

May 7, 1996

TO: DEFENSE TECHNICAL INFORMATION CENTER
ATTN: DTIC-FDAC
CAMERON STATION, BG 5
ALEXANDRA, VA 22304-6145

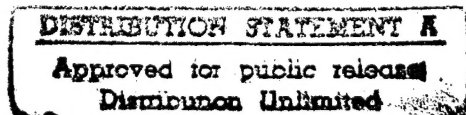
FROM: DR. ROGER L. SIMPSON
AEROSPACE AND OCEAN ENGINEERING
VIRGINIA POLYTECHNIC INSTITUTE AND
STATE UNIVERSITY
BLACKSBURG, VA 24061



SUBJECT: GRANT REPORT

ENCLOSED ARE TWO COPIES OF THE FOLLOWING TECHNICAL REPORT THAT
DESCRIBE WORK THAT WAS PERFORMED UNDER GRANT:

VPI-AOE-229 by Douglas J. Lewis and Roger L. Simpson
TITLE: AN EXPERIMENTAL INVESTIGATION OF HEAT TRANSFER IN
THREE-DIMENSIONAL AND SEPARATING TURBULENT BOUNDARY
LAYERS
GRANT: AFOSR-91-0310



19960520 005

DTIC QUALITY INSPECTED 1

REPORT DOCUMENTATION PAGE

Form Approved
OMB No. 0704-0188

Public reporting burden for this collection of information is estimated to average 1 hour per response, including the time for reviewing instructions, searching existing data sources, gathering and maintaining the data needed, and completing and reviewing the collection of information. Send comments regarding this burden estimate or any other aspect of this collection of information, including suggestions for reducing this burden, to Washington Headquarters Services, Directorate for Information Operations and Reports, 1215 Jefferson Davis Highway, Suite 1204, Arlington, VA 22202-4302, and to the Office of Management and Budget, Paperwork Reduction Project (0704-0188), Washington, DC 20503.

1. AGENCY USE ONLY (Leave blank) 2. REPORT DATE April 25, 1996 3. REPORT TYPE AND DATES COVERED Technical Report 6/91 - 12/95

4. TITLE AND SUBTITLE
An Experimental Investigation of Heat Transfer in Three-dimensional and Separating Turbulent Boundary Layers

5. FUNDING NUMBERS
AFOSR-91-0310

6. AUTHOR(S)
D.J. Lewis and R.L. Simpson

7. PERFORMING ORGANIZATION NAME(S) AND ADDRESS(ES)
Department of Aerospace and Ocean Engineering
Virginia Polytechnic Institute and State University
Blacksburg, VA 24061-0203

8. PERFORMING ORGANIZATION
REPORT NUMBER
VPI - AOE - 229

9. SPONSORING/MONITORING AGENCY NAME(S) AND ADDRESS(ES)
AFOSR/PA
110 Duncan Avenue, Suite B115
Bolling AFB, DC 20332-0001

10. SPONSORING/MONITORING
AGENCY REPORT NUMBER

11. SUPPLEMENTARY NOTES

12a. DISTRIBUTION/AVAILABILITY STATEMENT
Unlimited

12b. DISTRIBUTION CODE

13. ABSTRACT (Maximum 200 words)

The turbulence structure of convective heat transfer was studied experimentally in complex three-dimensional and separating turbulent boundary layers. Three test cases whose fluid dynamics have been well documented were examined. In case 1, time- and spatially-resolved surface heat transfer was measured in the nose region of a wing-body junction formed by a wing and a flat plate. Both the wing and the endwall were heated and held at a constant uniform temperature 20 °C above ambient temperature. Heat flux rates were increased up to a factor of 3 over the heat flux rates in the approach boundary layer. The rms of the heat flux fluctuations were as high as 25% of the mean heat flux in the vortex-dominated nose region. Away from the wing, upstream of the time-averaged vortex center, augmentation in the heat flux is due to increased turbulent mixing caused by large-scale unsteadiness of the vortex. Adjacent to the wing the augmentation in heat flux is due to a change in the mean velocity field.

In case 2, simultaneous surface heat flux and temperature profiles were measured at 8 locations in the spatially-developing pressure-driven three-dimensional turbulent boundary layer upstream of a wing-body junction. Mean heat transfer was decreased 10% by three-dimensionality. The turbulent Prandtl number in the near-wall region of logarithmic temperature variation was approximately 0.9 at all measurement locations in the three-dimensional boundary layer. Profiles of the skewness factor of temperature fluctuations and conditionally-averaged temperature signals during a sweep/ejection event suggest that the strength of ejections of hot fluid from the near-wall region are decreased by three-dimensionality. Time-delayed correlations of the surface heat flux and temperature signals over a range of y locations reveal a linear turbulent wavefront whose inclination angle increases with three-dimensionality.

In case 3, simultaneous surface heat flux and temperature profiles were measured at 14 stream-wise locations in a mean two-dimensional adverse-pressure-gradient separating turbulent boundary layer on a smooth, flat, uniform-temperature plate. Mean surface heat transfer near the location of time mean-detachment attains a minimum value which is 30 percent below attached-boundary-layer levels. Approaching separation, the turbulent Prandtl number decreases and the location of maximum temperature fluctuations occurs much closer to the wall than the location of maximum turbulent normal and shear stresses. The temperature profile law-of-the-wall based on skin friction fails. A length scale $y_{0,St}^{1/2}/v$ was found to correlate turbulent heat transfer in the near-wall region. A temperature defect-law is presented for the outer region.

14. SUBJECT TERMS

Turbulent Boundary Layers
Separation
Heat Transfer

Convection

Three-dimensional Flow

15. NUMBER OF PAGES
492

16. PRICE CODE

17. SECURITY CLASSIFICATION
OF REPORT

Unclassified

18. SECURITY CLASSIFICATION
OF THIS PAGE

Unclassified

19. SECURITY CLASSIFICATION
OF ABSTRACT

Unclassified

20. LIMITATION OF ABSTRACT

UL —

An Experimental Investigation of Heat Transfer in Three-Dimensional and Separating Turbulent Boundary Layers

by

Douglas J. Lewis and Roger L. Simpson

(ABSTRACT)

The turbulence structure of convective heat transfer was studied experimentally in complex three-dimensional and separating turbulent boundary layers. Three test cases whose fluid dynamics have been well documented were examined. In case 1, time- and spatially-resolved surface heat transfer was measured in the nose region of a wing-body junction formed by a wing and a flat plate. Both the wing and the endwall were heated and held at a constant uniform temperature 20°C above ambient temperature. Heat flux rates were increased up to a factor of 3 over the heat flux rates in the approach boundary layer. The rms of the heat flux fluctuations were as high as 25% of the mean heat flux in the vortex-dominated nose region. Away from the wing, upstream of the time-averaged vortex center, augmentation in the heat flux is due to increased turbulent mixing caused by large-scale unsteadiness of the vortex. Adjacent to the wing the augmentation in heat flux is due to a change in the mean velocity field.

In case 2, simultaneous surface heat flux and temperature profiles were measured at 8 locations in the spatially-developing pressure-driven three-dimensional turbulent boundary layer upstream of a wing-body junction. Mean heat transfer was decreased 10% by three-dimensionality. The turbulent Prandtl number in the near-wall region of logarithmic temperature variation was approximately 0.9 at all measurement locations in the three-dimensional boundary layer. Profiles of the skewness factor of temperature fluctuations and conditionally-averaged temperature signals during a sweep/ejection event suggest that the strength of ejections of hot fluid from the near-wall region are decreased by three-dimensionality. Time-delayed correlations of the surface heat flux and temperature signals over a range of y locations reveal a linear turbulent wavefront whose inclination angle increases with three-dimensionality.

In case 3, simultaneous surface heat flux and temperature profiles were measured at 14 stream-wise locations in a mean two-dimensional adverse-pressure-gradient separating turbulent boundary layer on a smooth, flat, uniform-temperature plate. Mean surface heat transfer near the location of time mean-detachment attains a minimum value which is 30 percent below attached-boundary-layer levels. Approaching separation, the turbulent Prandtl number decreases and the location of maximum temperature fluctuations occurs much closer to the wall than the location of maximum turbulent normal and shear stresses. The temperature profile law-of-the-wall based on skin friction fails. A length scale $yU_{\infty}St^{1/2}/\nu$ was found to correlate turbulent heat transfer in the near-wall region. A temperature defect-law is presented for the outer region.

Tables of Contents

Abstract	ii
Acknowledgements	iv
List of Tables	x
List of Figures	xiii
Nomenclature	xxxvi
1 Introduction	1
1.1 Literature Review	6
1.1.1 Heat Transfer in a Turbulent Wing/Body Junction Vortex System	6
1.1.2 Heat Transfer in Three-Dimensional Turbulent Boundary Layers	9
1.1.3 Heat Transfer in Two-Dimensional Separating Turbulent Boundary Layers	16
1.2 Objectives and Approach	23
1.2.1 Wing/Body Junction Vortex Flow	23
1.2.2 Three-Dimensional Turbulent Boundary Layer Flow	25
1.2.3 Two-Dimensional Separating Turbulent Boundary Layer Flow	26
2 Experimental Apparatus and Technique	28
2.1 Wind Tunnel	28
2.1.1 Wing/Body Junction Vortex Flow Test Section	28
2.1.2 3-D TBL Flow Test Section	30
2.1.3 2-D Separating TBL Flow Test Section	31
2.2 Appendage Shapes and Mounting	32
Tables of Contents	v

2.3	Sensors and Equipment	33
2.3.1	Heat Flux Microsensor	33
2.3.2	Schmidt-Boelter Gage	34
2.3.3	Thermocouple Temperature Sensor	35
2.3.4	Cold-Wire Resistance Thermometer	35
2.3.5	Data Acquisition	37
2.4	Experimental Technique	37
2.4.1	Wing/Body Junction Flow	38
2.4.2	Three-Dimensional Turbulent Bondary Layer Flow	40
2.4.3	Two-Dimensional Separating Turbulent Boundary Layer Flow	43
2.5	Signal Processing	45
2.5.1	Post Processing of Time-Series Data	45
2.5.2	Burst-Detection Algorithms	47
2.5.3	Processing of Spectral Data	49
2.6	Uncertainty Analysis	50
3	Flow Documentation	55
3.1	Wing/Body Junction Vortex Flow	55
3.2	Three-Dimensional Turbulent Bondary Layer Flow	56
3.3	Two-Dimensional Separating Turbulent Boundary Layer Flow	59
3.4	Heat Flux Surface Validation	63
4	Results and Discussion for Wing/Body Junction Vortex Flow	65
4.1	Mean Surface Heat Flux	65
4.2	Statistical Description of Surface Heat Flux	67
4.2.1.	Surface Heat Flux Fluctuations	67
4.2.2.	Probability Density Functions, Skewness, and Flatness Factors	67
4.3	Power Spectra of Surface Heat Flux Fluctuations	69
4.4	Discussion of Results	71

4.5	Correlation Between Mean Surface Heat Flux and Turbulence	72
5	Results and Discussion for 3-D TBL Flow	75
5.1	Mean Results	75
5.1.1	Temperature Profiles	75
5.1.2	Surface Heat Transfer	78
5.1.3	Enthalpy Thickness Vector Correlation	79
5.1.4	Effects of Mean Streamwise Pressure Gradient	82
5.2	Statistical Results	84
5.3	Spectral Results	87
5.3.1	Surface Heat Flux Power Spectra	87
5.3.2	Temperature Power Spectra	88
5.3.3	Comparison of u- and t- Power Spectra	90
5.4	Correlation Between Temperature and Velocity Fluctuations	93
5.5	Coherency and Coherence Length Scale	96
6	Examination of Coherent Structures in 3-D TBL Flow	99
6.1	Mean Sweep/Ejection Frequency	99
6.2	Conditional Averaging Analysis	100
6.3	Time-Averaged Wave-Front of Large-Scale Structures	102
6.4	Discussion of Heat Transfer Structure in Three-Dimensional Turbulent Boundary Layers	105
7	Results and Discussion for 2-D Separating TBL Flow	107
7.1	Surface Heat Flux	107
7.2	Mean Temperature Profiles	113
7.2.1	Upstream of Detachment	113
7.2.2	Downstream of Detachment	119

7.3	Temperature Fluctuation Profiles	120
7.3.1	Upstream of Detachment	120
7.3.2	Downstream of Detachment	121
7.4	Higher Order Statistics	123
7.4.1	Upstream of Detachment	123
7.4.2	Downstream of Detachment	124
7.5	Estimation of Normal Velocity-Temperature Correlation	125
7.6	Power Spectra	129
7.7	Characteristic Frequencies from Power Spectra	131
7.8	Spectral Coherency Between Surface Heat Flux and Temperature	133
8	Conclusions	135
8.1	Turbulent Wing/Body Junction Vortex Heat Transfer	135
8.2	Three-Dimensional Turbulent Boundary Layer Heat Transfer	136
8.3	Two-Dimensional Separating Turbulent Boundary Layer Heat Transfer	138
	References	141
	Tables	156
	Figures	182
	Appendix A. Calibrations	389
A.1	Convection Heat Flux Calibrations	389
A.1.1	Cylinder Stagnation Point Calibration	389
A.1.2	Jet Stagnation Point Calibration	391
A.2	Temperature Calibration	393
A.2.1	Static Temperature Calibration	393
A.2.2	Dynamic Temperature Calibration	394
	Tables of Contents	viii

Appendix B. Corrections to Heat Flux Power Spectrum	414
B.1 Correction Due to Background Noise	414
B.2 Correction Due to Finite Sensor Size	415
 Appendix C. Correction of Ha's Data	 428
C.1 Time-Averaged Turbulence Structure Wavefronts	428
C.2 Convection Velocity	430
C.2.1 Spectral Variation of Convection Velocity	430
C.2.2 Convection Velocity from Time-Delayed Autocorrelation	432
 Vita	 453

List of Tables

Table 2.1.	Characteristic dimensions of the wing models and results from oil flow visualizations.	157
Table 2.2.	Locations of surface heat flux measurement in the wing/body junction test case for the modified NACA 0020 model. Mean heat flux was measured at all measurement locations. Time-resolved surface heat flux was measured only in line #1. Distances are normalized by the maximum thickness of the wing.	158
Table 2.3.	Locations of surface heat flux measurement in the wing/body junction test case for the streamlined cylinder model. Distances are normalized by the maximum thickness of the wing.	160
Table 2.4.	Locations of surface heat flux measurement in the wing/body junction test case for the NACA 0015 model. Distances are normalized by the maximum thickness of the wing.	161
Table 2.5.	Positions of measurement stations for 3-D TBL test case in wind-tunnel coordinates.	162
Table 2.6.	Flow characteristics at measurement stations in 3-D TBL test case. (from Ölçmen and Simpson, 1994)	163
Table 2.7.	Locations of surface heat flux and temperature profile measurement for the 2-D separated TBL test case.	164
Table 2.8.	95% Confidence intervals.	165
Table 2.9.	Normalized 95% confidence intervals for spectral estimates of 3-D boundary layer flow.	166

Table 2.10.	Normalized 95% confidence intervals for spectral estimates of 2-D separating boundary layer flow.	167
Table 3.1.	Boundary layer characteristics in the 2-D separating TBL test case measured 163.2 cm downstream of the test section entrance.	168
Table 3.2.	Boundary layer characteristics in the 2-D separating TBL test case measured 301 cm downstream of the test section entrance.	169
Table 3.3.	Boundary layer characteristics in the 2-D separating TBL test case measured 352.4 cm downstream of the test section entrance.	170
Table 3.4.	Boundary layer characteristics in the 2-D separating TBL test case measured 397.2 cm downstream of the test section entrance.	171
Table 4.1.	Location and value of maximum and minimum St , St_{rms} , skewness, and flatness.	172
Table 5.1	Heat transfer parameters at each station in three-dimensional flow. β_H is relative to tunnel coordinate system.	173
Table 6.1	Bursting frequencies from first moment of corrected surface-heat-transfer spectra.	174
Table 6.2	Values of parameters k and T used in VITA "burst" detection algorithm.	175
Table 6.3	Angle of inclination of time-averaged wavefronts constructed from time-delayed correlations.	176
Table 7.1.	Values of mean, rms, skewness, and flatness of surface heat flux in two-dimensional separating turbulent boundary layer.	177
Table 7.2.	Parameters of the temperature profile development in two-dimensional separating turbulent boundary layer.	178
Table 7.3	Backflow velocity and temperature profile parameters.	179

Table 7.4.	Average value of turbulent Prandtl number in the log region computed from the slope of T^+ vs y^+ upstream of <i>intermittent transitory detachment</i> .	180
Table 7.5.	Streamwise variation of temperature scale and length scale used in empirical temperature defect law, Eq. (7.23).	181
Table A.1.	Sensitivities of heat flux gages.	399
Table B.1.	Values of parameter "A" used in Eq. (B.4). Taken from Corcos (1963).	418
Table B.2.	Values of parameter "B" used in Eq. (B.5). Taken from Corcos (1963).	419
Table B.3.	Attenuation of the frequency-spectral density by rectangular transducers of various aspect ratios.	420
Table C.1.	Angle of maximum coherency between upstream and downstream sensors of parallel sensor probe.	434

List of Figures

Fig. 1.1.	Sketch illustrating phenomena affecting convective heat transfer in a gas turbine engine.	183
Fig. 1.2.	Sketch of simplified wing/body junction vortex showing the horseshoe vortex and the tunnel coordinate system.	184
Fig. 1.3.	Sketch of typical velocity profile in a three-dimensional turbulent boundary layer and definitions of coordinate systems used in 3-D test case: TC denotes tunnel coordinate system; FS denotes local free-stream coordinate system; WC denotes local wall-stress coordinates.	185
Fig. 1.4.	Plan view of measurement locations for the 3-D TBL test case. The scale of the plot is in inches.	186
Fig. 1.5.	Time-mean velocity vectors in the plane of symmetry upstream of wing used for wing/body junction vortex flow. Oil-flow visualizations show separation occurs at $X/T = -0.47$ and a line of low shear at $X/T = -0.28$. Histograms of X-component velocity fluctuations at $X/T = -0.204$, $Y/T = 0.0046$ <i>inset</i> . Solid line shows region of bimodal X-component velocity fluctuations. (from Devenport and Simpson, 1989).	187
Fig. 1.6.	Surface oil flow visualization performed on the test wall around the 3:2 elliptic nosed NACA 0020 tailed airfoil (from Devenport and Simpson, 1990 a). The line farthest upstream is the line of separation. The line nearer the nose of the wing is the line of low shear.	188
Fig. 1.7.	Distribution of coherent vortical structures through a two-dimensional, turbulent boundary layer (from Robinson, 1991).	189

Fig. 1.8.	Generation of ejections and sweeps in a 2-D turbulent boundary layer by: (a) an arch-like vortical structure in the outer region; (b) a single near-wall quasi-streamwise vortex (from Robinson, 1991).	190
Fig. 1.9.	Schematic showing proposed mechanisms which lead to reductions in Reynolds stresses in a three-dimensional turbulent boundary layer. (from Sendstad and Moin, 1992).	191
Fig. 1.10.	Typical profiles of variance, skewness and flatness factors of streamwise velocity fluctuations u in a two-dimensional turbulent boundary layer. (Durst et al., 1992)	192
Fig. 2.1.	Side view of the boundary layer tunnel test section configuration used for the wing/body junction test case and the wing shapes.	193
Fig. 2.2.	Heat Flux Microsensor mounted in cam system beneath the modified NACA 0020 wing in wind tunnel test section.	194
Fig. 2.3.	Sketch of cam system used to position the heat flux gage on the endwall upstream of the wing/body junction.	195
Fig. 2.4.	Side view of the boundary layer tunnel test section configuration used for the pressure-driven 3-D turbulent boundary layer test case. Heated surface begins 1.22 m downstream of test section entrance.	196
Fig. 2.5.	Side view of the boundary layer tunnel test section configuration used for the 2-D separating turbulent boundary layer test case. Heated surface begins 1.22 m downstream of test section entrance. Boundary layer control side-wall jets and suction are located at beginning of each 244-cm-long section. Major divisions on scales are 25.4 cm.	197
Fig. 2.6.	Isometric view of the Heat Flux Microsensor thermocouple junctions. (from Hager et al., 1991b)	198
Fig. 2.7.	Heat Flux Microsensor pattern. (from Hager et al, 1991a)	199

Fig. 2.8.	Locations where surface heat flux was measured in the wing/body junction test case for the modified NACA 0020 wing.	200
Fig. 3.1.	Streamwise velocity variation in the potential core of the test section used for the 3-D TBL test case. \square - current data; X - Devenport and Simpson, (1990 a).	201
Fig. 3.2.	Spanwise variation of surface shear stress coefficient measured 0.75 chord lengths upstream of the modified NACA 0020 model mounted in the test section used for the 3-D TBL test case. \circ - from Preston tube; Δ - from law-of-the-wall velocity profile.	202
Fig. 3.3.	Sketch of sawdust accumulated on test section floor near mean detachment location in 2-D separating TBL test case.	203
Fig. 3.4.	Streamwise velocity variation in the potential core of the test section used for the 2-D separating TBL test case. \circ current data; + Simpson et al. (1981 a).	204
Fig. 3.5.	Streamwise pressure gradient variation in the test section used for the 2-D separating TBL test case. \circ current data; + Simpson et al. (1981 a).	205
Fig. 3.6.	Mean velocity profile measured 163.2 cm downstream from the test section entrance in the 2-D separating TBL test section. \circ current data; + Simpson et al. (1981 a).	206
Fig. 3.7.	Fluctuating velocity profile measured 163.2 cm downstream from the test section entrance in the 2-D separating TBL test section. \circ current data; + Simpson et al. (1981 a).	207
Fig. 3.8.	Mean velocity profile measured at $x = 301.0$ cm in the 2-D separating TBL test section. \bullet current data; Δ Simpson et al. (1981 a).	208
Fig. 3.9.	Flucuating velocity profile measured at $x = 301.0$ cm in the 2-D separating TBL test section. \bullet current data; Δ Simpson et al. (1981 a)	209

Fig. 3.10.	Clauser plot of mean velocity profile at $x = 163.2$ cm in 2-D separating TBL test section.	210
Fig. 3.11.	Semi-logarithmic wall law plot of mean velocity profile at $x = 163.2$ cm in 2-D separating TBL test section.	211
Fig. 3.12.	Mean velocity profile in the 2-D separating TBL test case measured at $x = 352.4$ cm in the separated flow outer region above where near-wall flow reversal occurs. \circ Current data; \square Simpson et al. (1981 a).	212
Fig. 3.13.	Turbulence intensity profile in the 2-D separating TBL test case measured at $x = 352.4$ cm in the separated flow outer region above where near-wall flow reversal occurs. \circ Current data; \square Simpson et al. (1981 a).	213
Fig. 3.14.	Profile of skewness factor S_u of velocity fluctuations in the 2-D separating TBL test case measured at $x = 352.4$ cm in the separated flow outer region above where near-wall flow reversal occurs. \circ Current data; \square Simpson et al. (1981 a).	214
Fig. 3.15.	Profile of flatness factor F_u of velocity fluctuations in the 2-D separating TBL test case measured at $x = 352.4$ cm in the separated flow outer region above where near-wall flow reversal occurs. \circ Current data; \square Simpson et al. (1981 a).	215
Fig. 3.16.	Mean velocity profile in the 2-D separating TBL test case measured at $X = 397.2$ cm in the separated flow outer region above where near-wall flow reversal occurs. \circ Current data; \square Simpson et al. (1981 a).	216
Fig. 3.17.	Turbulence intensity profile in the 2-D separating TBL test case measured at $X = 397.2$ cm in the separated flow outer region above where near-wall flow reversal occurs. \circ Current data; \square Simpson et al. (1981 a).	217
Fig. 3.18.	Profile of skewness factor S_u of velocity fluctuations in the 2-D separating TBL test case measured at $X = 397.2$ cm in the separated flow outer region above where near-wall flow reversal occurs. \circ Current data; \square Simpson et al. (1981a).	218

Fig. 3.19.	Profile of flatness factor F_u of velocity fluctuations in the 2-D separating TBL test case measured at $X = 397.2$ cm in the separated flow outer region above where near-wall flow reversal occurs. \circ Current data; \square Simpson et al. (1981 a).	219
Fig. 3.20.	Streamwise variation of surface skin-friction coefficient in the 2-D separating TBL test case. \bullet Simpson et al (1981 a); Δ Preston tube; \square Ludwig-Tillman equation.	220
Fig. 3.21.	Streamwise variation in normalized wall temperature for the 3-D TBL test section.	221
Fig. 3.22.	Streamwise variation in Stanton number for the 3-D TBL test section with the wing removed.	222
Fig. 4.1.	Contours of constant time-mean Stanton number $\times 10^3$ for the modified NACA 0020 wing; — — — - line of separation, +++++ - line of low shear, \bullet - locations of heat flux measurements.	223
Fig. 4.2.	Time-mean Stanton number distribution along the stagnation streamline upstream of each model. Distances are normalized with x_{sep} which is different for each model.	224
Fig. 4.3.	Fluctuations in Stanton number measured along the stagnation streamline upstream of each model. Distances are normalized with x_{sep} which is different for each model.	225
Fig. 4.4.	Probability density functions of heat flux fluctuations measured on the stagnation streamline upstream of the modified NACA 0020 wing.	226
Fig. 4.5.	Probability density functions of heat flux fluctuations measured on the stagnation streamline upstream of the streamlined cylinder.	227
Fig. 4.6.	Probability density functions of heat flux fluctuations measured on the stagnation streamline upstream of the NACA 0015 wing.	228

Fig. 4.7.	Distributions of the skewness factor of the heat flux pdfs measured along the symmetry line upstream of each model.	229
Fig. 4.8.	Distributions of the flatness factor of the heat flux pdfs measured along the symmetry line upstream of each model.	230
Fig. 4.9.	Mean flux spectra measured along the line of symmetry upstream of the modified NACA 0020 wing.	231
Fig. 4.10.	Heat flux spectra measured along the line of symmetry upstream of the streamlined cylinder wing.	232
Fig. 4.11.	Heat flux spectra measured along the line of symmetry upstream of the NACA 0015 wing.	233
Fig. 4.12.	A comparison of heat flux spectra measured in the approach boundary layer ($x/x_{sep}=-1.465$), in the region between the separation line and the line of low shear ($x/x_{sep}=-0.659$), and near the junction ($x/x_{sep}=-0.189$) for the modified NACA 0020 wing.	234
Fig. 4.13.	Relation between surface heat flux and $k_{rms,max}$ in the region outside of the line of low shear for the modified NACA 0020 wing. Lines 1,4,6, and 7 are defined in Fig. 2.7.	235
Fig. 4.14.	St' correlation for surface heat flux in the region outside of the line of low shear for the modified NACA 0020 wing. Lines 1,4,6, and 7 are defined in Fig. 2.7. Solid line is Eq. (4.4). Dashed lines are $\pm 15\%$ error bands.	236
Figure 5.1.	Mean temperature profiles at each station in the 3-D turbulent boundary layer.	237
Figure 5.2.	Near-wall variation of eddy viscosity in wall-stress direction at each station in the 3-D turbulent boundary layer. Straight line denotes $\epsilon_m/\nu = 0.41 y^+$.	238
Figure 5.3.	Mean temperature profiles at each station in the three-dimensional turbulent boundary layer calculated from the eddy viscosity.	239

Figure 5.4.	Stanton number distribution in 3-D boundary layer. ○ - measured St; □ - calculated from enthalpy thickness vector magnitude and Eq. (5.14); — Eq. (3.11); --- Eq. (5.16).	240
Figure 5.5.	Stanton number determined from mean temperature profile at station #0.	241
Figure 5.6.	Correlation between surface heat transfer and magnitude of enthalpy thickness vector in 3-D Turbulent boundary layer.	242
Figure 5.7.	Direction of enthalpy thickness vector compared to free-stream and wall-shear-stress directions relative to tunnel coordinate system.	243
Figure 5.8a.	Temperature fluctuation profiles at each station in the 3D TBL. Y-axis scale applies to the profile at station 0. Remaining profiles are offset successively by 0.06.	244
Figure 5.8b.	Temperature fluctuation profiles at each station in the 3D TBL. Y-axis scale applies to the profile at station 4. Remaining profiles are offset successively by 0.06.	245
Figure 5.9.	Profiles of the skewness factor of temperature fluctuations at stations #0 - #6 in the 3D turbulent boundary layer.	246
Figure 5.10.	Profiles of the flatness factor of temperature fluctuations at stations #0 - #6 in the 3D turbulent boundary layer.	247
Figure 5.11.	Plot of flatness factor as a function of skewness factor of temperature fluctuations at stations 0 - 6 in the 3D TBL. Solid line is parabola fit to data.	248
Figure 5.12.	Power spectra of surface heat flux fluctuations measured at stations 0 - 6 in the 3D TBL.	249
Figure 5.13a.	Temperature spectra measured in the wall-region of station 0 normalized with outer scaling parameters.	250
Figure 5.13b.	Temperature spectra measured in the wall-region of station 1 normalized with outer scaling parameters.	251

Figure 5.13c. Temperature spectra measured in the wall-region of station 2 normalized with outer scaling parameters.	252
Figure 5.13d. Temperature spectra measured in the wall-region of station 3 normalized with outer scaling parameters.	253
Figure 5.13e. Temperature spectra measured in the wall-region of station 4 normalized with outer scaling parameters.	254
Figure 5.13f. Temperature spectra measured in the wall-region of station 5 normalized with outer scaling parameters.	255
Figure 5.13g. Temperature spectra measured in the wall-region of station 6 normalized with outer scaling parameters.	256
Figure 5.14a. Temperature spectra measured in the wall-region of station 0 normalized with inner scaling parameters.	257
Figure 5.14b. Temperature spectra measured in the wall-region of station 1 normalized with inner scaling parameters.	258
Figure 5.14c. Temperature spectra measured in the wall-region of station 2 normalized with inner scaling parameters.	259
Figure 5.14d. Temperature spectra measured in the wall-region of station 3 normalized with inner scaling parameters.	260
Figure 5.14e. Temperature spectra measured in the wall-region of station 4 normalized with inner scaling parameters.	261
Figure 5.14f. Temperature spectra measured in the wall-region of station 5 normalized with inner scaling parameters.	262
Figure 5.14g. Temperature spectra measured in the wall-region of station 6 normalized with inner scaling parameters.	263
Figure 5.15a. Comparison of temperature spectra at station 0 normalized by t' in (a) the near-wall region; (b) the log-region; and (c) the wake region.	264
Figure 5.15b. Comparison of temperature spectra at station 1 normalized by t' in (a) the near-wall region; (b) the log-region; and (c) the wake region.	265

Figure 5.15c. Comparison of temperature spectra at station 2 normalized by t' in (a) the near-wall region; (b) the log-region; and (c) the wake region.	266
Figure 5.15d. Comparison of temperature spectra at station 3 normalized by t' in (a) the near-wall region; (b) the log-region; and (c) the wake region.	267
Figure 5.15e. Comparison of temperature spectra at station 4 normalized by t' in (a) the near-wall region; (b) the log-region; and (c) the wake region.	268
Figure 5.15f. Comparison of temperature spectra at station 5 normalized by t' in (a) the near-wall region; (b) the log-region; and (c) the wake region.	269
Figure 5.15g. Comparison of temperature spectra at station 6 normalized by t' in (a) the near-wall region; (b) the log-region; and (c) the wake region.	270
Figure 5.16a. Comparison of first moment of temperature and u-spectra measured at several positions across the boundary layer at station 0.	271
Figure 5.16b. Comparison of first moment of temperature and u-spectra measured at several positions across the boundary layer at station 1.	272
Figure 5.16c. Comparison of first moment of temperature and u-spectra measured at several positions across the boundary layer at station 2.	273
Figure 5.16d. Comparison of first moment of temperature and u-spectra measured at several positions across the boundary layer at station 3.	274
Figure 5.16e. Comparison of first moment of temperature and u-spectra measured at several positions across the boundary layer at station 4.	275
Figure 5.16f. Comparison of first moment of temperature and u-spectra measured at several positions across the boundary layer at station 5.	276

Figure 5.16g.	Comparison of first moment of temperature and u-spectra measured at several positions across the boundary layer at station 6.	277
Figure 5.17.	Distributions of B parameter across the boundary layer at stations 0 - 6 in the 3D TBL. (a) inner region; (b) outer region.	278
Figure 5.18.	Distributions of B_Q parameter across the boundary layer at stations 0 - 6 in the 3D TBL. (a) inner region; (b) outer region.	279
Figure 5.19.	Distributions of B_v parameter across the boundary layer at stations 0 - 6 in the 3D TBL. (a) inner region; (b) outer region.	280
Figure 5.20.	Spectral variation of coherency between surface heat flux and temperature at several points across the boundary layer measured at station 0. (a) near-all region; (b) outer region.	281
Figure 5.21.	Spectral variation of coherency between surface heat flux and temperature at several points across the boundary layer measured at station 6. (a) near-wall region; (b) outer region.	282
Figure 5.22a.	Spectral variation of coherence length scale at all stations in 3D turbulent boundary layer.	283
Figure 5.22b.	Spectral variation of coherence length scale from at all stations in 3D turbulent boundary layer from Ha and Simpson (1993). Y/δ vaues on legend apply to the bottom sensor of the hot-wire rake.	284
Figure 5.23a.	Spatial variation of coherency in the y direction between surface heat flux and temperature for selected frequencies at station 0. Solid line represents exponential decay model with $k_0 = 1.26$.	285
Figure 5.23b.	Spatial variation of coherency in the y direction between surface heat flux and temperature for selected frequencies at station 1. Solid line represents exponential decay model with $k_0 = 1.28$.	286

Figure 5.23c.	Spatial variation of coherency in the y direction between surface heat flux and temperature for selected frequencies at station 2. Solid line represents exponential decay model with $k_0 = 1.33$.	287
Figure 5.23d.	Spatial variation of coherency in the y direction between surface heat flux and temperature for selected frequencies at station 3. Solid line represents exponential decay model with $k_0 = 1.33$.	288
Figure 5.23e.	Spatial variation of coherency in the y direction between surface heat flux and temperature for selected frequencies at station 4. Solid line represents exponential decay model with $k_0 = 1.33$.	289
Figure 5.23f.	Spatial variation of coherency in the y direction between surface heat flux and temperature for selected frequencies at station 5. Solid line represents exponential decay model with $k_0 = 1.33$.	290
Figure 5.23g.	Spatial variation of coherency in the y direction between surface heat flux and temperature for selected frequencies at station 6. Solid line represents exponential decay model with $k_0 = 1.33$.	291
Figure 6.1a.	Conditionally averaged temperature time records during a sweep/ejection event at several y locations across the boundary layer at station 0.	292
Figure 6.1b.	Conditionally averaged temperature time records during a sweep/ejection event at several y locations across the boundary layer at station 1.	293
Figure 6.1c.	Conditionally averaged temperature time records during a sweep/ejection event at several y locations across the boundary layer at station 2.	294
Figure 6.1d.	Conditionally averaged temperature time records during a sweep/ejection event at several y locations across the boundary layer at station 3.	295

Figure 6.1e.	Conditionally averaged temperature time records during a sweep/ejection event at several y locations across the boundary layer at station 4.	296
Figure 6.1f.	Conditionally averaged temperature time records during a sweep/ejection event at several y locations across the boundary layer at station 5.	297
Figure 6.1g.	Conditionally averaged temperature time records during a sweep/ejection event at several y locations across the boundary layer at station 6.	298
Figure 6.2a.	Long-time average time-delayed correlation coefficient between surface heat flux and temperature at several y locations across the boundary layer at station 0.	299
Figure 6.2b.	Long-time average time-delayed correlation coefficient between surface heat flux and temperature at several y locations across the boundary layer at station 1.	300
Figure 6.2c.	Long-time average time-delayed correlation coefficient between surface heat flux and temperature at several y locations across the boundary layer at station 2.	301
Figure 6.2d.	Long-time average time-delayed correlation coefficient between surface heat flux and temperature at several y locations across the boundary layer at station 3.	302
Figure 6.2e.	Long-time average time-delayed correlation coefficient between surface heat flux and temperature at several y locations across the boundary layer at station 4.	303
Figure 6.2f.	Long-time average time-delayed correlation coefficient between surface heat flux and temperature at several y locations across the boundary layer at station 5.	304
Figure 6.2g.	Long-time average time-delayed correlation coefficient between surface heat flux and temperature at several y locations across the boundary layer at station 6.	305

Figure 6.3.	Time-averaged wavefronts in x-y plane constructed from time-delayed correlations of surface heat flux and temperature at station (a) 0; (b) 1; (c) 2; (d) 3; (e) 4; (f) 5; and (g) 6.	306
Fig. 7.1.	Mean heat transfer coefficient in two-dimensional separating turbulent boundary layer. Solid line is from integral method of Kays and Crawford (1980). ID, location of <i>incipient detachment</i> ; ITD, location of <i>intermittent transitory detachment</i> ; TD, location of <i>transitory detachment</i> .	307
Fig. 7.2.	Mean and rms Stanton numbers in the two-dimensional separating turbulent boundary layer. Solid line is from integral method of Kays and Crawford (1980). ID, location of <i>incipient detachment</i> ; ITD, location of <i>intermittent transitory detachment</i> ; TD, location of <i>transitory detachment</i> .	308
Fig. 7.3.	Skewness and flatness factors of surface heat flux fluctuations in two-dimensional separating turbulent boundary layer. ID, location of <i>incipient detachment</i> ; ITD, location of <i>intermittent transitory detachment</i> ; TD, location of <i>transitory detachment</i> .	309
Fig. 7.4.	Streamwise variation of length scale Δ_l in two-dimensional separating turbulent boundary layer. TD is location of <i>transitory detachment</i> .	310
Fig. 7.5.	Streamwise variation of enthalpy thickness upstream of detachment in two-dimensional separating turbulent boundary layer. TD is location of <i>transitory detachment</i> .	311
Fig. 7.6	Comparison of streamwise variation of temperature profile shape factor with velocity profile shape factor in two-dimensional separating turbulent boundary layer. TD is location of <i>transitory detachment</i> .	312
Fig. 7.7.	Stanton number versus enthalpy thickness Reynolds number upstream of detachment. Solid line is correlation of Kays and Crawford (1980).	313

Fig. 7.8.	Profiles of the integrand of the enthalpy thickness.	314
Fig. 7.9.	Streamwise variation of the product of enthalpy thickness and free-stream velocity upstream of detachment. Solid line is polynomial least-squares curve fit.	315
Fig. 7.10.	Comparison of directly measured Stanton numbers with Stanton numbers computed from integral energy equation, Eq. (7.5). Solid line is from integral method of Kays and Crawford (1980). ID, location of <i>incipient detachment</i> ; ITD, location of <i>intermittent transitory detachment</i> ; TD, location of <i>transitory detachment</i> .	316
Fig. 7.11.	Backflow Stanton number versus backflow enthalpy thickness Reynolds number downstream of detachment. Solid line is laminar correlation. Dashed line is turbulent correlation, Eq. (7.4) (Kays and Crawford, 1980). \circ measured St_N ; Δ St_N from St' correlation (Maciejewski and Moffat, 1992).	317
Fig. 7.12.	Temperature profiles upstream of <i>incipient detachment</i> in conventional wall-law coordinates.	318
Fig. 7.13.	Temperature profiles in the region between <i>incipient detachment</i> and detachment in conventional wall-law coordinates.	319
Fig. 7.14.	Temperature profiles upstream of <i>incipient detachment</i> in wall-law coordinates proposed by Blackwell et al. (1972).	320
Fig. 7.15.	Temperature profiles in the region between <i>incipient detachment</i> and detachment in wall-law coordinates proposed by Blackwell et al. (1972).	321
Fig. 7.16.	Temperature profiles upstream of detachment in wall-law coordinates based on the near-wall value of turbulent kinetic energy. See Eq. (7.20).	322
Fig. 7.17.	Temperature defect profiles upstream of detachment in conventional temperature-defect coordinates. (See Eq. (7.21)). (a) semi-logarithmic axis; (b) linear axis.	323

Fig. 7.18.	Streamwise variation of temperature scale $T_r/(T_w - T_\infty) = St/(C_p/2)^{1/2}$ used in conventional defect law upstream of detachment.	324
Fig. 7.19.	Streamwise variation of length scale Δ_3 upstream of detachment.	325
Fig. 7.20.	Temperature defect profiles upstream of detachment in modified temperature-defect coordinates. (a) semi-logarithmic axis; (b) linear axis.	326
Fig. 7.21.	Temperature defect profiles upstream of detachment in Perry-Schofield coordinates. (See Eq. (7.23)). (a) semi-logarithmic axis; (b) linear axis.	327
Fig. 7.22.	Streamwise variation of temperature scale Θ_s used in Eq. (5.23) upstream of detachment.	328
Fig. 7.23.	Temperature profiles downstream of detachment plotted in outer variables.	329
Fig. 7.24.	Temperature profiles downstream of detachment in wall-law coordinates proposed by Blackwell et al. (1972). Solid line is molecular sublayer equation $T^* = Pr y^*$.	330
Fig. 7.25.	Temperature profiles downstream of detachment in "law-of-the-backflow" coordinates. See Eq. (7.24).	331
Fig. 7.26.	Temperature fluctuation profiles upstream of <i>incipient</i> detachment in outer-region coordinate.	332
Fig. 7.27.	Temperature fluctuation profiles upstream of <i>incipient</i> detachment in conventional wall-law coordinate.	333
Fig. 7.28.	Temperature fluctuation profiles upstream of <i>incipient</i> detachment in wall-law coordinate proposed by Blackwell et al. (1972).	334
Fig. 7.29a.	Temperature fluctuation profiles downstream of detachment in outer-region coordinates plotted on logarithmic x-axis.	335

Fig. 7.29b.	Temperature fluctuation profiles downstream of detachment in outer-region coordinates plotted on linear x-axis.	336
Fig. 7.30.	Temperature fluctuation profiles downstream of detachment plotted in wall-law coordinate proposed by Blackwell et al. (1972).	337
Fig. 7.31.	Profiles of the skewness factor of temperature fluctuations upstream of <i>incipient</i> detachment plotted in outer-region coordinates.	338
Fig. 7.32.	Profiles of the flatness factor of temperature fluctuations upstream of <i>incipient</i> detachment plotted in outer-region coordinates.	339
Fig. 7.33.	Profiles of skewness factor of streamwise velocity fluctuations S_u (a) upstream and (b) downstream from detachment. (from Simpson et al., 1981 b)	340
Fig. 7.34.	Profiles of flatness factor of streamwise velocity fluctuations F_u (a) upstream and (b) downstream from detachment. (from Simpson et al., 1981 b)	341
Fig. 7.35.	Profiles of the skewness factor of temperature fluctuations upstream of <i>incipient</i> detachment plotted in conventional wall-law coordinates.	342
Fig. 7.36.	Profiles of the flatness factor of temperature fluctuations upstream of <i>incipient</i> detachment plotted in conventional wall-law coordinates.	343
Fig. 7.37.	Profiles of the skewness factor of temperature fluctuations upstream of <i>incipient</i> detachment plotted in wall-law coordinates proposed by Blackwell et al. (1972).	344
Fig. 7.38.	Profiles of the skewness factor of temperature fluctuations upstream of <i>incipient</i> detachment plotted in wall-law coordinates proposed by Blackwell et al. (1972).	345
Fig. 7.39.	Profiles of the skewness factor of temperature fluctuations downstream of detachment plotted in outer-region coordinates.	346

Fig. 7.40.	Profiles of the flatness factor of temperature fluctuations downstream of detachment plotted in outer-region coordinates.	347
Fig. 7.41.	Profiles of the skewness factor of temperature fluctuations downstream of detachment plotted in wall-law coordinates proposed by Blackwell et al. (1972).	348
Fig. 7.42.	Profiles of the flatness factor of temperature fluctuations downstream of detachment plotted in wall-law coordinates proposed by Blackwell et al. (1972).	349
Fig. 7.43.	Profiles of each term on the right-hand-side of Eq. (7.29) that contribute to $\overline{v\theta}/U_\infty$ at streamwise location $x = 285.4$ cm.	350
Fig. 7.44.	Profiles of each term on the right-hand-side of Eq. (7.29) that contribute to $\overline{v\theta}/U_\infty$ at streamwise location $x = 301.0$ cm.	351
Fig. 7.45.	Profiles of each term on the right-hand-side of Eq. (7.29) that contribute to $\overline{v\theta}/U_\infty$ at streamwise location $x = 341.63$ cm.	352
Fig. 7.46.	Profiles of $\overline{v\theta}/U_\infty$ upstream of <i>incipient detachment</i> computed from integrating the energy equation. (a) inner region; (b) outer region.	353
Fig. 7.47.	Profiles of $\overline{v\theta}/U_\infty$ in the region between <i>incipient detachment</i> and detachment computed from integrating the energy equation. (a) inner region; (b) outer region.	354
Fig. 7.48.	Profiles of total, turbulent, and molecular heat transfer at streamwise location $x = 285.43$ cm.	355
Fig. 7.49.	Profiles of total, turbulent, and molecular heat transfer at streamwise location $x = 341.63$ cm.	356
Fig. 7.50a,b.	Normalized t power spectral distribution far upstream of detachment, at $x = 285.4$ cm. (a) in the buffer region; (b) in the fully turbulent region; (c) in the outer region.	357

Fig. 7.50c.	Normalized t power spectral distribution far upstream of detachment, at $x = 285.4$ cm. (a) in the buffer region; (b) in the fully turbulent region; (c) in the outer region.	358
Fig. 7.51a,b.	Normalized t power spectral distribution just upstream of detachment, at $x = 341.6$ cm. (a) in the buffer region; (b) in the fully turbulent region; (c) in the outer region.	359
Fig. 7.51c.	Normalized t power spectral distribution measured just upstream of detachment, at $x = 341.6$ cm. (a) in the buffer region; (b) in the fully turbulent region; (c) in the outer region.	360
Fig. 7.52a,b.	Normalized t power spectral distribution downstream of detachment, $x = 407.03$ cm. (a) in the near-wall region of the backflow; (b) in the outer backflow; (c) in transitional region; (d) in the outer region.	361
Fig. 7.52c,d.	Normalized t power spectral distribution downstream of detachment, $x = 407.03$ cm. (a) in the near-wall region of the backflow; (b) in the outer backflow; (c) in transitional region; (d) in the outer region.	362
Fig. 7.53.	Normalized first moment of q_0'' and t power spectral distribution far upstream of detachment, at $x = 285.4$ cm. Y-axis applies to surface heat flux spectra. Temperature spectra are offset successively by 0.15.	363
Fig. 7.54.	Normalized first moment of q_0'' and t power spectral distribution just upstream of detachment, at $x = 341.6$ cm. Y-axis applies to surface heat flux spectra. Temperature spectra are offset successively by 0.15.	364
Fig. 7.55.	Normalized first moment of q_0'' and t power spectral distribution downstream of detachment, at $x = 407.0$ cm. Y-axis applies to surface heat flux spectra. Temperature spectra are offset successively by 0.15.	365
Fig. 7.56.	Streamwise distribution of characteristic frequency from spectra of surface heat flux fluctuations. (a) dimensional period; (b) characteristic period normalized with outer flow velocity and length scale.	366

Fig. 7.57a.	Profiles of characteristic frequency from spectra of temperature fluctuations at $x = 188.60$ cm.	367
Fig. 7.57b.	Profiles of characteristic frequency from spectra of temperature fluctuations at $x = 222.57$ cm.	368
Fig. 7.57c.	Profiles of characteristic frequency from spectra of temperature fluctuations at $x = 285.43$ cm.	369
Fig. 7.57d.	Profiles of characteristic frequency from spectra of temperature fluctuations at $x = 300.99$ cm.	370
Fig. 7.57e.	Profiles of characteristic frequency from spectra of temperature fluctuations at $x = 306.07$ cm.	371
Fig. 7.57f.	Profiles of characteristic frequency from spectra of temperature fluctuations at $x = 309.56$ cm.	372
Fig. 7.57g.	Profiles of characteristic frequency from spectra of temperature fluctuations at $x = 323.22$ cm.	373
Fig. 7.57h.	Profiles of characteristic frequency from spectra of temperature fluctuations at $x = 328.61$ cm.	374
Fig. 7.57i.	Profiles of characteristic frequency from spectra of temperature fluctuations at $x = 332.42$ cm.	375
Fig. 7.57j.	Profiles of characteristic frequency from spectra of temperature fluctuations at $x = 341.63$ cm.	376
Fig. 7.57k.	Profiles of characteristic frequency from spectra of temperature fluctuations at $x = 352.43$ cm.	377
Fig. 7.57l.	Profiles of characteristic frequency from spectra of temperature fluctuations at $x = 364.49$ cm.	378
Fig. 7.57m.	Profiles of characteristic frequency from spectra of temperature fluctuations at $x = 407.04$ cm.	379
Fig. 7.57n.	Profiles of characteristic frequency from spectra of temperature fluctuations at $x = 440.01$ cm.	380

Fig 7.58.	Characteristic frequency parameter $U_{\infty}/f_b\delta$ at (a) 285.50 cm., (b) 341.63 cm., and (c) 398.27 cm. Note the log-linear abscissa. (from Simpson et al., 1981 b)	381
Fig 7.58c.	Characteristic frequency parameter $U_{\infty}/f_b\delta$ at (a) 285.50 cm., (b) 341.63 cm., and (c) 398.27 cm. Note the log-linear abscissa. (from Simpson et al., 1981 b)	382
Fig. 7.59a.	Spectral variation of coherency between surface heat flux and temperature at several distances from the wall far upstream of detachment, at $x = 285.4$ cm.	383
Fig. 7.59b.	Spectral variation of coherency between surface heat flux and temperature at several distances from the wall just upstream of detachment, at $x = 341.6$ cm.	384
Fig. 7.59c.	Spectral variation of coherency between surface heat flux and temperature at several distances from the wall downstream of detachment, at $x = 407.0$ cm.	385
Fig. 7.60a.	Spectral variation of coherence length scale far upstream of detachment.	386
Fig. 7.60b.	Spectral variation of coherence length scale in the region between <i>insipient detachment</i> and detachment.	387
Fig. 7.60c.	Spectral variation of coherence length scale downstream of detachment.	388
Fig. A.1.	Sketch of test cylinder used for static convection calibration of Schmidt-Boelter gauge. (from Gundappa and Diller, 1985).	400
Fig. A.2.	Static convection calibration of Schmidt-Boelter gauge using cylinder apparatus.	401
Fig. A.3.	Sketch of the impinging-jet calibration apparatus. (from Hager et al., 1991c).	402
Fig. A.4.	Static convection calibration of Heat Flux Microsensor in impinging-jet apparatus.	403
Fig. A.5.	Static calibration of cold-wire temperature sensor.	404

Fig. A.6.	Static calibration of resistance temperature sensor on heat flux micorsensor.	405
Fig. A.7.	Sketch of passive dynamic compensation network.	406
Fig. A.8.	Compensation optimization scheme. (from Doebelin, 1990)	407
Fig. A.9.	Apparatus used for pulsed-laser dynamic calibration of cold-wire sensor.	408
Fig. A.10.	Dynamic calibration of 5- μ m dia. cold wire using pulsed-laser technique.	409
Fig. A.11.	Apparatus used for current-injection technique for dynamic calibration of cold-wire sensor.	410
Fig. A.12.	Response of cold-wire temperature probe to current injection of 300 Hz square wave. (a) uncompensated signal; (b) compensated signal.	411
Fig. A.13.	Response of cold-wire temperature probe to current injection of 2000 Hz square wave. (a) uncompensated signal; (b) compensated signal.	412
Fig. A.14.	Response of cold-wire temperature probe to current injection of 4000 Hz square wave. (a) uncompensated signal; (b) compensated signal.	413
Fig. B.1.	Corrections to surface heat flux fluctuation spectra at station #0 in 3-D TBL test case. \circ raw spectrum; Δ spectrum after white noise floor has been subtracted; \square spectrum after corrections for finite gage size.	422
Fig. B.2.	Corrections to first moment of surface heat flux fluctuation spectrum at station #0 in 3-D TBL test case..	423
Fig. B.3.	Values of parameter "A" which relates the frequency-spectral density to the longitudinal cross-spectral density through Eq. (B.4). \circ data from Corcos (1963); — curve fit to data, Eq. (A.6).	424

Fig. B.4.	Values of parameter "B" which relates the frequency-spectral density to the lateral cross-spectral density through Eq. (B.5). O data from Corcos (1963); — curve fit to data, Eq. (A.7).	425
Fig. B.5.	Attenuation of the frequency-spectral density due to finite surface area by a round and a square transducer. — Corcos (1963); ---- Integration of Eq. (A.1).	426
Fig. B.6.	Attenuation of the frequency-spectral density due to finite surface area by a rectangular transducer of aspect ratio L_z/L_x .	427
Fig. C.1.	Time-delayed correlation coefficients between u fluctuations measured by the sensor closest to the wall and u fluctuations measured by each sensor of hot-wire rake.	435
Fig. C.2.	Time-averaged wavefronts in x_{FS} -y plane constructed from time-delayed correlations of u-fluctuations of hot-wire rake.	436
Fig. C.3a.	Spectral variation of convective wave speed at station 0 normalized with outer scaling. $\beta = \beta_m$.	437
Fig. C.3b.	Spectral variation of convective wave speed at station 1 normalized with outer scaling. $\beta = \beta_m$.	438
Fig. C.3c.	Spectral variation of convective wave speed at station 2 normalized with outer scaling. $\beta = \beta_m$.	439
Fig. C.3d.	Spectral variation of convective wave speed at station 3 normalized with outer scaling. $\beta = \beta_m$.	440
Fig. C.3e.	Spectral variation of convective wave speed at station 4 normalized with outer scaling. $\beta = \beta_m$.	441
Fig. C.3f.	Spectral variation of convective wave speed at station 5 normalized with outer scaling. $\beta = \beta_m$.	442
Fig. C.3g.	Spectral variation of convective wave speed at station 6 normalized with outer scaling. $\beta = \beta_m$.	443

Fig. C.4a.	Spectral variation of convective wave speed at station 0 normalized with inner scaling. $\beta = \beta_m$.	444
Fig. C.4b.	Spectral variation of convective wave speed at station 1 normalized with inner scaling. $\beta = \beta_m$.	445
Fig. C.4c.	Spectral variation of convective wave speed at station 2 normalized with inner scaling. $\beta = \beta_m$.	446
Fig. C.4d.	Spectral variation of convective wave speed at station 3 normalized with inner scaling. $\beta = \beta_m$.	447
Fig. C.4e.	Spectral variation of convective wave speed at station 4 normalized with inner scaling. $\beta = \beta_m$.	448
Fig. C.4f.	Spectral variation of convective wave speed at station 5 normalized with inner scaling. $\beta = \beta_m$.	449
Fig. C.4g.	Spectral variation of convective wave speed at station 6 normalized with inner scaling. $\beta = \beta_m$.	450
Fig. C.5.	Profiles of convection velocity normalized with free-stream velocity measured by the parallel sensor probe aligned in (a) free-stream direction and (b) maximum-coherency direction.	451
Fig. C.6	Profiles of convection velocity normalized with friction velocity measured by the parallel sensor probe aligned in (a) free-stream direction and (b) maximum-coherency direction.	452

Nomenclature

A, B	hot-wire calibration constants
a_l	Townstends structural parameter
a_θ	see Eq. (5.26)
B	see Eq. (5.23)
B_{3D}	see Eq. (5.27)
B_Q	see Eq. (5.28)
B_v	see Eq. (5.29)
C	constant used in Eq. (7.22) = 0.132
C_D	drag coefficient
C_f	skin friction coefficient
$C_{xy}(f)$	imaginary component of complex $G_{xy}(f)$
C_p	pressure coefficient
C_p	specific heat
E	output voltage of sensor
f	frequency, Hz
$f()$	a function of an independent variable
f_b	characteristic frequency
$F_{()}$	flatness factor of variable (). See Eq. (2.5).

$G_{xx}(f)$	auto spectral density function of $x(t)$
$G_{xy}(f)$	cross spectral density functions of $x(t)$ and $y(t)$
h	convection film coefficient = $\overline{q_0''}/(T_w - T_\infty)$, W/(m ² K)
H	shape factor = δ^*/θ
H_T	temperature profile shape factor = Δ_1/Δ_2
\mathbf{H}	enthalpy thickness vector, see Eq. (5.15)
i	enthalpy, J/kg
i_s	stagnation enthalpy, J/kg
$i_{s,0}$	stagnation enthalpy at the wall, J/kg
K	acceleration parameter, Eq. (5.17)
k	turbulent kinetic energy, $k = (u'^2 + v'^2 + w'^2)/2$; also wave number = $2\pi f/U$; also threshold level in VITA burst-detection algorithm
k'_{\max}	maximum value of square root of turbulent kinetic energy in boundary layer
L_γ	coherence length scale
L	threshold level in modified u-level burst-detection algorithm
N	distance from the wall to location of maximum negative velocity in backflow region; also sample size
N_c	number samples in calibration
n_d	number of ensemble averages
p	mean static pressure
p_0	mean stagnation pressure

Pr	Prandtl number
Pr_t	turbulent Prandtl number
$(Pr_t)_l$	average value of Pr_t in log-region
Q	magnitude of velocity parallel to the surface, $(U^2 + W^2)^{1/2}$
$Q_{xy}(f)$	real component of complex $G_{xy}(f)$
q	square root of twice the turbulent kinetic energy, $q = (\overline{u^2} + \overline{v^2} + \overline{w^2})^{1/2}$
$\overline{q''}$	time-mean heat flux, W/m^2
q''	instantaneous heat flux, W/m^2
$(q'')'$	rms value of q'' , W/m^2
$\overline{q_0''}$	time-mean wall heat flux, W/m^2
q_0''	instantaneous wall heat flux, W/m^2
$(q_0'')'$	rms value of wall heat flux, W/m^2
$R_{xy}(\tau)$	time-averaged correlation coefficient between signals $x(t)$ and $y(t)$ at time shift τ .
$Re_{()}$	Reynolds number based on ()
S	heat flux gage sensitivity, $S = E / \overline{q_0''}$, $V \cdot m^2/W$
s	distance measured along path connecting measurement locations in 3-D TBL flow.
$S_{()}$	skewness factor of variable (). See Eq. (2.4).
St	Stanton number = $h / (\rho C_p U_{ref})$ for wing/body junction; = $h / (\rho C_p U_\infty)$ otherwise
St_{rms}	rms of fluctuation Stanton number = $(q'')' / (\rho C_p \Delta T U)$

St'	Stanton Prime correlation = $h/(\rho C_p \Delta T u'_{\max})$
T	local time-averaged temperature; also averaging time in VITA burst-detection algorithm
T_f	film temperature = $(T_w + T_\infty)/2$
T_g	gage surface temperature
T_∞	temperature of free-stream air
T_w	temperature of wall
T_τ	friction temperature = $= \overline{q_0''}/(\rho C_p U_\tau)$
T^*	see Eq. (7.15)
T^{**}	see Eq. (7.19)
T^+	temperature in inner coordinates $(T_w - T)/T_\tau$
t	time; also instantaneous fluctuating component of T
t'	rms of t
t'^+	t'/T_τ
t''^*	$\theta'/(St)^{1/2}$
t_{\max}	maximum thickness of wing section
Tu	turbulence intensity = u'/U
U, V, W	local time-averaged velocity components in x,y,z directions, respectively
U_c	celerity of convected turbulence structures
U_{ref}	reference velocity measured at throat of test section
U_∞	time-mean velocity at edge of boundary layer

U_τ	friction velocity = $(\tau_w/\rho)^{1/2}$
U_N	mean streamwise velocity at $y = N$.
u, v, w	instantaneous fluctuating velocity components in x, y, and z direction, respectively
u', v', w'	rms values of u, v, and w, respectively
u'_{\max}	maximum value of u' in boundary layer
u_τ^*	friction velocity based on fluctuating component of wall shear stress = $\sqrt{\tau_{w,rms}/\rho}$
x, y, z	cartesian coordinate system axis
x_{FS}, y_{FS}, z_{FS}	local free-stream coordinates (Fig. 1.4)
x_{TC}, y_{TC}, z_{TC}	wind-tunnel coordinates (Fig. 1.4)
x_{WC}, y_{WC}, z_{WC}	local wall shear-stress coordinates (Fig. 1.4)
$x(t), y(t)$	general time-dependent signals
$X(f), Y(f)$	complex Fourier Transforms of $x(t), y(t)$
x_{lols}	distance measured along line of symmetry of wing from wing leading edge to line of low shear
x_{sep}	distance measured along line of symmetry of wing from wing leading edge to line of separation
y^+	yU_τ/ν
y^*	$yU_\infty St^{1/2}/\nu$
y^{**}	see Eq. (7.19)
$z_{\alpha/2}$	standardized normal random variable

Greek Letters

β_{FS}	angle between local free-stream direction and tunnel axis, See Fig. 1.4.
β_H	angle between enthalpy thickness vector direction and tunnel axis, See Fig. 1.4.
β_m	angle of maximum coherency between velocities measured by parallel sensor probe. See Appendix C.
β_{ws}	angle between local wall shear stress direction and tunnel axis, See Fig. 1.4.
γ^2	spectral coherency between surface heat flux and temperature, Eq. (2.17)
γ_{pu}	fraction of time that the instantaneous streamwise velocity at location y is positive
δ^*	displacement thickness $= \int_0^{\infty} (1 - U/U_{\infty}) dy$
$\delta, \delta_{0.995}$	velocity boundary layer thickness defined by $U = 0.995U_{\infty}$
$\delta_{0.99}$	velocity boundary layer thickness defined by $U = 0.990U_{\infty}$
δ_s	length scale used in Eq. (7.22) $= y\Theta_s C/\Delta_1$
δ_T	thermal boundary layer thickness defined by $\Theta = 0.995$
$\delta(\)$	95% confidence interval in quantity ()
Δ_1	temperature displacement thickness, see Eq. (7.3)
Δ_2	enthalpy thickness $= \int_0^{\infty} (1 - \Theta) \frac{U}{U_{\infty}} dy$

Δ_{1N}	backflow temperature displacement thickness, see Eq. (7.6)
Δ_{2N}	backflow enthalpy thickness, see Eq. (7.6)
Δ_3	length scale, see Eq. (7.21)
ΔT	Temperature difference = $T_w - T_\infty$
ϵ_h	turbulent diffusivity for heat transport = $\overline{v\theta}/(\partial\theta/\partial y)$, m^2/s
ϵ_m	kinematic eddy viscosity for two-dimensional boundary layer, m^2/s
$ \epsilon_m $	magnitude kinematic eddy viscosity used for 3-D boundary layer. See Eq. (5.6), m^2/s
η	normalized distance = y/δ_s
η_g	gage emissivity
Θ	local time-averaged normalized temperature = $(T_w - T)/(T_w - T_\infty)$
$\langle\Theta\rangle$	conditionally-averaged temperature. See Eq. (2.12)
θ	instantaneous non-dimensional fluctuating temperature, $t/(T_w - T_\infty)$; also momentum thickness = $\int_0^\infty (1 - U/U_\infty)U/U_\infty dy$
θ'	rms value of non-dimensional temperature θ
κ	von Karman constant = 0.41
κ_n	heat transfer constant analogous to κ , See Eq. (5.4)
μ	molecular viscosity, $N\ s/m^2$; also mean value
μ_T	turbulent eddy viscosity, $N\ s/m^2$
ν	molecular kinematic viscosity, μ/ρ , m^2/s

ρ	density, kg/m^3
σ	Steffan Boltzmann constant = $5.67 \times 10^{-8} \text{ W/(m}^2 \text{ K}^4)$; also variance of a quantity
τ	total shear stress, N/m^2 also time shift
τ_w	wall shear stress, N/m^2
$\tau_{w,\text{rms}}$	root mean square of fluctuating component of wall shear stress, N/m^2
$\phi(ky)$	power spectrum of t as a function of ky
$\phi(k\delta)$	power spectrum of t as a function of $k\delta$
ϕ_{xy}	cross-spectral phase angle between signals $x(t)$ and $y(t)$ at frequency f . See Eq. (2.16).

1 Introduction

It is well known that in complex three-dimensional and separated turbulent flows, the turbulence structure is significantly different than that observed in attached two-dimensional boundary layers. Since the invention of laser-Doppler velocimetry, much research has focused on the changes in turbulent momentum transport in complex flows. Significantly less attention has been paid to the turbulent transport of heat. While there are global heat transfer measurements for such cases, no detailed study of the relationships between the fluid turbulence and the heat transfer have been made.

Basic research on convective heat transport in complex three-dimensional and separated turbulent flows is of value to both basic and applied issues. The basic issues of turbulent transport of a passive scalar (temperature) in turbulent flow is of primary scientific merit. A well-known example of practical engineering interest where heat transport through a complex turbulent boundary layer occurs is in a turbine engine as illustrated in Fig. 1.1. The flow field in a turbine engine is extremely complicated and includes three-dimensionality caused by spanwise pressure gradients and surface shearing forces, boundary layer separation from a smooth surface caused by adverse streamwise pressure gradients on the suction side of the blades, and vortical structures at the blade/hub junction. Other phenomena which affect heat transfer include the high free-

stream turbulence of the air entering the turbine and periodic unsteadiness of the free stream due to the angular rotation of the turbine. The combined, interacting, and often conflicting effects of these phenomena on surface heat transfer are extremely difficult to unravel in a such a complicated flow field. Instead, it is more useful to study each phenomenon separately in a simple geometry.

In the present study, the turbulence structure of convective heat transfer was examined in three low speed complex turbulent boundary layer test cases for which detailed laser velocimeter flow-field measurements were already available:

(1) Wing/Body Junction Vortex Flow

A wing/body junction flow is formed when the boundary layer on a surface encounters the blunt nose of an airfoil shaped body or strut protruding from that surface as illustrated in Fig. 1.2. When the approach boundary layer encounters the wing, it separates in front of the nose and the separation line stretches around the sides of the wing. Closer to the nose a horseshoe vortex forms which stretches around the wing. The junction vortex system is of interest in many practical engineering applications. This flow pattern is present at aircraft wing roots, ship and submarine appendage/hull junctions, in gas turbines at the blade/hub junction, and in flows with injection normal to the mean flow. Because of the complexity and unsteadiness of the flow in this region, analysis of the flow and heat transfer is difficult.

In the present study, time- and spatially-resolved heat flux measurements are made

at various positions on the endwall surface in the nose region of the wing body junction flow previously studied by Devenport and Simpson (1987, 1990 a) and Ölçmen and Simpson (1994). Statistical and spectral characteristics of the heat flux fluctuations are presented and are compared to the velocity and turbulence fields. Several wing shapes are used to study the effects of nose geometry on endwall heat transfer.

(2) Three-Dimensional Turbulent Boundary Layer Flow

Three-dimensional turbulent boundary layers (TBLs) occur in many practical applications where convective heat transfer is significant. Flow in a gas-turbine engine is one well-known example. The mean flowfield in a 3D TBL is characterized by a flow direction which varies with distance from the wall as shown in Fig. 1.3. Three-dimensional TBLs are created by either the presence of a spanwise pressure gradient (referred to as a pressure-driven 3D TBL) or by a streamwise shear applied to the fluid by a moving surface (shear-driven 3D TBL). The changing direction of the flow with distance from the wall results in some features that are distinctly different from two-dimensional TBLs.

The flow case studied here is the spatially developing pressure-driven three-dimensional boundary layer upstream of a wing-body junction previously studied by Ölçmen and Simpson (1990, 1995a) and Ha and Simpson (1993). Outside of the plane of symmetry, a three-dimensional boundary layer is created by the spanwise pressure gradient imposed on the flow by the presence of the wing (Fig. 1.4). Closer to the nose

of the wing, a horseshoe vortex forms. The region of flow studied by Ölçmen and Simpson (1990, 1995a) is upstream of the vortex-dominated separated region close to the wing studied in flow case (1).

Surface heat flux and temperature are measured at various locations across the boundary layer at 8 streamwise locations in the spatially-developing flow. The correlation between surface heat flux and the turbulence structure is determined from the spectral coherency function between surface heat flux and temperature. The statistical and spectral characteristics of the surface heat flux and temperature field are compared to the turbulence structure data from previous studies.

(3) Two-Dimensional Separating Turbulent Boundary Layer Flow

Boundary layer separation is often unavoidable in many engineering applications where convection heat transfer is of interest. Examples include heat exchangers, coaxial and dump combustors, gas turbine engines, ramjets, disk drives, electronics cooling systems, continuous laser cavities, and housings for optical instruments in space vehicles (Aung, 1982). As pointed out by Hacker and Eaton (1995) current CFD codes employing the turbulent Prandtl number fail in separated flows. Little research has been done to establish values for the turbulent Prandtl number in separated flows or even to determine if the turbulent Prandtl number approach is valid. Current turbulence models are only good in the region away from the wall and often over-predict surface heat transfer (Shishov et al, 1988; Launder, 1988). Over the last fifty years, a large amount of research

on heat transfer in basic separated turbulent flows has been reported. Few studies have included coupled heat transfer and fluid mechanics data. Almost all previous heat transfer studies have been in cases where the separation point is fixed by a sharp corner such as flow over a backward facing step. No previous studies of heat transfer in flows separating from smooth surfaces have included surface heat transfer, the detailed temperature field and detailed fluid mechanics data.

The case studied in the current investigation is the mean two-dimensional, steady free-stream velocity, adverse-pressure-gradient-induced separated flow of Simpson, Chew, and Shivaprasad (1981 a, b). Simultaneous surface heat flux and temperature are measured at various locations across the boundary layer at several streamwise locations from far upstream of detachment to downstream of detachment. The correlation between surface heat flux and the turbulence structure is determined from the coherency between surface heat flux and temperature. The statistical and spectral characteristics of the surface heat flux and temperature field are compared to the turbulence structure data from previous studies.

1.1 Literature Review

1.1.1 Heat Transfer in a Turbulent Wing/Body Junction Vortex System

The flowfield in the wing/body junction is dominated by large-scale, aperiodic motions. Devenport and Simpson (1990 a,b) measured velocities in the plane of symmetry upstream of a wing/body junction and observed bimodal (double peaked) velocity probability histograms (Fig. 1.5, inset). Further research showed that the flow at a given point in this zone switched aperiodically from one mode to the other. This double-peaked structure has also been found in histograms of surface pressure fluctuation measurements made on the endwall upstream of a wing/body junction (Ölçmen and Simpson, 1994; Rife, 1992). Hydrogen bubble flow visualizations by Kim (1991) revealed that the aperiodic motions were caused by stretching of the horseshoe vortex about the wing and by interaction of the horseshoe vortex with co-rotating separation vortices which form between the horseshoe vortex and the line of separation. This aperiodic phenomenon is responsible for the observed high turbulence intensities and high surface pressure fluctuations and may be responsible for high heat transfer rates.

Figure 1.6 shows an oil flow visualization performed by Devenport and Simpson (1990 a) on the test wall around a 3:2 elliptic nosed/NACA 0020 tailed airfoil. The free-stream velocity was 27 m/s and the approach boundary layer momentum thickness measured 2.15 wing thicknesses upstream of the wing was 6700. Two prominent lines are visible in the oil flow. Upstream of the model a separation line originates from a saddle

point. Closer to the wing, a second line appears which Devenport and Simpson have shown to mark a location of minimum local streamwise shear. This line, called the "line of low shear," divides the flow into two distinct regions. Downstream of the line-of-low shear, the vortex brings high-momentum fluid down to the endwall, producing a region of high streamwise shear. The fluid transported toward the endwall on the downwash side of the vortex impinges on the wing/endwall junction and is deflected radially in the spanwise direction and back upstream in a near-wall jet of fluid. Turbulent stresses reach comparatively small values and the boundary layer in this region is very thin due to the transport of outer fluid toward the endwall. Upstream of the line of low shear, a crescent-shaped region of low shear exists. This is a region of intense backflow and very large turbulent stresses. The backflow velocity reaches a maximum value at a streamwise location near the mean flow vortex center and then decelerates as it moves upstream to the separation point. Backflow in the region between the line of low shear and the line of separation is an intermittently forward and reverse unsteady flow. Peak values in the turbulent normal stresses were found to exist much closer to the wall in this region than elsewhere in the flow.

Few studies of the effects of the horseshoe vortex on endwall heat flux have been made. Time-averaged heat flux measurements in turbine cascades have been made by several researchers. Blair (1974) and Dunn and Stoddard (1979) measured endwall heat flux rates between blades in a turbine cascade and found that the horseshoe vortex increased heat flux by a factor of 3 near the leading edge of the turbine/endwall junction.

The effects of the approach boundary layer thickness on heat flux to the endwall

in turbine cascades have been investigated with inconclusive results. Grazianni et al. (1980) found that minimum and maximum Stanton number levels were independent of the approach boundary layer thickness. Grazianni et al. (1980) also found that the area of influence of the horseshoe vortex was increased with increasing approach boundary layer thickness. In contrast, Georgiou et al. (1979) found that the effect of reducing the inlet boundary layer thickness was to uniformly increase the local heat flux rate, but that the shape of the iso-heat-transfer contours were unaffected by boundary layer thickness. Georgiou et al. (1979) also found changes in free-stream turbulence levels to have only a minimal effect on heat flux rates in the horseshoe vortex.

Gaugler and Russell (1983) compared their measured turbine/endwall heat flux rates with flow visualizations of Hylton et al. (1981). The only obvious correlation between the horseshoe vortex and endwall heat flux was found near the vane leading edge where a local peak in heat flux occurred. The three-dimensional separation line was found to not correlate with any endwall heat flux features. Hippensteele and Russell (1988) measured turbine/endwall heat flux rates using high spatial resolution liquid crystal sheets for the same turbine cascade used by Gaugler and Russell and obtained similar results.

Eibeck and Eaton (1987) examined surface heat transfer beneath a streamwise vortex embedded in a turbulent boundary layer. They observed an augmentation in surface heat flux on the downwash side of the vortex and a decrease in heat flux on the upwash side. They attributed the change in surface heat transfer to a thinning of the boundary layer on the downwash side of the vortex and a thickening of the boundary layer on the upwash side of the vortex. Fisher and Eibeck (1990) and Wroblewski and Eibeck (1992)

have examined surface heat transfer in the wake downstream of a wing/body junction. They observed that both the mean flow field created by the horseshoe vortex and the large-scale unsteadiness arising from vortex shedding augmented the surface heat transfer.

Only recently have time-resolved heat flux measurements been made in the junction vortex. A high-frequency-response heat flux gage called the Heat Flux Microsensor was recently used by Swisher et al. (1992) to measure time-resolved endwall heat flux along the stagnation streamline upstream of a streamlined cylinder. The rms of the heat flux unsteadiness was found to be as high as 30% of the mean heat flux in the horseshoe vortex.

1.1.2 Heat Transfer in Three-Dimensional Turbulent Boundary Layers

As previously mentioned, a three-dimensional boundary layer is characterized by a flow direction which varies with distance from the wall. The changing direction of the flow with distance from the wall results in some features that are distinctly different from two-dimensional TBLs. Mean-velocity profiles do not collapse onto a single law-of-the-wall profile (Ölçmen and Simpson; 1990, 1992). The mean turbulent shearing stress direction generally lags the mean velocity gradient direction so that an isotropic eddy viscosity model cannot reflect the correct physics of the stress-producing structures (Ölçmen and Simpson; 1990, 1995a). Also there is a decrease in the ratio of the shear stress to twice the turbulent kinetic energy, called the structure parameter a_1 (Ölçmen and Simpson; 1990, 1993). This ratio has a near-constant value of 0.15 in the outer part of 2D

TBLs and has been used in turbulence modelling (Bradshaw et al., 1967). The decrease in a_1 suggests a decrease in the ability of the 3D TBL to transfer momentum and heat.

Currently, turbulence models extended from two-dimensional models are often applied to three-dimensional TBLs with poor results, particularly when strong crossflows are encountered (Ölçmen and Simpson, 1993; Bettelini and Fannelöp, 1993). Future turbulence models for convective heat transfer in 3D TBLs must incorporate the physics that occurs in 3D TBLs. A large amount of past research has been aimed at investigating the flow physics in unheated 3D TBLs. Reviews of recent experiments in 3D TBLs have been presented by Anderson and Eaton (1989) and Johnston and Flack (1994). Considerably less research has focused on understanding heat transfer in simple 3D TBLs. Development of turbulence models for heat transfer and accurate but general heat transfer correlations requires research into the detailed mechanisms of turbulent heat transport in simple three-dimensional boundary layers.

Since the flow visualization experiments of Kline et al. (1967), much attention has been paid to the quasi-periodic repeating patterns of coherent motion observed in the near-wall region of TBLs. Many of the observed differences in three-dimensional and two-dimensional TBLs are thought to be the result of changes in these coherent motions. These coherent motions consist of the well-documented low-speed streaky structures in the sublayer and the sweep/ejection sequence which consists of ejections of low-speed fluid from the near-wall region followed by sweeps of high speed fluid from the outer layer and log-regions. The majority of turbulence production in the entire boundary layer is known to occur in the buffer region during this sweep/ejection cycle (Corino and

Brodkey, 1969; Kim et al., 1971). A comprehensive summary of the current state of knowledge of two-dimensional boundary layer structure may be found in Kline (1992).

Robinson (1991) examined the flow structure in the two-dimensional low-Reynolds-number flat-plate boundary layer from the direct numerical simulation (DNS) data of Spalart (1988). Robinson observed several types of vortical structures distributed throughout the boundary layer and devised a conceptual model to account for the kinematics of the coherent motions. According to this model, quasi-streamwise vortices occur primarily in the buffer region of the boundary layer while transverse vortical arches occur primarily in the outer wake region (see Fig. 1.7). Both types of vortical structures occur in the log region.

Nychas et al. (1973) observed a close spatial association between the passage of transverse vortices and the occurrence of sweep/ejection motions in the near-wall region which implicated transverse vortices as the key structural element connecting the near-wall activity with the outer-region flow (Fig. 1.8a). This result was supported by the work of Praturi and Brodkey (1978) and Brown and Thomas (1977). In contrast, Robinson's (1991) results showed that the sweep/ejection process observed at a stationary location is primarily created by the passage of a single quasi-streamwise vortex which ejects fluid away from the wall by vortex induction as illustrated in Fig. 1.8b. The exact relation between near-wall quasi-streamwise vortices, outer-region transverse vortices, and the sweep/ejection process is still unresolved. As a result, there exists some uncertainty over proper scaling of the mean sweep/ejection frequency (Gad-el-Hak and Bandyopadhyay, 1994). Some research groups have concluded that the mean sweep/ejection frequency

should scale on outer variables (U_∞ and δ) while other groups have found that inner scaling (u_τ and v) should be used.

Many of the observed differences in three-dimensional and two-dimensional TBLs are thought to be the result of changes in the coherent structures. Several recent experiments have examined coherent structure in 3D TBLs. Ölçmen and Simpson (1995 a,b,c,d) used a five-component fiber-optic Laser Doppler Velocimeter to make three-velocity component measurements. Ölçmen and Simpson (1995 c) performed an octant analysis on their data in u , v , and w coordinates and found that in the 3-D flow, a greater fraction of the Reynolds stresses across the layer, particularly \overline{uw} and \overline{vw} , were created by sweep ($u>0$, $v<0$) and ejection ($u<0$, $v>0$) motions than in the 2-D TBL upstream.

Ha and Simpson (1993) employed a number of experimental techniques to measure length scales and the convective wave speed and direction of coherent structures in the same 3D TBL studied by Ölçmen and Simpson (1990). They found that length scales were reduced and that the coherent structures are convected in the direction of the local mean flow. Ha and Simpson observed that the coherency between the inner and outer regions of the TBL was decreased by three dimensionality. Fleming and Simpson (1994) and Fleming et al. (1995) made and examined videos of hydrogen-bubble flow visualizations of the near-wall streaky structure region in low Reynolds number 2D and 3D TBLs. Fleming and Simpson (1994) observed decreased activity in the high speed sweep region for the 3D case which supports the idea that the presence of a transverse, near-wall mean velocity component leads to a more "organized" flow structure with less interaction between the inner and outer regions. Fleming and Simpson also observed that

the low-speed streaks in the three-dimensional case appear to be more stable with less movement in the spanwise direction.

Sendstad and Moin (1992) examined results from a DNS of a low-Reynolds number 3D TBL. They found that the key mechanisms responsible for the reduction in Reynolds stresses are a reduction in the distance which sweeps and ejections penetrate the boundary layer as illustrated in Fig. 1.9. Sweeps by vortices whose sign of rotation is the same as the mean near-wall streamwise vorticity do not get as close to the wall because the fluid is forced toward the vortex center by the mean flow and therefore have a lower vortex-induced vertical velocity (Fig. 1.9 a). Ejections by vortices whose sign of rotation is the opposite of the mean near-wall streamwise vorticity do not carry as much momentum because they originate at a higher distance from the wall (Fig. 1.9 b). The streamwise vortices are shifted with respect to the wall-layer streaks below them so that the vortices pump high- rather than low-speed fluid away from the wall (Fig. 1.9 c). Sweeps by vortices whose sign of rotation is the opposite as the mean near-wall streamwise vorticity do not get as close to the wall because the fluid is forced away from the vortex by the mean flow and does not reach as close to the wall (Fig. 1.9 d).

Flack and Johnston (1995) made and examined videos of hydrogen-bubble flow visualizations of the ejection process in the wall-region of low-Reynolds number 2D and 3D TBLs. In contrast to the observations of Sendstad and Moin (1992), Flack and Johnston did not observe a difference in the distance from the wall that ejections penetrate. Rather, they observed that the frequency of ejections was decreased by three dimensionality.

Several authors have compared the statistical characteristics of temperature and velocity fluctuations in two-dimensional TBLs. Zaric (1972, 1975), Fulachier and Dumas (1976), Antonia, Krishnamoorthy, and Fulachier (1988), and Hishida and Nagano (1979) have reported temperature and velocity fluctuation measurements for turbulent flow over a heated flat plate. Similarity between histograms of temperature and streamwise velocity fluctuations in the near-wall region have been reported. Typical 2D turbulent boundary layer profiles of variance, skewness, and flatness of streamwise velocity histograms reported by Durst et al. (1992) are shown in Fig. 1.10. Profiles of the variance, skewness, and flatness of temperature fluctuation histograms are very similar to those of streamwise velocity (Nagano and Tagawa, 1988). The histograms are skewed positively in the near-wall region and become skewed negatively further away from the wall. Zaric (1972) has proposed that the positive and negative skewness of the histograms is the result of coherent motions. Skewness of temperature and streamwise velocity fluctuations attain large positive values in the near-wall region due to the frequent occurrence of sweeps of high-momentum, cold fluid from the outer region of the boundary layer. In the log-region, the histograms become nearly Gaussian due to equal occurrence and strength of sweeps and ejections. Further from the wall, the histograms are skewed negatively due to the increasing frequency of ejections of low-momentum, warm fluid from the near-wall region. Near the edge of the boundary layer, flatness factors become very large due to the intermittent passage of turbulent bulges. It is notable that the skewness factor changes sign at approximately the location where flatness factor is minimal and variance attains a maximum (Zaric, 1972; Durst et al., 1985) and that this location moves further from the

wall as Reynolds number increases (Andreopoulos et al, 1984). Skewness and flatness factors of temperature fluctuations are also of interest in modelling the triple products which appear in the turbulent diffusion terms of the Reynolds-stress and scalar-flux equations. Nagano and Tagawa (1990, 1991) have shown that these triple products can be related to the Reynolds stresses and skewness factors of u , v , and θ .

In comparison to the amount of fluid mechanics research done in 3D TBLs, the work done on heat transfer through them is very sparse. The majority of previous work has primarily involved two types of flow: flows around obstructions and flow on a rotating disk. A review of some of this work is given in Abrahamson and Eaton (1993). The research in flows around an obstruction has generally centered on heat transfer in the vortical structure in the wall/obstruction junction region and downstream of the obstruction in the wake vortex. This flow case, encountered in turbine cascades, is too complicated to extract general information on three-dimensional boundary layers. The heat transfer from a rotating disk is fundamentally different than many typical 3D TBLs of interest in that the boundary layer begins, undergoes transition to turbulent, and develops fully in a three-dimensional state rather than developing as a two-dimensional TBL being driven to its three-dimensional state.

Few heat transfer experiments have been made in simple three-dimensional boundary layers. The single previous experiment is the work of Abrahamson and Eaton (1993). Abrahamson and Eaton measured mean surface heat flux and temperature profiles in a spatially developing pressure-driven three-dimensional TBL upstream of 60° and 90° wedges. Abrahamson and Eaton found that the mean surface heat transfer decreased with

distance downstream faster in a three-dimensional boundary layer than in a two-dimensional zero-pressure-gradient boundary layer and that this decrease was greater with stronger three-dimensionality. Abrahamson and Eaton proposed that the heat transfer correlates with a Reynolds number based on the magnitude of an enthalpy thickness vector defined:

$$\mathbf{H} \equiv \left[\frac{\int_0^\infty \rho U i_s dy}{\rho_\infty i_{s,0} (U_\infty^2 + W_\infty^2)^{1/2}}, 0, \frac{\int_0^\infty \rho W i_s dy}{\rho_\infty i_{s,0} (U_\infty^2 + W_\infty^2)^{1/2}} \right]. \quad (1.1)$$

Further, Abrahamson and Eaton found that the enthalpy thickness vector, which points in the direction of the mean thermal energy flux across the boundary layer, is aligned with the direction of the collateral flow in the near-wall region, indicating that the majority of thermal energy transfer occurs in the near-wall region.

1.1.3 Heat Transfer in Separating Two-Dimensional Turbulent Boundary Layers

Almost all previous heat transfer studies have been in cases where the separation point is fixed by a sharp corner such as flow over a backward facing step. This differs from the case where flow over a smooth wall separates due to an adverse pressure gradient. As pointed out by Simpson (1989), turbulent boundary layer separation due to an adverse pressure gradient is the entire process of "*departure or breakaway or the breakdown of boundary-layer flow*" and occurs over a significant streamwise distance.

The separation point is very unsteady and the whole region surrounding separation is one of intermittently forward and reverse flow. Simpson (1981) defines four streamwise locations in a separating TBL. *Incipient detachment* (ID) occurs with instantaneous backflow 1% of the time; *intermittent transitory detachment* (ITD) occurs with instantaneous backflow 20% of the time; *transitory detachment* (TD) occurs with instantaneous backflow 50% of the time; and *detachment* (D) occurs where the time-averaged wall shearing stress is 0. Data suggest TD and D occur at the same location (Simpson, 1981). The length of the region between ID, ITD, TD, and D points will depend on the geometry of the flow.

The boundary layer upstream of ID is similar to a "normal" attached turbulent boundary layer (Simpson, 1989). The mean flow obeys the "law-of-the-wall" and the "law-of-the-wake" as long as the maximum shearing stress is less than 1.5 times the wall shear stress. Since wall shearing stress approaches 0 at detachment, it is a poor parameter to use in describing mean velocity profiles away from the near-wall region. When $-\overline{p u v} > 1.5 \tau_w$, the Perry & Schofield (1973) mean-velocity profile correlation for the outer flow, the law of the wall for the near-wall flow, and the Ludwig-Tillman skin-friction equation apply upstream of ID and remain approximately valid upstream of ITD. The qualitative turbulence structure is not markedly different from a flat plate TBL except that the maximum turbulent fluctuations occur in the middle of the boundary layer.

Separation begins only intermittently at a given streamwise location i.e., flow reversal at that location occurs only a fraction of the time. At progressively farther downstream locations, the fraction of time that the flow moves downstream is

progressively less. A spanwise line of detachment does not move up and downstream as a unit. Small three-dimensional elements of flow move upstream for a distance and are later carried downstream. Large eddies grow rapidly and agglomerate with one another. These large-scale structures supply turbulence energy to the near-wall detaching flow. The velocity fluctuations in the backflow regions are greater than or at least comparable to the mean backflow velocities. Intermittent backflow occurs as far away from the wall as the maximum shearing-stress location $y/\delta > 0.5$. Due to the large-scale unsteadiness, mean flow streamlines do not represent pathlines for elements of fluid. Fluid is supplied locally rather than from far downstream as mean flow streamlines suggest (Simpson, 1989).

The near-wall region downstream of separation lacks many characteristics normally associated with turbulent boundary layers. Profiles of turbulence intensity do not have a peak close to the wall. Profiles of mean velocity do not have a log region related to the friction velocity. The Reynolds shearing stress remains small and turbulent bursts are relatively infrequent. There is little production or convection of turbulence kinetic energy. Turbulence energy dissipated here is supplied by diffusion from the separated shear layer above rather than by production due to the mean velocity gradient (Simpson, 1989). Mixing-length and eddy viscosity models fail because the Reynolds shearing stress is related to the turbulence structure and not the local mean velocity.

Lack of Reynolds stress suggests that viscous shear stress is significant. Based on maximum mean backflow velocity U_N and distance from the wall where it occurs, N , the low Reynolds number and high skin friction coefficient of the near-wall flow also suggest viscous dominated structure. Adams and Johnston (1988) measured velocity profiles in

the near-wall region downstream of a backward-facing step and observed that the acceleration parameter based on the maximum backflow velocity, $K = (v/U_N^2)(dU_N/dx)$ is two orders of magnitude larger than required for relaminarization. By treating each velocity profile in the region from the wall out to N as a boundary layer profile, Adams and Johnston calculated the integral parameters δ , θ , and δ^* . Variation of δ , θ , and δ^* was nearly linear in the streamwise direction and the shape factor, $H = \delta^*/\theta$, had a nearly constant value of $H = 2.05$. The integral lengths were very small. Momentum thickness Reynolds number in the backflow varied from 12 to 55.

Simpson (1983) has proposed that mean streamwise velocity profiles in the backflow region scale on U_N and N . A U^+ vs. y^+ law-of-the-wall velocity profile is not valid since both the velocity scale $|U_N|$ and the length scale N increase with streamwise distance while the law-of-the-wall length scale v/U_τ varies inversely with the velocity scale U_τ . For $0.02 < y/N < 1.0$, Simpson (1987) has proposed the mean-flow velocity profile

$$\frac{U}{|U|_N} = A \left(\frac{y}{N} - \ln \left| \frac{y}{N} \right| - 1 \right) - 1 \quad (1.2)$$

with the value of $A = 0.3$. Dianat and Castro (1989) have found Eqn (1.2) to correlate their data with $A = 0.235$. Devenport and Sutton (1987) have shown that the constant A in Simpson's law-of-the backflow is a function of C_f , N , and dp/dx .

The values of u are as large as U in the near-wall region while the v fluctuations are small. Peak energy in u spectra occurs at very low frequencies, suggesting large scales

on the order of the separation bubble (Simpson et al., 1981b; Adams and Johnston, 1988). These observations suggest that the velocity fluctuations in the near-wall region are produced by large-scale vortices which do not produce Reynolds stress in the near-wall region. Devenport and Sutton (1991) observed that when fluctuating streamwise velocity is scaled on U_τ , profiles do not collapse even for $y^+ < 10$. Since, the velocity fluctuations in the near-wall region are dominated by large-amplitude low frequency motions parallel to the wall, the fluctuations should scale on a parameter directly related to the large scale unsteadiness. Devenport and Sutton (1991) reasoned that since the flow is like an unsteady laminar flow in the near-wall region, the unsteady skin friction should be related to the large-scale unsteadiness. Devenport and Sutton therefore use a friction velocity based on the intensity of the wall shear-stress fluctuations, $u_\tau^* = \sqrt{\tau_{w,rms}/\rho}$. Devenport and Sutton further show that the profile of the fluctuating streamwise velocity is a function of the fluctuating skin friction and the frequency of the fluctuations imposed by the large-scale unsteadiness.

Almost all previous heat transfer studies have been in cases where the separation point is fixed by a sharp corner such as flow over a backward facing step. When the flow separates at the sharp edge, a shear layer forms which on one side bounds the main stream and on the other encloses a region of time-mean backflow. The shear layer reattaches some distance downstream. The turbulence structures in the backflow regions of backstep flows and flows where the boundary layer separates from a smooth surface are very similar (Adams and Johnston, 1988). It is therefore worthwhile to review previous heat transfer work in backstep flows. One important difference is that the

important length scale in a backward-facing step flow is the distance from reattachment while in a flow separating from a smooth surface the important length scale is the distance from separation (Adams and Johnston, 1988). Also, the near-wall velocity fluctuations in the backflow region downstream of a backstep are created by a "flapping" of the entire shear layer while the near-wall fluctuations in the backflow region downstream of separation from a smooth surface are due to turbulence within the separated shear layer (Simpson et al., 1981 a)

Reviews of heat transfer studies in the separated region downstream of a backward-facing step have been made by Aung and Watkins (1978), Aung (1982), Ota and Nishiyama (1987), and more recently, by Hacker and Eaton (1995). An augmentation of the heat transfer coefficient occurs with a peak in the vicinity of reattachment. The peak heat transfer is well correlated by a Reynolds number based on reattachment length. The dominant resistance to heat transfer in separated flows is concentrated very near the wall and the conventional wall similarity laws fail. The large heat transfer rates are due to high turbulence diffusivity and a low thermal resistance of a fresh newly developing thermal boundary layer starting from the location of reattachment.

Recent experiments in backstep flow heat transfer have included coupled fluid mechanics data. Vogel and Eaton (1984, 1985) coupled local heat transfer measurements with temperature and velocity profiles downstream of a backward-facing step using laser anemometry and constant-current resistance thermometers. They observed that the peak heat transfer occurs a short distance upstream of mean reattachment where turbulent intensities and length scales are maximum. Vogel and Eaton (1985) found that the heat

transfer rate near reattachment was correlated with the level of fluctuating skin friction. Moving upstream from reattachment, the near-wall layer grows as a laminar boundary layer, thickening as it approaches the center of the recirculation bubble. The Stanton number drops as the layer thickens. A secondary peak in heat transfer was observed just downstream of the step, caused by the strong mean normal convection. The location of peak heat transfer just upstream of reattachment has been reported by other workers (Garcia and Sparrow, 1987; Sparrow and Ohadi, 1987; Sparrow, 1988; Mori et al., 1986). Mori et al. (1986) concluded that the shift of the peak heat transfer upstream of the mean reattachment point had to do with the intermittent motions of the reattaching shear layer.

Baughn et al. (1984, 1989) measured heat transfer downstream of a sudden pipe expansion for both constant heat flux and constant temperature boundary conditions. They found that the change in boundary conditions caused only slight change in the Nusselt number distribution. They also found the secondary peak in heat transfer just downstream of the step. Shishov et al. (1988) used hot wire anemometers and constant-current resistance thermometers to simultaneously measure velocity and temperature profiles in the separated region downstream of a backward-facing step. Heat flux and surface skin friction coefficients were determined from the slope of profiles. They observed that the development of the heat transfer and friction coefficient was similar to a laminar boundary layer growing from the reattachment point.

Little detailed study of heat transfer exists in flows where separation from a smooth wall occurs. Globally averaged heat transfer rates have been measured in flows containing smooth wall separation. Only one known experiment exists where local heat

transfer measurements were coupled with velocity profiles. Rivir et al. (1994) made measurements of mean local heat transfer at 7 streamwise locations from upstream of separation to downstream of reattachment. Their results showed that the heat transfer coefficient decreased very rapidly and monotonically approaching separation. A minimum in heat transfer coefficient was observed very near the time-mean detachment point. The heat transfer coefficient increased slightly in the center of the separation bubble and increased rapidly in the reattachment region. The maximum heat transfer rate was observed slightly downstream of the mean reattachment point.

1.2 Objectives

The overall objective of the present study was to examine the relation between the turbulence field, the temperature field, and the surface heat transfer for three test cases involving complex turbulent boundary layers. The purpose of the work was to determine the underlying physics or mechanisms responsible for heat transport. Knowledge of the correct flow physics is necessary both to develop general turbulence models and to develop novel schemes to control convective heat transfer by manipulating the boundary layer.

1.2.1 Wing/Body Junction Vortex Flow

All of the previous studies have shown similar levels and patterns of wing/endwall

heat flux. High levels of heat flux were found in the horseshoe vortex with peak levels occurring near the wing. Free-stream turbulence and approach boundary layer thickness have been found to have little effect on heat flux to the endwall but these effects are still poorly understood. The relationship between the fluid dynamics and the heat flux has not been established.

The case studied here was the thin-boundary-layer ($Re_\theta = 3730$) wing/body junction vortex studied by Ölçmen and Simpson (1993). The objective of this study was to relate the turbulent heat flux to the fluid dynamics in a horseshoe vortex. No attempt was made to predict the fluid dynamics as this has been the subject of many previous papers (Baker, 1980; Devenport and Simpson, 1990; Kim, 1991; Fleming et al., 1993). It was therefore assumed that the fluid dynamics (location and strength of the vortex) were known and the heat flux was related to these parameters. The specific objectives of this work were:

1. to examine both time-averaged and fluctuating heat transfer through detailed time- and spatially-resolved surface heat flux measurements in the horseshoe vortex.
2. to determine if the bimodal phenomenon caused by a bistable velocity variation is responsible for the augmentation in surface heat transfer.
3. to examine the effects of wing geometry on both the mean heat transfer and heat transfer turbulence levels.
4. to examine correlations between the surface heat transfer and the fluid mechanics.
5. to examine spectral characteristics of surface heat transfer.

1.2.2 Three-Dimensional Turbulent Boundary Layer Flow

None of the previous heat transfer studies in 3D TBLs have examined the structure of the turbulent temperature and heat flux fluctuations. Few of the heat transfer studies have made detailed measurements of the fluid mechanics. The case studied here was the spatially-developing pressure-driven 3D TBL upstream of a wing/body junction formed by a modified NACA 0020 wing and a flat plate. The fluid mechanics of this test flow are extremely well documented from previous studies (Ölçmen and Simpson, 1990, 1993, 1995 a,b,c,d; Devenport and Simpson, 1989, 1990a; Fleming and Simpson, 1994, 1995; Ailinger, 1990, Ha and Simpson, 1993). This test case differs from many other experimentally examined three-dimensional flows in that the mean flow variables depend on three spatial axes rather than two axes, such as flows in which the three-dimensionality of the flow has been generated either by a rotating cylinder or by a spanwise pressure gradient in one direction only throughout the flow. For these "degenerate" 3D flows, a local near-wall equilibrium exists which causes the mean velocity profiles to be self-similar in wall coordinates (Simpson, 1995, 1996). Ölçmen and Simpson (1992) found that a universal law-of-the-wall exists only for the beginning stages of 3D flow. This is the result of the inner and outer regions coming from different directions and having different histories, i.e, the sweeps from the outer region and the ejections from the inner region are not related (Simpson, 1995).

The overall objective of this work was to examine the effect that the changes in turbulence structure caused by three-dimensionality have on heat transfer. The specific

objectives of this work were:

1. to examine the effects of mean three-dimensionality on mean surface heat transfer and temperature profiles.
2. to determine appropriate scaling laws for temperature profiles.
3. to determine differences in the near-wall sweep/ejection process caused by three-dimensionality.
4. to examine changes in the outer-layer structure caused by three-dimensionality.
5. to examine the relationship between the inner and outer regions.

1.2.3 Two-Dimensional Separating Turbulent Boundary Layer Flow

None of the previous studies of heat transfer from a smooth surface have examined the structure of the temperature and heat flux fluctuations. The case studied here was the mean 2-D steady free-stream velocity adverse-pressure-gradient-induced separated flow of Simpson, Chew, and Shivaprasad (1981 a, b), which was a computational test case for the 1980-81 AFOSR-Stanford Conferences on Complex Turbulent Flows. The specific objectives for this work were:

1. to find out what happens to the surface heat transfer coefficient in the neighborhood of a simple smooth-wall separation point.
2. to determine appropriate temperature profile scaling laws for the inner and outer regions both upstream and downstream of detachment.
3. to determine if the turbulent Prandtl number approach is valid for separating

turbulent boundary layers.

4. to determine the nature of heat transfer in the near-wall backflow region, i.e., to determine if heat transfer in the backflow behaves like an unsteady laminar-like flow.

2 Experimental Apparatus and Technique

2.1 Wind Tunnel

The wind tunnel is an open-circuit type and is powered by a centrifugal blower. Air from the blower is supplied to the test section after passing through a fixed-setting damper, a plenum, a section of honeycomb, 7 screens which are used to remove much of the turbulence intensity, and a 4:1 contraction nozzle to further reduce the turbulence and to accelerate the flow to test speed. The potential core of the flow entering the test section is uniform to within 0.5% in the spanwise direction and 1% in the vertical direction with a turbulence intensity of 0.1% at 27 m/s (Devenport and Simpson, 1990 a).

2.1.1 Wing/Body Junction Vortex Flow Test Section

Figure 2.1 is a side view of the 6-m-long and 0.91-m-wide test section. The upper wall is made from plexiglass reinforced with aluminum channel. The glass side walls are lined internally with removable 6.4-mm thick plexiglass sheets. The lower wall is made from 19-mm thick fin-form plywood. Flow entering the test section is subjected to a further 1.5:1 contraction produced by the shape of the upper wall. A throat is reached

1.63 m downstream of the entrance where the section is 254 mm in height. Downstream of the throat the upper wall is almost parallel to the flat lower wall, diverging gradually from it with distance downstream to account for boundary layer growth.

In order to create a new fluid boundary layer at the beginning of the heat flux surface, a heated false floor is placed in the tunnel and a suction slot is opened in the tunnel floor as shown in Fig. 2.1. The upstream boundary layer formed on the tunnel floor is sucked out through the slot and a new boundary layer develops from the rounded leading edge of the false floor. The thin boundary layer is tripped by a 12.7-mm-wide strip of 120-grade sandpaper, located with its leading edge 70 mm downstream of the false floor leading edge. The forward edge of the suction slot is located 145 mm downstream of the throat of the test section. The false floor rests with its upper surface 34.9 mm above the tunnel floor and its leading edge 116 mm downstream of the throat. The false floor is made of 3 sections of 1.59-cm-thick aluminum plate. A trailing edge flap set at an angle of 7° is used to produce a constant static pressure on the tunnel floor throughout the test section.

The aluminum false floor is heated and held at a constant and uniform temperature. Silicone-rubber-insulated electric resistance heaters (Watlow Co., power density = 32.26 W/cm^2) are epoxied to the bottom of the floor using Silicone RTV epoxy. The heaters are insulated from beneath by 1.9-cm-thick styrofoam sheet which is secured to the plates by bolts. T-type thermocouples are soldered into 3.18-mm-diameter brass tube and press fit into the aluminum floor for feedback control. Power to the heaters is controlled by 5, Eurotherm 810, 3-mode process controllers, each connected to a

Eurotherm 831 SCR power supply. Because of the high thermal conductivity of aluminum and the thickness of the false floor, the surface is nearly isothermal. The automatic controllers hold the surface temperature constant and uniform to within $\pm 0.5^{\circ}\text{C}$.

The heat flux probe is mounted in a cam system installed in the false floor beneath the wing (Fig 2.2). The cam system is made of two 1.59-cm-thick aluminum discs, with the smaller disc fitting into the larger disc with an offset from the center of 4.44 cm. The probe holder containing the heat flux gage is mounted through a 2.86-cm dia hole in the smaller cam and secured by a set screw. A hole is drilled through the center of the larger cam to secure the airfoil. Rotating one or both cams allows the probe to be positioned throughout a 12.5 cm radius region in front of the wing. Scribe lines milled on the cams and the center plate are used to measure the cam yaw angle. The cams are heated from beneath by electric resistance heaters. Dimensions of the cam system are given in Fig 2.3.

2.1.2 Three-Dimensional Turbulent Boundary Layer Flow Test Section

To increase the momentum Reynolds number to match the flow conditions of Ölçmen and Simpson (1990), the heated false floor used in the wing/body junction case is lengthened as shown in Figure 2.4. The aluminum floor of the tunnel is heated from a distance 121.9 cm downstream of the test section entrance (41.07 cm upstream of the throat) for a distance of 335.3 cm. The roof of the test section is raised upward 34.9 mm to match the flow conditions of Ölçmen and Simpson (1990). Since the height of the roof at the leading edge of the test section entrance can not be adjusted, a ramp is installed

upstream of the aluminum floor to gradually adjust from the height of the leading edge of the test section entrance to the height of the heated floor. The ramp is 121.9 cm long and 34.9 mm high. The ramp consists of a plexiglass surface supported by an aluminum frame. The cam system used in the wing/body junction test section is replaced with a heated plate with eight 2.54-cm dia holes milled at the locations where heat flux was to be measured. The heat flux gage is press-fit into these holes and leveled by shims.

2.1.3 Two-Dimensional Separating TBL Flow Test Section

For this test case, the side-wall liners of the test section are removed and the upper wall is adjusted as shown in Fig. 2.5 to reproduce the flow of Simpson et al. (1981a). Flow entering the test section is subjected to a 1.5:1 contraction. A throat is reached 1.63 m downstream of the test section entrance where the section is 245 mm in height. An active suction and tangential wall-jet boundary layer control system, described by Simpson, Chew, and Shivaprasad (1980), is used to eliminate preferential separation of the curved-top-wall and side-wall boundary layers. Highly two-dimensional wall jets of high-velocity air are introduced into the upper-wall and side-wall boundary layers at the beginning of each of the 244-cm-long sections. At the latter two streamwise locations the oncoming upper-wall and side-wall boundary layers are partially removed by highly two-dimensional suction systems.

2.2 Appendage Shapes and Appendage Mounting

The wing shapes used were a modified NACA 0020 tailed wing, a streamlined cylinder shape, and an NACA 0015. The modified NACA 0020 wing consists of a 3:2 elliptical nose (with its major axis aligned with the chord) and an NACA 0020 tail joined at the maximum thickness. The streamlined cylinder shape had a circular nose of diameter 12.7 cm with the tail of the body after $x/c = 0.235$ made out of planar surfaces. The shapes of the NACA profiles may be found in Abbott and Von Doenhoff (1949). The height of each model was 22.9 cm. The models were each made of aluminum and were heated with silicone-rubber-insulated electric resistance heaters (power density = 32.26 W/cm^2) epoxied inside the models. The flow over each model was tripped with a strip of 120-grade sandpaper to prevent unsteadiness due to natural flow transition. The chord length, maximum thickness, leading edge radius, trip width, and trip location of each wing shape are given in Table 2.1. Results from oil flow visualizations (Ölçmen and Simpson, 1994) on the false floor in front of each wing are also given in Table 2.1. These oil visualizations revealed the location of primary separation of the approach boundary layer, x_{sep} , and the location of the "line of low shear", x_{ols} , measured from the wing leading edge along the line of symmetry in front of each wing. The wing shapes are illustrated in Fig. 2.1.

The wing was mounted in the test section at zero incidence and sweep with its leading edge 3.02 m downstream of the leading edge of the test section entrance. Since the measurements were made only with the wing at a zero angle of attack, it was possible

to reduce blockage-induced pressure gradients by contouring the side walls of the wind tunnel to approximately follow the streamlines produced by the 3:2 elliptic nose/NACA 0020 tailed wing in unbounded potential flow. This was accomplished by removing the 6.4-mm-thick plexiglass sheets which line the tunnel sidewalls from the region surrounding the wing. This effectively increased the width of the test section by 12.7 mm from a location 330 mm upstream of the wing leading edge to another 203 mm downstream of its trailing edge. The abrupt corners at the edges of the liner were faired over using adhesive tape. This same arrangement was used for the wing/body vortex flow junction and 3-D TBL flow test cases.

2.3 Sensors and Equipment

2.3.1 Heat Flux Microsensor

The Heat Flux Microsensor (Vatell Corp., Blacksburg, VA) is a layered type gage which operates by relating the heat flux to the measured temperature drop across a thin thermal resistance layer. The gage consists of several thin-film metal layers which form a differential thermopile across a thin thermal resistance layer as illustrated in Fig. 2.6. The layers of the gage are sputter coated onto a 2.54-cm diameter, 6.35-mm thick aluminum nitride disk. Feed-through leads are used to bring the signal through the substrate. The thin construction of the gage ($<2\mu\text{m}$) is physically unobtrusive in the flow and causes minimal disruption of the flow or the thermal boundary layer. The Heat Flux

Microsensor (HFM) has a flat electronic frequency response up to 50 kHz (Hager et al., 1991 b) and produces a continuous voltage linearly related to the heat flux. The surface pattern of the HFM is illustrated in Fig. 2.7. For the wing/body junction test case, the microsensor used was a model HFM-1 which has 40 thermocouple pairs and a sensing area of 3 mm by 4 mm. For the 3-D TBL and the 2-D separating TBL test cases a model HFM-3 microsensor with 100 thermocouple pairs and a 4 mm by 6.5 mm sensing area was used. The microsensor was always aligned so that the smaller length was in the streamwise direction. A platinum resistance temperature sensor (RTS) sputter coated onto the aluminum nitride disk near the heat flux sensor measures gage surface temperature. Differential amplifiers built by Vatec specifically for the heat flux microsensor are used to provide a small constant current to the RTS and to amplify the RTS output voltage. Potentiometers on the amplifier are used to null the heat flux and RTS temperature output. Calibration of the HFM is described in Appendix A.

2.3.2 Schmidt-Boelter gage

Due to the low output voltage of the HFM used in the wing/body junction vortex flow, a second, high-sensitivity Schmidt-Boelter gage manufactured by Medtherm Corp. (Model # 8-2-.625-36-20893T) was used to measure the mean time-averaged heat flux for this test case. The Schmidt-Boelter gage has an output voltage directly proportional to the heat flux with a sensitivity of $3.9 \pm 0.2 \text{ mV}/(\text{W}/\text{cm}^2)$ and a response time of approximately 250 msec. The diameter of the sensing area of the gage is 3.18 mm.

Temperature of the gage was measured by a T-type thermocouple mounted inside the gage by the manufacturer. Calibration is described in Appendix A.

2.3.3 Thermocouple Temperature Sensors

The test section floor surface temperature T_w and free-stream air temperature T_∞ were measured with 0.5106-mm diameter, copper/constantan thermocouples (Omega Engineering, part No. TT-T-24). The thermocouple temperature was read by a TEGAM 821 microprocessor-based digital thermometer. Free-stream temperature was measured by a thermocouple inserted through the roof at the throat of the test section. The heated floor surface temperature was measured by thermocouples soldered into 3.18-mm dia brass tube and press-fit into the aluminum floor.

2.3.4 Cold Wire Resistance Thermometer

Flow temperature inside the thermal boundary layer was measured using a hot-wire anemometer operating in the constant-current mode. To obtain information concerning the structure of turbulent heat transfer, a temperature sensor must have both fine spatial and temporal resolution. A small diameter wire provides greater frequency response due to its small thermal inertia. A small sensing length reduces spatial averaging of small turbulent structures. Blackwelder and Haritonitus (1983) suggest that the wire length must be less than 20 viscous units (the width of the smallest low-speed streaks) to capture the near-

wall coherent motions. Gad-el-Hak and Bandyopadhyay (1994) state that a probe length much larger than the viscous sublayer is not acceptable for accurately measuring turbulence levels and spectra anywhere across the boundary layer. However, as the sensor length decreases, the sensitivity of the wire also decreases due to the decrease in resistance. This causes a higher signal to noise ratio. Also, the length-to-diameter ratio must be sufficiently large to reduce heat conduction to the support needles. Bremhorst and Gilmore (1978) found that for platinum wires a length-to-diameter ratio (L/d) of 400 was necessary to measure temperature fluctuations with an accuracy of 5% while for tungsten wires a length to diameter ratio of 800 was required.

The probe used was a TSI 1261A - P.5 miniature boundary layer probe which has been modified by TSI. The original TSI 1261A - T1.5 probe was modified by replacing the 5 μm diameter x 1.5 mm length tungsten wire ($L/d = 300$) with a 1.25 μm dia. x 0.5 mm length platinum wire ($L/d = 400$). For the 3-D TBL test case, this wire length corresponds to 26 viscous units in the approach boundary layer. A Dantec 56C01 anemometer with a Dantec 56C20 constant-current bridge was used to provide a constant 0.2 mA current to the probe. The frequency response of the wire was measured by both an external heating method and a current injection method described in Appendix A. The wire frequency response was flat up to approximately 2 kHz at all velocities and turbulence intensities of interest.

2.3.5 Data Acquisition

Data were sampled for all three test cases by an HP 3562A Dynamic Signal Analyzer. The HP 3562A has a 14-bit digitization resolution over a range which is adjustable from ± 31 V to ± 3.99 mV. The sampling rate is adjustable from 26.21 mHz to 256 kHz. The HP3562A samples data at fixed rate of 256 kHz and uses a digital filter to adjust the data to slower sampling frequencies. In this way only one fixed analog filter is required to provide anti-aliasing protection at all sampling frequencies.

In the A/D mode, the HP 3562A collects data from one or two channels, each in blocks of 2048 samples each, and records the data in binary form on a 3.5 inch floppy disk. The HP 3562A has a fast Fourier transform processor which provides real-time time domain to frequency domain transformation and a floating point processor which allows real-time frequency-domain data processing to be performed.

2.4 Experimental Technique

To keep daily conditions as uniform as possible, the wind tunnel, heated floor, and laboratory air conditioner were always run for approximately 30 minutes before taking data to allow the free-stream temperature to stabilize. For all of the measurements made, the free-stream temperature was held constant at 25 ± 1 °C. The heated floor of the tunnel was held constant and uniform at 45 ± 0.5 °C except near the leading edge of the heated floor. (See chapter 3 for complete flow documentation.) Dynamic pressure of the wind

tunnel was monitored by a pitot-static probe located at the throat of the wind tunnel, 1.63 m downstream of the test section entrance. The daily atmospheric pressure was approximately 945 ± 10 mb. Small changes in U_{ref} , and T_∞ were constantly updated as measurements were made. Tunnel speed was adjusted to keep the reference dynamic pressure constant. Post processing of data was performed on an IBM RT work station and a 50 MHz 80486 based microcomputer using codes written in FORTRAN.

2.4.1 Wing/Body Junction Vortex Flow

The heat transfer in the nose region of a wing/body junction was studied experimentally by making time- and spatially-resolved surface heat flux measurements on the endwall surface in the nose region of a wing/body junction formed by a wing and a flat plate. The wing is mounted on the test section floor at zero angle of attack and zero sweep. The nominal air speed in the test section upstream of the wing is 32.5 m/s and the momentum thickness Reynolds number Re_θ measured 215.8 mm upstream of the nose of the wing with the wing in place is 3730.

Data are presented in the coordinate system (shown in Fig. 1.2) defined as having the x axis parallel to the wind-tunnel centerline and positive in the downstream direction. The y axis is normal to the test wall and positive away from the wall. The z axis completes a right-hand coordinate system. The origin of the coordinate system is located at the junction between the wing leading edge and the test section floor.

Mean surface heat flux measurements were taken with the Schmidt-Boelter gage

at the 60 locations along the 7 lines on the floor in front of the modified NACA 0020 model shown in Fig. 2.8. The lines are numbered clockwise from the line of symmetry. Lines 1, 4, 6, and 7 correspond to the same locations where Devenport and Simpson (1990 a) made 3-component velocity profile measurements for a thick approach boundary layer ($Re_\theta = 6700$). The Schmidt-Boelter gauge was also used to measure mean surface heat flux on the centerline upstream of the other two models at the same locations where Ölçmen and Simpson (1994) measured pressure fluctuations. Time-resolved heat flux measurements were made with the heat flux microsensor along the centerline upstream of each of the three models. Measurement locations are summarized for the modified NACA 0020 model, the streamlined cylinder, and NACA 0015 model in Tables 2.2, 2.3, and 2.4 respectively.

Output from the thermocouples used to measure the free-stream temperature and wall temperature was monitored by a Doric Model 410 thermocouple readout. The cam yaw angles were adjusted from outside the tunnel so that both the tunnel and the heaters remained on throughout the test. After moving the heat flux gauge to a new location, approximately 5 min were allowed for the heat flux gauge to reach thermal equilibrium in the new location.

The signal from the Heat Flux Microsensor was amplified 1000 times by Vatel AMP-4 amplifier and sampled by the HP 3562A Dynamic Signal Analyzer at a frequency of 10240 hz. The input range of the HP 3562A was set to ± 100 mV. One hundred segments of 2048 samples were taken over a period of approximately 1 min and recorded on floppy disk for post-processing. Output from the RTS on the Heat Flux Microsensor

was amplified 500 times and read by an HP multimeter.

The output voltage from the Schmidt-Boelter gage was amplified 1000 times by a Tektronix AM 502 differential amplifier and filtered by a 300 Hz low-pass filter. The signal was sampled at a frequency of 600 Hz and recorded by an IBM PC AT using a 12 bit Data Translation DT2801A A/D converter.

2.4.2 Three-Dimensional Turbulent Boundary Layer Flow

The pressure-driven three-dimensional turbulent boundary layer upstream of a wing/body junction was studied experimentally by making simultaneous time-resolved temperature and surface heat flux measurements. The wing is mounted on the test section floor at zero angle of attack and zero sweep. The nominal air speed at the test section throat upstream of the wing is 27.5 m/s and the momentum thickness Reynolds number Re_θ measured 228.6 mm upstream of the nose of the wing with the wing in place is 6960. Data are presented in three different coordinate systems shown in Fig. 1.4. The wind tunnel coordinate system (TC) is defined as having the x axis parallel to the wind-tunnel centerline and positive in the downstream direction. The y axis is normal to the test wall and positive away from the wall. The z axis completes a right-hand coordinate system. The origin of the tunnel coordinate system is located at the junction between the wing leading edge and the test section floor. The local free-stream coordinate system (FS) has its y axis coincident to the tunnel coordinate system y axis and its x axis pointing in the direction of the local free-stream velocity vector, parallel to the tunnel floor. The z axis

completes a right-hand coordinate system. The local wall-stress coordinate system (WC) has its y axis normal to the tunnel wall, its x axis parallel to the local wall shear-stress vector and its z axis completing a right-hand coordinate system.

Surface heat flux and temperature profiles were measured at 8 locations shown in Fig. 1.4, where Ölçmen and Simpson (1990, 1995a) made three-component velocity measurements using a fibre-optic laser-Doppler velocimeter and where Ha and Simpson (1993) used a variety of multiple sensor hot-wire/hot-film probes to study the coherent structure. Following Ölçmen and Simpson (1990), the locations will be referred to as stations #0 through #7 starting with the most upstream location. As explained by Ölçmen and Simpson, these stations lie along a line determined by the mean velocity vector component parallel to the wall in the layer at a location where the $\overline{u^2}$ kinematic normal stress is maximum. The measurement locations, in tunnel coordinates, are summarized in Table 2.5. This test case is unique in that the flow is subjected to a strong spanwise pressure gradient which changes sign for the downstream locations. Initially, the spanwise pressure gradient turns the flow away from the wing. Further downstream, the spanwise pressure gradient changes sign and turns the flow back toward the wing. Both adverse and favorable streamwise pressure gradients also occur. The important flow parameters at the measurement stations obtained by Ölçmen and Simpson (1995 a) and Ailinger (1991) are given in Table 2.6.

At each measurement station, the heat flux microsensor was press fit into a 25.4-mm-diameter, 6.4-mm-deep hole milled in the heated floor of the tunnel. A thin layer of zinc-oxide heatsink ointment was applied to the outside perimeter of the heat flux

microsensor substrate to ensure good thermal contact between the heat flux gage and the floor. The holes at the other measurement stations were filled with aluminum plugs. The cold wire was positioned directly above the heat flux microsensor and aligned parallel to the wall and perpendicular to the local free-stream velocity vector. Temperature measurements were started nearest the wall and traversed outward. The initial location of the wire was determined using a cathetometer to measure the distance between the wire and its reflected image from the tunnel floor. Temperature measurements were made at approximately 30 logarithmically spaced locations across the boundary layer at each of the 8 stations.

While taking data, the heaters were turned off to reduce electrical noise in the heat flux signal. Data collection took approximately one minute. During this time the surface temperature of the wall and the heat flux gage fell approximately 1 °C. The trend removal algorithm described by Bendat and Piersol (1986, pp. 362 - 365) was used to correct the data for temperature drift. Approximately 15 min were required to reheat the wall and reach thermal equilibrium between each measurement.

Output from the thermocouples used to measure the free-stream temperature and wall temperature was monitored by a TEGAM thermocouple readout. The heat flux signal from the Heat Flux Microsensor was amplified 1000 times and the RTS signal was multiplied 500 times by a Vatell AMP-5 amplifier. The signal from the RTS was read by an HP multimeter. The cold-wire and heat-flux signals were sampled simultaneously by an HP 3562A Dynamic Signal Analyzer. The input range for the cold wire was ± 12.6 V and the input range for the heat flux signal was ± 15.9 mV. Sixty segments of 2048

samples of each signal were taken at a frequency of 10240 hz and recorded on floppy disk for post-processing. Spectral analysis was performed in real time by the HP 3562A. Two hundred ensemble averages of the heat flux and temperature power spectra, co-spectra, and coherence were calculated from segments of 2048 samples of each signal at a sampling frequency of 10240 hz and recorded.

2.4.3 Two-Dimensional Separating Turbulent Boundary Layer Flow

Data are presented in the coordinate system defined as having the x axis parallel to the wind-tunnel centerline and positive in the downstream direction. The y axis is normal to the test wall and positive away from the wall. The z axis completes a right-hand coordinate system. The origin of the coordinate system is located on the centerline of the test section floor at the entrance to the test section.

All measurements were performed at a reference speed of 21.9 m/s measured at the throat of the tunnel. Surface heat flux and temperature profiles were measured at 14 streamwise locations in the adverse-pressure-gradient region downstream of the throat. The streamwise locations of the measurements are summarized in Table 2.7. At each streamwise station, the heat flux microsensor was press fit into a hole milled in the heated floor of the tunnel. Zinc oxide heat sink paste was used to ensure good thermal contact between the heat flux gauge and the floor. The cold wire was aligned parallel to the wall and perpendicular to the freestream directly above the heat flux microsensor. Temperature measurements were made at approximately 30 logarithmically space locations across the

boundary layer at each streamwise location. Temperature measurements were started nearest the wall and traversed outward. The initial location of the wire was measured with a cathetometer.

Output from the thermocouples used to measure the free-stream temperature and wall temperature was monitored by a TEGAM thermocouple readout. The heat flux signal from the Heat Flux Microsensor was amplified 5000 times and the RTS signal was multiplied 500 times by a Vatel AMP-6 amplifier. The signal from the RTS was read by an HP multimeter. Due to the long sampling time required to resolve the low-frequency large-scale unsteadiness that occurs in the separated region of this flow, the heaters were left on during data collection. To reduce noise caused by the heaters, the signal from the cold wire was passed through a unity-gain amplifier with a -5 Volt offset, which made it possible to decrease the digitization range by a factor of 10. The cold-wire and heat-flux signals were sampled simultaneously by a HP 3562A Dynamic Signal Analyzer. The input range for the cold wire was ± 1 V and the input range for the heat flux signal was ± 100 Mv. In the separating region, downstream of $x = 400$ cm, 60 segments of 2048 samples of each signal were taken at a frequency of 409.6 hz and recorded on floppy disk for post-processing. Upstream of $x = 400$ cm, 60 segments of 2048 samples of each signal were taken at a frequency of 1024 hz and recorded on floppy disk. Spectral analysis was performed in real time at all streamwise locations by the HP 3562A. One thousand ensemble averages of the heat flux and temperature power spectra, co-spectra, and coherence were calculated from segments of 2048 samples of each signal at a sampling frequency of 10240 hz and recorded.

2.5 Data Reduction and Signal Processing

2.5.1 Post Processing of Time-Series Data

Heat transfer coefficients h were calculated from the measured heat-flux after subtracting the radiated heat flux using

$$h = \frac{E/S - \eta_g \sigma (T_g^4 - T_\infty^4)}{T_g - T_\infty} \quad (2.1)$$

where E is the output voltage of the heat flux gage, S is the sensitivity of the gage, η_g is the emissivity of the gage, and σ is the Boltzman constant. The convection heat transfer coefficients were converted to Stanton numbers where C_p and ρ were evaluated at the film temperature. The emissivity of the Schmidt-Boelter gauge was 0.97. The emissivity of the Heat Flux Microsensor was not precisely known and was assumed to be approximately 0. However, due to the small temperature difference between the heated wall and the free-stream air, the heat flux due to radiation was less than the uncertainty in the measurement of total heat flux.

The mean μ , standard deviation σ , skewness factor S , and flatness factor F of the temperature and heat flux were computed from the time records using (Tennekes and Lumley, 1972):

$$\mu = \frac{1}{N} \sum_{n=1}^N x_n \quad (2.2)$$

$$\sigma = \frac{1}{N} \sum_{n=1}^N (x - \mu)^2 \quad (2.3)$$

$$S = \frac{\frac{1}{N} \sum_{n=1}^N (x - \mu)^3}{\sigma^{3/2}} \quad (2.4)$$

$$F = \frac{\frac{1}{N} \sum_{n=1}^N (x - \mu)^4}{\sigma^2} \quad (2.5)$$

where x is the digitized data (either temperature or heat flux) and N is the total number of samples.

Histograms of the signals were computed by breaking the discretization range into 4096 bins counting the number of samples that fall within each bin. The probability density was then computed by normalizing the histogram so that the area under the histogram is equal to 1. The value of the probability density for a given bin represents the probability of finding the signal in that bin. The probability density is always positive.

The long time-averaged time-delayed cross-correlation coefficient between two signals $x(t)$ and $y(t)$, defined:

$$R_{xy}(\tau) = \frac{\overline{x(t+\tau)y(t)}}{\sqrt{\overline{x(t)^2}} \sqrt{\overline{y(t)^2}}}. \quad (2.6)$$

is a measure of the correlation between the signal $y(t)$ and the time-delayed signal $x(t+\tau)$. R_{xy} has a value between 1 and -1 with a value of 1 indicating perfect correlation, a value of 0 indicating no correlation, and a value of -1 indicating perfect correlation but 180° out of phase. A maximum value of R_{xy} occurring for a positive value of τ indicates that $x(t)$ lags $y(t)$.

2.5.2 Burst Detection Algorithms

Several algorithms were used with the cold-wire signals to detect the occurrence of a sweep/ejection event. The variable interval time average (VITA) algorithm of Blackwelder and Kaplan (1976) detects coherent motions from the high level of variance of the streamwise velocity component associated with sweep/ejection events. Chen and Blackwelder (1978) used the technique on the output of a cold wire used to measure temperature and obtained results similar to Blackwelder and Kaplan. The technique in its functional form is given by

$$\text{VAR}(t) = [\theta^2] - [\theta]^2 \quad (2.7)$$

where

$$[\theta(t)] = \frac{1}{T} \int_{t-T/2}^{t+T/2} \theta(t) dt. \quad (2.8)$$

The detection function $D(t)$ is defined as

$$\begin{aligned} D(t) &= 1 \quad \text{if } \text{VAR}(t) > k\overline{\theta^2}, \\ &= 0 \quad \text{otherwise,} \end{aligned} \quad (2.9)$$

where the detection function equals 1 during a sweep/ejection event. Blackwelder and Kaplan recommended $0.9 < k < 1.2$ and $T = 10v/U_t^2$.

For the modified u-level burst-detection algorithm described by Luchik and Tiederman (1987), the detector function is turned on ($D(t) = 1$) when

$$\theta(t) < -L\sqrt{\overline{\theta^2}} \quad (2.10)$$

and turned off ($D(t) = 0$) when

$$\theta(t) \geq -0.25L\sqrt{\overline{\theta^2}}. \quad (2.11)$$

Luchik and Tiederman recommended $0.5 < L < 1.25$.

Once the detection function $D(t)$ has been determined, the ensemble average of the temperature during a sweep/ejection event is determined from

$$\langle \theta(\tau) \rangle = \frac{1}{N} \sum_{j=1}^N \theta(t_j + \tau), \quad (2.12)$$

where the time t_j is taken to be midway between the beginning and end of the period during which $D(t) = 1$.

2.5.3 Processing of Spectral Data

Spectral estimates were performed in real time by the HP 3562A Dynamic Signal Analyzer for the 3-D TBL and 2-D separating TBL test cases. For the wing/body junction test case, spectral estimates were computed by post-processing the digitized time-series data using algorithms from Bendat and Piersol (1986).

The power spectrum of a time-dependent signal, $x(t)$ is computed from

$$G_{xx}(f) = X(f)X^*(f) \quad (2.13)$$

where $X(f)$ is the complex Fourier Transform of $x(t)$ at frequency f and $X^*(f)$ is the complex conjugate of $X(f)$. The power spectrum represents the frequency distribution of x^2 and satisfies

$$\overline{x^2} = \int_{-\infty}^{\infty} G_{xx}(f) df. \quad (2.14)$$

The cross spectrum between two time-dependent signals $x(t)$ and $y(t)$ is defined

$$G_{xy}(f) = X(f)Y^*(f) \quad (2.15)$$

which is, in general, a complex number. The phase shift between $x(t)$ and $y(t)$ is determined from

$$\Phi_{xy}(f) = \tan^{-1} \left(\frac{Q_{xy}(f)}{C_{xy}(f)} \right) \quad (2.16)$$

where $Q_{xy}(f)$ and $C_{xy}(f)$ are the imaginary and real parts of $G_{xy}(f)$, respectively. A positive value of Φ_{xy} indicates that $x(t)$ lags $y(t)$.

The coherence function between $x(t)$ and $y(t)$ is defined

$$\gamma^2(f) = \frac{G_{xy}(f) G_{yx}(f)}{G_{xx}(f) G_{yy}(f)} \quad (2.17)$$

and represents the correlation between $x(t)$ and $y(t)$ at frequency f with the effects of phase removed. The value of $\gamma^2(f)$ ranges between 0 (no correlation) and 1 (perfect positive correlation).

If $x(t)$ and $y(t)$ represent quantities measured at two locations in a turbulent flow, then $\gamma^2(f)$ will be a function of the spacing between the two locations, Δs . The coherency, which is a function of f and Δs , will equal 1 for $\Delta s = 0$ and decreases as Δs increases. Ha and Simpson (1993) defined a coherence length scale for turbulent flow, $L_\gamma(f)$ as the distance Δs where the coherence between $x(t)$ and $y(t)$ becomes statistically insignificant. Ha (1993) chose this critical value as $\gamma_{cr}^2 = 0.27$. The coherence length scale is then defined as

$$L_\gamma(f) = \Delta s_{xy} \text{ where } \gamma_{xy}^2(f, \Delta s_{xy}) = 0.27. \quad (2.18)$$

2.6 Uncertainty Analysis

All uncertainties presented were estimated at 20:1 odds. The uncertainty of a quantity which is a function of several measured variables was estimated from the combined uncertainties of the measured variables using the method from Kline and

McClintock (1953) described below.

For a quantity R which is a function of n independent variables of the form:

$$R = R(x_1, x_2, \dots x_n) \quad (2.19)$$

where the uncertainties in $x_1, x_2, \dots x_n$ are $\delta x_1, \delta x_2, \dots \delta x_n$ respectively, at the same odds, the uncertainty in R is given by:

$$\delta R = \sqrt{\left(\frac{\partial R}{\partial x_1} \delta x_1\right)^2 + \left(\frac{\partial R}{\partial x_2} \delta x_2\right)^2 + \dots + \left(\frac{\partial R}{\partial x_n} \delta x_n\right)^2} \quad (2.20)$$

The uncertainty in the mean and root mean-squared value of temperature and surface heat flux was computed from the sum of contributions from uncertainty due to finite sample size and uncertainty due to random error in calibration. The uncertainty due to finite sample size was estimated using the standard formulae given by Bendat and Piersol (1986). For a quantity R , the $100(1-\alpha)\%$ confidence intervals for the mean value estimate, is:

$$\delta \bar{R} = \frac{\sqrt{\bar{r}^2} z_{\alpha/2}}{\sqrt{N}} \quad (2.21)$$

and the uncertainty in the estimate of the variance is given by:

$$\delta \bar{r}^2 = \left(\frac{N-1}{\chi_{n,1-\alpha/2}^2} - 1 \right) \bar{r}^2. \quad (2.22)$$

where z_{α} is the standardized normal random variable and N is the number of samples.

The uncertainties due to random error in the linear calibrations were estimated using the method described by Doeblin (1990). For a linear least squares regression between an independent input variable q_i and a dependent output variable q_o of the form:

$$q_o = mq_i + b \quad (2.23)$$

the confidence intervals of the output q_o , the static sensitivity m , and the y-intercept b , are given by:

$$\delta q_o = z_{\alpha/2} \sqrt{\frac{1}{N_c} \sum (mq_i + b - q_o)^2} \quad (2.24)$$

$$\delta m = z_{\alpha/2} \sqrt{\frac{N_c s_{q_o}^2}{N_c \sum q_i^2 - (\sum q_i)^2}} \quad (2.25)$$

$$\delta b = z_{\alpha/2} \sqrt{\frac{s_{q_o}^2 \sum q_i^2}{N_c \sum q_i^2 - (\sum q_i)^2}} \quad (2.26)$$

where N_c is the number of data points in the calibration and $z_{\alpha/2}$ is the standardized normal random variable for a $100(1-\alpha)\%$ confidence interval. Confidence intervals for the estimates of mean and rms measurements are presented in Table 2.8.

Uncertainties of the spectral results were estimated using the formulas of Bendat and Piersol (1986). The normalized $100(1-\alpha)\%$ uncertainties of the power spectrum, cross

spectrum, coherence function, and phase shift are given by eqns. (2.27), (2.28), (2.29), and (2.30), respectively:

$$\frac{\delta G_{xx}}{G_{xx}} = \frac{z_{\alpha/2}}{\sqrt{n_d}} \quad (2.27)$$

$$\frac{\delta G_{xy}}{G_{xy}} = \frac{z_{\alpha/2}}{\gamma_{xy}\sqrt{n_d}} \quad (2.28)$$

$$\frac{\delta \gamma^2}{\gamma^2} = \frac{z_{\alpha/2}\sqrt{2(1-\gamma_{xy}^2)}}{\gamma_{xy}\sqrt{n_d}} \quad (2.29)$$

$$\frac{\delta \Phi_{xy}}{\Phi_{xy}} = \frac{z_{\alpha/2}\sqrt{(1-\gamma^2)}}{\gamma\sqrt{2n_d}} \quad (2.30)$$

Normalized 95% confidence intervals for the spectral results are given in Table 2.9 for the 3-D TBL test case and in Table 2.10 for the 2-D separating TBL test case.

The 95% confidence interval for the coherence length scale was estimated from:

$$\delta L_\gamma = \frac{\delta \gamma_{0.27}^2}{\left| \frac{d\gamma^2}{dy} \right|} \quad (2.31)$$

where $\delta \gamma_{0.27}^2$ is the 95% confidence interval in γ^2 at $\gamma^2=0.27$. The derivative in Eq. (2.31) was estimated by fitting a parabola through 5 consecutive data points using a least squares method and then evaluating the derivative of this curve fit at the central (third) point. For the 3-D test case, the uncertainty in L_γ was approximately 1.4 mm.

Uncertainty in sensor coordinates x , z was 0.5 mm. Uncertainty in the estimate starting location from the wall was 0.08 mm. The uncertainty in increments in y -locations was 0.03 mm.

3 Flow Validation

3.1 Wing/Body Junction Vortex Flow

For the wing/body junction test case, the approach boundary layer velocity profile upstream of the wing/body junction was measured to ensure that the test section with the heated false floor had the same flow characteristics as the test section with the false floor used by Devenport and Simpson (1990 a) and Ölçmen and Simpson (1994). The mean and fluctuating streamwise velocity profile was measured 215.8 mm upstream of the nose of the modified NACA 0020 wing. A TSI model 1218.T15 boundary layer probe was used for the measurements. The probe was operated with an AA LAB SYSTEMS model AN-1003 anemometer with a resistance ratio of approximately 1.7.

The probe was calibrated in the free stream against a pitot tube. The output was sampled with an RC ELECTRONICS A/D board model ISC-16 operating with an IBM PC-AT microcomputer. The constants A, B, and n in the King's law

$$E^2 = A + BU^n \quad (3.1)$$

were calculated by applying a least squares fit to the measured voltage E and velocity U. The least squares procedure was repeated for different values of the exponent n to obtain the maximum correlation coefficient. The linearized signal produced a correlation

coefficient in excess of 0.99999.

The velocity profile was measured by traversing the probe from a y location of 0.25 mm to 50.8 mm in twenty-five logarithmically spaced steps. At each y location, the output of the anemometer was sampled at 4 kHz for a record length of 20 s by the A/D board and logged onto the hard disk of the computer.

The skin friction was estimated by fitting the data to the semi-logarithmic law of the wall

$$U^+ = \frac{1}{\kappa} \ln(y^+) + C \quad (3.2)$$

where $\kappa = 0.41$ and $C = 5.0$ (Coles and Hirst, 1968). The friction velocity was estimated to be 1.32 m/s. The velocity profile was then numerically integrated, assuming a linear velocity variation in the sublayer, to obtain the momentum and displacement thickness. The nominal free-stream velocity was 32.3 m/s with a Reynolds number based on momentum thickness of 3730. The momentum thickness was 1.9 mm and the displacement thickness was 2.6 mm.

3.2 Three-Dimensional Turbulent Boundary Layer Flow

The streamwise velocity in the potential core of the test section was measured after the upper wall of the test section was raised to verify that the streamwise pressure gradient was zero. Velocity measurements were made using a TSI model 1210-T1.5 probe. The probe was operated with a DANTEC 56C01 constant temperature anemometer

at a resistance ratio of 1.7. The output of the anemometer was connected to a buck and gain amplifier. A dc component was subtracted from the signal and the signal was amplified by a gain of 20. The signal was sampled by a DATA Translation DT 2801A 12-bit A/D board installed in a PC. Calibrations were made on a TSI model 1125 calibrator at various flow speeds using the procedure described in section 3.1.

The probe was mounted on a cart at a 45° angle relative to the freestream at a position 10.47 cm above the test section floor. The cart was traversed in the streamwise direction using fishing line. The streamwise variation of velocity is shown in Figure 3.1. Also shown in Fig. 3.1 is the streamwise variation in velocity measured before the heated floor was installed (Devenport and Simpson, 1990 a).

The approach boundary layer velocity profile was measured at a location 0.75 chord lengths upstream of the nose of the modified NACA 0020 tailed wing with the wing in place. A TSI 1218-T1.5 boundary layer probe was used. The probe was traversed from a y location 0.020 cm to 7.62 cm in 30 logarithmically spaced steps. At each y location, the output of the anemometer was sampled at 1000 Hz for a length of 20 seconds. The data were fit to Eq. (3.2) by selecting U_τ such that $u^+ = 16.23$ at $y^+ = 100$. A value of $U_\tau = 0.978$ m/s was obtained for a boundary layer edge velocity of 27.4 m/s.

With the value of U_τ known, a total of 25 points were fitted between $y^+ = 0$ and $y^+ = 25$ in steps of $\Delta y^+ = 1$. The augmented velocity profile was then integrated numerically using a simple trapezoidal rule. The displacement and momentum thicknesses were 5.93 mm and 4.29 mm, respectively. The momentum thickness Reynolds number at a free-stream velocity of 27.4 m/s was 6960.

The boundary layer momentum thickness was estimated from the measured streamwise velocity variation to confirm velocity measurements. For favorable and zero-pressure gradient flows, the momentum thickness may be obtained from (Kays and Crawford, 1980):

$$\theta(x)^{5/4} U_{\infty}(x)^{4.11} v^{-1/4} - \theta(x_0)^{5/4} U_{\infty}(x_0)^{4.11} v^{-1/4} = 0.016 \int_{x_0}^x U_{\infty}(x)^{3.86} dx \quad (3.3)$$

where x_0 refers to conditions measured at the entrance to the test section. The momentum thickness at the test section entrance, $\theta(x_0)$, was estimated by taking a control volume around the initial step used to trip the flow. A force balance gives:

$$\text{Drag/unit width} = \rho \int_0^{\infty} U(y)[U_{\infty} - U(y)] dy = \theta \rho U_{\infty}^2 \quad (3.4)$$

Substituting $D = C_D (.5 \rho U_{\infty}^2) h$ into the above equation gives:

$$\theta = \frac{C_D h}{2} \quad (3.5)$$

Substituting the drag coefficient for a forward-facing step (Schlichting, 1968), $C_D = 0.5$ and $h = 6.35$ mm into Equation (3.5) gives $\theta_0 = 1.59$ mm.

The measured streamwise velocity variation was integrated using Eqn. (3.3) to obtain a momentum thickness $\theta = 4.03$ mm at the x -location where the velocity profile was measured. The Streamwise velocity variation reported by Devenport and Simpson (1990 a) was integrated to obtain $\theta = 4.02$ mm at the same location. These values compare favorably with the measured momentum thickness of $\theta = 4.29$ mm.

The spanwise skin-friction distribution was measured 0.75 chord lengths upstream

of the modified NACA 0020 wing with a 0.0508-cm-diameter Preston tube to verify that the approach boundary layer was uniform. Measurements were made at spanwise increments of 5 cm. The pressure difference from the Preston tube was measured by a Setra model 239 pressure transducer. The pressure difference was converted to a surface shear stress by

$$\frac{\Delta p}{\tau_w} = F\left(\frac{\Delta p d^2}{\rho \nu^2}\right) \quad (3.6)$$

where Δp is the measured pressure difference, d is the outer diameter of the Preston tube, ρ is the density, and ν is the viscosity of air. The function F in Eqn. (3.6) was obtained in Tabular form from Winter (1977). The spanwise variation of the shear stress coefficient is shown in Fig 3.2. The Shear stress is uniform in the spanwise direction and agrees with the skin friction coefficient obtained from the velocity profile.

3.3 Two-Dimensional Separating Turbulent Boundary Layer Flow

Tufts of yarn were taped to the upper and side walls of the test section to verify that boundary layer separation occurred only on the test section floor. Sawdust was used to verify that separation occurred at the correct streamwise location and that the separation line was reasonably two-dimensional and was comparable to the earlier setup and observations of Simpson et al. (1980) of the same flow. A thin layer of fine sawdust was spread evenly over the test section floor near the vicinity of the separation. After

running the tunnel for a few minutes, the sawdust accumulated in the pattern sketched in Fig. 3.3. The sawdust pattern shows that the separation occurs at a streamwise location $x \approx 343$ cm and is two-dimensional across the inner 75% of the test section.

The streamwise velocity variation in the potential core of the test section was measured using the same technique and equipment as in the 3-D TBL test case. A TSI model 1210-T1.5 probe was mounted on the cart a 0° angle to the free stream at a position 15 cm above the test section floor. In the separated region, the position of the probe was raised to keep the probe in the potential core. The measured streamwise velocity variation in the test section is compared to the velocity variation reported by Simpson et al. (1980) in Fig. 3.4. Figure 3.5 shows the variation in streamwise pressure gradient

$$\frac{dC_p}{dx} = -2U_\infty \frac{dU_\infty}{dx} \left(\frac{1}{U_{\infty,i}} \right)^2 \quad (3.7)$$

where the pressure coefficient C_p is defined:

$$C_p = 1 - \left(\frac{U_\infty}{U_{\infty,i}} \right)^2 \quad (3.8)$$

and $U_{\infty,i} = 15.06$ m/s is the value of the free-stream velocity at the test section entrance.

Boundary layer velocity profiles of mean and fluctuating streamwise velocity were measured using the same equipment and techniques used in the 3-D TBL test case. Measurements of mean and fluctuating streamwise velocity measured at the test section throat, $x = 163.2$ cm are compared with previous measurements (Simpson et al., 1981 a)

in Figures 3.6. and 3.7. respectively. Agreement is very good except that the maximum turbulence intensity in the buffer region is slightly higher than previously reported. Mean and fluctuating streamwise velocity profiles measured just upstream of incipient detachment, at $x = 300.4$ cm, are compared with velocity profiles from Simpson et al. (1981 a) in Fig. 3.8 and 3.9 respectively. Agreement is extremely good and within measurement uncertainties. The mean velocity profiles shown in Fig. 3.6 and 3.8 were numerically integrated (assuming linear velocity variation from the wall to the inner-most point) to obtain the momentum and displacement thicknesses. Boundary layer thicknesses $\delta_{0.995}$ were estimated by fitting a parabola through the outer 10 points and determining where the parabola passed through $U/U_\infty = 0.995$. The skin friction coefficient was estimated from a Clauser plot shown in Fig. 3.10 and from the Ludwig-Tillman equation:

$$C_f = 0.246 \times 10^{-0.678H} \text{Re}_\theta^{-0.268} \quad (3.9)$$

where $H = \delta^*/\theta$ is the shape factor. The skin friction coefficient was also estimated by fitting the data to the semi-logarithmic law, Eq. (3.2), as shown in Fig. 3.11. Skin friction estimates from all three methods agreed to within 0.8 %. The boundary layer characteristics at $x = 163.2$ cm and $x = 300.4$ cm are summarized in Table 3.1 and 3.2 respectively.

The boundary layer velocity was measured in the separated flow outer region, at $x = 351.47$ cm and $x = 397.19$ cm at y locations above the near-wall region where mean flow reversal occurs. Mean and fluctuating velocity profiles at $x = 351.47$ cm are compared with previous measurements (Simpson et al., 1980) in Figs. 3.12 and 3.13,

respectively. Skewness and flatness factors of the velocity are shown in Figs. 3.14 and 3.15, respectively. The same measurements made further downstream at $x = 397.19$ cm are shown in Fig. 3.16 - 3.19. The boundary layer thicknesses estimated from the mean velocities shown in Fig. 3.12 and 3.16 are compared with previous results in Table 3.3 and 3.4.

A Preston tube was used to measure the streamwise variation of skin friction in the test section upstream of detachment. The same technique used for the 3-D TBL test case was repeated. The surface skin friction coefficient is compared to the results reported by Simpson et al. (1981) in Fig. 3.20. Also shown are the skin friction estimates from the Ludwig-Tillman equation, Eqn. (4.5).

All of the data collected agrees with the data with Simpson et al. (1981a,b) within the confidence intervals of the data. We assume therefore in the absence of any data in the backflow region, that the flow has been reproduced. The locations of insipient detachment, intermittent transitory detachment and transitory detachment are assumed to be the same as in the flow of Simpson et al., although no measurements are available to validate this assumption. The location of detachment is based on the observed sawdust pattern and on the velocity profiles approaching detachment and above the backflow region downstream of detachment. Every effort possible was made to keep ambient temperature and tunnel dynamic pressure constant to prevent wandering of the time-mean detachment point.

3.4. Heat Flux Surface Validation

The streamwise variation in normalized surface temperature for the heated floor of the tunnel is shown in Fig. 3.21. Except near the leading edge of the heated section, the temperature is uniform to within ± 0.5 °C. For the wing/body junction vortex test case, the location of a "virtual origin" was estimated from the measured boundary layer profile from (Kays and Crawford, 1980):

$$(\theta/x) = 0.036\text{Re}_x^{-0.2} \quad (3.10)$$

The virtual origin was 1 cm downstream of the leading edge of the false floor. The unheated starting length ξ was approximately 5 cm and was therefore negligible at the locations where surface heat flux was measured. The Stanton number at the most upstream heat flux measurement location (75.24 mm upstream of the nose of the wing) was calculated from (Kays and Crawford, 1980):

$$\text{St} = 0.0287(\text{Pr}^{-0.4})\text{Re}_{x_v}^{-0.2} \left[1 - \left(\frac{\xi}{x_v} \right)^{9/10} \right]^{-1/4} \quad (3.11)$$

where x_v is measured from the virtual origin. The Stanton number at $x_{\text{TC}} = -75.24$ mm ($x_v = 1077$ mm) was $\text{St} = 1.837 \times 10^{-3}$. The Stanton number measured at this location with the Schmidt-Boelter gauge was 1.84×10^{-3} .

The surface heat flux in the zero-pressure-gradient region of the test section used for the 3-D TBL test case with the wing removed was measured with the heat flux microsensor. The location of a virtual origin was estimated from the momentum thickness

and the Stanton number distribution was estimated from Eqn. (3.11). Figure 3.22 shows a comparison of the measured Stanton numbers with Eqn. (3.11). The good agreement shows that the heat surface obeys the zero-pressure-gradient constant temperature flat plate heat transfer relations.

4 Results and Discussion for Wing/Body Junction Vortex Flow

Experimental results are presented using the coordinate system shown in Fig. 1.2. Lengths are normalized using the distance from the model leading edge to the location of the primary separation line measured from oil-flow visualizations (Ölçmen and Simpson, 1994) presented in Table 2.1. Note that this distance is different for each model.

4.1 Mean Surface Heat Flux

Mean heat flux measurements were obtained from the Schmidt-Boelter gage. Contours of constant Stanton number are shown in Fig. 4.1 for the modified NACA 0020 model. The Stanton numbers, non-dimensionalized on the upstream free-stream velocity, represent lines of constant heat transfer coefficient. The region of the flow close to the wing is an area of high heat flux created by the presence of the horseshoe vortex. This high heat flux is the result of both highly turbulent mixing created by the vortex and cold free-stream air transported by the vortex down the front of the wing perpendicular to the endwall. The locations of maximum levels of heat flux were close to the wing, at the

wing/endwall junction. Upstream of the wing, the Stanton numbers approach the 2-D, zero pressure gradient boundary layer Stanton number, $St = 0.00184$, calculated using $St Pr^{0.4} = 0.0287 Re_x^{-0.2}$ and the estimated location of the virtual origin.

Distributions of mean surface heat flux on the centerline upstream of each model are shown in Fig. 4.2. The heat flux enhancement begins close to the separation line ($x/x_{sep} = -1.0$) for each model tested. Downstream of separation, the heat flux increases rapidly as the wing is approached, reaching a level almost 100 percent higher than in the approach boundary layer. This initial rise is followed by a plateau in the heat flux distributions. The heat flux levels attained here are approximately the same for the three models tested. For the modified NACA 0020 and the NACA 0015 models, this plateau appears to be centered around the line of low shear, at $x/x_{sep} = -0.60$ and $x/x_{sep} = -0.53$ respectively. An inflection point in the plot of Stanton number versus x/x_{sep} occurs just downstream of the line of low shear, approximately below the vortex center, followed by a second rapid increase in heat flux. The maximum value of Stanton number was found at the closest measurement location to the wing, where the maximum Stanton number measured was 0.0054, a 200 percent increase over the value measured in the approach boundary layer. For the tapered cylinder model, the plateau in heat flux extends into the wing/endwall junction with no second rise in heat flux.

4.2 Statistical Description of Surface Heat Flux

4.2.1 Surface Heat Flux Fluctuations

Fluctuations in endwall surface heat flux presented here were measured using the Heat Flux Microsensor. The fluctuating component of heat flux measured along the centerline in front of each model is shown in Fig 4.3. The fluctuations in heat flux increase rapidly after the separation line and reach a maximum value near the line of low shear. Fluctuations in heat flux decrease rapidly as the wing is approached. The fluctuating heat flux is a significant part of the total heat flux, reaching values as high as 25% of the mean heat flux near the line of low shear. The line of low shear has also been observed to be the location of maximum level of pressure fluctuations (Ölçmen and Simpson, 1994; Rife, 1992) and turbulence normal stresses (Devenport and Simpson, 1990 a).

4.2.2 Probability Density Functions, Skewness, and Flatness Factors

Distributions of the probability density function (pdf) of the heat flux fluctuations measured along the centerline in front of the modified NACA 0020 model, streamlined cylinder, and NACA 0015 model are shown in Fig. 4.4 - 4.6 respectively. The pdfs of heat flux fluctuations do not show the bimodal or "double-peaked" structure that have been found in the velocity pdfs and in pdfs of pressure fluctuations measured on the

endwall upstream of the wing.

While the heat flux pdfs are not bimodal, the effects of large scale unsteadiness are seen in the distortion of the pdfs. Distributions of the skewness and flatness factors of the heat flux pdfs are shown for each model in Fig. 4.7 and Fig. 4.8, respectively. Maximum values of skewness and flatness of the heat flux pdfs were found in the vicinity of separation and are caused by the highly intermittent forward and reverse flow which exists in this region. A second local maxima occurs further downstream, near the line of low shear where the maximum value of St_{rms} also occurs. For the modified NACA 0020 wing and the NACA 0015 wing, skewness factors decrease to near zero and flatness factors near 3 in the near-wing region. For the streamlined cylinder model, large values of skewness and flatness were also observed in the near-wing region. This may indicate some unsteadiness in the near-wing region for the streamlined cylinder model. Table 4.1 presents the locations and values of the maximum mean Stanton number, rms Stanton number, skewness and flatness for each wing. Upstream of the wing, in the approach boundary layer, the flatness approaches the Gaussian value of 3 and the skewness factor is approximately 0.35. The positive skewness in the approach boundary layer is caused by the sweeps of high momentum, cold fluid from the outer region which occur in the near-wall layer.

4.3 Power Spectra of Surface Heat Flux Fluctuations

One-sided autospectral density functions (power spectra) of the heat flux fluctuations were computed. Figure 4.9 - 4.11 show spectra measured on the line of symmetry upstream of each model. Figure 4.12 presents a comparison of non-dimensional spectra of the heat flux fluctuations measured in the approach boundary layer, in the region between the separation line and the vortex center, and near the wing/endwall junction for the modified NACA 0020 wing. Frequency has been normalized by t/U_{ref} which is the time it takes the free-stream flow to travel one wing thickness. The spectra have been normalized by $(U_{ref}/t)(\rho U_{ref} C_p \Delta T)^2$ so that the area under the spectrum is equal to the variance of the local Stanton number. The spectra have been non-dimensionalized in this way to allow direct comparison of spectral levels measured at different streamwise locations. Lines indicating -1, -5/3, and -8/3 power-law slopes are include in Fig. 4.12 for comparison.

In general the spectra have a region of almost constant spectral level at low frequencies followed by a roll-off with a -8/3 slope. While no spectra of heat flux fluctuations were available in the literature, the -8/3 power law has been found in the spectra for temperature fluctuations measured in fully-developed pipe flow (Rust and Sesonske, 1966; Bremhorst and Bullock, 1969; Hishida and Nagano, 1987). Note that the results have not been corrected for the effects of the finite size of the heat flux sensor and that the spectra at high frequencies may be attenuated. Upstream of separation, in the approach boundary layer, the region of near constant spectral level extends up to a

dimensionless frequency of $ft/U_{ref} \approx 0.3$ followed by the $-8/3$ roll-off. Downstream of separation, between the line of separation and the vortex center, there is a dramatic increase in spectral density, particularly at low frequencies. Further downstream, between the vortex center and the wing/end-wall junction, there is an increase in spectral density at high frequencies.

The high levels of spectral density found in the region between the separation line and the vortex center are associated with the high heat flux fluctuations shown in Fig. 4.3. The high spectral levels at low frequencies suggest that the heat flux fluctuations in this region are created by large-scale, low-frequency, aperiodic, coherent motions. Spectra of the normal and streamwise velocity components measured by a laser-Doppler velocimeter in this region (Devenport and Simpson, 1990 a; Rife, 1992) show a similarly dramatic increase in spectral density at low frequencies.

Near the wing/endwall junction, spectral energy exists at higher frequencies than elsewhere in the flow-field. At low frequencies, the spectral density levels are the same as in the approach boundary layer. However, the region of constant spectral density extends further, to a dimensionless frequency value of $ft/U_{ref}=1.0$. This high frequency energy could be the effect of a small counter rotating vortex trapped in the junction, or the effect of small structures from the outer boundary layer region, transported by the main vortex, down the wing and into the junction.

For the streamlined cylinder model, spectra in the near-wing region show a large contribution from low frequency energy. This further supports the idea of some large-scale unsteadiness in the near-wing region for the streamlined cylinder.

4.4 Discussion of Results

From the results presented above and the available velocity data, a description of the augmentation in heat flux across the horseshoe vortex can be summarized by breaking the flowfield into three regions. In the first region, upstream of the line of separation, the heat flux is as would be expected for a two-dimensional, adverse pressure gradient boundary layer.

The second region, between the line of separation and the line of low shear, is dominated by the large-scale aperiodic motions of the horseshoe vortex. This region is characterized by highly intermittent forward and reverse flow. Turbulence energy production and turbulent stresses an order of magnitude higher than upstream were found in this region although surface shear stresses are small. Mean heat flux levels are increased over upstream values by a factor of two and fluctuations of the heat flux are increased by a factor of 3. The augmentation in heat transfer in this region is due to turbulent mixing created by the unsteadiness of the recirculating flow.

Downstream of the line of low shear, in the third region, the heat flux increases rapidly and reaches a maximum value in the immediate vicinity of the wing/endwall junction while turbulence energy and fluctuations in heat flux decrease rapidly as the wing is approached. Skin friction values in this region are very large (Devenport and Simpson, 1989). The velocity field in this region is similar to an impinging jet. The fluid transported toward the endwall on the downwash side of the vortex impinges on the wing/endwall junction and is deflected radially in the spanwise direction and back

upstream in a near-wall jet of fluid. The heat flux in this region is determined by the effects of the vortex on the mean flow. The increase in heat flux in this third region is due to a thinning of the thermal boundary layer as cold fluid from the outer boundary layer or freestream is transported by the vortex to the near wall region.

This may explain the differences in mean heat flux in the near-wing region for each wing shown Figure 4.2. The time-mean heat flux in this near-wing region appears to be controlled by the size and location of the primary vortex. The size of the primary vortex is proportional to the location of the line of separation x_{sep} , which was 3.23 cm, 2.71 cm, and 6.59 cm for the modified NACA 0020, NACA 0015, and streamlined cylinder models respectively. For the streamlined cylinder, the vortex is located much farther upstream, away from the wing than for the other two models. This may lead to a lower downwash velocity in the near-wing region for the streamlined cylinder model. Unfortunately, no detailed velocity data are available for this model to verify this conclusion.

4.5 Correlation between Surface Heat Flux and Turbulence

Since the heat flux rate upstream of the line of low shear (in the first and second regions defined above) is believed to be primarily due to turbulence generated by the large-scale unsteadiness of the horseshoe vortex, one would expect a correlation between the turbulent stresses and the time-averaged heat flux. For two-dimensional boundary layer flows, Maciejewski and Moffat (1992) relate the local heat flux to the streamwise

component of the turbulent normal stress through the use of a Stanton number based on u'_{\max} as

$$St' \equiv h/(\rho C_p u'_{\max}) \quad (4.1)$$

where h is the local convection coefficient and u'_{\max} is the maximum value of u' found in the boundary layer or freestream at the location where h is measured. Note that St' is not to be confused with St_{rms} which is the nondimensional rms value of the fluctuations in heat flux. The St' correlation is of limited practical value since it requires a detailed knowledge of the turbulence structure which is usually not available.

Maciejewski and Moffat (1992) suggest a functional form of the relation between St' and turbulence intensity $Tu = u'_{\max}/U_{ref}$ for air ($Pr=0.71$) as

$$St' = 0.0184 + 0.0092 \exp[-(Tu - 0.11)/0.055]^2 \quad (4.2)$$

This form has a peak value at a turbulence level of 11%. For turbulence intensities above 0.20, $St' \approx 0.0184$. Maciejewski and Moffat applied this correlation to heat flux experiments for various complex flow situations from the literature and found Eq. (4.2) to be valid to within 15% at (20:1) odds independent of flow geometry or Reynolds number.

To extend the St' correlation to three-dimensional flows, the author chose to substitute the maximum value of the square root of the turbulent kinetic energy present in the boundary layer, k'_{\max} , in place of u'_{\max} , in Eq.(4.1). The value of k'_{\max}/U_{ref} was obtained from the LDV data of Devenport and Simpson (1990 a) which were measured at a free-stream velocity of 27 m/s and an approach Reynolds number based on momentum thickness of 6700. This value of k'_{\max}/U_{ref} may not be the same as the value

of k'_{\max}/U_{ref} for the present data for which $U_{\text{ref}}=32.3$ m/s and $Re_{\theta}=3700$. It is assumed, however that k'_{\max}/U_{ref} is not a strong function of Reynolds number for this flow. This assumption is supported by the fact that the locations of the line of low shear and the line of separation revealed by the oil flow visualizations performed at the lower Reynolds number (Ölçmen and Simpson, 1994) were found to agree with the locations of these lines obtained from oil flow visualizations of Devenport and Simpson (1990 a). This suggests that the size and location of the primary vortex, and presumably the turbulence structure, is the same for the flowfield of Devenport and Simpson and the flowfield of the current study.

Figure 4.13 shows the local heat transfer coefficient as a function of k'_{\max}/U_{ref} for data measured along lines 1, 4, 6, and 7 upstream of the modified NACA 0020 model. Only data from regions I and II, outside of the line of low shear, were used. The heat flux in this region varies by a factor of 2.5. A linear relation is seen to exist between St and k'_{\max}/U_{ref} . St' correlations were computed from the heat transfer coefficients in Fig 4.13 and are shown as a function of k'_{\max}/U_{ref} in Fig. 4.14. The solid line in Fig. 4.14 represents Eq. (4.2) and the dashed lines represent $\pm 15\%$ error bounds. The values of St' have a mean value of 0.0217 and a standard deviation of 11%. A peak in St' does seem to appear around a turbulence level of 10%.

5 Results and Discussion for Three-Dimensional Turbulent Boundary Layer Flow

5.1 Mean Results

Results from the mean heat flux and temperature profile measurements are summarized in Table 5.1.

5.1.1 Temperature Profiles

Figures 5.1 shows mean temperature profiles measured at the 8 locations in the three-dimensional turbulent boundary layer plotted in wall coordinates where

$$T^+ \equiv \frac{T_w - T}{T_\tau} = \frac{\Theta \sqrt{C_f/2}}{St} \quad (5.1)$$

and

$$\Theta \equiv \frac{T_w - T}{T_w - T_\infty}. \quad (5.2)$$

T_τ is the friction temperature defined:

$$T_\tau \equiv \frac{\overline{q_0''}}{\rho C_p U_\tau} = \frac{St(T_w - T_\infty)}{\sqrt{C_f/2}}. \quad (5.3)$$

Also shown in Fig. 5.1 is the logarithmic temperature law of the wall:

$$T^+ = \frac{1}{k_n} \ln(y^+) + B. \quad (5.4)$$

where $k_n = 0.4556$, $B = 3.654$ for air (Kays and Crawford, 1980) and the molecular conduction sublayer equation:

$$T^+ = Pr y^+. \quad (5.5)$$

When plotted in inner variables, the profiles collapse only in the sublayer and buffer regions. In the semi-logarithmic region, the slope decreases from stations 0 to station 2 and then increases monotonically from stations 2 to 7. This increase in slope is caused by a decrease in mean surface heat flux as one proceeds downstream. This result differs from the finding of Abrahamson and Eaton (1991) that temperature profiles in a three-dimensional boundary layer obey the two-dimensional scaling laws quite well.

The semi-logarithmic temperature profile is the result of a linear variation of eddy diffusivity for heat, ϵ_h , near the wall. The increase in slope of the semi-logarithmic region indicates a decrease in ϵ_h . In two-dimensional boundary layers, the eddy diffusivity, ϵ_h , is related to the kinematic eddy viscosity, ϵ_m , by the turbulent Prandtl number, $Pr_t = \epsilon_m/\epsilon_h$. For a three-dimensional boundary layer, we can related the eddy diffusivity to a

"magnitude" kinematic eddy viscosity, $|\epsilon_m|$, which is defined as the ratio of the magnitude of the total turbulent shear stress to the magnitude of the total strain rate:

$$|\epsilon_m| = \frac{[(-\overline{uv})^2 + (-\overline{vw})^2]^{1/2}}{\left[\left(\frac{\partial U}{\partial y}\right)^2 + \left(\frac{\partial W}{\partial y}\right)^2\right]^{1/2}}. \quad (5.6)$$

The magnitude eddy viscosity defined in Eq. (5.6) is invariant with rotation about an axis perpendicular to the wall. If wall-shear-stress coordinates are used in Eq. (5.6), the terms $\partial W/\partial y$ and $(-\overline{vw})^2$ are negligible in the near-wall region and $|\epsilon_m|$ is equal to the streamwise eddy viscosity.

Figure 5.2 shows profiles of the magnitude kinematic eddy viscosity $|\epsilon_m|$ at stations 1 through 7 calculated from the data of Ölçmen and Simpson (1995a). The solid line in Fig. 5.2 is the relation $|\epsilon_m| = 0.41 y^+$ which is valid for 2D TBLs. The magnitude kinematic eddy viscosity in the near-wall region decreases from stations 1 to 7. We would like to know if the decrease in ϵ_h is the result of the decrease in $|\epsilon_m|$ alone or also the result of a change in $(Pr_t)_l$, the average value of Pr_t in the log-region. We can use the magnitude eddy viscosity shown in Fig. 5.2 to calculate the mean temperature profile at each station. In the constant heat flux region near the wall,

$$T^+ = \int_0^{y^+} \frac{dy^+}{\frac{1}{Pr} + \frac{\epsilon_h}{v}}. \quad (5.7)$$

If we assume, that $(Pr_t)_l \epsilon_h = |\epsilon_m| = \kappa v y^+$, integration of Eq. (5.7) leads to Eq. (5.4) where $\kappa_n = \kappa/(Pr_t)_l$. Figure 5.2 shows that $\epsilon_m < \kappa v y^+$ in the near-wall region at the

downstream locations. Equation (5.7) was numerically integrated by assuming $\epsilon_h = |\epsilon_m|/(Pr_t)_l$ and using the measured values of ϵ_m with $(Pr_t)_l = 0.9$. Results are shown in Fig. 5.3. Equation (5.7) is valid only in the constant-heat-flux region out to about $y^+ = 300$. At stations 0 - 6, agreement is very good between the measured and predicted values of T^+ . At station 7, the measured values are slightly higher than the predicted values, indicating $(Pr_t)_l > 0.9$. However, the difference is within the uncertainty in the measured values of T^+ . Therefore, the agreement between the calculated and directly measured temperature profiles suggests that the assumption $(Pr_t)_l = 0.9$ is still valid in 3-D flows. The significance of this is that any turbulence model which correctly predicts the shear stresses $-\overline{uv}$ and $-\overline{wv}$ can be used with Eq. (5.6) and $(Pr_t)_l = 0.9$ to predict the surface heat transfer.

5.1.2 Surface Heat Transfer

Figure 5.4 is a plot of the development of the Stanton number in the three-dimensional boundary layer. The Stanton numbers are normalized on local free-stream velocity U_∞ . The two-dimensional, zero-pressure-gradient correlation valid upstream of the wing, Eq. (3.11) is shown for comparison. The coordinate "s" in Fig. 5.4 is defined by the path connecting the measurement locations with $s = 0$ at the beginning of the heated floor. This path is not actually a streamline of either the free-stream or near-wall flow but is useful for comparison with the 2-D correlation between St and s , Eq. (3.11). The Stanton number distribution follows the 2-D correlation from station 0 to station 4

and then decreases faster than the 2-D correlation.

As a check on the surface heat flux and temperature measurements, the Stanton number at station zero, which is nominally two dimensional, was estimated from the measured temperature profile by fitting the temperature profile to the temperature law of the wall, Eq. (5.4). By substituting the definition of T^+ , Eq. (5.2), into Eq. (5.4) and solving for Stanton number, we get

$$St = \frac{\Theta \sqrt{\frac{C_f}{2}}}{\frac{1}{\kappa_n} \ln(y^+) + B} \quad (5.8)$$

Figure 5.5 shows the value computed from Eq. (5.8) versus y^+ for station number 0. In the log-region where Eq. (5.4) is valid, Eq. (5.8) has a constant value which is equal to the Stanton number. Different values of κ_n , and B in Eq. (5.4) give different Stanton numbers. The constants $\kappa_n = 0.4556$, $B = 3.654$ (Kays and Crawford, 1980) give $St = 0.00168$. The constants $\kappa_n = 0.47$, $B = 3.8$ (Kader and Yaglom, 1972) give $St = 0.00172$. These numbers are 4% and 1.7% less than the directly measured value of $St = 0.00175$.

5.1.3 Enthalpy Thickness Vector Correlation

For an incompressible, constant property turbulent boundary layer flow, the continuity and energy equations can be expressed as:

$$\frac{\partial U}{\partial x} + \frac{\partial V}{\partial y} + \frac{\partial W}{\partial z} = 0 \quad (5.9)$$

$$\frac{\partial(U\Theta)}{\partial x} + \frac{\partial(V\Theta)}{\partial y} + \frac{\partial(W\Theta)}{\partial z} = \frac{1}{\rho C_p (T_w - T_\infty)} \frac{\partial \bar{q}''}{\partial y}. \quad (5.10)$$

Integrating with respect to y between the wall and infinity and using the continuity equation to eliminate V_∞ from the integral energy equation yields:

$$St = \frac{1}{U_\infty} \frac{d}{dx} \int_0^\infty U(1 - \Theta) dy + \frac{1}{U_\infty} \frac{d}{dz} \int_0^\infty W(1 - \Theta) dy. \quad (5.11)$$

For two-dimensional flow, Eq. (5.11) reduces to:

$$St = \frac{1}{U_\infty} \frac{d(U_\infty \Delta_2)}{dx} \quad (5.12)$$

where Δ_2 is the enthalpy thickness defined:

$$\Delta_2 \equiv \frac{1}{U_\infty} \int_0^\infty U(1 - \Theta) dy. \quad (5.13)$$

In 2-D TBL's with moderate pressure gradients, the Stanton number is related to Δ_2 through the relation (Kays and Crawford, 1980):

$$St = 0.125 Pr^{-0.5} Re_{\Delta_2}^{-0.25}. \quad (5.14)$$

For 3-D TBL's, Abrahamson and Eaton (1991) have proposed that the heat transfer is related to an enthalpy thickness vector, which for an incompressible constant property flow is defined:

$$\mathbf{H} = \left[\frac{1}{U_\infty} \int_0^\infty U(1 - \Theta) dy, 0, \frac{1}{U_\infty} \int_0^\infty W(1 - \Theta) dy \right] \quad (5.15)$$

in local free-stream coordinates. Abrahamson and Eaton propose that the 2-D Stanton number/enthalpy thickness relation, Eq. (5.14), extends to three-dimensional flows by substituting the magnitude of the enthalpy thickness vector in place of Δ_2 . Further, Abrahamson and Eaton show that the enthalpy thickness vector is aligned with the direction of mean energy flux across the boundary layer.

To calculate the enthalpy thickness vector, the U and W components of the velocity vector (Ölçmen and Simpson, 1995a) were fit to piece-wise cubic splines and interpolated onto the temperature data set. The interpolated data were then combined according to Eq. (5.15) and numerically integrated to form the components of \mathbf{H} .

Figure 5.6 shows the relationship between the directly measured Stanton numbers and the Reynolds number based on magnitude of the enthalpy thickness vector. The data of Abrahamson and Eaton (1991) are also included. The three-dimensional data lie very close to the two-dimensional correlation. Note that the two points of Abrahamson and Eaton which lie furthest away from the correlation were attributed by those authors to an unheated starting length effect. Stanton numbers computed from the magnitude of the enthalpy thickness vector and the two-dimensional correlation are shown in Fig. 5.4. The calculated Stanton number distribution shows good agreement with the measured Stanton numbers. This finding disagrees with the results Abrahamson and Eaton who found that the relationship between St and Re_H did not follow the spatial development of St in either

x or s.

Figure 5.7 shows the direction of the enthalpy thickness vector in tunnel coordinates. At stations 0 through 5, the direction of the enthalpy thickness vector is between the free-stream direction and the wall-shear-stress direction. In their experiment, Abrahamson and Eaton (1991) observed that the enthalpy thickness vector was closely aligned with the near-wall flow. The current results show that in the flow studied here, a significant amount of enthalpy is convected by the outer flow. At stations 6 and 7, the enthalpy thickness vector direction lags the free-stream and wall-shear-stress directions. This is caused by transport of enthalpy away from the wing by the middle region of the boundary layer at stations 6 and 7.

The enthalpy thickness correlation developed by Abrahamson and Eaton shows that the two-dimensional relationship between enthalpy thickness and heat transfer is still valid in a three-dimensional boundary layer. However, it does not illuminate the mechanism by which enthalpy thickness is increased (heat transfer is reduced) in a three-dimensional boundary layer. For this, we must look at the statistical and spectral description of turbulent heat transfer.

5.1.4 Effects of Mean Streamwise Pressure Gradient

Since the flow experiences both streamwise and spanwise pressure gradients we must separate the effects of the streamwise and spanwise pressure gradients on surface heat transfer. The free-stream flow decelerates mildly from station 0 to station 2 and then

accelerates strongly to station 7. To account for the stream-wise pressure gradient, the integral method suggested by Ambrok (1957) and described by Crawford and Kays (1980) was used:

$$\int_{x_0}^x d(U_{\infty} \Delta_2)^{1.25} = \left(\frac{0.8}{0.0287 \text{ Pr}^{-0.4}} \right)^{-1.25} v^{0.25} \int_{x_0}^s U_{\infty}(s) ds. \quad (5.16)$$

Equation (5.16) was integrated from the measured enthalpy thickness at station 0 using the free-stream velocity distribution given in Table 2.6. The Stanton numbers were then determined from Eq. (5.14). The use of Eq. (5.16) is only approximate since the "path" from station 0 to station 7 is not a streamline. The resulting Stanton number distribution is plotted in Fig. 5.4. The Stanton number distribution is indistinguishable from the Stanton number distribution obtained from Eq. (3.11). The streamwise pressure gradients have very little effect on the Stanton number distribution due to the limited streamwise distances traveled. This suggests that it is the spanwise pressure gradient is responsible for the reduction in surface heat transfer.

It should be noted however, that Eq. (5.16) is not valid for strongly accelerated flows characterized by large magnitudes of the acceleration parameter K defined:

$$K \equiv \frac{v}{U_{\infty}^2} \frac{dU_{\infty}}{ds} \quad (5.17)$$

For values of $K > 1 \times 10^6$, the favorable pressure gradient stretches vortex filaments in the stream wise direction and causes the viscous sublayer to thicken, resulting in a "laminar-like" decrease in Stanton number after some distance along the flow (Kays and

Crawford, 1980). From the results of a numerical investigation, Hanjalić et al. (1994) suggest that for a pressure-driven 3-D TBL, laminarization should occur for even lower streamwise acceleration since both the favorable streamwise pressure gradient and the spanwise pressure gradient reduce turbulence stresses. As shown in Table 2.6, the value of K exceeds 1×10^{-6} at stations 3, 4, and 5.

However, the temperature profiles shown in Fig. 5.1 (and the velocity profiles of Ölçmen and Simpson (1995a)) show no thickening of the viscous sublayer or laminar-like shape. The shape factor, H , for the eight stations decreases from the maximum value of 1.48 at station 2 to 1.27 at station 7 while the shape factor for a typical laminar profile has a value of about 2. Also, the turbulent relation between the enthalpy thickness and heat transfer described above appears to be valid. The reason the favorable streamwise pressure gradient does not cause relaminarization is because the pressure gradient does not act over a sufficiently large streamwise distance (Simpson, 1979).

5.2 Statistical Results

Figure 5.8 is a plot of normalized temperature fluctuation profiles measured at stations 0 through 6 where the normalized temperature fluctuation θ is defined:

$$\theta = \frac{t}{T_w - T_\infty} \quad (5.18)$$

and θ' is the rms of θ . For all of the stations the near-wall profiles are similar with the peak value of θ' occurring in the buffer region at a y^+ value close to 20. As the flow

proceeds downstream, a plateau develops in the temperature profile between $y^+ = 100$ and $y^+ = 400$ and the temperature fluctuations extend further into the outer boundary layer. The peak value of θ' and the y -location of peak θ' do not change significantly as the flow proceeds downstream.

Figure 5.9 shows skewness factor profiles of the normalized temperature fluctuations for stations 0 - 6. Skewness values attain a maximum values of 1.0 near $y^+ = 6$ and decrease rapidly through the buffer region. At stations 0 through 3 the skewness changes sign at approximately $y^+ = 40$. Proceeding further downstream, the location where skewness changes sign increases. At stations 4 and 5, positive skewness values persist through the log-region to values of $y^+ = 150$ and 200, respectively. At station 6, the skewness values are not as large near the wall. Moving away from the wall, the skewness decreases slower than at the upstream locations and remains at a value near 0.2 up to a y^+ value of 300. The positive skewness which develops from stations 3 to 6 may indicate that sweeps of outer-layer cold fluid occur more frequently than ejections of near-wall warm fluid in the region $20 < y^+ < 400$. The octant analysis of Ölçmen and Simpson (1995c) shows that this is not the case. Another possible explanation is that sweeps are stronger than ejections in this region. From the results of a DNS, Sendstad and Moin (1992) have suggested that ejections in a 3-D boundary layer originate from a further distance from the wall and therefore have less momentum and temperature difference (See Fig. 1.7).

Figure 5.10 shows the flatness factor profiles for stations 0 through 6. At stations 0 through 5, the flatness profiles are very similar to flatness profiles of temperature and

streamwise velocity fluctuations measured in two-dimensional flows (See Fig. 1.8). Flatness values attain a maximum value of 4 at the y -locations nearest the wall. Moving away from the wall, flatness values decrease and reach a minimum value near $y^+ = 25$. The flatness values then increase slightly, reaching a local maximum near $y^+ = 100$ and then decrease to a second local minimum at $y^+ = 200 - 400$. Flatness values increase rapidly near the edge of the boundary layer.

For streamwise velocity fluctuations (Durst et al., 1987) and temperature fluctuations (Zaric, 1975; Nagano and Tagawa, 1988) in a two-dimensional, zero-pressure gradient boundary layer, the first minimum in flatness occurs at the same y -location where the variance attains a maximum and skewness becomes zero (see Fig. 1.8). The second local maximum appears to occur at the location where an inflection point occurs in the variance. The temperature flatness factors at stations 0 through 5 agree with these 2-D results. At station 6, the flatness profile is somewhat different. The near-wall flatness values are not as large and the flatness decreases somewhat slower moving away from the wall. The second local minimum is lower than the first minimum. Interestingly, the skewness changes sign at the location of the second minimum, indicating that there may be some relationship between skewness and flatness.

From their results as well as the results of other authors, Durst et al. (1987) found that a relationship existed between the flatness and skewness factors of streamwise velocity fluctuations in a two-dimensional zero-pressure-gradient boundary layer. Figure 5.11 is a plot of the flatness factor as a function of the skewness factor of temperature fluctuations for stations 0 - 6. A least-squares regression to the data shown in Fig. 5.11

yields

$$F = 1.372 S^2 + 2.694. \quad (5.19)$$

Note that the flatness factor in Eq. (5.19) attains a minimum value when $S = 0$. It is of note that this minimum F occurs at the same y locations where $S = 0$ even for station 6 where the skewness factor changes sign far away from the wall at $y^+ = 400$. It is also of note that when $S = 0$, Eq. (5.19) predicts a flatness $F = 2.69$ instead of the Gaussian value $F = 3.0$.

5.3 Spectral Results

5.3.1 Surface Heat Flux Power Spectra

Spectra of the surface heat flux fluctuations are shown in Fig. 5.12 for the stations 0 - 6. The corrections for background noise and finite sensor size described in Appendix B have been applied. The spectra have been normalized such that the area under the curves shown in Fig. 5.13 is equal to 1. The spectra at all stations have a region of near-constant level at low frequencies followed by a continuous roll-off with no definite power law. The high frequency spectra appear to obey a $-5/3$ power law. The spectra at stations 4, 5 and 6 have less low-frequency energy from large outer-region structures.

5.3.2 Temperature Power Spectra

Several scaling laws were investigated for the temperature fluctuation spectra.

Following the work of Perry, et al. (1985), scaling laws of the form:

$$\frac{G_u U}{2\pi \delta T_\tau^2} = \phi(k\delta) \quad (5.20)$$

$$\frac{G_u U}{2\pi Y T_\tau^2} = \phi(ky), \quad (5.21)$$

were investigated where $k = 2\pi f/U$ is the wave number and $\phi(k\delta)$ and $\phi(ky)$ represent the power spectrum given as a function of $k\delta$ and ky , respectively. Perry et al. (1985) used similar scaling laws (with U_τ replacing T_τ in Eq. (5.20) and (5.21)) to scale velocity spectra of the u , v , and w velocity components measured in the region, $y^+ > 140$; $y/\delta < 0.14$, of two-dimensional turbulent pipe flow. Using a Λ -vortex model based on Townsend's (1976) attached eddy hypothesis, Perry et al. (1985) argued that large δ -scale vortices contribute only to u fluctuations in the near-wall region. Thus, both structures of size $O(\delta)$ and $O(y)$ contribute to u fluctuations while only structures of size $O(y)$ contribute to w and v at a location y . Since these large δ -scale structures do not create v -motions, they do not contribute to the Reynolds stress. They contribute low frequency energy to u spectra which has been termed "inactive" motion by Bradshaw (1967). The low frequency end of the u -spectrum scales on the outer length scale δ and time scale

δ/U_τ . Structures of $O(y)$ contribute to a middle range of frequencies for u -spectra so the spectra scale on the length scale y and time scale y/U_τ . The high wave-number end of the spectrum is dependant on viscosity dominated motions and spectra scale on the Kolmogoroff (1941) length scale $\eta = (v^3/\epsilon)^{1/4}$ and velocity scale $v = (v\epsilon)^{1/4}$. The overlap region between outer and inner scaling laws gives rise to the -1 power law. The overlap region between the inner and Kolmogoroff scaling laws gives rise to the -5/3 power law. The w and v fluctuations are unaffected by δ -scale motions and neither scale on outer variables at low frequencies nor exhibit a -1 slope region.

Since temperature fluctuations have been shown to be similar to streamwise velocity fluctuations, one would expect similar scaling laws for temperature spectra, ie., Eq. (5.20) should collapse temperature spectra at low frequencies and in the -1 slope region while Eq. (5.21) should collapse temperature spectra in the -1 and -5/3 regions.

Power spectra of the temperature fluctuations measured in the region $y^+ > 100$, $y/\delta < 0.2$, are shown in Fig. 5.13a - 5.13g for stations 0 - 6 respectively, normalized with outer scaling parameters. The temperature spectra collapse only slightly at low frequencies when scaled with outer variables. This is because the temperature fluctuations are created by u fluctuations and by v and w fluctuations which do not scale on outer variables.

Power spectra of the temperature fluctuations measured in the region $y^+ > 100$; $y/\delta < 0.2$, are shown in Fig. 5.14a - 5.14g for stations 0 - 6 respectively, normalized with inner scaling parameters. The spectra appear to collapse in the -5/3 slope region but do not collapse in the -1 slope region as expected.

Following the example of Hishida and Nagano (1979) temperature spectra were

also normalized by the temperature variance and plotted versus frequency in Fig. 5.15a - 5.15g for stations 0 - 6 respectively. Three regions of the boundary layer are evident. Near the wall, $y^+ < 30$ and in the wake region $y^+ > 700$, a continuously curved spectra is observed which exhibits neither a -1 nor -5/3 power-law region. In the log-region, a strong -1 power-law region (which corresponds to the energy-containing range of eddies) exists over a large frequency range. At high frequencies, a -8/3 power-law is observed for the temperature spectra across the whole boundary layer. The -8/3 slope has been previously documented for temperature spectra in pipe flows by Rust and Sesonske (1966), Bremhorst and Bullock (1970), and Hishida and Nagano (1979). As the flow moves downstream, no noticeable change was observed in the temperature power spectra due to three-dimensionality.

5.3.3 Comparison of u- and t-Power Spectra

The first moment of the spectra shown in Figs. 5.15a - 5.15g are shown in Figs. 5.16a - 5.16g. Also shown are the first moment of the streamwise velocity fluctuations at approximately the same y-location from Ha (1993). The first moment of the spectrum is very sensitive to changes in the energy distribution and the area under any section of the $f \cdot G_u(f)$ plot represents the fraction of total energy in that frequency range. Fulachier and Dumas (1976) have compared temperature spectra with the spectra of streamwise, spanwise and normal velocity components in two dimensional boundary layers. The temperature spectrum was found to correlate with a velocity vector spectrum formed from

the sum of the three velocity spectrum weighted by twice the total turbulent kinetic energy:

$$\frac{G_t(f)}{\overline{t^2}} = \frac{G_{uu}(f)}{\overline{q^2}} + \frac{G_{vv}(f)}{\overline{q^2}} + \frac{G_{ww}(f)}{\overline{q^2}} \quad (5.22)$$

where $\overline{q^2} = \overline{u^2} + \overline{v^2} + \overline{w^2}$. In general, the energy-containing eddies in the temperature spectra are associated with higher frequencies than the energy-containing eddies for streamwise velocity spectra. This is due to the fact that energy-containing eddies for spanwise and normal velocity spectra are at higher frequencies and reflects the fact that spanwise and normal velocity fluctuations are associated with smaller scale motions than the streamwise fluctuations.

The temperature and streamwise velocity spectra shown in Fig. 5.15a - 5.15g are similar to those observed in two-dimensional boundary layers by Bremhorst and Bullock (1970) and Fulachier and Dumas (1976). In the outer region of the boundary layer, the peak in temperature and streamwise velocity spectra is well defined and extends over a narrow frequency range. The peak in the temperature spectrum occurs at a higher frequency than the peak in the streamwise velocity spectrum. Nearer the wall, in the log-region, the peaks flatten and a second low-frequency peak appears in the temperature spectrum at a frequency near the initial peak in the u spectrum. A second high-frequency peak appears in the streamwise velocity spectrum at a frequency near the initial peak in the temperature spectrum. As y decreases further, this second peak grows and reaches a maximum value near $y^+ = 130$. Below this location, the second peak again diminishes and

the original peak grows so that the spectra again become single-peaked with the peak occurring at the same frequency as the outer-region peak. At the locations closest to the wall where velocity fluctuation spectra were measured ($y^+ = 17$) the peak in temperature spectra still occurs at a higher frequency than the peak in streamwise velocity spectra. As shown by Antonia et al. (1988) the temperature spectra and streamwise velocity spectra must be correlated at the wall since $\overline{u^2} \gg \overline{w^2} \gg \overline{v^2}$ as $y \rightarrow 0$ and the correlation coefficient between u and θ approaches unity at the wall. At $y^+ = 9$ the peak in the temperature spectra still occurs at high frequency. However, Antonia et al. (1988) found that the location of the peak in the near-wall region temperature and velocity spectra decreases as $y \rightarrow 0$ due to the declining contribution from the ejection phase of the bursting cycle. Therefore, the peak in the temperature spectrum should decrease as the wall is approached and agree with the peak in the streamwise velocity spectrum.

The location of the peak in the temperature spectrum appears to be unaffected by three dimensionality. This indicates that the mean sweep/ejection frequency is unaltered by three-dimensionality. At the downstream locations, the streamwise velocity spectra change in the buffer region. The high-frequency peak which appears in the log region continues to grow and the original low frequency peak disappears. The streamwise velocity fluctuations are therefore generated by smaller-scale motions. This suggests that the large-scale motions are either suppressed or do not effect the near-wall flow at stations 3 - 6. This result agrees with the decrease in surface heat flux spectra at low frequencies observed in Fig. 5.12.

5.4 Correlation Between Temperature and Velocity Fluctuations

Based on the spectral similarity between q and θ , Fulachier and Dumas (1976) have proposed that in a two-dimensional turbulent boundary layer, the parameter B , defined:

$$B \equiv \left(\frac{\overline{q^2}}{\overline{\theta^2}} \right)^{1/2} \left| \frac{\partial \theta / \partial y}{\partial U / \partial y} \right| \quad (5.23)$$

is approximately a constant equal to 1.5 in the entire region $0 < y/\delta < 0.8$. Experiments by Elena (1977) indicate that the limiting value of B at $y^+ = 0$ is 1.5. Examination of the DNS data of Kim and Moin (1989) by Antonia and Kim (1991) suggests that the limiting value of B at the wall is 1.2. Further, Fulachier and Dumas (1976) show $B = \text{Pr}_t a_\theta / a_1$ where Pr_t is the turbulent Prandtl number which, in a three-dimensional flow, is defined:

$$\text{Pr}_t = \frac{\epsilon_m}{\epsilon_h} = \frac{L_m}{L_h} = \frac{[(\overline{-uv})^2 + (\overline{-vw})^2]^{1/2}}{\overline{\theta v}} \frac{\partial \theta / \partial y}{[(\partial U / \partial y)^2 + (\partial W / \partial y)^2]^{1/2}} \quad (5.24)$$

which is invariant with rotation about the y -axis. The term a_1 is a turbulence structural parameter defined as the ratio of turbulent shearing stress to twice the turbulent kinetic energy (Bradshaw, et al., 1967):

$$\tau / \rho = [(\overline{-uv})^2 + (\overline{-vw})^2]^{1/2} = a_1 \overline{q^2} \quad (5.25)$$

and a_θ is a similar parameter for turbulent thermal energy transfer (Townsend 1976, p.357):

$$\overline{\theta v} = a_\theta (\overline{\theta^2})^{1/2} (\overline{q^2})^{1/2} \quad (5.26)$$

Fulachier and Dumas (1976) propose that the assumption that B is constant across the boundary layer is better than the assumptions that a_1 , a_θ , and Pr_t are constant. The significance of a constant value of B with regards to turbulence modeling is that θ' can be estimated in the wall region provided q' is known.

For a three-dimensional boundary layer, the parameter B_{3D} is defined

$$B_{3D} \equiv \left(\frac{\overline{q^2}}{\overline{\theta^2}} \right)^{1/2} \left| \frac{\partial \theta / \partial y}{\sqrt{(\partial U / \partial y)^2 + (\partial W / \partial y)^2}} \right| \quad (5.27)$$

and is invariant with coordinate system rotation about an axis normal to the wall. Values of B_{3D} calculated using U and W data from Ölçmen and Simpson (1995a) are plotted in Fig. 5.17. Figure 5.17a shows the near-wall region and Fig. 5.17b shows the outer region. Only at the two most upstream stations does B_{3D} have an approximately constant value of 1.5. As the flow moves downstream, the value of B_{3D} increases across the entire layer. Values of B_{3D} in the outer region generally fall in the region $1.5 < B_{3D} < 2.2$. As y approaches zero, the scatter in the measured values of B_{3D} increases but the values of B_{3D} appears to remain close to 1.5.

Two other parameters similar to B were evaluated. In the first, the gradients $\partial U / \partial y$ and $\partial W / \partial y$ in Eq. (5.27) were replaced with the single gradient $\partial Q / \partial y$, where $Q = (U^2 + W^2)^{1/2}$ to obtain:

$$B_Q \equiv \left(\frac{\overline{q^2}}{\theta^2} \right)^{1/2} \left| \frac{\partial \Theta / \partial y}{\partial Q / \partial y} \right|. \quad (5.28)$$

This resulted in greater scatter in the parameter as shown in Figs. 5.18. As the flow moves downstream, a peak appears in the profile in the region $100 < y^+ < 400$. The maximum value of this peak increases and the location moves upward in the profile as the flow moves from station 0 to station 6.

The ratio $\overline{v^2}/|\tau/\rho|$, which is a correlation between the momentum transporting velocity and the magnitude of the resulting shear stress, was found by Ölçmen and Simpson (1995a) to have a nearly constant value of 1.6 over the middle region ($y^+ > 50$ to $y/\delta < 0.5$) of the boundary layer for several 3-D experiments. The velocity v is also responsible for the turbulent transport of heat. This suggests a correlation of the form

$$B_v \equiv \left(\frac{\overline{v^2}}{\theta^2} \right)^{1/2} \left| \frac{\partial \Theta / \partial y}{\partial U / \partial y} \right| \quad (5.29)$$

which is shown in Fig. 5.19 for stations 0 - 6. This correlation appears to be no better than B_{3D} . At the upstream locations, B_v has a near-constant value of 0.7 for $y^+ > 100$. Near the wall, $B_v \sim y$ since $v \sim y^2$ and $\theta \sim y$. As the flow moves downstream, B_v increases in the outer region to values near 1.0.

5.5 Coherency and Coherence Length Scale

Figures 5.20 and 5.21 show the spectral variation of coherency between the surface heat flux and the temperature at selected points in the boundary layer for stations 0 and 6 respectively. A common feature of the spectral variation of coherency is a region of near-constant coherency at low frequencies followed by a rapid fall of coherency with frequency in a constant slope region. The band-width of the near-constant coherency region does not appear to be affected by three-dimensionality. The coherency decreases with increasing separation distance due to the decrease in the number of turbulence structures which impact both the cold wire and the heat flux gage.

An unexpected phenomenon shown in Figs. 5.20 and 5.21 is that the measured coherency does not increase to a value of 1 as the separation distance between the heat flux gauge and cold wire goes to zero. Instead, the coherency increases as the separation distance becomes smaller until the cold wire reaches a location in the range $100 < y^+ < 200$ ($y/\delta \approx 0.07$, $y \approx 2.6$ mm). After this point, the coherency decreases at low frequencies as the cold wire moves toward the wall. It is believed that this phenomenon is caused by the large size of the heat flux gage although no proof of this hypothesis has been obtained. A similar phenomena was observed by Brooks and Hodgson (1981).

The coherency at station 0 is representative of the spectral coherency at stations 1 and 2. The spectral variation of coherency at stations 6 is representative of the coherency at stations 4 and 5. Comparing Fig 5.20 to Fig 5.21, we see that the coherency between the surface heat flux and the temperature in the boundary layer is decreased at

all frequencies by the three dimensionality. The maximum coherency measured is less at station 6 than at station 0 and the coherency falls off more rapidly as distance from the wall is increased. At station 0, the surface heat flux is correlated with the temperature fluctuations ($\gamma^2 > 0.27$) all the way to the outer edge of the log-region ($y^+ = 900$) while at station 6 the surface heat flux is correlated with temperature fluctuations only out to a location $y^+ = 400$.

Coherence length scales were computed for selected frequencies from the spatial variation of coherency. The spectral variation of coherence length scales are presented in Fig 5.22a for stations 0 through 6. The most noticeable feature of this plot is the 50 % reduction in coherence length at low frequencies as the flow progresses downstream from station 0 to station 6. At stations 0 through 2 the coherency extends to almost half the boundary layer thickness ($y^+ = 900$). At the latter three stations, the coherency extends over only the inner 20% of the boundary layer ($y^+ = 400$).

Ha and Simpson (1993) used a hot-wire rake to simultaneously measure velocity at 16 logarithmically spaced locations across the boundary layer at stations 0 - 7 in the same flow studied here. Ha and Simpson (1993) computed coherence length scales based on the coherency between the hot-wire sensor closest to the wall and each of the other hot-wire sensors. The spectral variation of coherence lengths scales obtained by Ha and Simpson (1993) are shown in Fig. 5.22b. At stations 0 - 2, the coherence length scales at low frequencies obtained by Ha and Simpson (1993) are approximately 20% lower than the coherence length scales obtained here. The same decrease in coherence length scale as the flow moves from station 0 to station 6 observed in Fig. 5.22a was observed by Ha

and Simpson (1993).

Figures 5.23a - 5.23g show the spatial variation of coherency at selected frequencies for stations 0 through 6 respectively. Distance from the wall has been normalized by the coherence length scales for each station. Except in the inner region where coherency decreases, the spatial variation of coherency is close to the exponential decay model proposed by Ha (1993)

$$\gamma^2 = \exp(-ky/L_\gamma) \quad (5.30)$$

which is represented by the solid lines in Fig. 5.23. The decay constant k was determined by least squares for each station. The value of k varies only slightly from station to station with a value of $k = 1.28$ giving a good fit to the data at all stations. Ha (1993) reported vales of k in the range 1.11 - 1.44 with no noticeable change due to three-dimensionality.

6 Examination of Coherent Structures in 3-D TBL

6.1 Mean Sweep/Ejection Event Frequency

The heat flux spectra were used to estimate the mean sweep/ejection frequency in the near-wall region using the method described by Strickland and Simpson (1975). Strickland and Simpson have shown that the time scales indicated by the location of the peak in the long-sampling-time first-moment spectral density is statistically equivalent to the time scale obtained from the ensemble average of time scales obtained from short-sampling-time autocorrelations. Simpson and Strickland found that sweep/ejection frequencies obtained by these two methods agreed within 15% with the frequency obtained by the former method usually, but not always, being slightly larger. Sweep/ejection frequencies obtained from the surface heat flux spectra are given in Table 6.1. The mean sweep/ejection frequency increases from station 0 to 6 as the flow accelerates.

There still exists some uncertainty over proper scaling of the sweep/ejection frequencies (Gad-el-Hak and Bandyopadhyay, 1994). Some research groups have concluded that the sweep/ejection frequency should scale on outer variables (U_∞ and δ) while other groups have found that inner scaling (U_τ and ν) should be used. Physically,

the confusion reflects the fact that the cause of the sweep/ejection process is still unresolved. Some researchers suggest that the passage of large-scale outer structures trigger the sweep/ejection sequence at the wall (for example, Brown and Thomas, 1977) while others believe vortical structures in the near-wall region are responsible (Robinson, 1991). Both inner and outer scaling are presented in Table 6.1. Neither collapses the data very well. The frequencies vary by 14 % when normalized with inner scaling and by 18 % when normalized by outer scaling while the streamwise momentum thickness Reynolds number varies by only 2.3 %. Three-dimensionality does not appear to strongly affect the mean normalized sweep/ejection frequency.

6.2 Conditional Averaging Analysis

The distribution of skewness and flatness factors of normalized temperature fluctuations across the boundary layer are related to the relative frequency of the sweep/ejection motions. Conditional averaging techniques have been used by Andreopoulos et al. (1984) and Johansson and Alfredsson (1982) to explain the distribution of skewness and flatness of streamwise velocity fluctuations across a two-dimensional turbulent boundary layer. A similar analysis was performed here. Both the variable interval time average (VITA) algorithm of Blackwelder and Kaplan (1976) and the modified u-level technique of Luchik and Tiederman (1987) were used to detect the presence of a sweep/ejection event. Once, the sweep/ejection events were detected, the ensemble-average temperature signal during a sweep/ejection event was calculated by Eq.

(2.12). The shape of the ensemble-averaged temperature during a sweep/ejection event was found to be very sensitive to the choice of the parameters T , k , and L used in Eqns (2.8) - (2.11). Several values of these parameters were investigated and although the number of bursts detected and the shapes of the conditionally-averaged temperature varied, the trends discussed below were found for all values of T , k , and L used.

Normalized ensemble-averaged values of temperature during a sweep/ejection event at selected y -locations across the boundary layer are shown in Fig. 6.1a - 6.1g for stations 0 to 6 respectively. These results were obtained using the VITA technique with the parameters k and T assigned the values shown in Table 6.2 based on the findings of Blackwelder and Kaplan (1976). At each y -location, the inrush of cold fluid is preceded by an ejection of warm fluid from the near-wall region. Both sweeps and ejections are evident in the ensemble-averaged temperature at the measurement locations closest to the wall. Andreopoulos et al (1984) found that only sweeps occur below $y^+ = 6$.

At stations 0 through 3, as distance from the wall increases, the magnitude of the sweep event (relative to the local variance of the temperature fluctuation) decreases and the relative magnitude ejection event increases slightly. In the near-wall region, the relative magnitude of the ensemble-averaged temperature is larger during the sweep event. At the y -location where the skewness factor equals zero, the relative magnitude of the ensemble-averaged temperature during the sweep and ejection events are equal. Above this y -location, the ejection event becomes stronger. At stations 4 through 6, the sweep event is also strongest nearest the wall and decreases in strength with increasing distance from the wall. In contrast to the upstream locations, the ejection event is also strongest

nearest the wall and decreases in strength with increasing distance from the wall. The location where the relative magnitude of the sweep and ejection events are equal moves further from the wall. At station 6, the strength of the ejection events decreases swiftly as distance from the wall is increased. This may explain the large positive skewness factors observed at station 6. This suggests that three dimensionality somehow changes the structure of the turbulence to reduce the magnitude of the ejection events in the log-region, in agreement with the findings of Flack (1995) and Sendsted and Moin (1992).

It should be noted that the sweep/ejection event detection algorithms can not be used to determine the mean sweep/ejection event frequency since almost any bursting frequency can be obtained by adjusting the threshold level used in the detection algorithm (Blackwelder and Haritonitus, 1983). Further, any decrease in the strength of ejections due to an alteration of the trajectory (as suggested by Sendsted and Moin, 1992) would cause a decreased number of ejections to be detected and would be incorrectly interpreted as a decrease in the sweep/ejection frequency.

6.3 Time-Averaged Wave-Front of Large-Scale Structures

In order to determine whether or not the large-scale outer structure has been changed by three-dimensionality, the shape of the time-averaged wavefront of the large-scale structures was estimated using the method described by Brown and Thomas (1977). Brown and Thomas (1977) measured time-resolved surface wall shear stress simultaneously with velocity in a 2-D zero-pressure-gradient boundary layer with a

momentum thickness Reynolds number, $Re_\theta = 10160$. Brown and Thomas then computed the time-delayed correlation coefficient between the surface wall shear stress and velocity at several points across the boundary layer between $0.05 < y/\delta < 0.75$. They observed that the correlation coefficient peaked at increasing time delay as the point of the velocity measurement moved further away from the wall. Similar results were reported by Blackwelder and Kovasznay (1972) using a wire at $y^+ = 24$ instead of a wall shear probe. Brown and Thomas assumed that this observation was due to the passage of some organized structure at an oblique angle to wall. As a first estimate they assumed that this structure was convected downstream at a speed $U_c = 0.7 U_\infty$. They then moved the hot wire downstream a distance equal to $U_c \times \Delta T$ where ΔT is the time delay corresponding to the peak in the correlation coefficient. The correlation coefficient between the wall-shear stress and the velocity at this downstream location was found to peak at a time delay near $\Delta T = 0$. After a few iterations, Brown and Thomas found the streamwise location where the peak in the time-delayed correlation coefficient occurred for zero time delay for each y -location. The convection velocities obtained from these locations ($U_c = \Delta X/\Delta T$) ranged from $0.65 U_\infty$ at $y/\delta = 0.05$ to $0.75 U_\infty$ at $y/\delta = 0.75$. Plotting the streamwise displacement of the probes which gave $\Delta T = 0$ as a function of distance from the wall showed that the structure was a straight line inclined at 18° to the wall. This angle was found to agree with the wave fronts of large-scale structures observed in flow visualizations performed by Falco (1977). The inclination angle was observed to be 20° by Head and Bandyopadhyay (1979). Bagheri and White (1993) measured the inclination angle of the turbulent temperature structure in a 2-D flat plate boundary layer and

obtained an angle of 30° , indicating that the temperature structure is inclined at a slightly greater angle than the turbulence structure.

In the present study, a method similar to the one used by Brown and Thomas (1977) was used. For each y -location where the temperature was measured, the long-time averaged correlation coefficient between temperature and surface heat flux defined by Eq. (2.6) was determined. The results for each station are shown in Fig. 6.2a - 6.2g. Note that the peak in the correlation coefficient occurs at increasing time delays as the point of temperature measurement moves away from the wall. This is the result of the time delay between large structures hitting the point where temperature was measured and the surface where heat flux was measured. The increasing time delay as y increases implies that the structure is inclined to the wall. Also note that the correlation decreases rapidly with distance from the wall at the downstream three-dimensional locations. At stations 0 - 2, as distance from the wall increases the peaks become broader due to increased length scales. At the downstream stations, the peak does not become broader as distance from the wall increases indicating no increase in length scale. At stations 4 - 6, the correlation coefficient becomes negative for large time delays.

The location of the wave front of the structures at each y -location was estimated by assuming that the convection speed was $0.7 U_\infty$. (Brown and Thomas, 1979); Bagheri et al., 1992). The estimated position of the wave fronts at the time delay corresponding to maximum correlation coefficient are shown for each measurement station in Fig. 6.3a - 6.3g. At station 0, the wave front is a straight line inclined at 24.7° to the wall. As the flow moves and downstream and becomes more three dimensional the inclination angles

increase to values near 50° . At stations 4, 5, and 6, the wave front is not linear. Near the wall ($y/\delta < 0.2$) where the surface heat flux and temperature are coherent, the wave front is inclined at a smaller angle. This may be the result of over-estimating the convection speed in the inner layer or it could be the result of the structures in the inner layer coming from a different direction than the structures in the outer layer.

Ha (1993) used an array of hot-wires to simultaneously measure streamwise velocity at 16 locations across the boundary layer at the same locations in the 3D boundary layer studied here. Time-average wave fronts calculated from his velocity measurements (see Appendix C) agreed well with the results obtained here except that the temperature structures are inclined at a slightly greater angle as expected. The angles of the velocity turbulence structure range from 17.1° at station 0 to values near 35° at stations 4 through 6. Mean inclination angles of the temperature and turbulence wave fronts are presented in Table 6.3 for all measurement stations.

6.4 Discussion of Heat Transfer Structure in Three-Dimensional Turbulent Boundary Layers

From the results discussed above, it appears that mean three-dimensionality reduces surface heat flux by altering the sweep/ejection process in the wall region. High levels of the skewness factor of normalized temperature fluctuations suggest that the strength of ejections is decreased by three-dimensionality. Conditionally-averaged temperature signals during a sweep/ejection suggest that ejections do not penetrate as far

from the wall-region. The mean sweep/ejection frequency determined from first moment of surface heat flux and temperature spectra was not affected by three-dimensionality, indicating that the frequency of ejections has not been decreased. Rather, it seems likely that the ejections do not carry as much temperature difference since they originate from further out in the boundary layer and do not penetrate as far into the outer boundary layer because the spanwise velocity alters their trajectory. The mean inclination angle of the large structures was found to increase and the shape of the wavefront became nonlinear as the three-dimensionality of the flow increased. How this affects the near-wall flow is still unknown. Coherency between the surface heat transfer and the outer region flow is reduced by three-dimensionality. The structure of both the inner and outer flow has been changed by three dimensionality and the coherency between the inner and outer regions has been reduced due to the fact that inner and outer regions come from different directions. Whether the change in the inner region causes the change in the outer region or visa versa is still unclear.

7 Results and Discussion for 2-D Separating TBL

7.1 Surface Heat Flux

The streamwise variation of the heat transfer coefficient is shown in Fig. 7.1.

Figure 7.2 shows the streamwise variation of the Stanton number, defined:

$$St = \frac{\overline{q_0''}}{\rho C_p (T_w - T_\infty) U_\infty} \quad (7.1)$$

with C_p and ρ evaluated at the film temperature. The solid line in Figs. 7.1 and 7.2 show the heat transfer predicted from the streamwise velocity variation using Eq. (5.16) with $x = x_0$ at the beginning of the heated section. The heat transfer starts to decrease slightly below the predicted values downstream of $x = 285$ cm and falls rapidly downstream of *incipient detachment* ($x = 311.5$ cm). The mean heat transfer attains a broad minimum near detachment ($x = 345.4$ cm) and increases rapidly in the backflow region. Figure 7.2 also shows the streamwise variation of heat flux fluctuations, St_{rms} defined:

$$St_{rms} = \frac{(q_0'')'}{\rho C_p (T_w - T_\infty) U_\infty} \quad (7.2)$$

The rms Stanton number increases approaching separation and remains constant in the separated region. The rms value of h attains a maximum value near the location of time-

mean detachment and decreases slightly downstream of detachment.

Figures 7.3 shows the streamwise variation of the skewness and flatness factors of surface heat flux fluctuations. The skewness and flatness factors increase monotonically approaching separation, from near Gaussian values upstream to relatively large values in the backflow region. The large skewness and flatness values are the result of large-scale unsteadiness in the backflow region. Mean Stanton numbers, rms Stanton numbers, and skewness and flatness factors of surface heat flux are presented in Table 7.1.

The mean temperature and velocity profiles upstream of detachment were integrated to calculate the enthalpy thickness, Δ_2 , at each station. Velocity profiles were interpolated onto the temperature data set and integrated numerically. The temperature profiles were also integrated to calculate a length scale defined:

$$\Delta_1 = \int_0^{\infty} (1 - \Theta) dy \quad (7.3)$$

which is analogous to the displacement thickness. Values of Δ_1 , Δ_2 , and a temperature shape factor defined $H_\Delta = \Delta_1/\Delta_2$, are presented in Table 7.2. Figures 7.4 and 7.5 show the streamwise variation of Δ_1 and Δ_2 , respectively. The Δ_1 length scale increases monotonically through detachment and levels off in the backflow region. The Δ_2 length scale increases approaching separation, although there is some scatter in Δ_2 in the region between ID and TD so the streamwise derivative of Δ_2 is uncertain in this region. Figure 7.6 compares the temperature shape factor with the velocity shape factor, $H = \delta_1/\delta_2$. The streamwise variation is very similar except that H_Δ is slightly larger than H .

Figure 7.7 shows the Stanton number upstream of detachment as a function of enthalpy thickness Reynolds number. Also shown is the 2-D flat plate correlation (Kays and Crawford, 1980):

$$St = 0.0125 Pr^{-0.5} Re_{\Delta_2}^{-0.25} \quad (7.4)$$

which is also valid for mild adverse pressure gradients (Moffat and Kays, 1984). The relation is valid in the region upstream of incipient detachment. Downstream of incipient detachment, the Stanton numbers are reduced below predicted values.

Figure 7.8 presents profiles of the integrand of the enthalpy thickness, $(1 - \Theta)(U/U_\infty)$, upstream of detachment. At the most upstream location, $(1 - \Theta)(U/U_\infty)$ is largest in the near-wall region, i.e. Δ_2 is determined more by the flow close to the wall. Proceeding downstream, the near-wall value of $(1 - \Theta)(U/U_\infty)$ decreases and the enthalpy thickness is determined more by the flow in the outer region. This is a probable reason for the breakdown of the relation between Stanton number and Δ_2 shown in Eq. (7.4).

The streamwise variation of enthalpy thickness was used to check the surface heat flux measurements. For a 2-D boundary layer the integral energy equation is:

$$St = \frac{1}{U_\infty} \frac{d(\Delta_2 U_\infty)}{dx}. \quad (7.5)$$

Figure 7.9 shows the streamwise variation of $U_\infty \Delta_2$ upstream of detachment. The streamwise derivative of $U_\infty \Delta_2$ was estimated from a quadratic curve fit to the data shown in Fig. 7.9. The data point at $x = 332.4$ cm was omitted from the curve fit. Stanton numbers computed from Eq. (7.5) are compared with the measured Stanton numbers in

Fig. 7.10. Agreement is within 5% for all of the measured Stanton numbers.

Integral parameters were calculated in the backflow region by treating each velocity and temperature profile in the near-wall region from the wall out to the location of maximum backflow velocity, N , as a boundary layer profile. The backflow temperature displacement thickness and backflow enthalpy thickness were defined by:

$$\Delta_{1N} \equiv \int_0^N \left(1 - \frac{\Theta}{\Theta_N}\right) dy; \quad \Delta_{2N} \equiv \int_0^N \frac{U}{U_N} \left(1 - \frac{\Theta}{\Theta_N}\right) dy. \quad (7.6)$$

where U_N and Θ_N are the values of U and Θ at $y = N$. Backflow velocity profiles at $x = 407$ cm and $x = 440$ cm were obtained from the backflow velocity profiles measured at $x = 397$ cm and $x = 434$ cm (Simpson et al., 1981) by assuming that the backflow similarity law (Simpson, 1983) remains valid. Values of N and U_N at $x = 407$ cm and 440 cm were obtained from a curve fit to the streamwise variation of N and U_N in Simpson et al. (1981). Values of Δ_{1N} , Δ_{2N} , and the backflow temperature profile shape factor $H_{\Delta N}$ are presented in Table 7.3. The temperature shape factor for the backflow ranges from 1.48 at the most downstream location to 1.73 just downstream of detachment.

Stanton number and enthalpy thickness Reynolds number for the backflow were defined:

$$St_N \equiv \frac{\overline{q_0''}}{\rho C_p U_N (T_w - T_N)}, \quad Re_{\Delta N} \equiv \frac{U_N \Delta_{2N}}{\nu}. \quad (7.7)$$

and are presented in Table 7.3. The enthalpy thickness Reynolds numbers ranged from 10 at the location just downstream of separation to 160 at the most downstream location.

Figure 7.11 shows St_N versus $Re_{\Delta N}$ for the measurement locations in the backflow region. Also shown are the turbulent relation for St as a function of Re_{Δ} , Eq. (7.4) and the laminar relation (Kays and Crawford, 1980):

$$St = 0.2204 Pr^{-4/3} Re_{\Delta_2}^{-1}. \quad (7.8)$$

Except for the first location, St_N follows the turbulent relation $St_N \sim Re_{\Delta N}^{-1/4}$ but the proportionality factor is approximately 4 times larger than the constant in Eq. (7.4).

Previous work (Devenport and Sutton, 1991; Adams and Johnston, 1988; Shishov et al., 1988) suggests that the observed increase in St is due to the high external turbulence. It was therefore decided to treat the backflow region as a turbulent boundary layer with high free-stream turbulence. Simonich and Bradshaw (1978) describe the increase in Stanton number due to free-stream turbulence in terms of the turbulence intensity alone using the simple linear model

$$\frac{\Delta St_0}{St_0} = 5 Tu \quad (7.9)$$

where Tu is the free-stream turbulence intensity, St_0 is the Stanton number for a standard boundary layer at enthalpy thickness Δ_2 , and ΔSt is the increase in Stanton number due to free-stream turbulence. Values of "free-stream" turbulence for each backflow velocity profile, $Tu_N = u_N/U_N$, were taken as the turbulence intensity at the location of maximum backflow velocity given in Table 7.3. The turbulence intensity ranges from 2.77 at the location just downstream of separation to 0.76 at the most downstream measurement location. It is unknown whether Eq. (7.9) is valid for the large turbulence levels greater

than 0.6. The increase in St_N for each station according to Eq. (7.9) are also given in Table 7.3 and range from $St/St_0 = 14.85$ at the most upstream station to $St/St_0 = 4.75$ at the most downstream station.

The St' correlation (Maciejewski and Moffat, 1992) described in Chapter 4 also relates the Stanton number to the free-stream turbulence level alone. St' is defined:

$$St' \equiv h/(\rho C_p u_\infty') \quad (7.10)$$

and is related to the turbulence intensity by:

$$St' = 0.0184 + 0.0092 \exp -[(Tu - .11)/0.055]^2. \quad (7.11)$$

For large turbulence intensities, Eq. (7.11) predicts $St' = 0.0184$. Values of St' for the backflow region were computed using:

$$St'_N = \frac{\overline{q_0''}}{\rho C_p (T_w - T_N) u'_N} \quad (7.12)$$

and range from 0.020 to 0.025. Values of St_N were calculated from Eqs. (7.11) and (7.12) and are compared with the measured values of St_N in Fig. 7.11. The calculated values are 10% to 25% lower than the measured values, but agree qualitatively with the St_N distribution. This agreement supports the idea that the backflow region is similar to a turbulent boundary layer with high free-stream turbulence.

7.2 Mean Temperature Profiles

7.2.1 Upstream of Detachment

Inner Region

Figure 7.12 shows mean temperature profiles upstream of ID plotted in conventional wall coordinates:

$$T^+ = \frac{\Theta \sqrt{C_f/2}}{St}; \quad y^+ = \frac{yU_\infty}{\nu} \sqrt{C_f/2} \quad (7.13)$$

Figure 7.13 shows T^+ vs y^+ profiles in the region between ID and detachment. Approaching detachment ($x = 345.4$ cm), the temperature profiles progressively fall further below the standard temperature law of the wall:

$$T^+ = \frac{(\text{Pr}_t)_1}{\kappa} \ln(y^+) + B \quad (7.14)$$

(($\text{Pr}_t)_1 = 0.9$, $B = 3.654$, $\kappa = 0.41$) because Stanton number does not decrease as rapidly with streamwise distance as the skin friction coefficient. In Eq. (7.14) ($\text{Pr}_t)_1$ is the average turbulent Prandtl number in the region of semi-logarithmic temperature variation. The semi-logarithmic region of the temperature profile still exists but the slope is lower. Simpson et al. (1980) have shown that upstream of the location of intermittent transitory detachment ($\gamma = 0.8$), the law-of-the-wall velocity profile, Eq. (3.2) and the near-wall variation of eddy viscosity, $\nu_T = \kappa U_\tau y$, remain valid. The decrease in slope of the temperature profiles is therefore created by a decrease in the average turbulent Prandtl

number. Turbulent Prandtl numbers were estimated by fitting the semi-logarithmic portion of the temperature profiles to Eq. (7.14). Values of $(Pr_t)_t$, given in Table 7.2, decrease from 0.80 at $x = 222.6$ cm to 0.23 near ITD. This indicates that the boundary layer loses its ability to transport momentum more than its ability to transport heat. Upstream of ID, the molecular conduction sublayer equation, $T^+ = Pr y^+$ remains valid. Downstream of ID the values of T^+ are greater than $Pr y^+$ near the wall.

Blackwell et al. (1972) observed that the conventional temperature wall law fails in an adverse pressure gradient. Blackwell et al. (1972) defined temperature and distance variables as:

$$T^* = \frac{\Theta}{\sqrt{St}}, \quad y^* = \frac{yU_\infty}{\nu} \sqrt{St} \quad (7.15)$$

and observed that T^* vs y^* collapsed temperature profiles much better in the near-wall and semi-logarithmic regions than T^+ vs y^+ . Blackwell et al. also showed that the molecular conduction sublayer equation, which can be written as:

$$\Theta \frac{\sqrt{C_f/2}}{St} = Pr \frac{yU_\infty}{\nu} \sqrt{C_f/2} \quad (7.16)$$

reduces to

$$T^* = Pr y^* \quad (7.17)$$

since $(C_f/2)^{1/2}$ appears on both sides of Eq. (7.16) and can be canceled out. Thus the sublayer equations is the same for both (T^+, y^+) and (T^*, y^*) .

Figure 7.14 shows T^* vs y^* upstream of incipient detachment. The data collapse

fairly well in the buffer and semi-logarithmic regions. Figure 7.15 presents T^* vs y^* in the region between *incipient detachment* and detachment. The data do not collapse with the profiles upstream of ID and fall above the sublayer equation, Eq. (7.17). This observation can not be attributed to uncertainty in initial distance from the wall or mean surface heat flux. To make the profiles collapse with the sublayer equation by adjusting the Stanton number alone, the Stanton number would have to be more than twice the measured value. To collapse the profiles by adjusting both the initial y -location and Stanton number would require a y shift of + 0.2 mm and a 20% increase in St at all measurement locations between ID and TD. Therefore, the observed $T^* > Pr y^*$ in the sublayer must result from either (1) the turbulent heat transfer in the near-wall region is negative ($\overline{v\theta} > 0$) and thus the molecular heat transfer is greater than the total heat transfer or (2) convective terms in the turbulent thermal energy equation are significant at the closest distances from the wall where temperature was measured and the heat transfer is not uniform in this region. At some location closer to the wall than the nearest measurement location, the sublayer equation must remain valid.

A common approach to obtain a wall law which is valid near detachment is to use the near-wall value of turbulent kinetic energy instead of the friction velocity as a velocity scale (Launder, 1988). In a fully turbulent region of constant stress, the turbulent kinetic energy is essentially uniform. Launder proposed the wall law:

$$T^{**} = \frac{(Pr_t)_l}{\kappa^{**}} \ln(y^{**}) + C^{**} \quad (7.18)$$

where

$$y^{**} \equiv \frac{y k_v^{1/2}}{\nu}; \quad T^{**} \equiv \frac{\rho C_p (T_w - T) k_v^{1/2}}{q_0''} \quad (7.19)$$

and y_v is the value of y at the edge of the viscous layer, k_v is the value of turbulent kinetic energy at $y = y_v$, $\kappa^{**} = 0.22$ and C^{**} is a constant determined by satisfying both Eq. (7.18) and the molecular conduction sublayer relation $T^{**} = \text{Pr } y^{**}$. In a numerical computation, it is often more convenient to use the value of k at the near-wall node rather than k_v in evaluating Eqs. (7.18) and (7.19). The value of k at the near-wall node is determined by solving a transport equation for k . In a constant-stress flow where generation and dissipation rates of k are in balance, $k \sim U_\tau$ and Eqn. (7.18) and (7.19) give identical results to Eqns. (7.12) and (7.13).

In the flow case studied here, no region of uniform k exists near the wall. The peak value occurs further from the wall and k increases monotonically throughout the region of logarithmic temperature variation. To be consistent, y_v was chosen at $y^+ = 13.2$. Since w' data were unavailable at most stations upstream of separation, the assumption $w' = v'$ was made. Shiloh et al. (1980) have shown that this is true in the semi-logarithmic region. Figure 7.16 shows temperature profiles upstream of detachment normalized using Eqs. (7.18) and (7.19). Profiles at the first two locations are not included because v' data were unavailable. The profiles upstream of incipient detachment collapse onto a single curve. Downstream of incipient detachment, profiles shift upward approaching separation and do not obey the sublayer equation.

Outer region

Upstream of detachment, in the region where the Perry-Schofield similarity law holds for streamwise velocity profiles, the mean temperature varies linearly with distance from the wall over a significant portion of the boundary layer. This suggests that a temperature defect law may be used to scale the temperature profiles in the outer boundary layer. Figure 7.17 shows temperature profiles normalized using the defect coordinates for an equilibrium turbulent thermal boundary layer (Moffat and Kays, 1984):

$$T_d^+ \equiv \frac{T - T_\infty}{T_\tau} = (1 - \Theta) \frac{\sqrt{C_f/2}}{St} = f\left(\frac{y}{\Delta_3}\right) \quad (7.20)$$

where the length scale Δ_3 is given by

$$\Delta_3 \equiv \int_0^\infty \frac{T - T_\infty}{T_\tau} dy = \frac{\sqrt{C_f/2}}{St} \Delta_1 \quad (7.21)$$

and T_τ is the friction temperature defined in Eq. (5.3). This form for $f(y/\Delta_3)$ is analogous to the Clauser defect law for momentum. The temperature profiles do not exhibit similarity when scaled using Eqs. (7.20) and (7.21). The streamwise variation of temperature scale T_τ and length scale Δ_3 are shown in Figs 7.18 and 7.19, respectively. The temperature scale increases by 110% and the length scale by 50% over the streamwise distance studied.

Figure 7.20 shows the temperature defect profile, $(1 - \Theta)$, plotted as a function of the length scale Δ_1 . This removes the analogy between momentum and thermal transport that was used in Eqs. (7.20) - (7.21) by removing the length- and temperature-scale

dependence on the term $St/(C_p/2)^{1/2}$. The profiles collapse much better in the outer 97% of the boundary layer. As shown in Fig. 7.4, Δ_1 increases by 200% over the streamwise distance. The thermal length scale used in Fig. 7.20 is constant. This makes sense physically because the Stanton number does not decrease as fast as the skin friction coefficient with streamwise distance.

A temperature defect correlation of the form:

$$\frac{(1 - \Theta)}{\Theta_s(x)} = f\left(\frac{y\Theta_s(x)C}{\Delta_1(x)}\right) = f\left(\frac{y}{\delta_s(x)}\right) = f(\eta), \quad (7.22)$$

(where $f(\eta)$ is not to be confused with $f(y/\Delta_3)$ in Eq. (7.20)) was obtained empirically by choosing the thermal scale Θ_s to give the best possible collapse of the data. This correlation is similar in form to the Perry-Schofield velocity correlation. The constant C ($= 0.132$) does nothing to improve the correlation of the profiles and is used only to make $y/\delta_s \approx 1$ at the edge of the boundary layer. Figure 7.21 shows temperature defect profiles normalized as in Eq. (7.22) using the temperature scales given in Table 7.5. The defect profiles collapse very well over the outer 97% of the boundary layer. The collapse is slightly better in the outer region than the profiles scaled using Δ_1 alone. The temperature scale Θ_s is plotted versus streamwise distance x in Fig. 7.22. The length scale δ_s varies by 200% while the thermal scale varies by only 15% over the region of profile similarity.

7.2.2 Downstream of Detachment

Mean temperature profiles downstream of detachment are shown in Fig. 7.23. The greatest fraction of the temperature recovery between the wall and freestream occurs in the near-wall region. At the two most-downstream locations the temperature profile away from the wall resembles that of a simple shear layer. A region of uniform temperature exists across the backflow region which is centered around the y -location where the mean streamwise velocity changes sign. This region is a buffer between the near-wall backflow and the outer shear layer. The zero-temperature gradient is the result of a change in scaling laws between the inner and outer regions. Turbulent mixing by large structures brings cold fluid very close to the wall at $x = 407$ cm and $x = 440$ cm and results in enhanced heat transfer. There appears to be outer-region similarity in the temperature profiles.

Figure 7.24 shows T^* plotted versus y^* (Eq. 7.15) downstream of separation. The data collapse only in the viscous sublayer and fall slightly above the sublayer equation $T^* = \text{Pr } y^*$. In the backflow region, the sublayer equation is valid only very near the wall. Simpson et al. (1981a) have shown that turbulent transport is negligible only below $y/N < 0.02$. The temperature profiles at the two most downstream locations collapse from the wall out through the region where $d\Theta/dy = 0$.

Simpson (1983) has shown that velocity profiles in the backflow region scale on the maximum backflow velocity U_N and the distance from the wall, N , where the U_N occurs. Figure 7.25 shows temperature profiles in the backflow region scaled using:

$$\frac{\Theta}{\Theta_N} = \frac{T - T_w}{T_N - T_w} \quad (7.23)$$

where T_N is the temperature at $y = N$ plotted versus y/N . Figure 25a shows the temperature profiles plotted on a semi-logarithmic scale and Fig 7.25b shows a linear scale. The temperature profiles do not collapse in the near-wall backflow region using Eq. (7.23). This suggests that the mechanisms responsible for heat and momentum transport are different.

Adams and Johnston have shown that velocity profiles in the near-wall backflow region downstream of a backward step fit a laminar Falkner-Skan profile closer than the one-seventh power law profile. They conclude that the turbulent transport of momentum is negligible in the near-wall backflow region. For comparison purposes, Fig. 7.25b shows a one-seventh power-law profile. The temperature profiles in the near-wall backflow region are fuller in shape than the one-seventh power-law profile. This suggests that turbulent exchange of heat is significant in the near-wall backflow region.

7.3 Temperature Fluctuation Profiles

7.3.1 Upstream of Detachment

Figure 7.26 presents temperature fluctuations upstream of detachment normalized as outer variable $\theta' = t'/(T_w - T_\infty)$ plotted versus y/δ . At the first two locations, the peak in θ' occurs at the same y/δ where the peak u' occur (Simpson et al., 1981 a). Moving

downstream, the peak in temperature fluctuations moves closer to the wall while the peak in u' moves away from the wall. It seems plausible that the peak θ' occurs closer to the wall than the peak u' because the mean temperature profile is much steeper near the wall than the mean velocity profile approaching separation. The location of peak θ' coincides with a local near-wall maxima observed in u' and w' profiles (Shiloh et al., 1980). The intensity of the temperature fluctuations increases with streamwise distance to $x = 300.1$ cm and then decreases slightly approaching separation. Near detachment ($x = 345.4$ cm), a plateau where $\partial\Theta/\partial y \approx 0$ develops in the region $0.2 < y/\delta < 0.5$.

Figure 7.27 presents the temperature fluctuations upstream of detachment plotted in conventional wall coordinates $t'^+ = t'/T_\tau$ plotted versus y^+ . The peak value of t'^+ decreases with streamwise distance and the location of the peak moves closer to the wall from a y location $y^+ = 20$ at the upstream-most location to $y^+ = 4$ near detachment.

Figure 7.28 presents the temperature fluctuation profiles upstream of detachment plotted in the wall coordinates of Blackwell et al. (1972) where $t'^* = \theta'/(St)^{1/2}$ and y^* is defined in Eq. (7.15). When plotted versus y^* the location of peak temperature fluctuations occurs in the range $20 < y^* < 30$ for all measurement locations. The profiles in the strong-adverse-pressure-gradient region upstream of detachment, $285 \text{ cm} < x < 341$, collapse fairly well.

7.3.2 Downstream of Detachment

Profiles of temperature fluctuations downstream of detachment are present in Fig.

7.29a,b plotted in outer variables. The maximum value of θ' occurs in the near-wall region. This location corresponds to the location where an inflection point in profiles of u' and w' occurs (Shiloh et al., 1980). This location is slightly closer to the wall than the location of maximum mean backflow velocity and the location of minimum upstream-downstream intermittency, γ_{pu} , defined as the fraction of time that the flow moves downstream. Moving downstream, away from the location of time-mean detachment, the maximum value θ' decreases. The location of peak θ' moves closer to the wall and the values of θ' decrease across the entire layer for $y/\delta < 0.8$.

At the measurement location just downstream of time-mean detachment, a plateau in the temperature fluctuation profile is observed in the region $0.1 < y/\delta < 0.6$. Proceeding further downstream, the temperature fluctuations in this region decrease. The mean temperature gradient, $\partial\Theta/\partial y = 0$ in this same region. Since $\partial\Theta/\partial y = 0$, there is little turbulent transport of thermal energy. A second local maxima develops further from the wall around $y/\delta = 0.8$ due to the increase in $\partial\Theta/\partial y$ in the outer layer. The location of the second peak is further from the wall than the location of maximum u' , v' and \overline{uv} ($y/\delta \approx 0.6$).

Figure 7.30 presents temperature fluctuation profiles downstream of detachment plotted in the inner coordinates of Blackwell et al. (1972). In y^* coordinates the location of the peak temperature fluctuations occurs near $y^* = 20$ for all temperature profiles both upstream and downstream of detachment.

7.4 Higher Order Statistics

7.4.1 Upstream of Detachment

Skewness S_θ and flatness F_θ profiles of normalized temperature fluctuations upstream of detachment are plotted versus y/δ in Fig. 7.31 and 7.32, respectively. These are compared to the skewness and flatness factors of streamwise velocity fluctuations from Simpson et al. (1981b) shown in Fig 7.33 and 7.34, respectively. Unlike zero-pressure-gradient turbulent boundary layers, similarity does not exist between profiles of S_θ and S_u and between F_θ and F_u . Far upstream of detachment, both S_θ and S_u near the wall are large but S_θ is larger than S_u . Both decrease moving away from the wall. Approaching separation, S_u nearest the wall decreases while S_θ nearest the wall increases. A likely explanation for this observation is that $\partial U/\partial y$ near the wall is very small approaching separation. Because of the uniform velocity profile, sweeps and ejections do not carry much momentum deficit or excess. The temperature gradient is much steeper than the velocity gradient approaching separation so S_θ remains large near the wall.

In the buffer region, the temperature data show a dip in the flatness factor and a change in sign in the skewness factor at the y -location where θ' attains a maximum value. S_u changes sign at a location much further from the wall ($y/\delta \approx 0.4$) which corresponds to the region where the turbulent normal stresses and the Reynolds shearing stress reach their maximum values. Approaching separation, the location where S_θ changes sign moves closer to the wall, as does the location of maximum θ' and the dip in F_θ . Further from the

wall, a local minima develops in the S_θ profiles at a location $y/\delta \approx 0.04$ and this minima becomes more prominent approaching separation. Simpson et al (1981a) have shown that the upstream/downstream intermittency, γ_{pu} reaches a minimum value at this same y -location. F_θ profiles develop a local maxima in the region slightly above where S_θ develops a minima. No such minima or maxima was observed in S_u , S_v , F_u or F_v . There appears to be some similarity in the outer region temperature skewness and flatness factor profiles plotted in outer coordinates.

Figure 7.35 and 7.36 show profiles of the skewness and flatness of temperature fluctuations, respectively, plotted in conventional wall coordinates. Figures 7.37 and 7.38 show the skewness and flatness profiles, respectively, plotted vs y^* . Similarity in the near-wall region of the temperature skewness and flatness profiles is observed when y^* is used. The skewness at all streamwise locations appears to change sign at a location near $y^* = 20$ and the dip in the flatness profiles occurs at the same location.

7.4.2 Downstream of Detachment

Skewness and flatness profiles of temperature fluctuations downstream of detachment are plotted versus y/δ in Fig. 7.39 and 7.40, respectively. Figures 7.41 and 7.42 show the skewness and flatness factor profiles downstream of detachment plotted vs y^* . Near the wall, skewness and flatness values are larger than near-wall values upstream of detachment while skewness factors of u are negative near the wall (Simpson et al., 1981b). This indicates that the backflow is supplied from the local outer cold flow and

not from far downstream. The skewness changes sign and the flatness has a minimum value at the location of maximum θ' ($y/\delta = 0.003 - 0.005$). Further from the wall, near the location of maximum backflow velocity, the skewness has a large negative peak and the flatness has a local maxima. A maxima in S_u and F_u occurs at this same location ($y/\delta = 0.04$). Skewness factors have a second zero point further out in the layer at the location where S_u also becomes zero ($y/\delta = 0.5$) followed by a local maxima. Flatness values attain a local minima at the same location. This point is near the location of maximum Reynolds shear stress (Simpson et al., 1981 a). At the outer edge of the boundary layer, S_θ becomes negative and F_θ attains large positive values. The inner region shows similarity when plotted vs y^* . The skewness changes sign and flatness has a dip near $y^* = 20$ for all temperature profiles both upstream and downstream of detachment. The outer region scales on y/δ .

7.5 Estimation of Normal Velocity-Temperature Correlation

The energy equation for a 2-D, steady, turbulent boundary layer flow is given by

$$U \frac{\partial \theta}{\partial x} + V \frac{\partial \theta}{\partial y} = - \frac{\partial (\overline{u\theta})}{\partial x} + \frac{\partial}{\partial y} \left(\frac{\overline{q'''}}{\rho C_p (T_w - T_\infty)} \right) \quad (7.24)$$

where

$$\frac{\overline{q'''}}{\rho C_p (T_w - T_\infty)} = \alpha \frac{\partial \theta}{\partial y} - \overline{v\theta}. \quad (7.25)$$

If we neglect or assume a value for the term involving $\overline{u\theta}$, numerical integration of Eq. (7.24) with respect to y yields profiles of the velocity-temperature correlation $\overline{v\theta}$. However, numerical differentiation of the measured temperature profiles with respect to x produces uncertain results when only a few streamwise measurement locations are available. We can take advantage of the outer-region temperature profile similarity described Eq. (7.22) to evaluate the streamwise derivatives. Where Eq. (7.22) is valid, the derivatives with respect to x are evaluated using only x -derivatives of the temperature scale Θ_s , the length scale δ_s , and derivatives with respect to the similarity variable η . Near the wall, where Eq. (7.22) is not valid, we assume the contributions from the terms containing streamwise derivatives are negligible. If we define

$$F_{u\theta}(\eta) = \frac{\overline{u\theta}}{U_\infty}; \quad F_q(\eta) = \frac{\overline{q''}}{\rho C_p U_\infty (T_w - T_\infty)} \quad (7.26)$$

and substitute the similarity variables into Equation (7.24), Eq. (7.24) becomes:

$$\begin{aligned} -\frac{U}{U_\infty} \left[\frac{(1-\Theta)}{\Theta_{sc}} \frac{d\Theta_{sc}}{dx} + \frac{\eta}{\delta_{sc}} \frac{d\delta_{sc}}{dx} \Theta' \right] + \frac{V}{U_\infty} \left[\frac{\Theta'}{\delta_{sc}} \right] = -\frac{1}{U_\infty} \frac{dU_\infty}{dx} F_{u\theta} \\ + \frac{\eta}{\delta_{sc}} \frac{d\delta_{sc}}{dx} F_{u\theta}' + \frac{1}{\delta_{sc}} F_q' \end{aligned} \quad (7.27)$$

where $()'$ denotes the derivative with respect to η . Equation (7.27) can be integrated from the wall outward to yield:

$$F_q(\eta) - St = -\frac{\delta_{sc}}{\theta_{sc}} \frac{d\theta_{sc}}{dx} \int_0^\eta (1 - \Theta) \frac{U}{U_\infty} d\eta + \int_0^\eta \left(\frac{V}{U_\infty} \right) \Theta' d\eta \quad (7.28)$$

$$- \int_0^\eta \left(\eta \frac{U}{U_\infty} \frac{d\delta_{sc}}{dx} \right) \Theta' d\eta + \left(\frac{d\delta_{sc}}{dx} + \frac{\delta_{sc}}{U_\infty} \frac{dU_\infty}{dx} \right) \int_0^\eta \frac{\overline{u\theta}}{U_\infty} d\eta + \frac{d\delta_{sc}}{dx} \eta \frac{\overline{u\theta}}{U_\infty}$$

after the boundary conditions $F_q(0) = St$ and $F_{u\theta}(0) = 0$ have been used. Equation (7.27)

can be integrated from the freestream inward to obtain:

$$F_q(\eta) = \frac{\delta_{sc}}{\theta_{sc}} \frac{d\theta_{sc}}{dx} \int_\eta^\infty (1 - \Theta) \frac{U}{U_\infty} d\eta - \int_\eta^\infty \left(\frac{V}{U_\infty} \right) \Theta' d\eta + \int_0^\eta \left(\eta \frac{U}{U_\infty} \frac{d\delta_{sc}}{dx} \right) \Theta' d\eta \quad (7.29)$$

$$- \left(\frac{d\delta_{sc}}{dx} + \frac{\delta_{sc}}{U_\infty} \frac{dU_\infty}{dx} \right) \int_\eta^\infty \frac{\overline{u\theta}}{U_\infty} d\eta - \frac{d\delta_{sc}}{dx} \eta \frac{\overline{u\theta}}{U_\infty}$$

after the boundary conditions $F_q(\infty) = 0$ and $F_{u\theta}(\infty) = 0$ have been used. Equations (7.28) and (7.29) involve only functions of the similarity variable η and x . The streamwise derivatives which must be evaluated are the thermal scale Θ_s , length scale δ_s , and free-stream velocity U_∞ . The streamwise derivatives were estimated by fitting second order regressions to the length and temperature scales shown in Figs. (7.4) and (7.22), respectively and evaluating the derivative at each streamwise location. Derivatives of Θ with respect to η were evaluated from 5-point second-order regressions with the derivative evaluated at the central point. The streamwise turbulent energy flux $\overline{u\theta}$ in Eq. (7.24) was estimated by assuming that the correlation coefficient between temperature and streamwise velocity variations, $\overline{v\theta}/(\overline{v^2} \overline{\theta^2})^{1/2} = 0.4$.

Equation (7.28) was numerically integrated to obtain profiles of $\overline{v\theta}$. Figure 7.43 is a plot of the five terms on the right-hand side of Eq. (7.28) versus y/δ at $x = 285.4$ cm.

Figure 7.44 and 7.45 show the same plots at $x = 301.0$ cm and just upstream of detachment, at $x = 341.6$ cm, respectively. In all three plots, the second and third integrals are much larger than the other three terms. Because the second and third terms are of opposite sign, the first integral involving $d\Theta_s/dx$ becomes significant in the outer part of the boundary layer. The terms involving $\overline{u\theta}$ are insignificant and can be dropped. Even if the maximum possible values of $\overline{u\theta}$ were used ($\overline{u\theta} = u'\theta'$), these terms are still insignificant.

Profiles of $\overline{v\theta}/U_\infty$ versus y/δ upstream of ID are presented in Fig. 7.46. Profiles of $\overline{v\theta}/U_\infty$ versus y/δ between ID and TD are presented in Fig. 7.47. Upstream of detachment, $\overline{v\theta}/U_\infty \approx 0$ at the location nearest the wall. Moving away from the wall, $\overline{v\theta}/U_\infty$ increases and reaches a plateau. The level of this plateau fluctuates randomly with streamwise distance. In the outer layer $\overline{v\theta}/U_\infty$ increases to unreasonably large values $> v'\theta'/U_\infty$. In the region between ID and TD, values of $\overline{v\theta}/U_\infty$ are positive near the wall. This results from the boundary condition $F_q(0) = St$ which is less than the laminar heat flux as shown in Figs. 7.48 and 7.49.

The increase in $\overline{v\theta}/U_\infty$ which occurs in the outer layer are the result of the second integral being larger than the first in the outer layer. Since $V_\infty > 0$ (by continuity), for $\overline{v\theta}$ to approach 0 at the edge of the boundary layer, the third integral in Eq. (7.28) must become greater than the second integral in the outer region. Figures 7.43 - 7.45 show that this is not the case. In the outer region the term V/U_∞ is larger than $(U/U_\infty)(y/\delta_s) d\delta_s/dx$. The error therefore must lie in either V/U_∞ , U/U_∞ , Θ , or $d\delta_s/dx$. Of these, the most uncertainty exists on V/U_∞ and $d\delta_s/dx$. The change with streamwise distance in the second

integral shown in Figs 7.43 and 7.44 suggest that the error comes from V/U_∞ . The value of $\overline{v\theta}$ calculated by Eq. (7.28) is very sensitive to error in either term since both the second and third integrals in Eq. (7.28) are much larger than $\overline{v\theta}$ and it is the difference between them that determines $\overline{v\theta}$. Small errors in either term lead to a large error in $\overline{v\theta}/U_\infty$. It is therefore unlikely that Eq. (7.28) can be used to estimate $\overline{v\theta}$.

Integration of Eq. (7.29) from the freestream inward yields $\overline{v\theta}/U_\infty$ profiles identical to those in Figs. 7.44 and 7.45 except that the boundary condition $F(\infty) = 0$ shifts each profile upward so that $\overline{v\theta}/U_\infty > 0$ across the boundary layer.

7.6 Power Spectra

Power spectra of temperature fluctuations well upstream of separation ($x = 285.43$ cm) are shown in Fig 7.50. The high-frequency spectra were formed from 1000 ensemble-averaged spectra sampled at 10240 samples/sec. The low frequency spectrum was obtained from 60 ensemble averaged spectra sampled at 409.8 samples/sec. Spectra have been normalized so that the area under the spectrum is equal to 1. In the buffer region near the wall ($y^* < 30$), shown in Fig. 7.50a, a low-frequency region of constant spectral level is observed. As frequency increases, a continuously curved spectra is observed which exhibits neither a -1 nor -5/3 power-law region.

Further from the wall, in the region of semi-logarithmic temperature variation, shown in Fig. 7.50b, a -1 power-law slope is observed. As distance from the wall increases, the fraction of energy contained in large eddies decreases and the fraction of

energy in small eddies increases. In the outer wake region, shown in Fig. 7.50c, the spectra do not fall on top of one another although an f^{-1} envelope bounds the top of each spectrum. This kind of envelope was reported by Simpson et al. (1988) for streamwise velocity spectra in a separating turbulent boundary layer flow. A $f^{-5/3}$ law is observed at higher frequencies in the wake region.

Figure 7.51 shows temperature power spectra measured just upstream of *transitory detachment*, at $x = 341.6$ cm. Near the wall, Fig. 7.51a, a continuously curved spectra is observed which exhibits neither a -1 nor $-5/3$ power-law region. The high-frequency spectra appear to obey a f^4 power law. Further from the wall, in the region of semi-logarithmic temperature variation, spectral energy at the lowest and highest frequencies is increased, while spectral energy in the inertial subrange ($f^{-5/3}$ spectral region) is decreased. In the wake region, shown in Fig. 7.51c, the spectra do not collapse. An f^{-1} envelope bounds the top of each spectrum and a $-5/3$ law dominates at higher frequencies.

Temperature power spectra downstream of detachment are presented in Fig. 7.52. Near the wall, Fig. 7.52a, continuously curved spectra are observed. Further from the wall, but still below the location of maximum backflow velocity, an $f^{-5/3}$ power-law region is observed. As distance from the wall increases, large eddies contain more energy and no low-frequency region of constant spectra level is observed. This implies that energy exists at frequencies below the 0.2 Hz frequency resolution. Figure 7.52c presents temperature power spectra in the region above the backflow where $\partial T/\partial y = 0$. An f^{-1} power-law region is observed at low frequencies followed by an $f^{-5/3}$ power law region. In the outer flow region where temperature profile similarity was observed, the energy in

large eddies decreases with distance from the wall. A low frequency region of -near-constant spectral level is observed. At higher frequencies an $f^{-5/3}$ region exists.

7.7 Characteristic Frequencies from Power Spectra

Strickland and Simpson (1975) have shown that the characteristic bursting frequency can be determined from the location of the peak in the first moment of spectra $fG(f)$ of wall shearing stress. Simpson et al. (1981 b) report characteristic frequencies in the separated flow studied here from the first moment of spectra of LDA velocity signals.

The significance of the first moment of the spectrum $fG(f)$ can be seen by noting that the area under the power spectrum of a quantity $x(t)$ can be written as

$$\int_0^{\infty} G_{xx}(f) df = \int_0^{\infty} f G_{xx}(f) d(\ln|f|) = \overline{x^2}. \quad (7.30)$$

We also note that the energy associated with an eddy of wave number k is distributed over a region of bandwidth k which is centered around k on a logarithmic scale (Tennekes and Lumley, p. 258). It is then apparent that the area under any frequency range of the $f \cdot G_{xx}(f)$ versus $\ln(f)$ plot represents the fraction of total turbulent energy contributed by eddies associated with that frequency range. The peak in $f \cdot G_{xx}(f)$ occurs at the frequency associated with eddies that contribute the greatest amount to x^2 .

Figure 7.53 shows the first moment of surface heat flux spectra and temperature spectra at several distances from the wall far upstream of detachment, at $x = 285.4$ cm.

The peak in the surface heat flux spectrum $fG_{qq}(f)$ occurs at a frequency approximately half the frequency where the peak in the temperature spectrum $fG_{tt}(f)$ occurs at the y -location nearest the wall. As distance from the wall increases, the location of the peak in $fG_{tt}(f)$ decreases slightly. In the middle region of the boundary layer, the peak in the temperature spectrum occurs over a broad range of frequencies. Figures 7.54 and 7.55 present the first moment of surface heat flux and temperature spectra just upstream of detachment and downstream of detachment, respectively.

For the surface heat flux and temperature measurements at each streamwise location, the first moment of each spectral distribution $fG(f)$ was obtained and the frequency of the peak was selected as the characteristic frequency f_b . Figure 7.56 presents the streamwise distribution of the characteristic frequency of the surface heat flux spectra. In dimensional variables, shown in Fig. 7.56a, the characteristic frequencies decrease continuously approaching detachment and reaches a plateau downstream of detachment. When normalized in outer flow velocity and length scales U_∞ and δ , $U_\infty/\delta f_b$ is approximately 4.6 ± 1.4 at all streamwise locations. The normalized characteristic frequency $U_\infty/\delta f_b$ decreases approaching incipient detachment, increases and levels off just downstream of detachment, and then decreases moving downstream from detachment.

Figure 7.57a - 7.57n shows the characteristic frequency $U_\infty/\delta f_b$ from the temperature spectra plotted versus y/δ for each streamwise measurement location. In many cases the $fG_{tt}(f)$ peak was constant over a frequency range which is represented in Fig. 7.57 by a line over the range of $U_\infty/\delta f_b$ values at a given y/δ .

At a fixed streamwise location, the value of $U_\infty/\delta f_b$ increase with distance from the

wall and reaches a maximum value near $y/\delta = 0.1$. In the outer layer $U_\infty/\delta f_b$ decreases. Upstream of detachment, the value of $U_\infty/\delta f_b$ across the inner boundary layer increases approaching detachment from $U_\infty/\delta f_b \approx 1.3$ at $x = 285.5$ cm to $U_\infty/\delta f_b \approx 5$ near detachment. Proceeding downstream from detachment, $U_\infty/\delta f_b$ initially continues to increase in the inner layer. At $x = 364.49$ cm, $U_\infty/\delta f_b$ ranges from 3.2 near the wall to 7 at $y/\delta = 0.1$. Downstream of $x = 364.49$ cm, values of $U_\infty/\delta f_b$ decrease with streamwise distance near the wall. Further from the wall, the peak in $fG_u(f)$ occurs over a broad range of frequencies where the upper value of $U_\infty/\delta f_b$ are about 40 and the lower values of $U_\infty/\delta f_b$ are about 5.

Figure 7.58 shows characteristic frequency $U_\infty/\delta f_b$ plotted versus y/δ obtained from spectra of streamwise velocity fluctuations (Simpson et al., 1981b). Comparing Figs 7.57 and 7.78, we note that the temperature peak occurs at a characteristic frequency parameter $U_\infty/\delta f_b$ approximately 1/5 of the peak in u -spectra and that the peak occurs over a narrower frequency range.

7.8 Spectral Coherency Between Surface Heat Flux and Temperature

Spectral variations of coherency between surface heat flux and temperature at several locations across the boundary layer at streamwise locations far upstream of detachment, just upstream of detachment, and downstream of detachment are shown in Fig. 7.59a - 7.59c, respectively. Far upstream of detachment, a region of constant coherency is observed at low frequencies followed by a continuous decrease in coherency

at high frequencies. As the location of temperature measurement moves away from the wall, the coherency and the size of the low-frequency region of constant coherence level is reduced. As separation is approached, the region of constant coherency is decreases so that coherency at higher frequencies is reduced.

The spatial variation of coherency was used to compute the coherence length scale for selected frequencies. The spectral variation of coherence length scale is shown for locations upstream of *incipient detachment* in Fig. 7.60a. The coherence length scales have peak value at a frequency between 1 and 10 Hz for all streamwise locations followed by a roll-off of coherence length scale with frequency. Approaching *incipient detachment* coherence lengths scales decrease at all frequencies. Figure 7.60b shows the spectral variation of coherence length scales in the flow region between incipient detachment and detachment. Figure 7.60c shows the spectral variation of coherence length scales in the flow region downstream of detachment. Coherence length scales at low frequencies grow from incipient detachment to slightly downstream of detachment. The maximum coherence lengths scales were observed at $x = 352.4$ cm. Proceeding further downstream past detachment, the coherence length scales decrease with streamwise distance. This agrees with the normalized characteristic frequencies from the surface heat flux spectra shown in Fig. 7.56b.

8 Conclusions

8.1 Turbulent Wing/Body Junction Vortex Heat Transfer

Time- and spatially-resolved heat flux measurements have been made on the endwall surface in a wing/body junction vortex system. Both the time-averaged and fluctuating components of the heat flux have been examined. The maximum value of time-averaged surface heat flux was observed in the immediate vicinity of the wing where the heat flux is three times that found in the approach boundary layer. The high level of heat flux in the region adjacent to the wing is due to the effect of the junction vortex on the mean velocity field. The position of the primary vortex center, and therefore the wing shape, was found to strongly affect the level of heat flux in this region. The near-wing heat flux is decreased by a blunt leading edge shape which moves the horseshoe vortex upstream and away from the wing.

Further upstream, between the separation line and the line of low shear, the time-averaged heat flux was found to be related to the high levels of turbulence stresses produced by the bimodal switching of the velocity field. The heat flux measured in this region was related to the turbulent stresses using a three-dimensional extension of the St' correlation of Maciejewski and Moffat (1992).

The rms of the heat flux fluctuations were as high as 25% of the time-mean heat flux. It was found that the line of low shear and the maximum value of fluctuations in heat flux, q_{rms} , occur at the same location. Histograms of the heat flux fluctuations were highly distorted in the region surrounding the separation line although no bimodal structure was found. Maximum values of skewness and flatness of the histograms of surface heat flux were located near the line of separation. Spectra of the heat flux fluctuations showed high levels of low frequency energy in this region.

8.2 Three-Dimensional Turbulent Boundary Layer Heat Transfer

Heat transfer in a high-Reynolds-number pressure-driven three-dimensional turbulent boundary layer generated by a 3:2 elliptic-nose NACA 0020 tail cylinder protruding from a flat plate was studied experimentally using a constant-current resistance thermometer and a fast response thin-layered surface heat flux gage. Simultaneous time-resolved surface heat flux and temperature profile measurements were taken at eight locations in the spatially-developing three-dimensional turbulent boundary layer upstream of the wing. The measurement locations were upstream of the region dominated by the junction vortex.

The time-mean surface heat flux was decreased approximately 10% by three-dimensionality. The decrease was attributed to a decrease in the near-wall turbulent eddy viscosity. Profiles of mean temperature suggest that the turbulent Prandtl number, $Pr = 0.9$, is unaltered by three-dimensionality. The correlation between mean surface heat

flux and Reynolds number based on the magnitude of an enthalpy thickness vector proposed by Abrahamson and Eaton (1993) collapsed the data.

The near-wall turbulence structure was altered by three dimensionality. Positive values of the skewness factor of temperature fluctuations S_θ and conditionally averaged temperature during a sweep/ejection event suggest that the strength of ejections of hot fluid from the near-wall region was decreased by mean three-dimensionality. The mean frequency of the sweep/ejection process, determined from the temperature and surface heat flux fluctuation spectra using the method of Strickland and Simpson (1977), was unaltered by three-dimensionality when normalized in inner variables. This suggests that ejections do not penetrate as far into the outer layer in a three-dimensional turbulent boundary layer.

Coherency between the inner and outer regions decreased with mean three dimensionality. The spatial variation of coherency between surface heat flux fluctuations and temperature fluctuations at various frequencies collapses onto a single curve when the separation distance is normalized by the coherence length scale. This curve is closely approximated by an exponential-decay model function. For low frequencies below $f\delta/U_\infty \approx 0.2$, the coherence length scale is reduced up to 0.3δ by the increasing three dimensionality of the flow.

In the early stages of development of three-dimensional flow, time-delayed correlations of the surface heat flux and temperature over a range of y locations in the boundary layer indicated the presence of a linear wavefront in the x - y plane inclined at 24° to the wall. The shape of the time-average wave front of the large-scale outer

structures changed with three-dimensionality. The wave front became nonlinear near the wall and the inclination angle of the wave-front increased with three dimensionality.

8.3 Two-Dimensional Separating Turbulent Boundary Layer Heat Transfer

Heat transfer in a two-dimensional, steady free-stream, turbulent boundary layer separating from a smooth surface was studied experimentally using a constant-current resistance thermometer and a fast response thin-layered heat flux gage. Measurements were performed at 14 streamwise locations from far upstream of the location of time-mean detachment to downstream of detachment. At each location time-resolved surface heat flux was measured simultaneously with temperature over a range of locations across the boundary layer.

The time-mean heat transfer decreases rapidly downstream of the location of *incipient detachment* and attains a broad minimum near the location of time-mean detachment, which is approximately 30% below attached-boundary-layer levels. The relation between enthalpy thickness Reynolds number and Stanton number valid for zero and mild adverse-pressure gradient flows breaks down downstream of the location of incipient detachment. Downstream of the location of time-mean detachment, heat transfer increases rapidly. The surface heat transfer under the backflow region was correlated to large near-wall velocity fluctuations.

The rms of surface heat flux fluctuations attain a maximum value near the location

of time-mean detachment. Skewness and flatness factors of surface heat flux fluctuations increase to large values downstream of detachment.

Profiles of mean temperature across the boundary layer revealed that the majority of temperature difference between the wall and freestream occurs in the near-wall region even near detachment. Similarity of streamwise velocity and temperature profiles breaks down in an adverse pressure gradient. The law-of-the-wall profile based on skin friction and St does not hold for mean temperature profiles in a strong adverse pressure gradient. Mean temperature profiles upstream of incipient detachment scale using the coordinates proposed by Blackwell et al. (1972). Mean temperature profiles in the outer 97% of the boundary layer upstream of detachment scale on a defect-law profile shape similar to the Perry-Schofield velocity correlation. Conventional defect laws involving C_f are not appropriate for temperature profiles for separating flows.

Downstream of incipient detachment, no similarity law was found for the inner region. Downstream of detachment, profiles of mean temperature have a large region where $\partial T/\partial y \approx 0$. Temperature profiles in the backflow region do not obey the same scaling laws as the backflow velocity profile. The large temperature gradient near the wall in the backflow region suggests that turbulent transport of heat is significant.

Upstream of detachment, the location of maximum temperature fluctuations occurs much closer to the wall than the location of maximum velocity fluctuations. Downstream of detachment, temperature fluctuations are very large near the wall and decrease in the region away from the wall where $dT/dy \approx 0$. Further away from the wall a second local maxima in profiles of the temperature fluctuations was observed where the dT/dy was

observed to increase.

Large values of the skewness factor of temperature fluctuations were observed in the near-wall region. The near-wall values of S_θ increase approaching and through detachment. Similarity in the θ' , S_θ , and F_θ was observed in the near wall region when the y^* coordinates proposed by Blackwell et al. (1972) were used. The location of maximum θ' , the location where S_θ changes sign, and the location of minimum F_θ all occur at $y^* \approx 20$ both upstream and downstream of detachment. Profiles of θ' , S_θ , and F_θ collapse in the outer region when plotted versus y/δ .

The characteristic frequency $U_\infty/f_b\delta$, determined from the first moment of surface heat flux fluctuation power spectra, decreases with streamwise distance to the location of insipient detachment, increases and reaches a maximum just downstream of the location of time-mean detachment, and decreases slightly in backflow. The same trend was observed in the coherence length scale at frequencies below 10 hz. In the backflow region, surface heat flux is not correlated with temperature fluctuations in the outer layer directly above.

REFERENCES

- Abbott, I.H., and Von Doenhoff, A.E, *Theory of Wing Sections*, Dover Publications, Inc., New York; 1949.
- Abrahamson, S.D., and Eaton, J.K., "Heat Transfer Through a Pressure-Driven Three-Dimensional Boundary Layer," *Journal of Heat Transfer*, Vol. 113, pp. 355-362, 1991.
- Adams, E.W, and Johnston, J.P., "Flow Structure on the Near-Wall Zone of a Turbulent Separated Flow," *AIAA Journal*, Vol. 21, pp. 932-935; 1988.
- Agarwal, N.K., and Simpson, R.L., "Backflow Structure and Unsteady Separating Turbulent Boundry Layers," *AIAA Journal*, Vol. 28, No. 10, pp. 1764 - 1771; 1990.
- Ahn, S., and Simpson, R. L., "Convective Wave Speed and Spectral Features of Turbulent Boundary Layers," AIAA Paper No. 87-0198; 1987.
- Ambrok, G.S, "Approximate Equation for the Thermal Boundary Layer with Variations in Boundary Layer Structure," *Soviet Physics, Technical Physics*, Vol. 2, No. 9, pp. 1979 - 1986; 1957.
- Ames, F. E., and Moffat, R. J., "Heat Transfer with High Intensity, Large Scale Turbulence: The Flat Plate Turbulent Boundary Layer and the Cylindrical Stagnation Point," Stanford University Report No. HMT-44; 1990.
- Ancraka, C. E., and Diller, T. E., "Heat-Transfer Distribution Around a Cylinder in Pulsating Crossflow," *Transactions of the ASME*, Vol. 107, pp. 976-982; 1985.
- Anderson, S., and Eaton, J.K., "Reynolds Stress Development in Pressure-Driven Three Dimensional Turbulent Boundary Layers," *J. Fluid Mech.*, Vol. 202, pp. 263 - 294; 1989.
- Andreopoulos, J., Durst, F., Zaric, Z., and Jovanovic, J., "Influence of Reynolds Number on Characteristics of Turbulent Wall Boundary Layers," *Experiments in Fluids*, Vol. 2, pp. 7 - 16; 1984.
- Antonia, R.A., Browne, L.W.B., and Chambers, A.J., "Determination of Time Constants of Cold Wires," *Rev. Sci. Instrum.*, Vol. 52, No. 9, pp. 1382 - 1385; 1981.

Antonia, R.A., Browne, L.W.B., and Chambers, A.J., "Use of Fine Cold-Wires for the Measurement of Dissipation of Temperature Fluctuations," *DISA Information No. 27*, pp. 27 - 30; 1982.

Antonia, R.A., and Kim, J., "Similarity between Turbulent Kinetic Energy and Temperature Spectra in the Near-Wall Region," *Phys. Fluids A*, Vol. 3., No. 5, pp.989 - 991; May, 1991.

Antonia, R.A., Krishnamoorthy, L.V., and Fulachier, L., "Correlation Between the Longitudinal Velocity Fluctuation and Temperature Fluctuation in the Near-Wall Region of a Turbulent Boundary Layer," *International Journal of Heat and Mass Transfer*, Vol. 31, No. 4, pp. 723 - 730; 1988

Aung, W., "Separated Forced Convection," Proceedings of ASME-JSME Joint Conference, Hawaii, v.2, pp. 499-515; 1982.

Aung, W., and Watkins, C.B., "heat Transfer Mechanisms in Separated Forced Convection," *Turbulent Forced Convection in Channels and Bundles - Theory and Applications to Heat Exchangers and Nuclear Reactors*, ed. S. Kakac and D.B. Spalding, Hemisphere Publishing Corp., pp. 233 - 256; 1989

Bagheri, N., Strataridakis, B.R., and White, B.R., (1992) "Turbulent Prandtl Number and Space-Time Temperature Correlation Measurements in an Incompressible Turbulent Boundary Layer," *AIAA Journal*, Vol. 30., pp. 35 - 42.

Bagheri, N., and White, B.R., "Experimental Measurements of Large-Scale Temperature Fluctuation Structures in a Heated Incompressible Turbulent Boundary Layer," *International Journal of Heat and Mass Transfer*, Vol. #, No. #, pp. 907 - 918; 1993

Bagheri, N., White, B.R., and Lei, T., "Nonisothermal Turbulent Boundary-Layer Adverse Pressure Gradient Large Scale Thermal Structure Measurement," *AIAA Journal of Thermophysics and Heat Transfer*, Vol 8, No. 1, pp. 68 - 74; 1994.

Baker, K., "Unsteady Surface Heat Flux and Temperature Measurement," M.S. thesis, Virginia Polytechnic Institute and State University, Blacksburg, VA; 1993.

Baughn, J.W., Hoffman, M.A., Launder, B.E., and Takaahashi, R.K., "Local Heat Transfer Downstream of an Abrupt Expansion in a Circular Channel with Constant Wall Heat Flux," *J. Heat Transfer*, Vol. 106, pp. 789-796; 1984.

Baughn, J.W., Hoffman, M.A., Launder, B.E., Lee, D., and C. Yap, "Heat Transfer, Temperature, and Velocity Measurements Downstream of an Abrupt Expansion in a Circular Tube at Uniform Wall Temperature," *J. Heat Transfer*, Vol. 3, pp. 870-876; 1989.

Bendat, J.S., and Piersol, A.G., *Random Data: Analysis and Measurement Procedures*, 2nd Ed., Wiley Intersciences, New York; 1986.

Bettelini, M.S.G., and Fanneløp, T.K., "Systematic Comparison of Mathematically Simple Turbulence Models for Three-Dimensional Boundary Layers," *AIAA Journal*, Vol. 31, No. 6, pp. 999 - 1006; 1993.

Blackwelder, R.F., and Haritonitus, J.H., "Scaling of the Bursting Frequency in Turbulent Boundary Layers," *J. Fluid Mech.*, Vol. 132, pp. 87 - 103; 1983.

Blackwelder, R.F., and Kaplan, R.E., "On the Wall Structure of the Turbulent Boundary Layer," *J. Fluid Mech.*, Vol. 76, part 1, pp. 89 - 112; 1976.

Blackwell, B.F., Kays, W.M., and Moffat, R.J., "The Turbulent Boundary Layer on a Porous Plate: An Experimental Study of the Heat Transfer Behavior with Adverse Pressure Gradients," Stanford University Report No. HMT-16; 1972

Blair, M. F., "An Experimental Study of Heat Transfer and Film Cooling on Large-Scale Turbine Endwalls," *ASME Journal of Heat*, pp. 524-529; 1984.

Borell, G. J., and Diller, T. E., "A Convection Calibration Method for Local Heat Flux Gages," *Journal of Heat Transfer*, Vol. 109, pp. 83-89; 1987.

Bradshaw, P., " 'Inactive' Motion and Pressure Fluctuations in Turbulent Boundary Layers," *J. Fluid Mech.*, Vol. 30, part 2., pp. 241 - 258; 1967.

Bradshaw, P., Ferriss, D.H., and Atwell, N.P., "Calculations of Boundary Layer Development Using the Turbulent Energy Equation," *J. Fluid Mech.*, Vol. 28, pp. 593 - 616; 1967.

Bremhorst, K., and Bullock, K. J., "Spectral Measurements of Temperature and Longitudinal Velocity Fluctuations in Fully Developed Pipe Flow," *Int. J. Heat Mass*, Vol. 13, pp. 1313-1329; 1969.

Bremhorst, K., and Gilmore, D.B., "Influence of End Conduction on the Sensitivity to Stream Temperature Fluctuations of a Hot-Wire Anemometer," *International Journal of Heat and Mass Transfer*, Vol. 21, pp. 145 - 154; 1978.

Bremhorst, K., and Graham, L.J.W., "A Fully Compensated Hot/Cold Wire Anemometer System for Unsteady Flow Velocity and Temperature Measurements," *Meas. Sci. Technol.*, Vol. 1, pp. 425 - 430; 1990.

Bremhorst, K., and Krebs, L., "Reconsideration of Constant Current Hot-Wire Anemometers for the Measurement of Fluid Temperature Fluctuations," *J. Phys. E.: Sci. Inst.*, Vol. 9, pp. 804-806, 1976.

Bremhorst, K., and Krebs, L., and Gilemore, D.B., "The Frequency Response of Hot-Wire Anemometer Sensors to Heating Current Fluctuations," *Int. J. Heat Mass Transfer*, Vol. 20, pp. 315 - 322; 1977.

Brooks, T.F., and Hodgson, T.H., "Trailing Edge Noise Prediction from Measured Surface Pressures," *Journal of Sound and Vibration*, Vol. 78, No. 1, pp. 69 - 117; 1981.

Brown, G.L., and Thomas, A.S.W., "Large Structure in a Turbulent Boundary Layer," *The Physics of Fluids*, Vol. 20, No. 10, Pt. II, pp. S243 - S252; 1977.

Chapman, D.R., and Kuhn, G.D., "The Limiting Behavior of Turbulence Near a Wall," *J. Fluid Mech.*, Vol. 170, pp. 265 - 292; 1986.

Chen, C.P., and Blackwelder, R.F., "Large-Scale Motion in a Turbulent Boundary layer: a Study using Temperature Contamination," *J. Fluid Mech.*, Vol. 89, part 1, pp. 1 - 31; 1978.

Chehroudi, B., and Simpson, R.L., "Space-Time Results for a Separating Turbulent Boundary Layer Using a Rapidly Scanning Laser Anemometer," *J. Fluid Mech.*, Vol. 160, pp. 77 - 92; 1985.

Coles, D.E., and Hirst, E.A., *Proceedings Computation of Turbulent Boundary Layers - 1968*, AFOSR-IFP-Stanford Conference, Vol. II, p. 49; Department of Mechanical Engineering, Stanford University, Stanford, CA; 1968.

Corcos, G.M., "Resolution of Pressure in Turbulence," *J. of the Acoustical Society of America*, Vol. 35, Number 2, pp. 192 - 199; 1963.

Corcos, G.M., "The Resolution of Turbulent Pressures at the Wall of a Boundary Layer," *J. Sound Vib.*, Vol. 6, No. 1, pp. 59 - 70; 1967.

Corino, G.M., and Brodkey, R.S., "A Visual Investigation of the Wall Region in Turbulent Flow," *J. Fluid Mech.*, Vol. 37, pp. 1 - 30; 1969.

Degani, A.T., Smith, F.T., and Walker, J.D.A., "The Structure of a Three-Dimensional Turbulent Boundary Layer," *J. Fluid Mech.*, Vol. 250, pp. 43 - 68; 1993.

Devenport, W. J., Agarwal, N. K., Dewitz, M. B., Simpson, R. L., and Poddar, K., "An Experimental Study of Devices For Controlling the Flow Past a Wing-Body Junction, (Edited Version: Baseline Case Only)," Preliminary Technical Report to The Office on Naval Research, Report AERO-170; 1989.

Devenport, W. J., and Simpson, R. L., "Turbulence Structure Near the Nose of a Wing/Body Junction," AIAA-87-1310; 1987.

Devenport, W.J., and Simpson, R.L., "Time-Dependent Structure in the Wing-Body Junction Flows," *Turbulent Shear Flows 6*, Springer-Verlag, Berlin, 1989, pp. 232 - 248; 1989.

Devenport, W. J. and Simpson, R. L., *An Experimental Investigation of the Flow Past an Idealized Wing-Body Junction: Preliminary Data Report v. 5*, VPI Technical Report No. VPI-AOE-172, VPI&SU, Blacksburg, VA, 24061; 1990a. (Available from DTIC)

Devenport, W. J., and Simpson, R. L., "Time-Dependent and Time-Averaged Turbulence Structure Near the Nose of a Wing-Body Junction," *J. of Fluid Mech.*, Vol. 210, pp. 23-55; 1990b.

Devenport, W. J., and Sutton, P.E., "Near-Wall Behavior of Separated and Reattaching Flows," *AIAA Journal*, Vol. 29, No. 1, pp. 25 - 31; 1991.

Dianat, M., and Castro, I.P., "Measurements in Separating Boundary Layers," *AIAA Journal*, Vol. 6, No. 27, pp. 719 - 724; May 1989.

Diller, T. E., and Telionis, D. P., "Time-Resolved Heat Transfer and Skin Friction Measurements in Unsteady Flow," in *Advances in Fluid Mechanics Measurements, Lecture Notes in Engineering*, Ed. M. Gadel-Hak, Springer-Verlag, Berlin, pp.323-355; 1989.

Doeblin, E.O., *Measurment Systems Application and Design*, 4th Ed., McGraw-Hill, New York; 1990.

Dunn, M. G., and Stoddard, F. J., "Measurement of Heat-Transfer Rate to a Gas Turbine Stator," *ASME Journal of Engineering for Power*, Vol. 101, pp. 275-280; 1979.

Durst, F., Jovanovic, J., and Kanevce, Lj., "Probability Density Distribution in Turbulent Wall Boundary-Layer Flows," *Turbulent Shear Flows 5*, Springer-Verlag, pp. 197 - 220; 1987

Eibeck, P.A., and Eaton, J.K., "Heat Transfer Effects of a Longitudinal Vortex Embedded in a Turbulent Boundary Layer," *J. of Heat Transfer*, Vol. 109, pp. 16 - 24; Feb. 1987.

Elena, M., "Title missing," *International Journal of Heat and Mass transfer*, Vol. 20, pp. 935; 1977.

Falco, R.E., *Phys. of Fluids*, Vol. 20, pp. S124; 1977

Fiedler, H., "On Data Acquisition in Heated Turbulent Flows," In *Proc. Dyn. Flow Conf.*, Skovlunde, Denmark, PP. 81-100, 1978.

Fiedler, H., "A Note on the Resistance Characteristics of Cold-Wire Probes," *DISA Information No. 27*, pp. 38 - 39; 1982.

Fiedler, H., "Coherent Structures in Turbulent Flows," *Prog. Aerospace Sci.*, Vol. 25, pp. 231 - 269; 1988.

Fisher, E.M., and Eibeck, P.A., "The Influence of a Horseshoe Vortex on Local Convective Heat Transfer," *J. of Heat Transfer*, Vol. 112, pp. 329 - 335; May 1990.

Flack, K.A., and Johnston, J.P., "Near-Wall Structure of Three-Dimensional Turbulent Boundary Layers," *9th Symposium on Turbulent Shear Flows*, University Park, PA; 1995.

Fleming, J. L., Simpson, R. L., and Devenport, W. J., "An Experimental Study of a Turbulent Wing-Body Junction and Wake Flow," AIAA Paper No. 92-0434; *Experiments in Fluids*, Vol. 14, pp. 366 - 378; 1993

Fleming, J.L., and Simpson, R.L., "Experimental Investigation of the Near Wall Flow Structure of a Low Reynolds Number 3-D Turbulent Boundary Layer," AIAA-94-0649, AIAA 32nd Aerospace Sciences Meeting, Reno, NV, Jan. 10-13, 1994.

Fleming, J.L., Simpson, R.L., and Shinpaugh, K., "Further Investigation of the Near Wall Flow Structure of a Low Reynolds Number 3-D Turbulent Boundary Layer," AIAA-95-0788, AIAA 33rd Aerospace Sciences Meeting, Reno, NV, Jan. 9-12, 1995.

Fulachier, L. and Antonia, R.A., "Spectral Analogy Between Temperature and Velocity Fluctuations in Several Turbulent Flows," *International Journal of Heat and Mass Transfer*, Vol. 27, No. 7, pp. 987 - 997; 1984.

Fulachier, L., and Dumas, R., "Spectral Analogy Between Temperature and Velocity Fluctuations in a Turbulent Boundary Layer," *J. Fluid Mech.*, Vol. 77, part 2, pp. 257-277, 1976.

Gad-el-Hak, M., and Bandyopadhyay, P.R., "Reynolds Number Effects in Wall-Bounded Turbulent Flows," *Appl Mech Rev*, Vol. 47, No. 8, pp. 307 - 364; 1994.

Garcia, A., and Sparrow, E.M., "Turbulent Heat Transfer Downstream of a Contraction-Related, Forward-Facing Step in a Duct," *J. Heat Transfer*, Vol. 109, pp. 621 - 626; 1987.

Gaugler, R. E., and Russell, L. M., "Comparison of Visualized Turbine Endwall Secondary Flows and Measured Heat Transfer Patterns," ASME paper No. 83-GT-83; 1983.

Georjoui, D. P., Godard, M., and Richards, B. E., "Experimental Study of the Iso-Heat-Transfer-Rate Lines on the End-Wall of a Turbine Cascade," ASME paper No. 79-GT-20; 1979.

Graziani, R.A., Blair, M.F., Taylor, J.R., and Mayle, R.E., "An Experimental Study of Endwall and Airfoil Surface Heat Transfer in a Large Scale Turbine Blade Cascade," *Journal of Engineering for Power*, Vol. 102, pp.257-267; 1980.

Gundappa, M., and Diller, T. E., "The Effects of Freestream Turbulence and Flow Pulsation on Heat Transfer to a Cylinder in Crossflow," *Augmentation of Heat Transfer in Energy Systems*, HTD Vol. 52, Editor: P. J. Bishop; 1985.

Ha, S.M., "Experimental Study of Coherent Structures in a Three-Dimensional Turbulent Boundary Layer," Ph.D. Dissertation, Department of Aerospace and Ocean Engineering, Va, Tech, Blacksburg, VA; 1993.

Ha, S., and Simpson, R.L., "An Experimental Investigation of a Three-Dimensional Turbulent Boundary Layer Using Multiple-Sensor Probes," Paper 2-3, *Ninth Symposium on Turbulent Shear Flows*, Kyoto, Japan, Aug. 16-18, 1993.

Haker, J.M., and Eaton, J.K., "Heat Transfer Measurements in a Backward Facing Step Flow with Arbitrary Wall Temperature Variations," Stanford Report No. MD-71, Department of Mechanical Engineering, Stanford University, Stanford, CA; 1995.

Hager, J.M., Langley, L.W., Onishi, S., and Diller, T.E., "High Temperature Heat Flux Measurements," AIAA paper 91-0165, AIAA 29th Aerospace Sciences Meeting, Reno, NV, Jan. 7 - 10; 1991a.

Hager, J. M., Simmons, S., Smith, D., Onishi, S., Langley, L. W., and Diller, T. E., "Experimental Performance of a Heat Flux Microsensor," *ASME Journal of Turbomachinery*, Vol. 113, 1991, pp. 246-250; 1991b.

Hager, J.M., Terrell, J.P., Langley, L.W., Onishi, S., and Diller, T.E., "Measurements with the Heat Flux Microsensor," *Proceedings of the 37th International Instrumentation Symposium*, Instrument Society of America, Research Triangle Park, NC, pp. 551-561, 1991c.

Hanjalić, K., Jakirlić, S., and Durst, F., "A Computational Study of Joint Effects of Transverse Shear and Streamwise Acceration on Three-Dimensioanl Boundary Layers," *Int. J. Heat and Fluid Flow*, Vol. 15, No. 4, Aug., pp. 269-282; 1994

Head, M.R., and Bandyopadhyay, P., (1979) AGARD Conference Proc., CP 271, 25.1.

Head, M.R., and Bandyopadhyay, P.R., "New Aspects of Turbulent Boundary layer Structure," *J. Fluid Mech.*, Vol. 107, pp. 297 - 338; 1981.

Hippensteele, S. A., and Russell, L. M., "High-Resolution Liquid-Crystal Heat-Transfer Measurements on the End Wall of a Turbine Passage with Variations in Reynolds Number," NASA Technical Memorandum 100827; 1988.

Hishida, M., and Nagano, Y., "Simultaneous Measurments of Velocity and Temperature in Nonisothermal Flows," *J. Heat Transfer*, Vol. 100, pp. 340 - 345; May 1978.

Hishida, M., and Nagano, Y., "Structure of Turbulent Velocity and Temperature Fluctuations in Fully Developed Pipe Flow," *Journal of Heat Transfer*, Vol. 101, No. 1, pp. 15-22; 1979.

Hishida, M., and Nagano, Y., "Structures of Turbulent Heat Transfer," *Heat Transfer in High Technology and Power Engineering*, (eds. W.J. Yang and Y. Mori), pp. 488 - 499; 1987.

Højstrup, J., Rasmussen, K., and Larsen, S.E., "Dynamic Calibration of Temperature Wires in Still Air," *DISA Information No. 20*, pp. 22 - 30; 1976.

Hylton, L.D., Mihelc, M.S., Turner, E.R., and York, R.E., "Experimental Investigation of the Turbine Endwall Heat Transfer," AFWAL-TR-81-2077, three volumes; 1981.

Johansson, A.V., and Alfredsson, P.H., "On the Structure of Turbulent Channel Flow," *J. Fluid Mech.*, Vol. 122, pp. 295 - 314; 1982.

Johnston, J.P., and Flack, K.A., "Advances in Three-Dimensional Turbulent Boundary Layers with Emphasis in the Wall-Layer Region," *Symposium on Boundary Layer and Free Shear Flows*, Lake Tahoe, NV, June 19 - 23; revision submitted to J. Fluids Engrg., TASME; 1994.

Kays, W. M., and Crawford, M. E., *Convection Heat and Mass Transfer*, 2nd Ed., McGraw-Hill, New York; 1980.

Kim, H.T., Kline, S.J., and Reynolds, W.C., "The Production of the Wall Region in Turbulent Flow," *J. Fluid Mech.*, Vol. 50, pp. 133 - 160; 1971.

Kim, S.A., "Observation and Measurement of Flow Structure in the Stagnation Region of a Wing-Body Junction," Ph.D. Dissertation, Department of Aerospace and Ocean Engineering, Virginia Polytechnic Institute and State University, Blacksburg, VA; 1991.

Kline, S.J., Reynolds, W.C., Schraub, F.A., and Runstadler, P.W., "The Structure of Turbulent Boundary Layers," *J. Fluid Mech.*, Vol. 30, pp. 741 - 773; 1967.

Kline, S.J., "Boundary Layer Structure - A Summary," unpublished *RINGI group report*; 1992.

Kline, S.J., and McClintock, F.A., "Describing Uncertainty in Single Sample Experiments," *Mechanical Engineering (ASME)*, Vol. 75, pp. 3-8; 1953.

Kolmogoroff, A.N., "The Local Structure of Turbulence in Incompressible Viscous Fluid for Very Large Reynolds Numbers," *C.R. Acad. Sci. U.R.S.S.*, Vol. 30, pp. 301 - 305; 1941.

Kovasznay, L.S.G., "Development of Turbulence Measuring Equipment," *National Advisory Committee for Aeronautics Report* 1209.

Kraabel, J. S., Baughn, J. W., and McKillop, A. A., "An Instrument for the Measurement of Heat Flux from a Surface with Uniform Temperature," *Journal of Heat Transfer*, Vol. 18, pp. 1387-1396; 1980.

Launder, B.E., "On the Computation of Convective Heat Transfer in Complex Turbulent Flows," *J. Heat Transfer*, Vol. 110, pp. 1112 - 1128; 1988.

Lewis, D.J., Simpson, R.L., and Diller, T.E., "Time-Resolved Surface Heat Flux Measurements in the Wing/Body Junction Vortex," AIAA-93-0918, AIAA 31st Aerospace Sciences Meeting, Reno, NV, Jan. 11 -14; 1993

Lewis, D.J., Simpson, R.L., and Diller, T.E., "Time-Resolved Surface Heat Flux Measurements in the Wing/Body Junction Vortex," *AIAA Journal of Thermophysics and Heat Transfer*, Vol. 8, No. 4, pp. 656 - 663; 1994.

Ligraini, P.M., Westphal, R.V., and Lemos, F.R., "Fabrication and Testing of Subminiature Multi-Sensor Hot-Wire Probes," *J. Phys. E: Sci. Instrum.*, Vol. 22, pp. 262 - 268; 1989.

Lomas, C.G., Fundamentals of Hot-Wire Anemometry, *Cambridge University Press*, 1990

Lu, S., and Willmarth, W.W., "Measurements of the Structure of Ejections and Bursts in Turbulent Channel Flows," *J. Fluid Mech.*, Vol. 174, pp. 529 - 552; 1987.

Luchik, T.S., and Tiederman, W.G., "Timescales and Structure of Ejections and Bursts in Turbulent Channel Flows," *J. Fluid Mech.*, Vol. 174, pp. 529 - 552; 1987.

Maciejewski, P. K., and Moffat, R. J., "Heat Transfer With Very High Turbulence Free-Stream Turbulence: Part II - Analysis of Results," *ASME Journal of Heat Transfer*, Vol. 114, pp. 834-839; 1992.

Moffat, R.J., and Kays, W.M. "A Review of Turbulent Boundary-Layer Heat Transfer Research at Stanford, 1958-1983," in *Advances in heat Transfer*, Edited by Hartnett, J.P., and Irvine, T.F., Vol. 16., Academic Press, New York; 1984.

Mori, Y., Uchida, Y., and Sakai, K., "A Study of the Time and Spatial Structure of Heat Transfer Performance near the Reattaching Point of Separated Flows," *Proceedings of the Int'l Heat Transfer Conf.*, Vol. 3, pp. 1083 - 1088; 1986.

Nagano, Y., and Hishida, M., "Turbulent Heat Transfer Associated with Coherent Structures Near the Wall," in *Near-Wall Turbulence*, Edited by Kline, S.J., and Afgan, N.H., Hemisphere Publishing Corp., New York, NY, pp. 568 - 589; 1990.

Nagano Y., and Tagawa, M., "Statistical Characteristics of Wall Turbulence with a Passive Scalar," *J. Fluid Mech.*, Vol. 196, pp. 157 - 185; 1988

Nagano, Y., and Tagawa, M., "A Structural Turbulence Model for Triple Products of Velocity and Scalar," *J. Fluid Mech.*, Vol. 215, pp. 639 - 657; 1990.

Nagano, Y., and Tagawa, M., "Turbulence Model for Triple Velocity and Scalar Correlations," *Turbulent Shear Flows 7*, Springer-Verlag, pp. 47 - 62; 1991.

Nagano, Y., and Tsuji, T., "Recent Developments in Hot- and Cold-Wire Techniques for Measurements in Turbulent Shear Flows near Walls," *Experimental Thermal and Fluid Science*, Vol. 9, pp. 94 - 110; 1994.

Nychas, S.G., Hershey, H.C., and Brodkey, R.S., "A Visual Study of Turbulent Shear Flow," *J. Fluid Mech.*, Vol. 61, pp. 513-540; 1973.

Ölçmen, M.S., and Simpson, R.L., *An Experimental Investigation of a Three-Dimensional Pressure Driven Turbulent Boundary Layer*, VPI Technical Report No. VPI-AOE-178, Virginia Polytechnic Institute and State University, Blacksburg, VA, 1990. (Available from DTIC)

Ölçmen, S. M., and Simpson, R. L., "Perspective: On the Near Wall Similarity of Three-Dimensional Turbulent Boundary Layers," *Journal of Fluids Engineering*, Vol. 114, pp. 487 - 495; 1992.

Ölçmen, S. M., and Simpson, R. L., "Evaluation of Algebraic Eddy-Viscosity Models in Three-Dimensional Turbulent Boundary Layer Flows," *AIAA Journal*, Vol. 31, pp. 1545 - 1544; 1993.

Ölçmen, S. M., and Simpson, R. L., "Influence of Wing Shapes on the Surface Pressure Fluctuations of a Wing-Body Junction," *AIAA Journal* Vol. 32. No. 1, pp. 6 - 15; 1994.

Ölçmen, S. M., and Simpson, R. L., "An Experimental Study of a Three-Dimensional Pressure-Driven Turbulent Boundary layer," *J. Fluid Mech.*, Vol. 290, pp. 225 - 262; 1995a.

Ölçmen, S. M., and Simpson, R. L., "Higher Order Turbulence Results for a Three-Dimensional Pressure-Driven Turbulent Boundary Layer," submitted to *J. Fluid Mech.*; 1995b.

Ölçmen, S. M., and Simpson, R. L., "Some Structural Features of a Three-Dimensional Pressure-Driven Turbulent Boundary Layer," manuscript in preparation for *J. Fluid Mech.*; 1995c.

Ölçmen, S. M., and Simpson, R. L., "A Five-Velocity-Component Laser-Doppler Velocimeter for Measurements of a Three-Dimensional Turbulent Boundary Layer," *Measurement Science and Technology*, Vol. 6, pp. 702 - 716; 1995d

Ota, T., and Hishiyama, M., "A Correlation of maximum Turbulent Heat Transfer Coefficient in Reattachment Flow Region," *International Journal of Heat and Mass Transfer*, Vol. 30, pp. 1193 - 1200; 1987.

Paranthoen, P., Lecordier, J.C., and Petit, C., "Influence of Dust Contamination on Frequency Response of Wire Resistance Thermometers," *DISA Information* No. 27; 1992.

Parihk, P.G., Kays, W.M., and Moffat, R.J., "A Study of Adverse Pressure Gradient Turbulent Boundary Layers with Outer Region Non-Equilibrium," Stanford Report No. HMT-26, Department of Mechanical Engineering, Stanford University, Stanford, CA; 1976.

Perry, A.E., Henbest, S., and Chong, M.S., "A Theoretical and Experimental Study of Wall Turbulence," *J. Fluid Mech.*, Vol. 165, pp. 163 - 199; 1986.

Perry, A.E., and Schofield, W.H., "Mean Velocity and Shear Stress Distributions in Turbulent Boundary Layers," *Phys. Fluids*, Vol. 16, pp. 2068 - 2074; 1973.

Praturi, A.K., and Brodkey, R.S., "A Stereoscopic Visual Study of Coherent Structures in Turbulent Shear Flow," *J. Fluid Mech.*, Vol. 89, pp. 251 - 272; 1978.

Rife, M. C., "An Experimental Study of the Relation-ship Between Velocity and Pressure Fluctuations in a Wing-Body Junction," M.S. Thesis, Aerospace and Ocean Engineering Department, Virginia Polytechnic Institute and State University, Blacksburg, VA 24061; 1992.

River, R.B., Johnston, J.P., and Eaton, J.K., "Heat Transfer on a Flat Surface Under a Region of Turbulent Separation," *Journal of Turbomachinery*, Vol. 116, pp. 57 - 62; 1994.

Robinson, S.K., "A Perspective on Coherent Structures and Conceptual Models for Turbulent Boundary Layer Physics," AIAA-90-1638; 1990.

Robinson, S.K., "Coherent Motions in the Turbulent Boundary layer," *Annu. Rev. Fluid Mech.*, Vol. 23, pp. 601 - 639; 1991.

Rust, J. H. and Sesonske, A., "Turbulent Temperature Fluctuations in Mercury and Ethylene Glycol in Pipe Flow," *Int. J. Heat Mass Transfer*, Vol. 9, pp. 215-227; 1966.

Schetz, J.A., *Boundary Layer Analysis*, Prentice-Hall, Englewood Cliffs, New Jersey, 1993.

Schlichting, H., *Boundary Layer Theory*, 6th Ed., McGraw-Hill, New York, p. 613; 1968.

Sendstad, O., and Moin, P., "The Near Wall Mechancis of Three-Dimensional Turbulent Boundary Layers," Stanford Report No. TF-57, Thermosciences Division, Department of Mechanical Engineering, Stanford University, Stanford, CA; 1992.

Shisov, E.V., Roganov, P.S., Grabarnik, S.I., and Zabolotsky, V.P., "Heat Transfer in the Recirculating Region Formed by a Backward-Facing Step," *Int. J. Heat Mass Transfer*, Vol. 31, pp. 1557-1562; 1988.

Shiloh, K., Shivaprasad, B.G., and Simpson, R.L., "The Structure of a Separating Turbulent Boundary Layer. Part 3. Transverse Velocity Measurements," *J. Fluid Mech.*, Vol. 113, pp. 75 - 90; 1981.

Simmons, S. G., Hager, J. M., and Diller, T. E., "Simultaneous Measurements of Time-Resolved Surface Heat Flux and Freestream Turbulence at a Stagnation Point," in *Heat Transfer* 1990, Vol. 2, Ed. G. Hetsroni, Hemisphere Pub. Corp., NY, pp. 375-380; 1990.

Simonich, J.C., and Bradshaw, P., "Effect of Free-Stream Turbulence on Heat Transfer Through a Turbulent Boundary Layer," *J. Heat Transfer*, Vol. 100, p. 673; 1978.

Simpson, R.L., "Some Features of Strongly Accelerated Turbulent Boundary Layers," paper 18.8, 2nd Symposium on Turbulent Shear Flows, London, July 2 - 4; 1979.

Simpson, R.L., "A Review of Some Phenomena in Turbulent Flow Separation," *J. Fluids Eng.*, Vol. 102, pp. 520 - 533; 1981.

Simpson, R.L., "A Model for the Backflow Mean Velocity Profile," *AIAA Journal*, Vol. 21, No. 1, pp. 142-143; 1983.

Simpson, R.L., "Two-Dimensional Turbulent Separated Flow," *AGARDograph* 287, Vol. 1; 1985.

Simpson, R.L., "A Review of Two-Dimensional Turbulent Separated Flow Calculation Methods," *IUTAM Symp. Boundary Layer Separation*, Springer-Verlag, London, ed. F.T. Smith, S.N. Brown, Berlin, pp. 179 - 196; 1987.

Simpson, R.L., "Turbulent Boundary-Layer Separation," *Ann. Rev. Fluid Mech.* Vol. 21, pp. 205 - 234; 1989.

Simpson, R.L., "Three-Dimensional Turbulent Boundary Layers and Separation," AIAA paper No. 95-0226, 33rd Aerospace Sciences Meeting and Exhibit, Reno, NV; 1995

Simpson, R.L., "Aspects of Turbulent Boundary-Layer Separation," *Progress in Aerospace Sciences*, July, 1996.

Simpson, R.L., Agarwal, N.K., Nagabushana, K.A., and Ölçmen, S., "Spectral Measurements and Other Features of Separating Turbulent Flows," *AIAA Journal*, Vol. 28, No. 3, pp. 446 - 452; 1988.

Simpson, R.L., Chew, Y.T., and Shivaprasad, B.G., *Measurements of a Separating Turbulent Boundary Layer*, Project SQUID Rep. SMU-4-PU, Southern Methodist University, Dallas, TX, DTIC number AD-A095-252/3; 1980.

Simpson, R.L., Chew, Y.T., and Shivaprasad, B.G., "The Structure of a Separating Turbulent Boundary Layer. Part 1. Mean Flow and Reynolds Stresses," *J. Fluid Mech.*, Vol. 113, pp. 23 - 51; 1981a.

Simpson, R. L., Chew, Y. T., and Shivaprasad, B. G., "The Structure of a Separating Turbulent Boundary Layer. Part 2. Higher-Order Turbulence Results," *J. Fluid Mech.*, Vol. 113, pp. 53 - 73; 1981b.

Simpson, R.L., Ghodbane, M., and McGrath, B.E., "Surface Pressure Fluctuations in a Separating Turbulent Boundary Layer," *J. Fluid Mech.*, Vol. 177, pp. 167 - 186; 1987.

Simpson, R.L, Whitten, D.G., and Moffat, R.J., "An Experimental Study of the Turbulent Prandtl Number of Air with Injection and Suction," *Int. J. Heat Mass Transfer*, Vol. 13, pp. 125 - 143; 1970.

Smits, A.J., Perry, A.E., and Hoffman, P.H., "The Responce to Temperature Fluctuations of a Constant-Current Hot-Wire Anemometer," *J. Phys. E.: Sci. Inst.*, Vol. 11, pp. 909-914, 1978.

Spalart, P.R., "Direct Simulation of a Turbulent Boundary Layer up to $Re_\theta = 1410$," *J. Fluid Mech.*, Vol. 187, p. 61; 1988.

Sparrow, E.M., "Heat Transfer in Fluid Flows which do not Follow the Contuor of Boundary Walls," *J. Heat Transfer*, Vol. 110, pp. 1145 - 1153; 1988.

Sparrow, E.M., and Ohadi, M.M., "Comparison of Turbulent Thermal Entrance Regions for Pipe Flows with Developed Velocity and Velocity Developing from a Sharp-Edged Inlet," *J. Heat Transfer*, Vol. 109, pp. 1028 - 1030; 1987.

Strickland, J.H., and Simpson, R.L., " 'Bursting' Frequencies Obtained From Wall Shear Stress Fluctuations in a Turbulent Boundary Layer," *The Physics of Fluids*, Vol. 18, No. 3, pp. 306 - 308; 1975.

Sucec, J., "Heat Transfer Across the Constant Property Boundary Layer," *Heat Transfer 1986*, Proc. Eighth Inter. Heat Transfer Conf., San Francisco, CA, Hemisphere Press, Washington, DC, Vol. 3, pp. 1109-1114; 1986

Sucec, J., and Lu, Y., "Heat Transfer Across Turbulent Boundary Layers With Pressure Gradients," *Journal of Heat Tansfer*, Vol. 112, Nov., pp. 906-912; 1990.

Swisher, S. E., Diller,T. E., and Pierce, F. J., "Time-Resolved Heat Flux Measurements in a Turbulent Junction Vortex," in *Topics in Heat Transfer*, Vol.1, Eds. M. Keyhani et al., ASME, N. Y., pp. 55-63; 1992.

Tennekes, H., and Lumley, J.L., *A First Course in Turbulence*, The Massachusetts Institute of Technology; 1972.

Townsend, A. A., *The Structure of Turbulent Shear Flow*, Cambridge University Press, Cambridge, U.K.; 1956.

Vogel, J.C., and Eaton, J.K., "Heat Transfer and fluid Mechanics Measurements in the Turbulent Reattaching Flow behind a Backward-Facing Step," Report MD-44, Department of Mechanical Engineering, Stanford University, Stanford, CA; 1984.

Vogel, J.C., and Eaton, J.K., "Combined Heat Transfer and Fluid Dynamics Measurements Downstream of a Backward-Facing Step," *J. Heat Transfer*, Vol. 107, pp.922-929; 1985

Walpole, R.E., and Myers, R.H., *Probability and Statistics for Engineers and Scientists*, 4th Ed., Macmillan, New York; 1985.

White, F.M., *Viscous Fluid Flow*, McGraw-Hill, New York; 1974.

Winter, K.G., "An Outline of the Techniques Available for the Measurement of Skin Friction in Turbulent Boundary Layers," *Prog. Aerospace Sci.*, Vol. 18, pp. 1 - 57; 1977.

Wroblewski, D.E., and Eibeck, P.A., "Turbulent Heat Transfer in a Boundary Layer Behind a Junction of a Streamlined Cylinder and a Wall," *J. of Heat Transfer*, Vol. 114, pp. 840 - 849; Nov. 1992.

Zaric, Z., "Wall Turbulence Studies," in *Advances in heat Transfer*, Edited by Hartnett, J.P., and Irvine, T.F., Vol. 8., Academic Press, New York; 1972

Zaric, Z., "Wall Turbulence Structure and Convection Heat Transfer," *International Journal of Heat and Mass Transfer*, Vol. 18, No. 6, pp. 831-842, 1975.

Tables

Table 2.1.Characteristic dimensions of the wing models and results from oil flow visualizations.

Model	Chord length, cm	Maximum thickness, cm	Maximum thickness/ location/ chord	Leading edge radius/ t_{\max}	Trip location/ chord	Trip length/ chord	x_{sep}^* , cm	x_{lots}^* , x/x_{sep}
modified NACA 0020	30.5	7.17	0.1983	0.333	0.1406	0.0208	3.23	0.60
Streamlined cylinder	29.8	12.70	0.2156	0.500	0.2542	0.0374	6.59	0.53
NACA 0015	60.8	9.21	0.3036	0.164	0.1152	0.0376	2.71	0.53

*From Ölçmen and Simpson (1994).

Table 2.2. Locations of surface heat flux measurement in the wing/body junction test case for the modified NACA 0020 model. Mean heat flux was measured at all measurement locations. Time-resolved surface heat flux was measured only in line #1. Distances are normalized by the maximum thickness of the wing.

	x/t_{\max}	z/t_{\max}
Line 1	-0.053	0.000
	-0.086	0.000
	-0.103	0.000
	-0.120	0.000
	-0.153	0.000
	-0.166	0.000
	-0.204	0.000
	-0.220	0.000
	-0.252	0.000
	-0.286	0.000
	-0.297	0.000
	-0.319	0.000
	-0.352	0.000
	-0.409	0.000
	-0.460	0.000
	-0.666	0.000
	-0.860	0.000

Table 2.2. Continued.

	x/t_{\max}	z/t_{\max}		x/t_{\max}	z/t_{\max}
Line 2	-0.169	-0.176	Line 5	0.196	-0.627
	-0.218	-0.188		0.171	-0.670
	-0.266	-0.200		0.147	-0.714
	-0.315	-0.212		0.123	-0.758
	-0.363	-0.224		0.074	-0.845
	-0.461	-0.247		0.001	-0.976
	-0.606	-0.283		-0.097	-1.151
	-0.800	-0.331	Line 6	0.428	-0.711
Line 3	-0.132	-0.353		0.419	-0.760
	-0.176	-0.376		0.410	-0.809
	-0.220	-0.399		0.400	-0.858
	-0.265	-0.422		0.382	-0.956
	-0.353	-0.469		0.361	-1.069
	-0.486	-0.538	Line 7	0.708	-0.775
	-0.664	-0.631		0.708	-0.850
Line 4	0.008	-0.490		0.708	-0.925
	-0.046	-0.523		0.708	-1.000
	-0.083	-0.556		0.708	-1.075
	-0.121	-0.589		0.708	-1.175
	-0.196	-0.655		0.708	-1.325
	-0.308	-0.755		0.708	-1.525
	-0.458	-0.887			

Table 2.3. Locations of surface heat flux measurement in the wing/body junction test case for the streamlined cylinder model. Distances are normalized by the maximum thickness of the wing.

X/t_{\max}	Z/t_{\max}
-0.017	0.00
-0.034	0.00
-0.050	0.00
-0.068	0.00
-0.102	0.00
-0.119	0.00
-0.135	0.00
-0.153	0.00
-0.173	0.00
-0.191	0.00
-0.207	0.00
-0.226	0.00
-0.242	0.00
-0.258	0.00
-0.276	0.00
-0.292	0.00
-0.311	0.00
-0.337	0.00
-0.348	0.00
-0.366	0.00
-0.382	0.00
-0.417	0.00
-0.437	0.00
-0.454	0.00
-0.471	0.00
-0.490	0.00
-0.506	0.00

Table 2.4. Locations of surface heat flux measurement in the wing/body junction test case for the NACA 0015 model. Distances are normalized by the maximum thickness of the wing.

x/t_{\max}	z/t_{\max}
-0.023	0.00
-0.047	0.00
-0.070	0.00
-0.094	0.00
-0.132	0.00
-0.154	0.00
-0.178	0.00
-0.201	0.00
-0.225	0.00
-0.239	0.00
-0.264	0.00
-0.286	0.00
-0.312	0.00
-0.334	0.00
-0.370	0.00
-0.395	0.00
-0.443	0.00
-0.817	0.00

Table 2.5. Positions of measurement stations for 3-D TBL test case in wind-tunnel coordinates.

Station #	X_{TC} (mm)	Z_{TC} (mm)
0	-114.0	33.4
1	-88.8	-36.8
2	-58.1	44.5
3	-33.7	-51.7
4	-12.0	65.5
5	6.6	-74.7
6	30.3	83.7
7	55.1	-89.7

Table 2.6. Flow characteristics at measurement stations in 3-D TBL test case. (from Ölçmen and Simpson, 1995a)

Station	U_{∞} (m/s)	β_{FS} (deg)	β_w (deg)	$\delta_{0.995}$ (mm)	U_{τ} (m/s)	$(\partial C_p / \partial X)_{FS}$ (m^{-1})	$(\partial C_p / \partial Z)_{FS}$ (m^{-1})	$K =$ $(v/U_{\infty}^2)(dU_{\infty}/ds)$ $\times 10^6 K$
0	26.3	1.68	6.1	38.6	0.92	0.778	0.916	-0.283
1	24.9	2.64	11.5	39.2	0.865	1.2	1.39	-0.514
2	24.8	4.81	24.0	40.2	0.865	0.204	2.99	-0.089
3	25.3	8.63	33.7	39.3	0.957	-3.91	4.07	1.598
4	27.3	9.45	30.6	39.0	1.11	-6.34	0.923	2.062
5	29.5	7.71	19.7	39.6	1.15	-6.25	-1.95	1.611
6	30.5	5.09	7.17	39.2	1.16	-4.06	-5.53	0.947
7	31.0	2.71	3.50	38.8	1.20	0.26	-6.69	-0.058

Table 2.7. Locations of surface heat flux and temperature profile measurement for the 2-D separated TBL test case.

x (cm)	z (cm)
188.6	0.0
222.6	0.0
285.4	0.0
301.0	0.0
306.1	0.0
309.6	0.0
323.2	0.0
328.6	0.0
332.4	0.0
341.6	0.0
352.4	0.0
364.5	0.0
407.0	0.0
440.1	0.0

Table 2.8. 95% Confidence intervals.

Variable	Uncertainty		
	Wing/Body Junction	3-D Boundary Layer	2-D Separating Boundary Layer
T (absolute)	$\pm 2\text{ }^{\circ}\text{C}$	$\pm 2\text{ }^{\circ}\text{C}$	$\pm 2\text{ }^{\circ}\text{C}$
ΔT	N.A.	$\pm 0.17\text{ }^{\circ}\text{C}$	$\pm 0.17\text{ }^{\circ}\text{C}$
θ	N.A.	± 0.01	± 0.01
q	$\pm 5.2\%$	$\pm 7.7\%$	$\pm 7.7\%$
St	$\pm 5.3\%$	$\pm 7.8\%$	$\pm 7.8\%$
T_{rms}	N.A.	$\pm 0.93\%$	$\pm 0.93\%$
q_{rms}	$\pm 15.2\%$	$\pm 5\%$	$\pm 5\%$
Skewness	± 0.025	± 0.025	± 0.025
Flatness	± 0.10	± 0.10	± 0.10
Re_H	N.A.	$\pm 9.3\%$	$\pm 10\%$
B	N.A.	± 0.07	N.A.
L_{γ}	N.A.	$\pm 1.4\text{ mm}$	$\pm 1.4\text{ mm}$

Table 2.9. Normalized 95% confidence intervals for spectral estimates of 3-D boundary layer flow.

γ^2	$\delta\gamma^2/\gamma^2$ (%)	$\delta G_{qq}/G_{qq}$ (%)	$\delta G_{qt}/G_{qt}$ (%)	$\delta\Phi_{qt}/\Phi_{qt}$ (%)
0.20	35.8	14.1	31.6	20.0
0.25	30.0	14.1	28.3	17.3
0.30	25.6	14.1	25.8	15.3
0.35	22.0	14.1	23.9	13.6
0.40	19.0	14.1	22.4	12.3
0.45	16.4	14.1	21.1	11.1
0.50	14.1	14.1	20.0	10.0
0.55	12.1	14.1	19.1	9.05
0.60	10.3	14.1	18.3	8.16
0.65	8.68	14.1	17.5	7.34
0.70	7.17	14.1	16.9	6.55
0.75	5.77	14.1	16.3	5.77
0.80	4.47	14.1	15.8	5.00
0.85	3.25	14.1	15.3	4.20
0.90	2.11	14.1	14.9	3.33
0.95	1.03	14.1	14.5	2.29
1.00	0.00	14.1	14.1	1.00

Table 2.10. Normalized 95% confidence intervals for spectral estimates of 2-D separating boundary layer flow.

γ^2	$\delta\gamma^2/\gamma^2$ (%)	$\delta G_{qq}/G_{qq}$ (%)	$\delta G_{qt}/G_{qt}$ (%)	$\delta\Phi_{qt}/\Phi_{qt}$ (%)
0.20	16.0	6.32	14.1	8.94
0.25	13.4	6.32	12.7	7.75
0.30	11.4	6.32	11.6	6.83
0.35	9.83	6.32	10.7	6.09
0.40	8.49	6.32	10.0	5.48
0.45	7.33	6.32	9.43	4.49
0.50	6.32	6.32	8.94	4.47
0.55	5.43	6.32	8.53	4.05
0.60	4.62	6.32	8.16	3.65
0.65	3.88	6.32	7.84	3.28
0.70	3.21	6.32	7.56	2.93
0.75	2.58	6.32	7.30	2.58
0.80	2.00	6.32	7.07	2.24
0.85	1.46	6.32	6.86	1.88
0.90	0.94	6.32	6.67	1.49
0.95	0.46	6.32	6.49	1.03
1.00	0.00	6.32	6.32	0.00

Table 3.1. Boundary layer characteristics in the 2-D separating TBL test case measured 163.2 cm downstream of the test section entrance.

	Simpson et al. (1981 a)	Current data
Free-stream velocity, U_∞ , (m/s)	21.82	21.46
dU_∞/dx (s^{-1})	-1.32	-0.84
$\delta_{0.990}$, (mm)	20.12	19.56
$\delta_{0.995}$, (mm)	21.39	21.34
displacement thickness (mm)	2.80	2.90
momentum thickness, (mm)	2.07	2.14
shape factor, H	1.375	1.355
Re_θ	2900.6	2750
$C_f/2 \times 10^3$	1.724	1.765

Table 3.2. Boundary layer characteristics in the 2-D separating TBL test case measured 301 cm downstream of the test section entrance.

	Simpson et al. (1981 a)	Current data
Free-stream velocity, U_∞ , (m/s)	16.18	16.25
dU_∞/dx (s^{-1})	-4.72	-4.95
$\delta_{0.990}$, (mm)	71.09	71.00
$\delta_{0.995}$, (mm)	72.19	72.14
displacement thickness (mm)	23.17	23.45
momentum thickness, (mm)	11.65	11.64
shape factor, H	1.989	2.015
Re_θ	11755	11240
$C_f/2 \times 10^3$	0.4469	0.4346

Table 3.3. Boundary layer characteristics in the 2-D separating TBL test case measured 352.4 cm downstream of the test section entrance.

	Simpson et al. (1981 a)	Current data
Free-stream velocity, U_{∞} , (m/s)	14.16	14.23
dU_{∞}/dx (s^{-1})	-2.05	-1.99
$\delta_{0.990}$, (mm)	146.8	145
$\delta_{0.995}$, (mm)	148.2	150

Table 3.4. Boundary layer characteristics in the 2-D separating TBL test case measured 397.2 cm downstream of the test section entrance.

	Simpson et al. (1981 a)	Current data
Free-stream velocity, U_{∞} , (m/s)	13.59	13.60
dU_{∞}/dx (s^{-1})	-1.28	-1.25
$\delta_{0.990}$, (mm)	237.4	235
$\delta_{0.995}$, (mm)	255.7	240

Table 4.1. Location and value of maximum and minimum St , St_{rms} , skewness, and flatness.

	Modified NACA 0020		Streamlined Cylinder		NACA 0015	
	value	x/x_{sep}	value	x/x_{sep}	value	x/x_{sep}
Maximum $St \times 10^3$	5.37	-0.118	3.51	-0.131	4.77	-0.078
Maximum $St_{rms} \times 10^3$	0.754	-0.636	0.833	-0.498	0.686	-0.524
Maximum Skewness	1.08	-0.909	1.23	-0.876	0.96	-0.898
Maximum Flatness	4.82	-1.022	5.61	-0.946	4.53	-0.973

Table 5.1 Heat transfer parameters at each station in three-dimensional flow. β_H is relative to tunnel coordinate system.

Station	$St \times 10^3$	T_τ (K)	δ_τ (mm)	$ \mathbf{H} $ (mm)	β_H (deg.)
0	1.75	1.00	36.0	2.79	-2.77
1	1.88	1.08	36.0	2.69	-4.68
2	1.84	1.06	37.7	2.95	-10.33
3	1.81	0.96	39.7	3.21	-16.72
4	1.80	0.88	39.8	3.52	-18.04
5	1.66	0.86	41.0	3.33	-15.10
6	1.60	0.84	40.9	3.67	-10.83
7	1.53	0.79	40.3	3.57	-6.80

Table 6.1 Bursting frequencies from first moment of corrected surface-heat-transfer spectra in three-dimensional TBL flow.

Station	f_b (hz)	$U_\infty/f_b\delta$	$U_\tau^2/f_b\nu$	$0.65Re_\theta^{.73}$
0	185	3.68	261	425
1	205	3.10	208	421
2	240	2.57	222	442
3	280	2.30	187	432
4	300	2.33	233	424
5	270	2.76	282	430
6	300	2.62	257	435

Table 6.2 Values of parameters k and T used in VITA "burst" detection algorithm.

Station #	T (msec)	$T^+ = TU^{*2}/v$	k
0	0.19	8.45	1
1	0.19	8.33	1
2	0.19	8.35	1
3	0.19	10.22	1
4	0.19	13.75	1
5	0.19	14.76	1
6	0.19	15.00	1

Table 6.3 Angle of inclination of time-averaged wavefronts constructed from time-delayed correlations.

Measurement Station #	α (degrees)		
	Temperature Structure	Turbulent Structure (current)	Turbulent Structure Ha (1993)
0	24.7	17.1	49.3
1	24.5	15.3	51.0
2	28.6	14.7	50.0
3	37.9	22.8	54.2
4	47.3	38.5	57.9
5	41.4	36.6	53.4
6	54.6	32.8	57.1

Table 7.1. Values of mean, rms, skewness, and flatness of surface heat flux in two-dimensional separating turbulent boundary layer.

x (cm)	$St \times 10^3$	$St_{rms} \times 10^3$	$S_{q''}$	$F_{q''}$
188.60	2.24	0.216	0.241	2.917
222.57	2.04	0.239	0.368	2.966
285.43	1.81	0.344	0.688	3.897
300.99	1.71	0.403	0.944	4.680
306.07	1.70	0.395	0.753	3.993
309.56	1.67	0.392	0.866	4.381
323.22	1.56	0.412	0.958	4.687
328.61	1.30	0.423	1.062	4.995
332.42	1.25	0.417	1.187	5.318
341.63	1.19	0.459	1.174	5.115
352.43	1.23	0.481	1.274	5.404
364.49	1.23	0.469	1.289	5.467
407.04	2.17	0.433	1.286	5.725
440.06	2.41	0.483	1.473	6.304

Table 7.2. Parameters of the temperature profile development in two-dimensional separating turbulent boundary layer.

x (cm)	$\delta_{T,0.995}$ (cm)	$\delta_{T,0.990}$ (cm)	Δ_1 (mm)	Δ_2 (mm)	H_Δ	Re_{Δ_2}
188.60	1.79	1.68	2.059	1.331	1.55	1632.1
222.57	2.77	2.58	2.959	1.932	1.53	2253.7
285.43	5.60	5.28	7.277	3.997	1.82	3790.7
300.99	6.72	6.40	9.544	4.502	2.12	4037.1
306.07	7.50	7.19	10.360	4.756	2.18	4203.7
309.56	8.12	7.72	11.224	4.807	2.33	4211.8
323.22	9.48	8.96	14.498	5.267	2.75	4467.5
328.61	10.13	9.72	15.665	5.048	3.10	4234.7
332.42	10.80	10.40	16.245	4.889	3.46	4070.7
341.63	12.70	12.15	20.326	5.448	3.73	4467.6
352.43	14.20	13.60	23.741	-	-	-
364.49	16.85	16.25	27.105	-	-	-
407.04	26.00	25.00	31.523	-	-	-
440.06	33.60	32.60	29.475	-	-	-

Table 7.3 Backflow velocity and temperature profile parameters.

x (cm)	N (cm)	U_N (m/s)	Tu_N	Θ_N	$Re_{\Delta N}$	Δ_{IN} (mm)	Δ_{2N} (mm)	$H_{\Delta N}$	St_N	St'
352.4	0.50	0.45	2.77	0.64	10.31	0.7052	0.4070	1.73	0.0606	0.219
364.5	1.00	1.11	1.10	0.70	32.88	0.9126	0.5240	1.74	0.0223	0.203
407.0	1.96	1.72	0.85	0.81	65.86	0.9819	0.6829	1.44	0.0211	0.248
440.1	2.64	1.90	0.76	0.89	163.68	2.268	1.5280	1.48	0.0187	0.246

Table 7.4. Average value of turbulent Prandtl number in the log region computed from the slope of T^+ vs y^+ upstream of *intermittent transitory detachment*.

x (cm)	$(Pr_t)_l$
188.60	0.705
222.57	0.803
285.43	0.467
300.99	0.428
306.07	0.384
309.56	0.327
323.22	0.226
328.61	0.232

Table 7.5. Streamwise variation of temperature scale and length scale used in empirical temperature defect law, Eq. (7.22).

x (cm)	θ_s	δ_s (mm)	$d\theta_s/dx$ (m^{-1})	$d\delta_s/dx$ $\times 10^3$
282.43	0.89	8.176	0.18762	9.64
300.99	0.92	10.375	0.21121	16.24
306.07	0.93	11.140	0.21892	18.26
309.56	0.94	11.941	0.22421	19.49
323.22	0.97	14.947	0.24491	24.22
328.61	0.98	15.984	0.25310	26.06
323.42	0.99	17.095	0.25887	27.15
341.63	1.02	19.928	0.27284	29.43

Figures

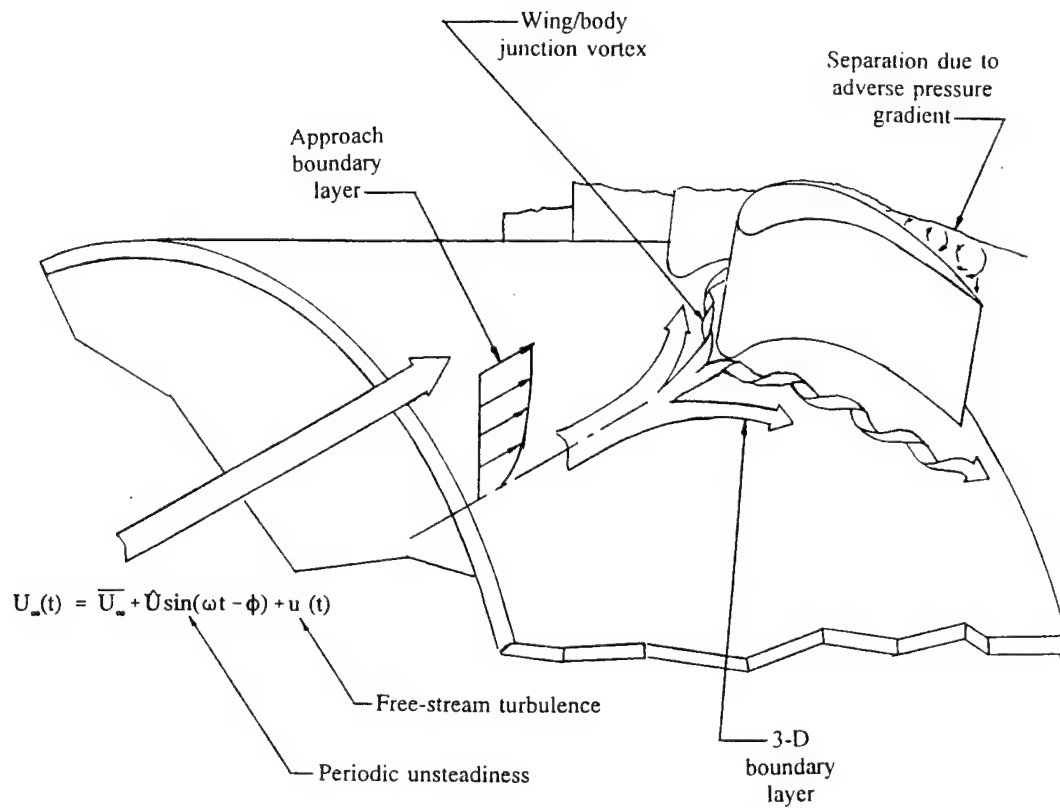


Fig. 1.1. Sketch illustrating phenomena affecting convective heat transfer in a gas turbine engine.

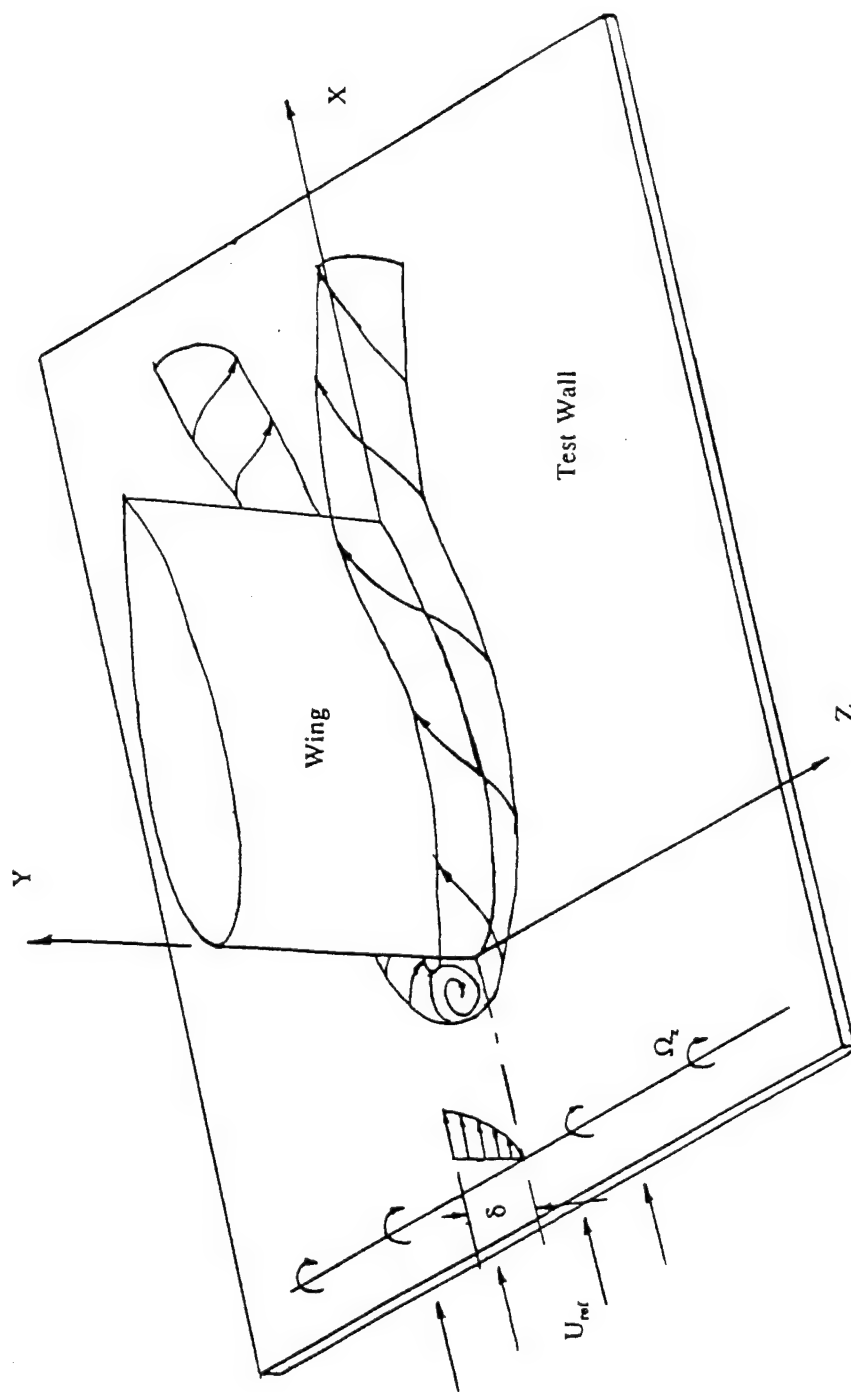


Fig. 1.2. Sketch of simplified wing/body junction vortex showing the horseshoe vortex and the tunnel coordinate system.

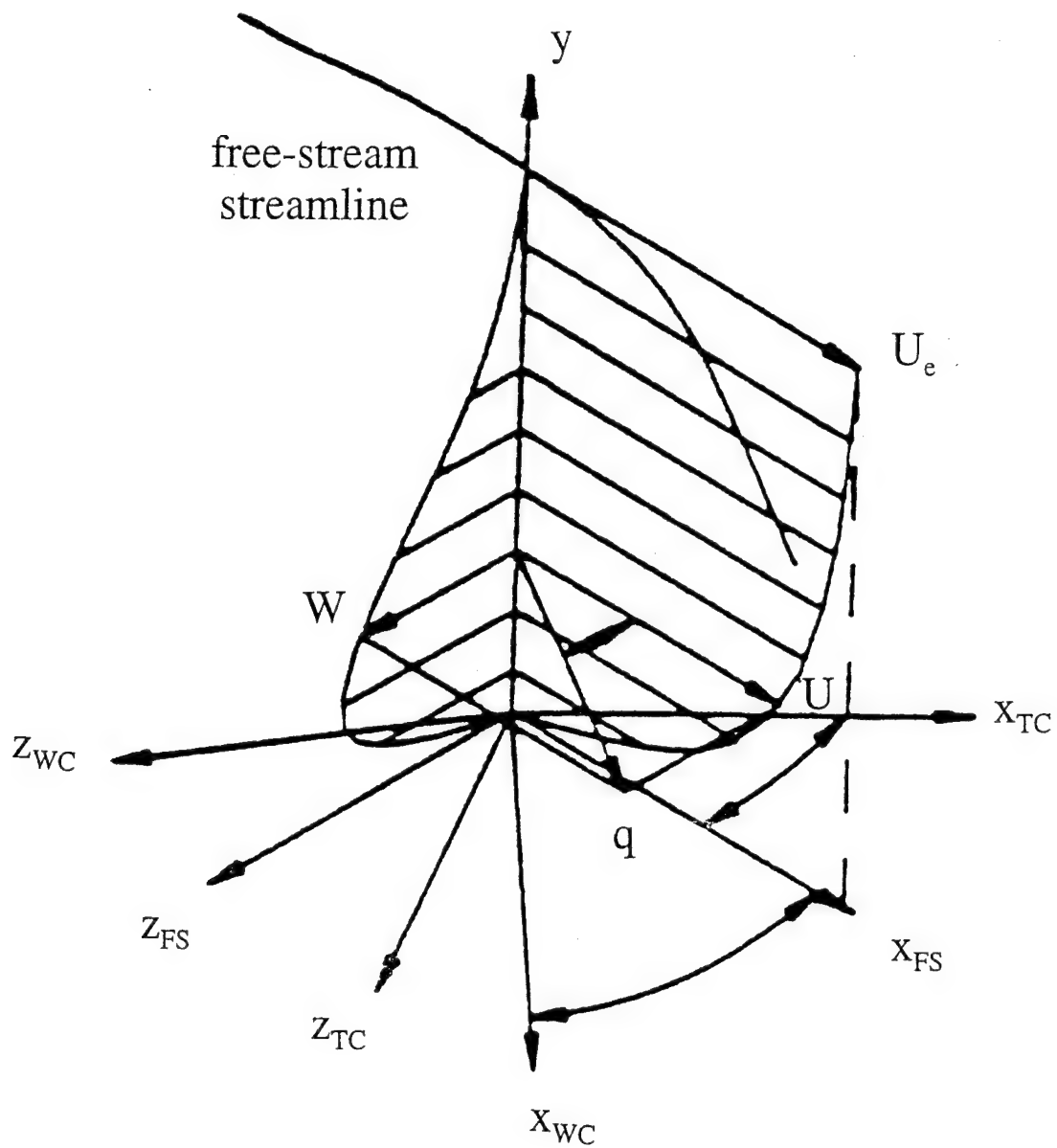


Fig. 1.3. Sketch of typical velocity profile in a three-dimensional turbulent boundary layer and definitions of coordinate systems used in 3-D test case: TC denotes tunnel coordinate system; FS denotes local free-stream coordinate system; WC denotes local wall-stress coordinates.

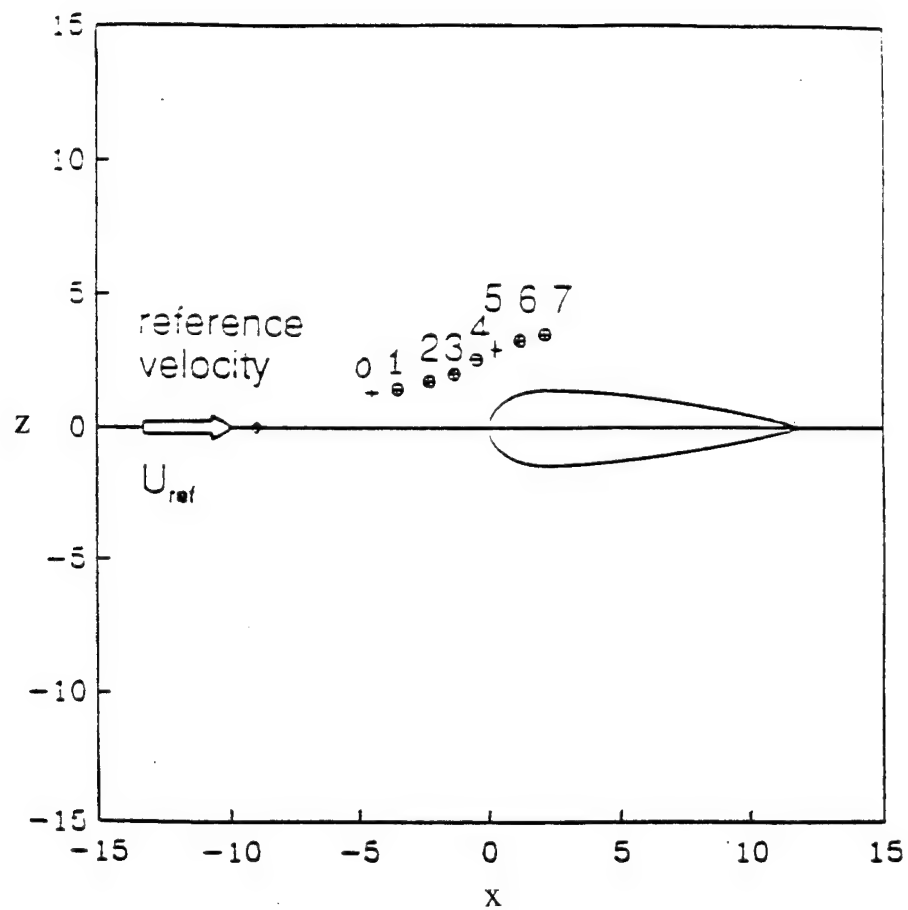


Fig. 1.4. Plan view of measurement locations for the 3-D TBL test case. The scale of the plot is in inches.

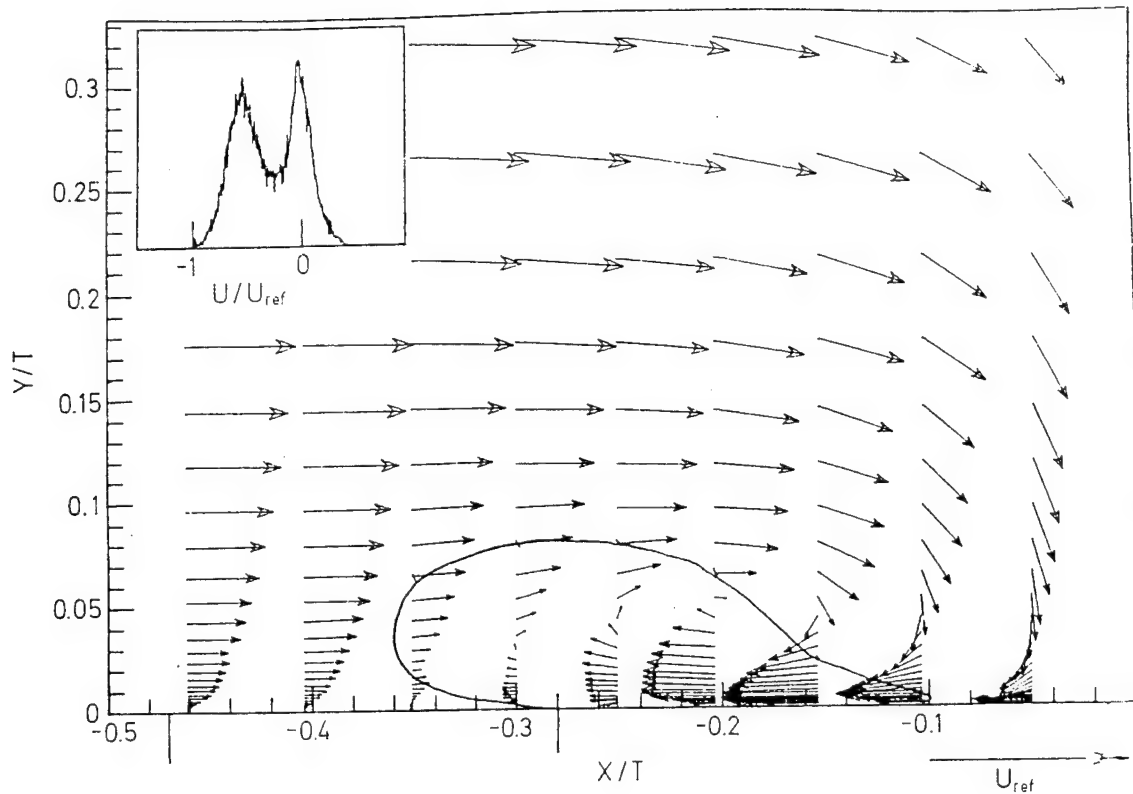


Fig. 1.5. Time-mean velocity vectors in the plane of symmetry upstream of wing used for wing/body junction vortex flow. Oil-flow visualizations show separation occurs at $X/T = -0.47$ and a line of low shear at $X/T = -0.28$. Histograms of X-component velocity fluctuations at $X/T = -0.204$, $Y/T = 0.0046$ *inset*. Solid line shows region of bimodal X-component velocity fluctuations. (from Devenport and Simpson, 1989).

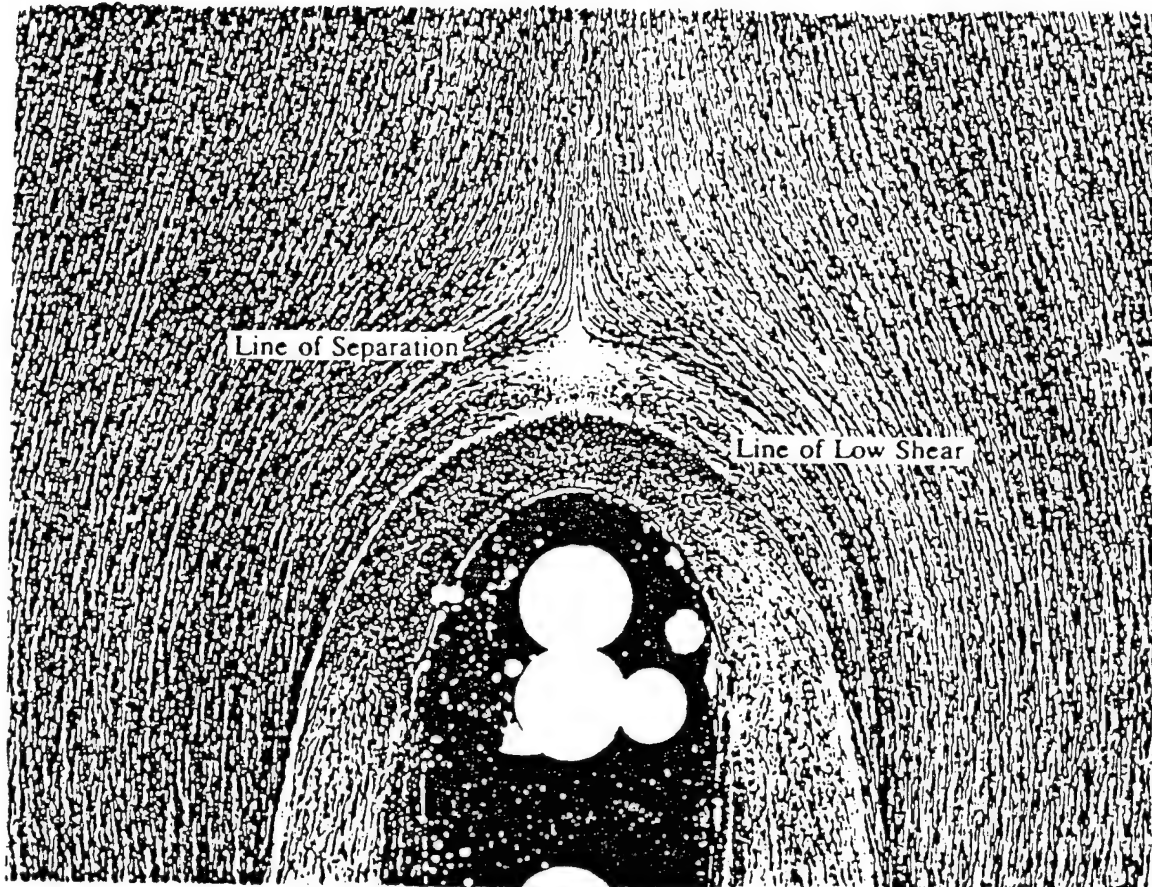


Fig. 1.6. Surface oil flow visualization performed on the test wall around the 3:2 elliptic nosed NACA 0020 tailed airfoil (from Devenport and Simpson, 1990 a). The line farthest upstream is the line of separation. The line nearer the nose of the wing is the line of low shear.

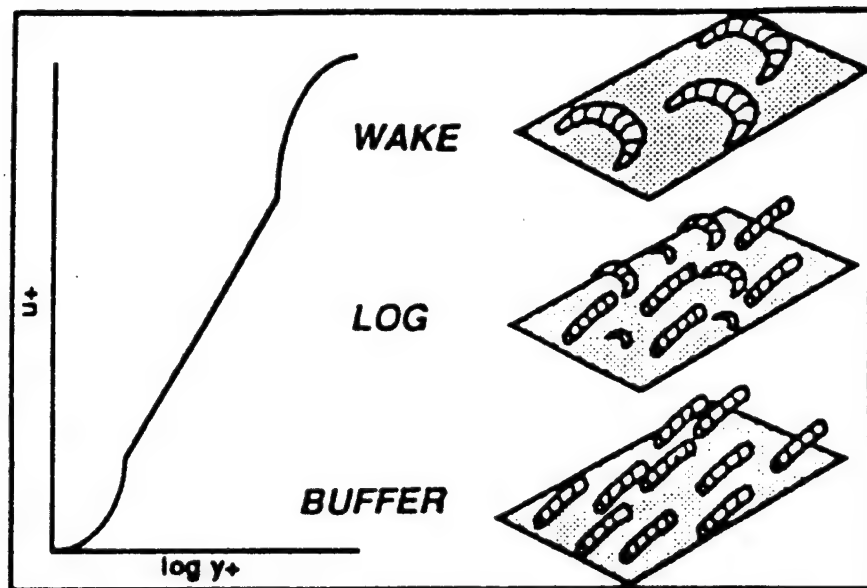


Fig. 1.7. Distribution of coherent vortical structures through a two-dimensional, turbulent boundary layer (from Robinson, 1991).

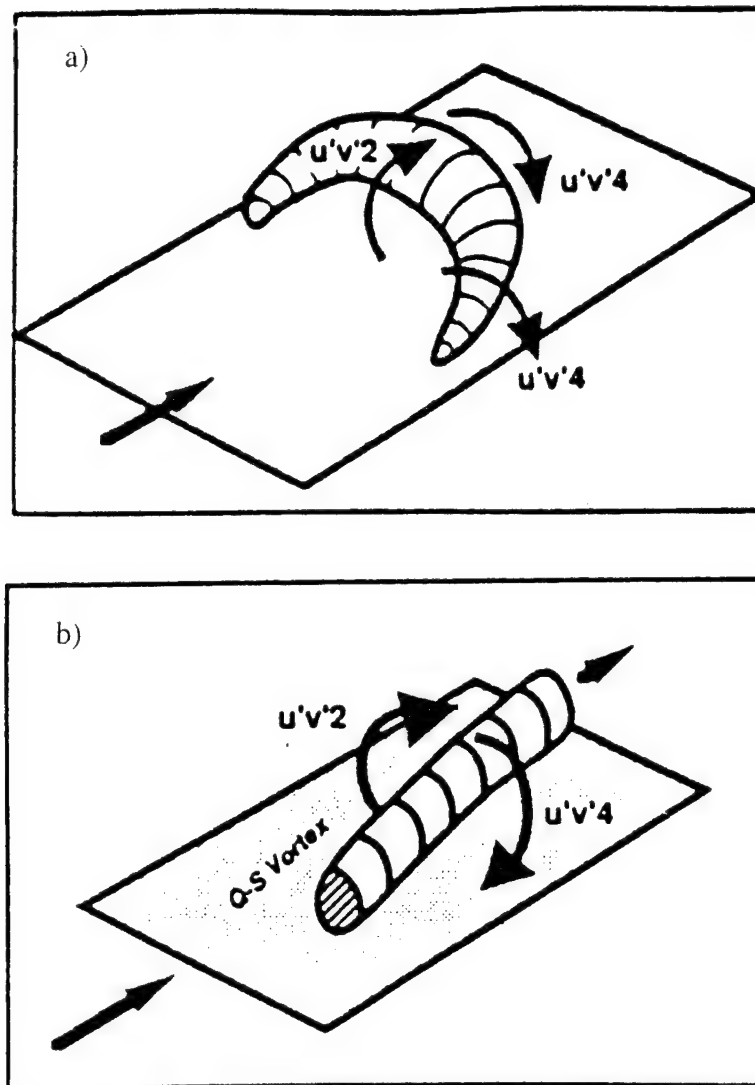


Fig. 1.8. Generation of ejections and sweeps in a 2-D turbulent boundary layer by: (a) an arch-like vortical structure in the outer region; (b) a single near-wall quasi-streamwise vortex (from Robinson, 1991).

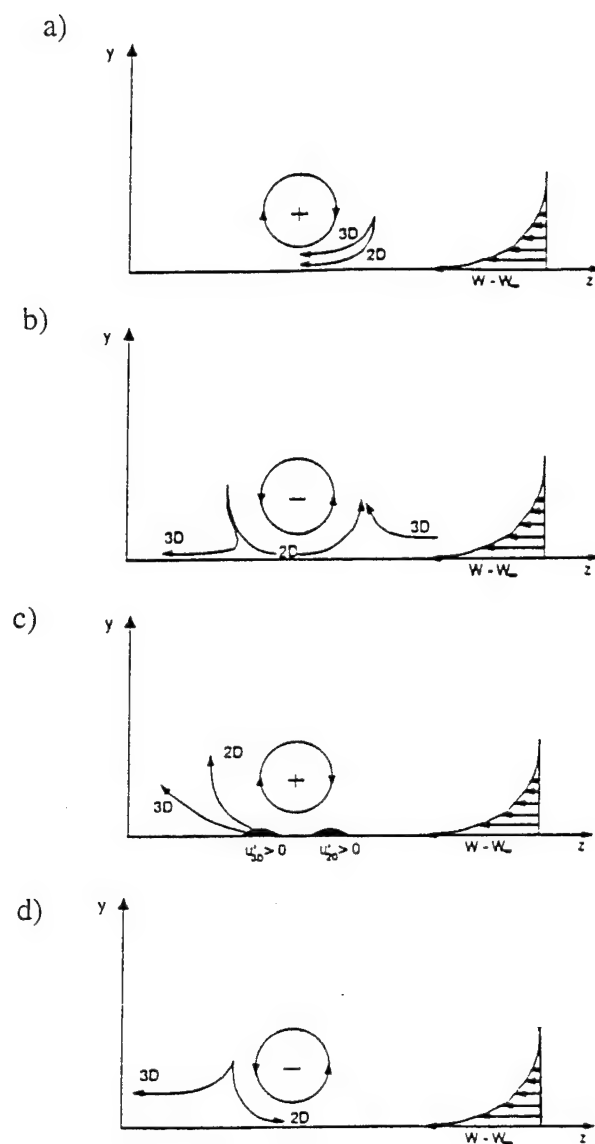


Fig. 1.9. Schematic showing proposed mechanisms which lead to reductions in Reynolds stresses in a three-dimensional turbulent boundary layer. (from Sendstad and Moin, 1992).

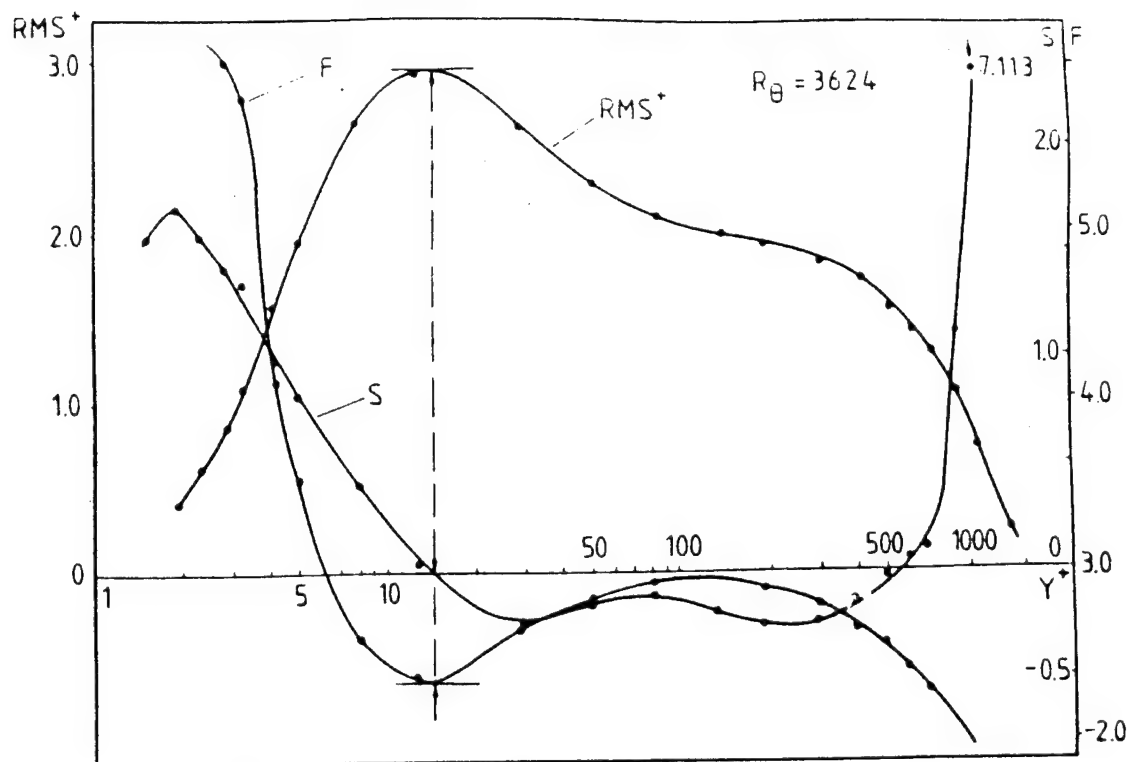


Fig. 1.10. Typical profiles of variance, skewness and flatness factors of streamwise velocity fluctuations u in a two-dimensional turbulent boundary layer. (Durst et al., 1992)

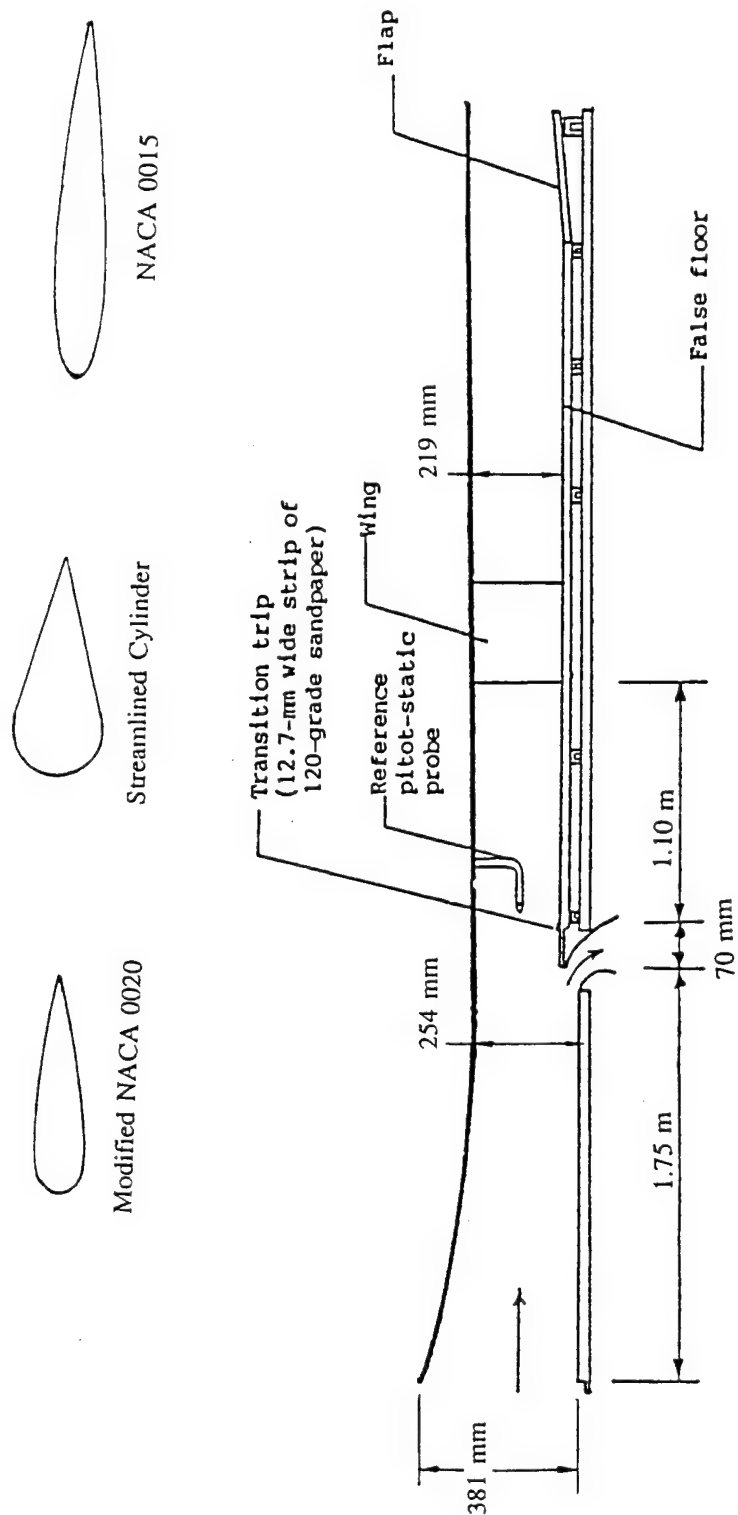


Fig. 2.1. Side view of the boundary layer tunnel test section configuration used for the wing/body junction test case and the wing shapes.

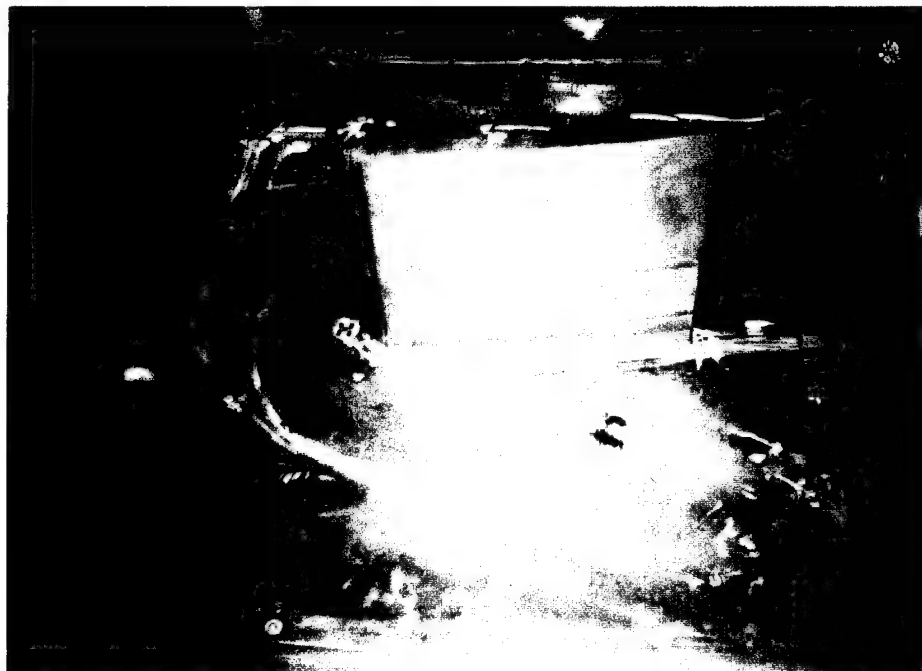


Fig. 2.2. Heat Flux Microsensor mounted in the cam system beneath the modified NACA 0020 wing in the wind tunnel test section.

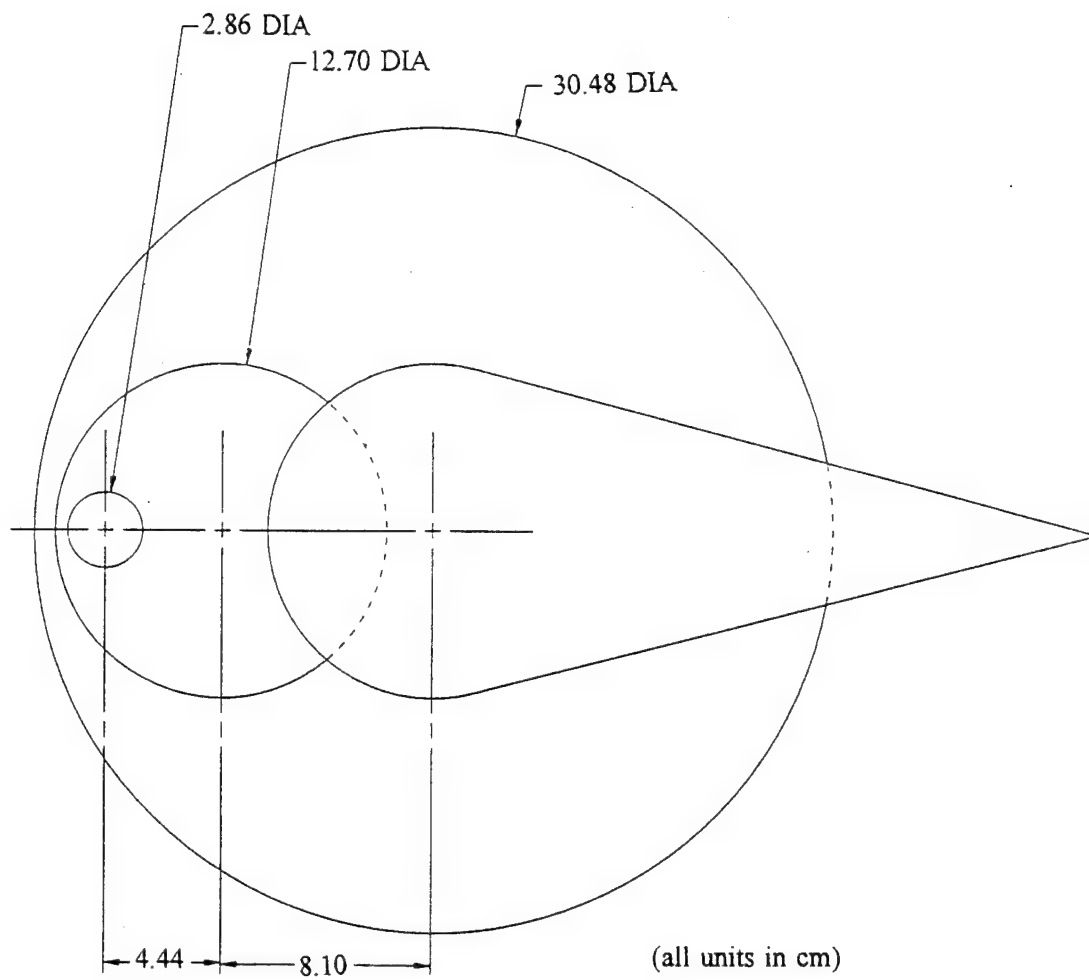


Fig. 2.3. Sketch of cam system used to position the heat flux gage on the endwall upstream of the wing/body junction.

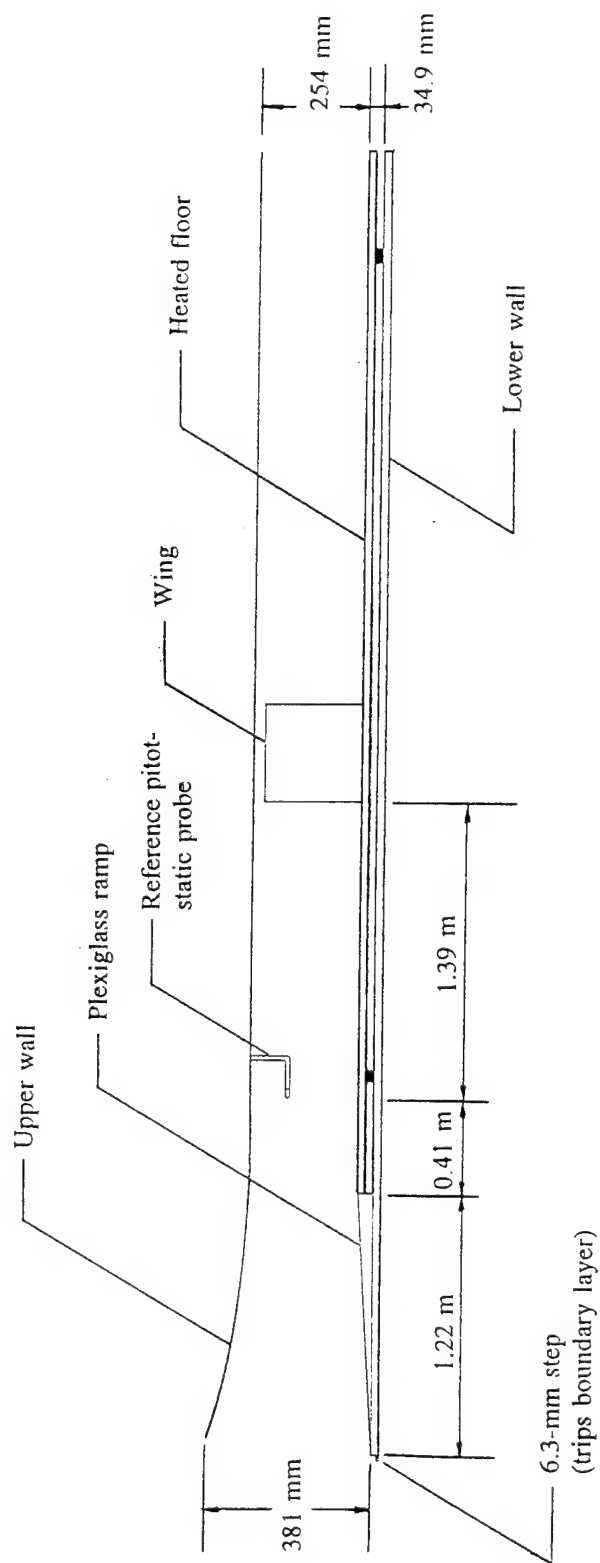


Fig. 2.4. Side view of the boundary layer tunnel test section configuration used for the pressure-driven 3-D turbulent boundary layer test case. Heated surface begins 1.22 m downstream of test section entrance.



Fig. 2.5. Side view of the boundary layer tunnel test section configuration used for the 2-D separating turbulent boundary layer test case. Heated surface begins 1.22 m downstream of test section entrance. Boundary layer control side-wall jets and suction are located at beginning of each 244-cm-long section. Major deviations on scales are 25.4 cm.

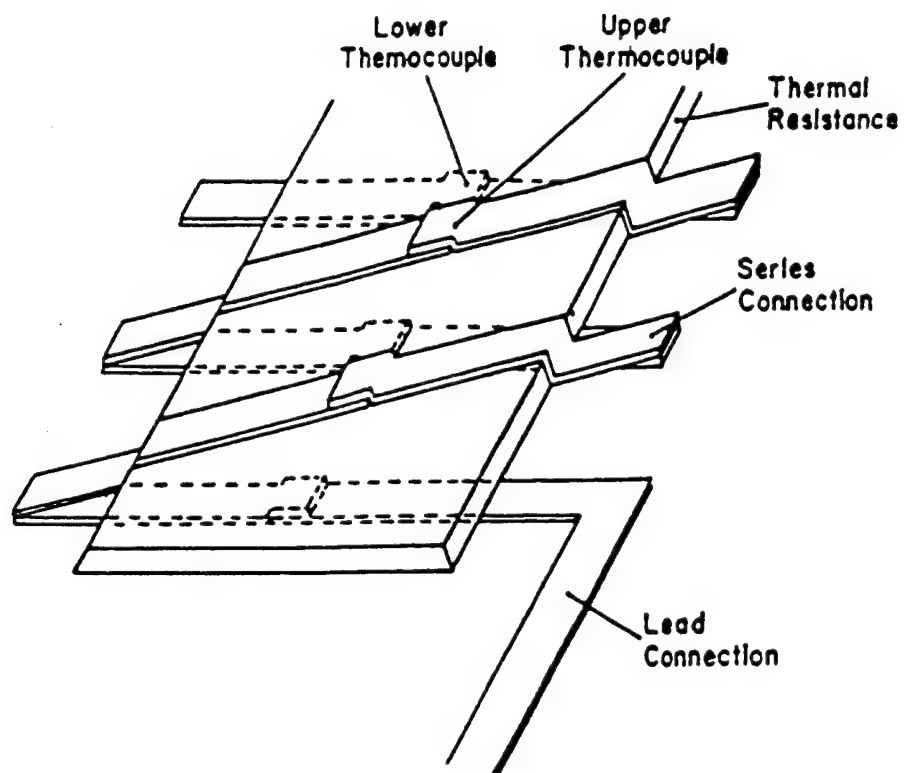


Fig. 2.6. Isometric view of the Heat Flux Microsensor thermocouple junctions.
(from Hager et al., 1991b)

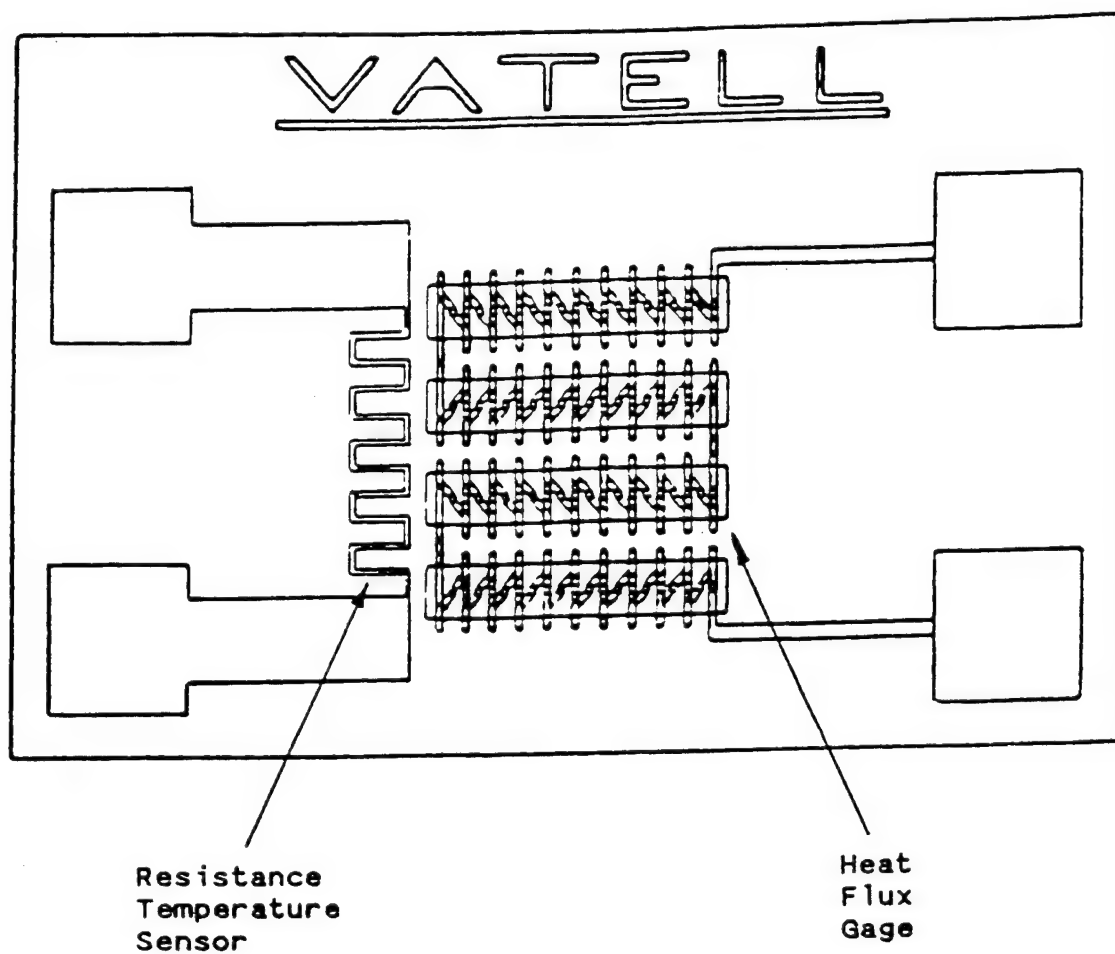


Fig. 2.7. Heat Flux Microsensor pattern. (from Hager et al, 1991a)

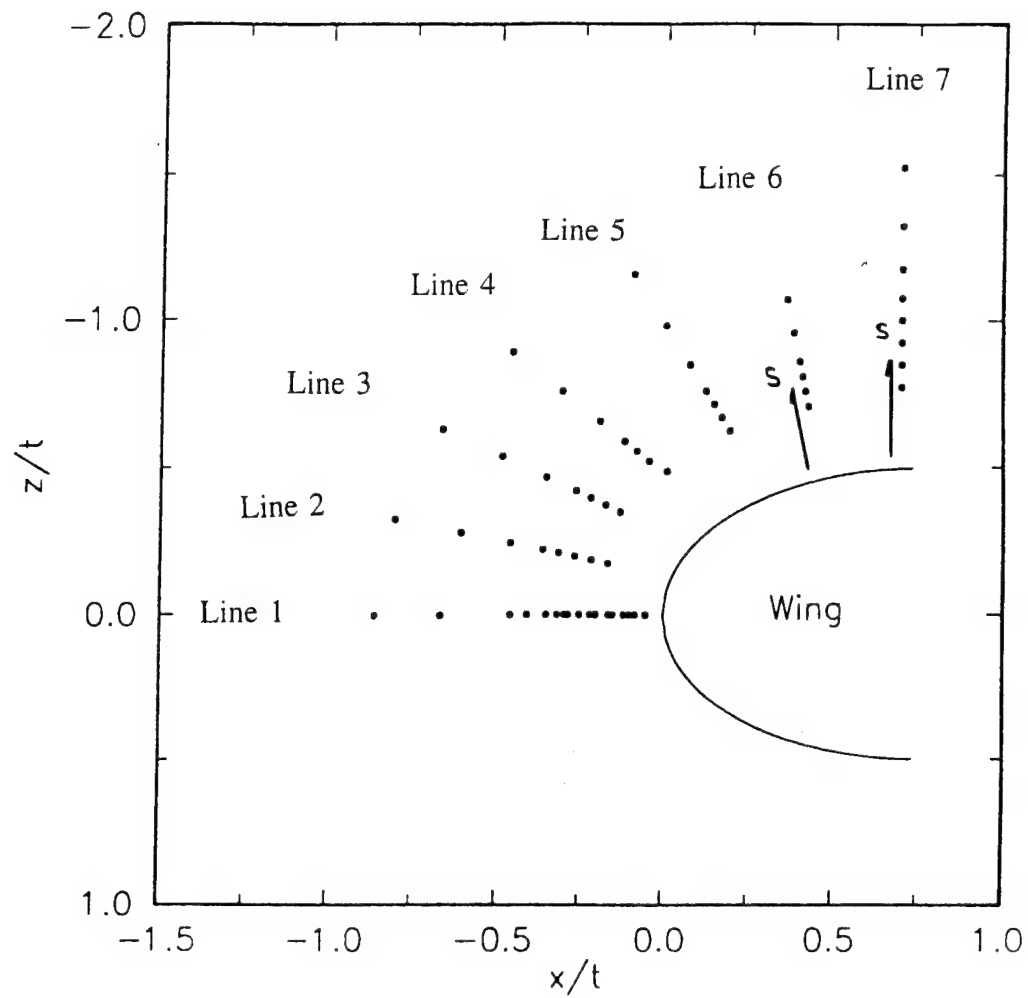


Fig. 2.8. Locations where surface heat flux was measured in the wing/body junction test case for the modified NACA 0020 wing.

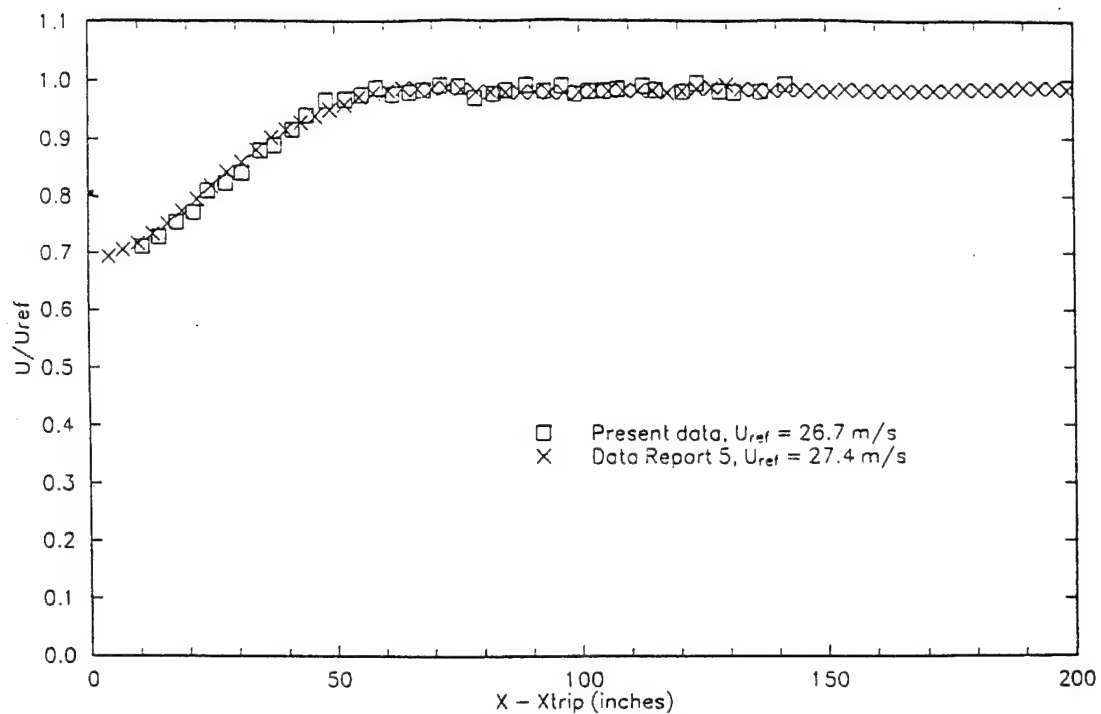


Fig. 3.1. Streamwise velocity variation in the potential core of the test section used for the 3-D TBL test case. \square - current data; X - Devenport and Simpson, (1990 a).

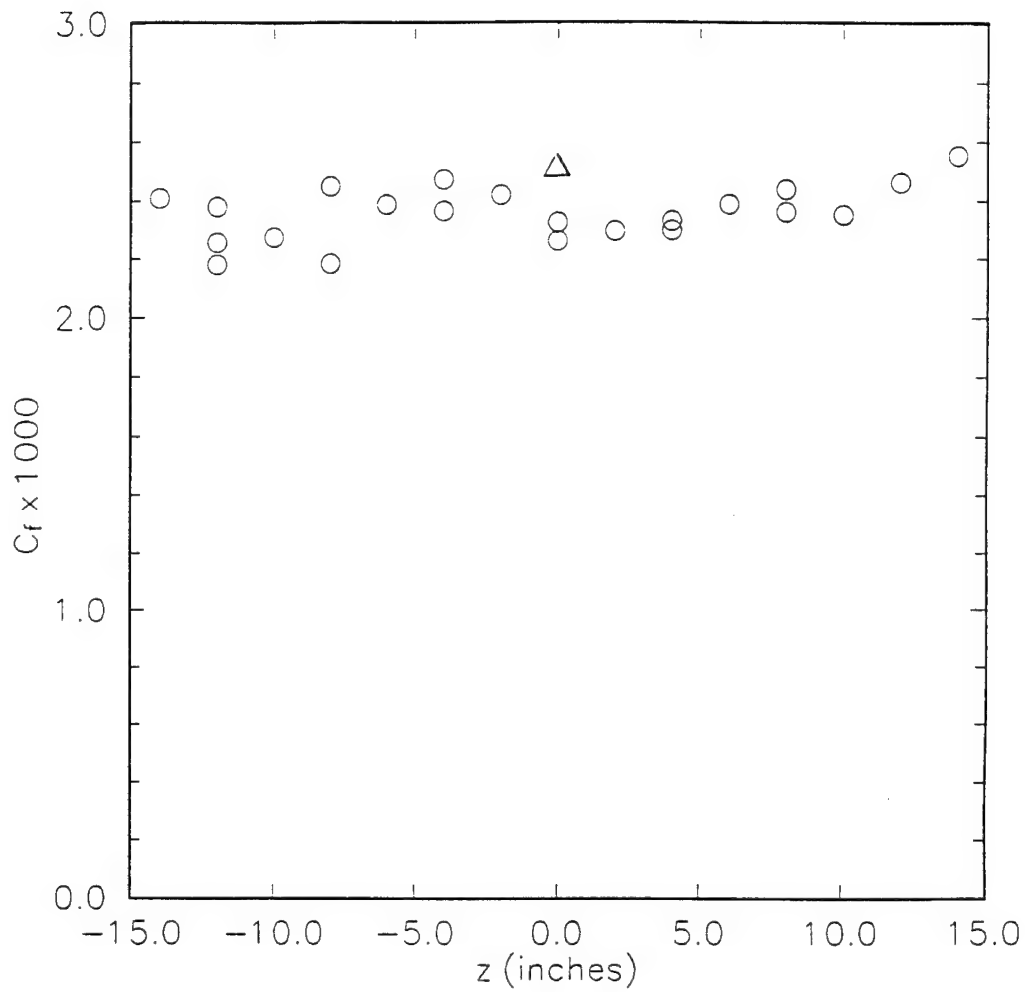


Fig. 3.2. Spanwise variation of surface shear stress coefficient measured 0.75 chord lengths upstream of the modified NACA 0020 model mounted in the test section used for the 3-D TBL test case. O - from Preston tube; Δ - from law-of-the-wall velocity profile.

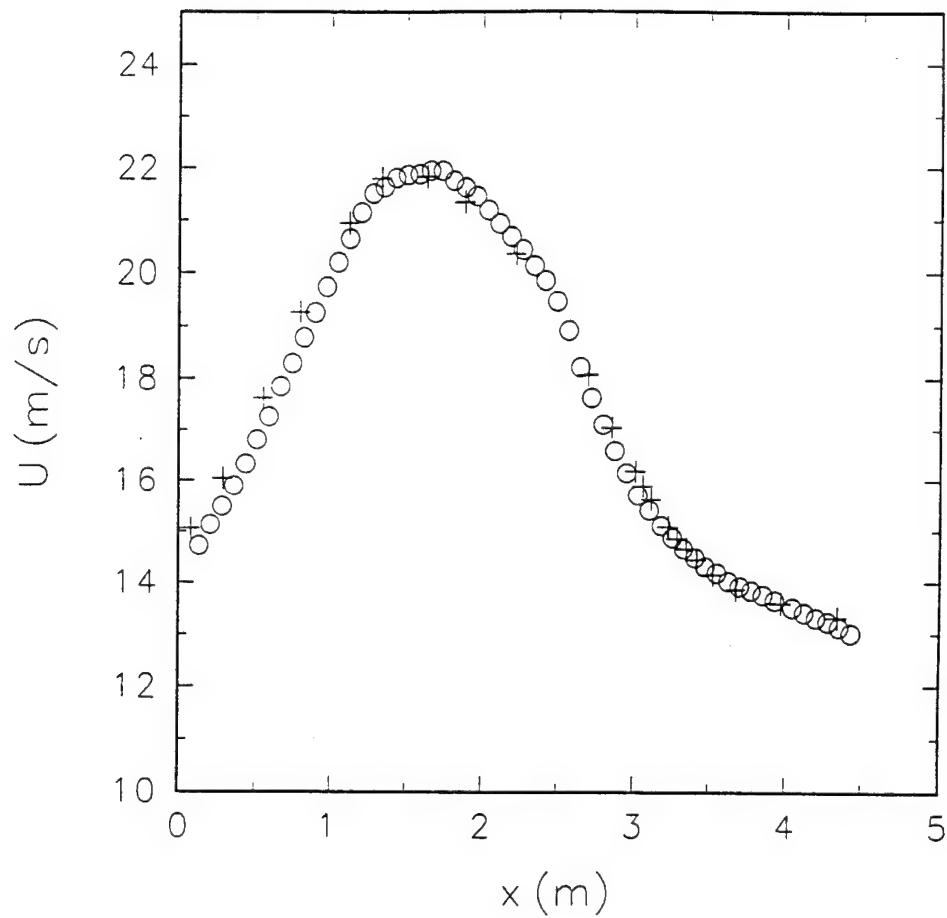


Fig. 3.4. Streamwise velocity variation in the potential core of the test section used for the 2-D separating TBL test case. O current data; + Simpson et al. (1981 a).

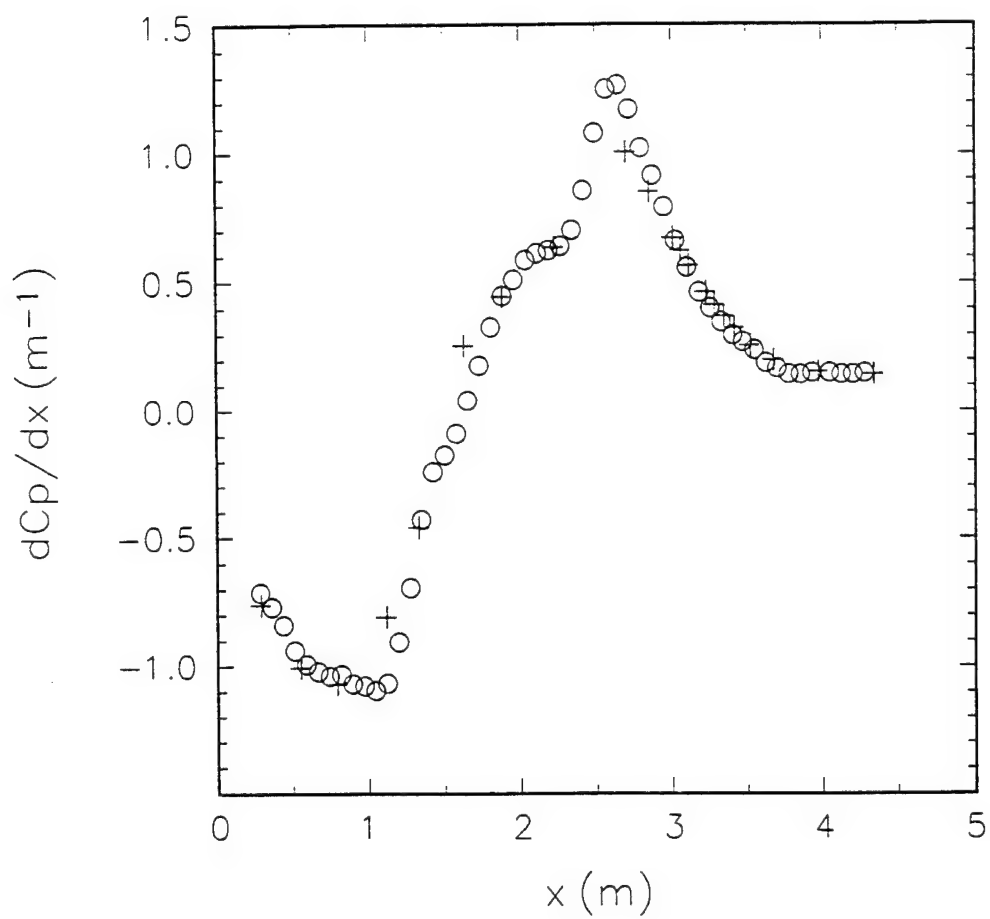


Fig. 3.5. Streamwise pressure gradient variation in the test section used for the 2-D separating TBL test case. O current data; + Simpson et al. (1981 a).

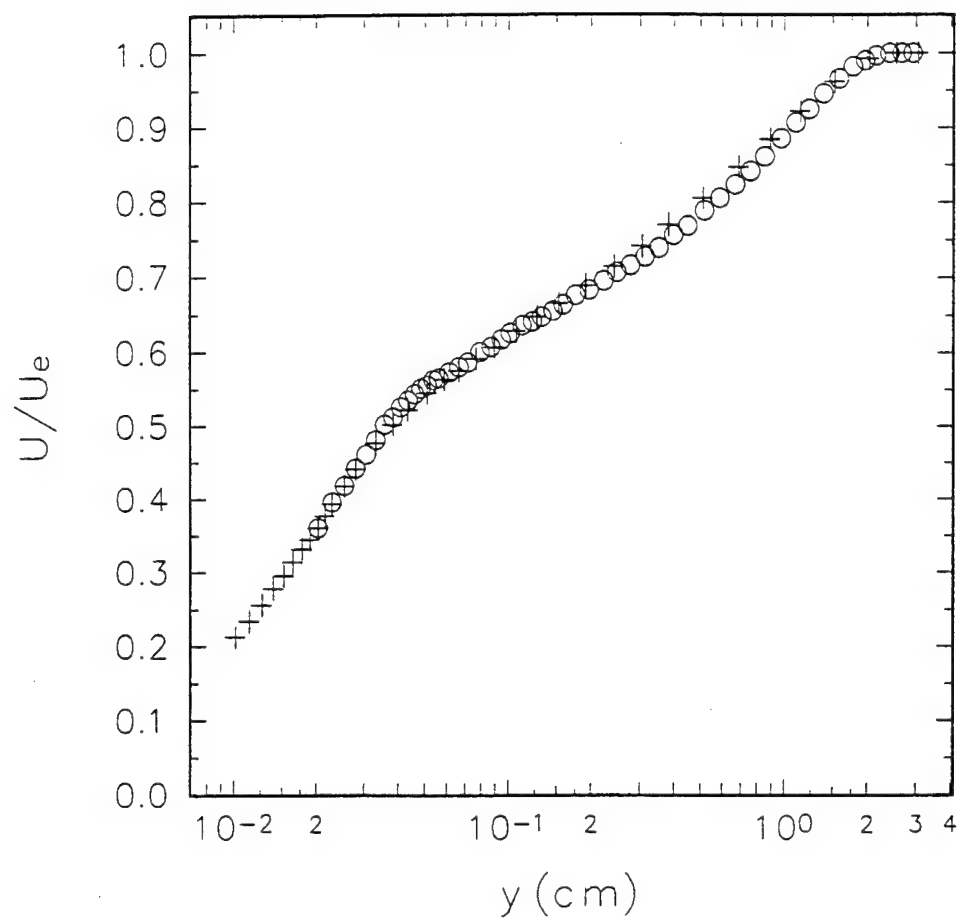


Fig. 3.6. Mean velocity profile measured 163.2 cm downstream from the test section entrance in the 2-D separating TBL test section. O current data; + Simpson et al. (1981 a).

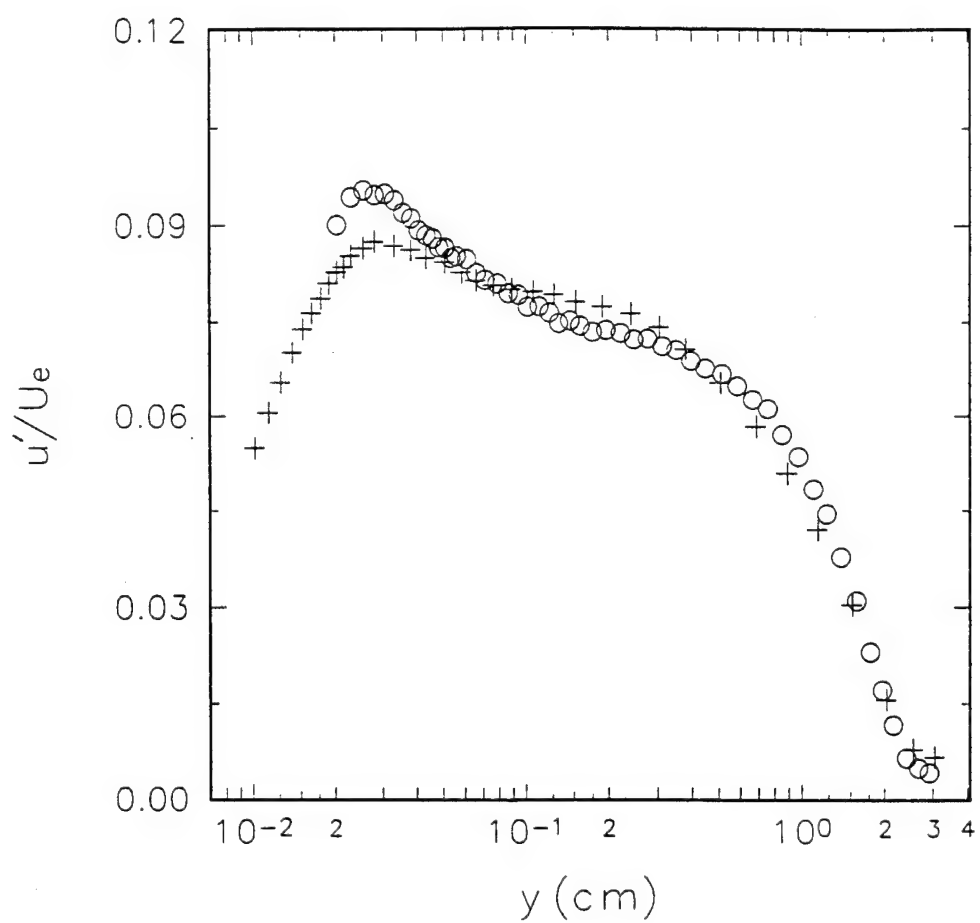


Fig. 3.7. Fluctuating velocity profile measured 163.2 cm downstream from the test section entrance in the 2-D separating TBL test section. O current data; + Simpson et al. (1981 a).

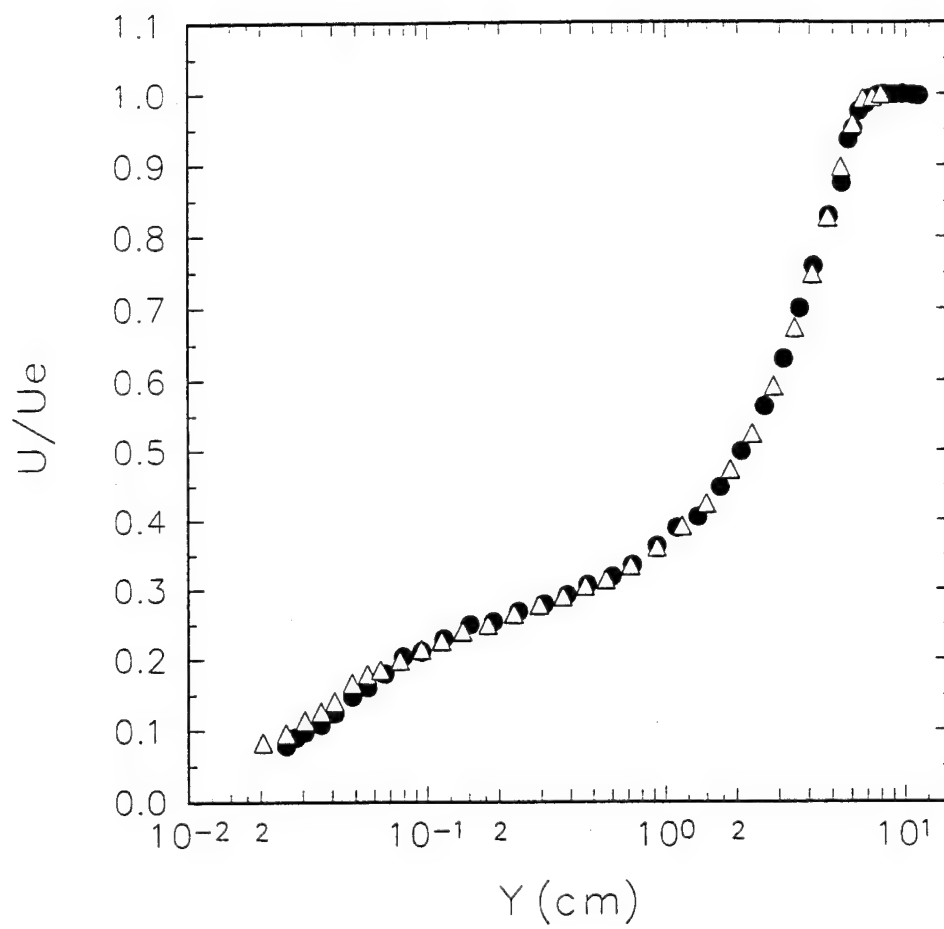


Fig. 3.8. Mean velocity profile measured at $x = 301.0$ cm in the 2-D separating TBL test section. ● current data; Δ Simpson et al. (1981 a).

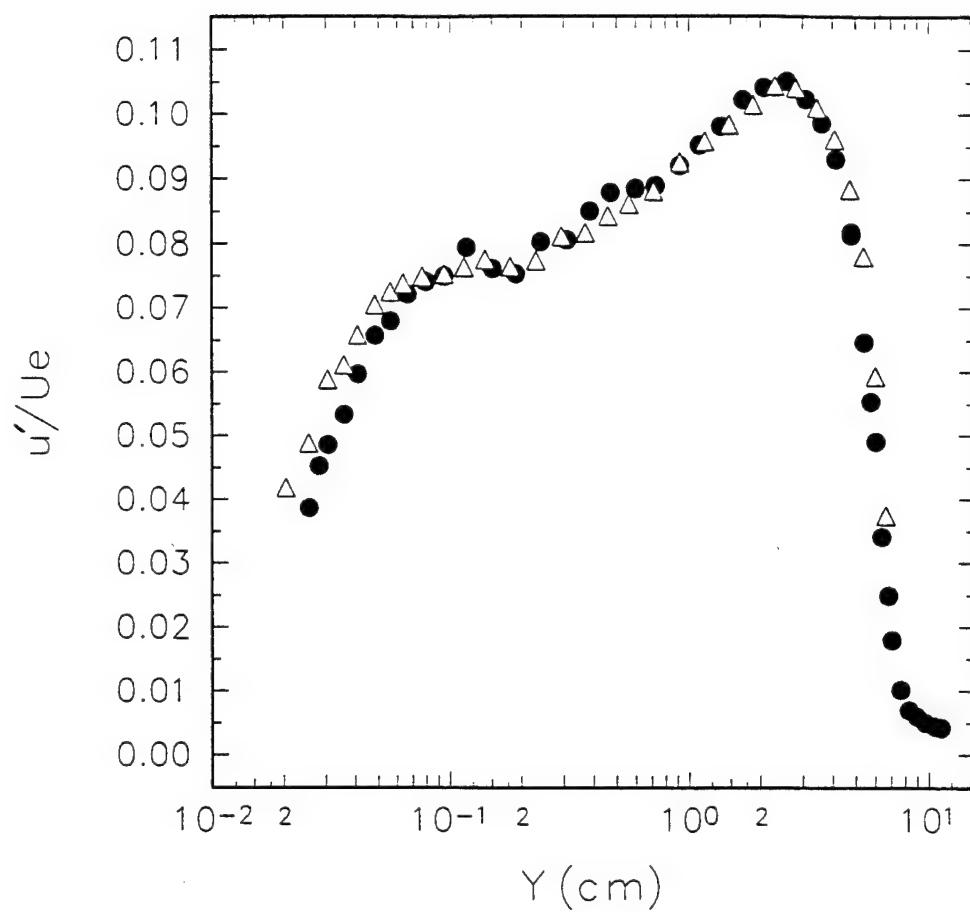


Fig. 3.9. Fluctuating velocity profile measured at $x = 301.0$ cm in the 2-D separating TBL test section. ● current data; Δ Simpson et al. (1981 a)

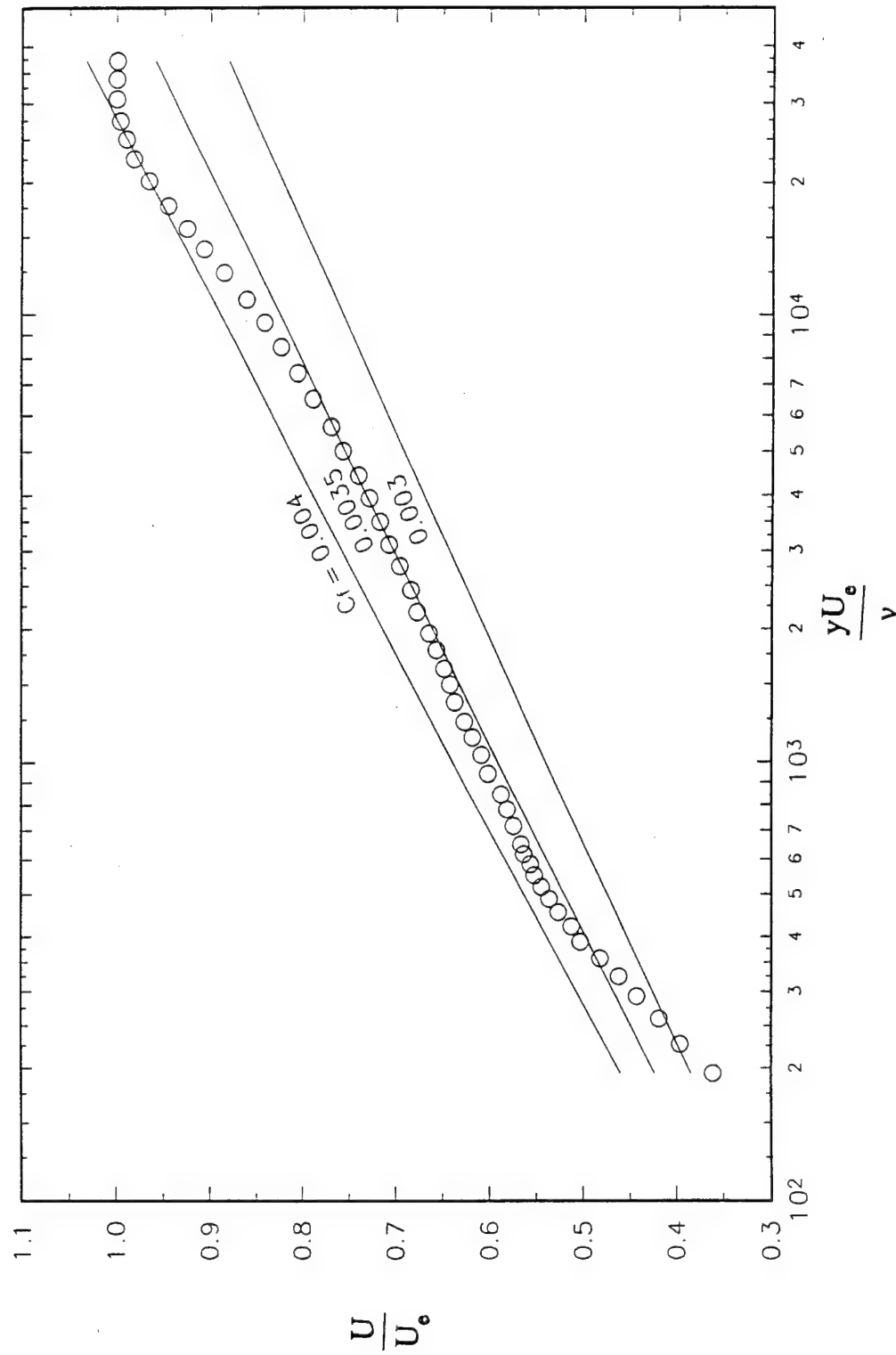


Fig. 3.10. Clauser plot of mean velocity profile at $x = 163.2$ cm in 2-D separating TBL test section.

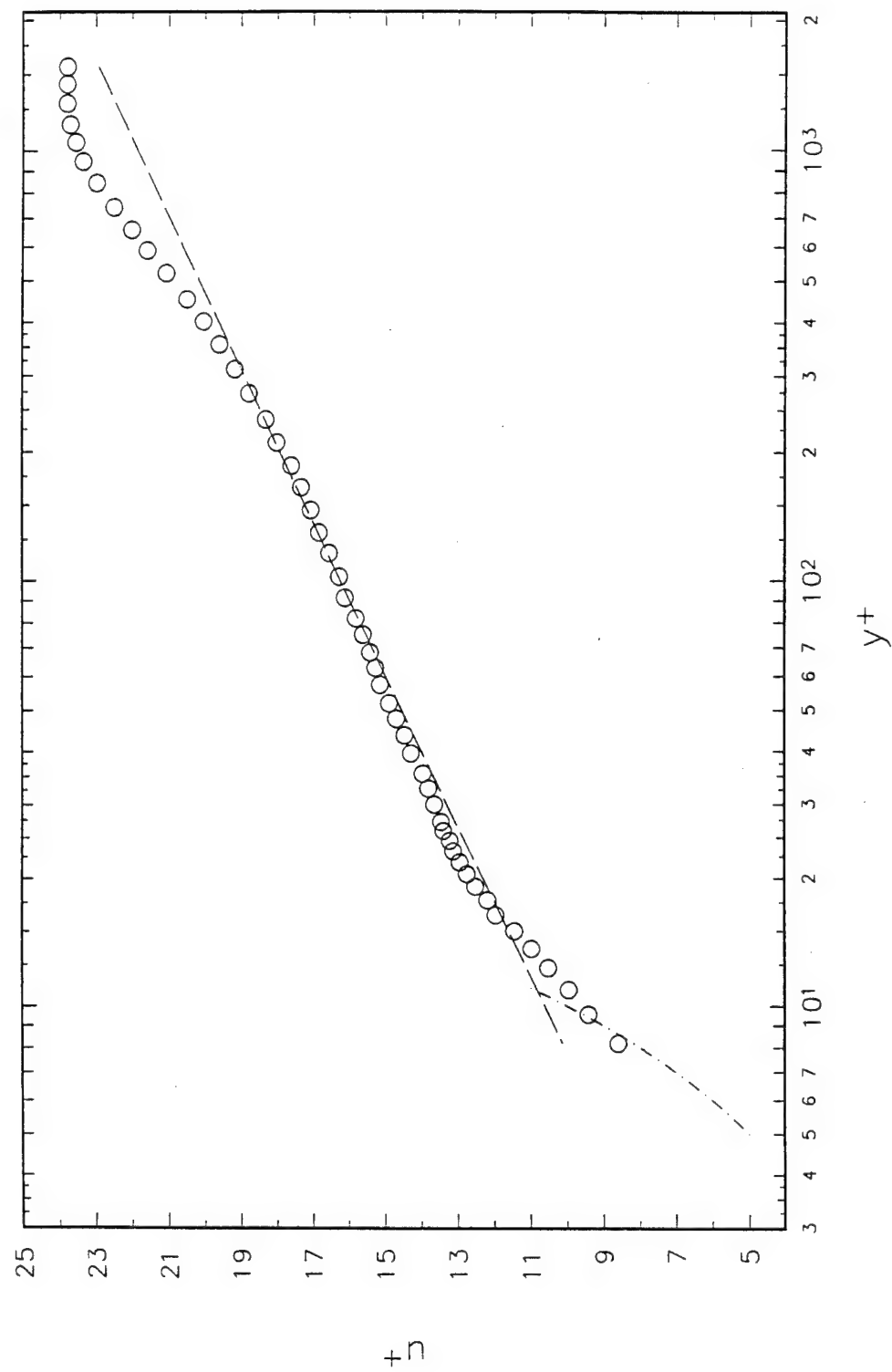


Fig. 3.11. Semi-logarithmic wall law plot of mean velocity profile at $x = 163.2$ cm in 2-D separating TBL test section.

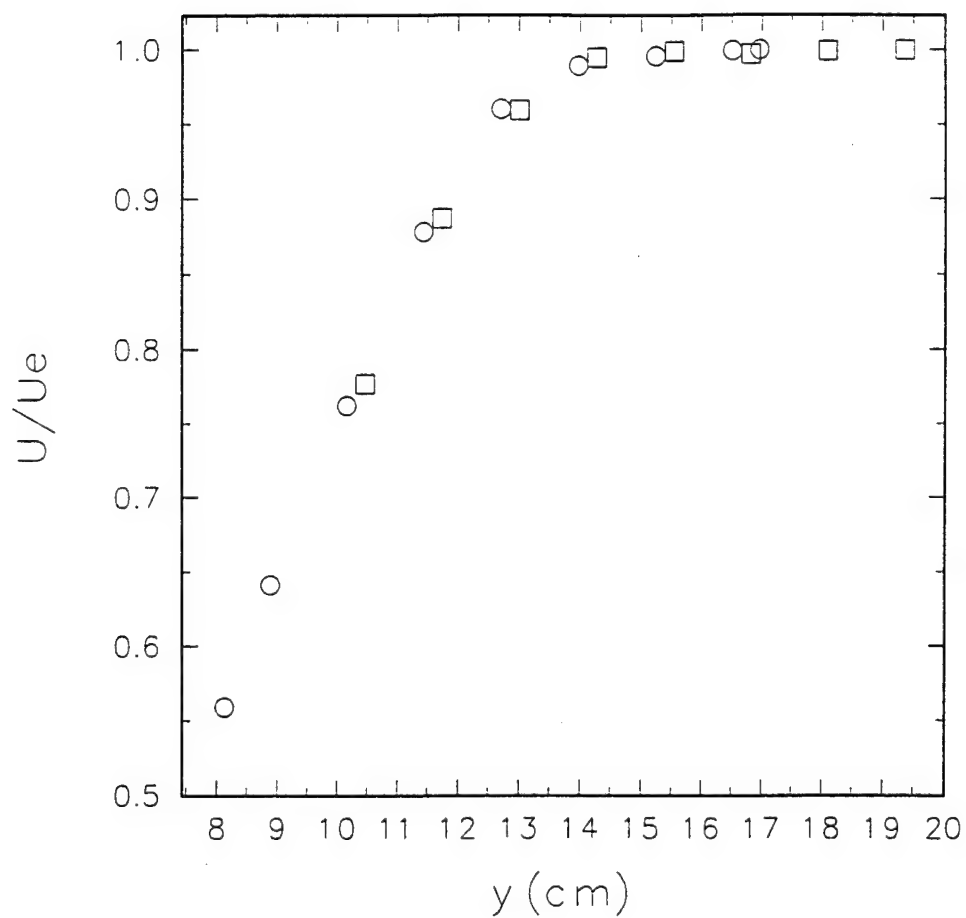


Fig. 3.12. Mean velocity profile in the 2-D separating TBL test case measured at $x = 352.4$ cm in the separated flow outer region above where near-wall flow reversal occurs. \circ Current data; \square Simpson et al. (1981 a).

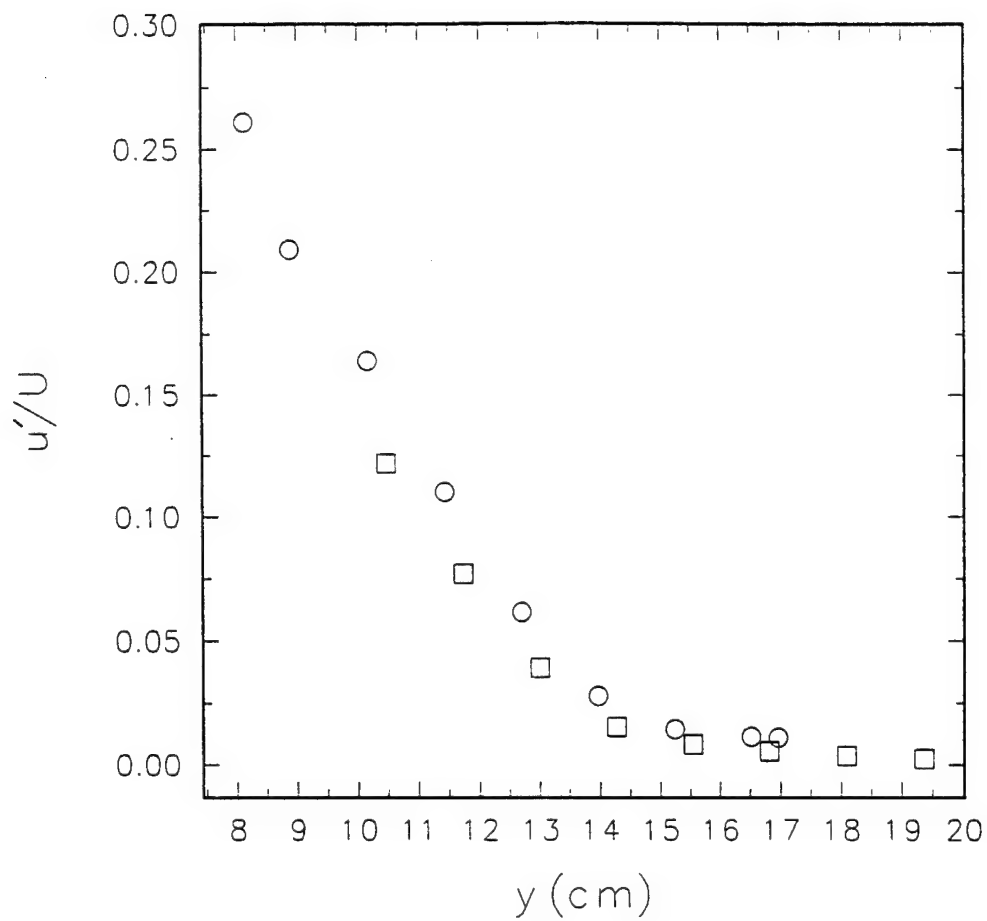


Fig. 3.13. Turbulence intensity profile in the 2-D separating TBL test case measured at $x = 352.4$ cm in the separated flow outer region above where near-wall flow reversal occurs. \circ Current data; \square Simpson et al. (1981 a).

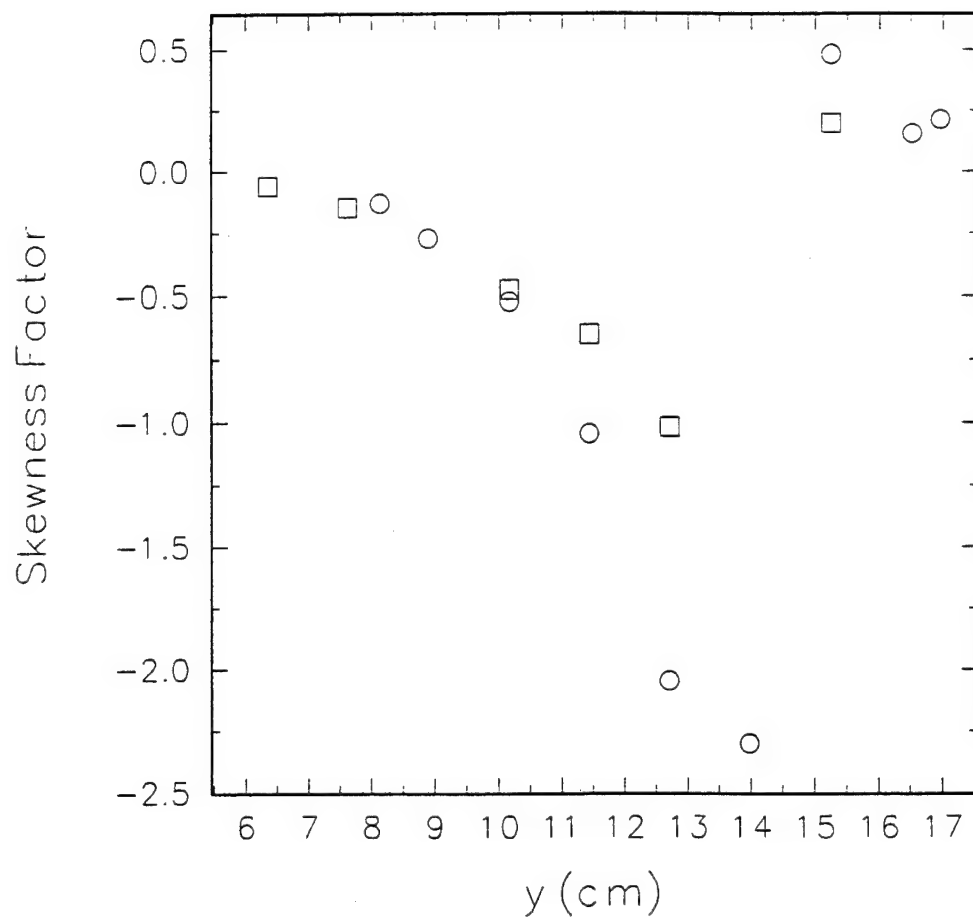


Fig. 3.14. Profile of skewness factor S_u of velocity fluctuations in the 2-D separating TBL test case measured at $x = 352.4$ cm in the separated flow outer region above where near-wall flow reversal occurs. \circ Current data; \square Simpson et al. (1981 a).

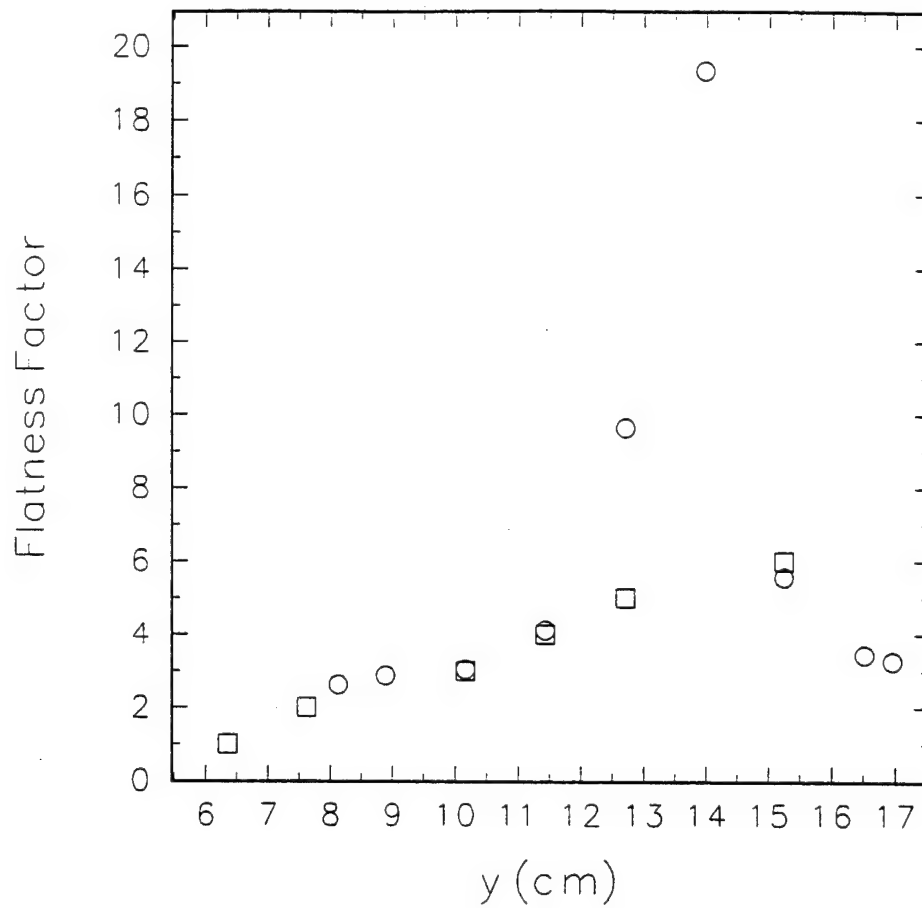


Fig. 3.15. Profile of flatness factor F_u of velocity fluctuations in the 2-D separating TBL test case measured at $x = 352.4$ cm in the separated flow outer region above where near-wall flow reversal occurs. \circ Current data; \square Simpson et al. (1981 a).

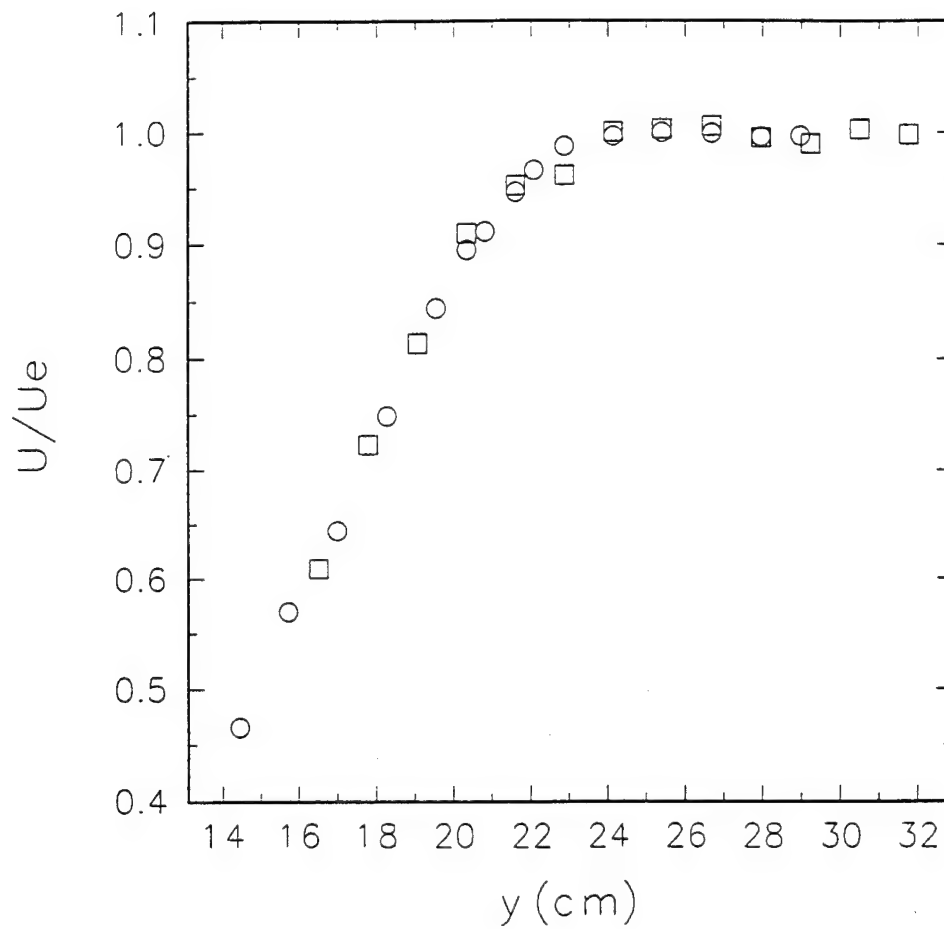


Fig. 3.16. Mean velocity profile in the 2-D separating TBL test case measured at $X = 397.2$ cm in the separated flow outer region above where near-wall flow reversal occurs. ○ Current data; □ Simpson et al. (1981 a).

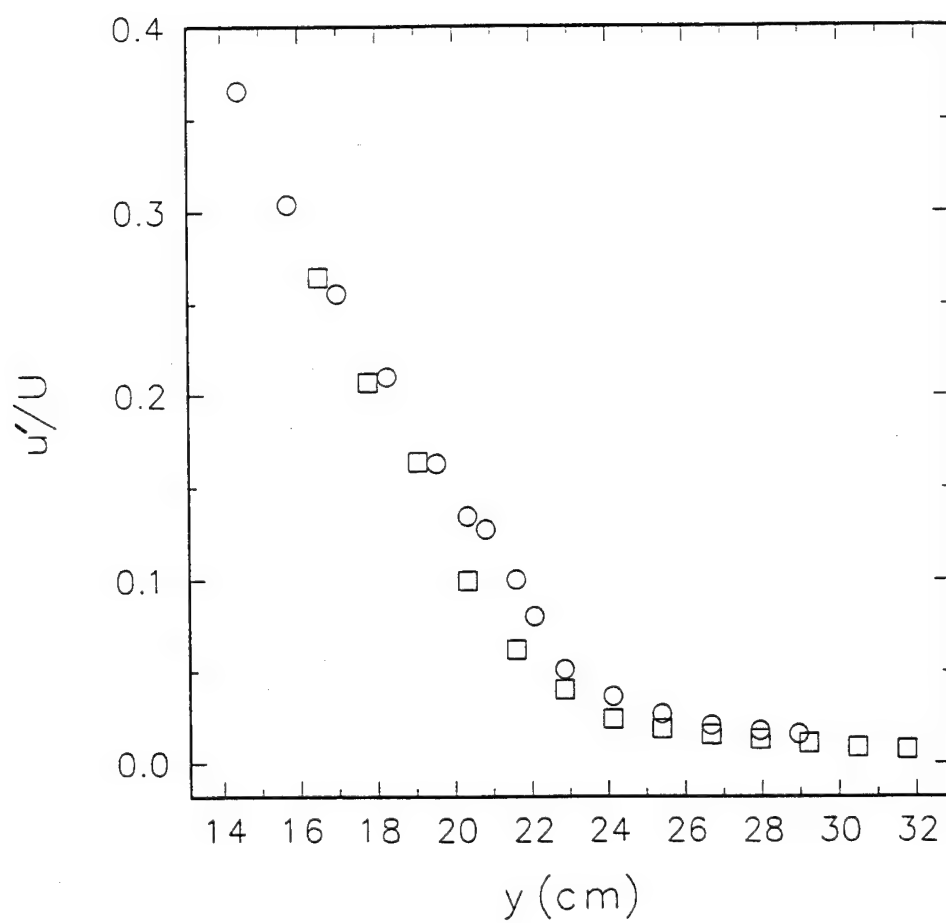


Fig. 3.17. Turbulence intensity profile in the 2-D separating TBL test case measured at $X = 397.2$ cm in the separated flow outer region above where near-wall flow reversal occurs. \circ Current data; \square Simpson et al. (1981 a).

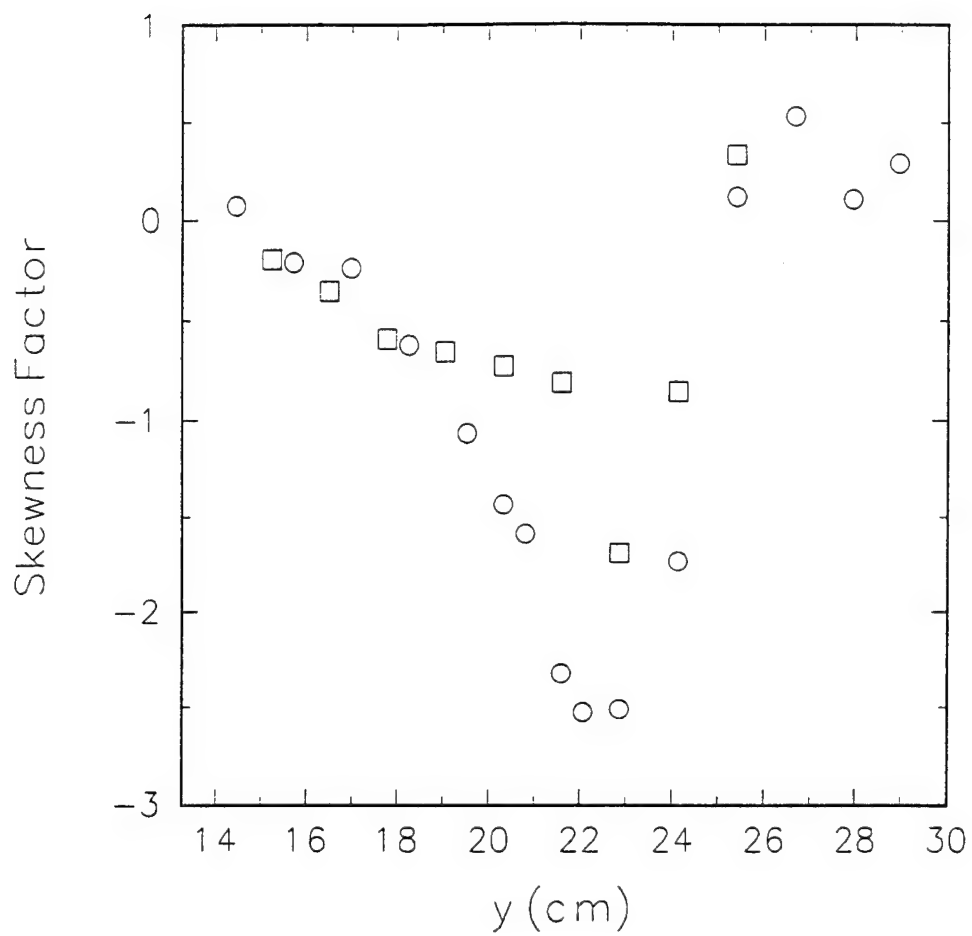


Fig. 3.18. Profile of skewness factor S_u of velocity fluctuations in the 2-D separating TBL test case measured at $X = 397.2$ cm in the separated flow outer region above where near-wall flow reversal occurs. \circ Current data; \square Simpson et al. (1981 a).

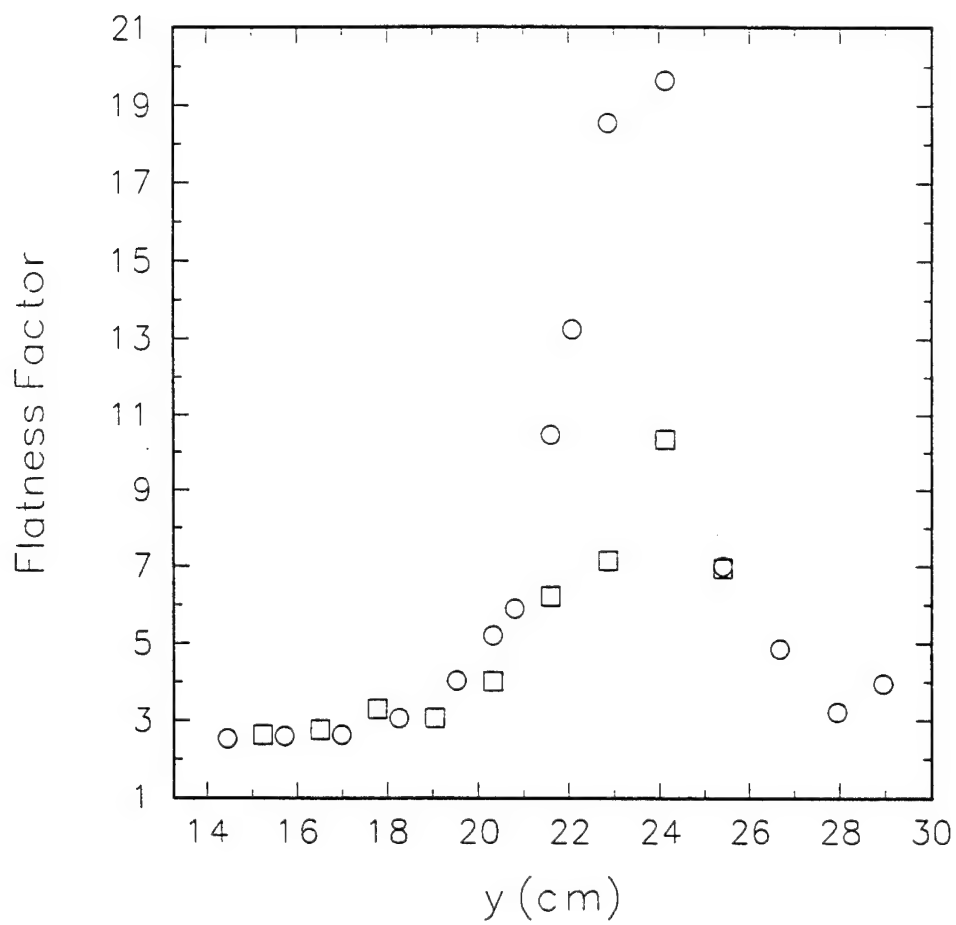


Fig. 3.19. Profile of flatness factor F_u of velocity fluctuations in the 2-D separating TBL test case measured at $X = 397.2$ cm in the separated flow outer region above where near-wall flow reversal occurs. \circ Current data; \square Simpson et al. (1981 a).

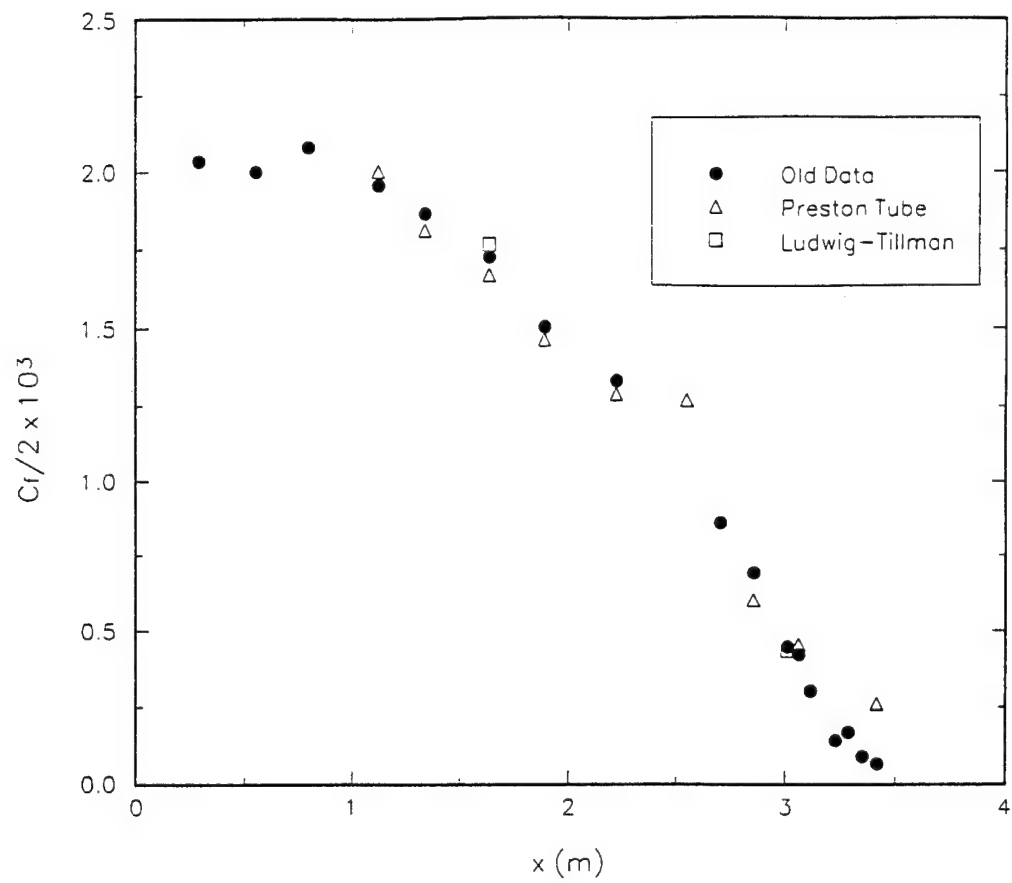


Fig. 3.20. Streamwise variation of surface skin-friction coefficient in the 2-D separating TBL test case. • Simpson et al (1981 a); Δ Preston tube; \square Ludwig-Tillman equation.

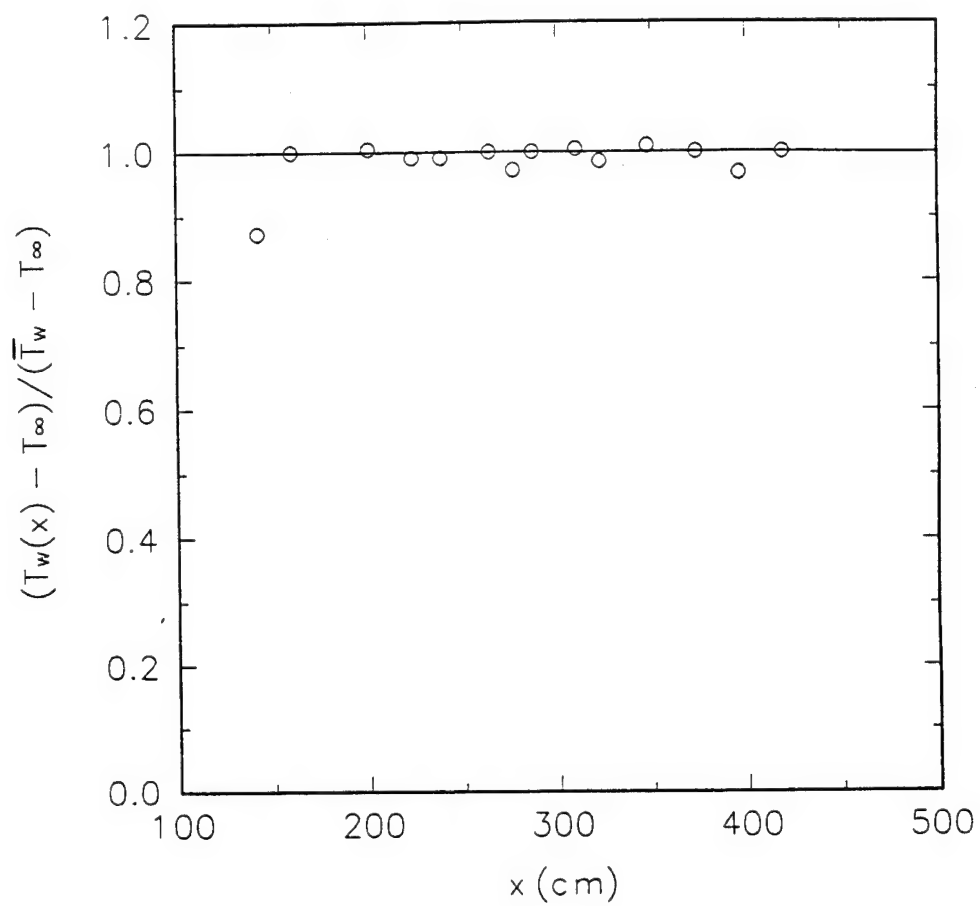


Fig. 3.21. Streamwise variation in normalized wall temperature for the 3-D TBL test section.

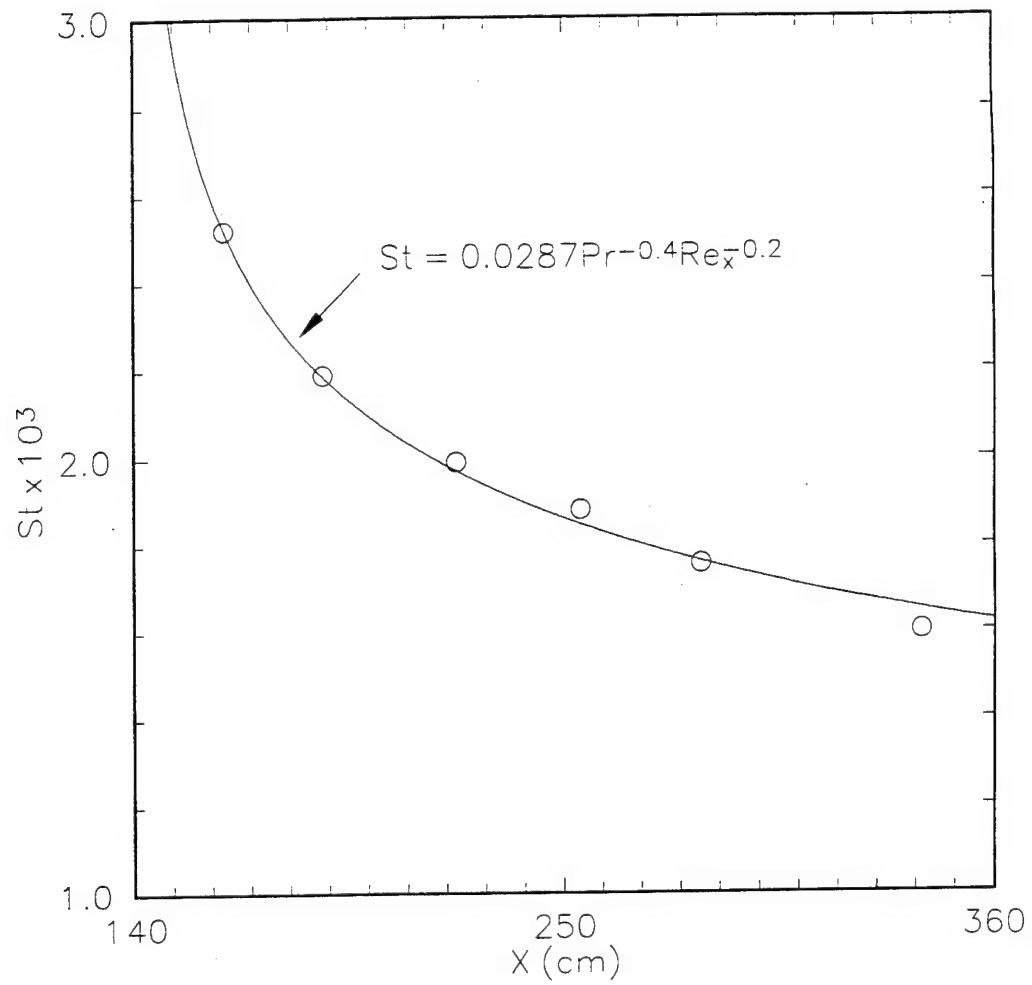


Fig. 3.22. Streamwise variation in Stanton number for the 3-D TBL test section with the wing removed.

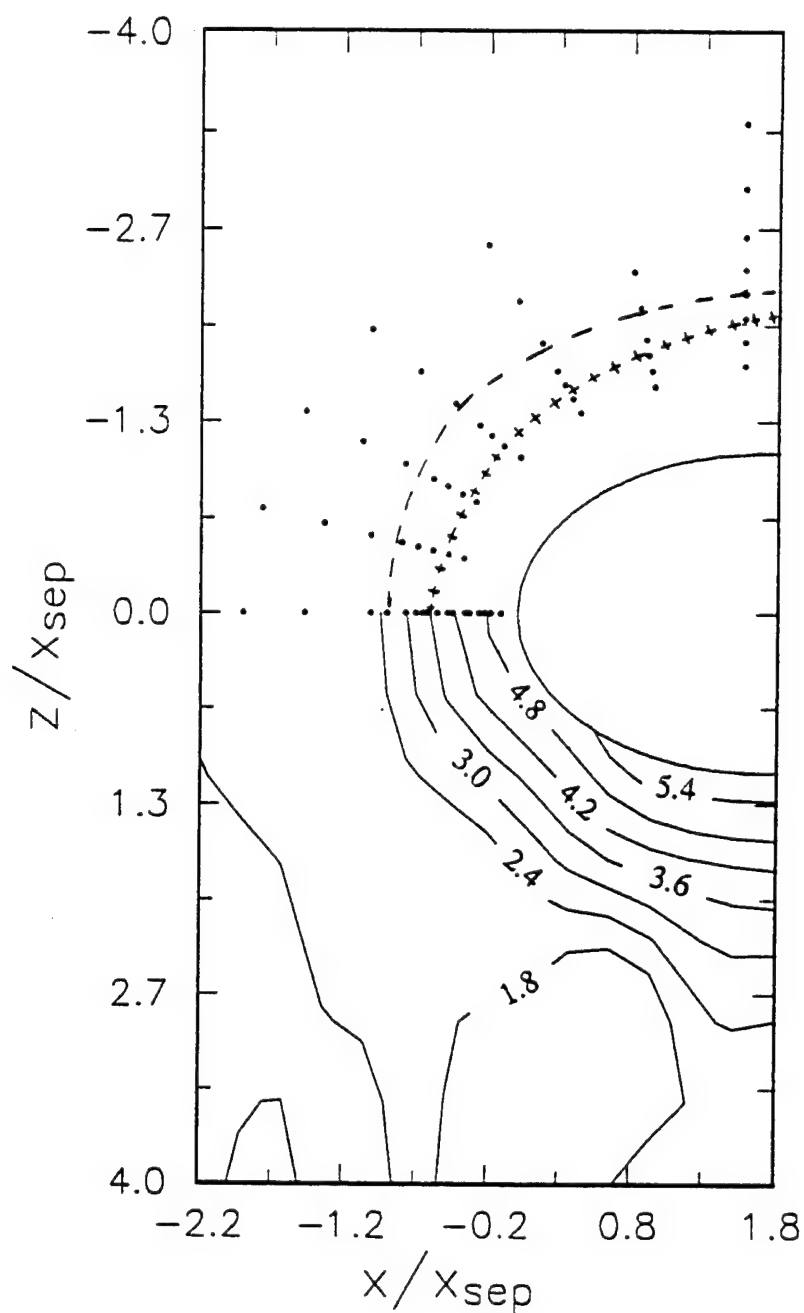


Fig. 4.1. Contours of constant time-mean Stanton number $\times 10^3$ for the modified NACA 0020 wing; — — — - line of separation, +++++ - line of low shear, • - locations of heat flux measurements.

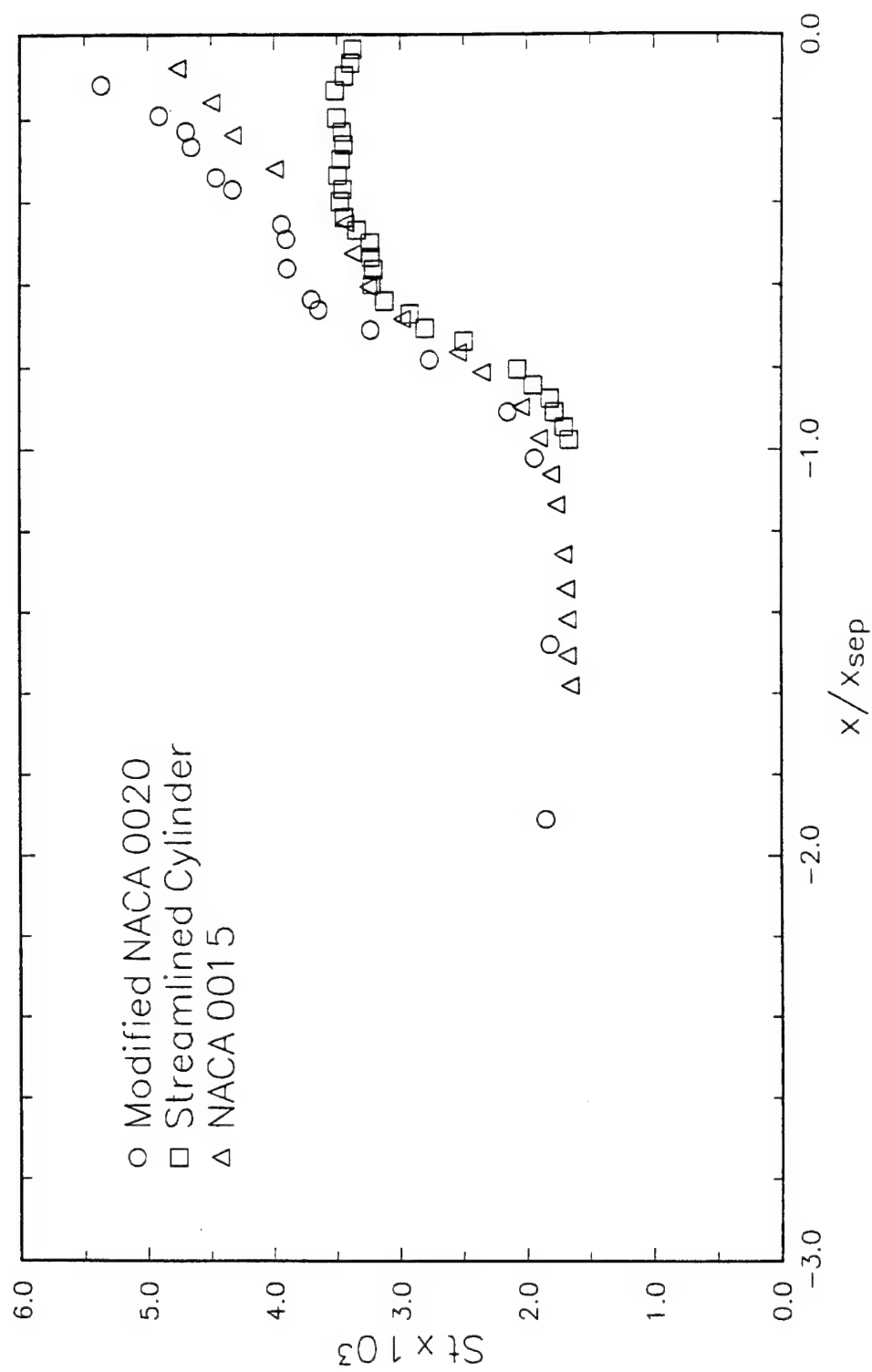


Fig. 4.2. Time-mean Stanton number distribution along the stagnation streamline upstream of each model. Distances are normalized with x_{sep} which is different for each model.

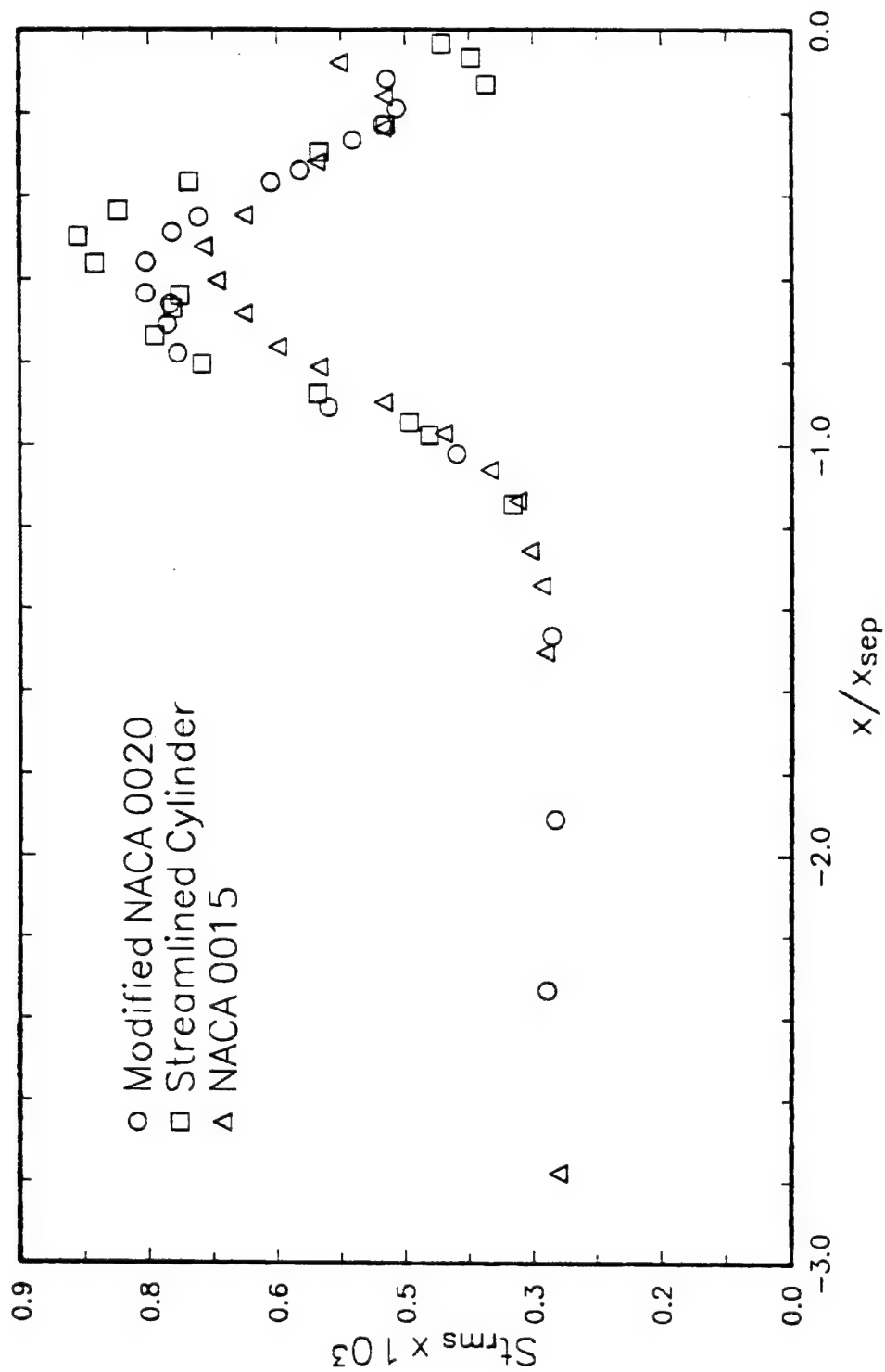


Fig. 4.3. Fluctuations in Stanton number measured along the stagnation streamline upstream of each model. Distances are normalized with x_{sep} which is different for each model.

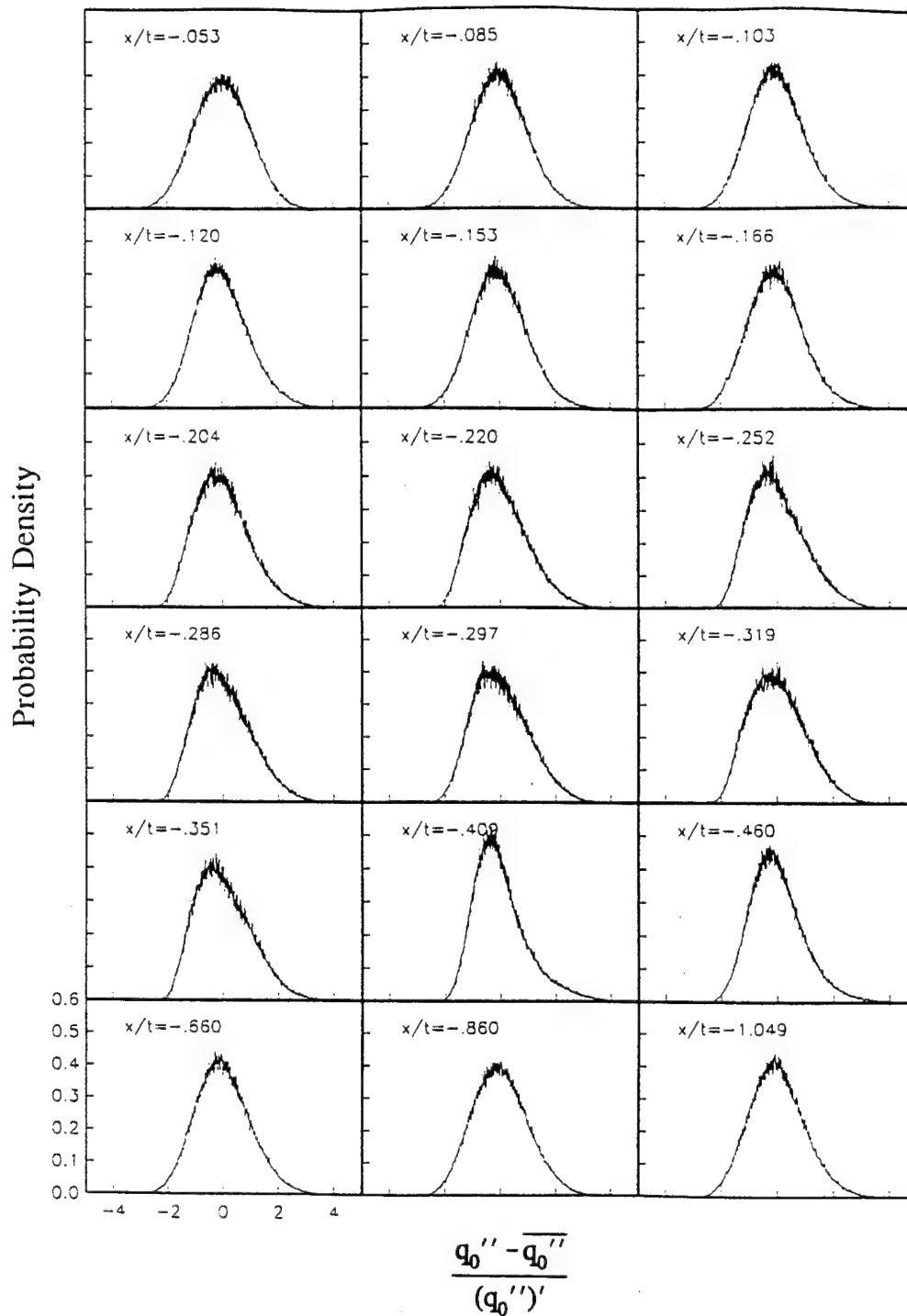


Fig. 4.4. Probability density functions of heat flux fluctuations measured on the stagnation streamline upstream of the modified NACA 0020 wing.

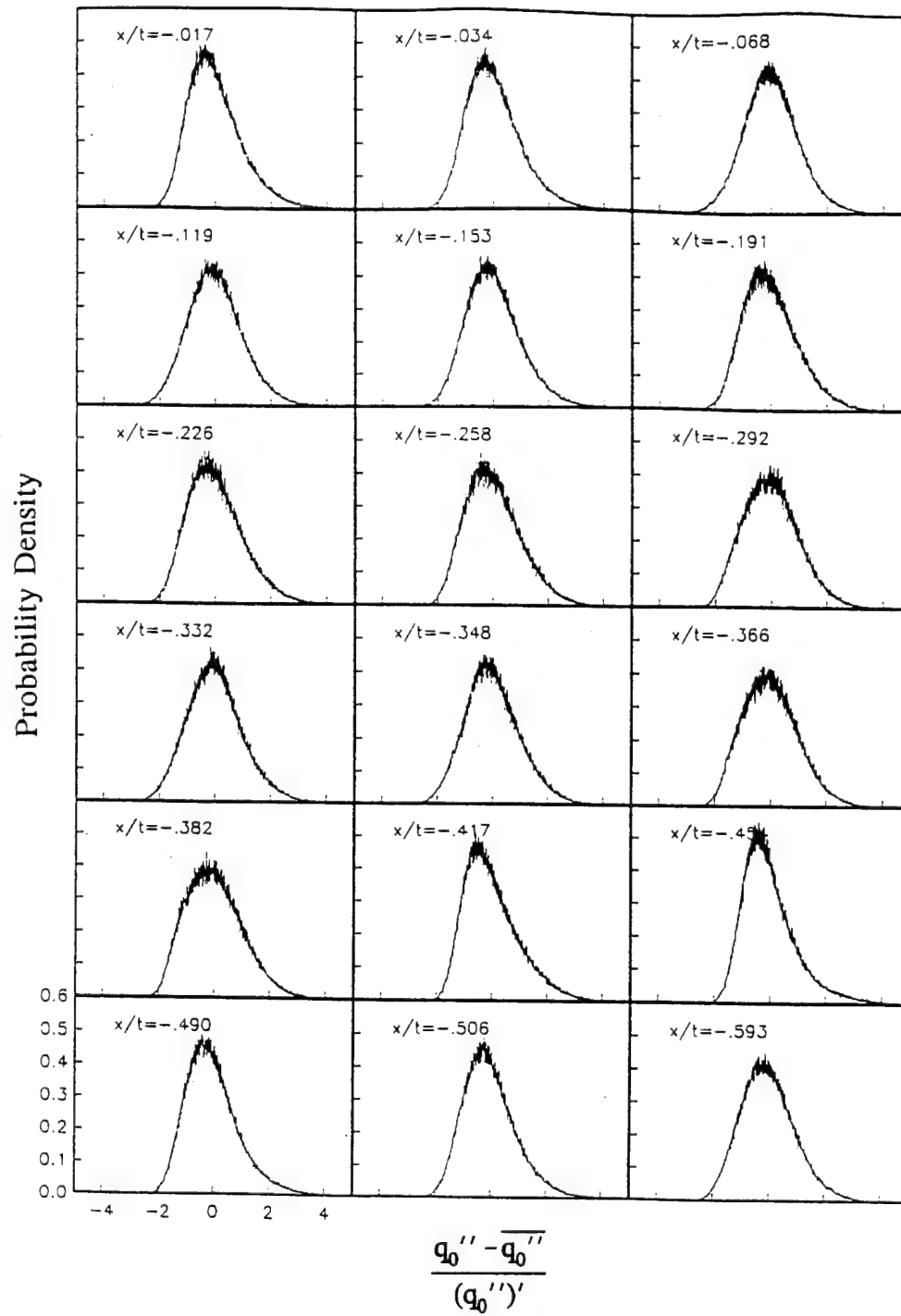


Fig. 4.5. Probability density functions of heat flux fluctuations measured on the stagnation streamline upstream of the streamlined cylinder.

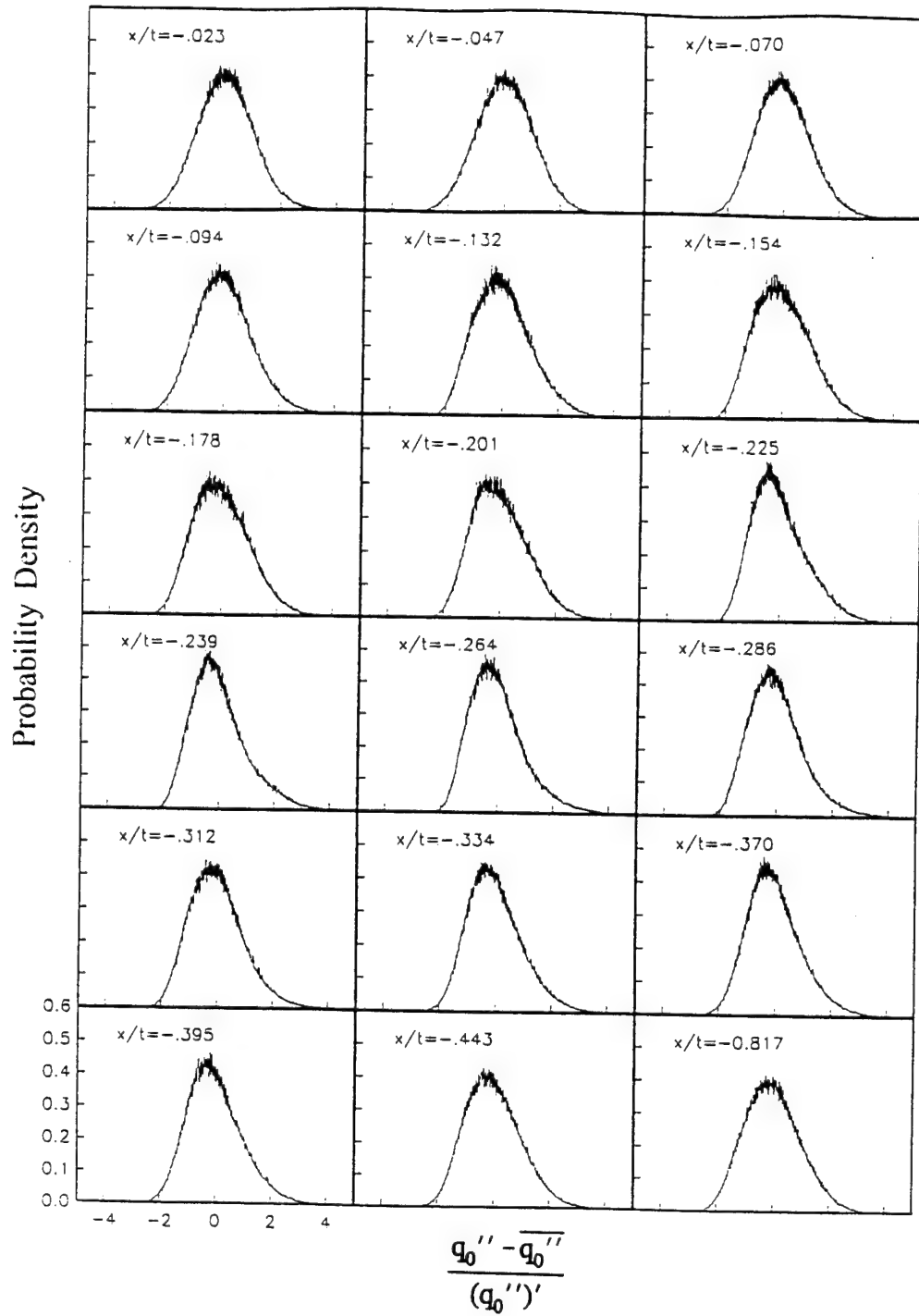


Fig. 4.6. Probability density functions of heat flux fluctuations measured on the stagnation streamline upstream of the NACA 0015 wing.

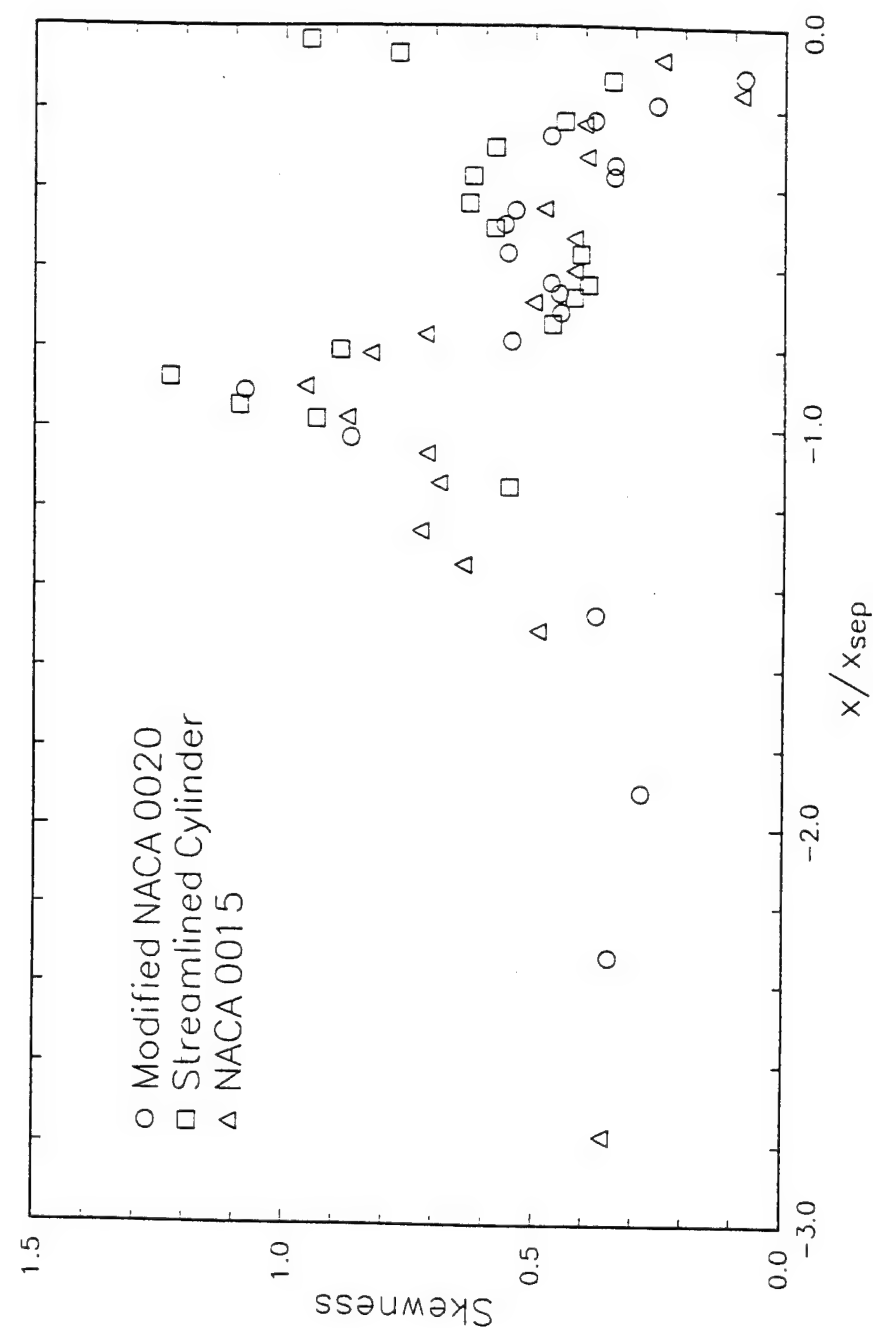


Fig. 4.7. Distributions of the skewness factor of the heat flux pdfs measured along the symmetry line upstream of each model.

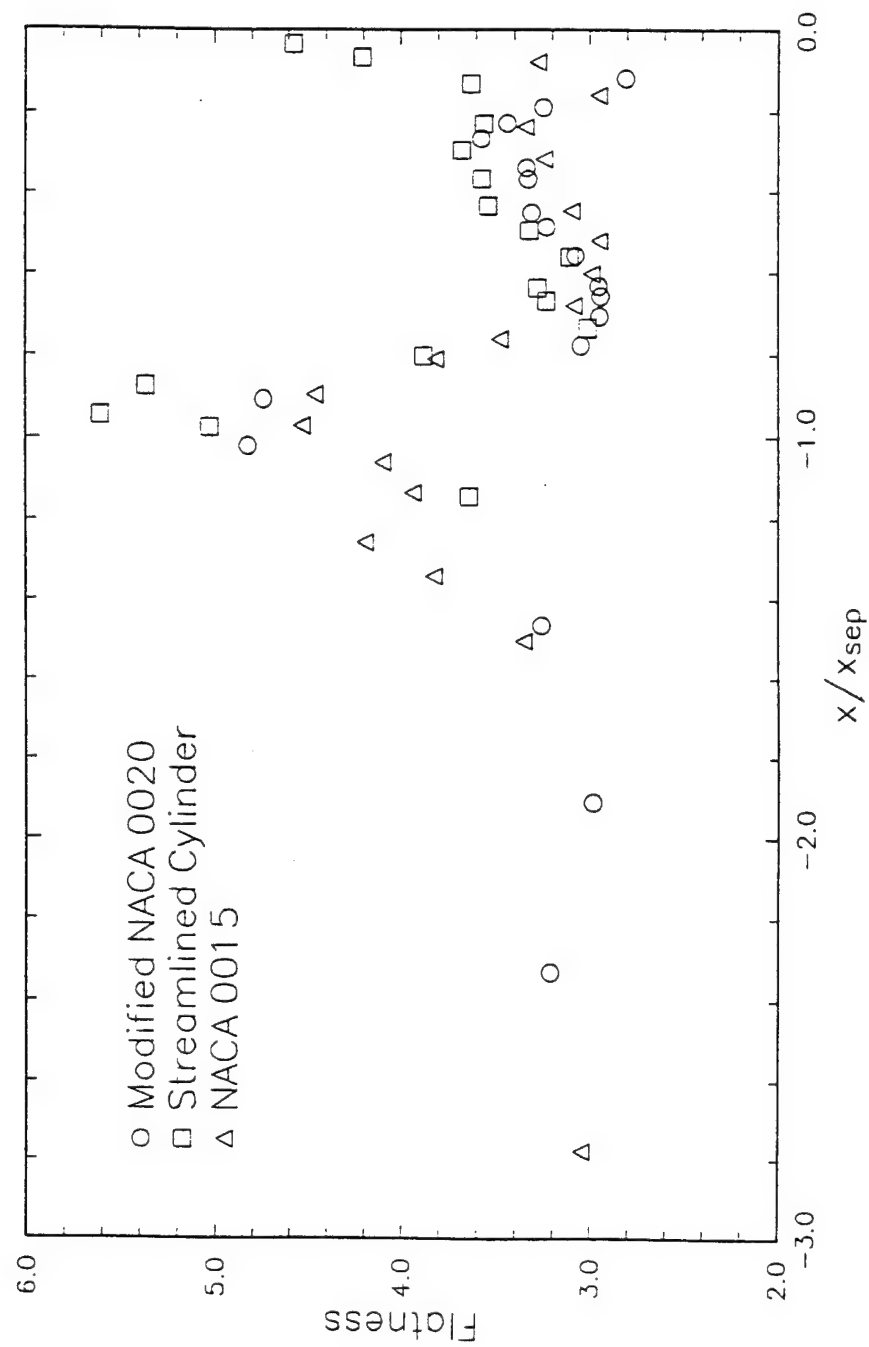


Fig. 4.8. Distributions of the flatness factor of the heat flux pdfs measured along the symmetry line upstream of each model.

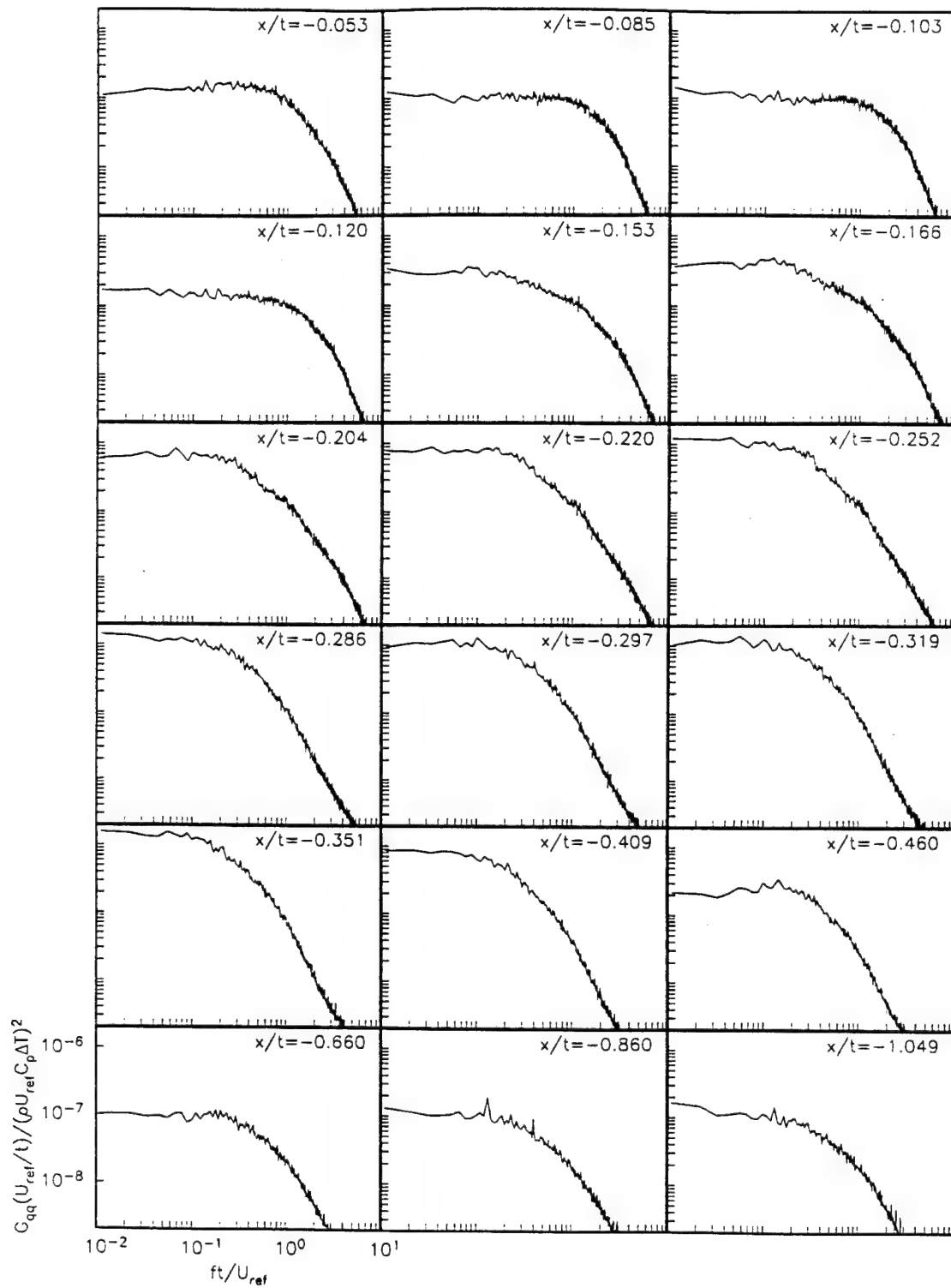


Fig. 4.9. Heat flux spectra measured along the line of symmetry upstream of the modified NACA 0020 wing.

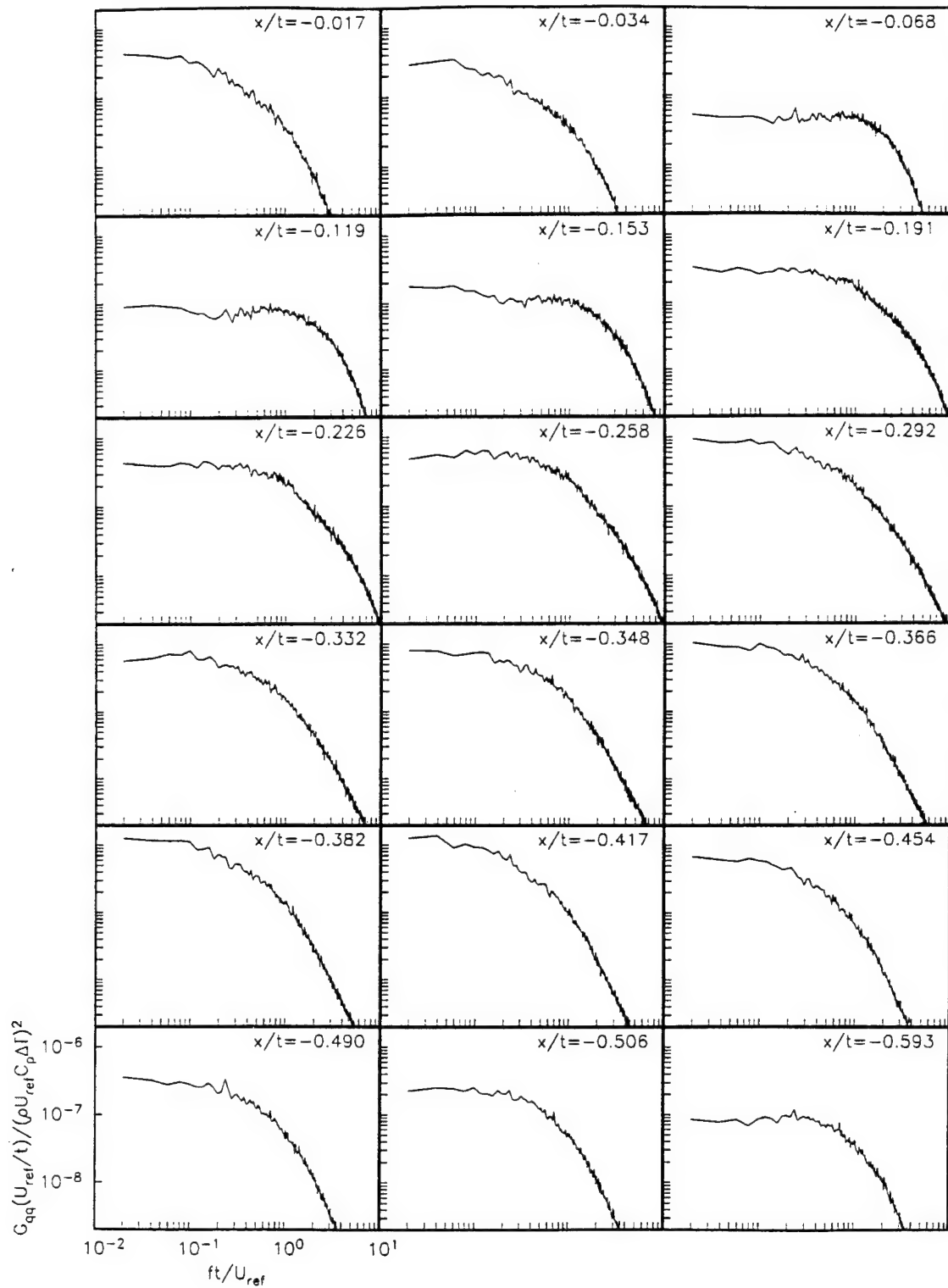


Fig. 4.10. Heat flux spectra measured along the line of symmetry upstream of the streamlined cylinder wing.

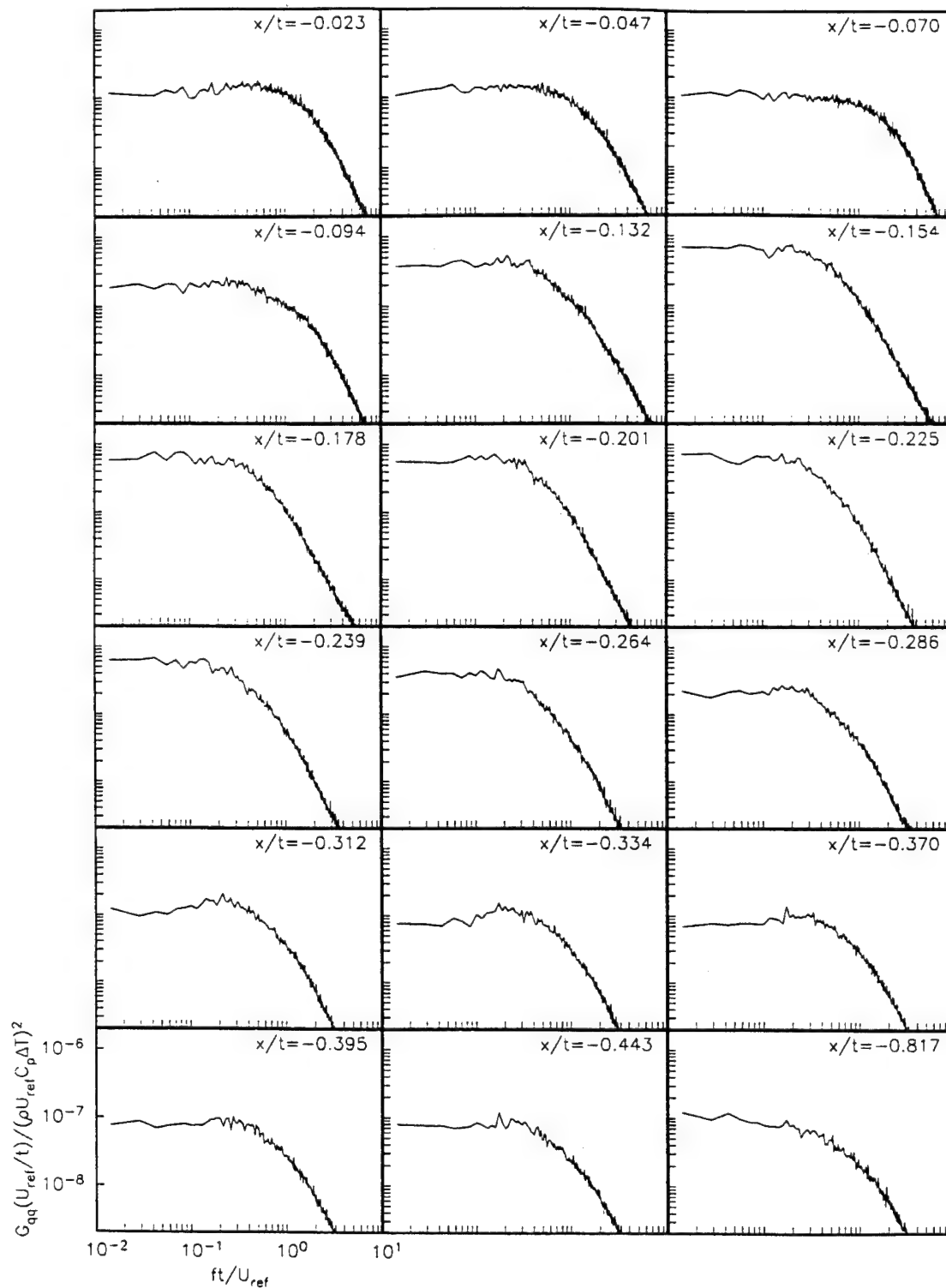


Fig. 4.11. Heat flux spectra measured along the line of symmetry upstream of the NACA 0015 wing.

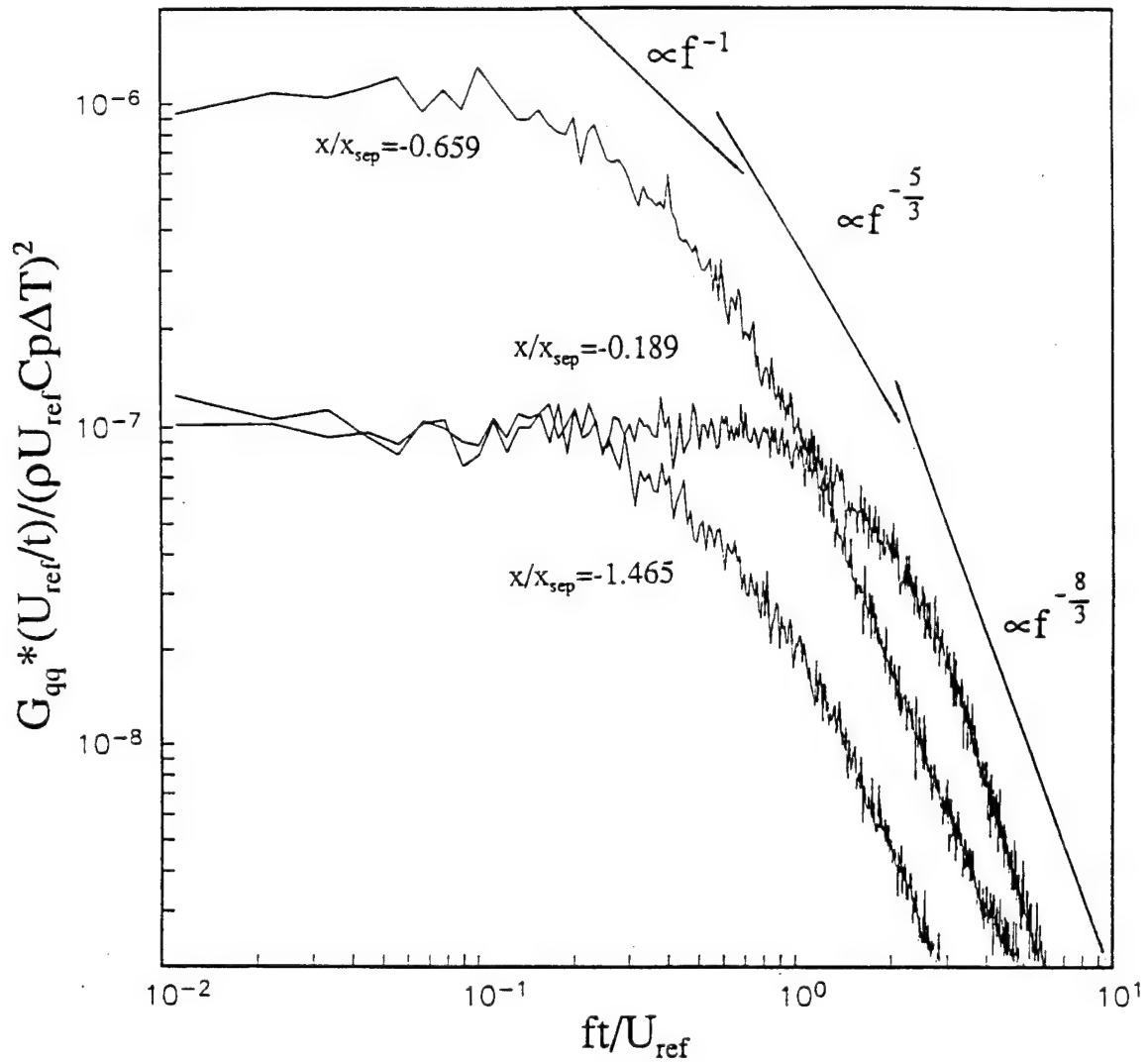


Fig. 4.12. A comparison of heat flux spectra measured in the approach boundary layer ($x/x_{sep}=-1.465$), in the region between the separation line and the line of low shear ($x/x_{sep}=-0.659$), and near the junction ($x/x_{sep}=-0.189$) for the modified NACA 0020 wing.

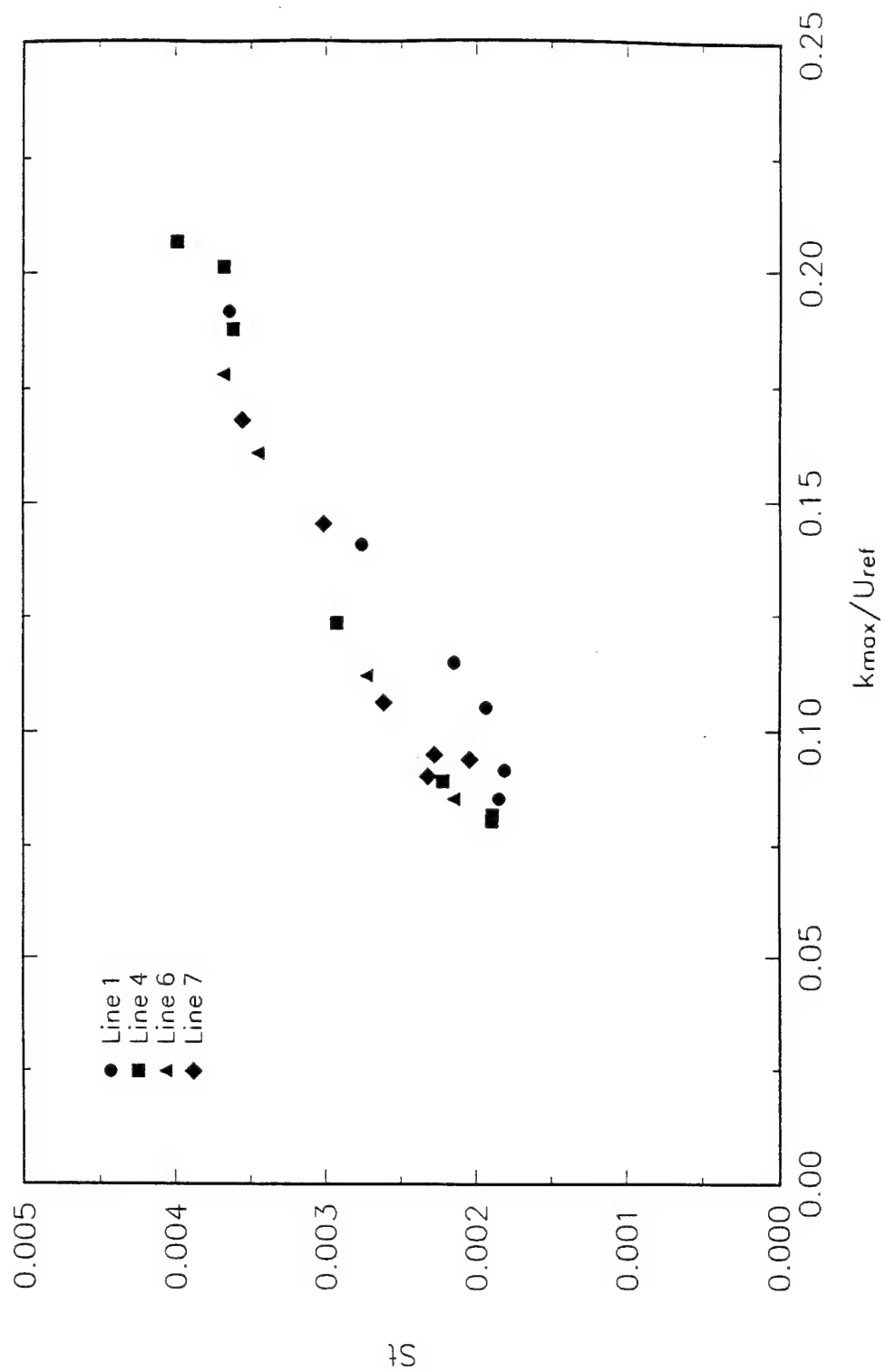


Fig. 4.13. Relation between surface heat flux and $k_{\text{rms,max}}$ in the region outside of the line of low shear for the modified NACA 0020 wing. Lines 1,4,6, and 7 are defined in Fig. 2.7.

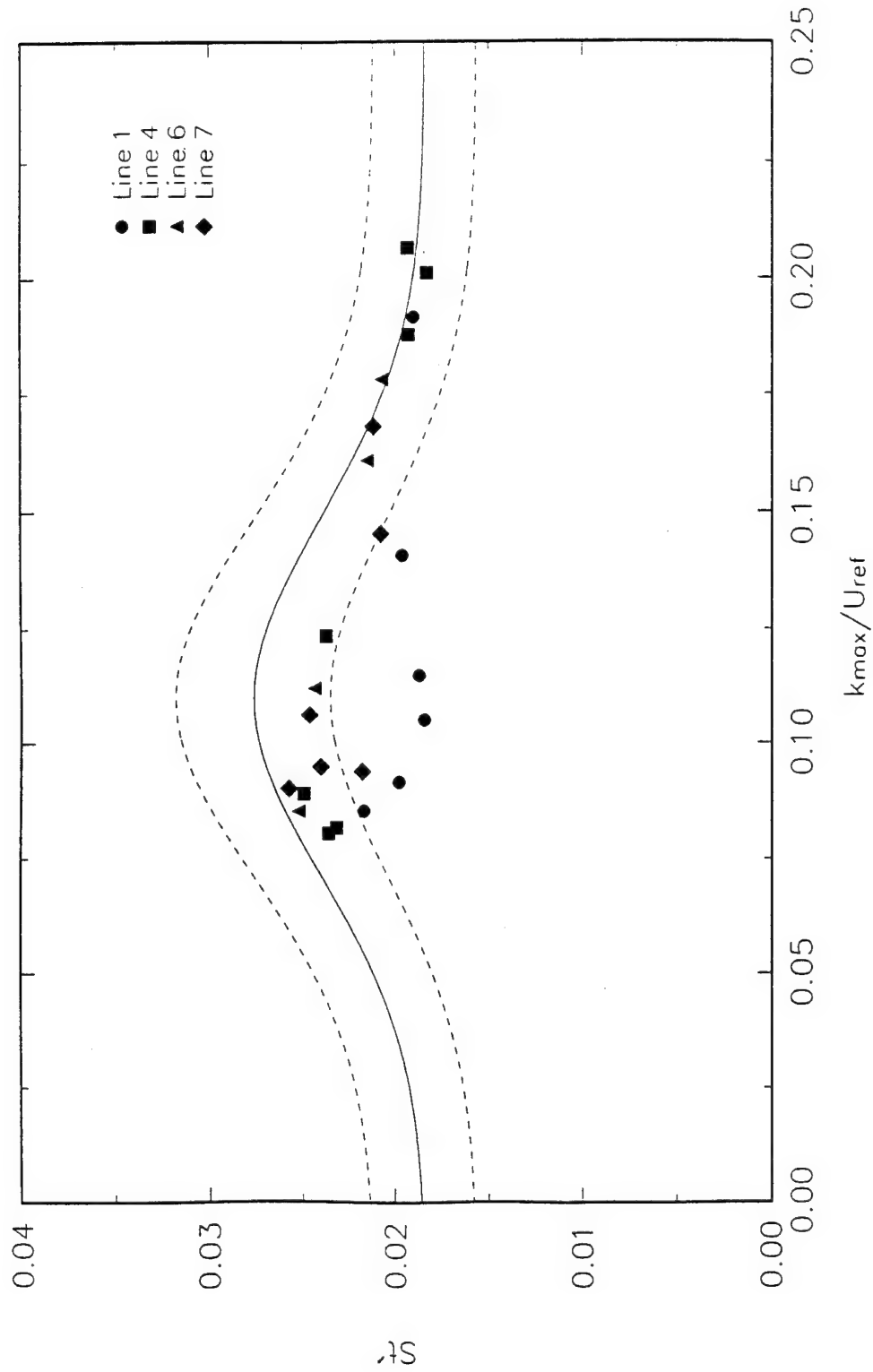


Fig. 4.14. St' correlation for surface heat flux in the region outside of the line of low shear for the modified NACA 0020 wing. Lines 1,4,6, and 7 are defined in Fig. 2.7. Solid line is Eq. (4.4). Dashed lines are $\pm 15\%$ error bands.

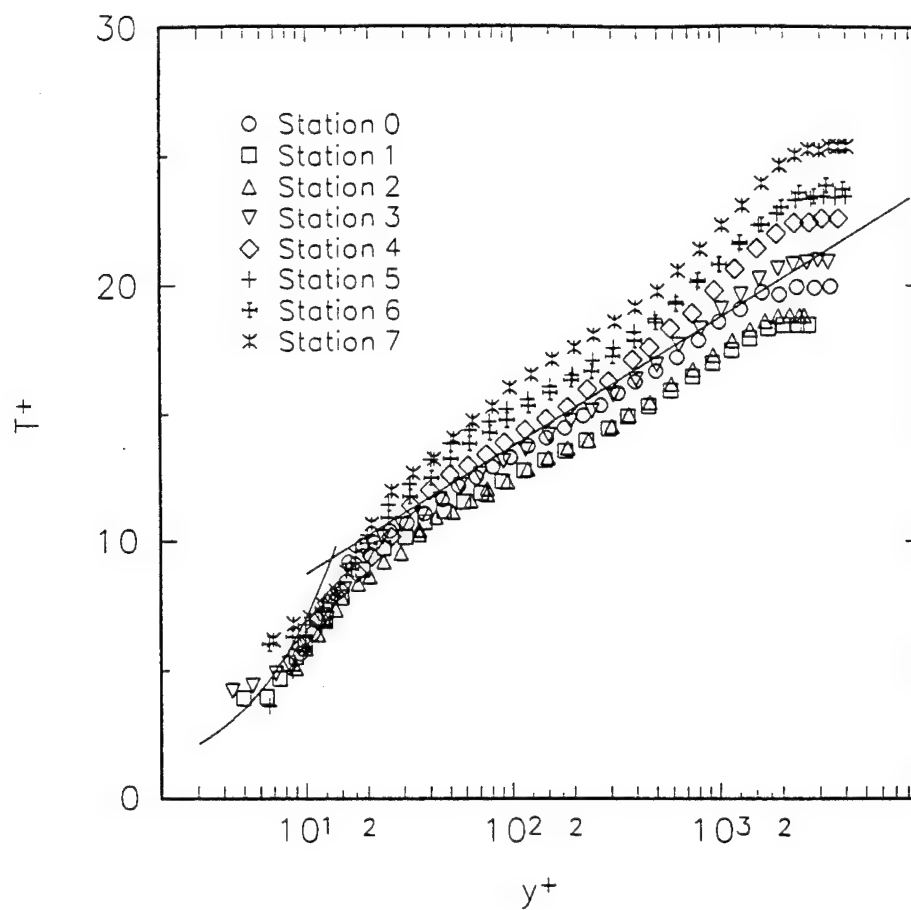


Figure 5.1. Mean temperature profiles at each station in the 3-D turbulent boundary layer.

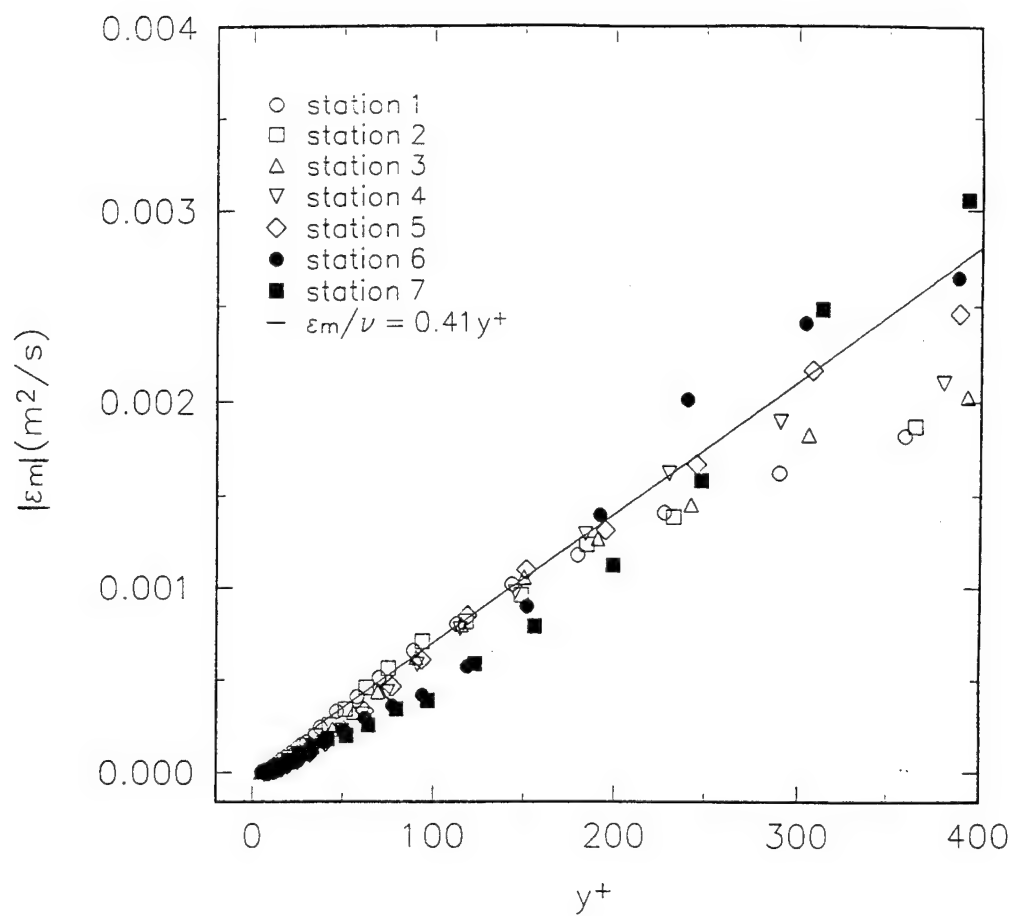


Figure 5.2. Near-wall variation of magnitude eddy viscosity at each station in the 3-D TBL flow. Straight line denotes $|\epsilon_m|/\nu = 0.41 y^+$. From data of Ölçmen and Simpson (1995a).

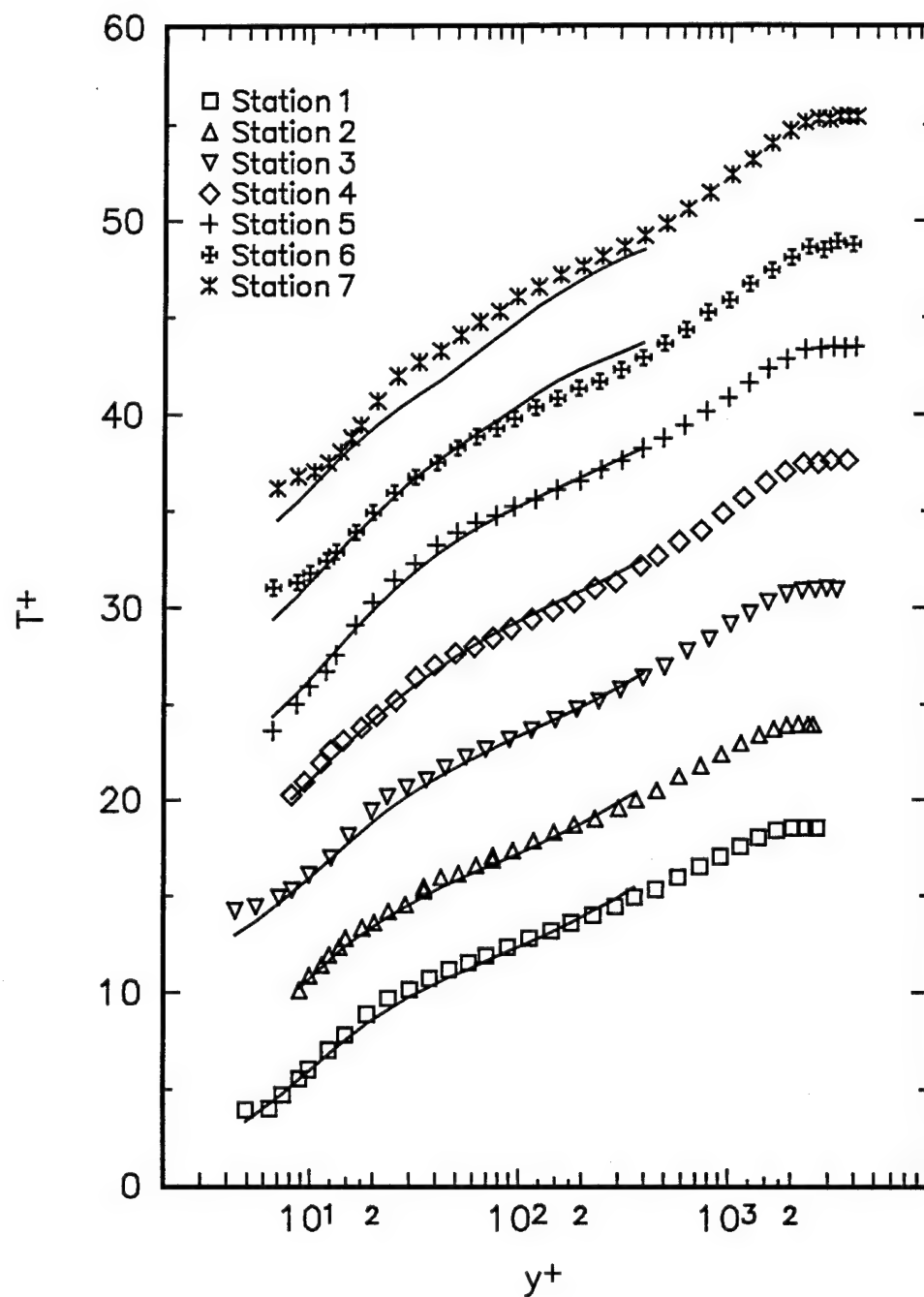


Figure 5.3. Mean temperature profiles at each station in the three-dimensional turbulent boundary layer calculated from the eddy viscosities of Fig. 5.2. Solid lines are from calculation. Symbols are data from Fig. 5.1.

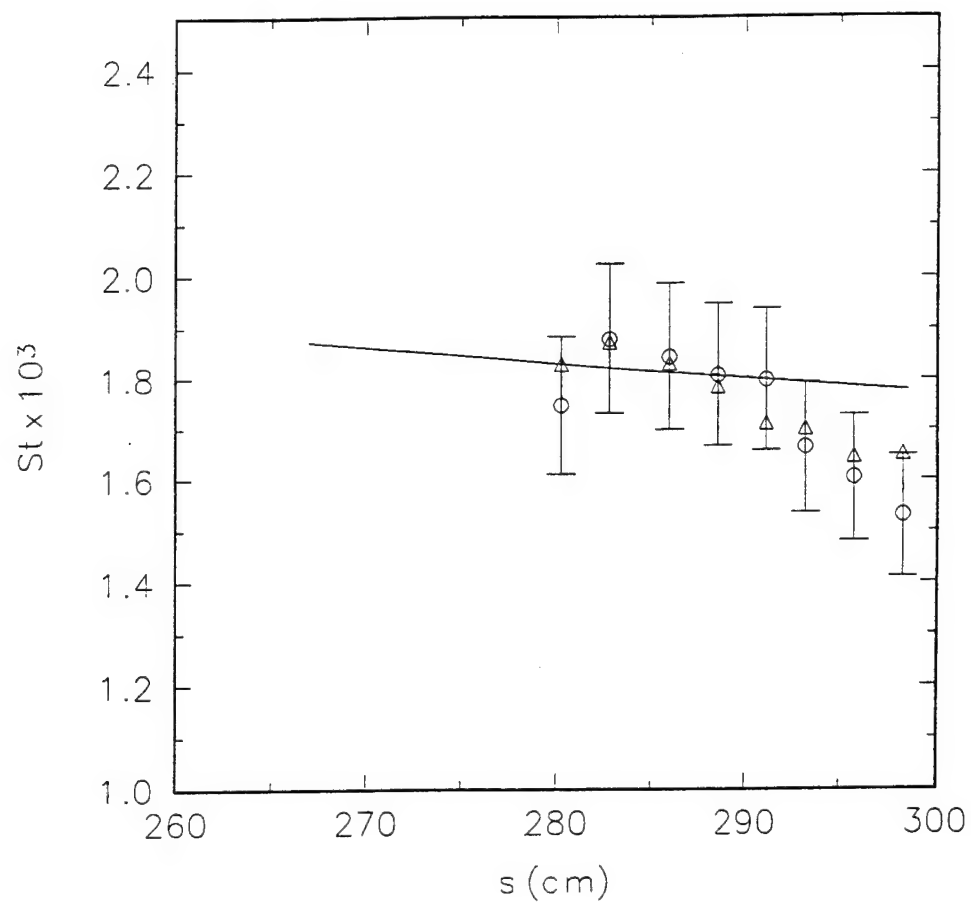


Figure 5.4. Stanton number distribution in 3-D boundary layer. O - measured St with uncertainty bars; Δ - calculated from enthalpy thickness vector magnitude and Eq. (5.14); — Eq. (3.11); --- Eq. (5.16) (indistinguishable from solid line).

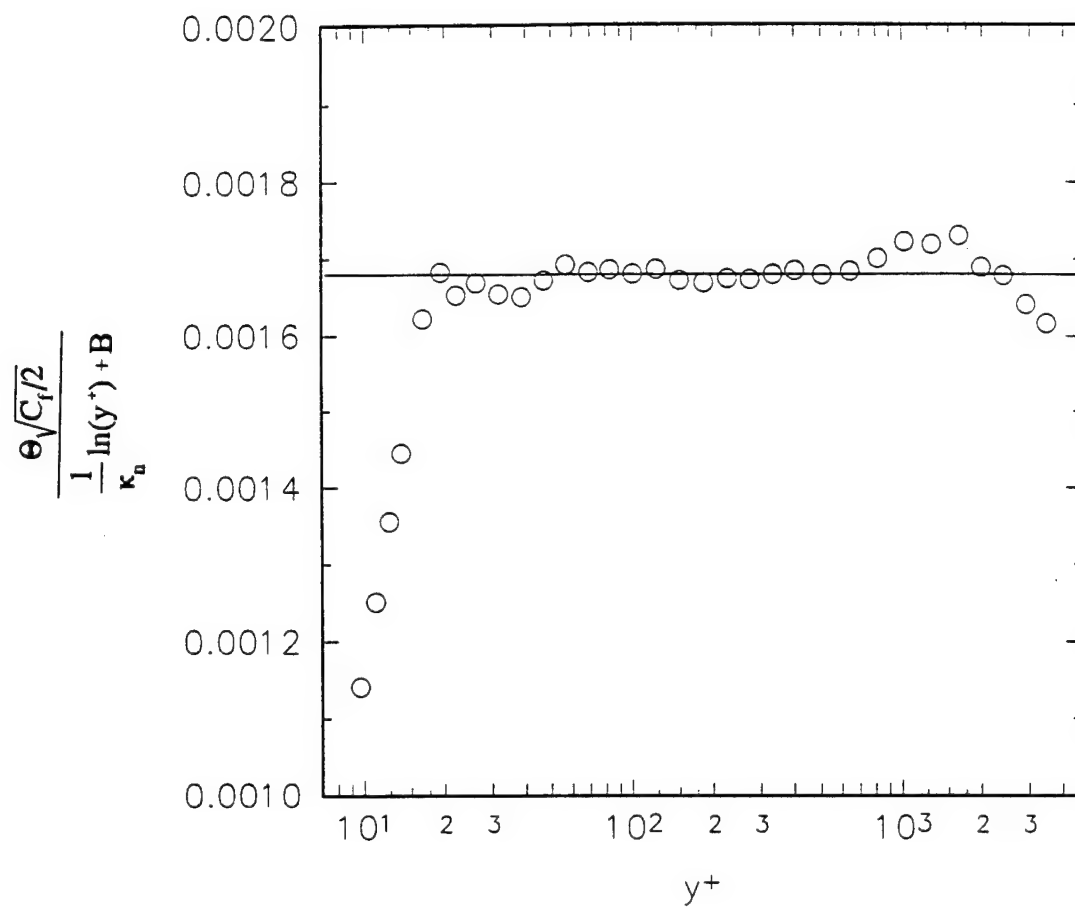


Figure 5.5. Stanton number determined from mean temperature profile at station #0.

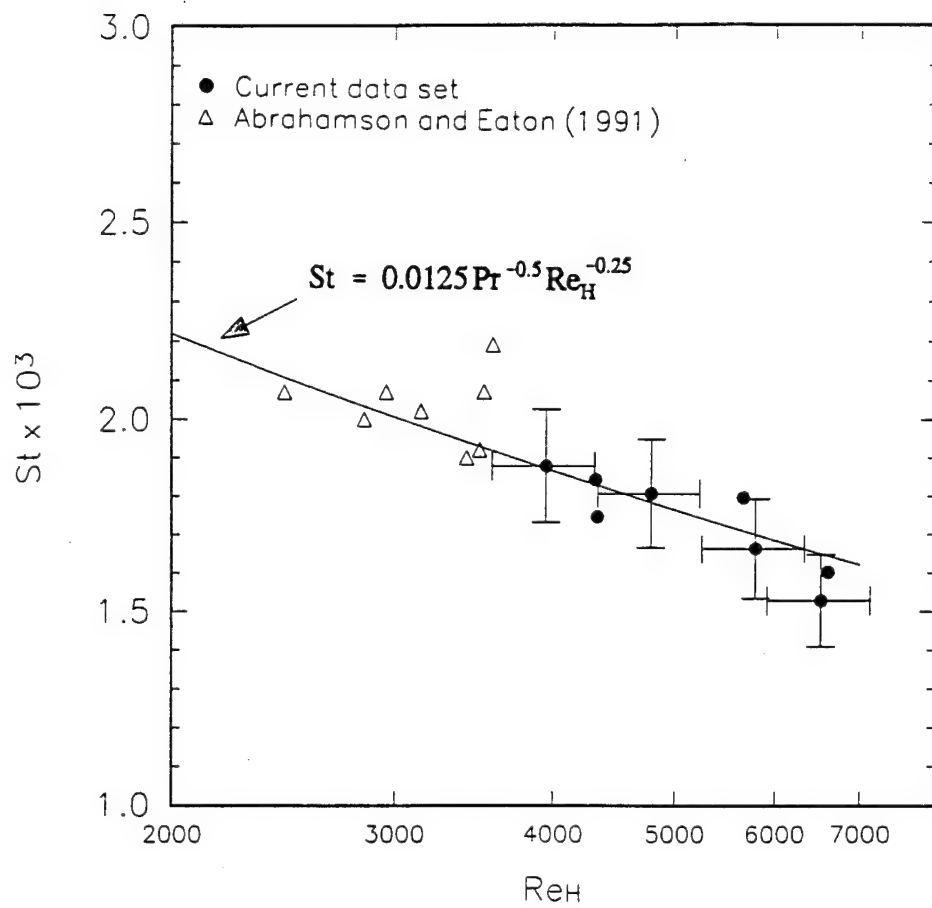


Figure 5.6. Correlation between surface heat transfer and magnitude of enthalpy thickness vector in 3-D Turbulent boundary layer.

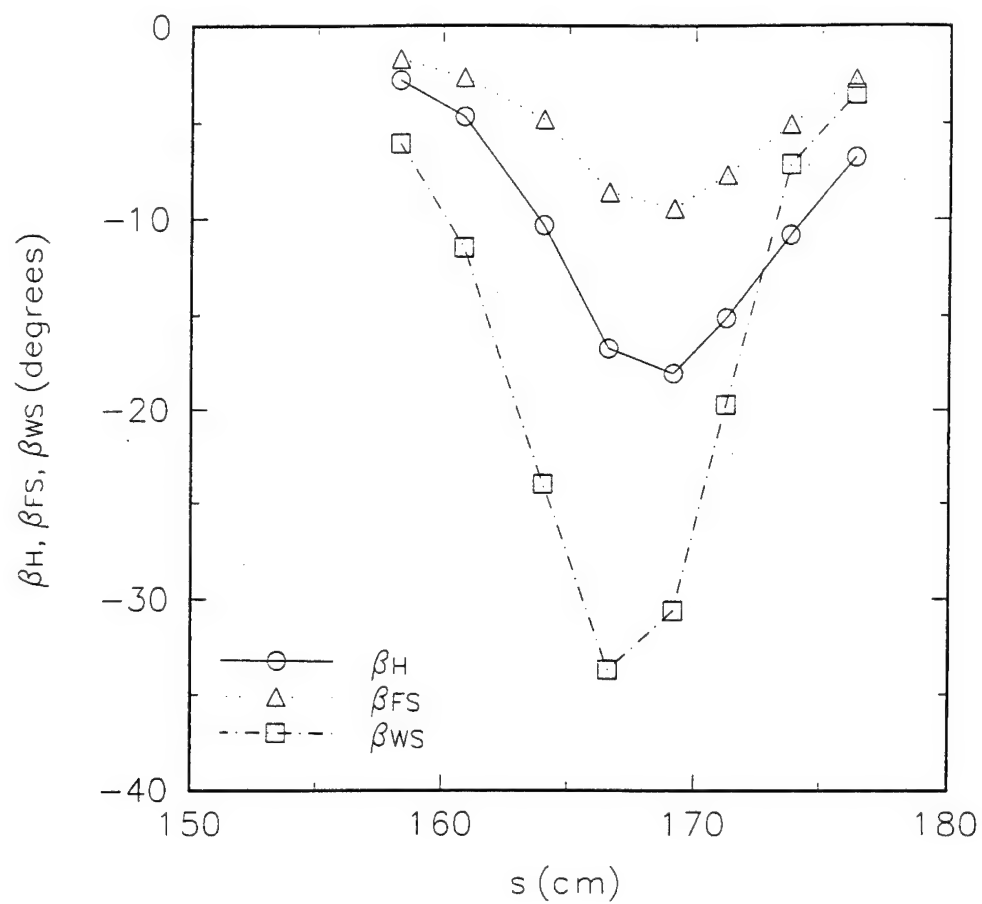


Figure 5.7. Direction of enthalpy thickness vector compared to free-stream and wall-shear-stress directions relative to tunnel coordinate system at stations 0 - 7.

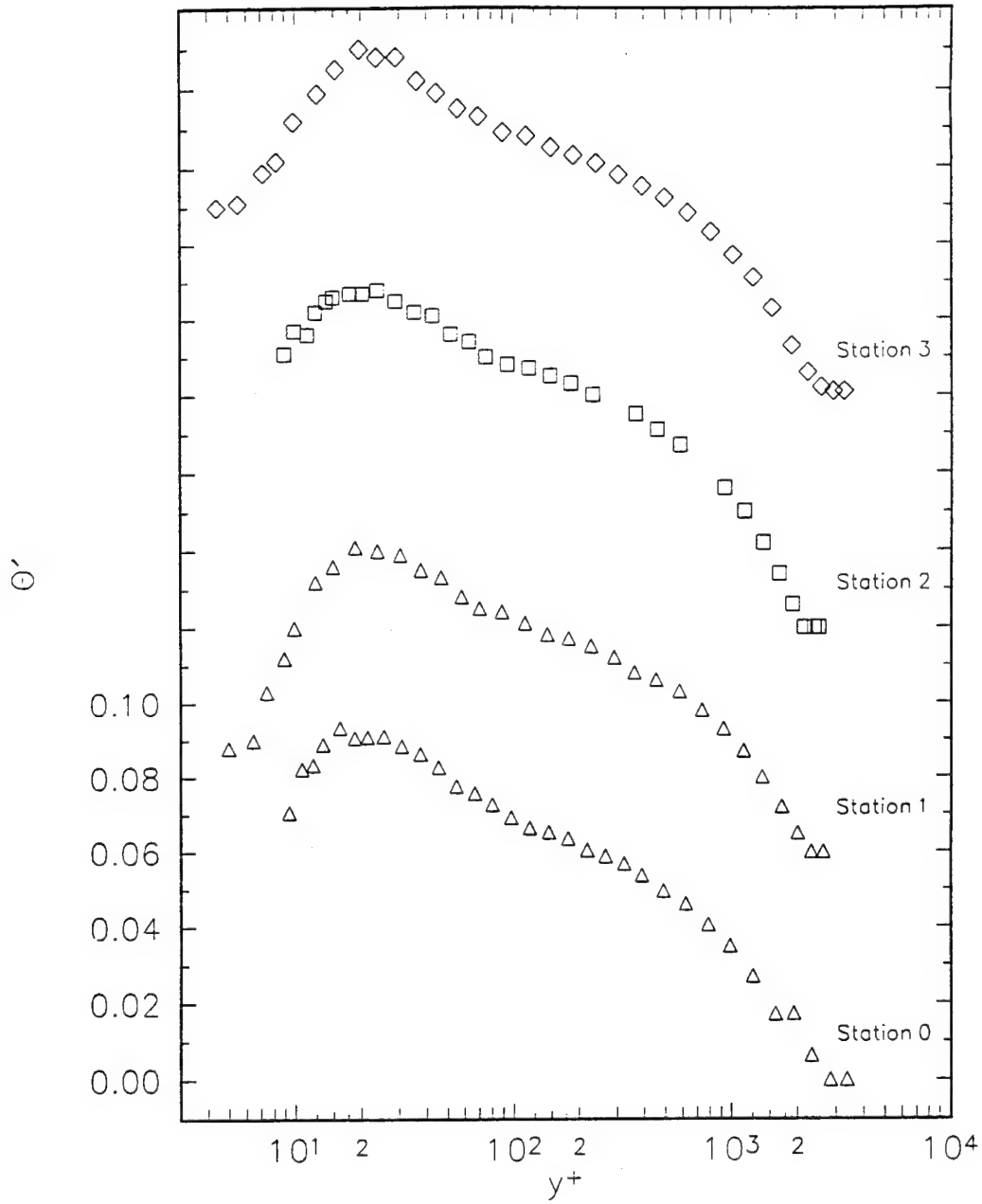


Figure 5.8a. Temperature fluctuation profiles at each station in the 3D TBL. Y-axis scale applies to the profile at station 0. Remaining profiles are offset successively by 0.06.

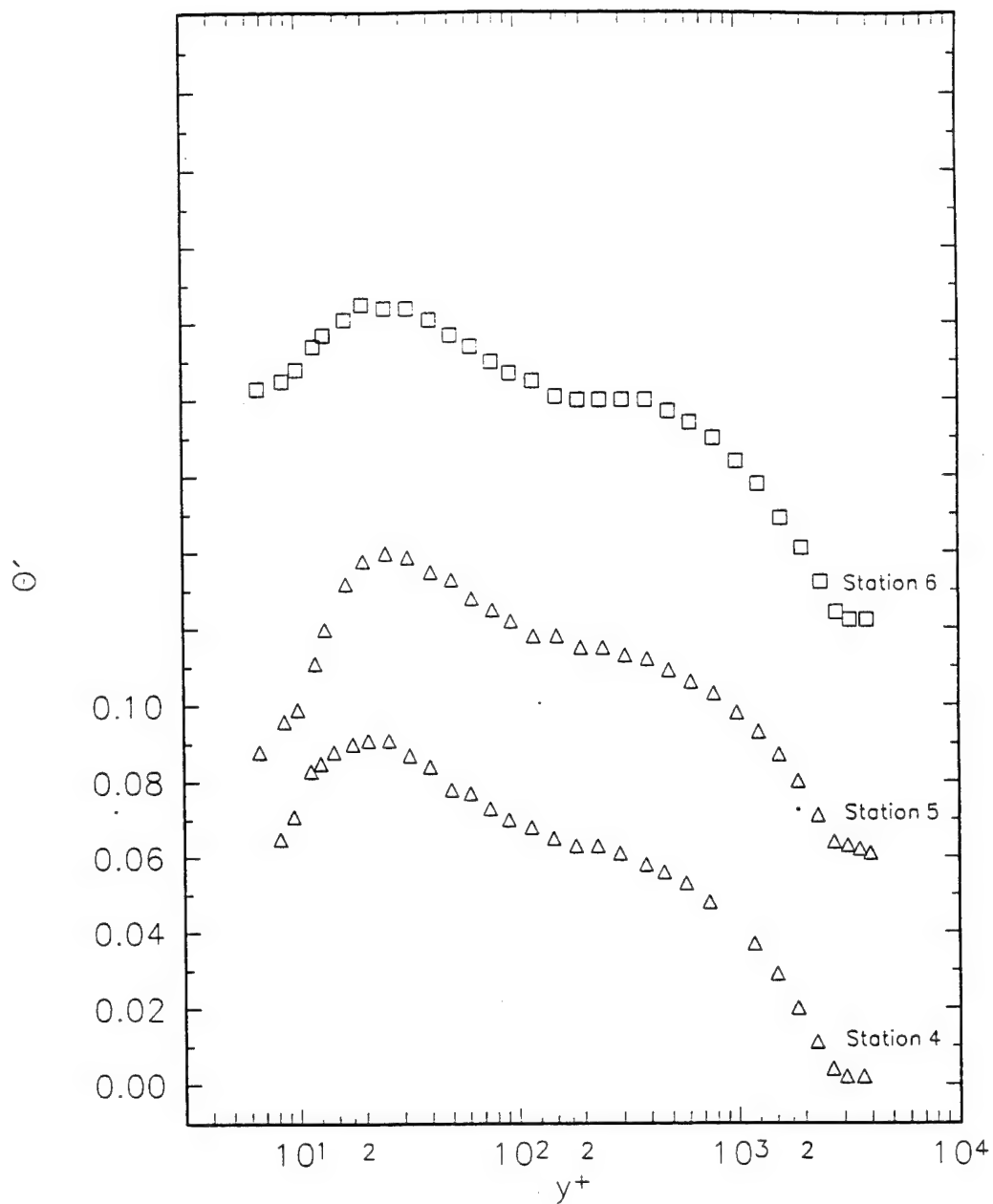


Figure 5.8b. Temperature fluctuation profiles at each station in the 3D TBL. Y-axis scale applies to the profile at station 4. Remaining profiles are offset successively by 0.06.

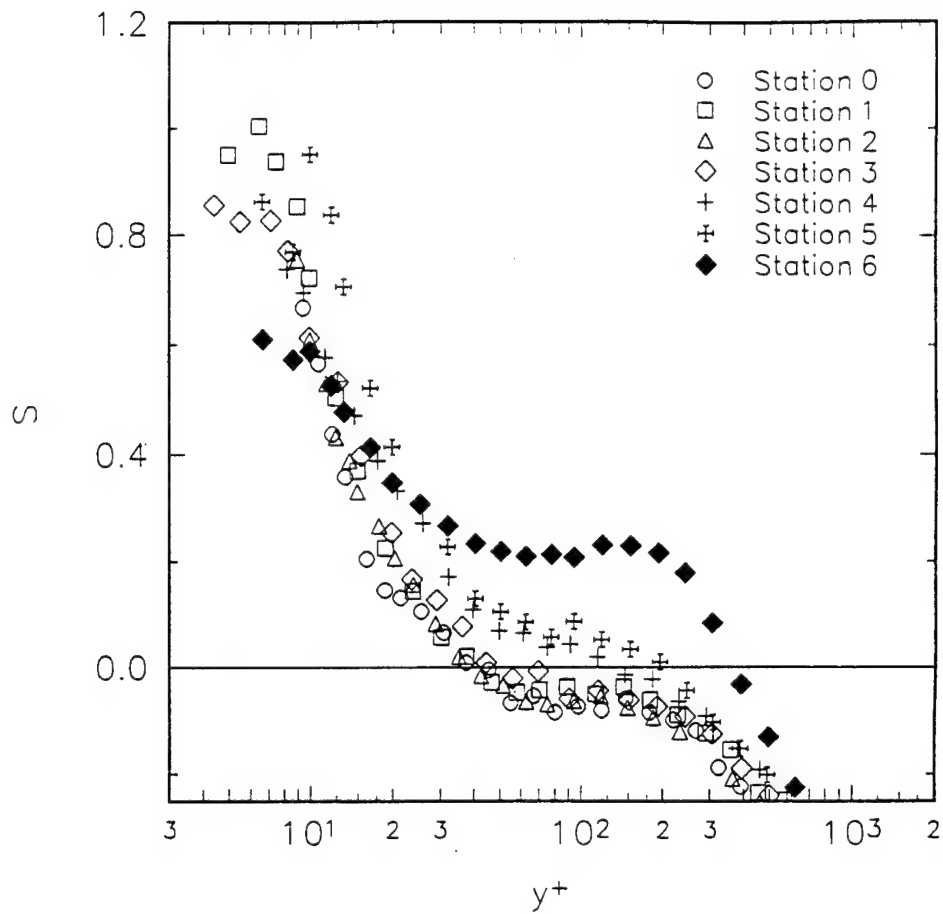


Figure 5.9. Profiles of the skewness factor of temperature fluctuations at stations #0 - #6 in the 3D turbulent boundary layer.

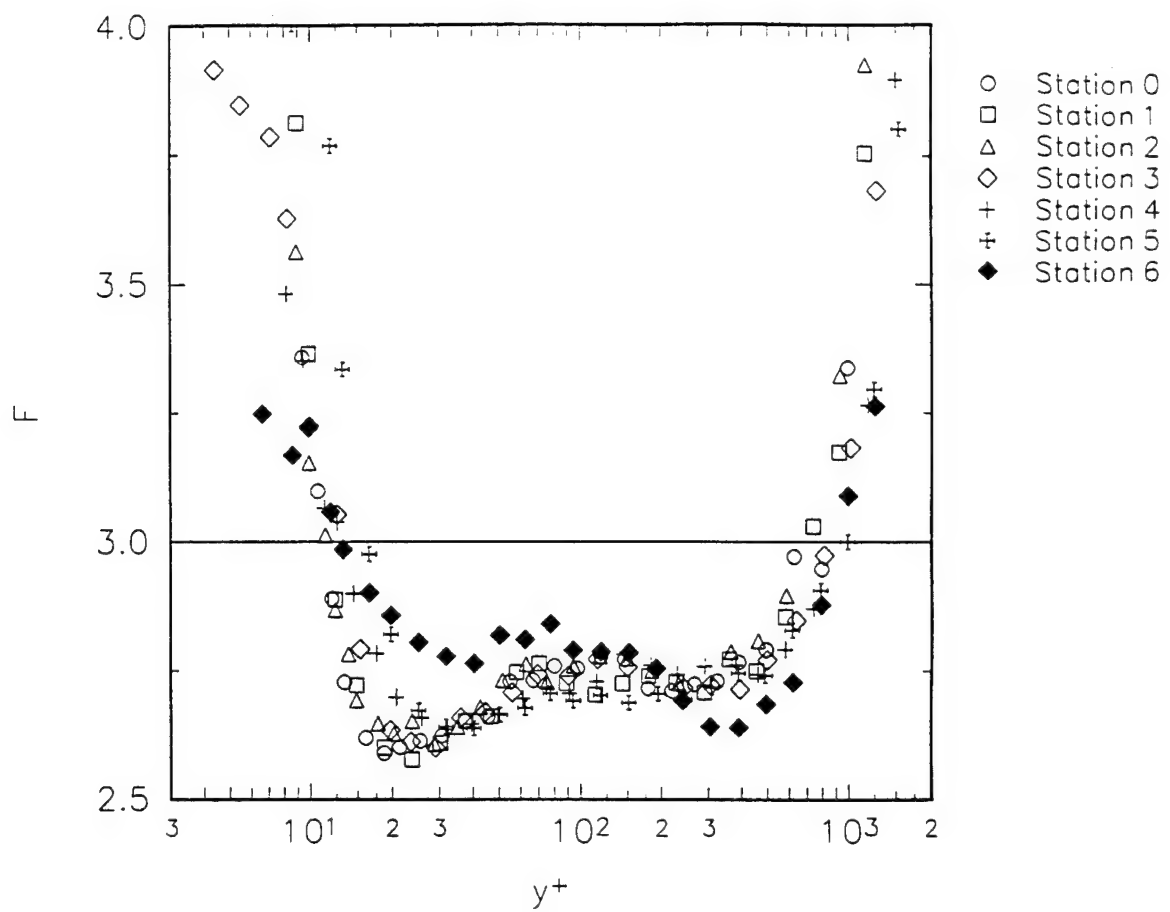


Figure 5.10. Profiles of the flatness factor of temperature fluctuations at stations #0 - #6 in the 3D turbulent boundary layer.

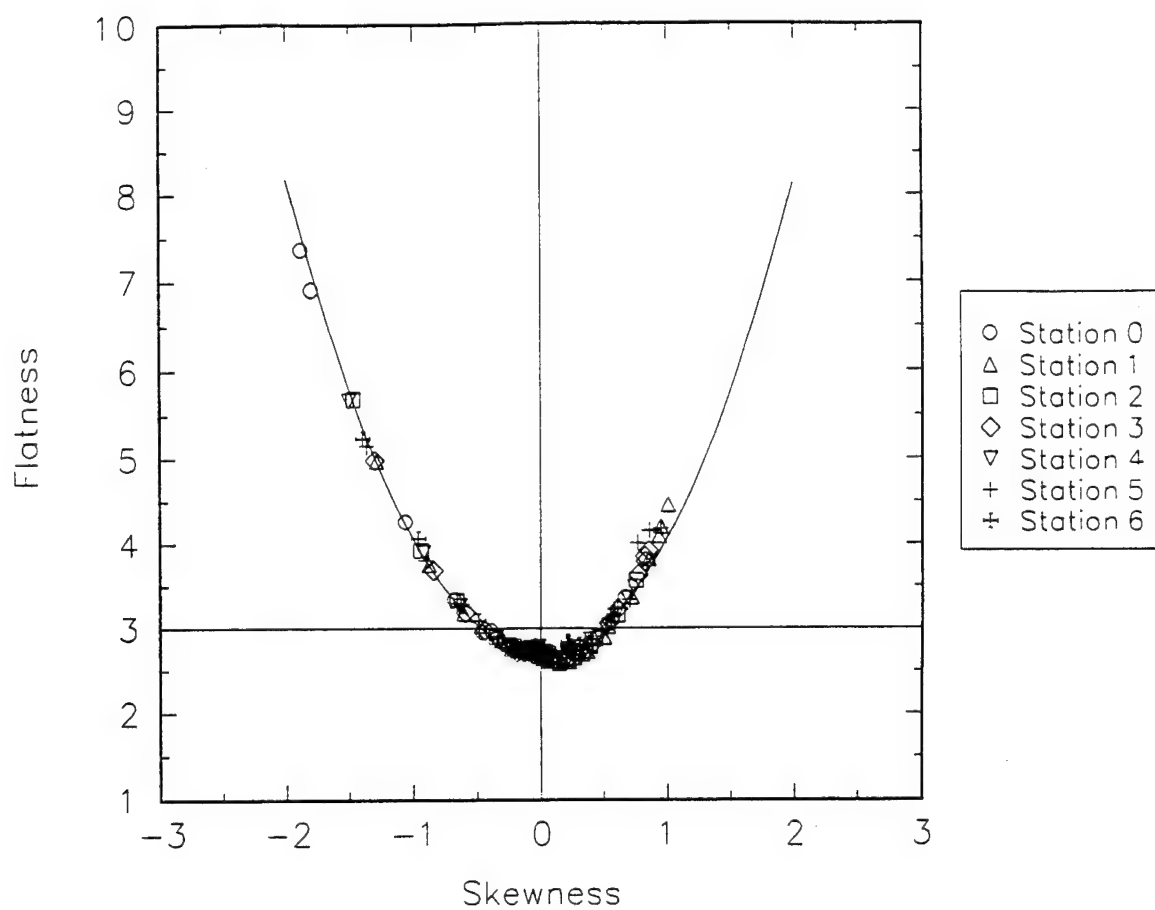


Figure 5.11. Plot of flatness factor as a function of skewness factor of temperature fluctuations at stations 0 - 6 in the 3D TBL. Solid line is parabola fit to data.

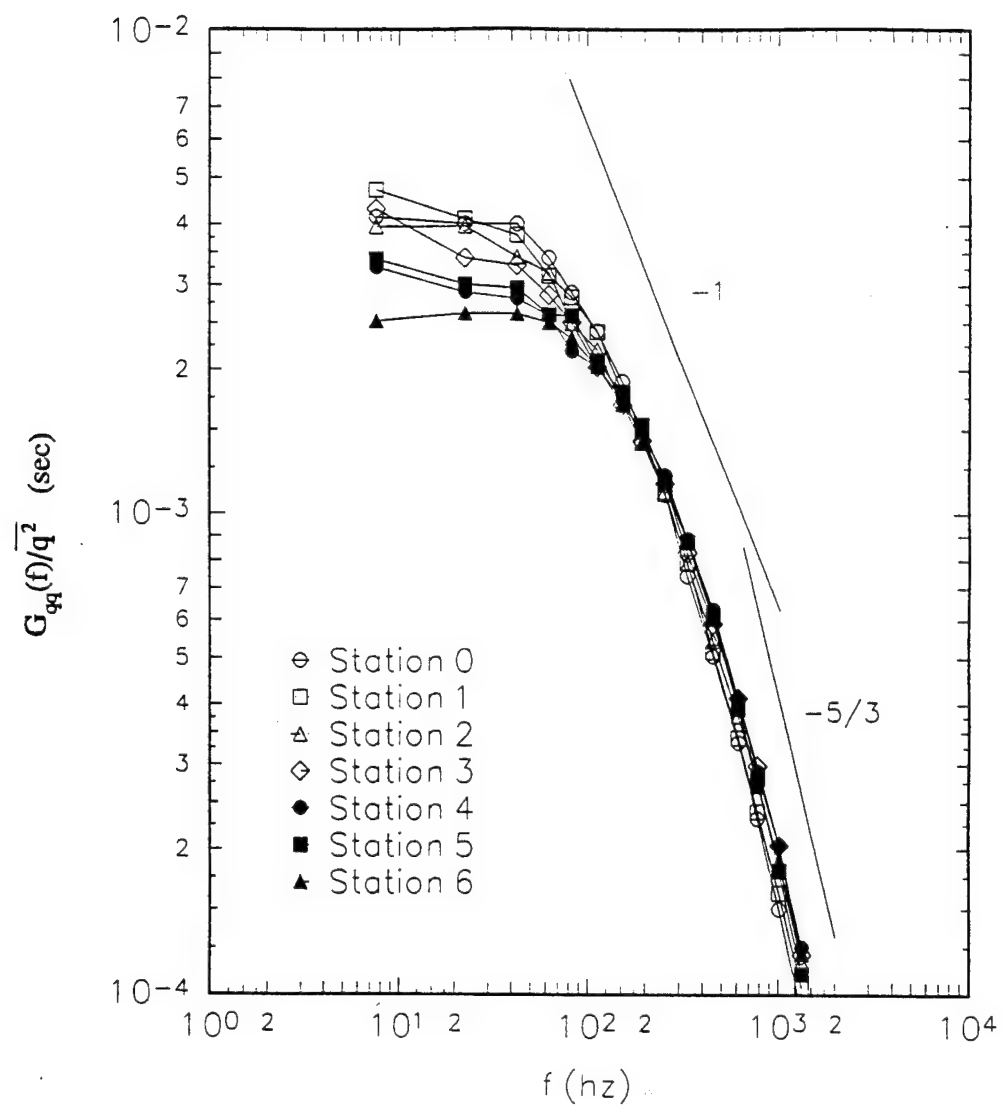


Figure 5.12. Power spectra of surface heat flux fluctuations measured at stations 0 - 6 in the 3D TBL.

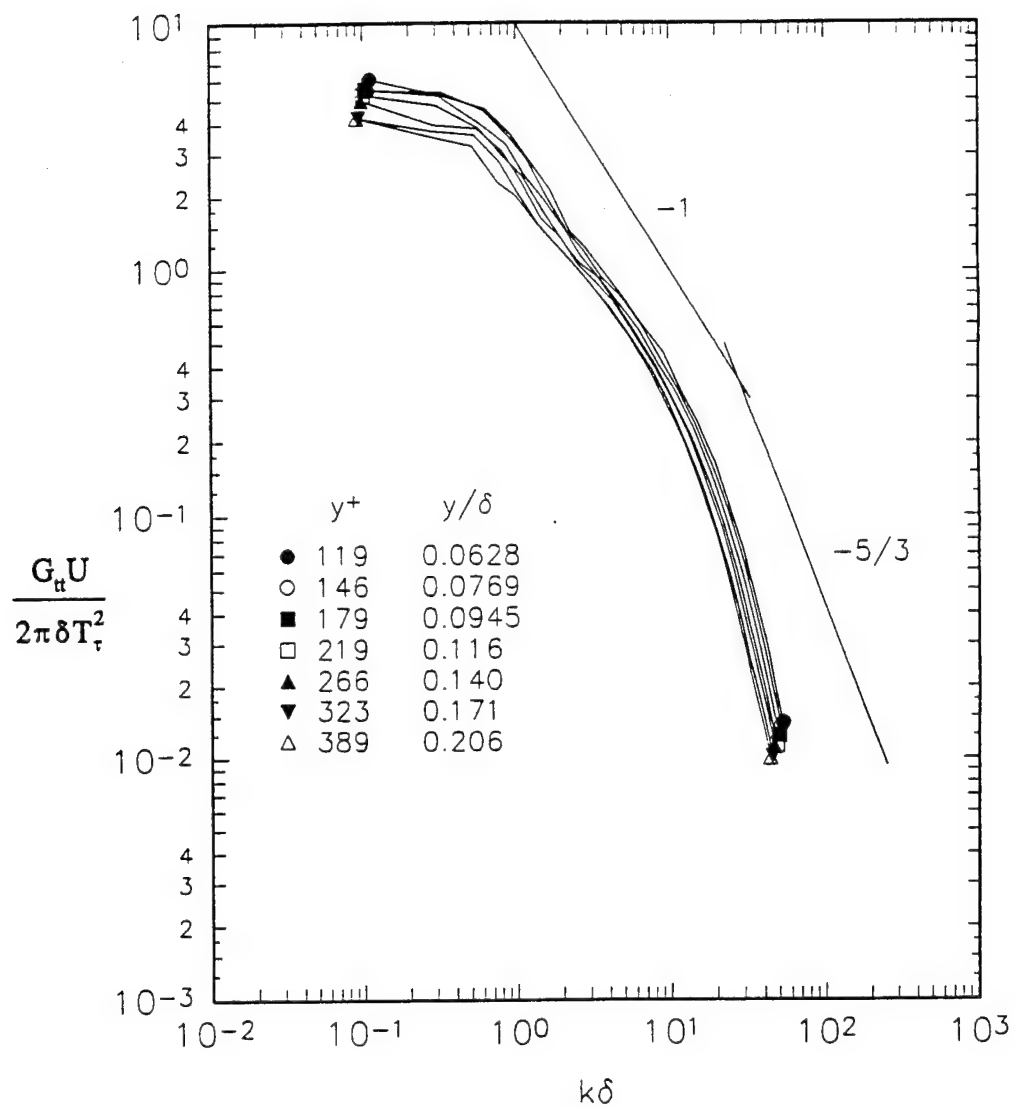


Figure 5.13a. Temperature spectra measured in the wall-region of station 0 normalized with outer scaling parameters.

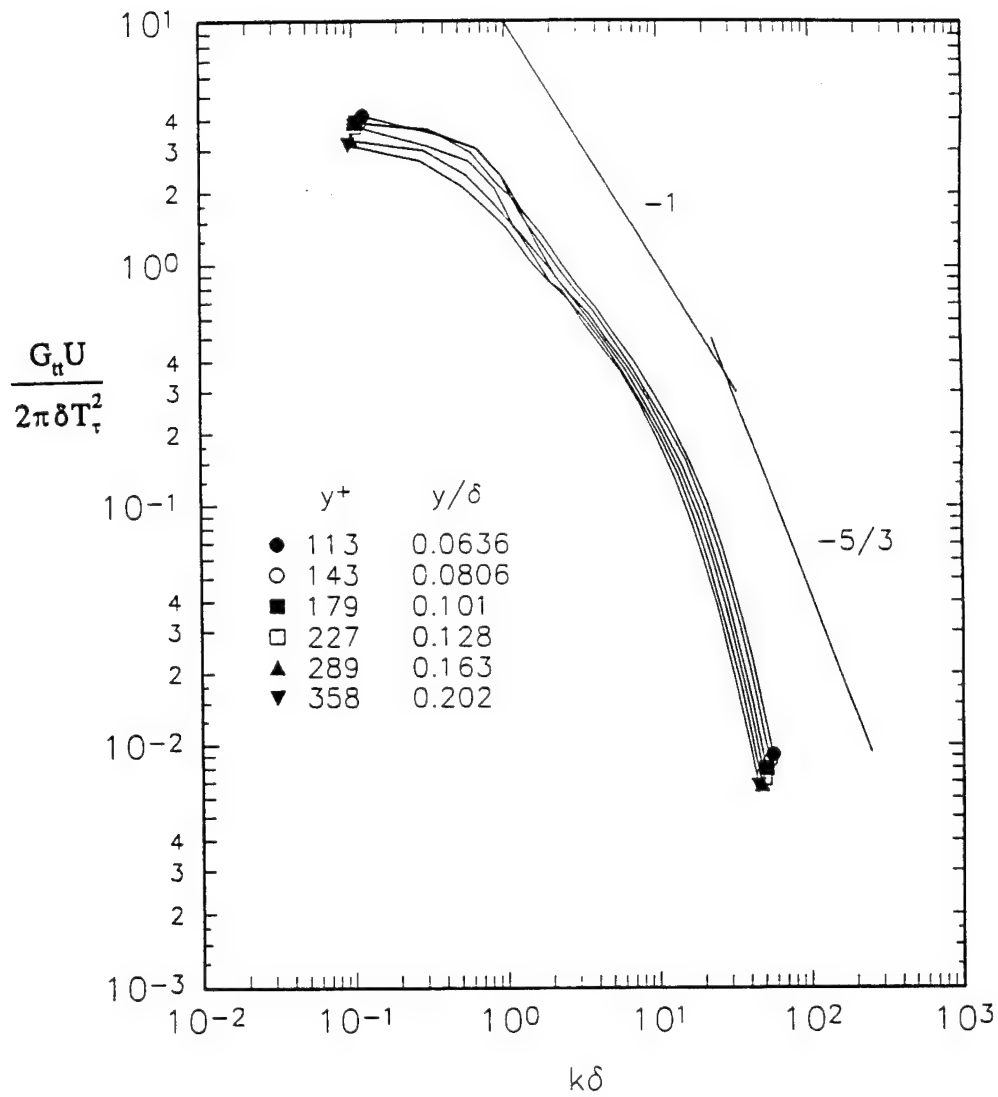


Figure 5.13b. Temperature spectra measured in the wall-region of station 1 normalized with outer scaling parameters.

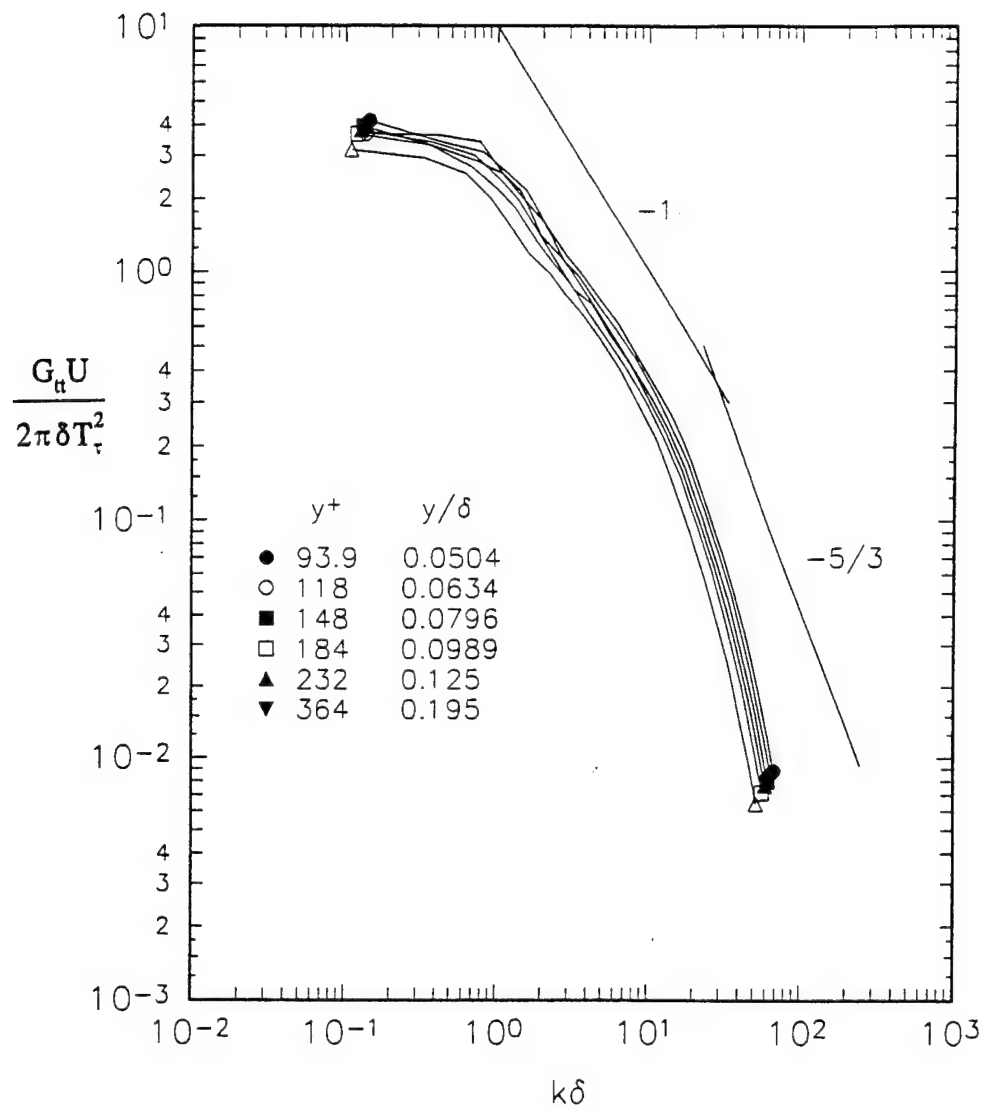


Figure 5.13c. Temperature spectra measured in the wall-region of station 2 normalized with outer scaling parameters.

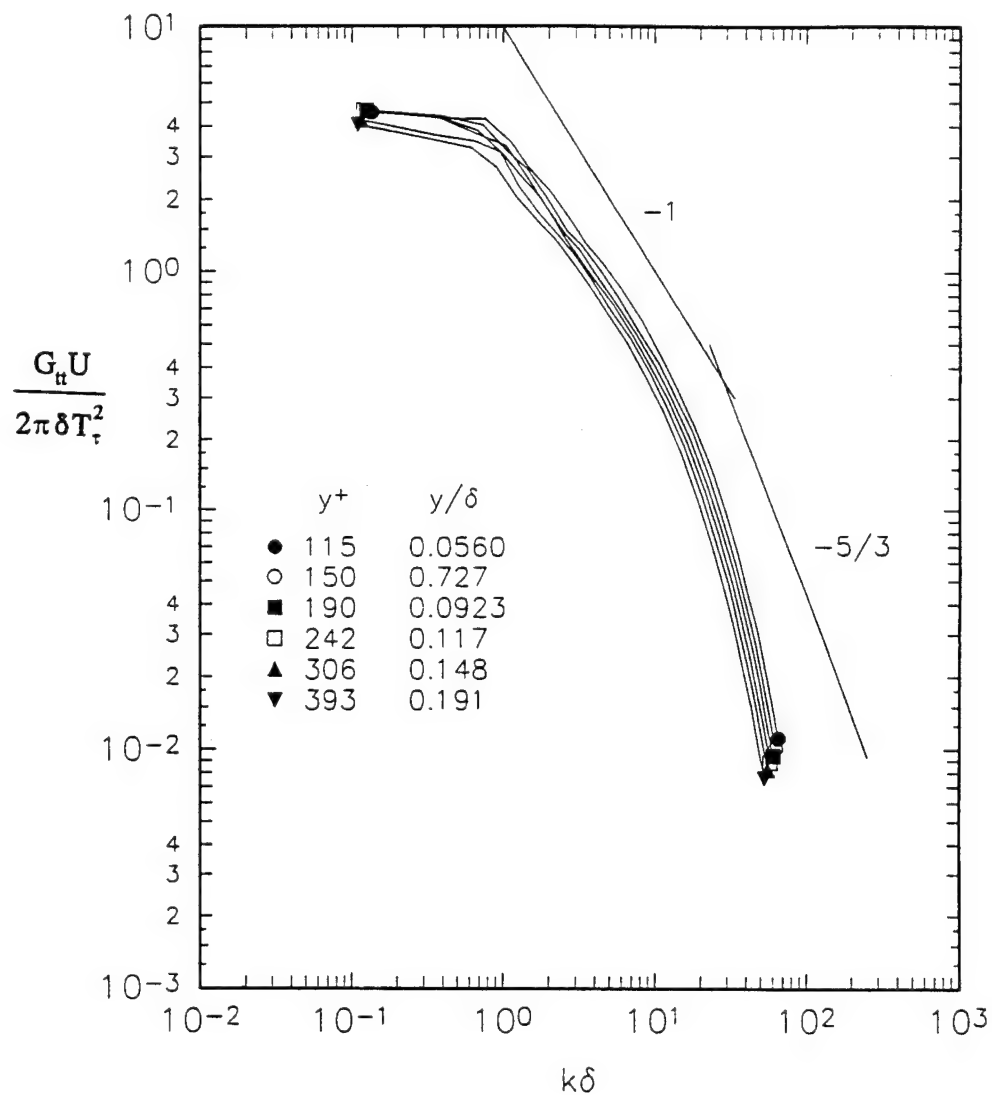


Figure 5.13d. Temperature spectra measured in the wall-region of station 3 normalized with outer scaling parameters.

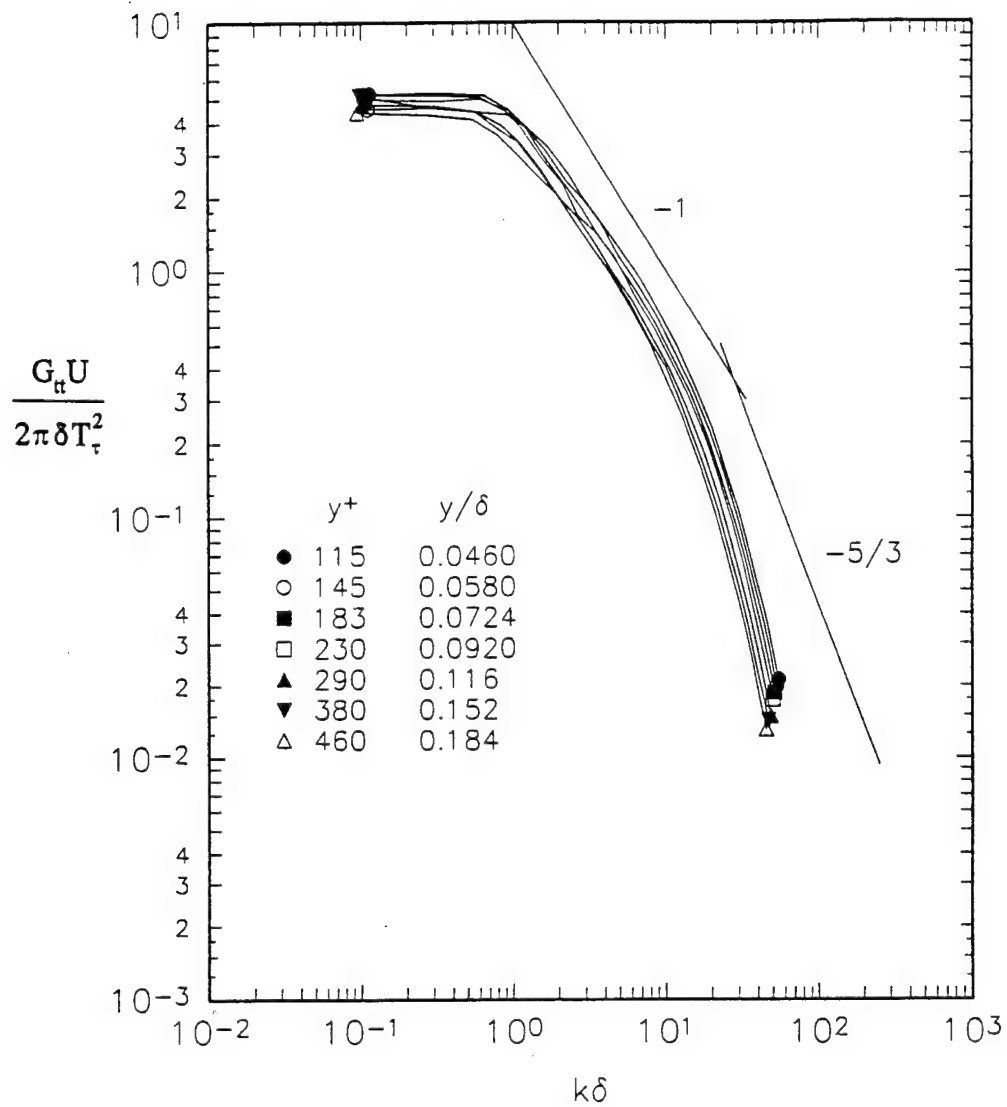


Figure 5.13e. Temperature spectra measured in the wall-region of station 4 normalized with outer scaling parameters.

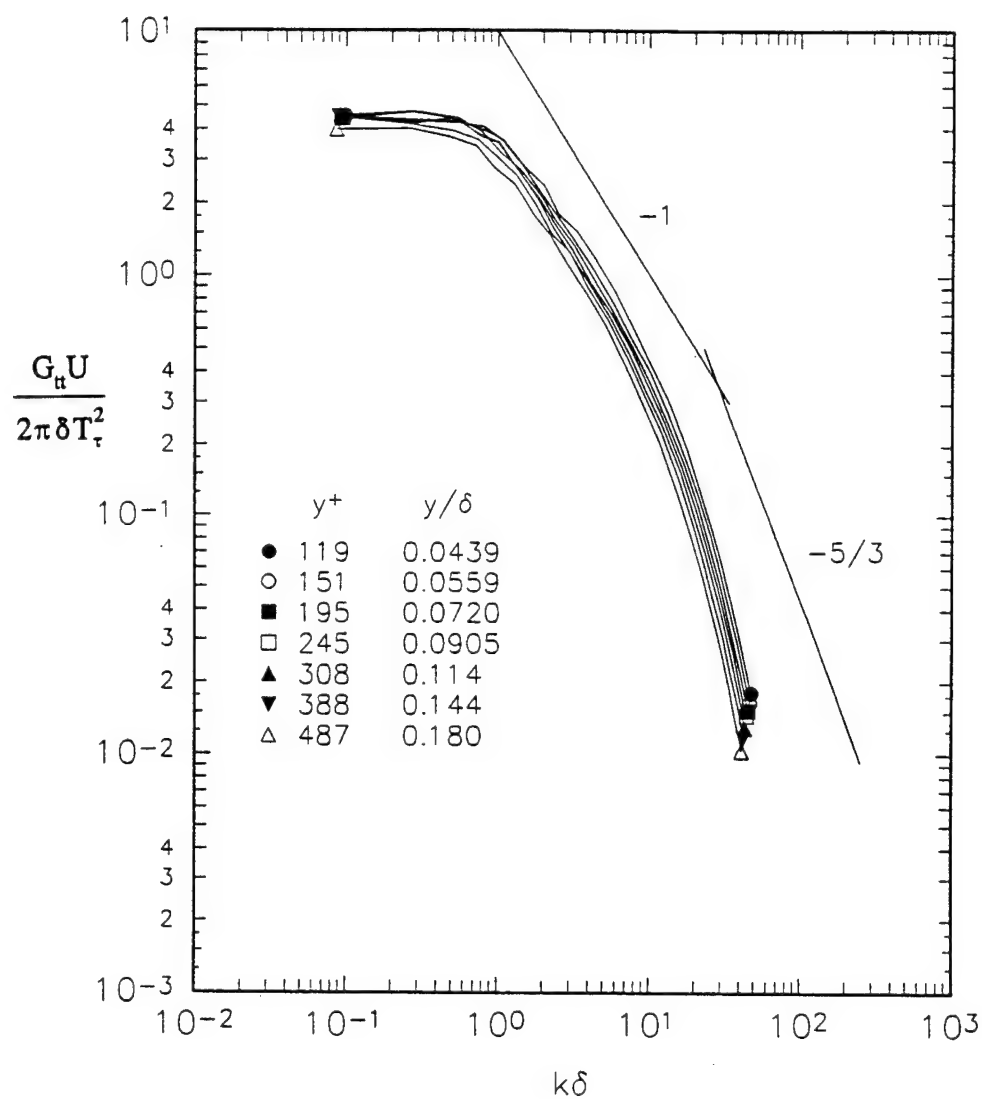


Figure 5.13f. Temperature spectra measured in the wall-region of station 5 normalized with outer scaling parameters.

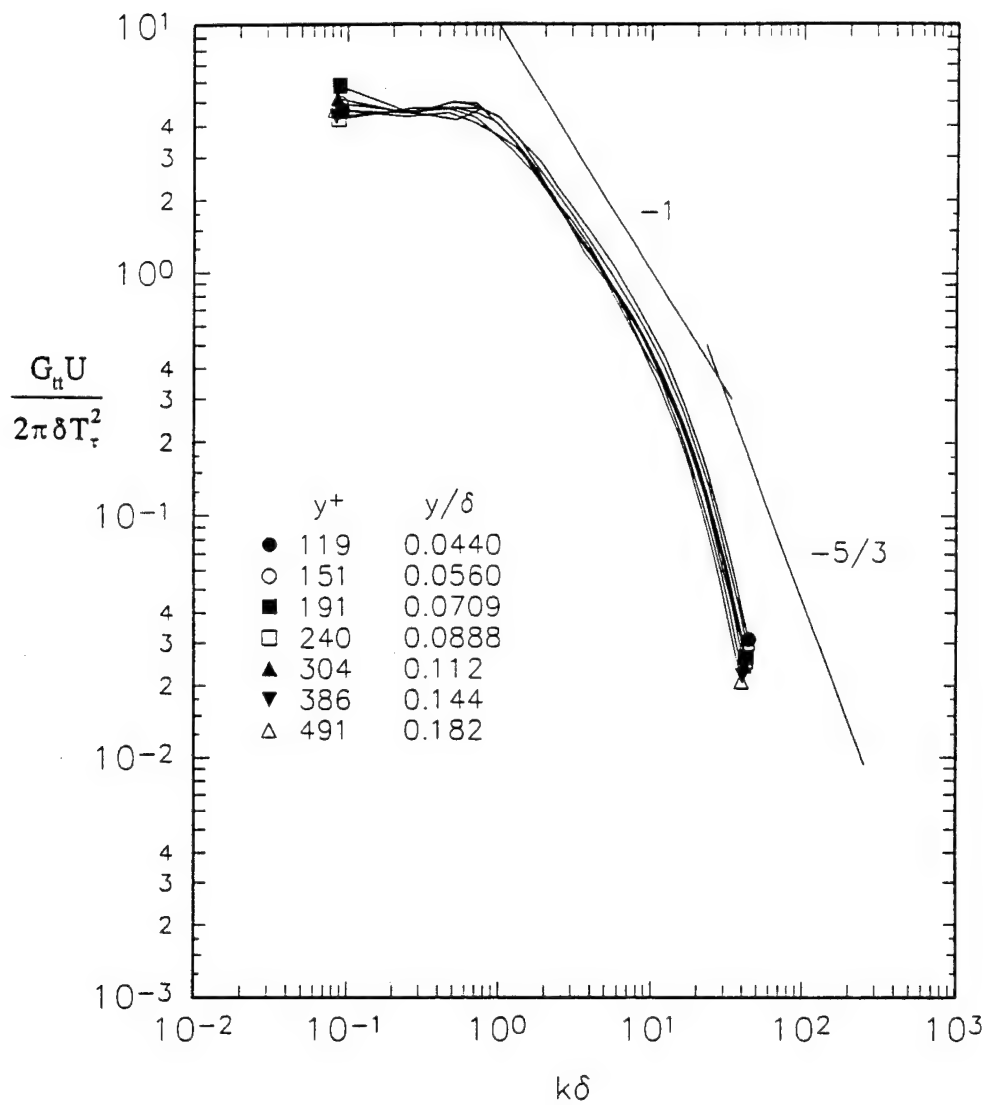


Figure 5.13g. Temperature spectra measured in the wall-region of station 6 normalized with outer scaling parameters.

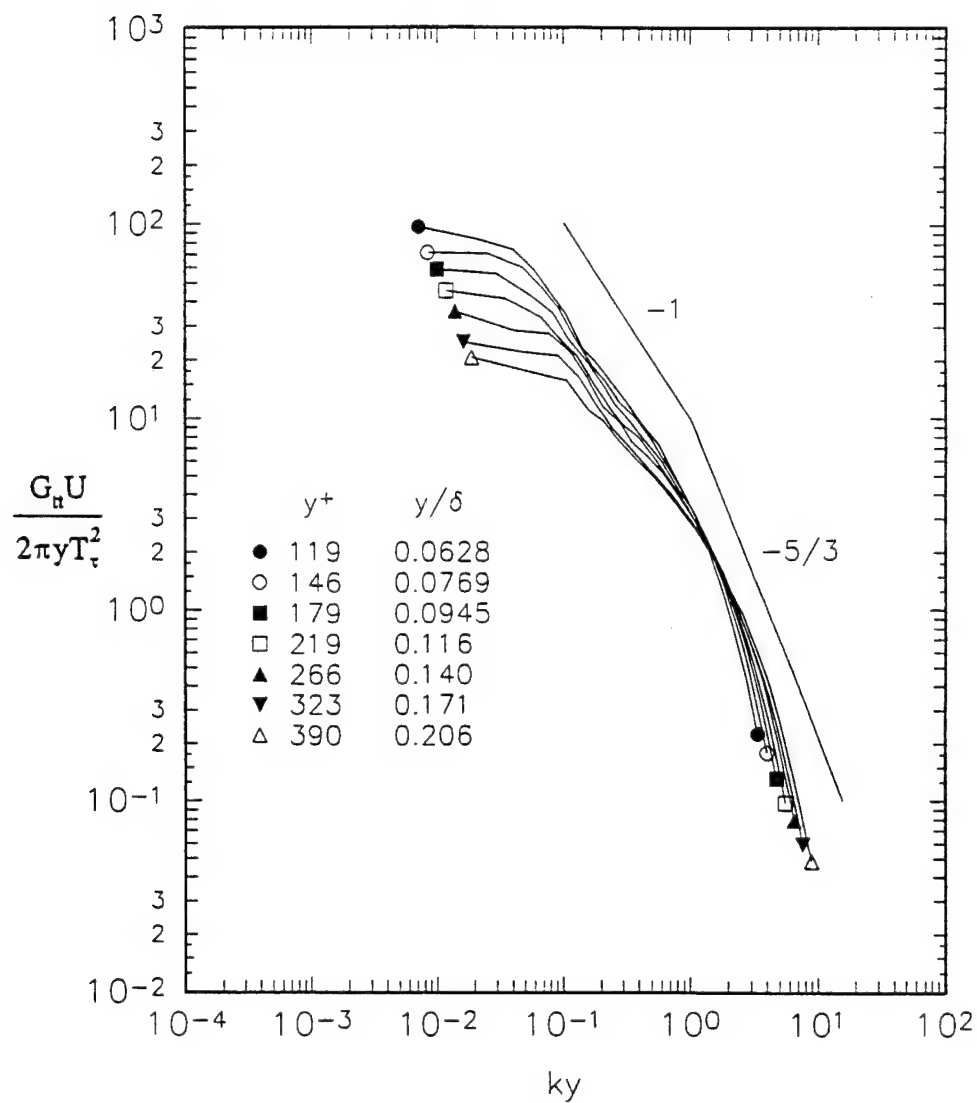


Figure 5.14a. Temperature spectra measured in the wall-region of station 0 normalized with inner scaling parameters.

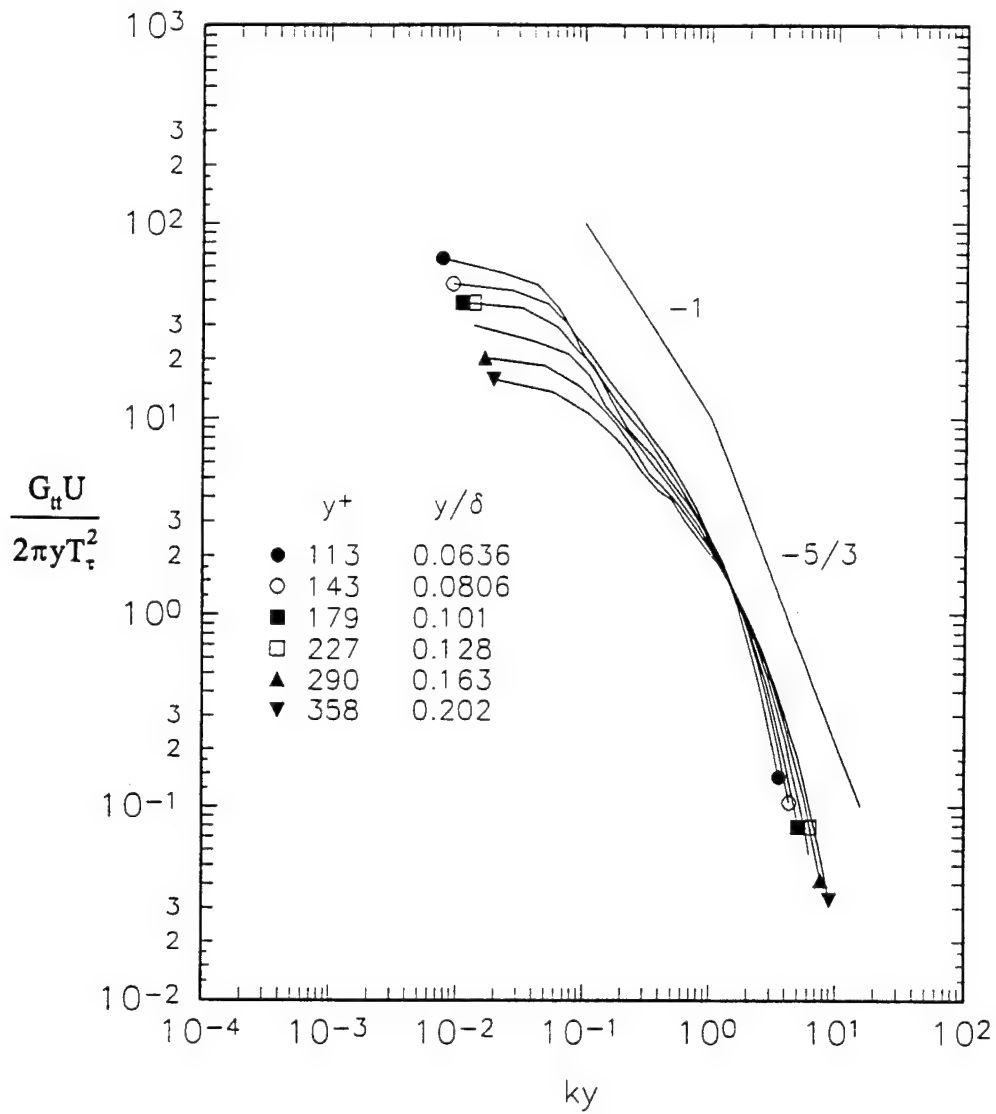


Figure 5.14b. Temperature spectra measured in the wall-region of station 1 normalized with inner scaling parameters.

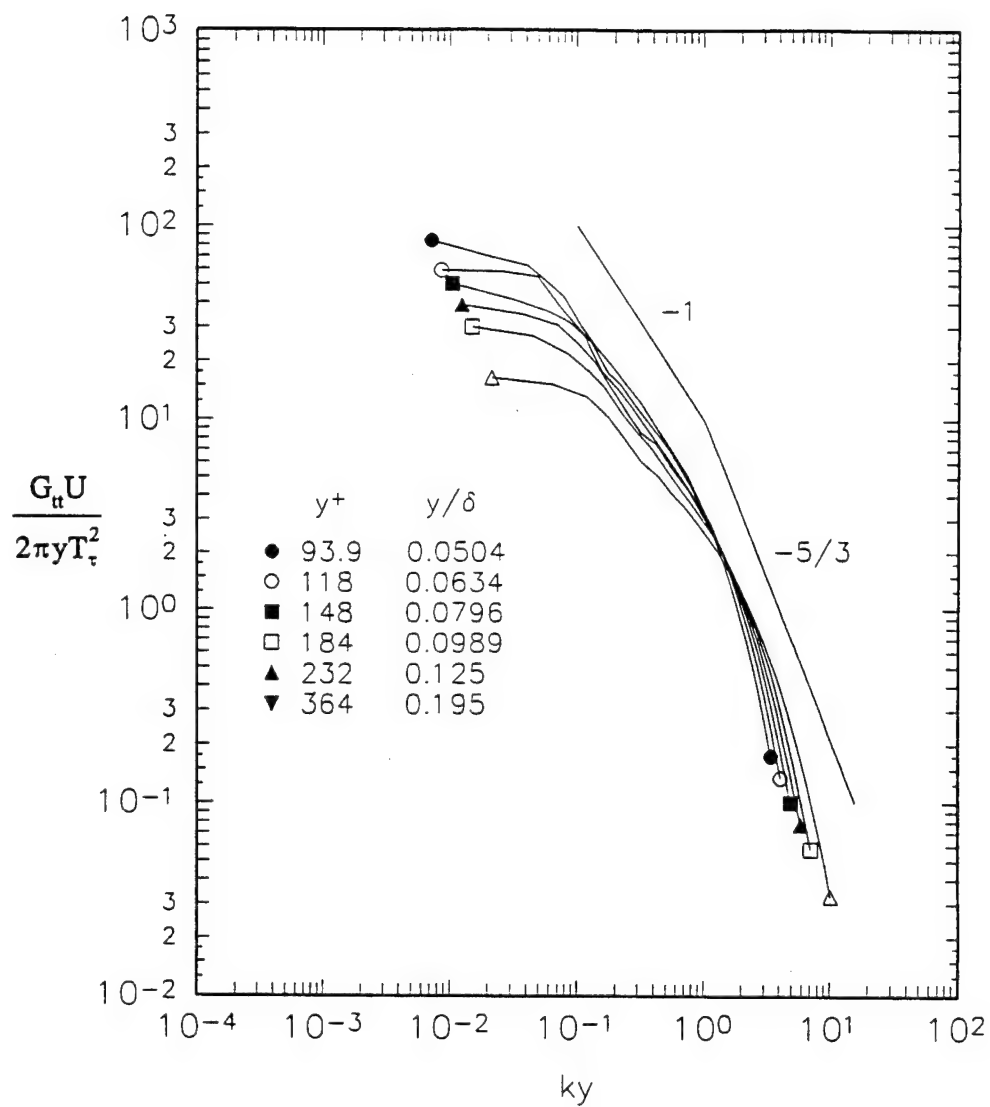


Figure 5.14c. Temperature spectra measured in the wall-region of station 2 normalized with inner scaling parameters.

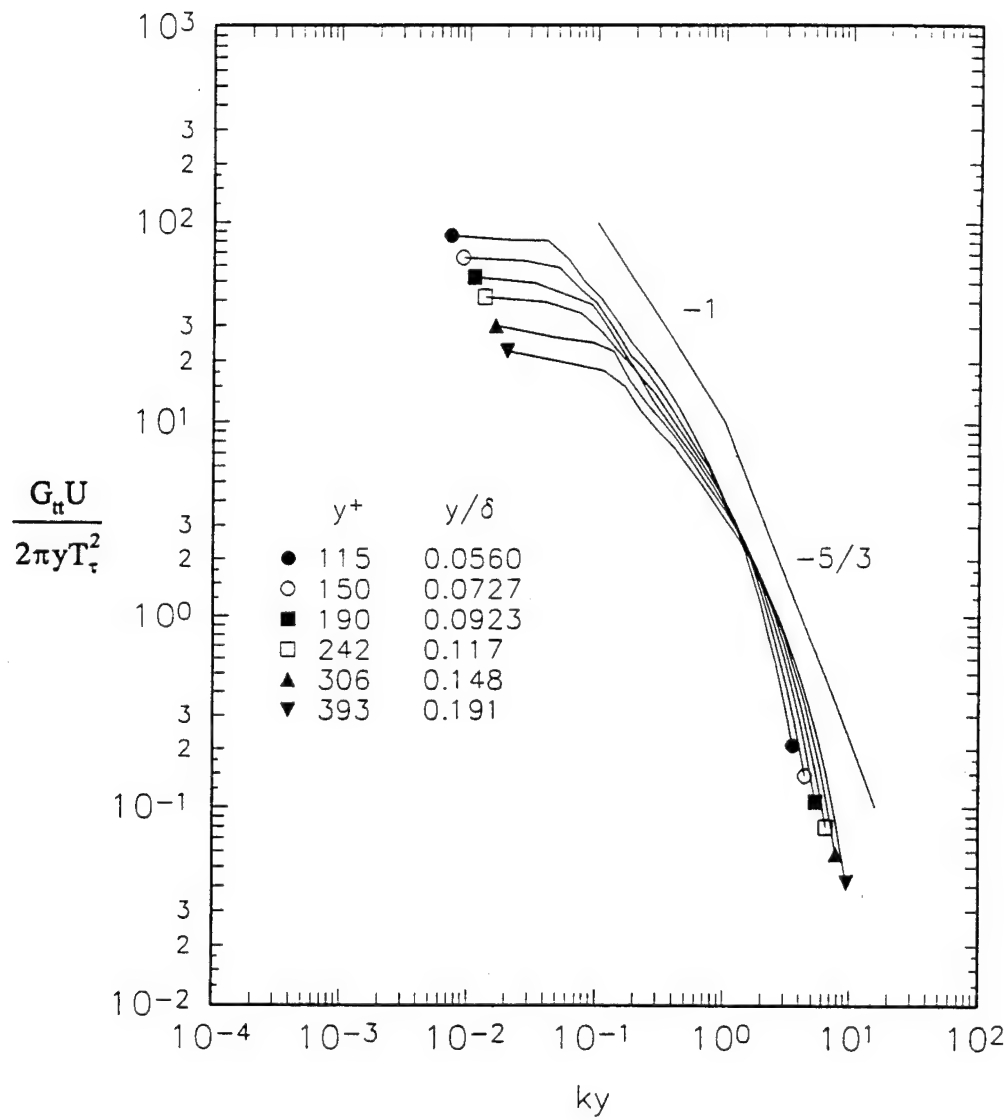


Figure 5.14d. Temperature spectra measured in the wall-region of station 3 normalized with inner scaling parameters.

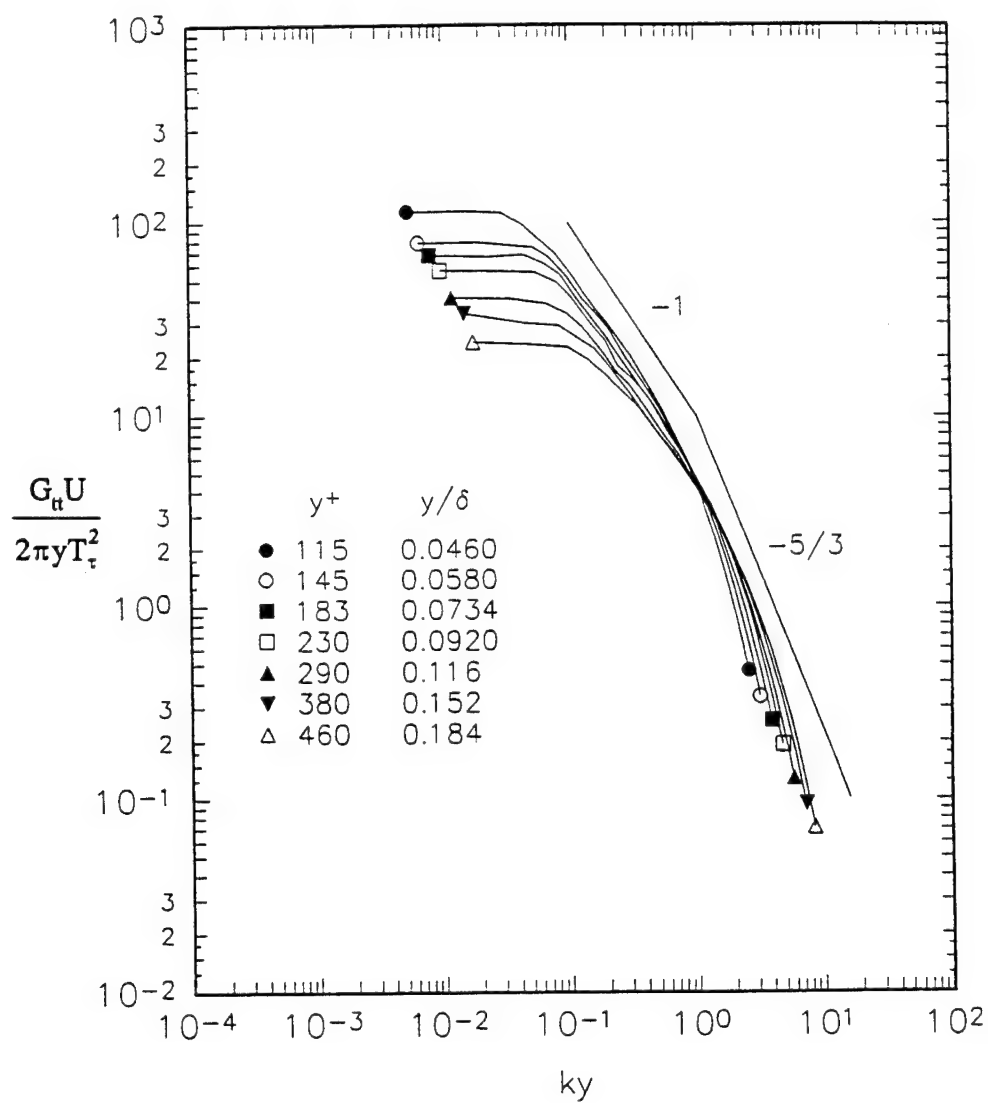


Figure 5.14e. Temperature spectra measured in the wall-region of station 4 normalized with inner scaling parameters.

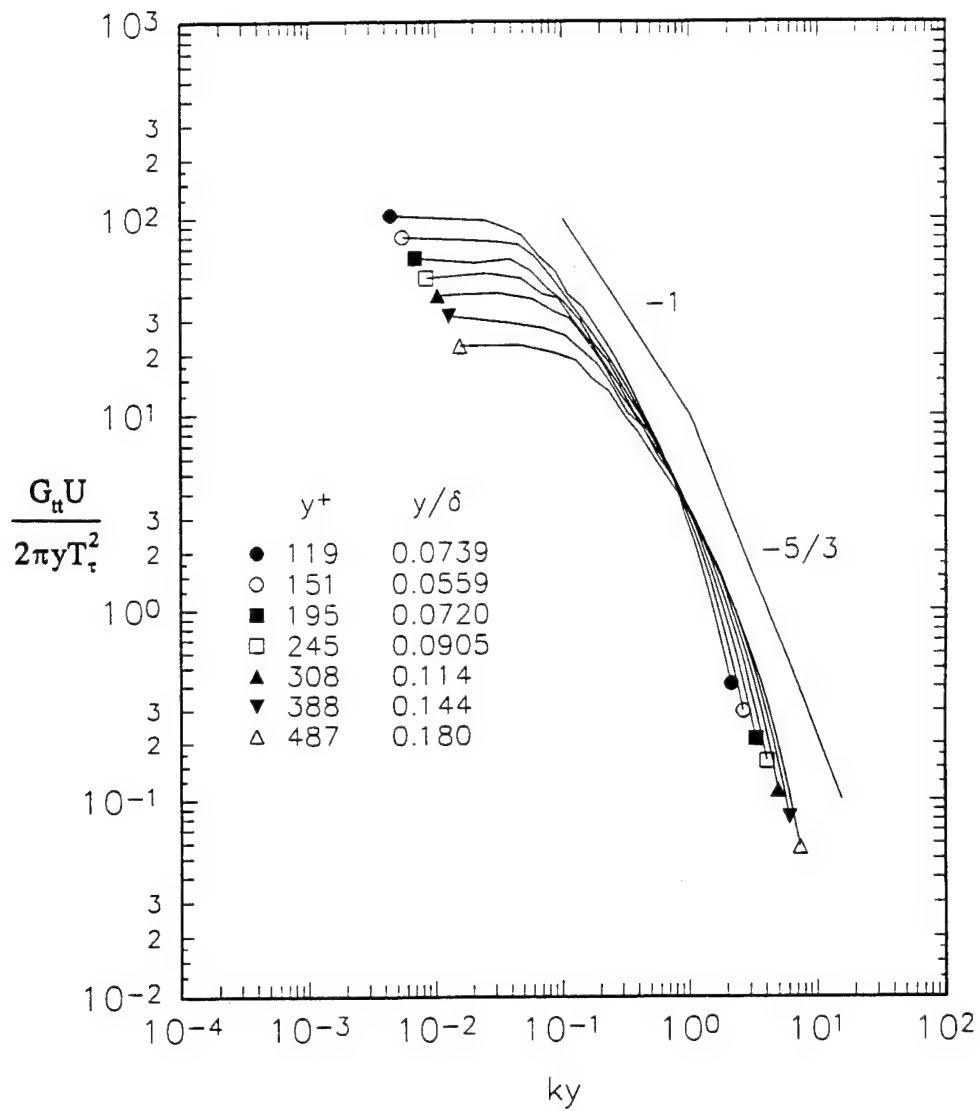


Figure 5.14f. Temperature spectra measured in the wall-region of station 5 normalized with inner scaling parameters.

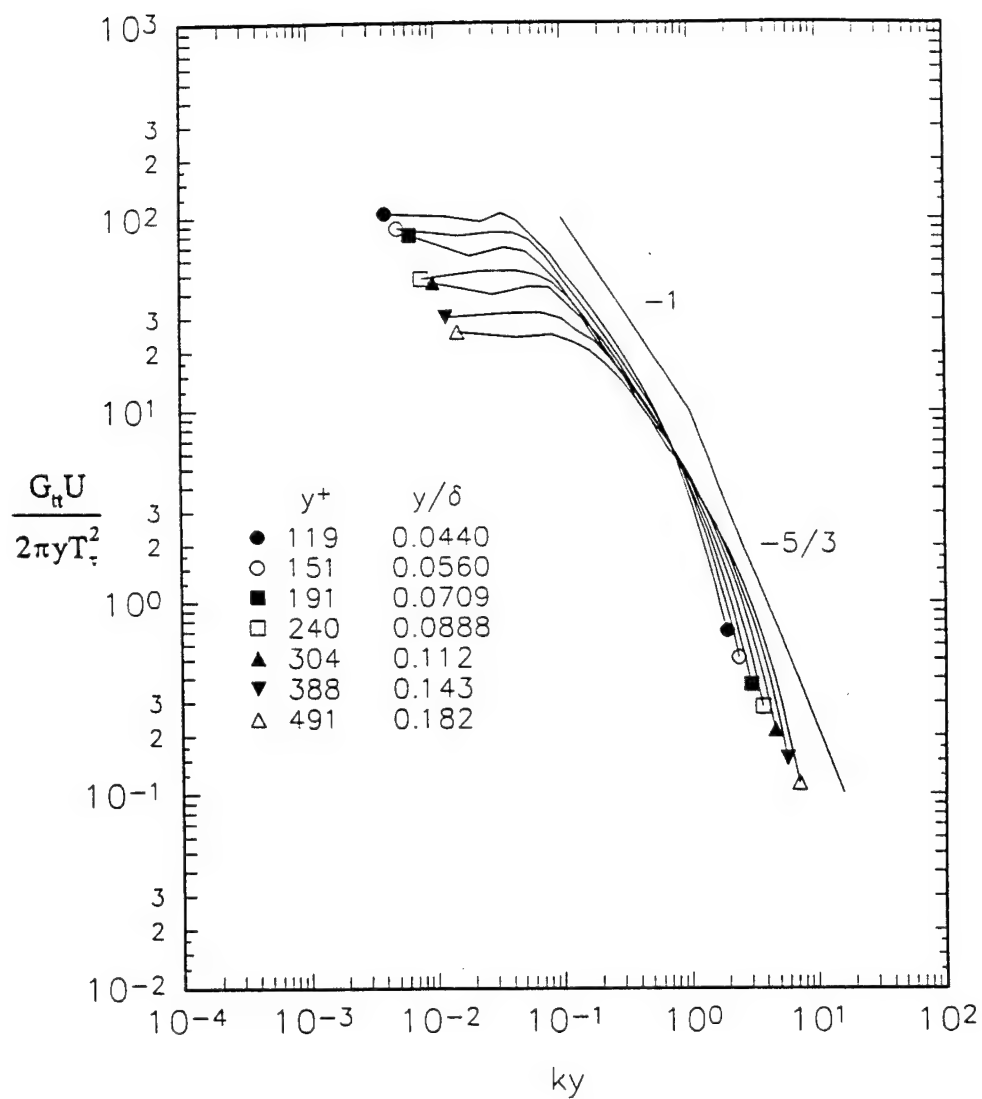


Figure 5.14g. Temperature spectra measured in the wall-region of station 6 normalized with inner scaling parameters.

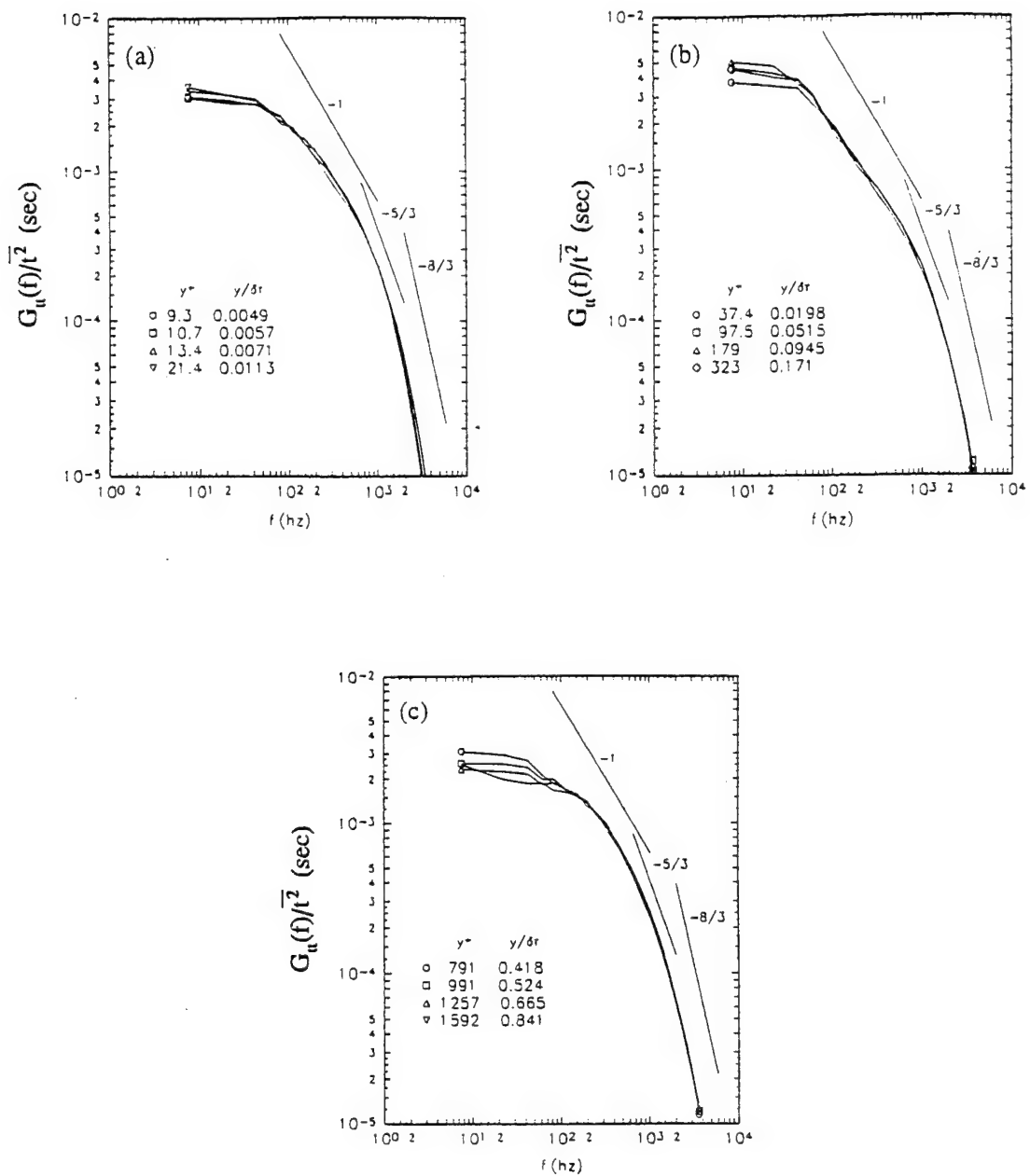


Figure 5.15a. Comparison of temperature spectra at station 0 normalized by t' in (a) the near-wall region; (b) the log-region; and (c) the wake region.

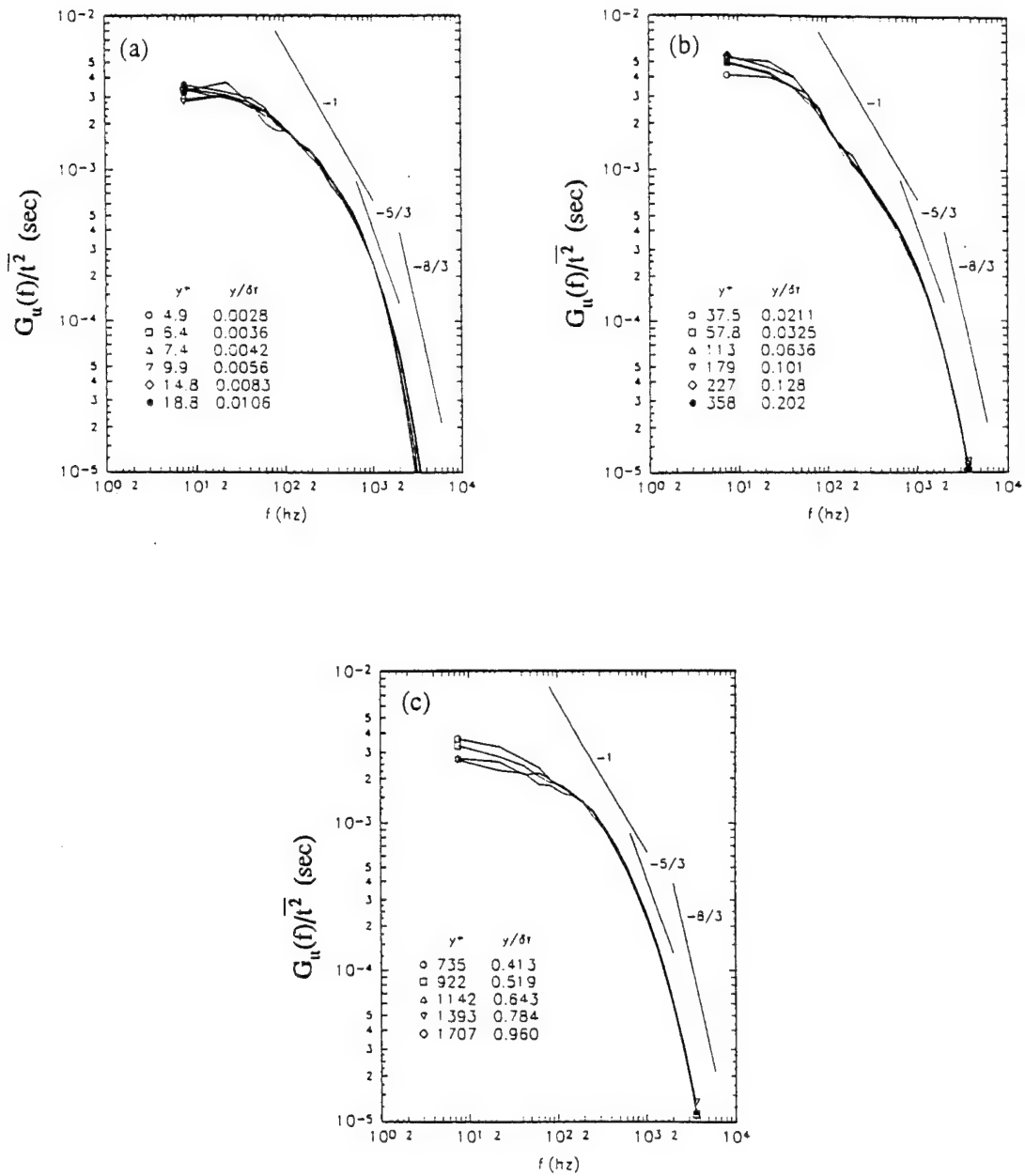


Figure 5.15b. Comparison of temperature spectra at station 1 normalized by t' in (a) the near-wall region; (b) the log-region; and (c) the wake region.

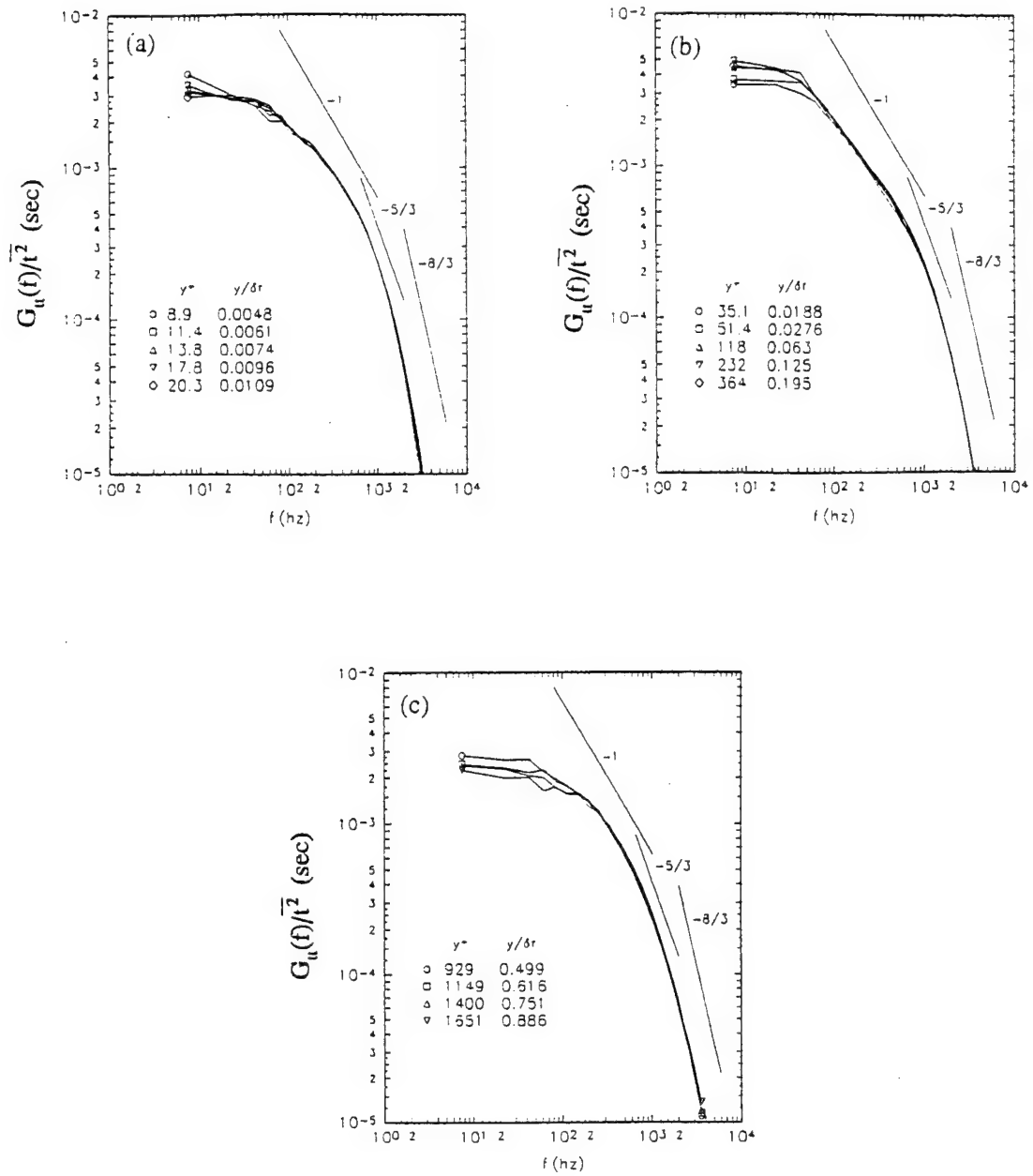


Figure 5.15c. Comparison of temperature spectra at station 2 normalized by t' in (a) the near-wall region; (b) the log-region; and (c) the wake region.

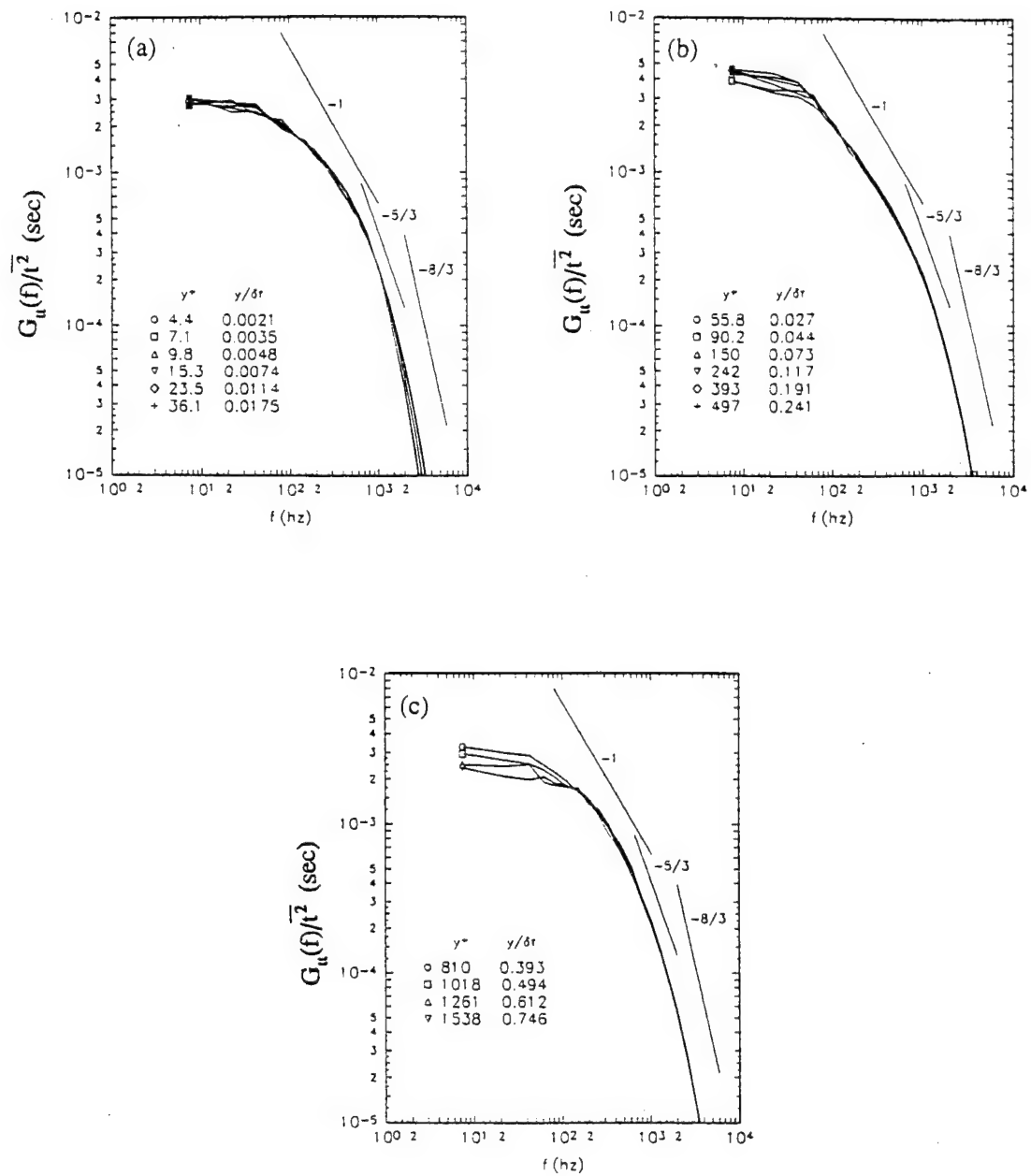


Figure 5.15d. Comparison of temperature spectra at station 3 normalized by t' in (a) the near-wall region; (b) the log-region; and (c) the wake region.

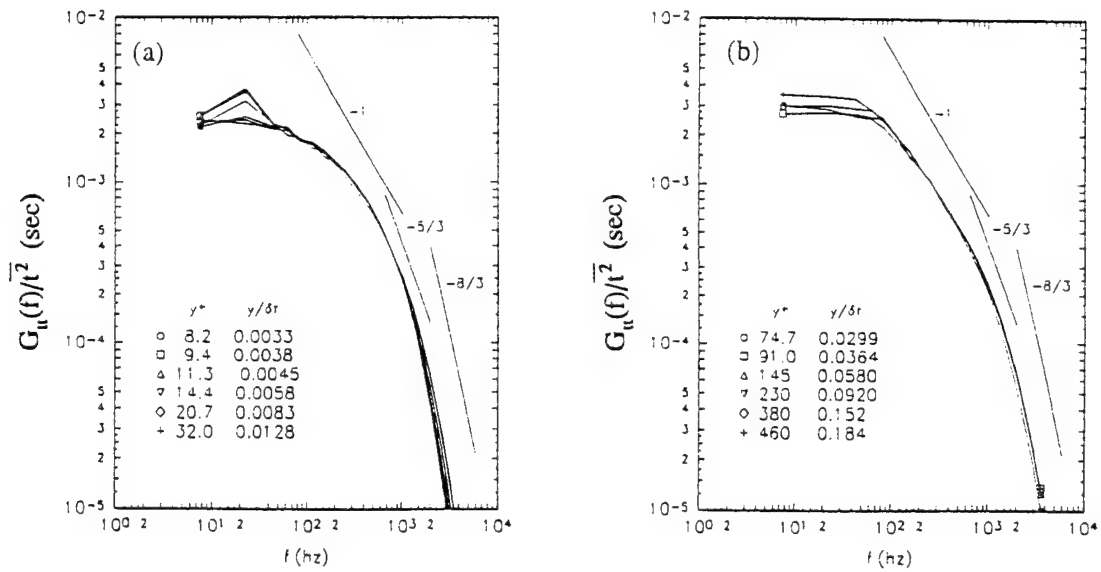


Figure 5.15e. Comparison of temperature spectra at station 4 normalized by t' in (a) the near-wall region; (b) the log-region; and (c) the wake region.

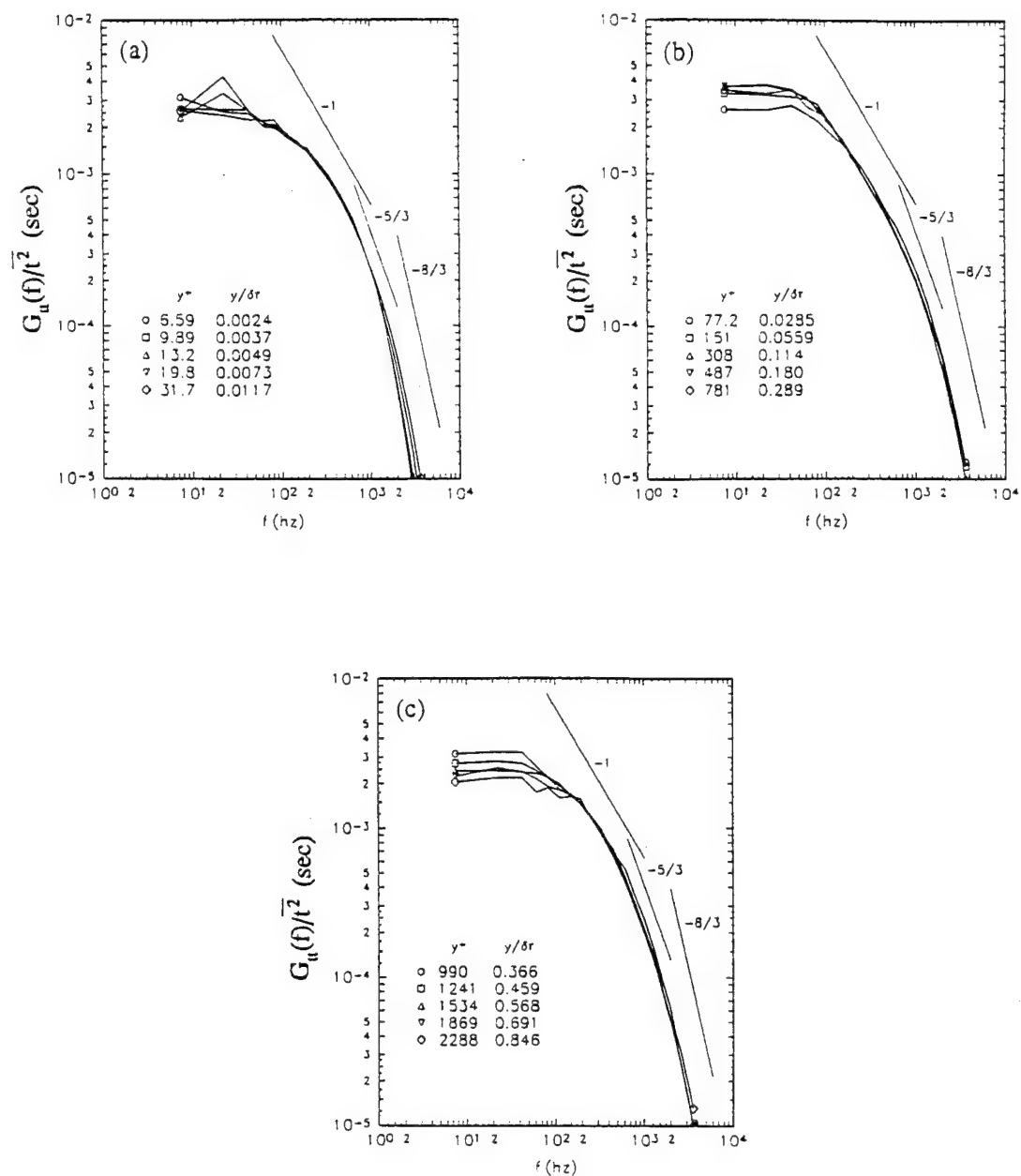


Figure 5.15f. Comparison of temperature spectra at station 5 normalized by t' in (a) the near-wall region; (b) the log-region; and (c) the wake region.

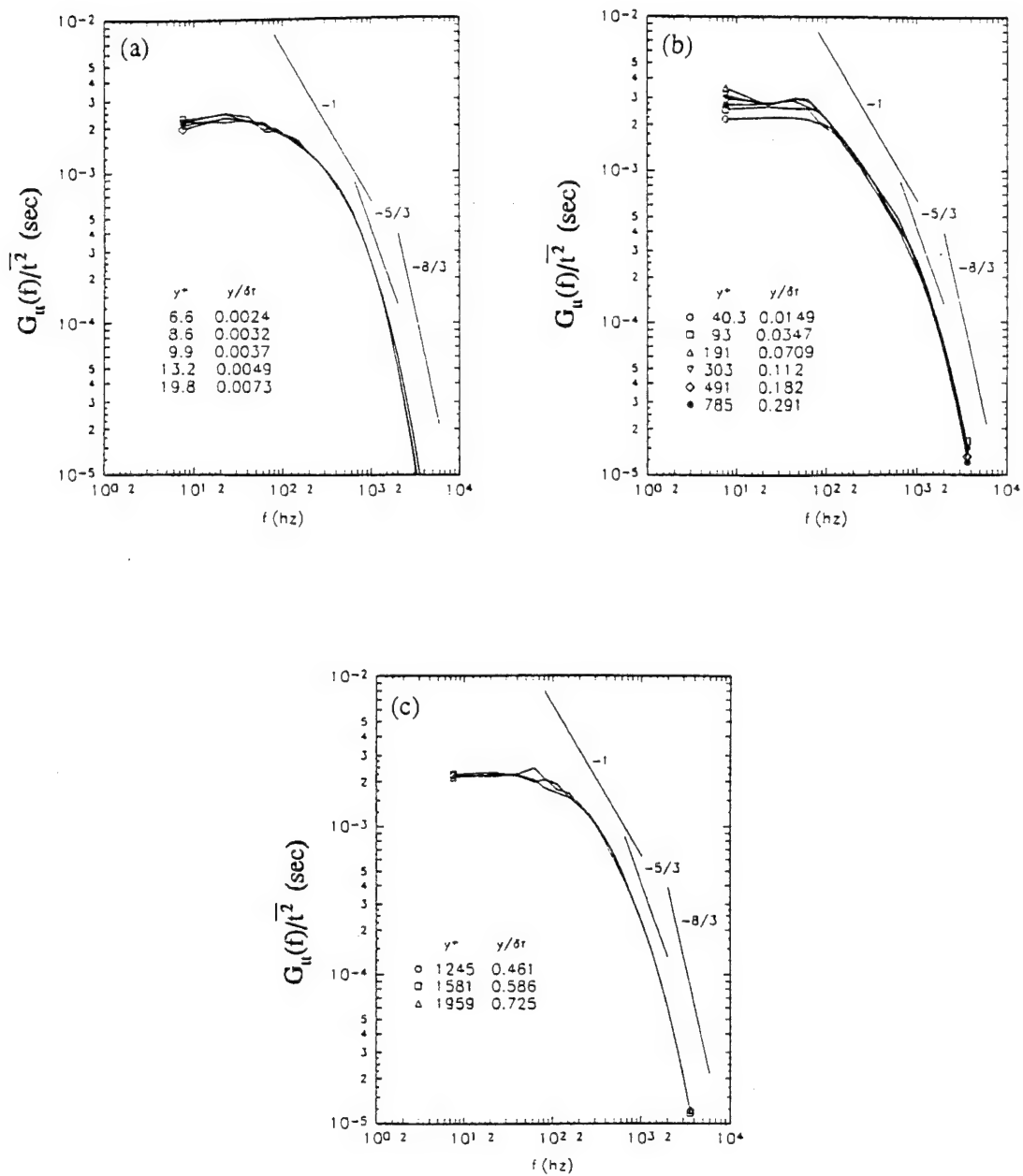


Figure 5.15g. Comparison of temperature spectra at station 6 normalized by t' in (a) the near-wall region; (b) the log-region; and (c) the wake region.

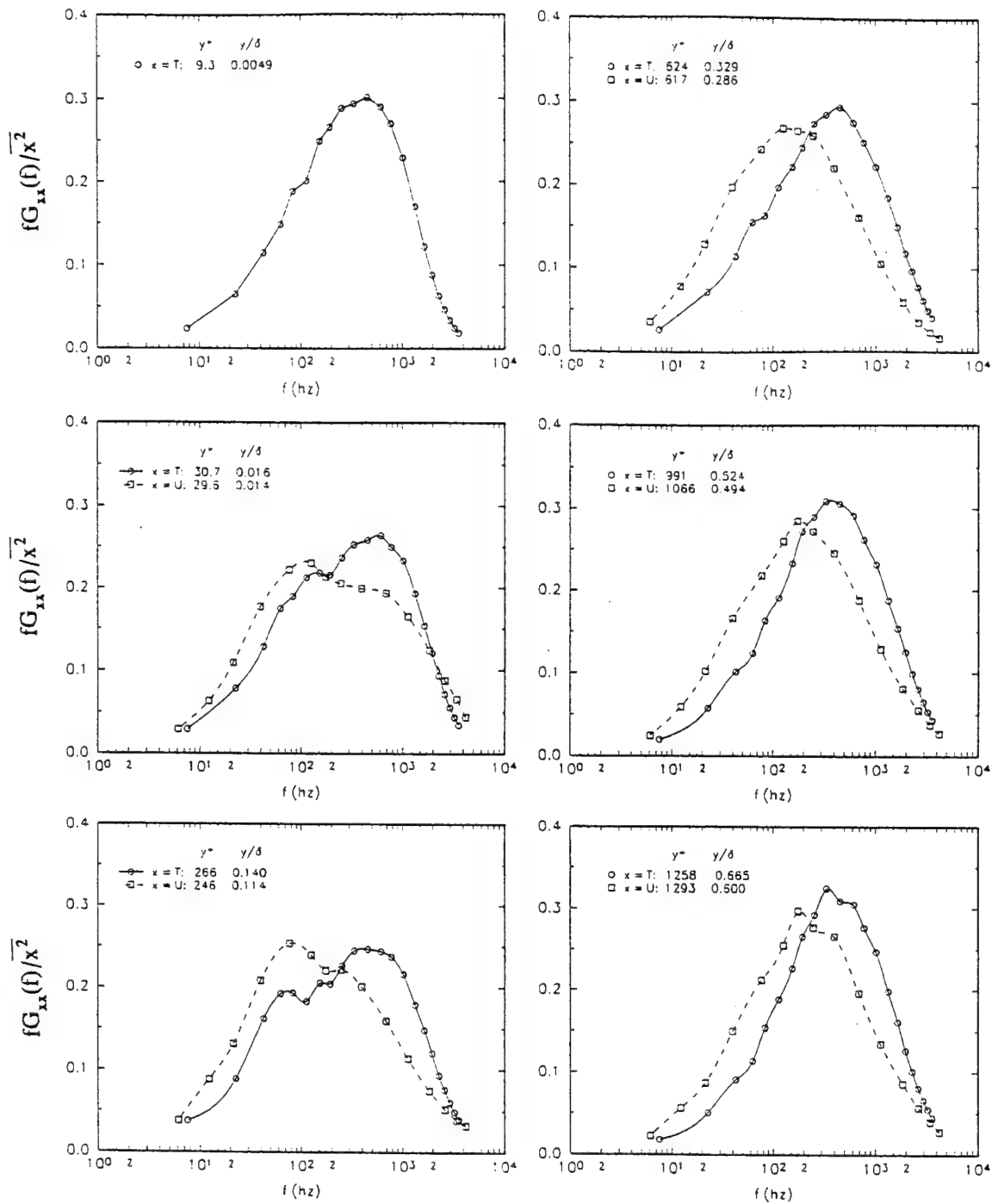


Figure 5.16a. Comparison of first moment of temperature and u-spectra measured at several positions across the boundary layer at station 0.

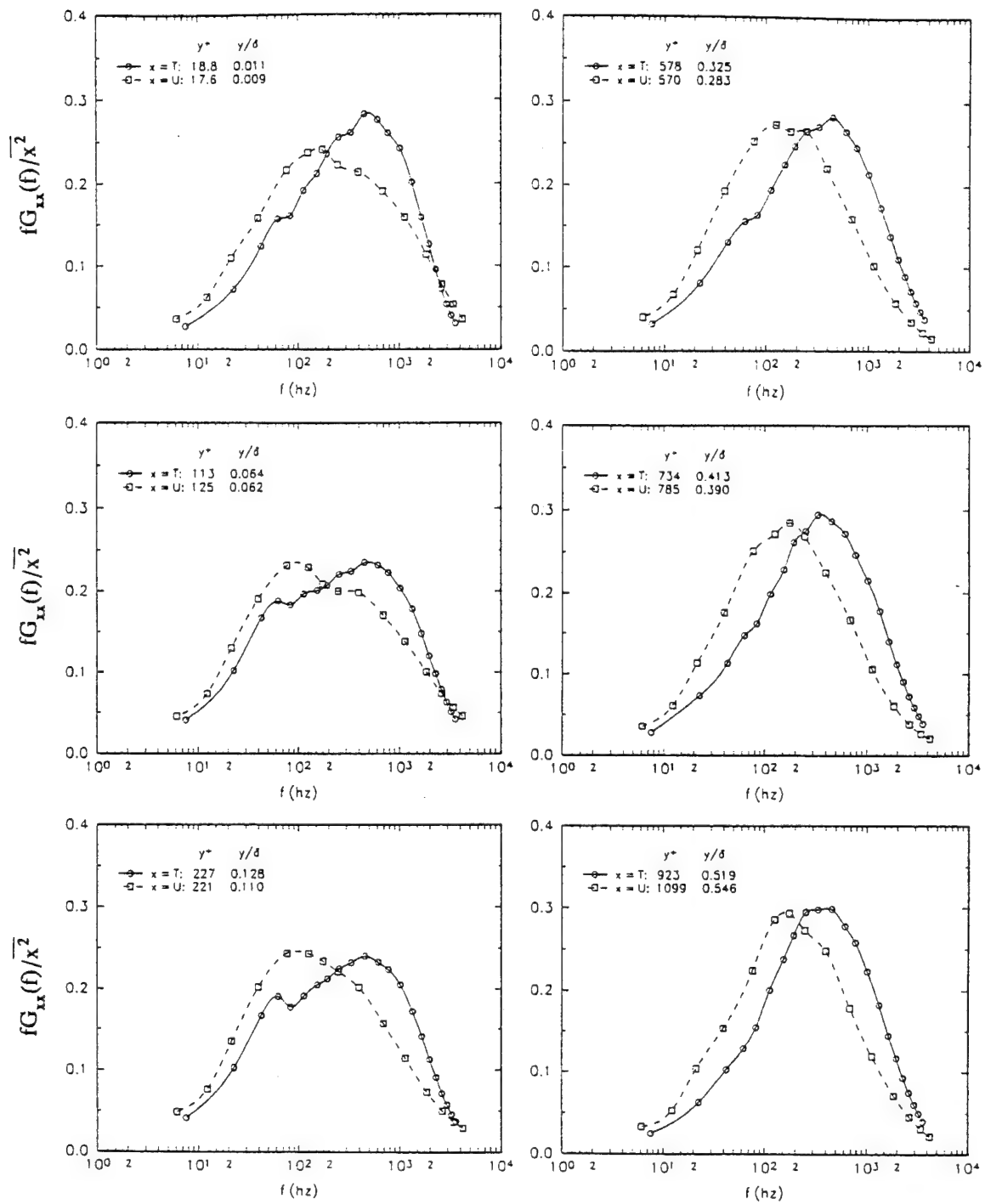


Figure 5.16b. Comparison of first moment of temperature and u-spectra measured at several positions across the boundary layer at station 1.

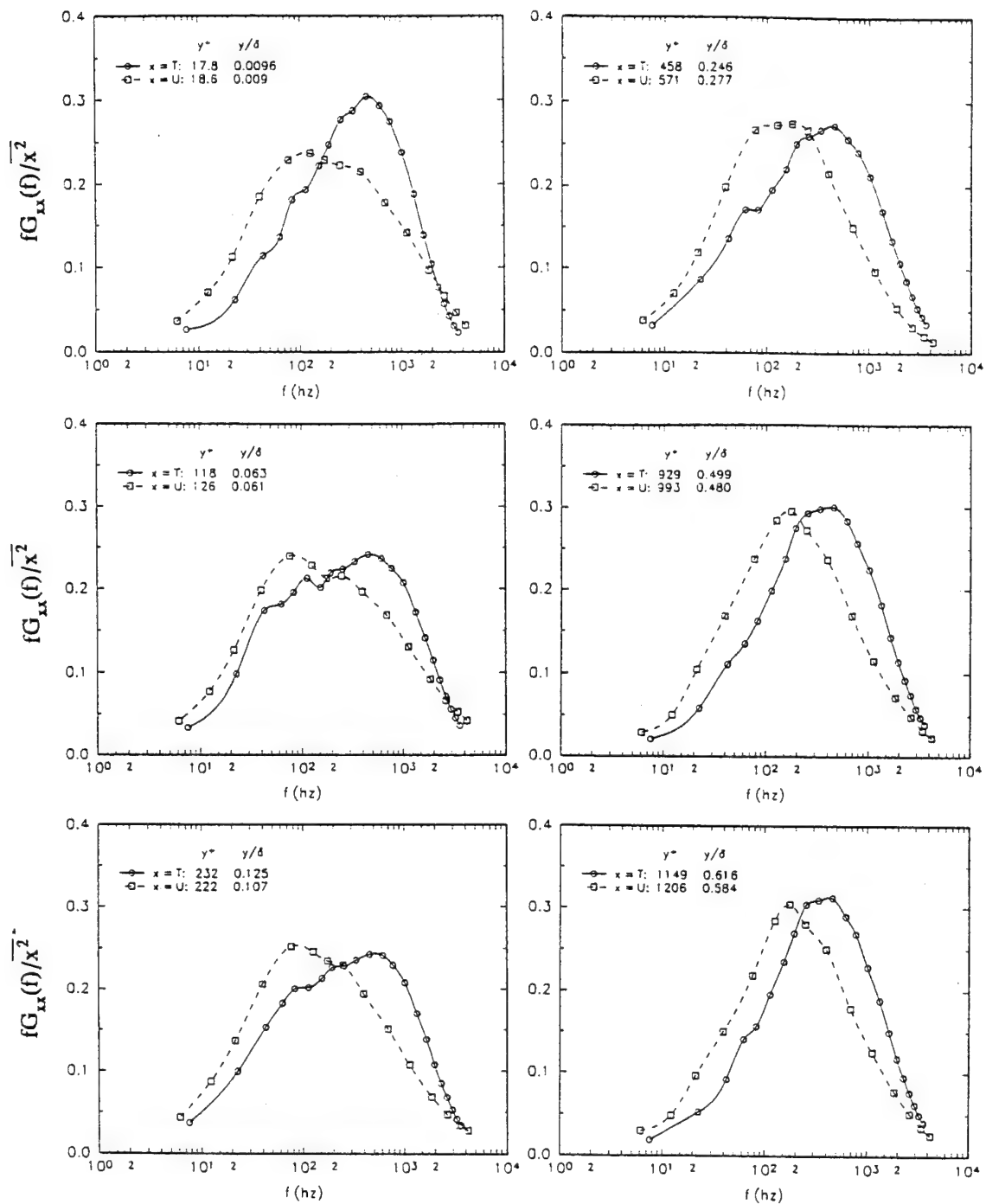


Figure 5.16c. Comparison of first moment of temperature and u-spectra measured at several positions across the boundary layer at station 2.

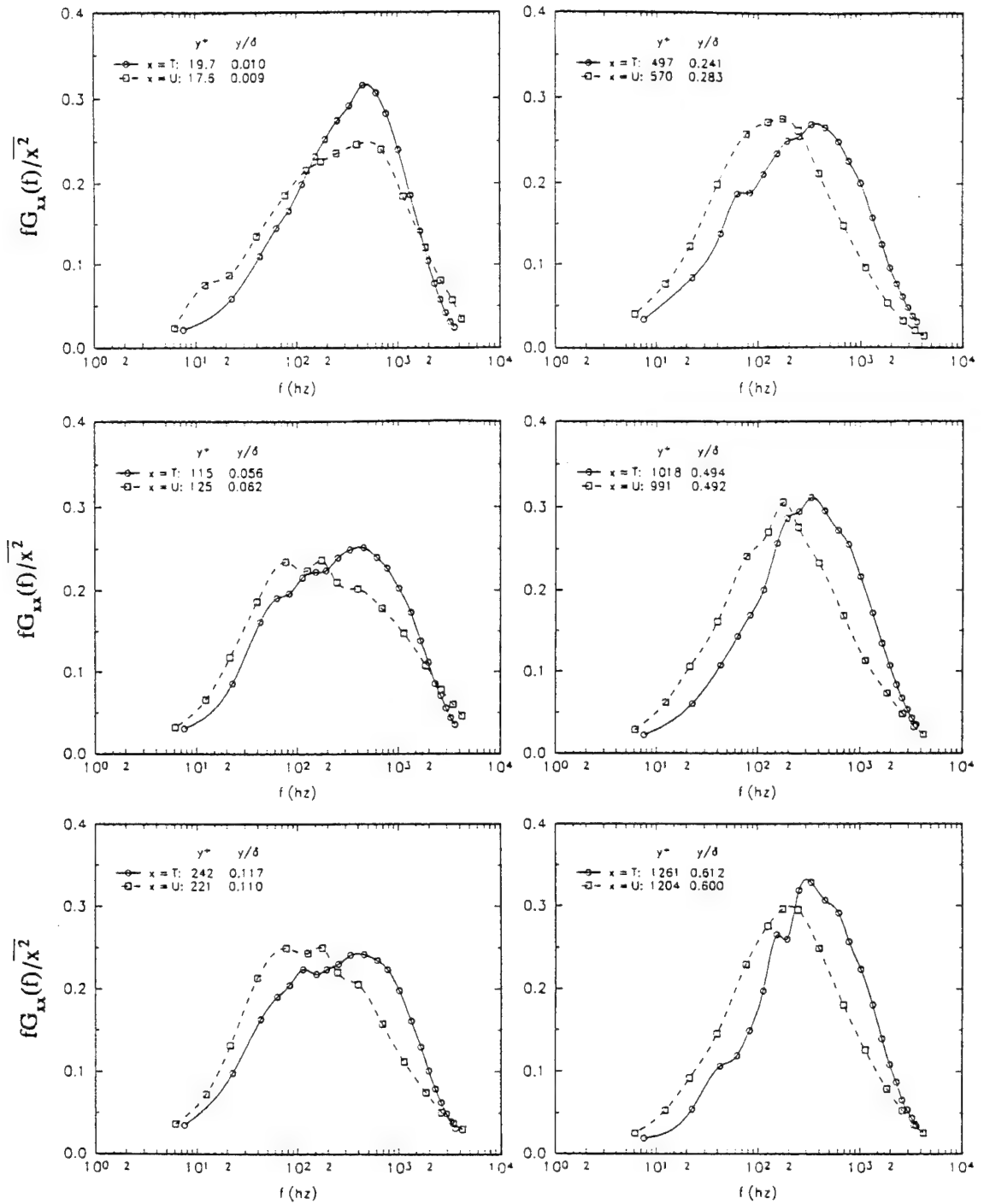


Figure 5.16d. Comparison of first moment of temperature and u-spectra measured at several positions across the boundary layer at station 3.

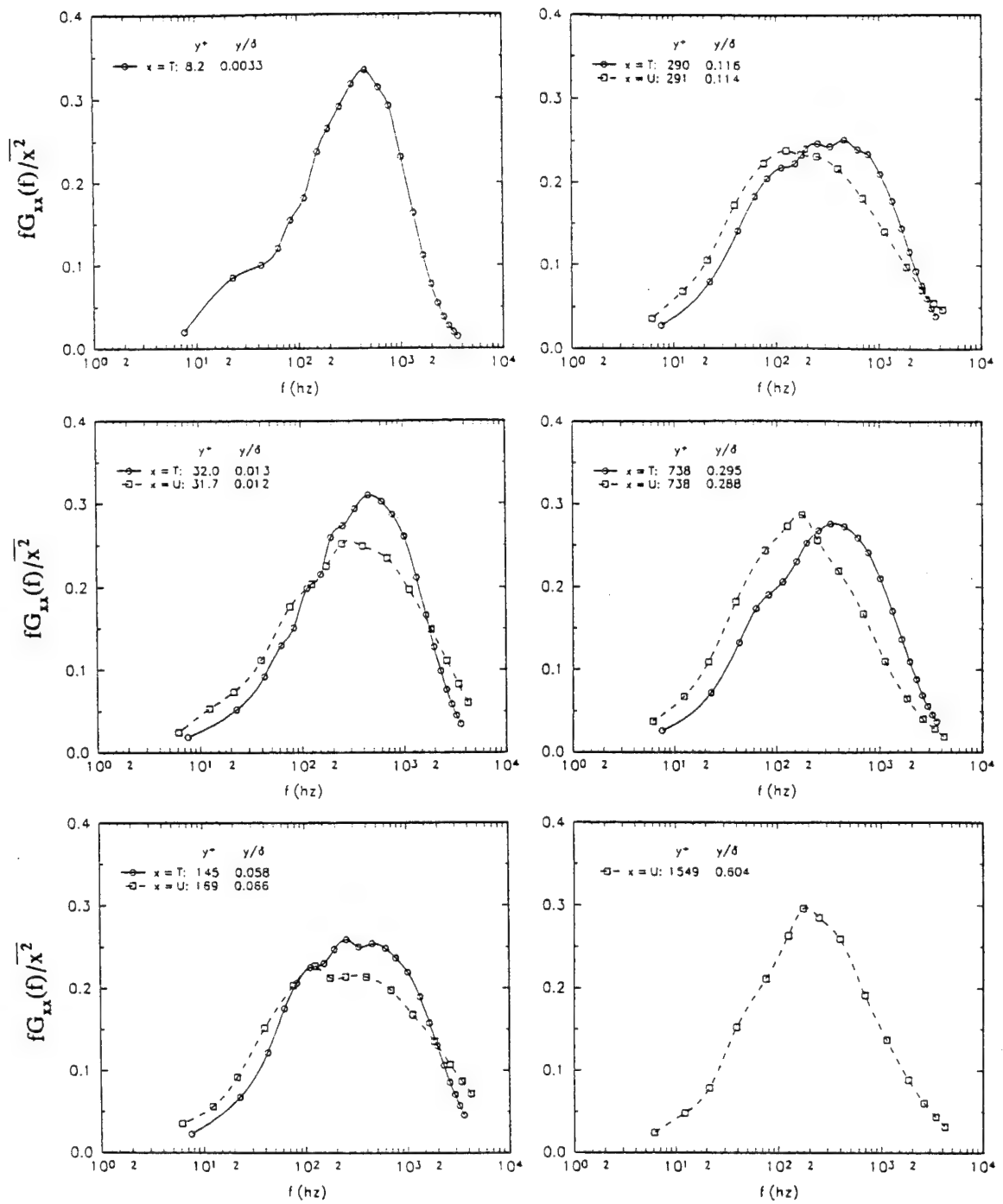


Figure 5.16e. Comparison of first moment of temperature and u-spectra measured at several positions across the boundary layer at station 4.

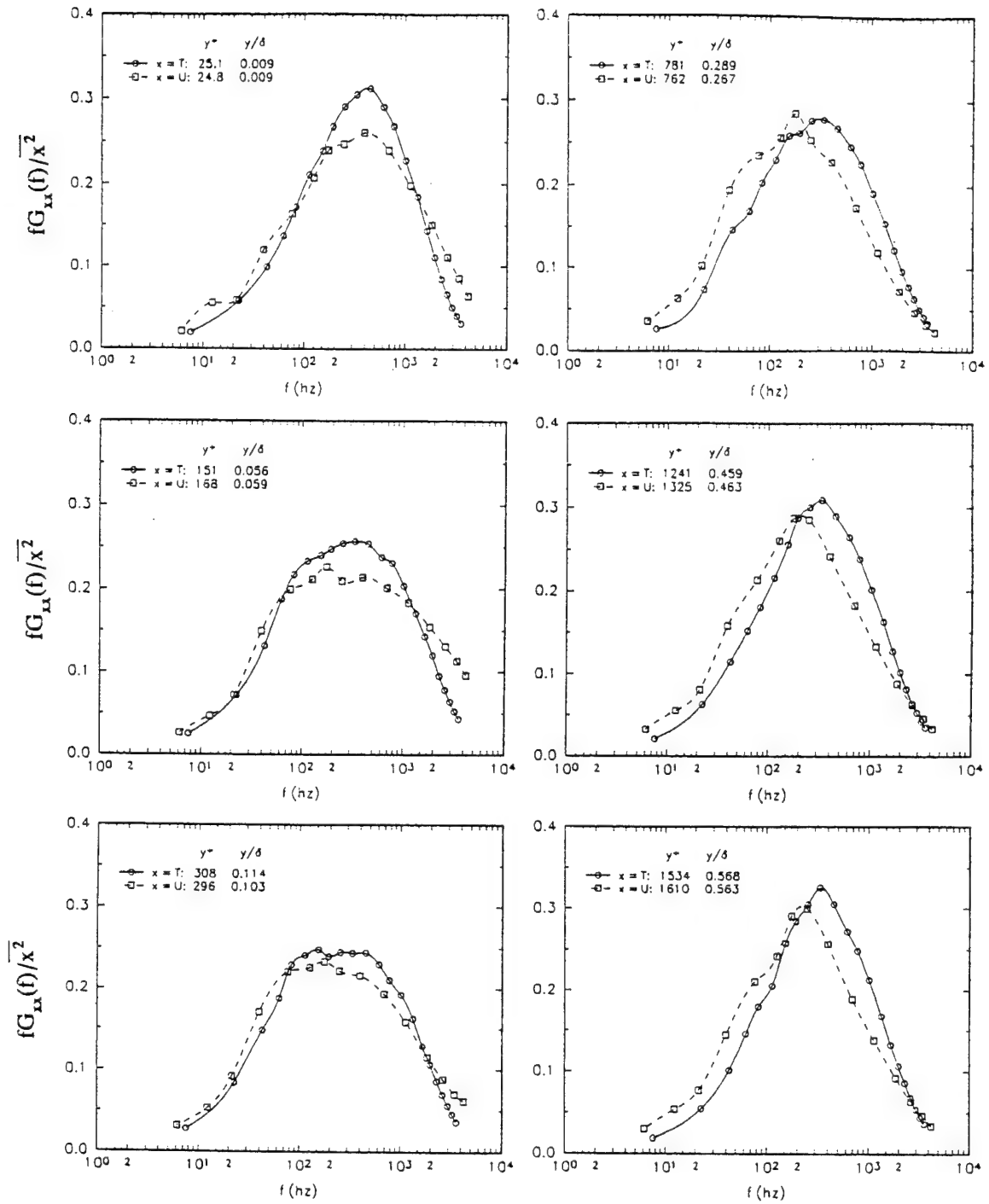


Figure 5.16f. Comparison of first moment of temperature and u-spectra measured at several positions across the boundary layer at station 5.

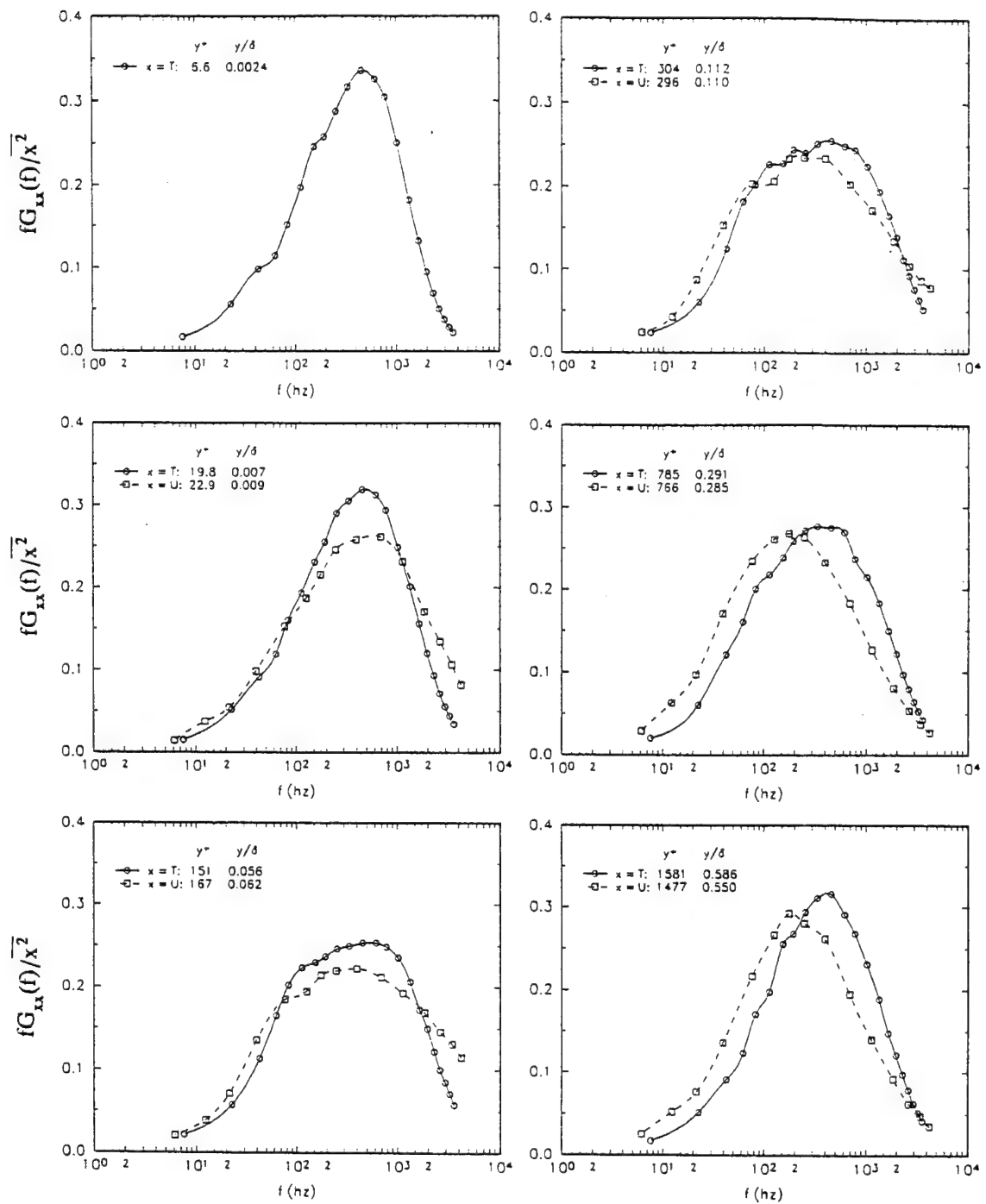


Figure 5.16g. Comparison of first moment of temperature and u-spectra measured at several positions across the boundary layer at station 6.

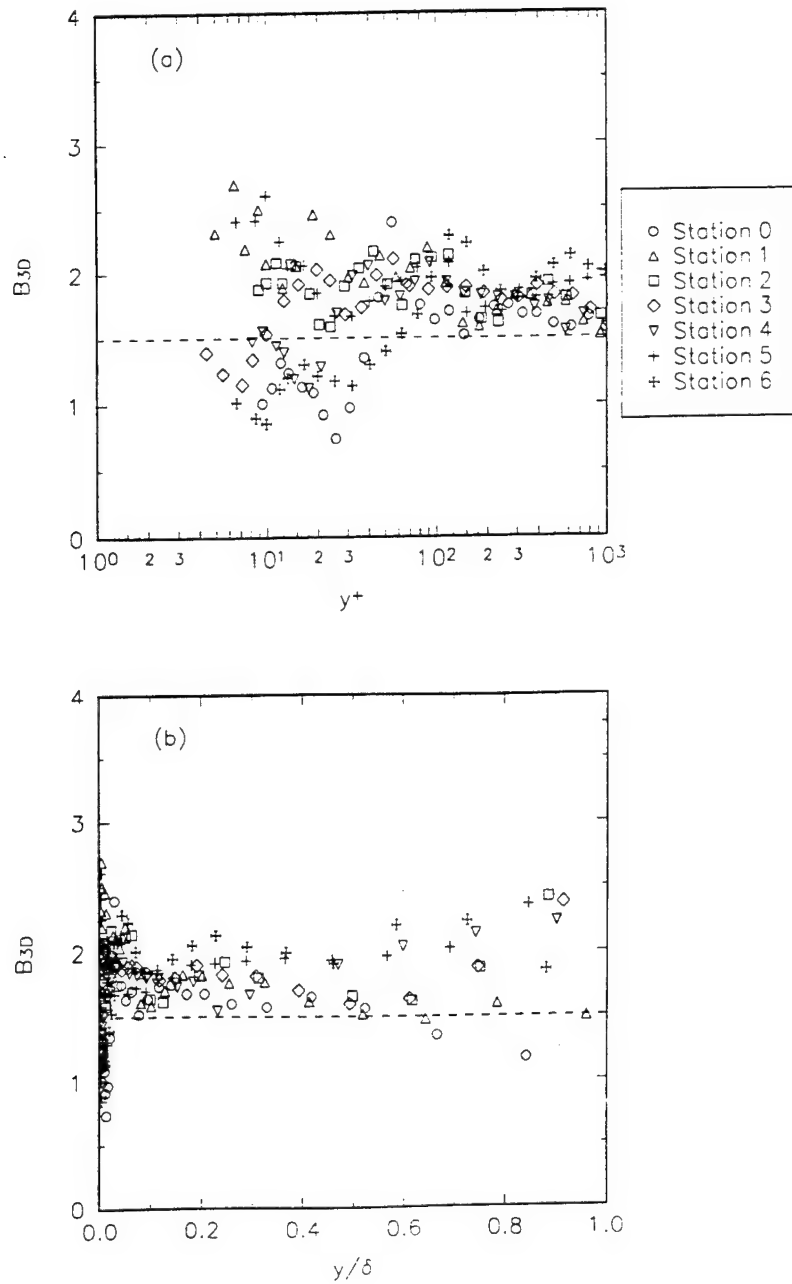


Figure 5.17. Distributions of B_{3D} parameter across the boundary layer at stations 0 - 6 in the 3D TBL. Dashed lines are Fulachier and Dumas (1976) value of 1.5. (a) inner region; (b) outer region.

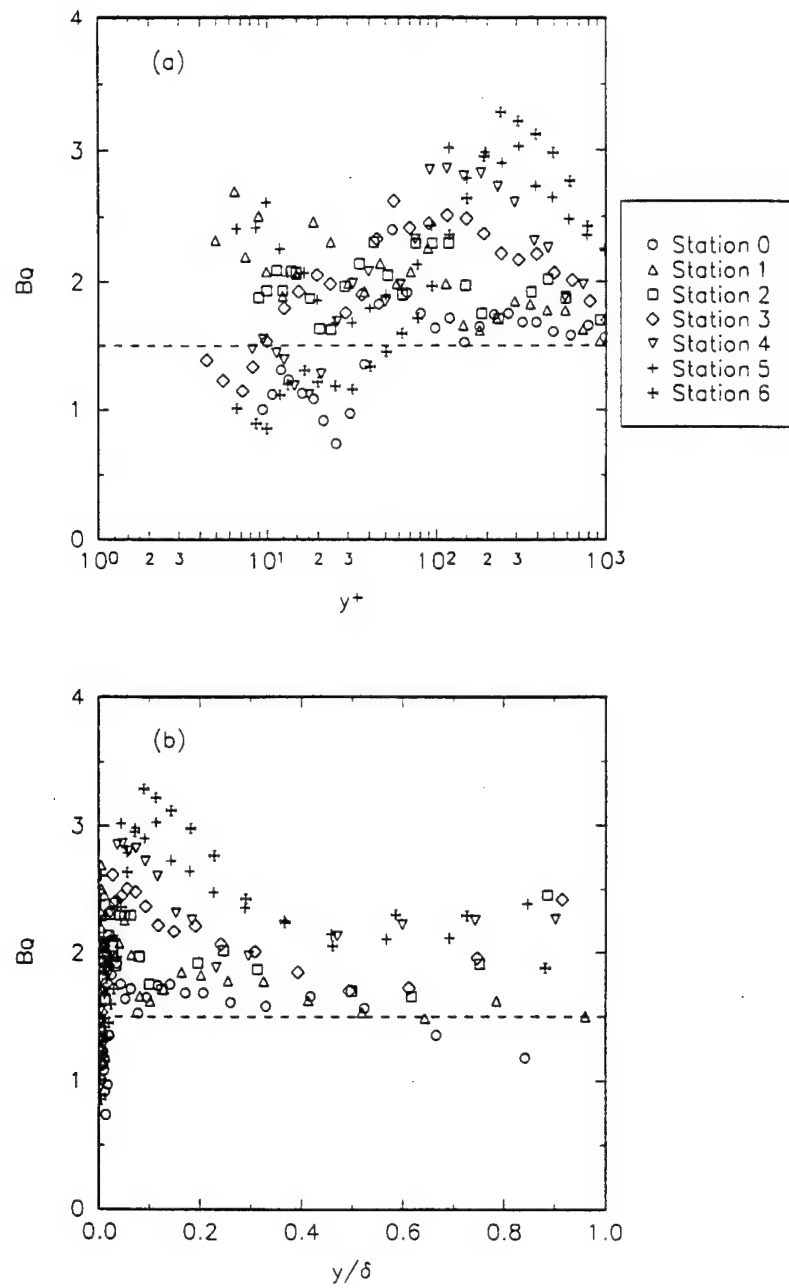


Figure 5.18. Distributions of B_Q parameter across the boundary layer at stations 0 - 6 in the 3D TBL. (a) inner region; (b) outer region.

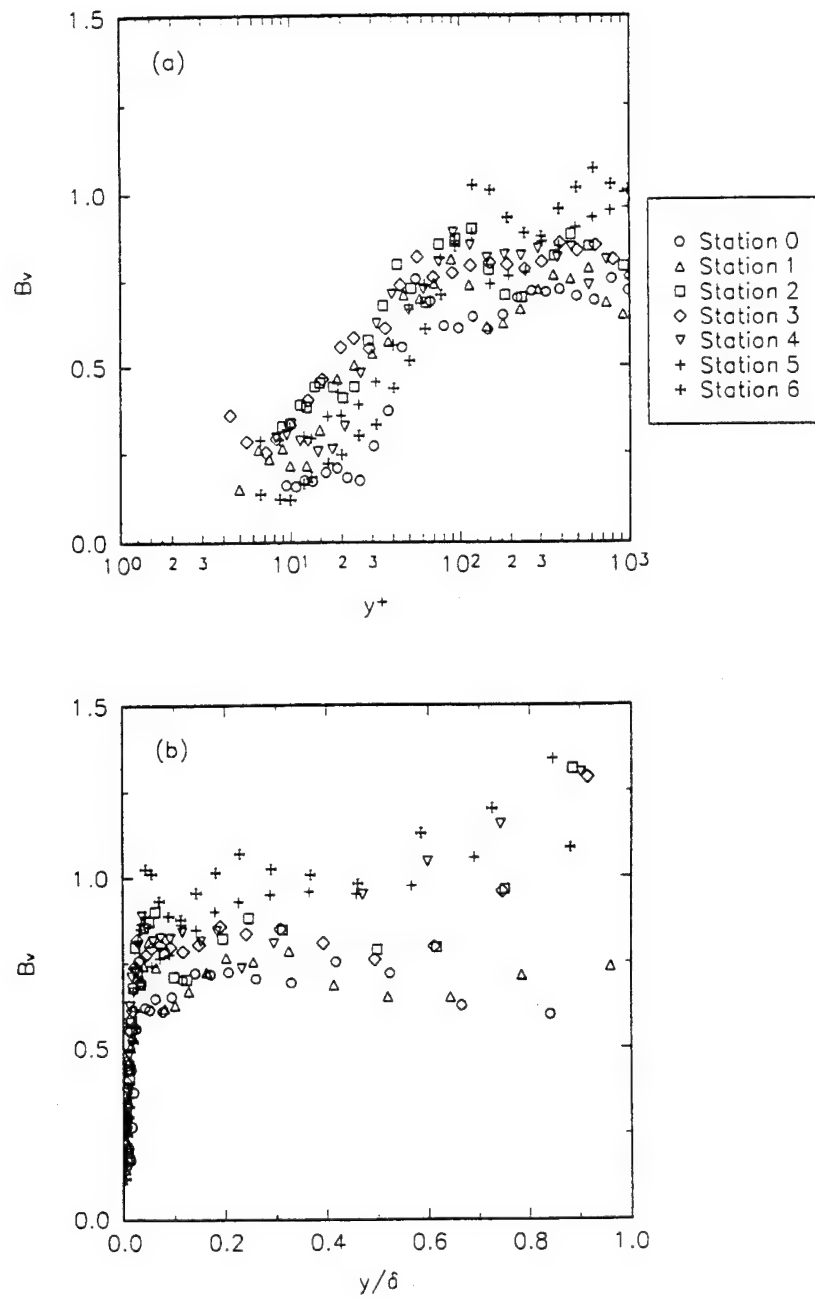


Figure 5.19. Distributions of B_v parameter across the boundary layer at stations 0 - 6 in the 3D TBL. (a) inner region; (b) outer region.

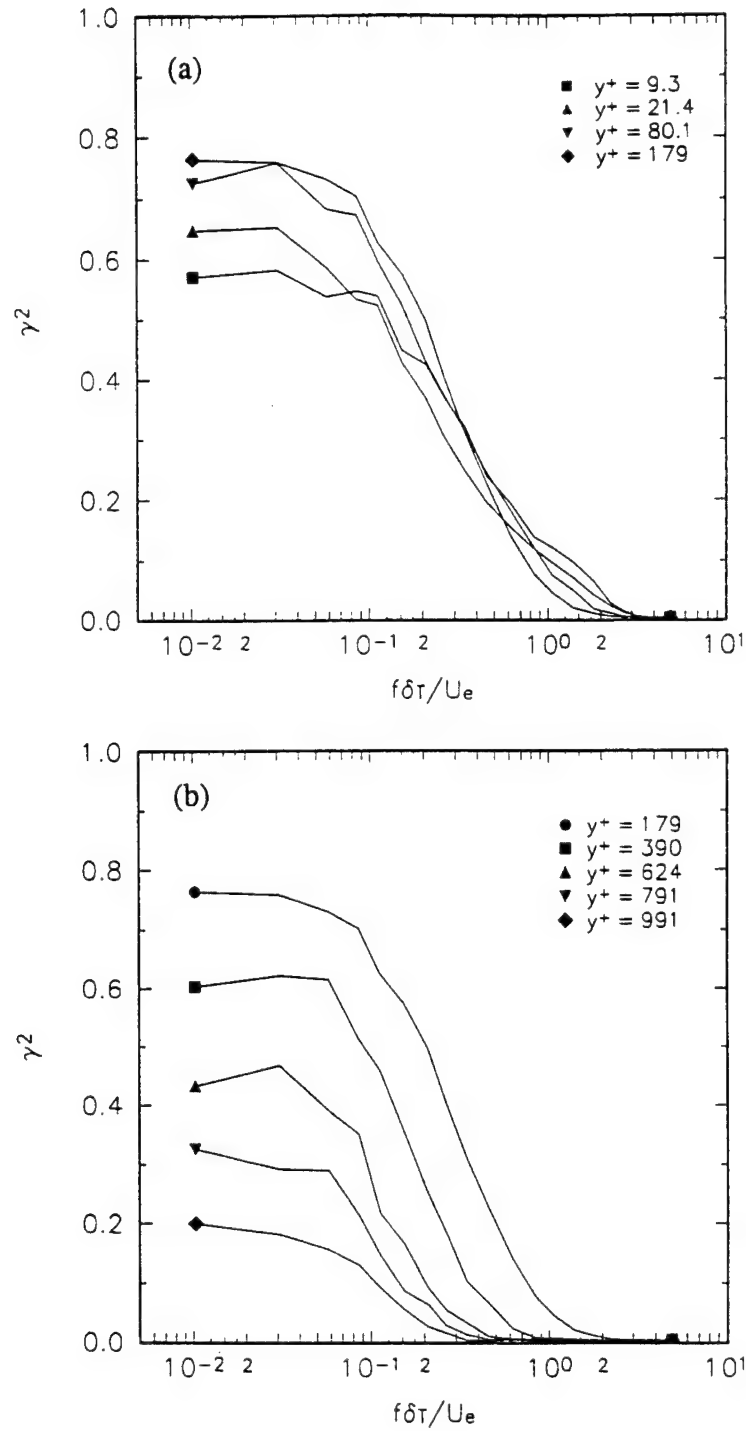


Figure 5.20. Spectral variation of coherency between surface heat flux and temperature at several points across the boundary layer measured at station 0. (a) near-wall region; (b) outer region.

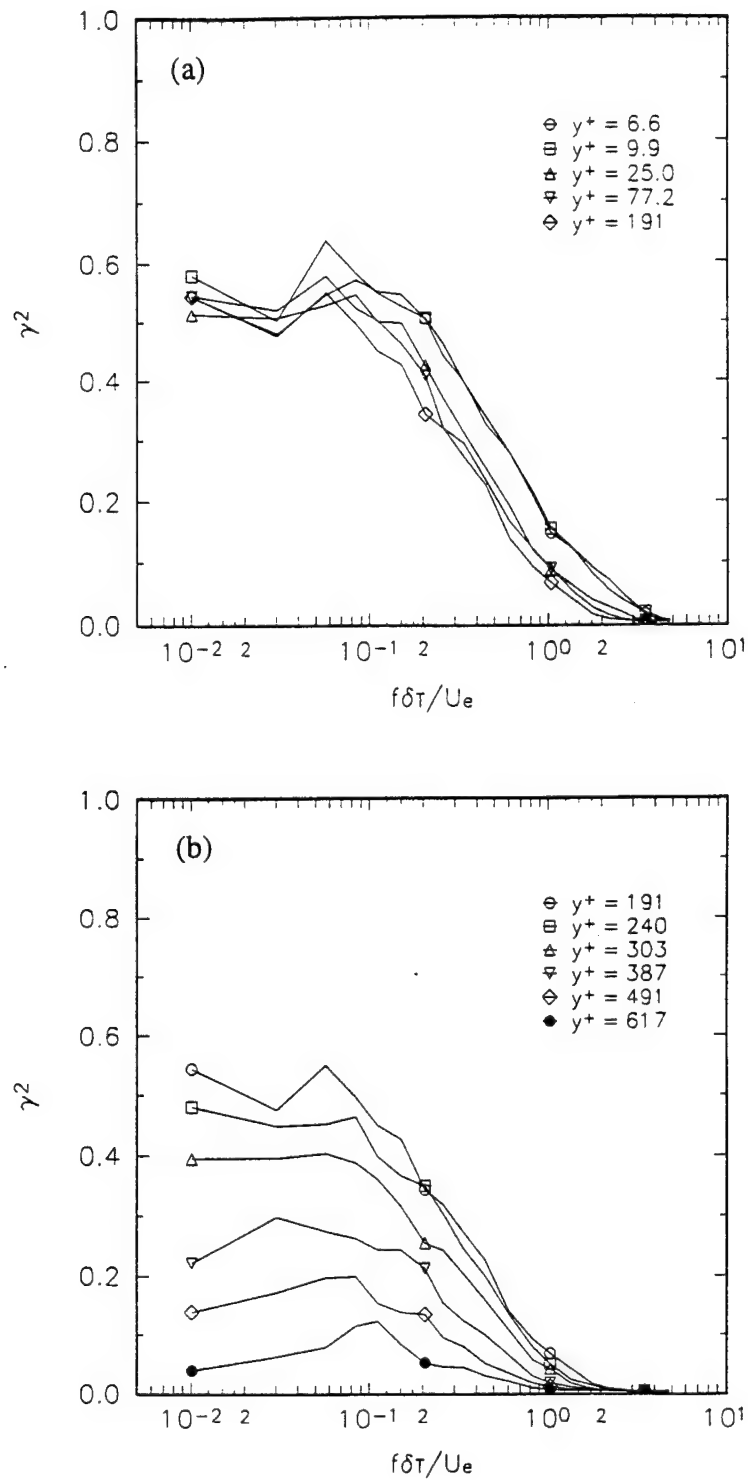


Figure 5.21. Spectral variation of coherency between surface heat flux and temperature at several points across the boundary layer measured at station 6. (a) near-wall region; (b) outer region.

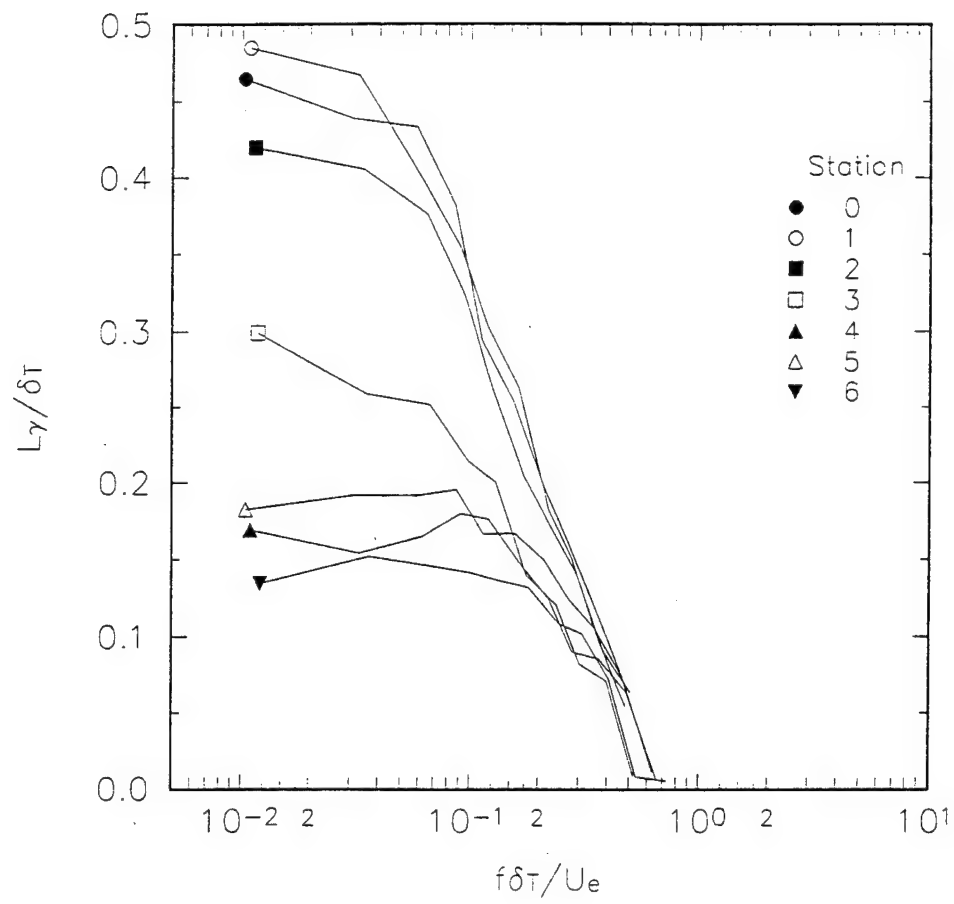


Figure 5.22a. Spectral variation of coherence length scale at all stations in 3D turbulent boundary layer.

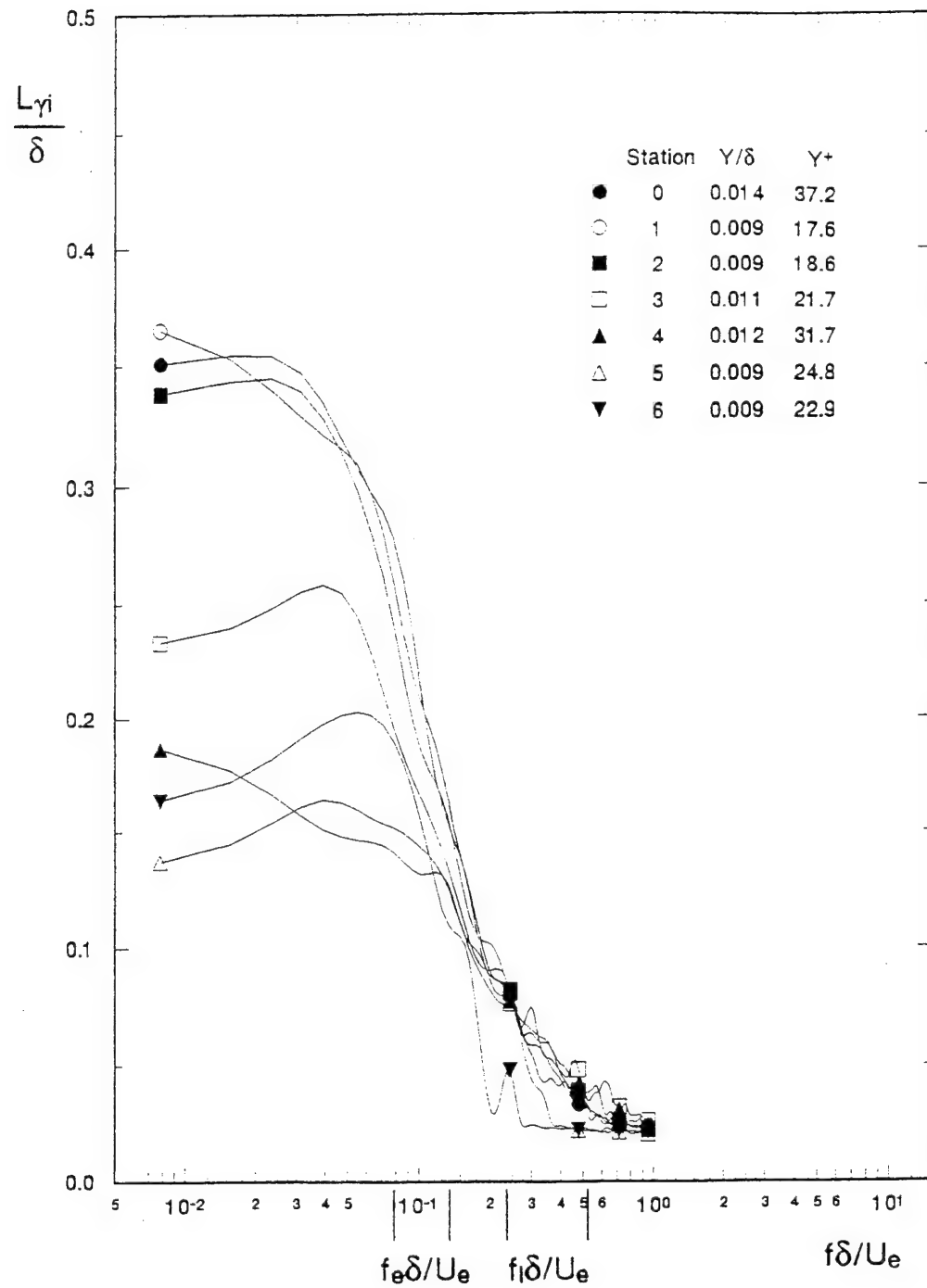


Figure 5.22b. Spectral variation of coherence length scale from at all stations in 3D turbulent boundary layer from Ha and Simpson (1993). Y/δ values on legend apply to the bottom sensor of the hot-wire rake.

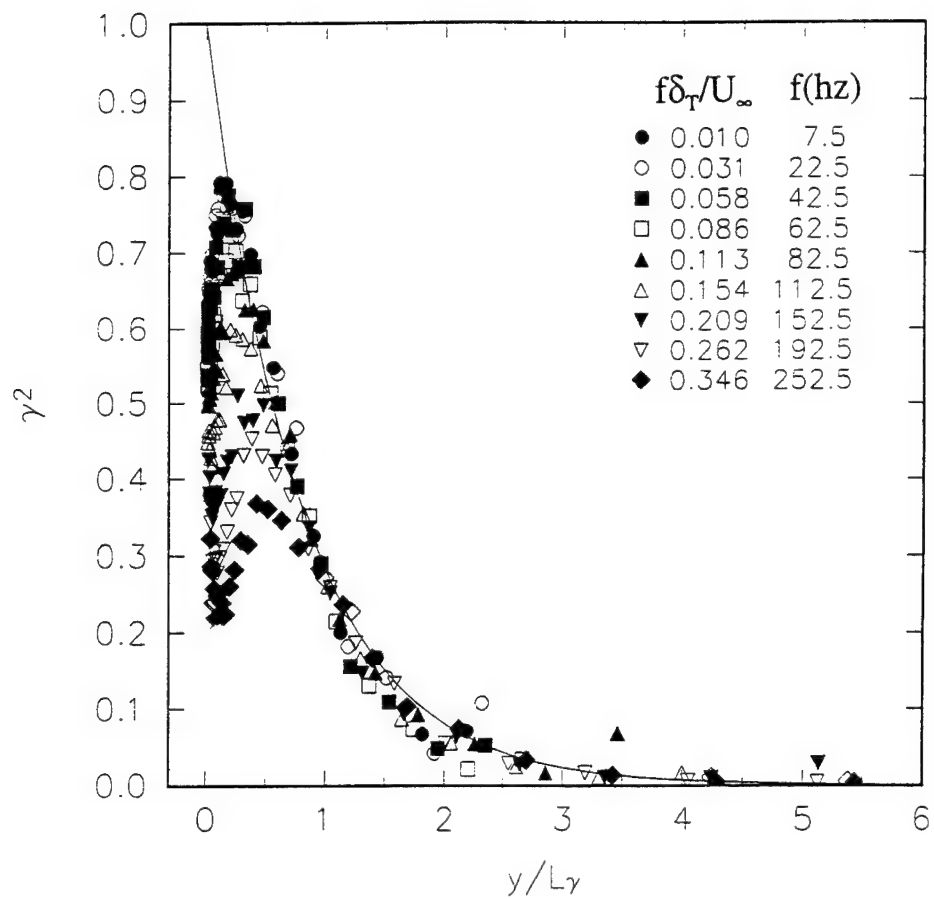


Figure 5.23a. Spatial variation of coherency in the y direction between surface heat flux and temperature for selected frequencies at station 0. Solid line represents exponential decay model with $k_0 = 1.26$.

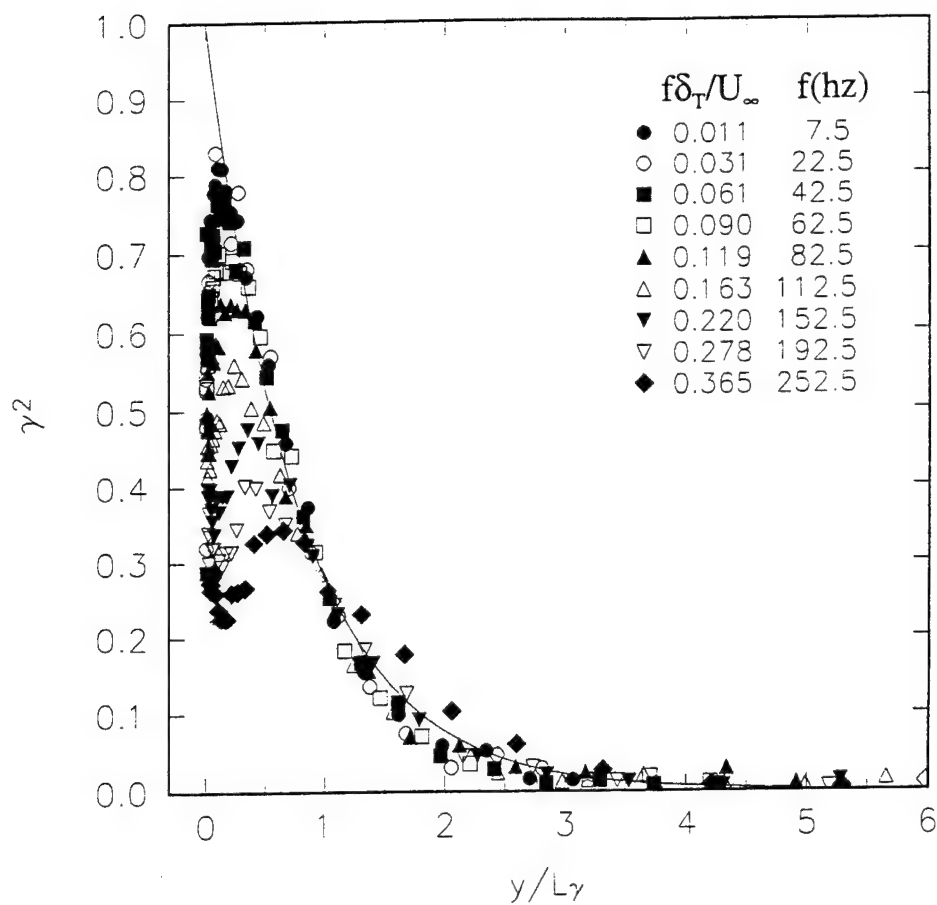


Figure 5.23b. Spatial variation of coherency in the y direction between surface heat flux and temperature for selected frequencies at station 1. Solid line represents exponential decay model with $k_0 = 1.28$.

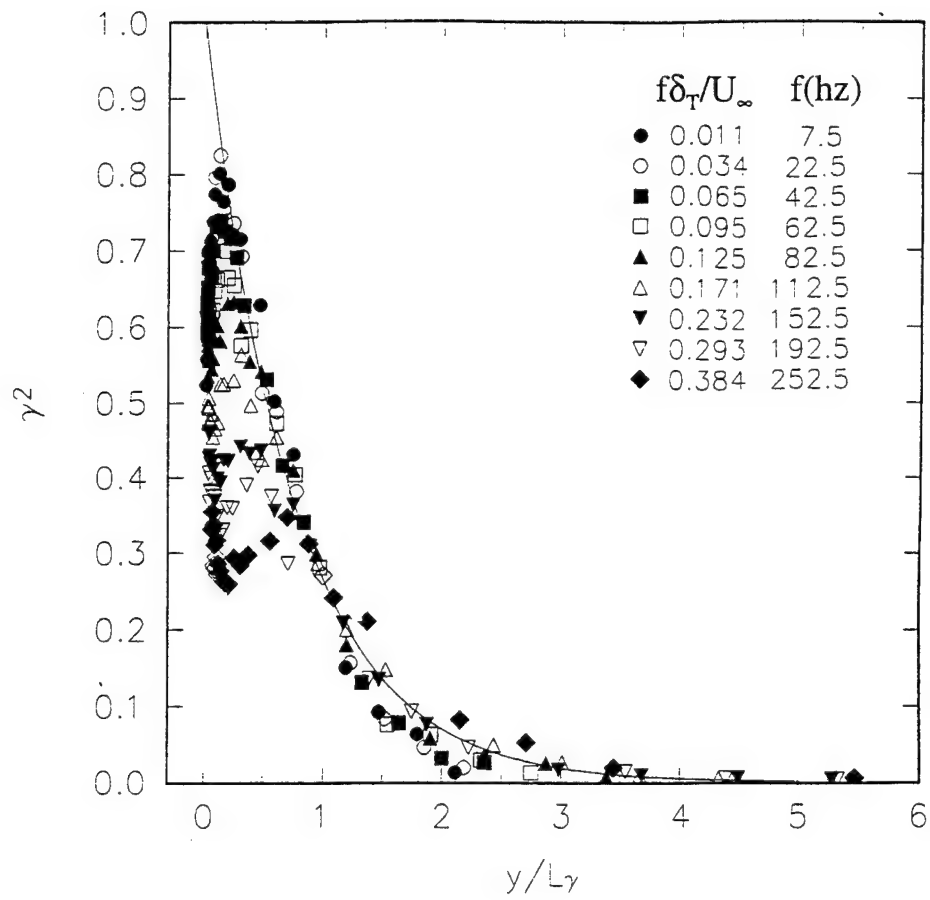


Figure 5.23c. Spatial variation of coherency in the y direction between surface heat flux and temperature for selected frequencies at station 2. Solid line represents exponential decay model with $k_0 = 1.33$.

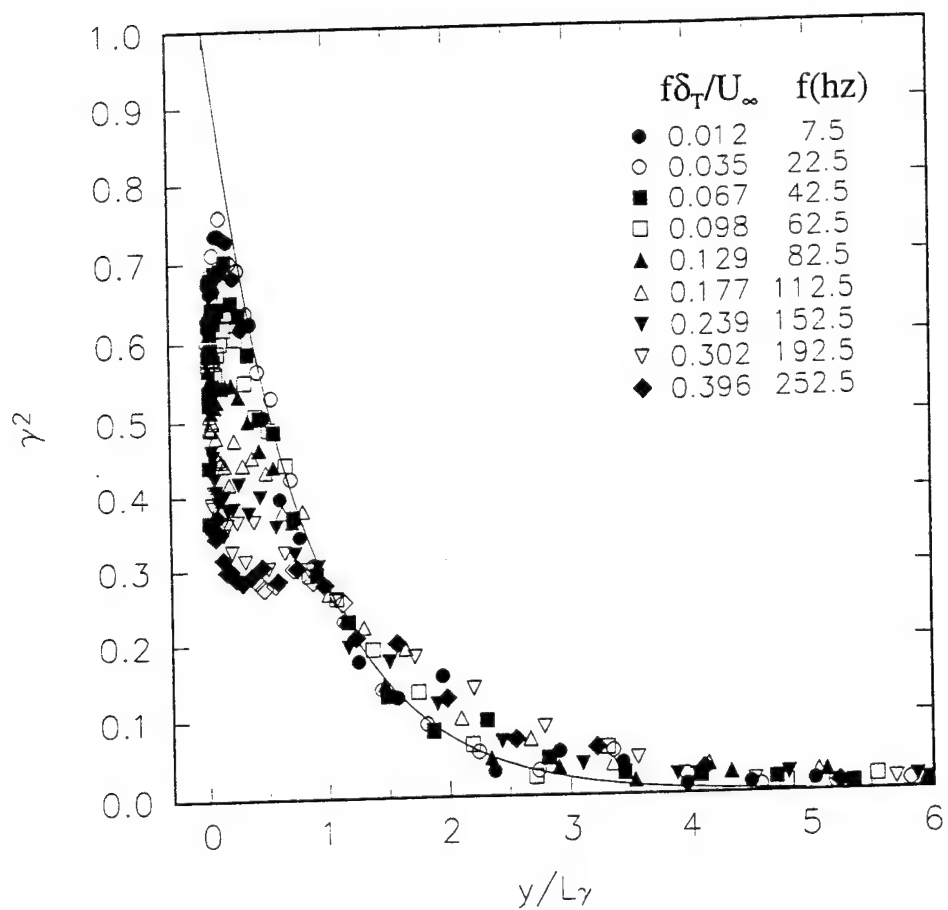


Figure 5.23d. Spatial variation of coherency in the y direction between surface heat flux and temperature for selected frequencies at station 3. Solid line represents exponential decay model with $k_0 = 1.33$.

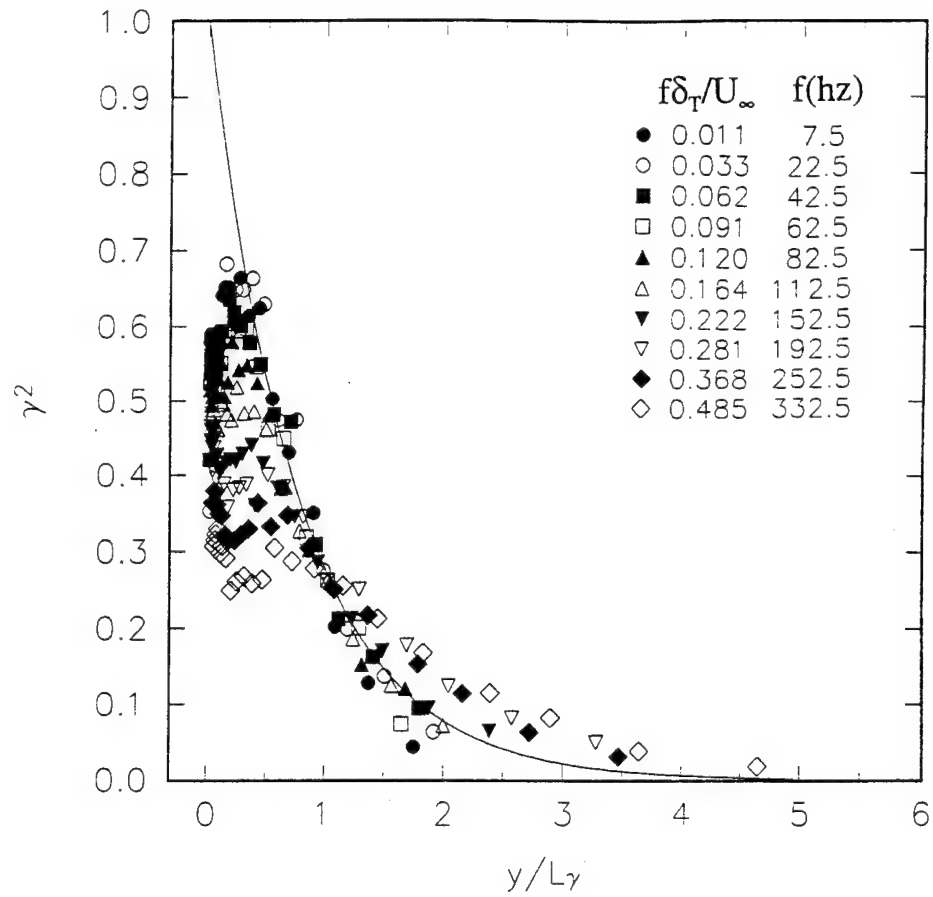


Figure 5.23e. Spatial variation of coherency in the y direction between surface heat flux and temperature for selected frequencies at station 4. Solid line represents exponential decay model with $k_0 = 1.33$.

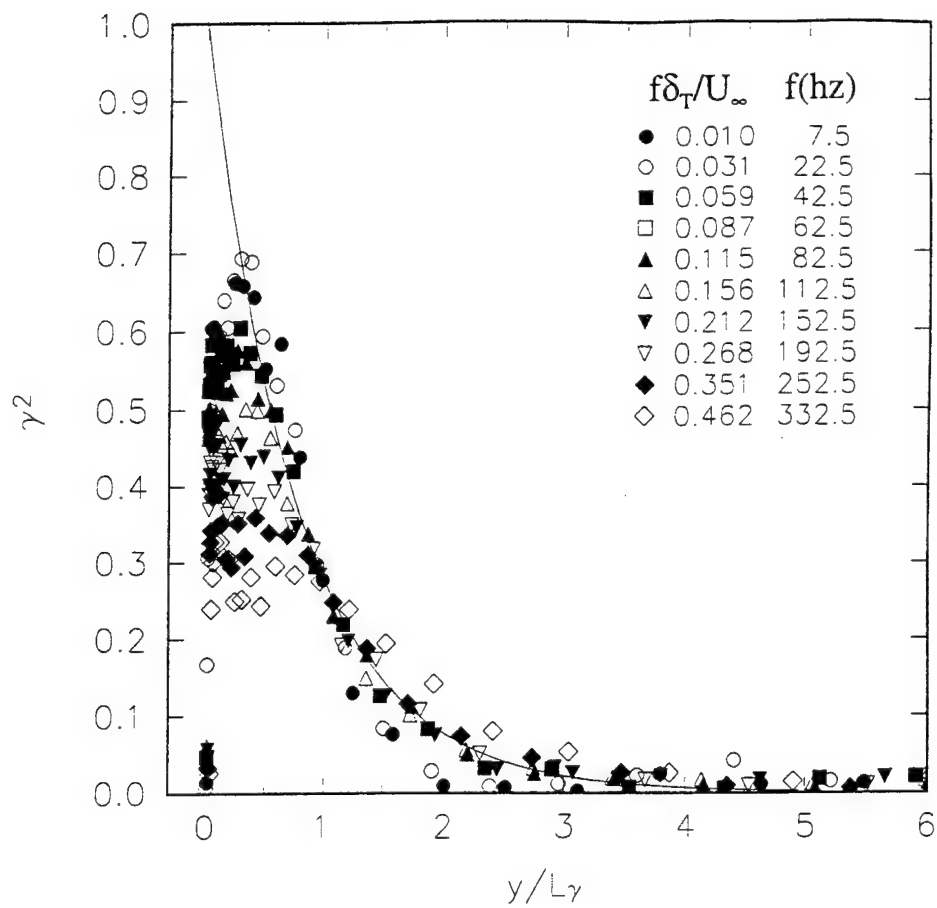


Figure 5.23f. Spatial variation of coherency in the y direction between surface heat flux and temperature for selected frequencies at station 5. Solid line represents exponential decay model with $k_0 = 1.33$.

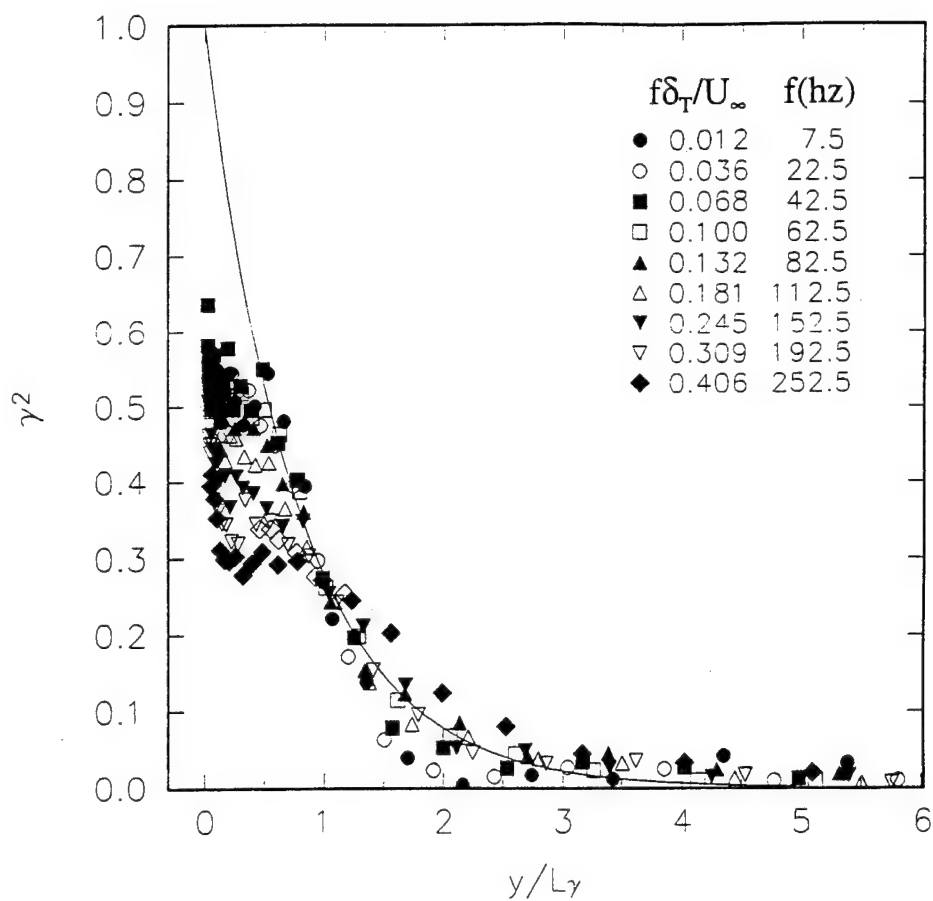


Figure 5.23g. Spatial variation of coherency in the y direction between surface heat flux and temperature for selected frequencies at station 6. Solid line represents exponential decay model with $k_0 = 1.33$.

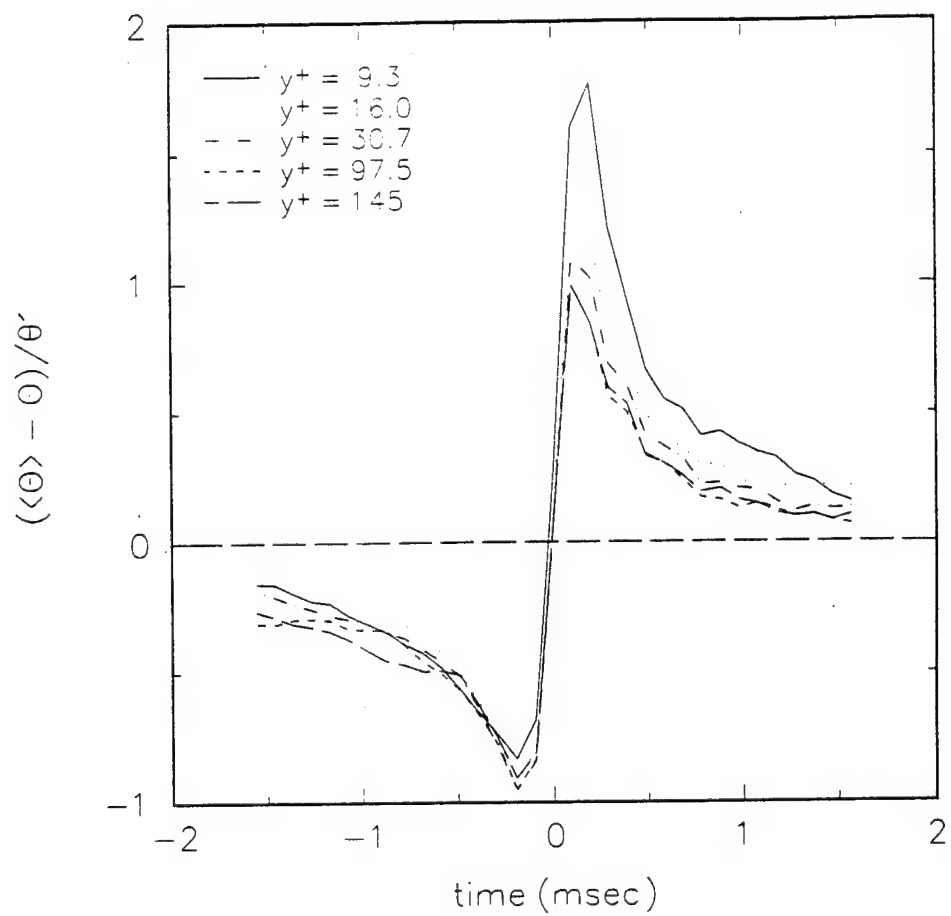


Figure 6.1a. Conditionally averaged temperature time records during a sweep/ejection event at several y locations across the boundary layer at station 0.

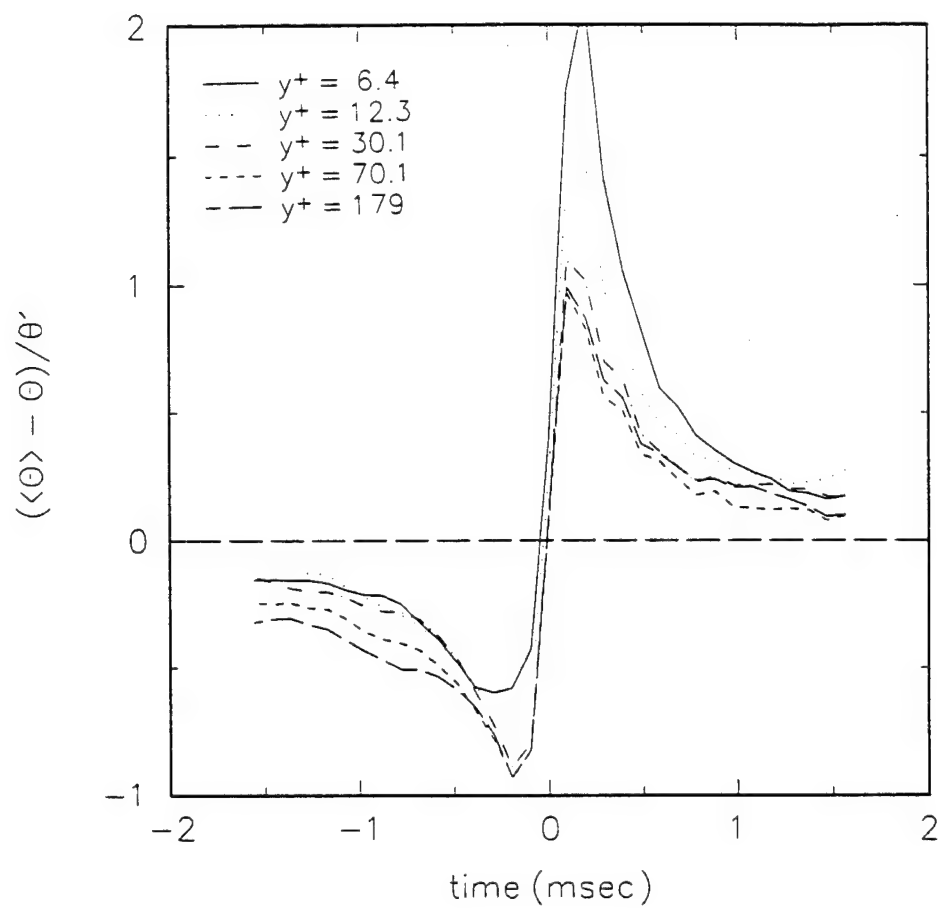


Figure 6.1b. Conditionally averaged temperature time records during a sweep/ejection event at several y locations across the boundary layer at station 1.

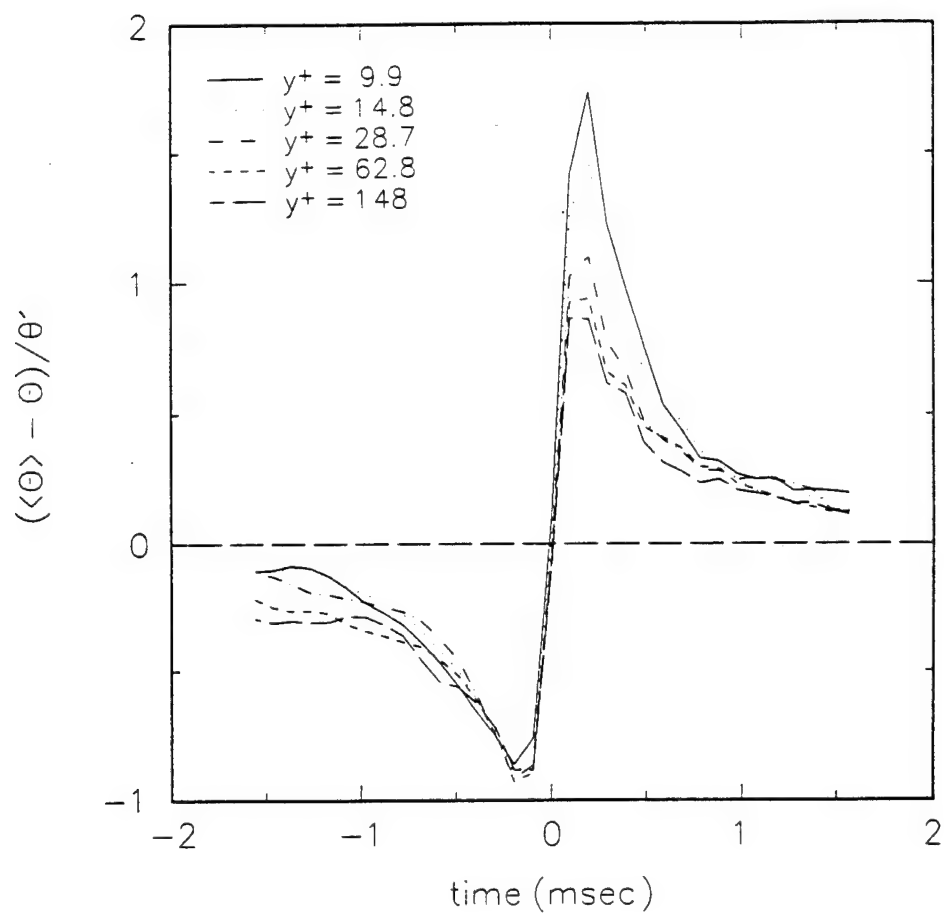


Figure 6.1c. Conditionally averaged temperature time records during a sweep/ejection event at several y locations across the boundary layer at station 2.

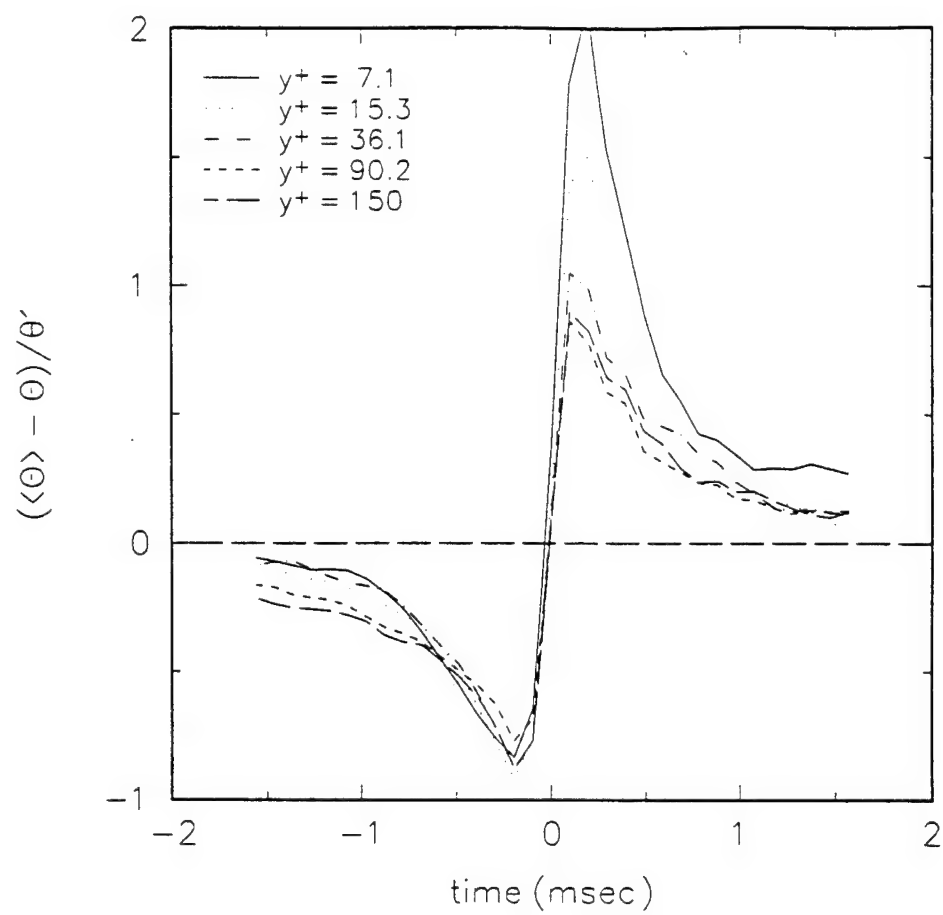


Figure 6.1d. Conditionally averaged temperature time records during a sweep/ejection event at several y locations across the boundary layer at station 3.

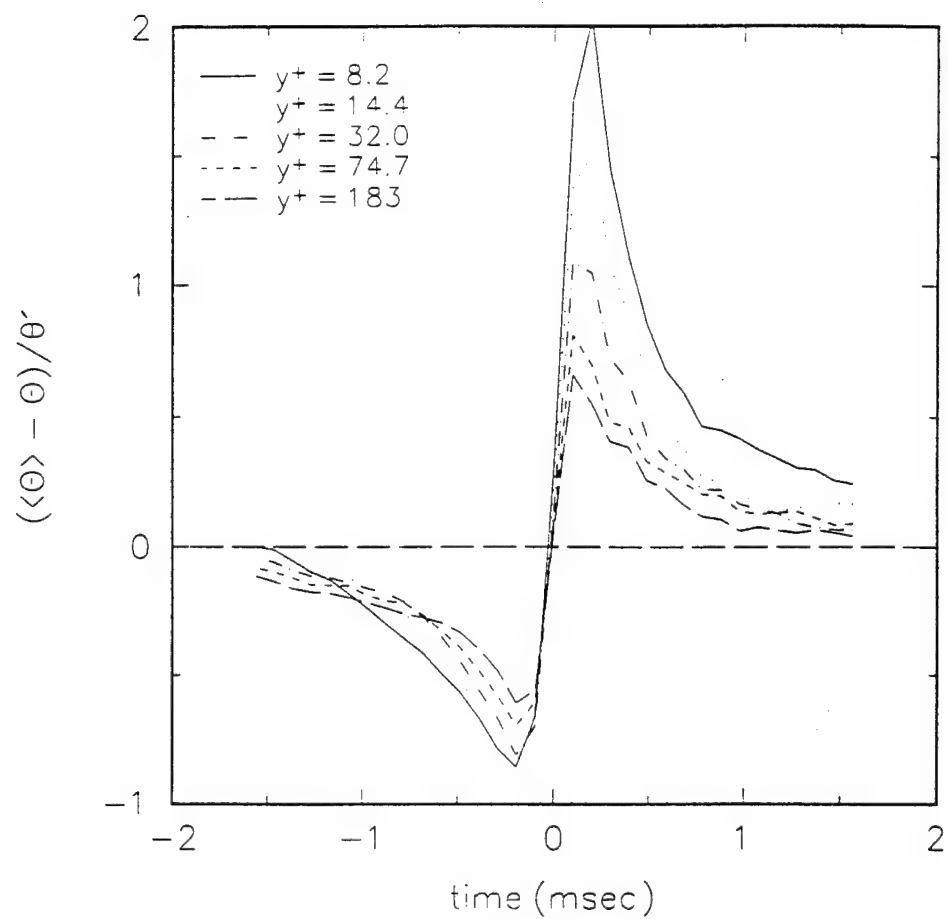


Figure 6.1e. Conditionally averaged temperature time records during a sweep/ejection event at several y locations across the boundary layer at station 4.

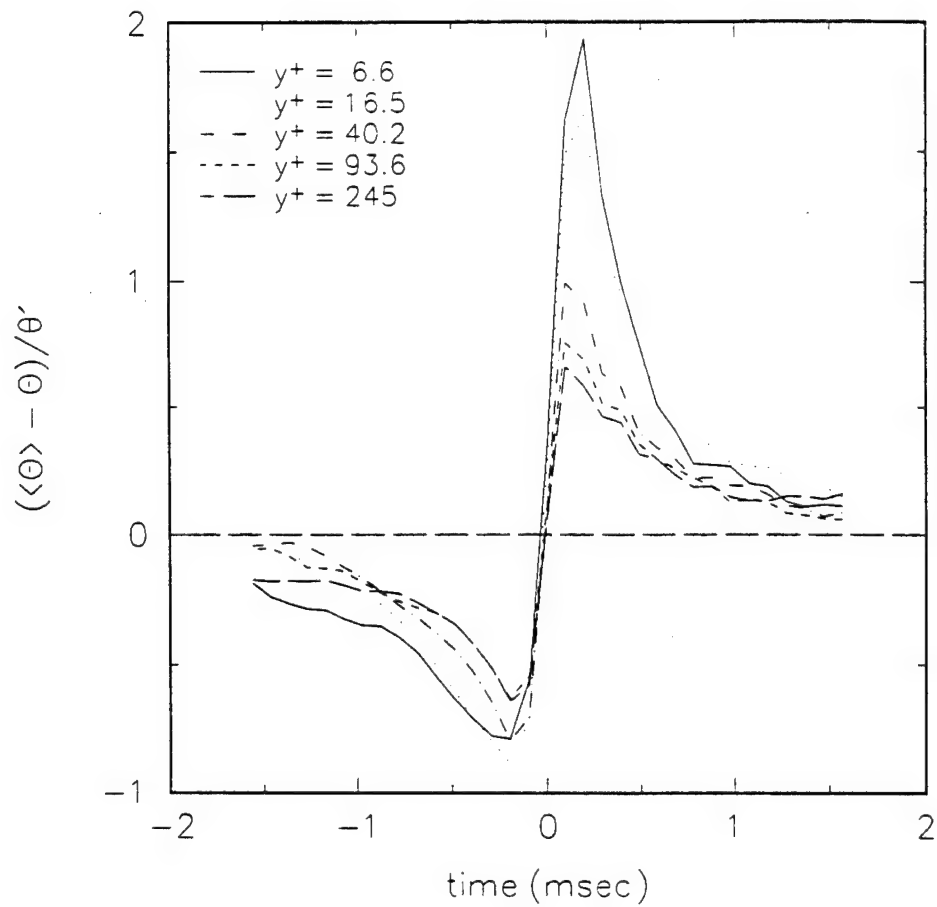


Figure 6.1f. Conditionally averaged temperature time records during a sweep/ejection event at several y locations across the boundary layer at station 5.

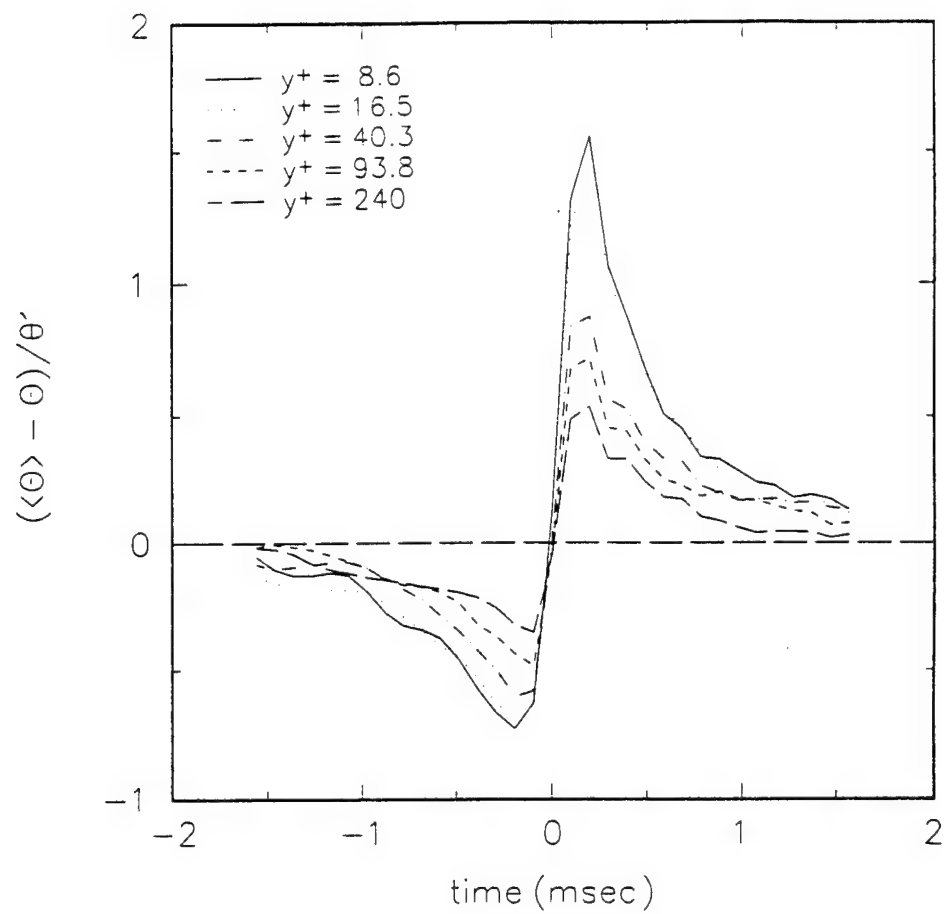


Figure 6.1g. Conditionally averaged temperature time records during a sweep/ejection event at several y locations across the boundary layer at station 6.

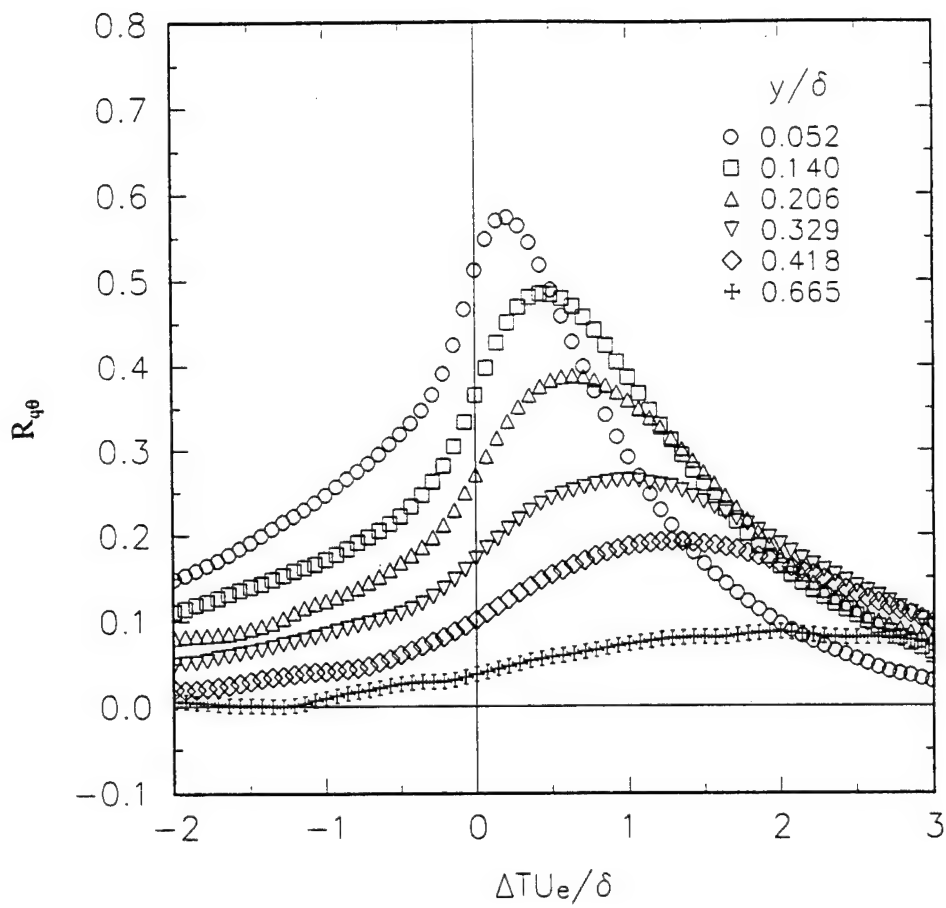


Figure 6.2a. Long-time average time-delayed correlation coefficient between surface heat flux and temperature at several y locations across the boundary layer at station 0.

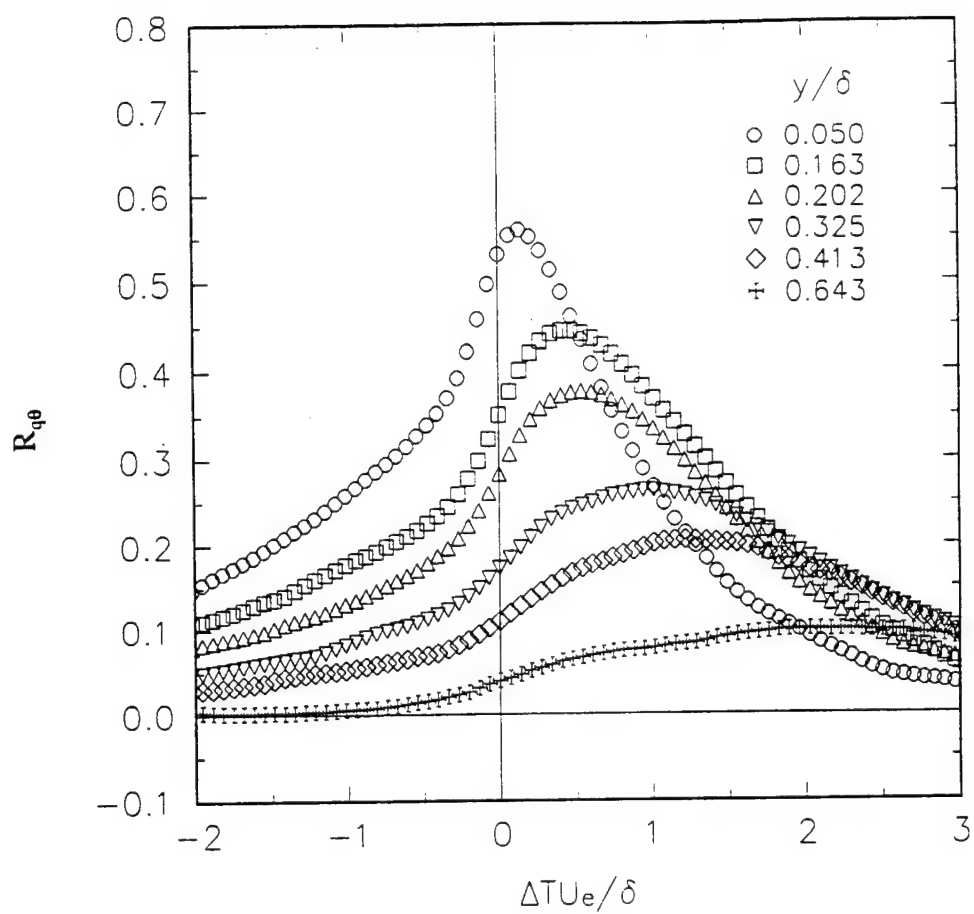


Figure 6.2b. Long-time average time-delayed correlation coefficient between surface heat flux and temperature at several y locations across the boundary layer at station 1.

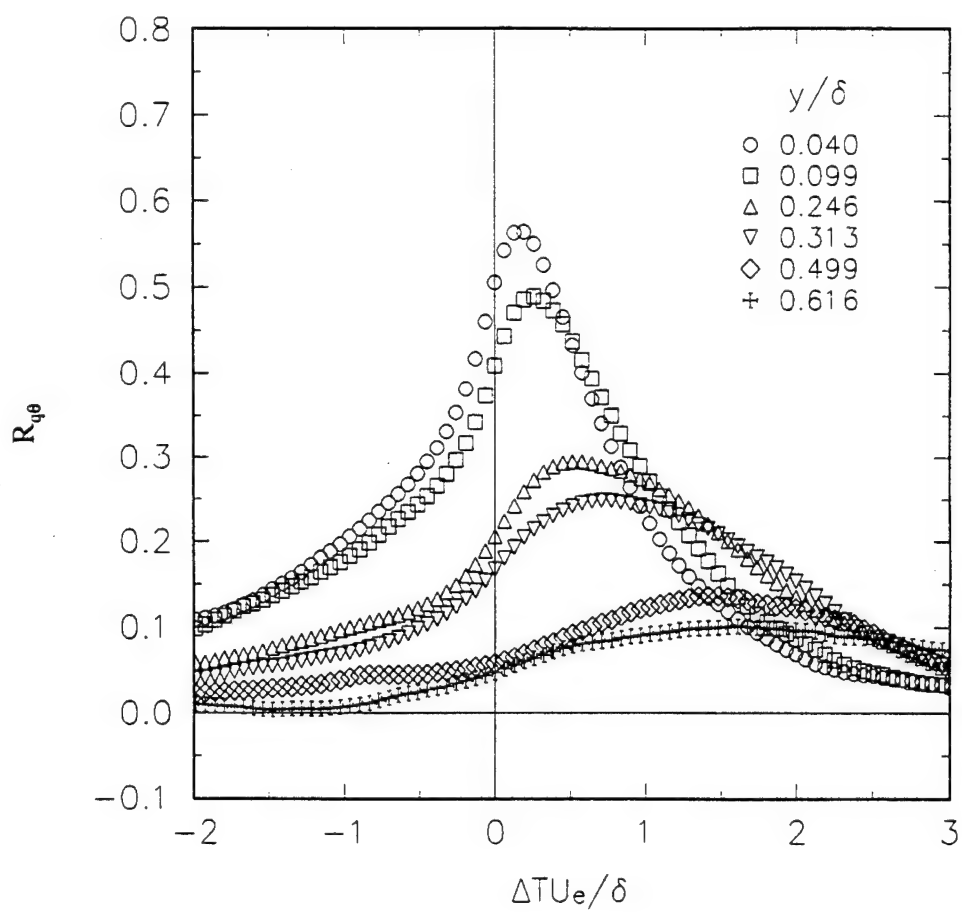


Figure 6.2c. Long-time average time-delayed correlation coefficient between surface heat flux and temperature at several y locations across the boundary layer at station 2.

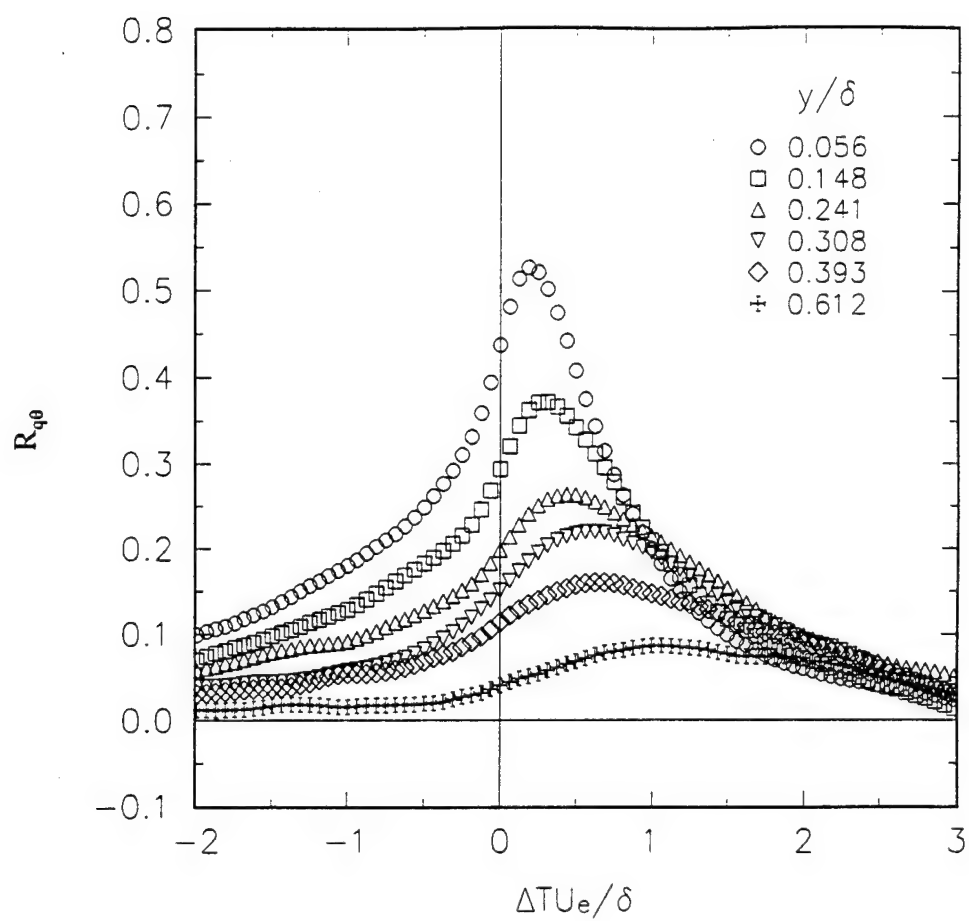


Figure 6.2d. Long-time average time-delayed correlation coefficient between surface heat flux and temperature at several y locations across the boundary layer at station 3.

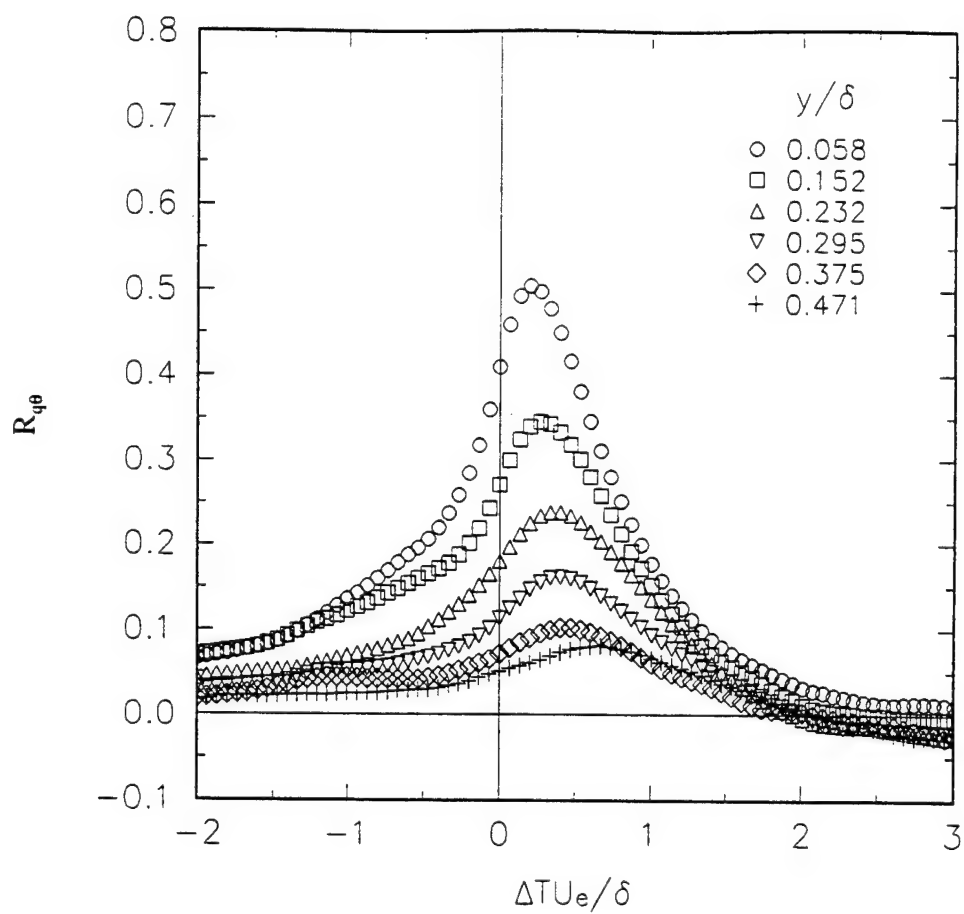


Figure 6.2e. Long-time average time-delayed correlation coefficient between surface heat flux and temperature at several y locations across the boundary layer at station 4.

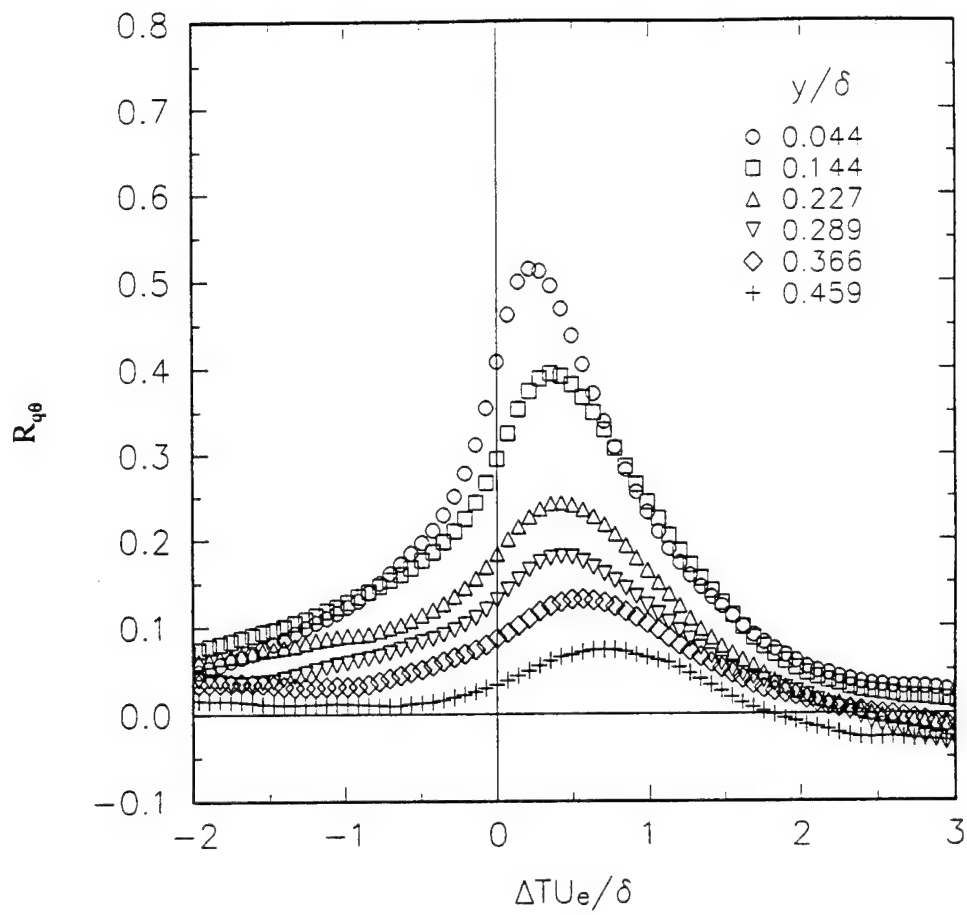


Figure 6.2f. Long-time average time-delayed correlation coefficient between surface heat flux and temperature at several y locations across the boundary layer at station 5.

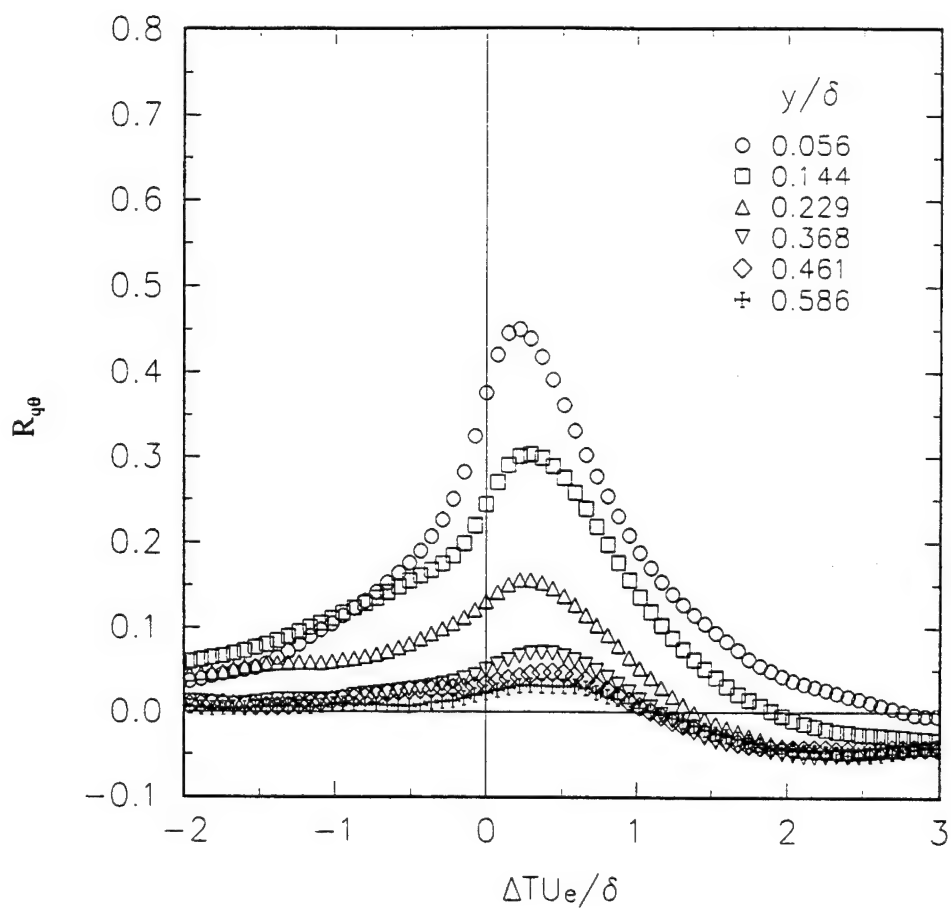


Figure 6.2g. Long-time average time-delayed correlation coefficient between surface heat flux and temperature at several y locations across the boundary layer at station 6.

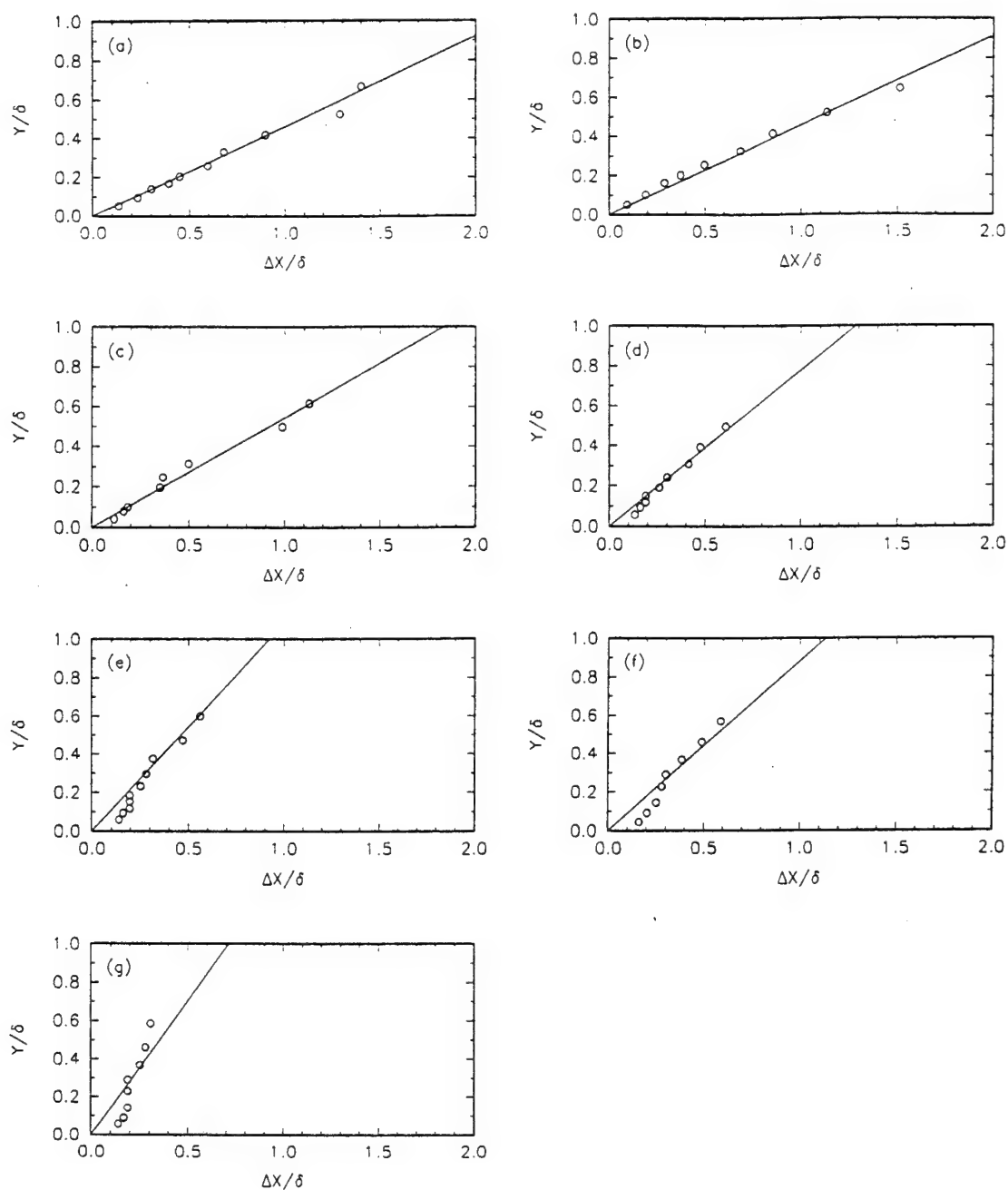


Figure 6.3. Time-averaged wavefronts in x-y plane constructed from time-delayed correlations of surface heat flux and temperature at station (a) 0; (b) 1; (c) 2; (d) 3; (e) 4; (f) 5; and (g) 6.

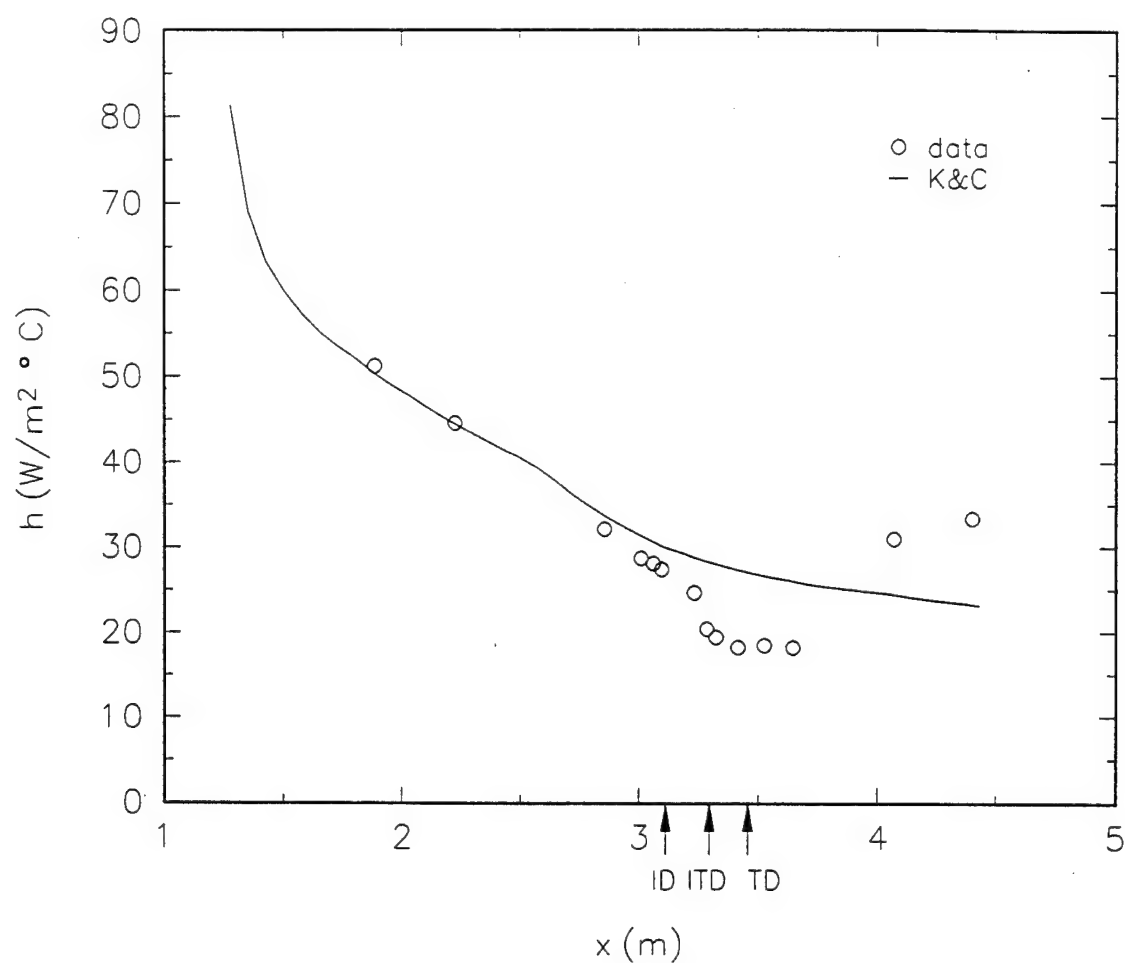


Fig. 7.1. Mean heat transfer coefficient in two-dimensional separating turbulent boundary layer. Solid line is from integral method of Kays and Crawford (1980). ID, location of *incipient detachment*; ITD, location of *intermittent transitory detachment*; TD, location of *transitory detachment*.

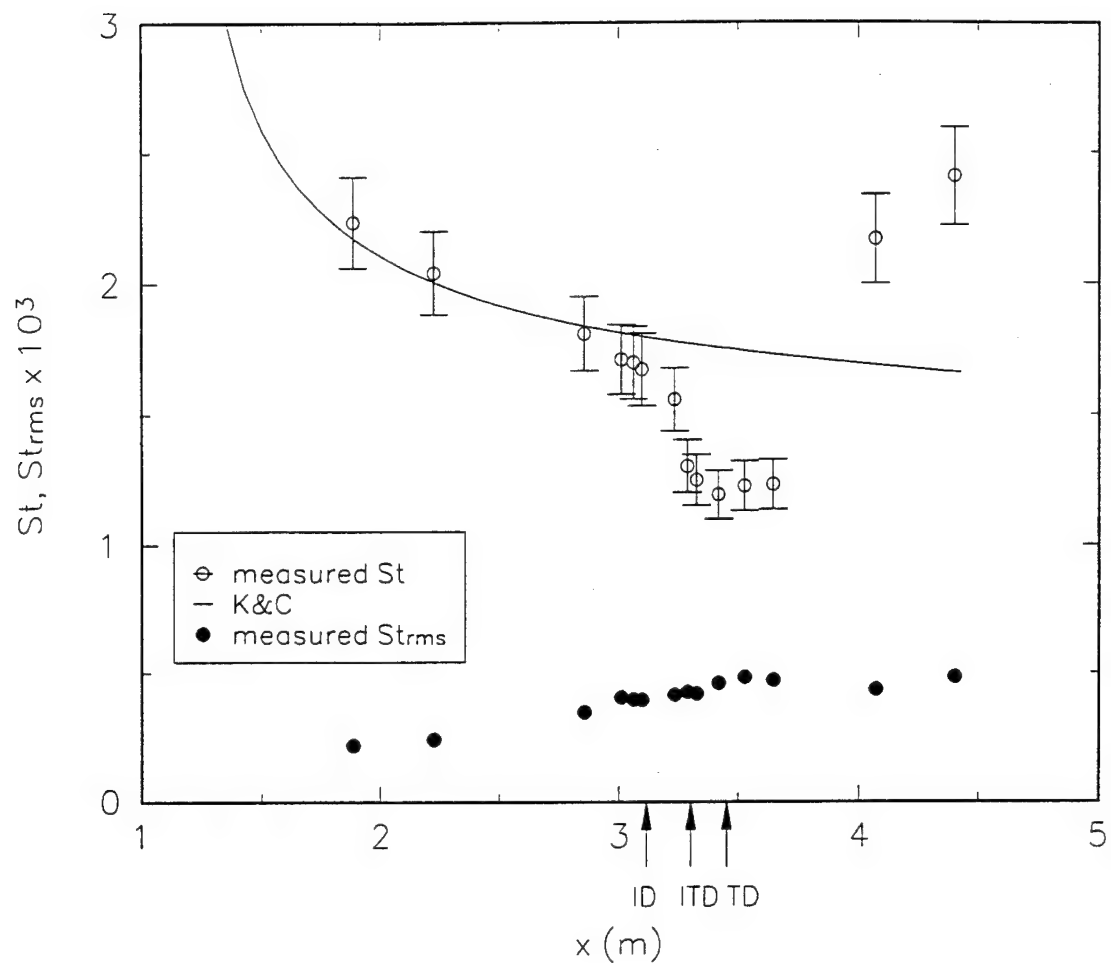


Fig. 7.2. Mean and rms Stanton numbers in the two-dimensional separating turbulent boundary layer. Solid line is from integral method of Kays and Crawford (1980). ID, location of *incipient detachment*; ITD, location of *intermittent transitory detachment*; TD, location of *transitory detachment*.

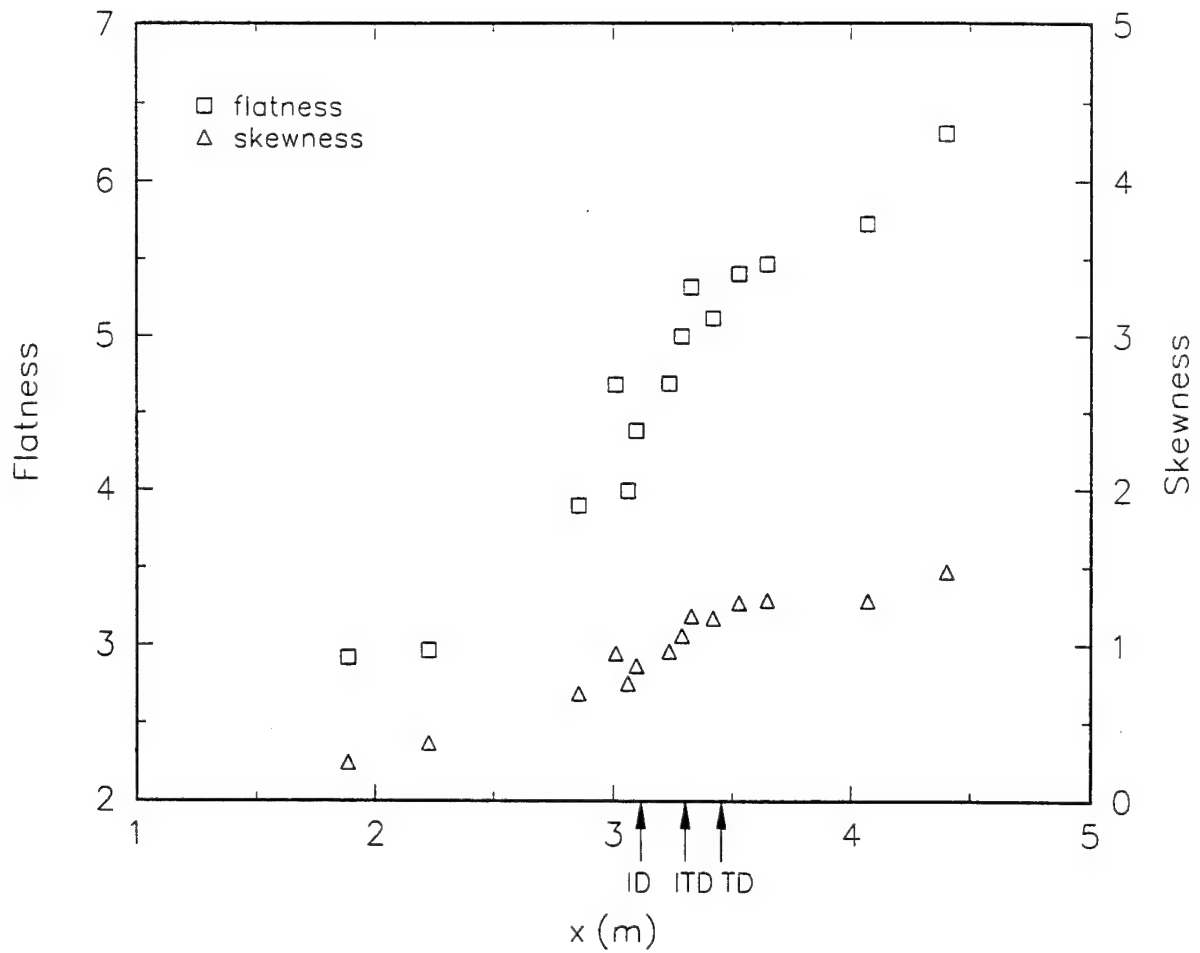


Fig. 7.3. Skewness and flatness factors of surface heat flux fluctuations in two-dimensional separating turbulent boundary layer. ID, location of *incipient detachment*; ITD, location of *intermittent transitory detachment*; TD, location of *transitory detachment*.

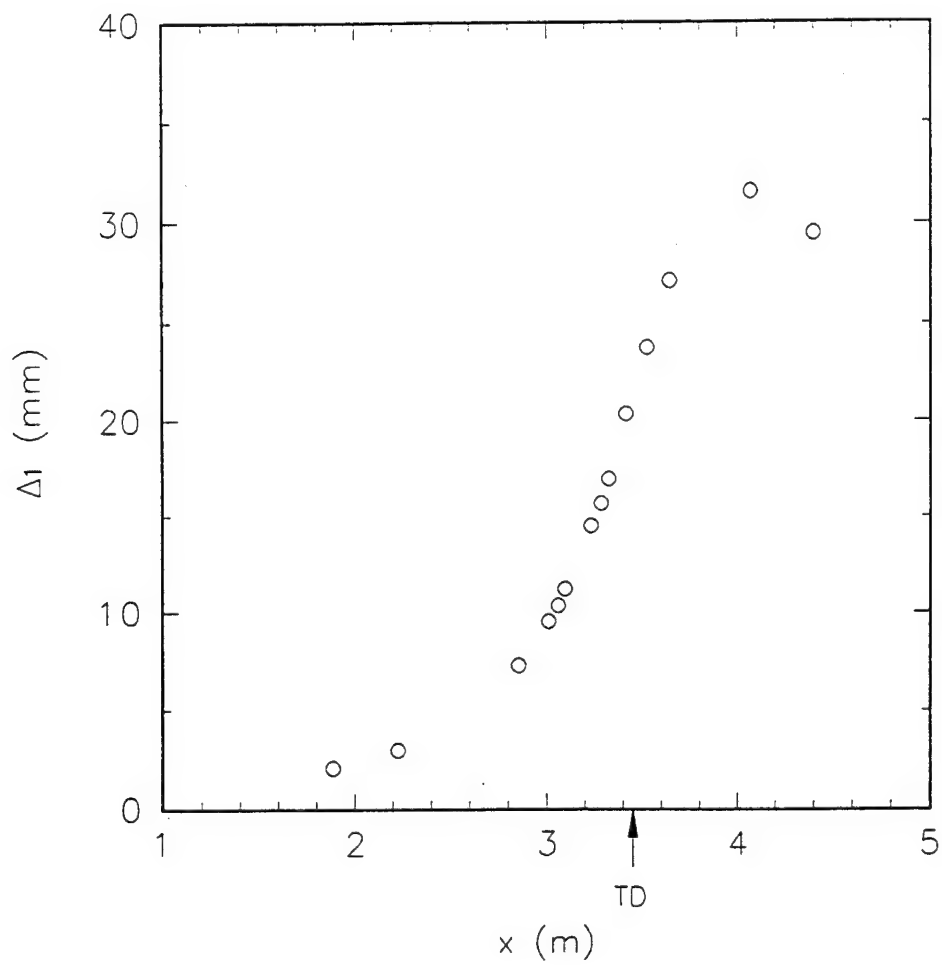


Fig. 7.4. Streamwise variation of length scale Δ_1 in two-dimensional separating turbulent boundary layer. TD is location of *transitory detachment*.

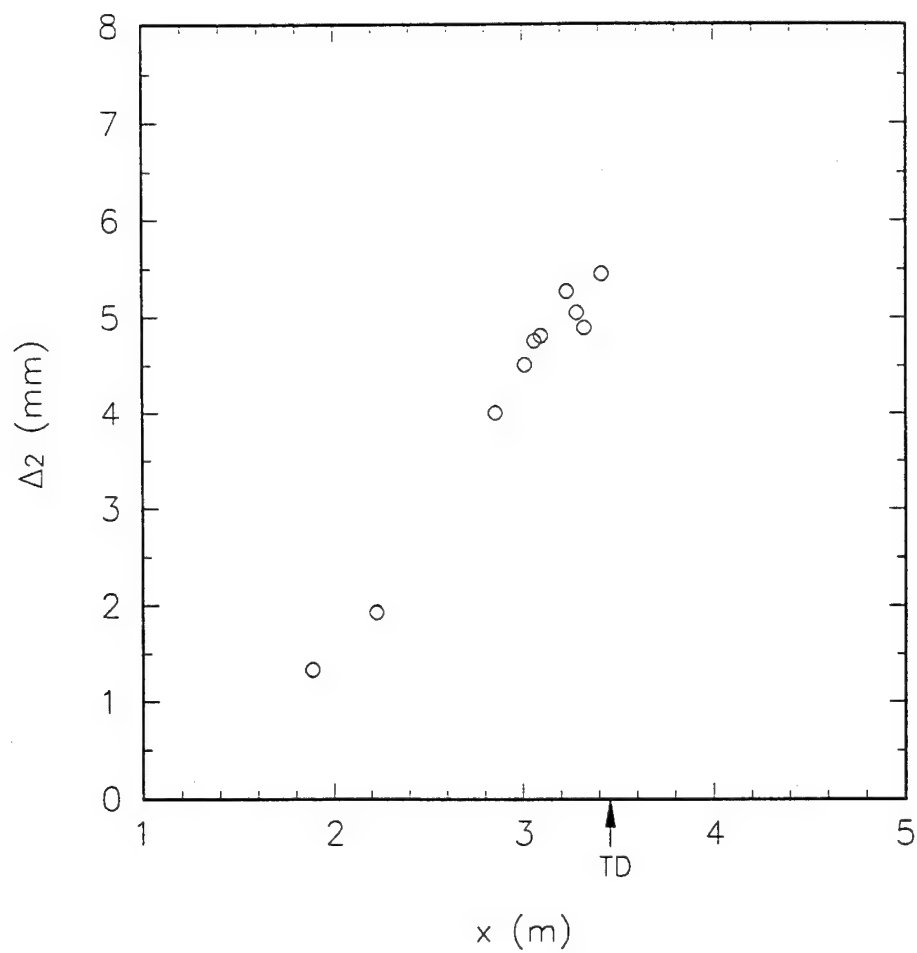


Fig. 7.5. Streamwise variation of enthalpy thickness upstream of detachment in two-dimensional separating turbulent boundary layer. TD is location of *transitory detachment*.

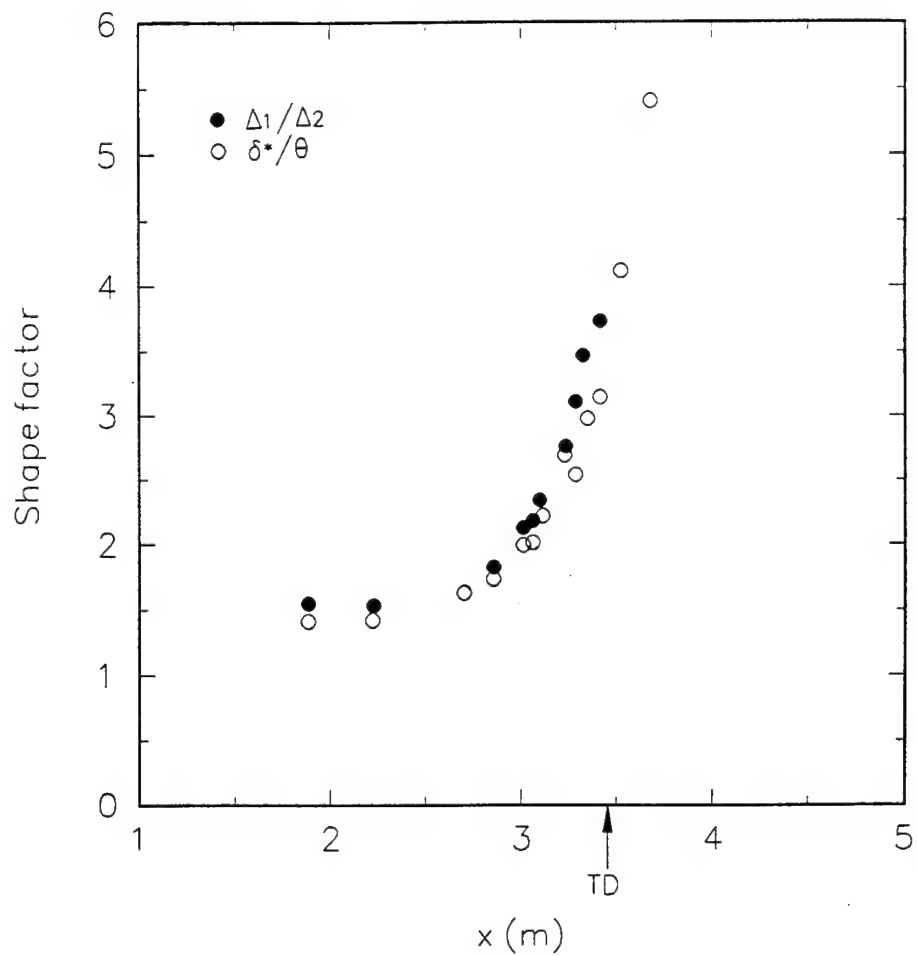


Fig. 7.6 Comparison of streamwise variation of temperature profile shape factor with velocity profile shape factor in two-dimensional separating turbulent boundary layer. TD is location of *transitory detachment*.

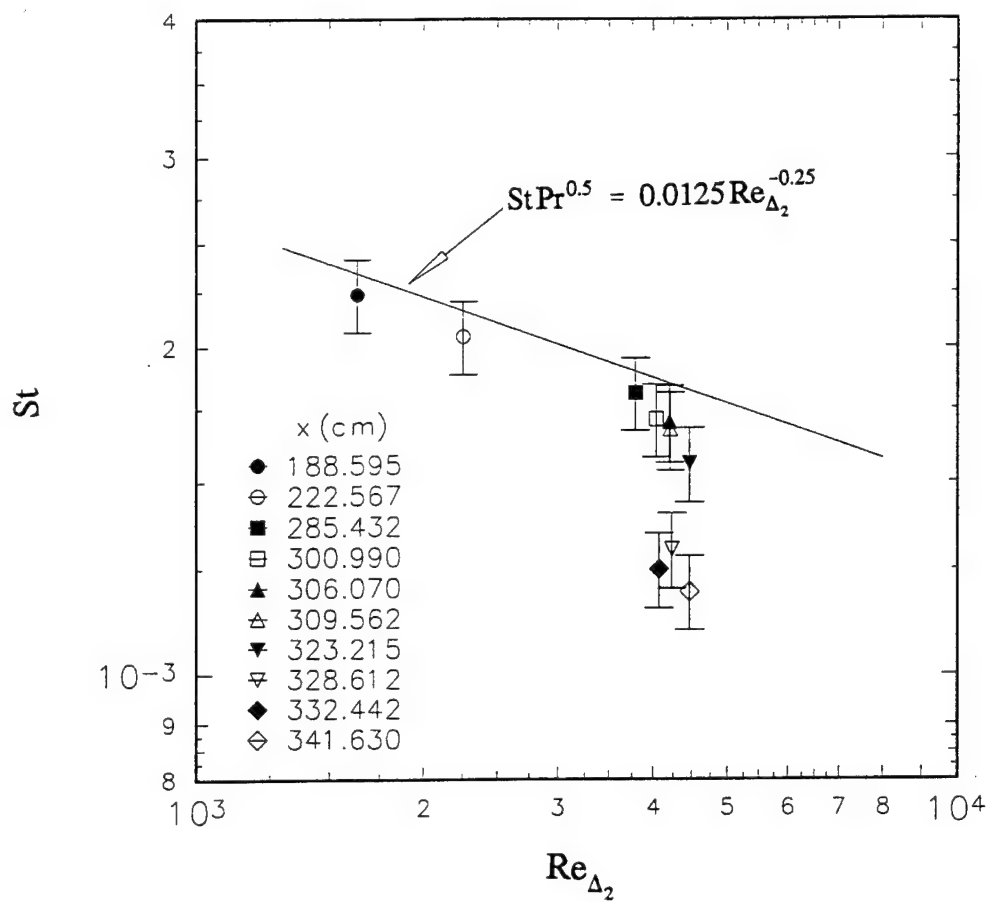


Fig. 7.7. Stanton number versus enthalpy thickness Reynolds number upstream of detachment. Solid line is correlation of Kays and Crawford (1980).

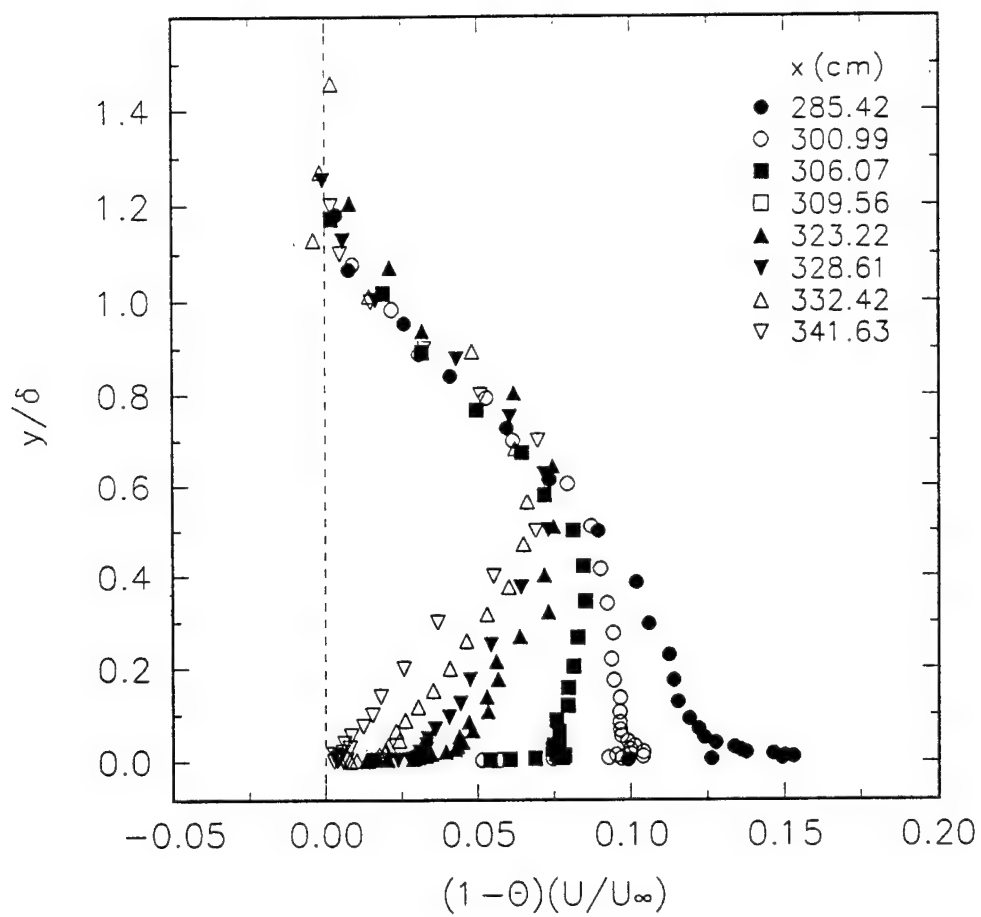


Fig. 7.8. Profiles of the integrand of the enthalpy thickness.

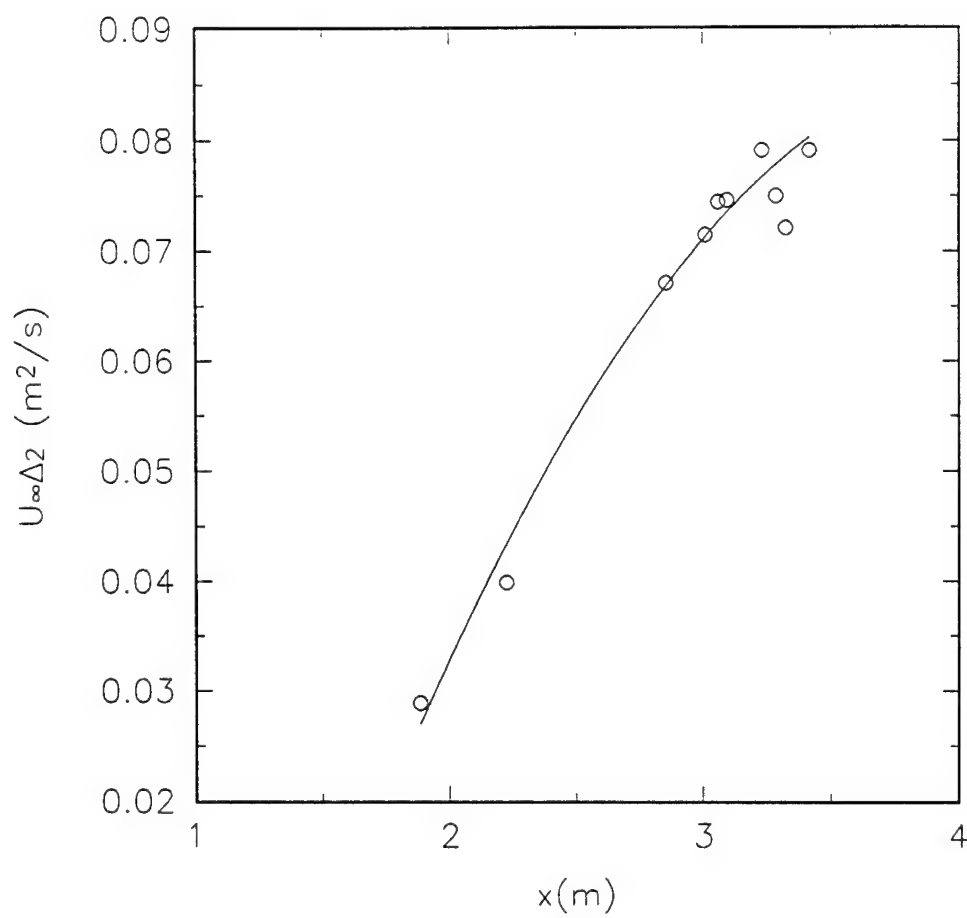


Fig. 7.9. Streamwise variation of the product of enthalpy thickness and free-stream velocity upstream of detachment. Solid line is polynomial least-squares curve fit.

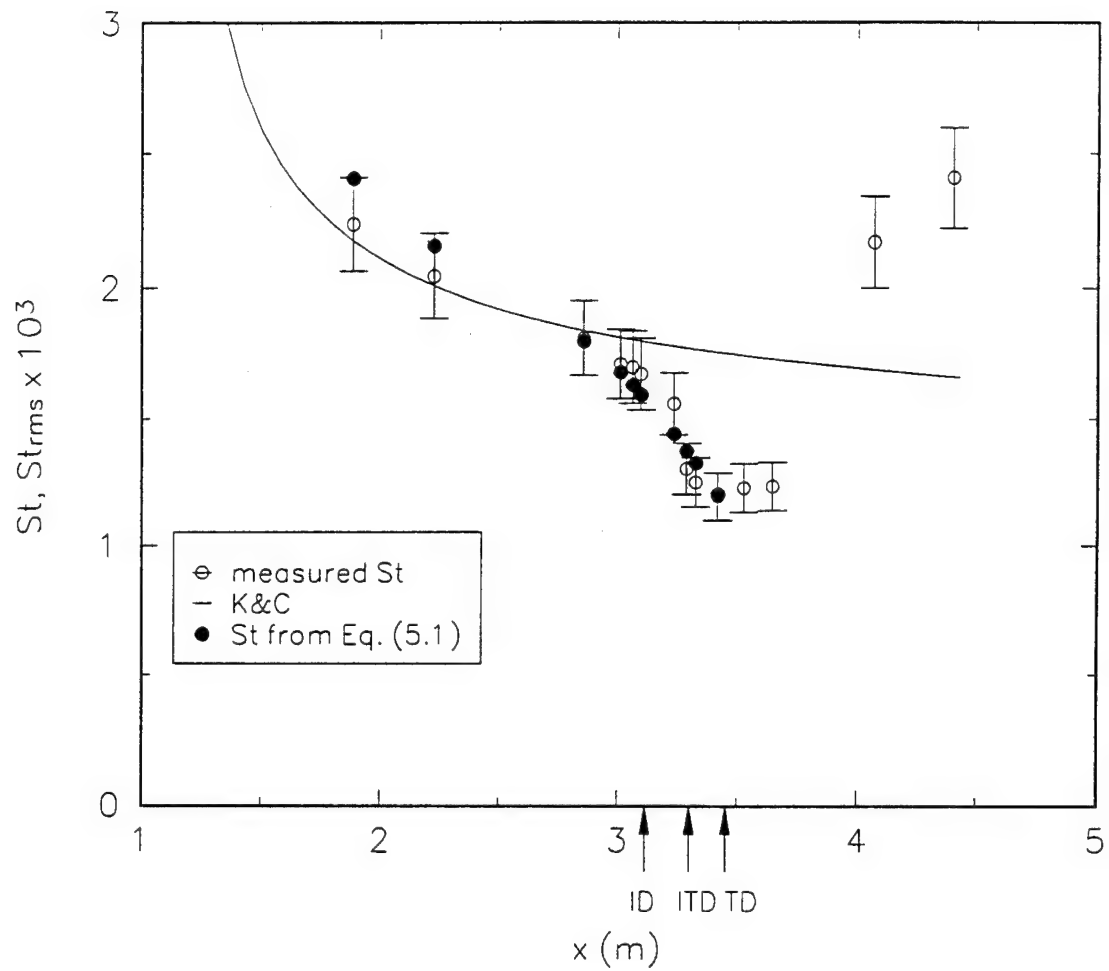


Fig. 7.10. Comparison of directly measured Stanton numbers with Stanton numbers computed from integral energy equation, Eq. (7.5). Solid line is from integral method of Kays and Crawford (1980). ID, location of *incipient detachment*; ITD, location of *intermittent transitory detachment*; TD, location of *transitory detachment*.

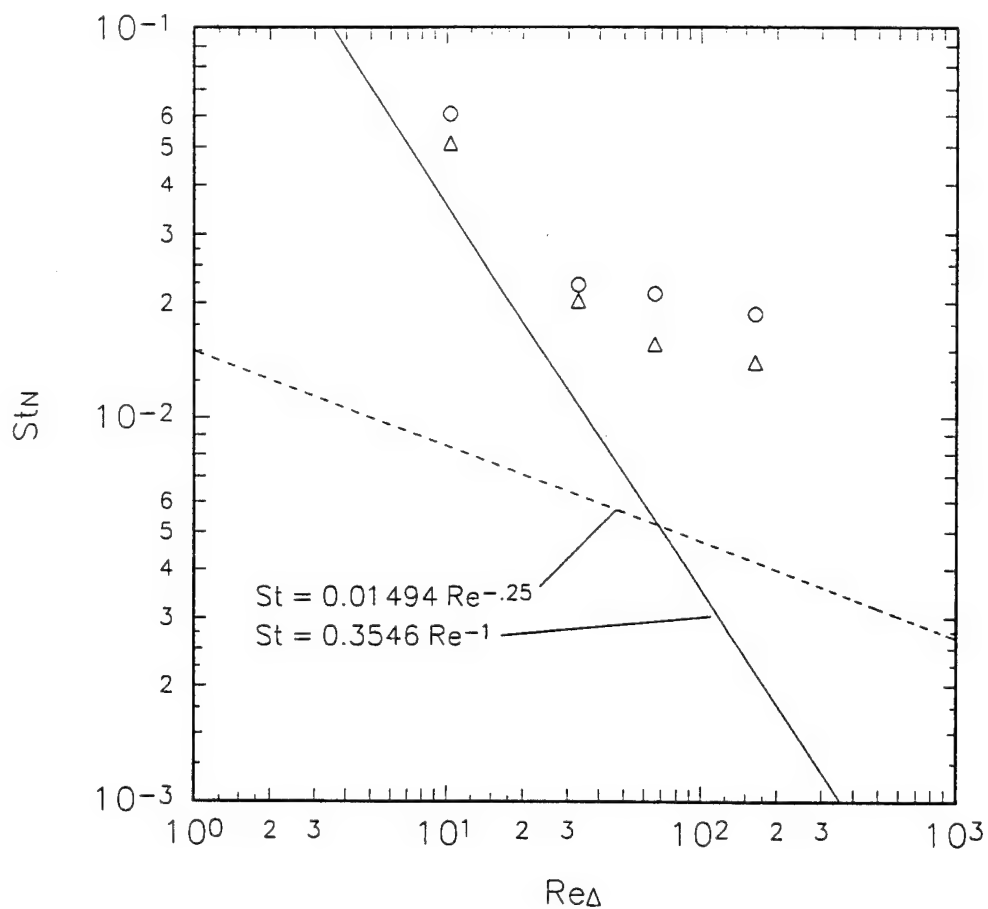


Fig. 7.11. Backflow Stanton number versus backflow enthalpy thickness Reynolds number downstream of detachment. Solid line is laminar correlation. Dashed line is turbulent correlation, Eq. (7.4) (Kays and Crawford, 1980). \circ measured St_N ; Δ St_N from St' correlation (Maciejewski and Moffat, 1992).

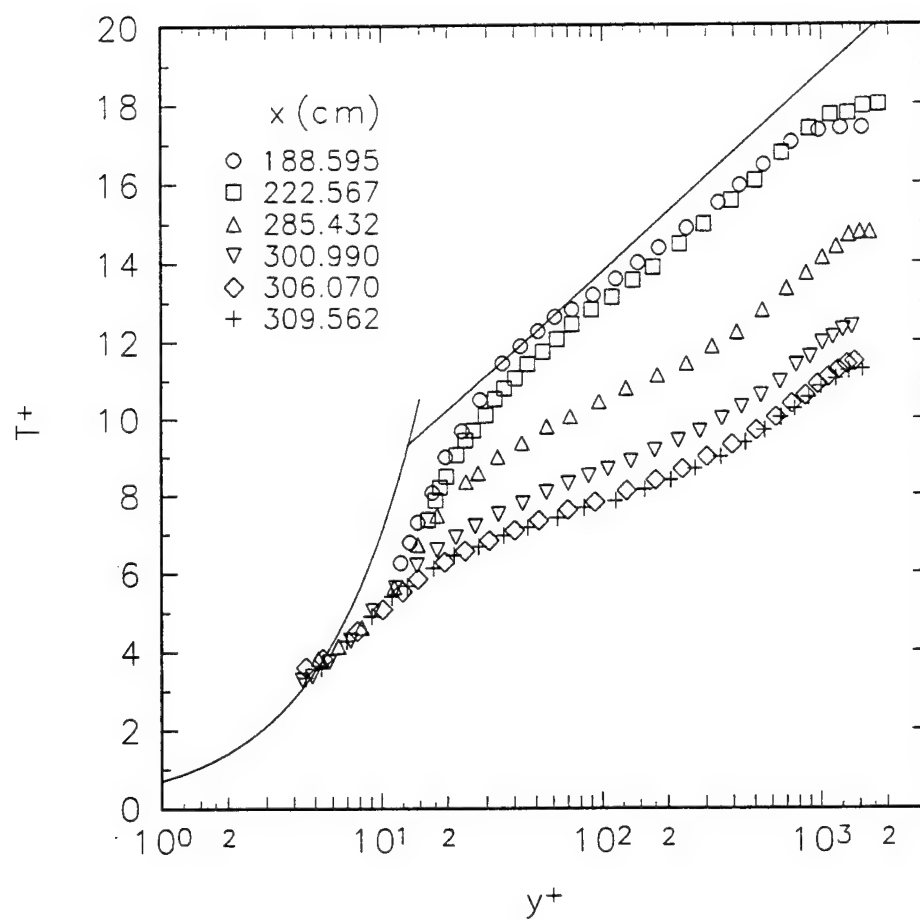


Fig. 7.12. Temperature profiles upstream of *incipient detachment* in conventional wall-law coordinates.

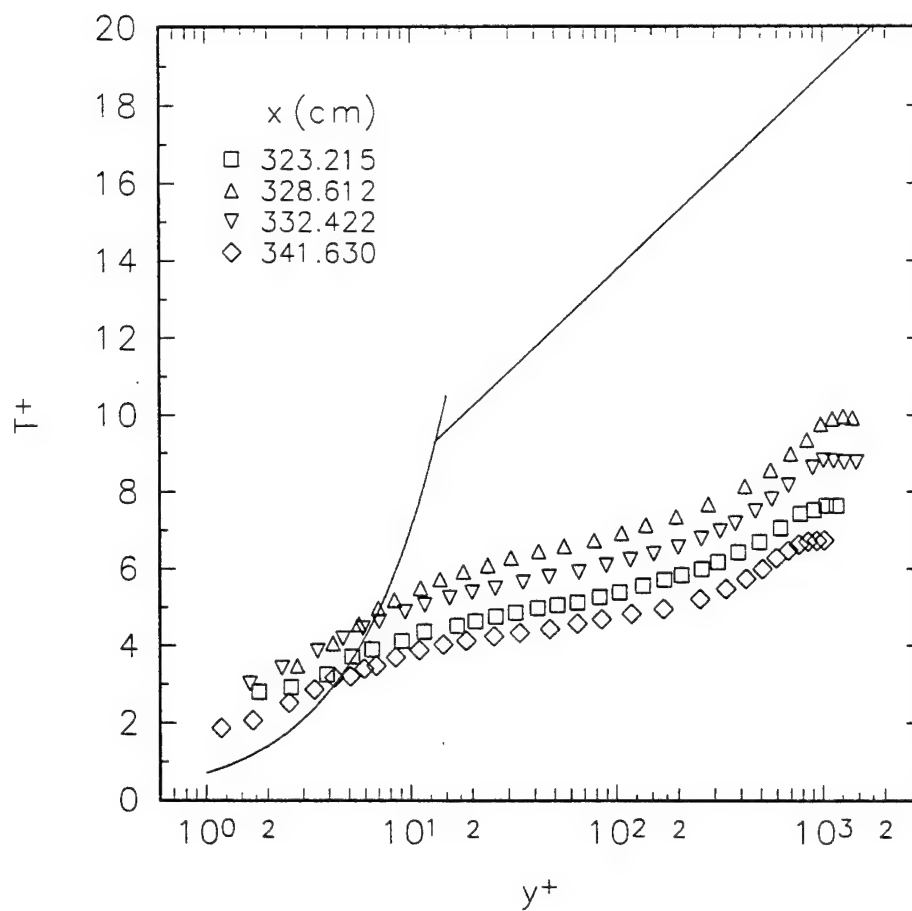


Fig. 7.13. Temperature profiles in the region between *incipient detachment* and detachment in conventional wall-law coordinates.

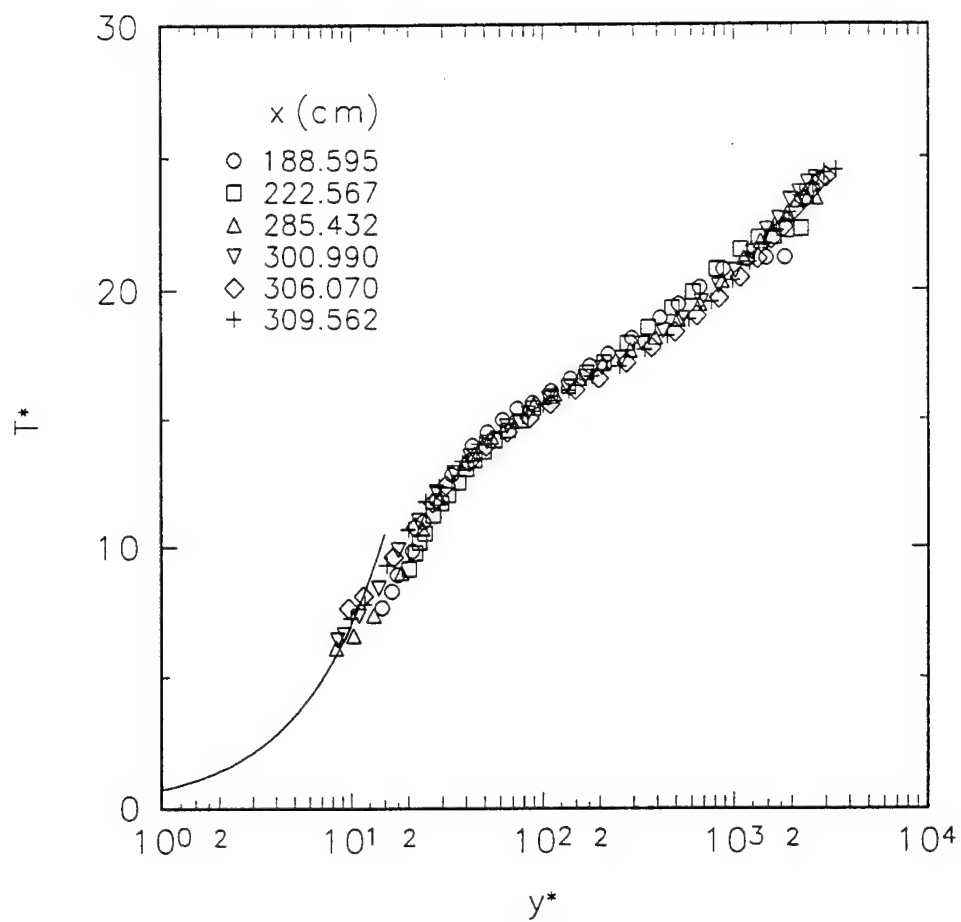


Fig. 7.14. Temperature profiles upstream of *incipient detachment* in wall-law coordinates proposed by Blackwell et al. (1972).

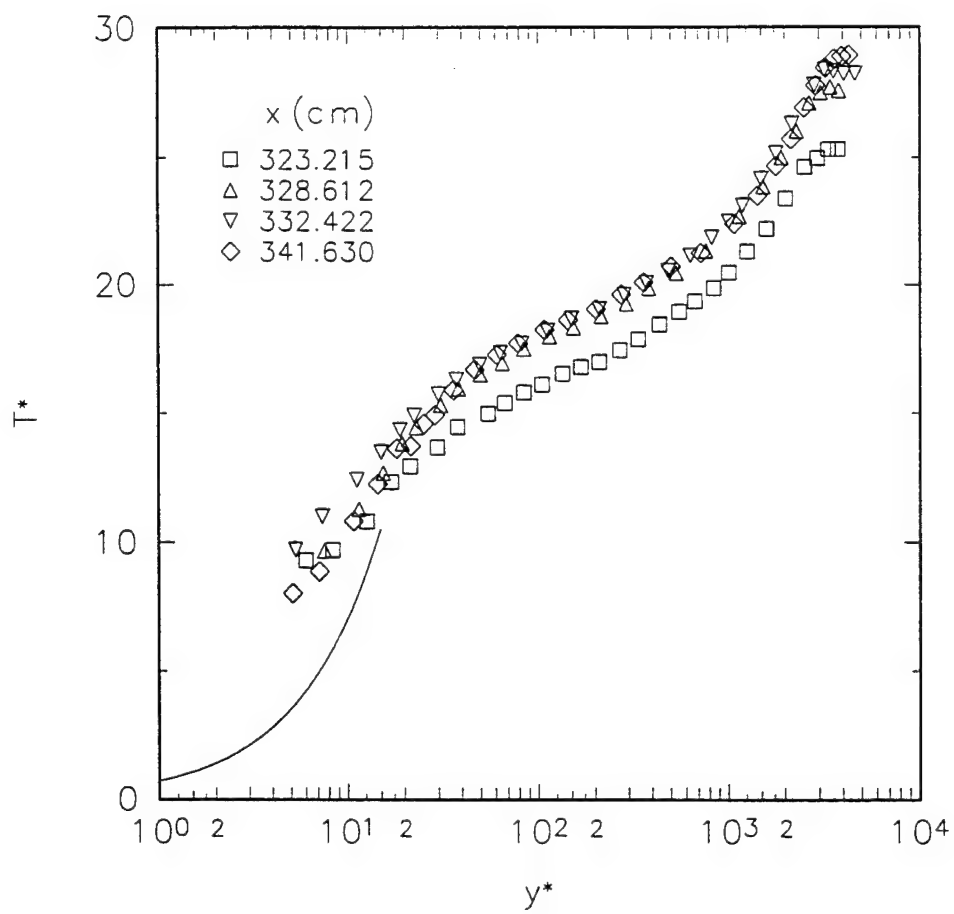


Fig. 7.15. Temperature profiles in the region between *incipient detachment* and detachment in wall-law coordinates proposed by Blackwell et al. (1972).

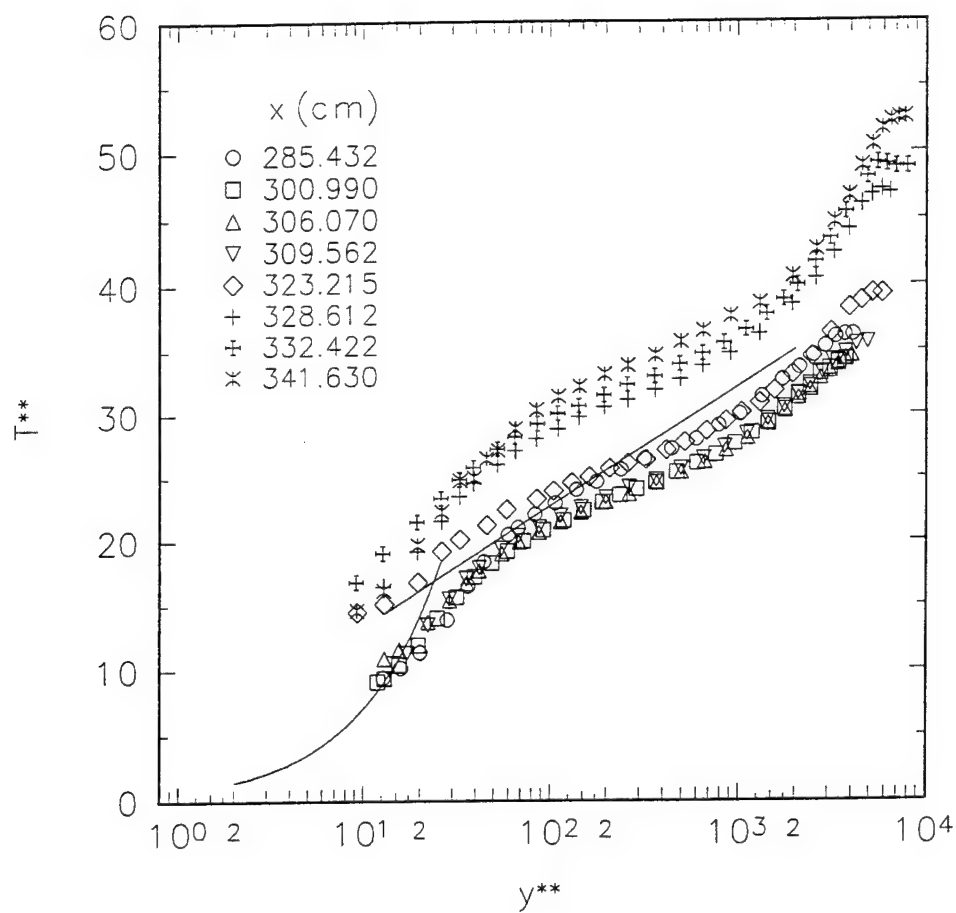


Fig. 7.16. Temperature profiles upstream of detachment in wall-law coordinates based on the near-wall value of turbulent kinetic energy. See Eq. (7.19).

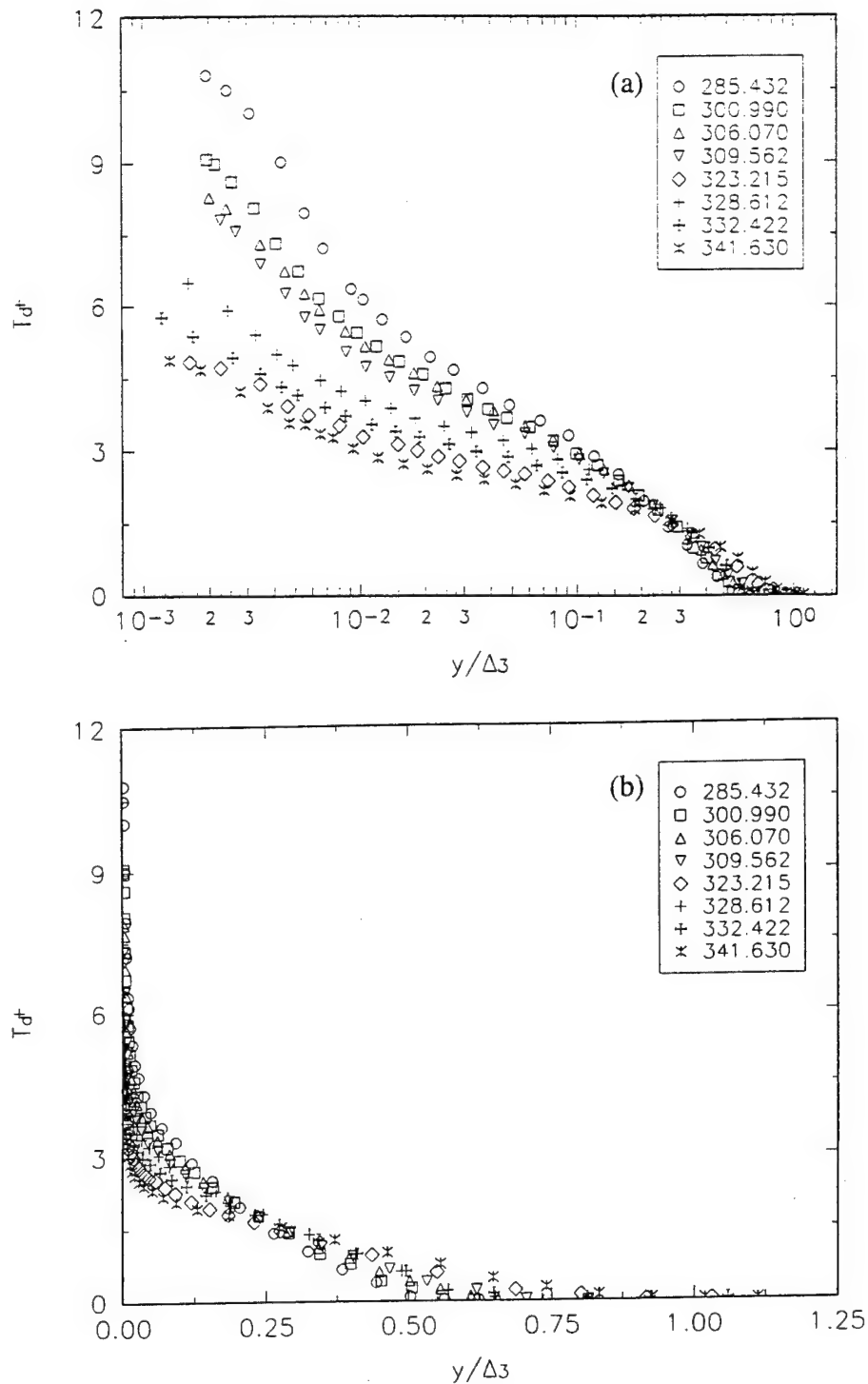


Fig. 7.17. Temperature defect profiles upstream of detachment in conventional temperature-defect coordinates. (See Eq. (7.20)). (a) semi-logarithmic axis; (b) linear axis.

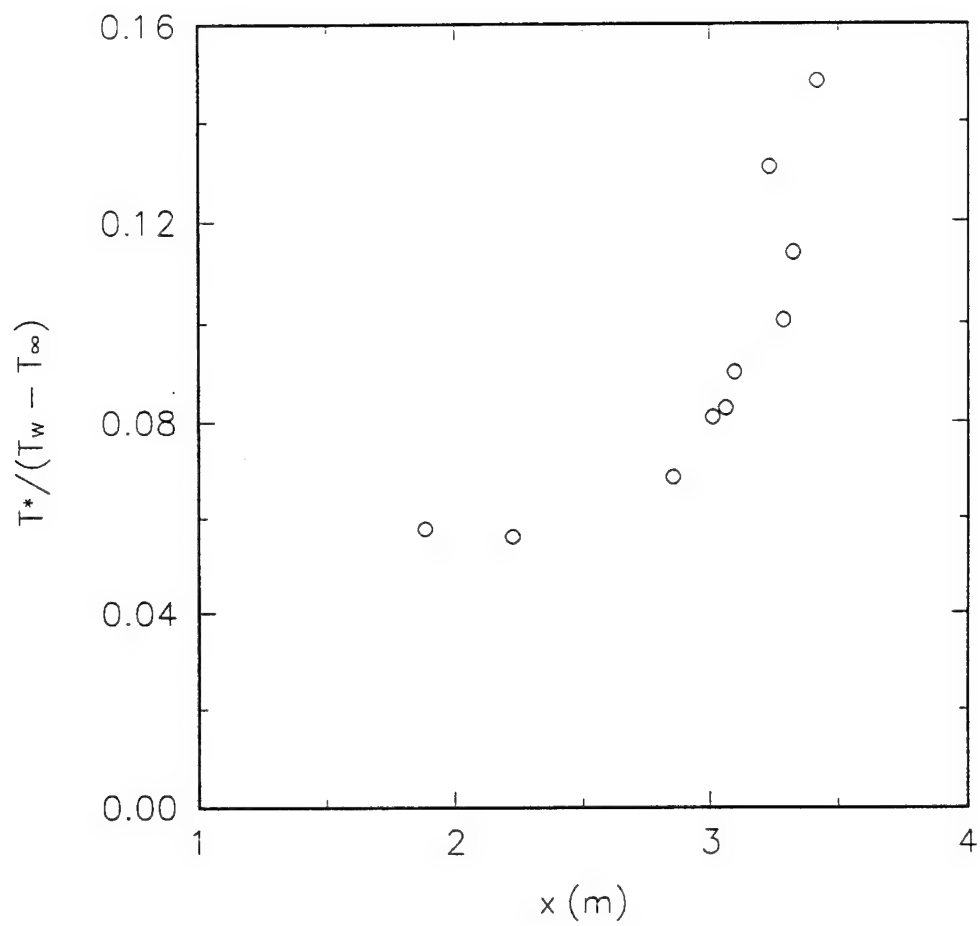


Fig. 7.18. Streamwise variation of temperature scale $T^*/(T_w - T_\infty) = St/(C_p/2)^{1/2}$ used in conventional defect law upstream of detachment.

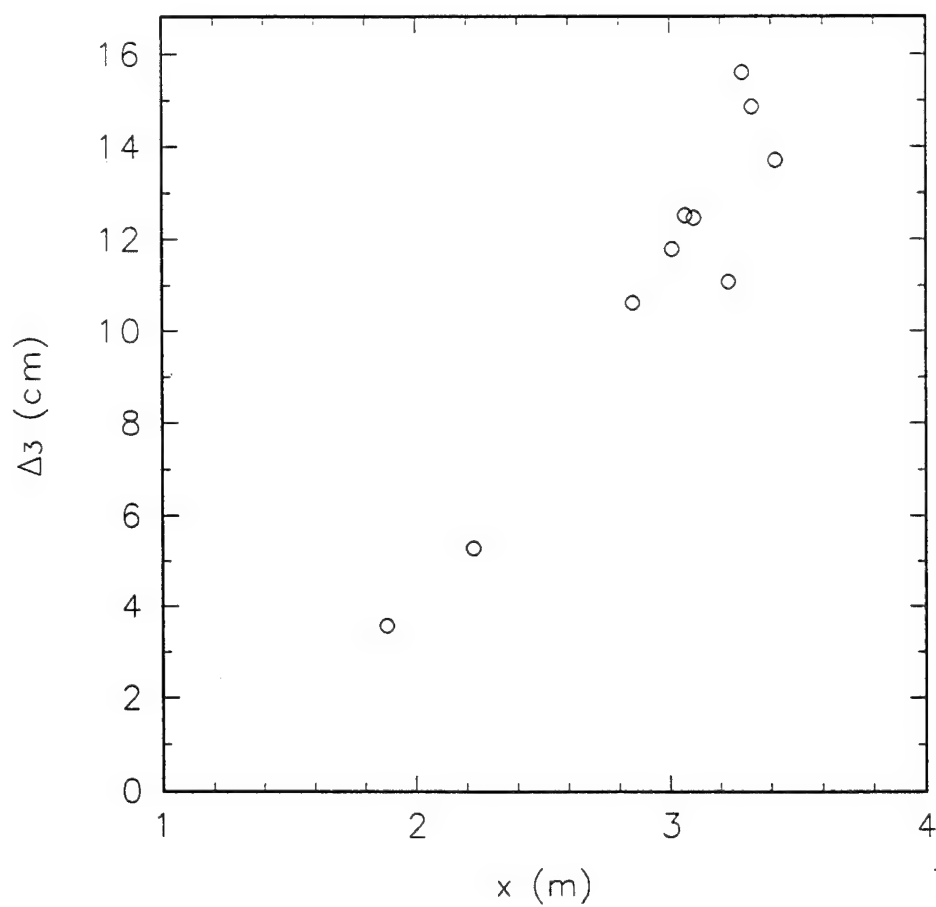


Fig. 7.19. Streamwise variation of length scale Δ_3 upstream of detachment.

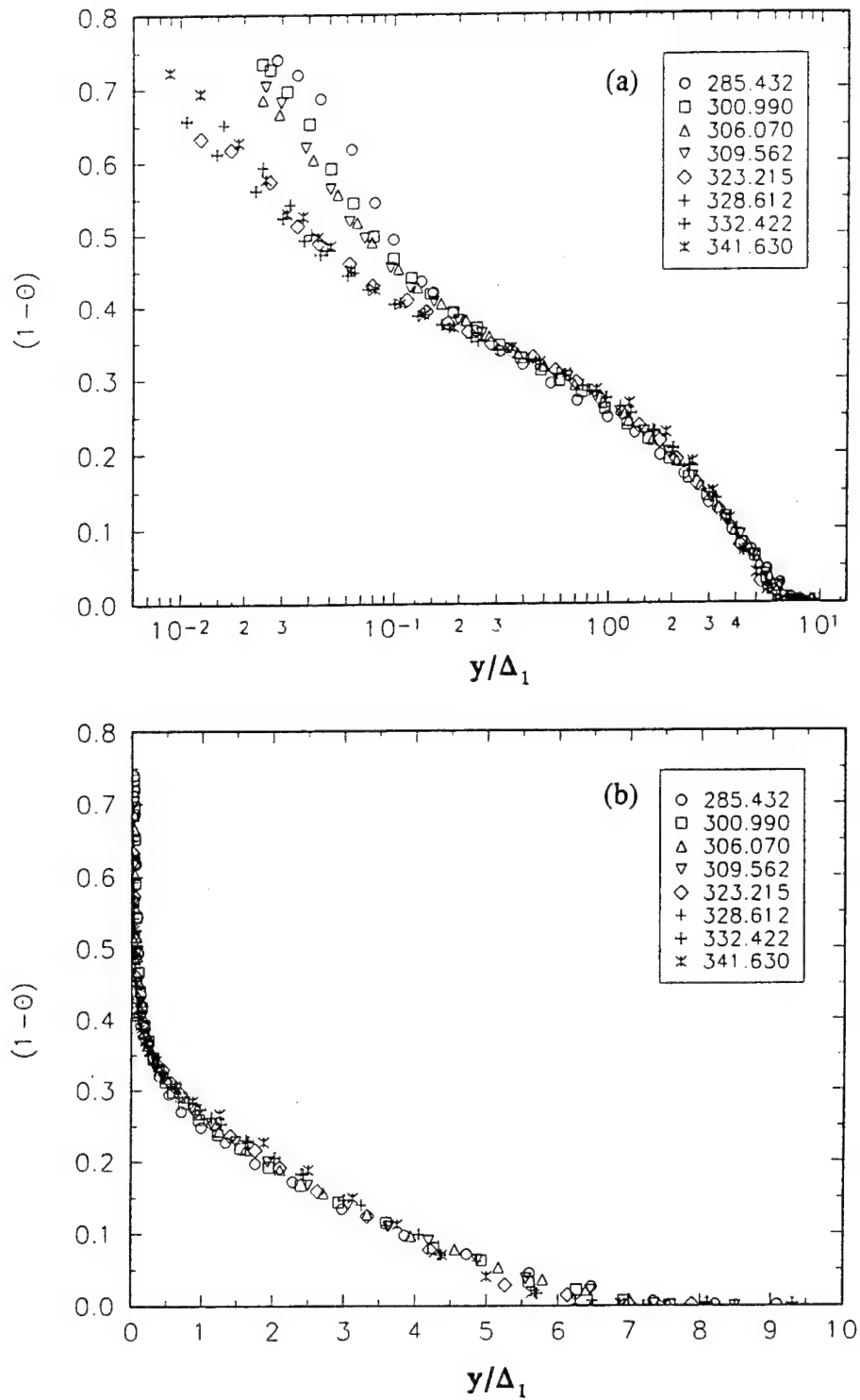


Fig. 7.20. Temperature defect profiles upstream of detachment in modified temperature-defect coordinates. (a) semi-logarithmic axis; (b) linear axis.

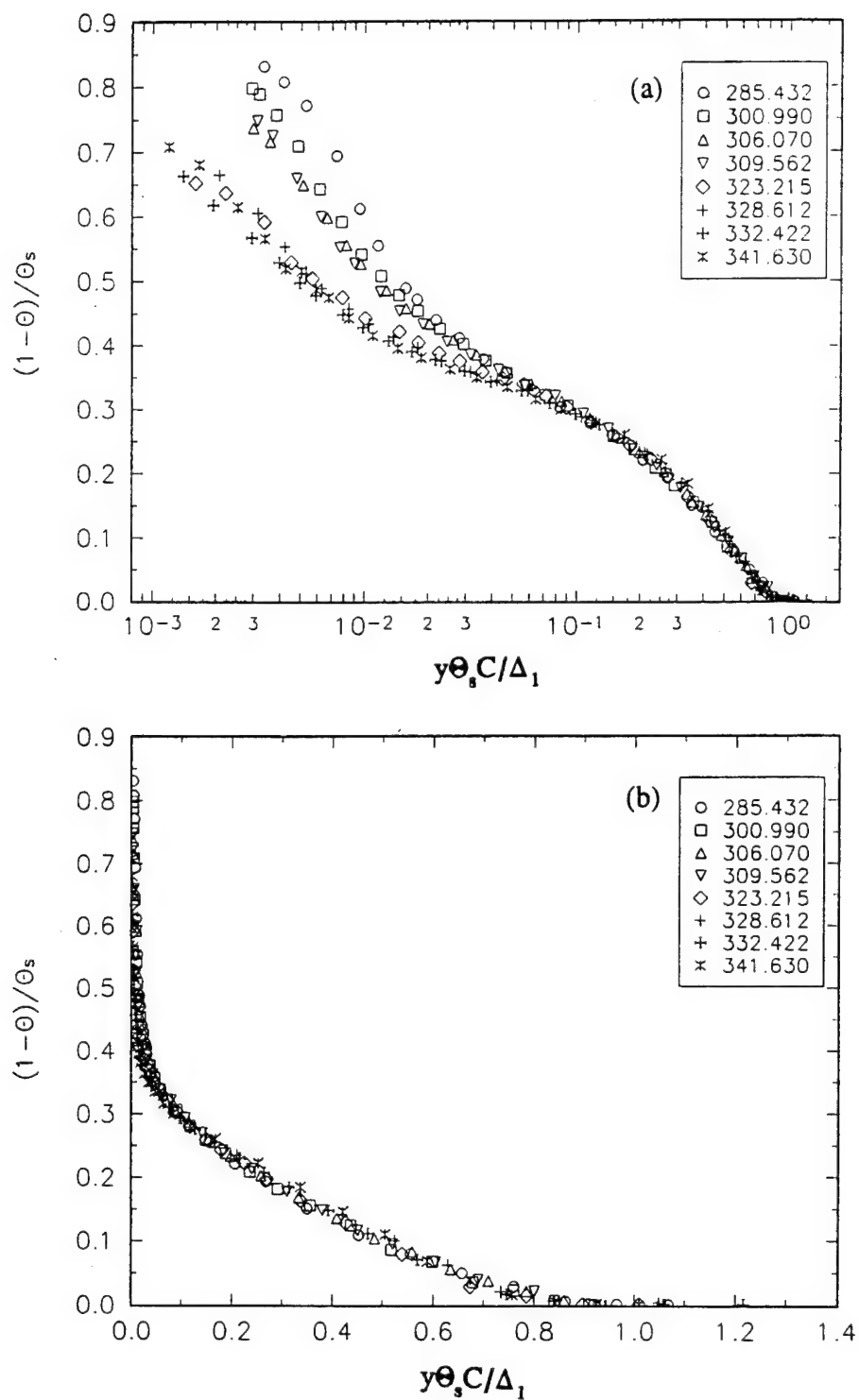


Fig. 7.21. Temperature defect profiles upstream of detachment in Perry-Schofield coordinates. (See Eq. (7.23)). (a) semi-logarithmic axis; (b) linear axis.

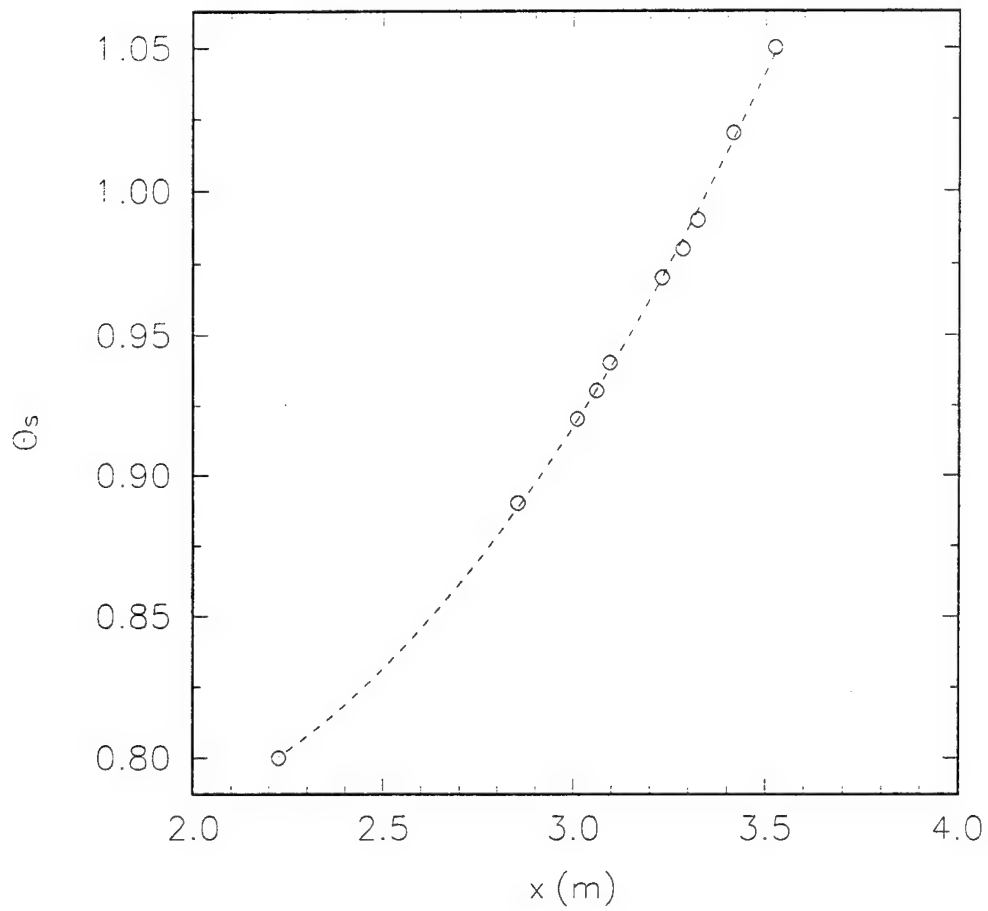


Fig. 7.22. Streamwise variation of temperature scale Θ_s used in Eq. (5.23) upstream of detachment.

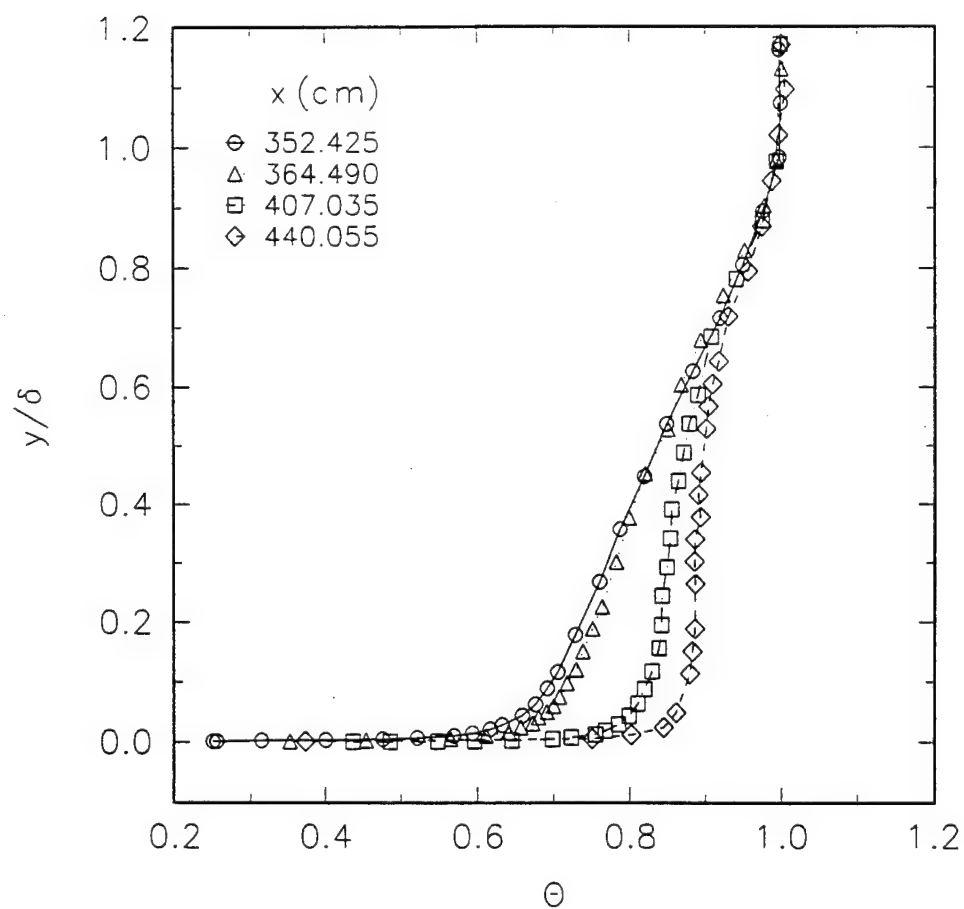


Fig. 7.23. Temperature profiles downstream of detachment plotted in outer variables.

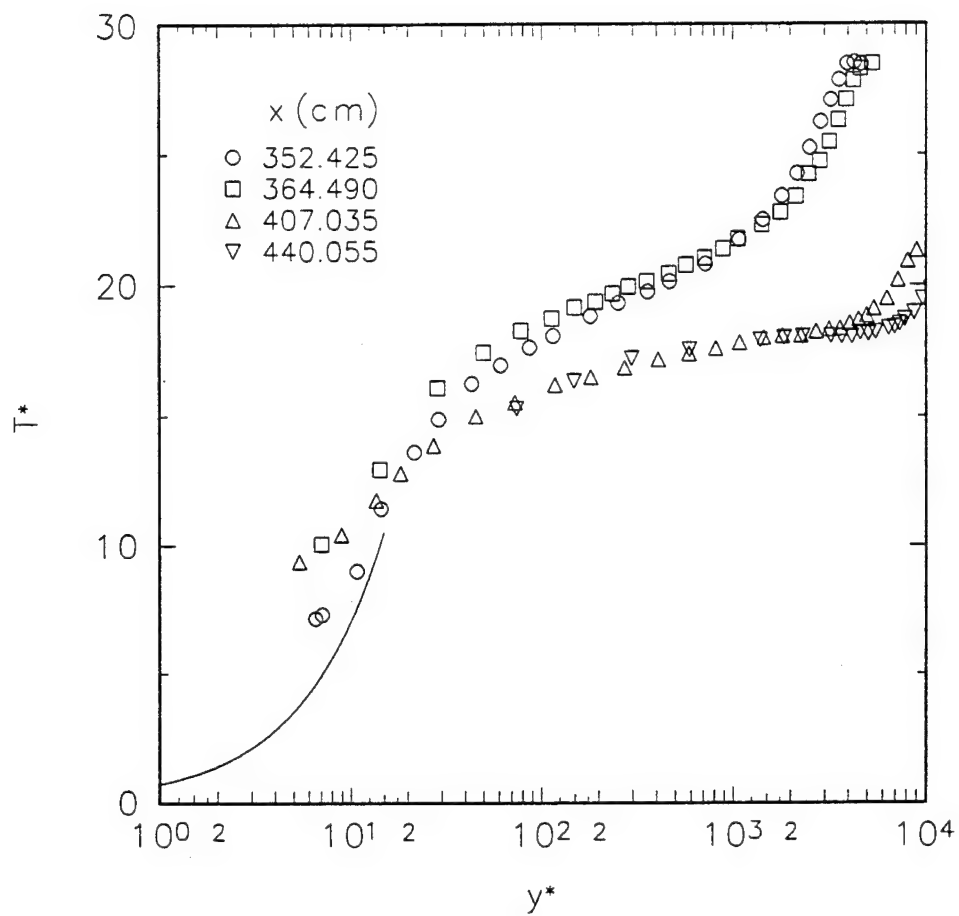


Fig. 7.24. Temperature profiles downstream of detachment in wall-law coordinates proposed by Blackwell et al. (1972). Solid line is molecular sublayer equation $T^* = \text{Pr } y^*$.

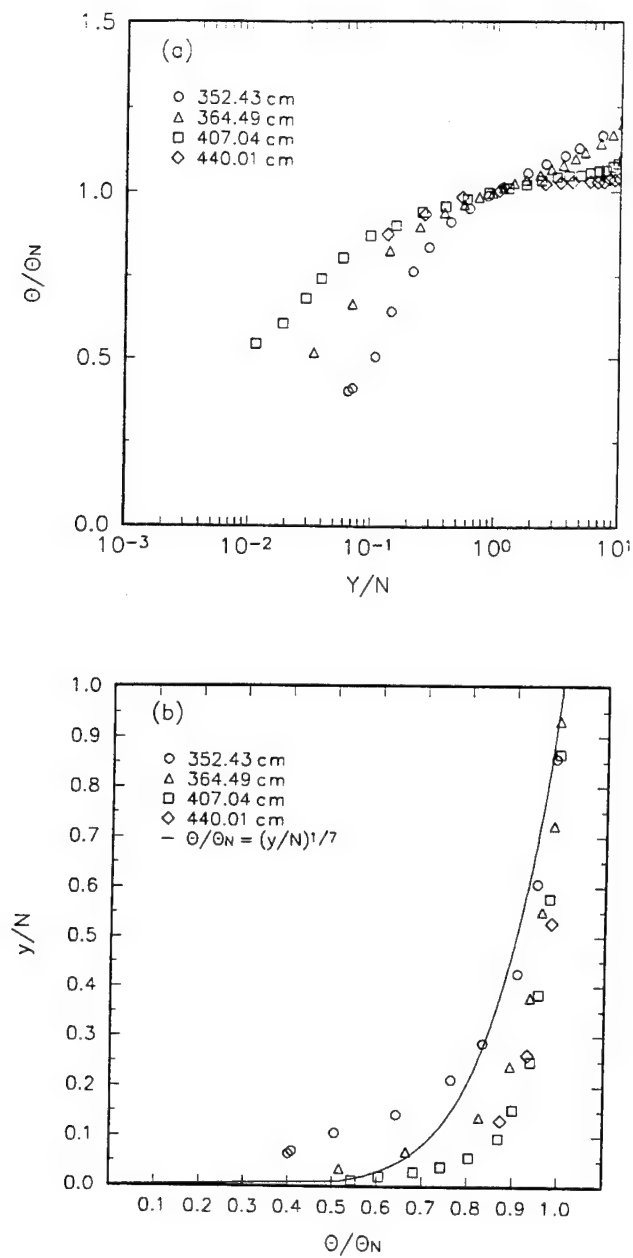


Fig. 7.25. Temperature profiles downstream of detachment in "law-of-the-backflow" coordinates. (a) near-wall region; (b) outer region.

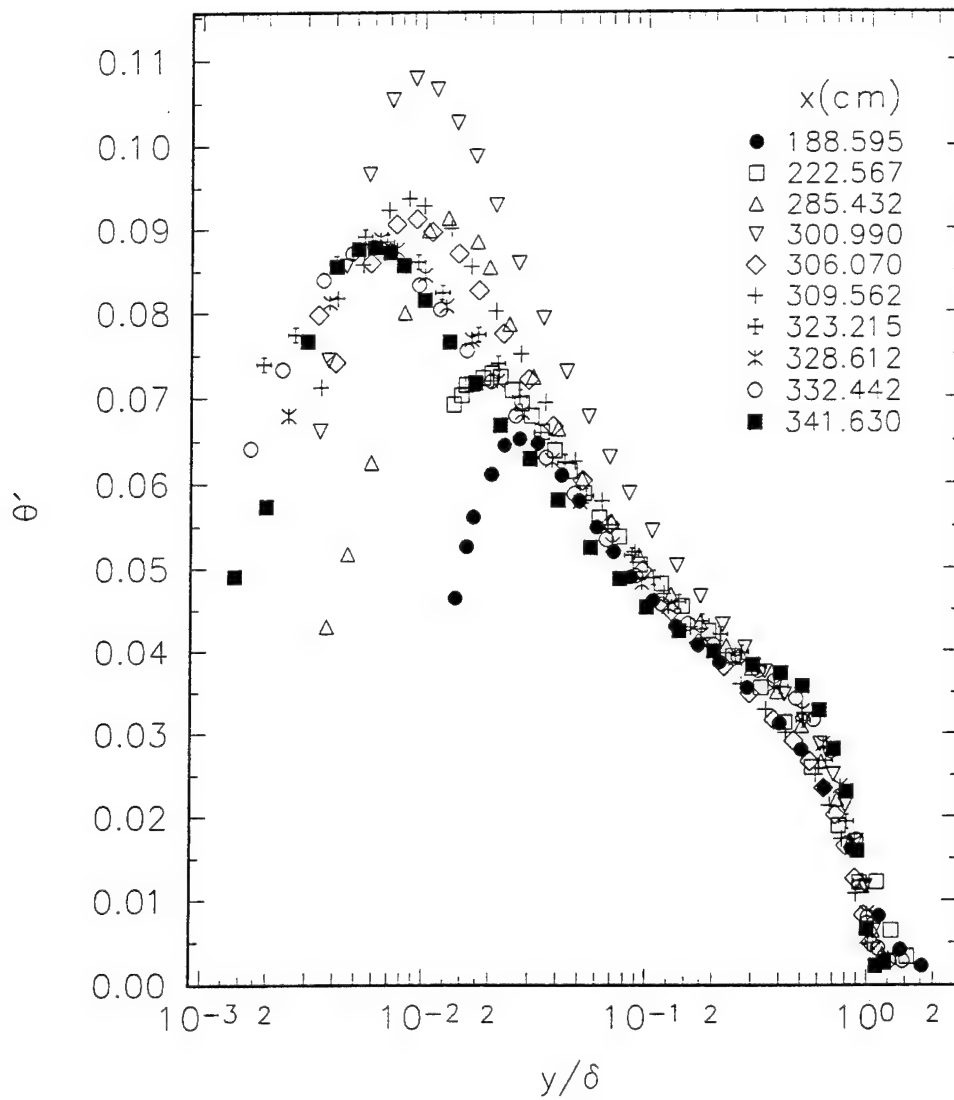


Fig. 7.26. Temperature fluctuation profiles upstream of *incipient* detachment in outer-region coordinate.

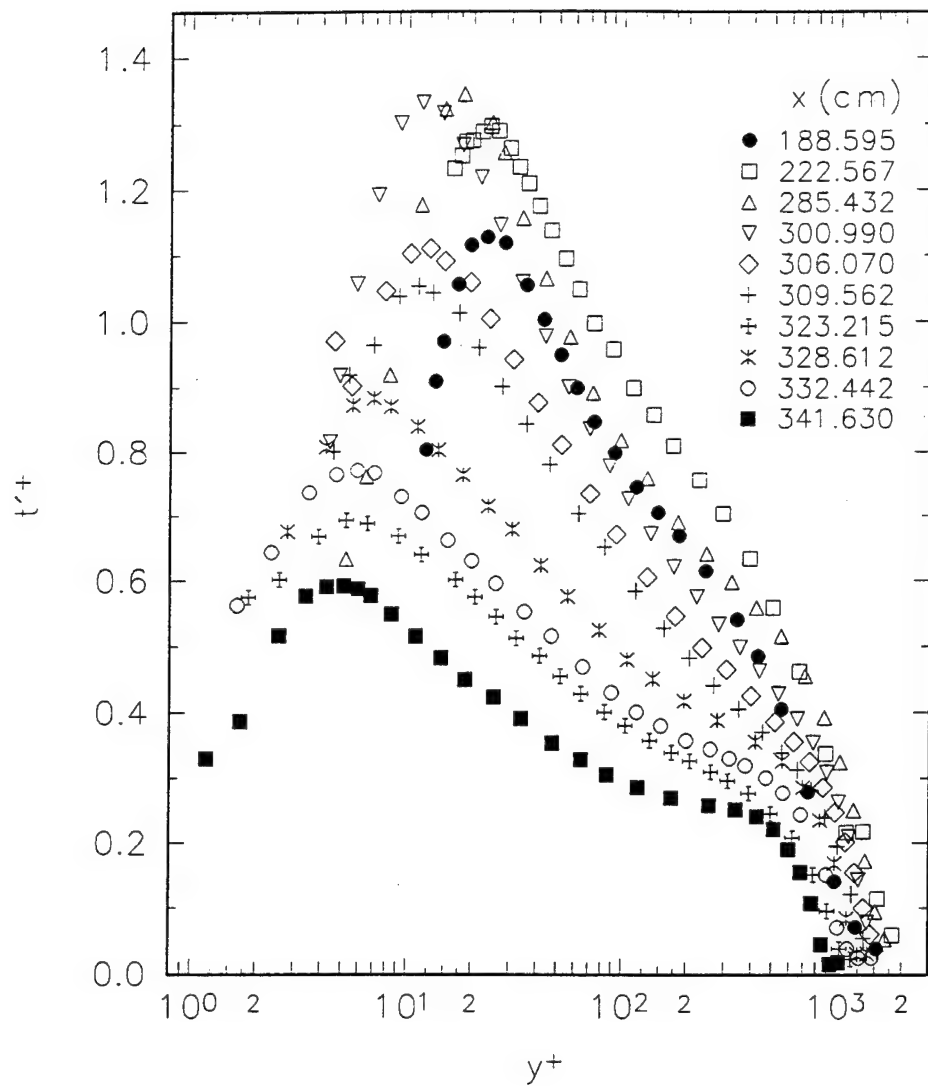


Fig. 7.27. Temperature fluctuation profiles upstream of *incipient* detachment in conventional wall-law coordinate.

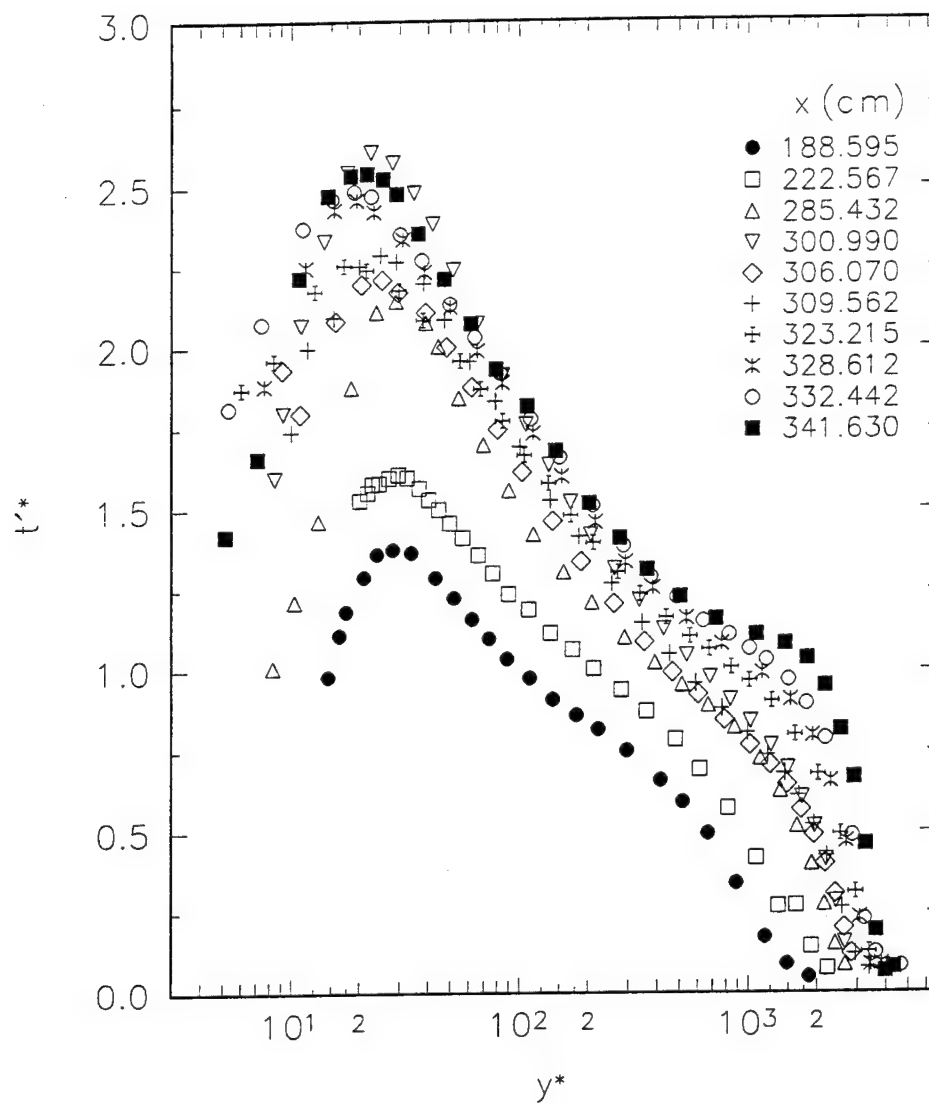


Fig. 7.28. Temperature fluctuation profiles upstream of *incipient* detachment in wall-law coordinate proposed by Blackwell et al. (1972).

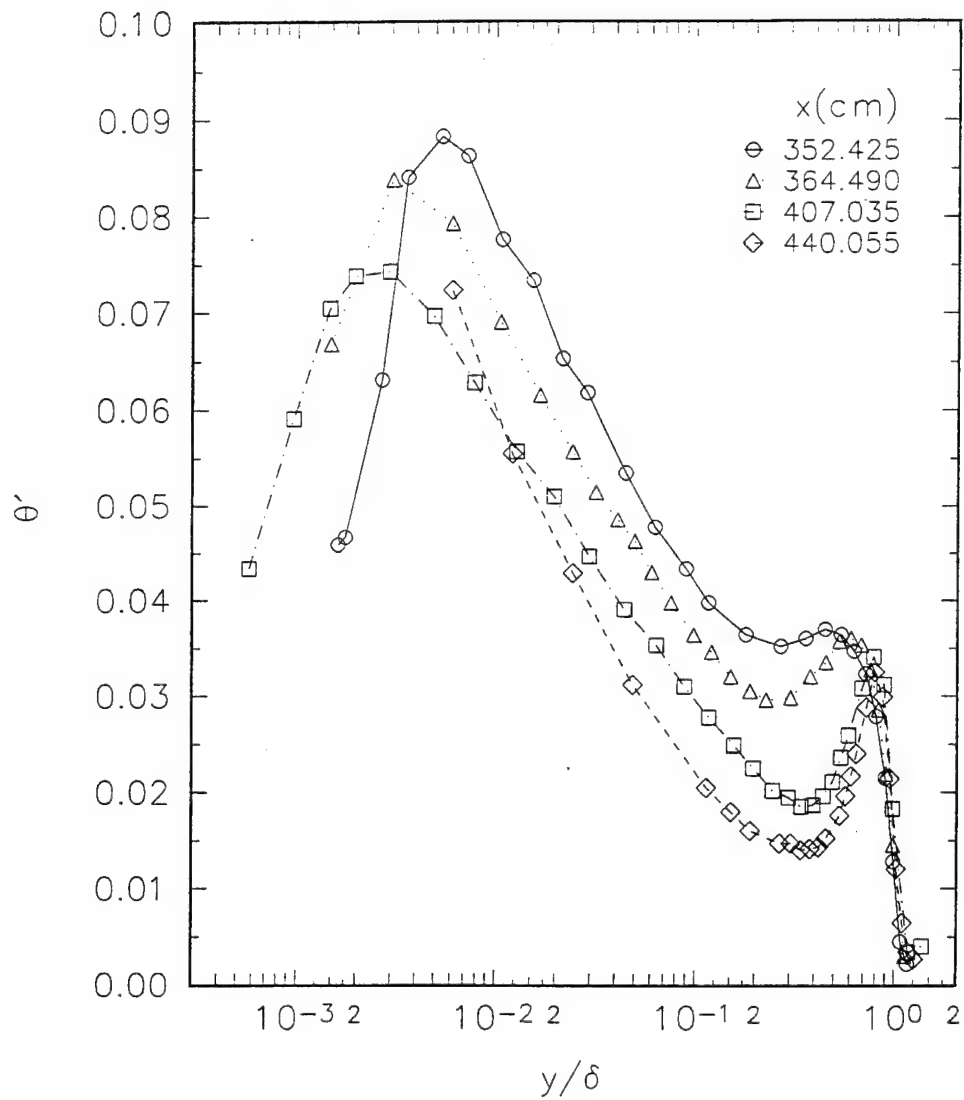


Fig. 7.29a. Temperature fluctuation profiles downstream of detachment in outer-region coordinates plotted on logarithmic abscissa.

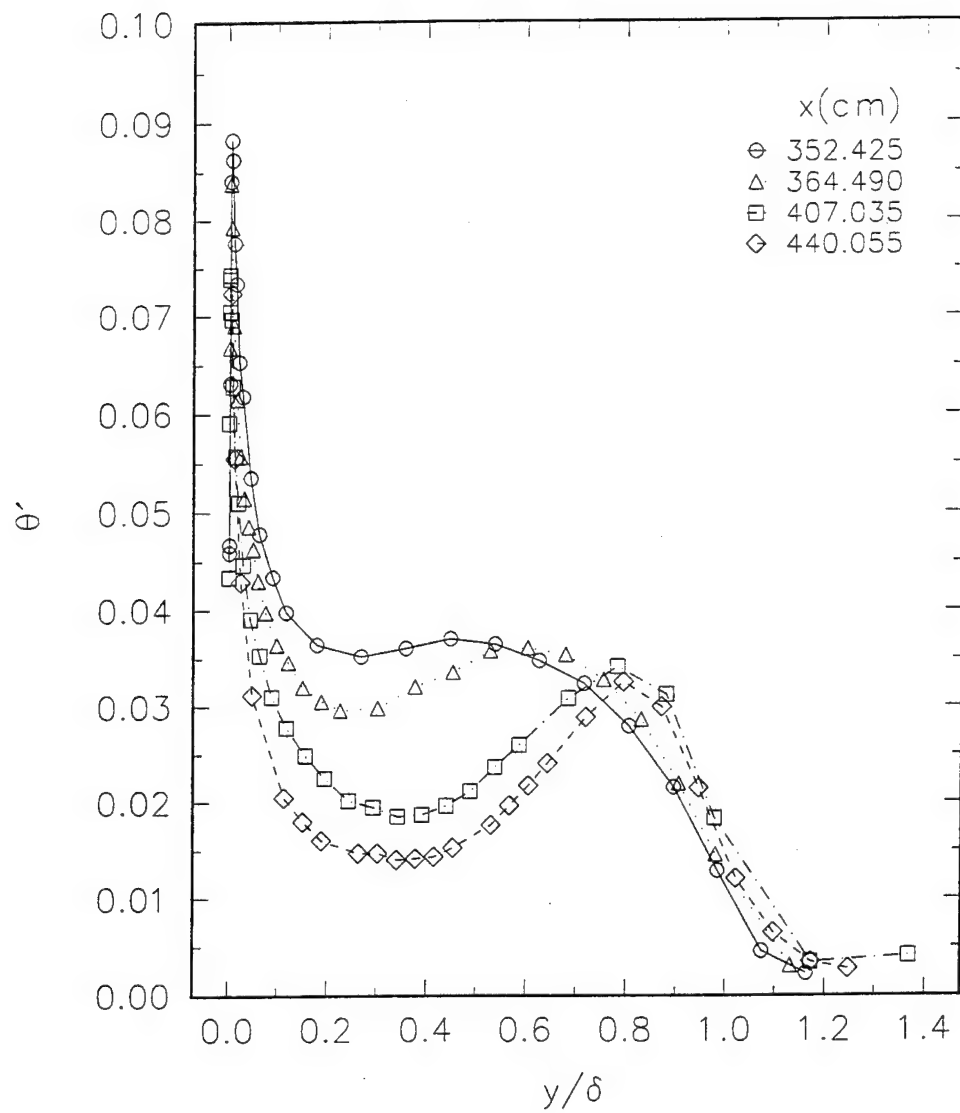


Fig. 7.29b. Temperature fluctuation profiles downstream of detachment in outer-region coordinates plotted on linear abscissa.

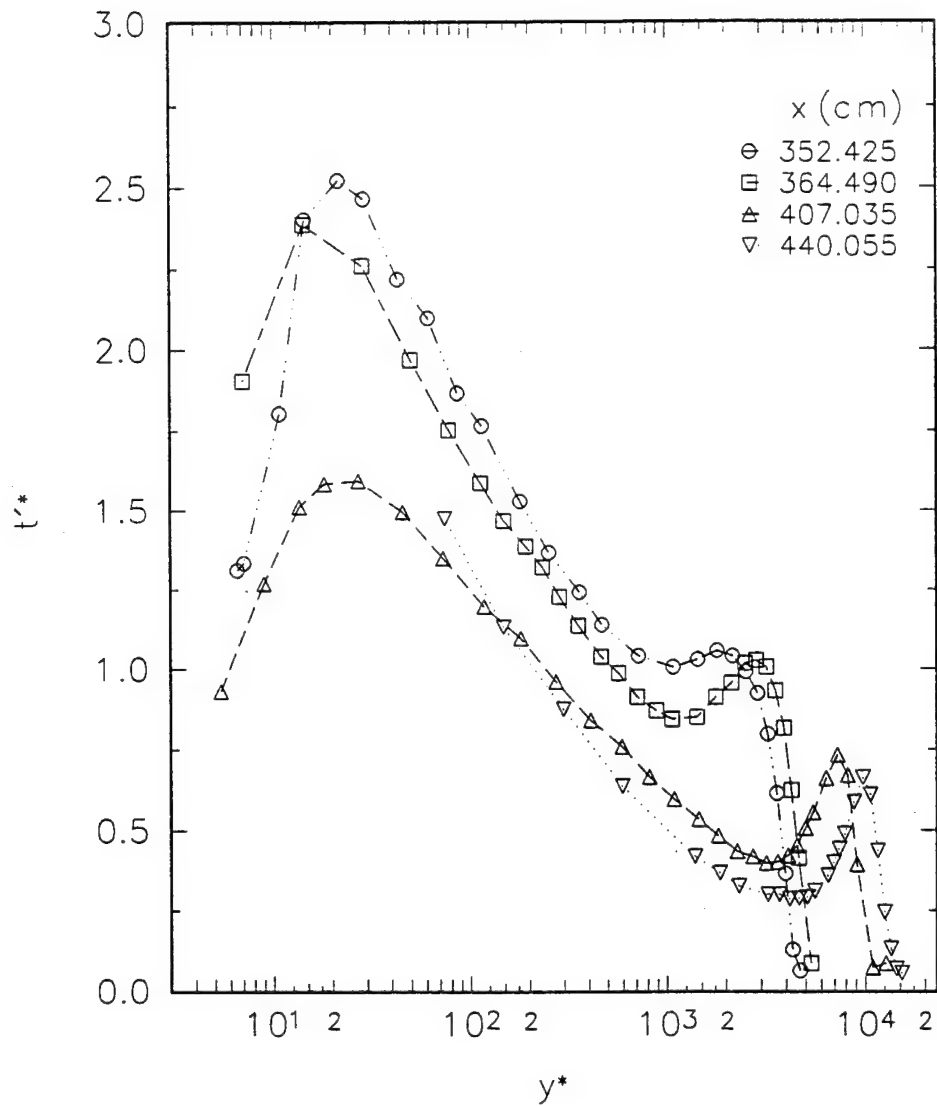


Fig. 7.30. Temperature fluctuation profiles downstream of detachment plotted in wall-law coordinate proposed by Blackwell et al. (1972).

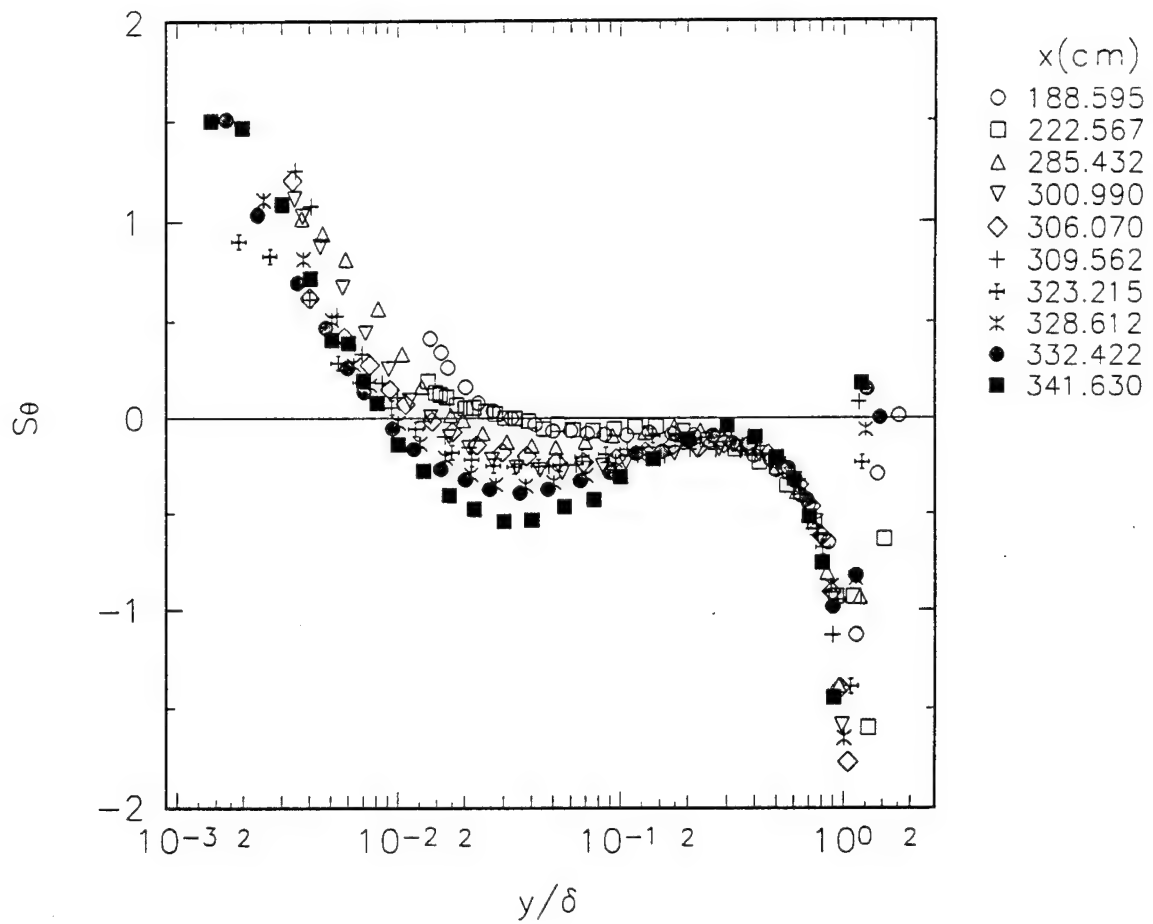


Fig. 7.31. Profiles of the skewness factor of temperature fluctuations upstream of incipient detachment plotted in outer-region coordinates.

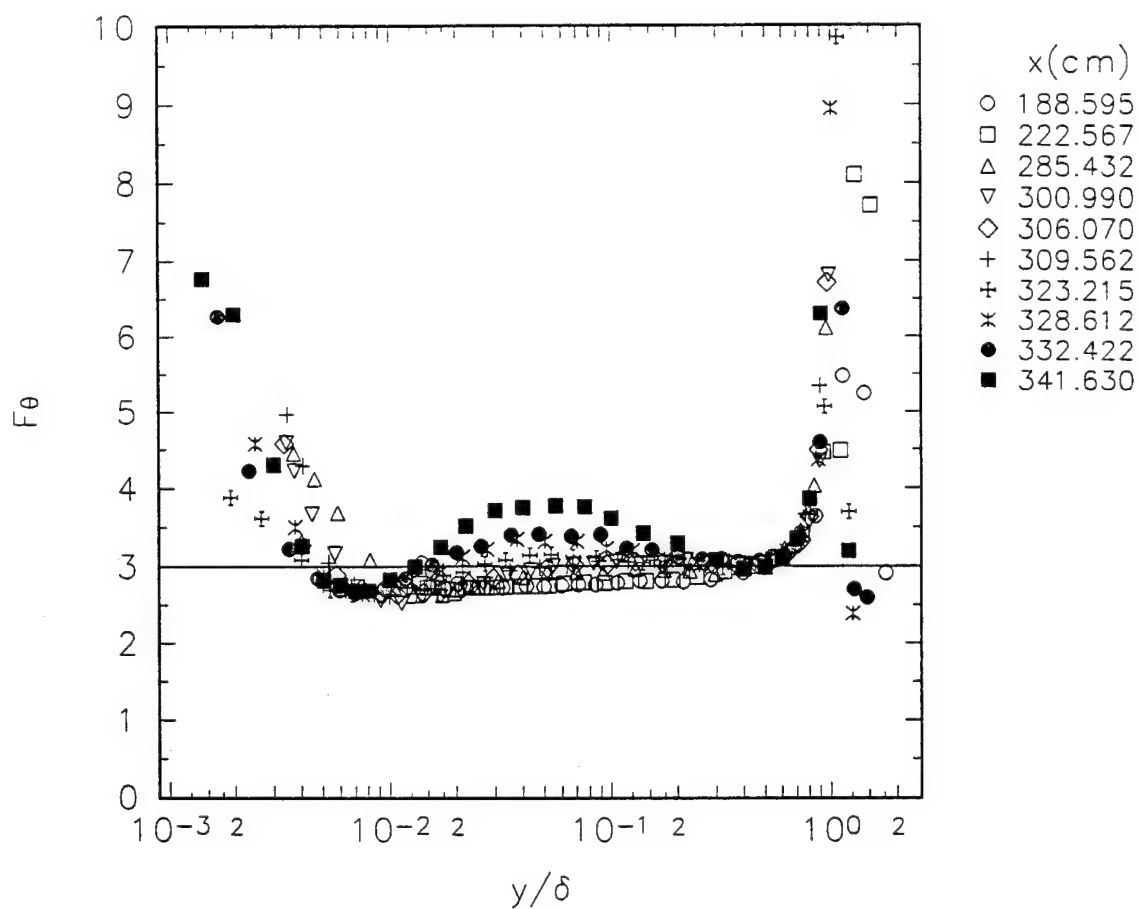


Fig. 7.32. Profiles of the flatness factor of temperature fluctuations upstream of *incipient* detachment plotted in outer-region coordinates.

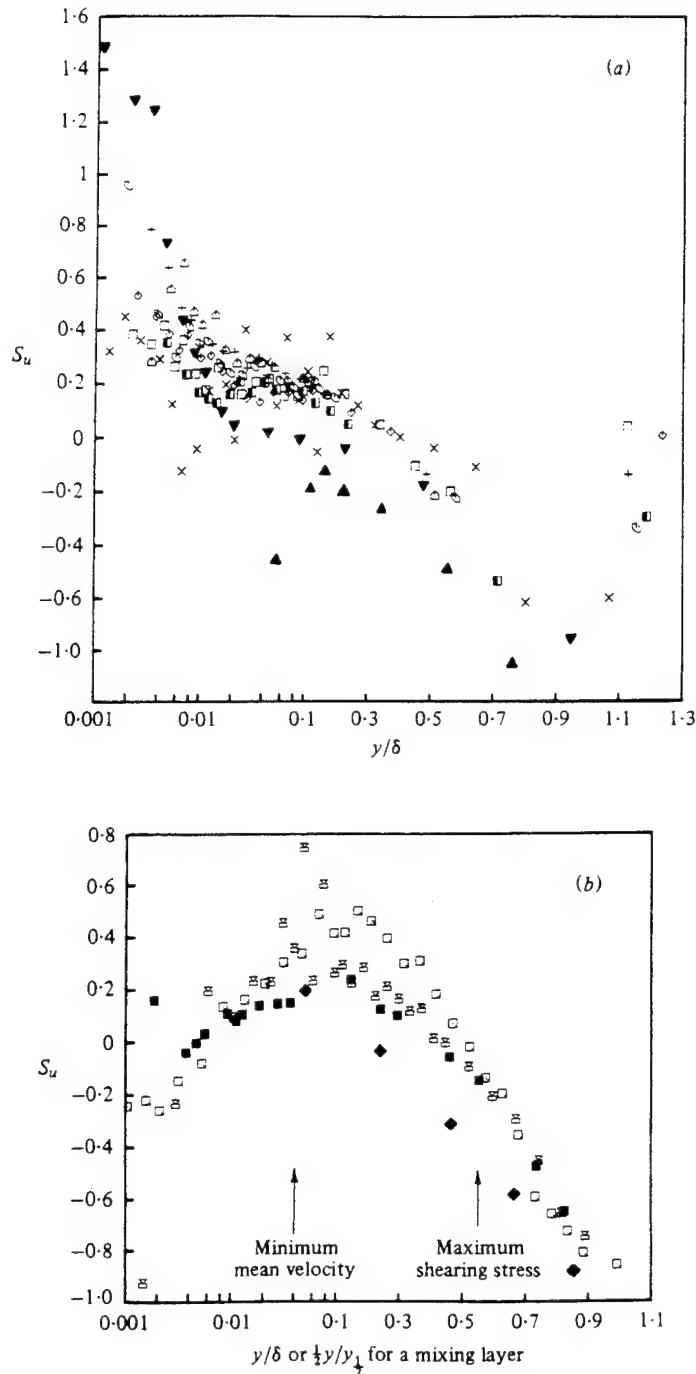


Figure 7.33. Skewness-factor, S_u , laser-anemometer data (a) upstream and (b) downstream from detachment. (a) \blacksquare , 112.4 in.; \square , 118.5; \triangle , 120.5; $+$, 122.6; \times , 127.1; \diamond , 129.4; \square , 131.9. \blacktriangle , Antonia (1973), $R_\delta = 31000$; \blacktriangledown , Dumas & Marciat (1966), $R_\delta = 32500$. Note the log-linear abscissa. (b) \blacksquare , 138.75 in.; \boxtimes , 144.9; \square , 156.4. \blacklozenge , Wygnanski & Fiedler (1970), mixing-layer data (from Simpson et al., 1981 b)

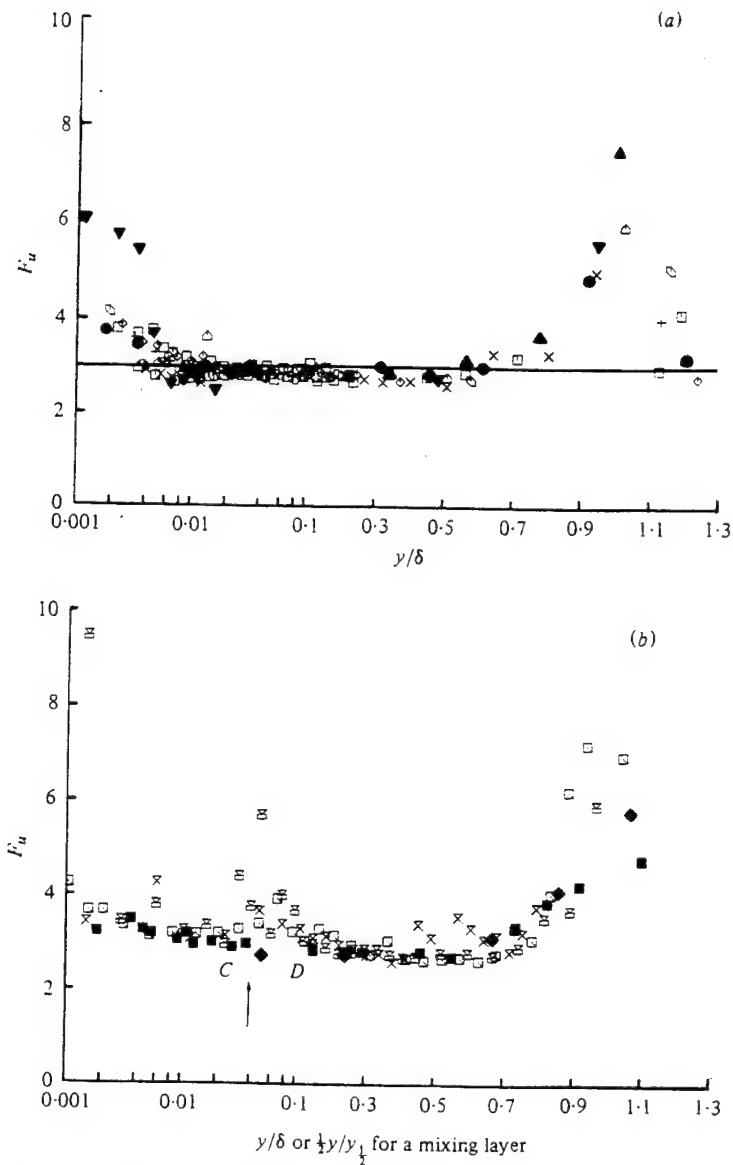


Figure 7.34. Flatness-factor, F_u , profiles (a) upstream and (b) downstream from separation. (a) \square , 112.4 in.; \circ , 118.5; \triangle , 120.5; +, 122.6; \times , 127.1; \diamond , 129.4; \square , 131.9. Sandborn (1959): \bullet , near separation, $Re_\delta = 5687$. Antonia (1973): \blacktriangle , $Re_\delta = 31000$. Dumas & Marcillat (1966): $Re_\delta = 32500$; —, value for Gaussian distribution. Note the log-linear abscissa. (b) C and D are the inflection points described by Shiloh *et al.* (1981) \blacksquare , 138.75 in.; \square , 144.9; \square , 156.4; \times , 170.9. The arrow denotes the location of minimum mean velocity U . \blacklozenge , Wygnanski & Fiedler (1970), mixing-layer data. (from Simpson *et al.*, 1981 b)

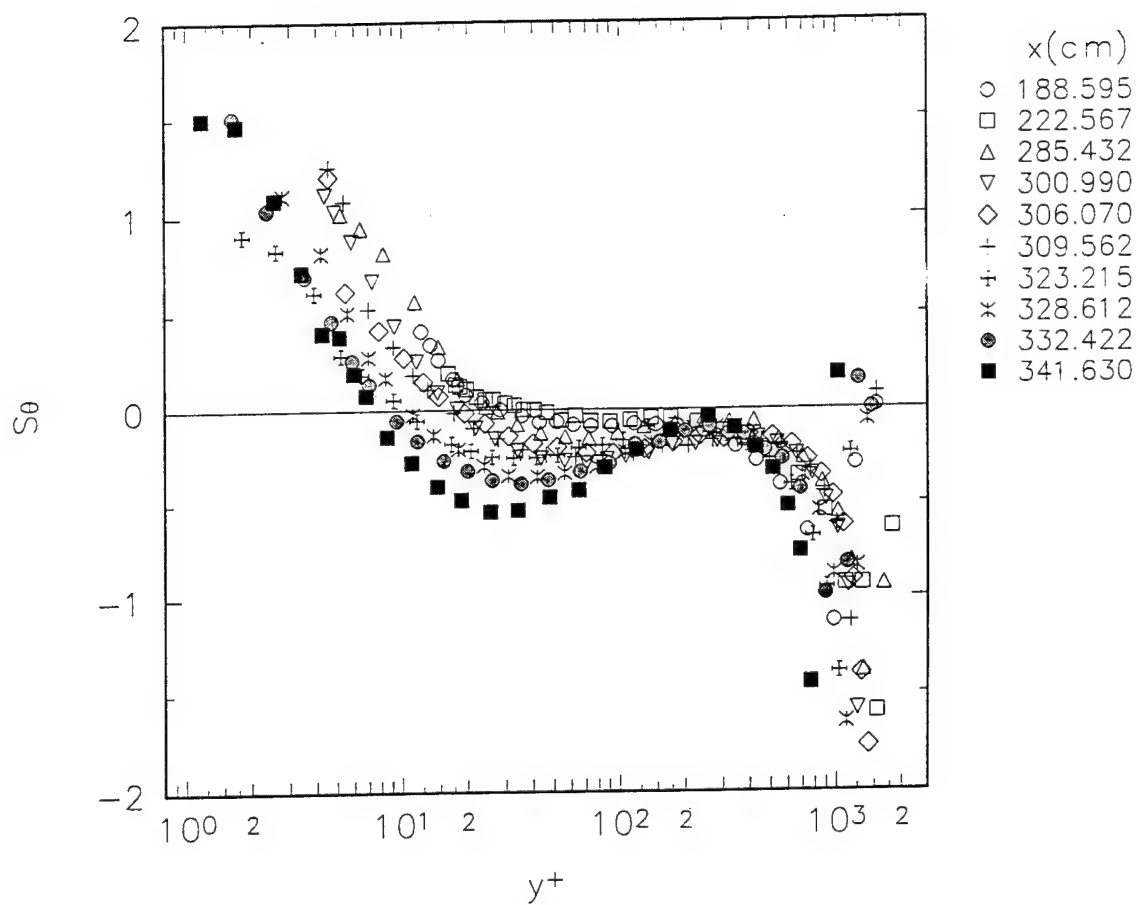


Fig. 7.35. Profiles of the skewness factor of temperature fluctuations upstream of *incipient* detachment plotted in conventional wall-law coordinates.

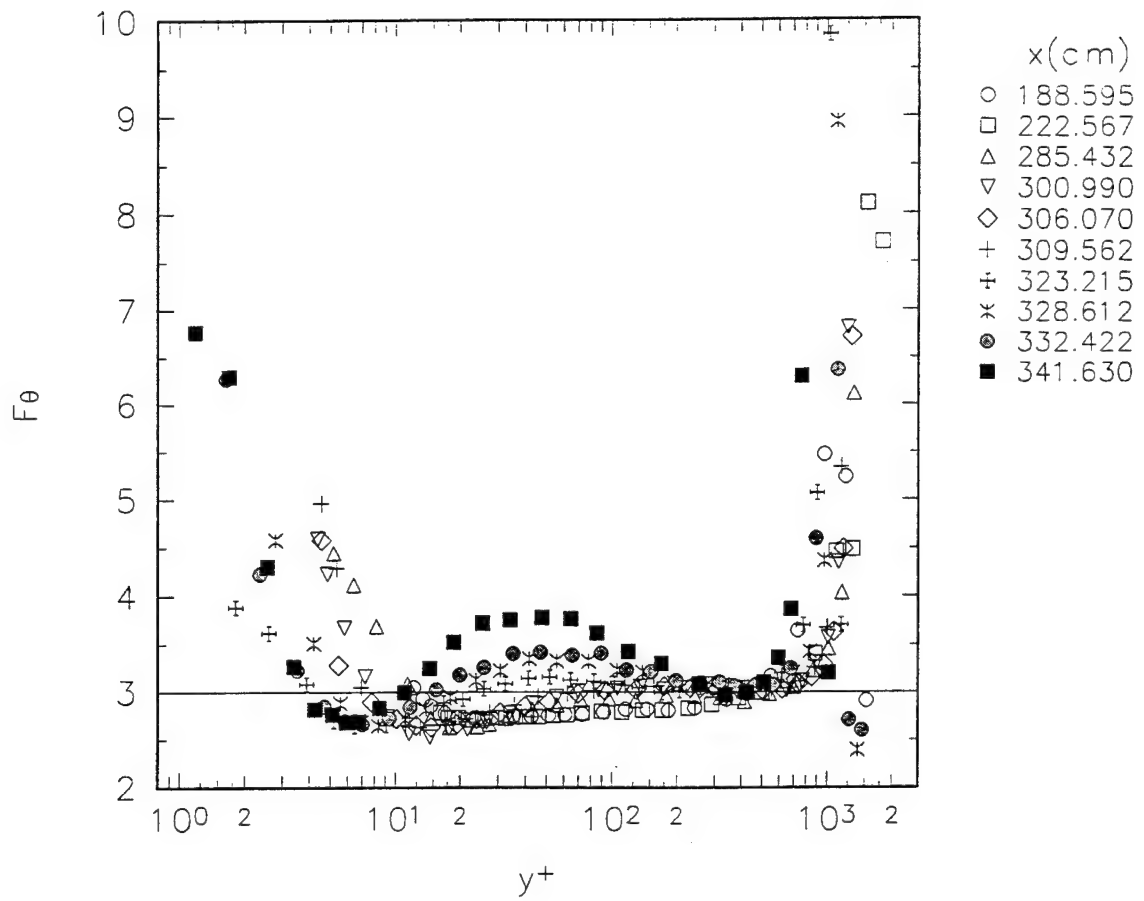


Fig. 7.36. Profiles of the flatness factor of temperature fluctuations upstream of *incipient* detachment plotted in conventional wall-law coordinates.

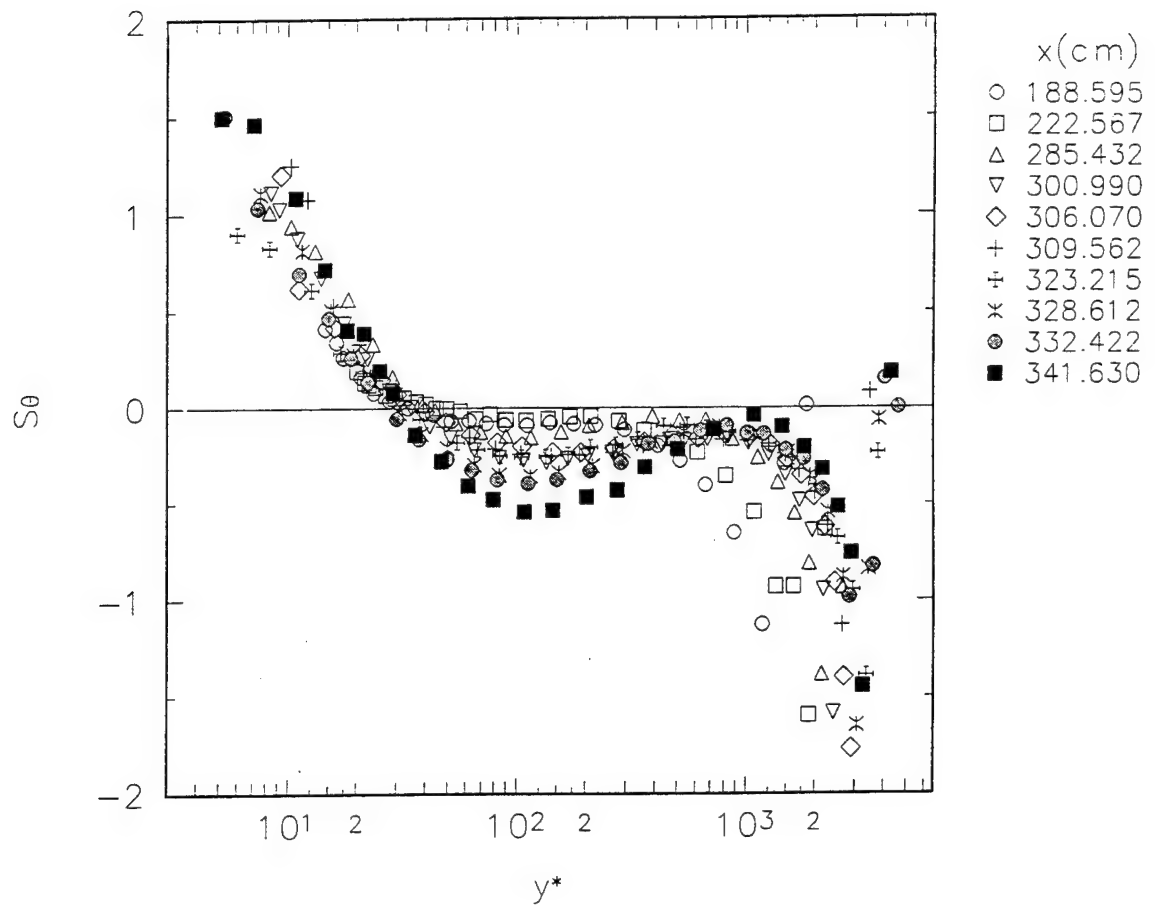


Fig. 7.37. Profiles of the skewness factor of temperature fluctuations upstream of *incipient* detachment plotted in wall-law coordinates proposed by Blackwell et al. (1972).

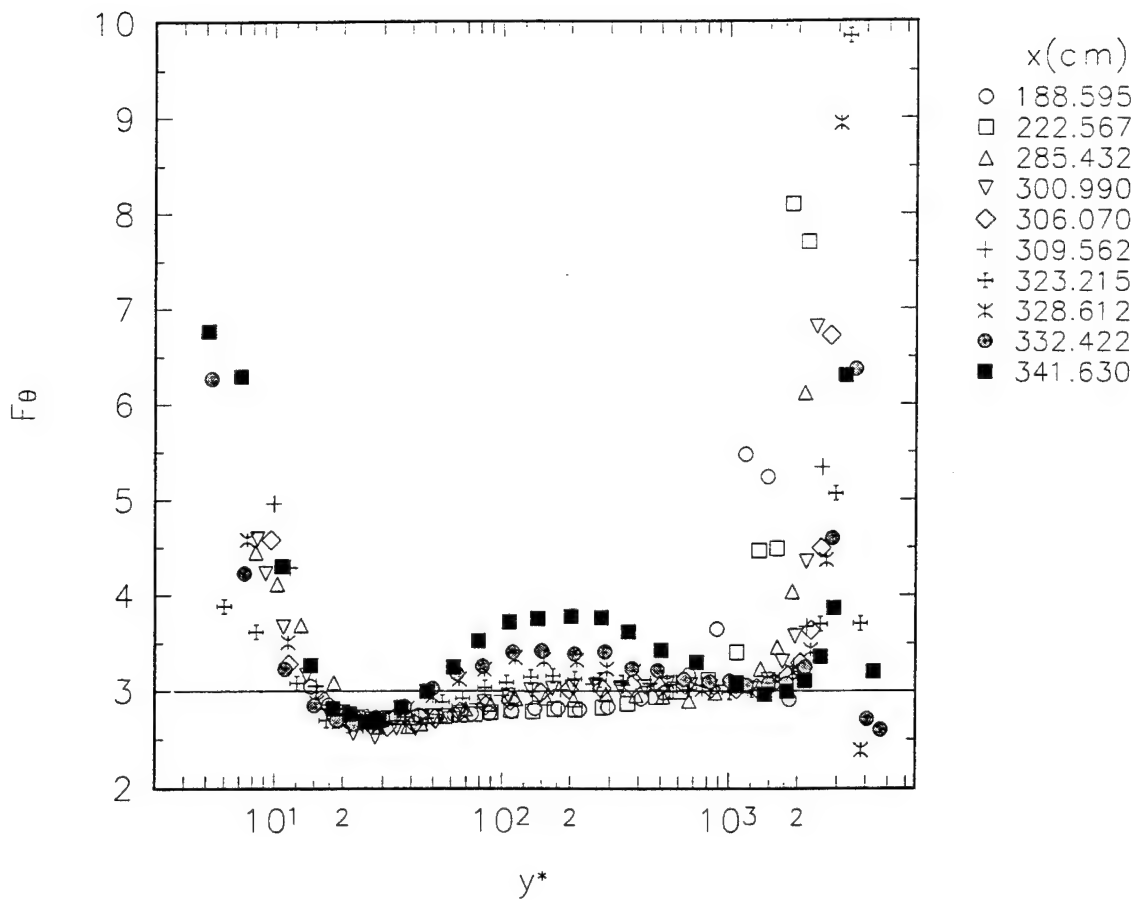


Fig. 7.38. Profiles of the skewness factor of temperature fluctuations upstream of *incipient* detachment plotted in wall-law coordinates proposed by Blackwell et al. (1972).

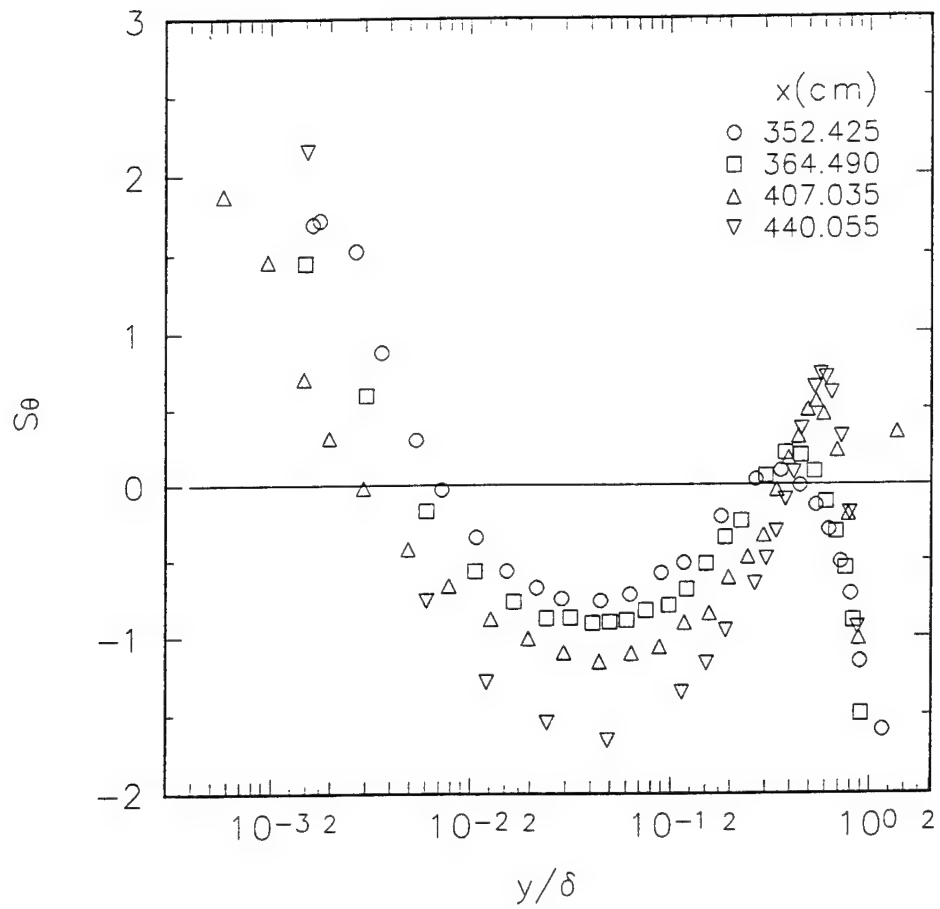


Fig. 7.39. Profiles of the skewness factor of temperature fluctuations downstream of detachment plotted in outer-region coordinates.

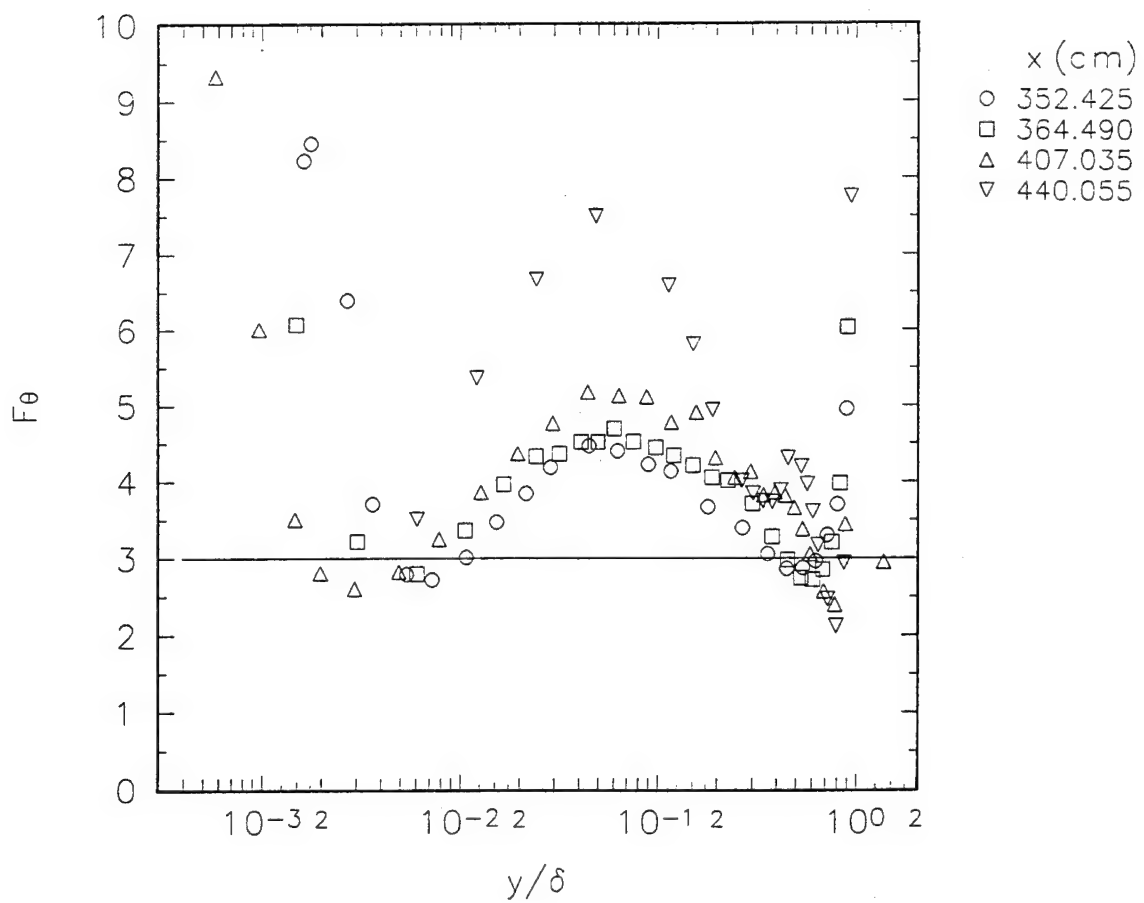


Fig. 7.40. Profiles of the flatness factor of temperature fluctuations downstream of detachment plotted in outer-region coordinates.

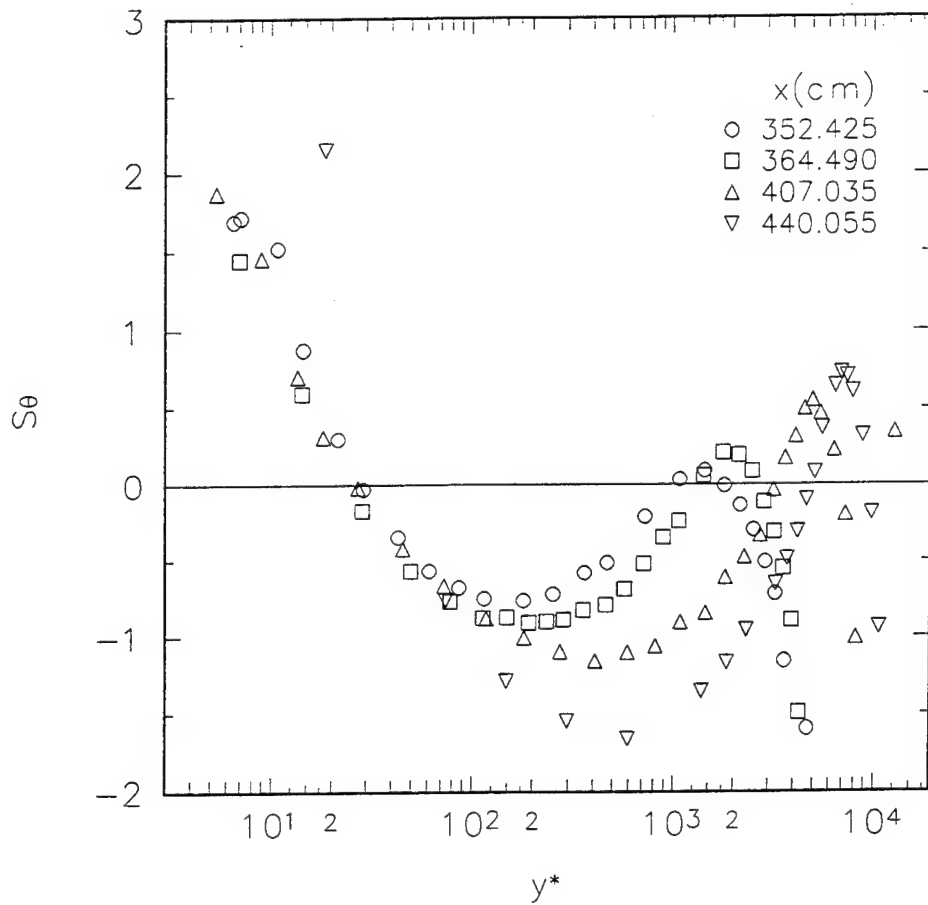


Fig. 7.41. Profiles of the skewness factor of temperature fluctuations downstream of detachment plotted in wall-law coordinates proposed by Blackwell et al. (1972).

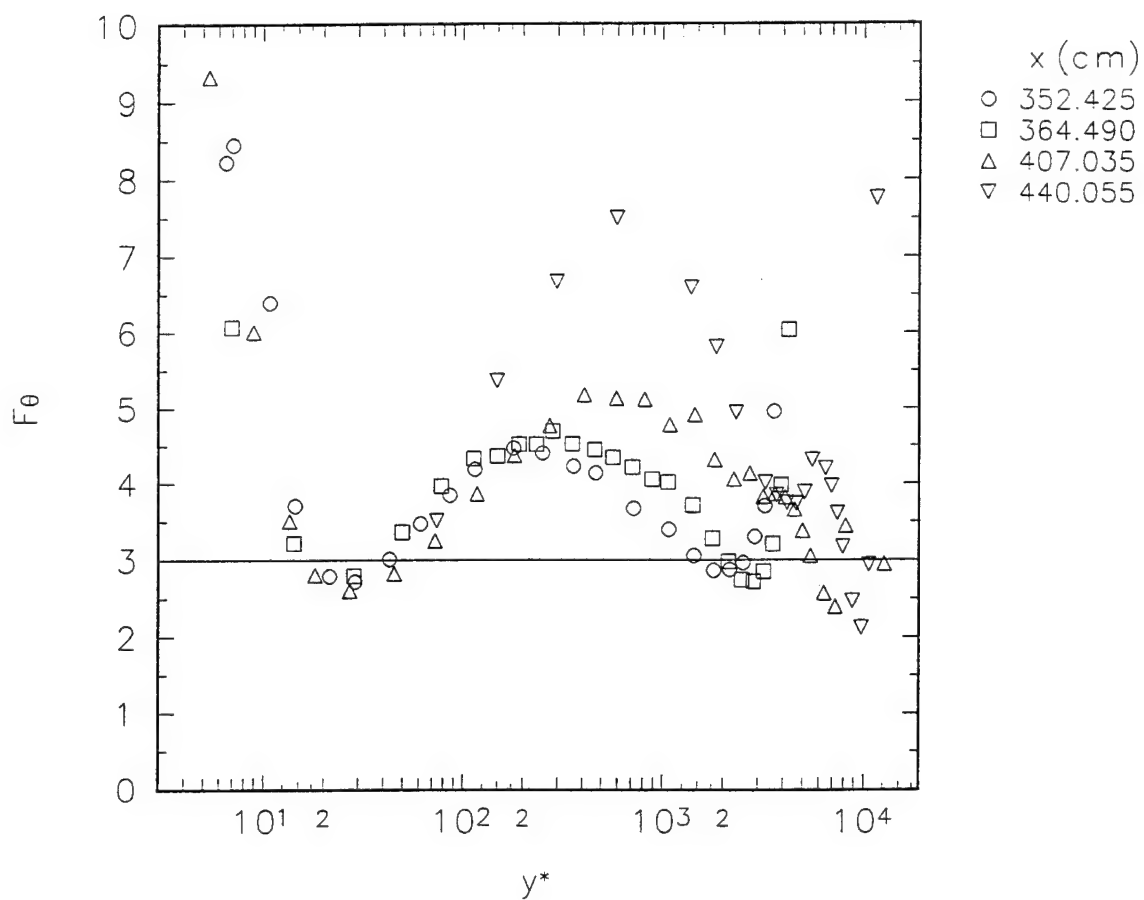


Fig. 7.42. Profiles of the flatness factor of temperature fluctuations downstream of detachment plotted in wall-law coordinates proposed by Blackwell et al. (1972).

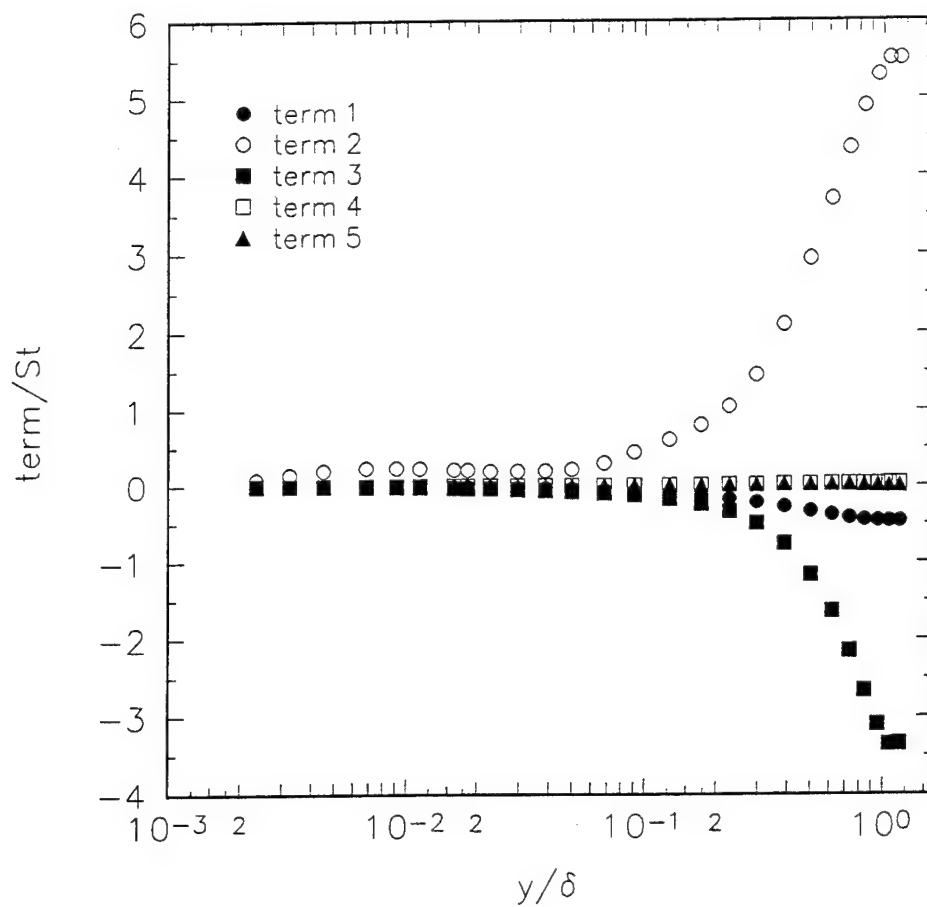


Fig. 7.43. Profiles of each term on the right-hand-side of Eq. (7.28) that contribute to $\overline{v\theta}/U_\infty$ at streamwise location $x = 285.4$ cm.

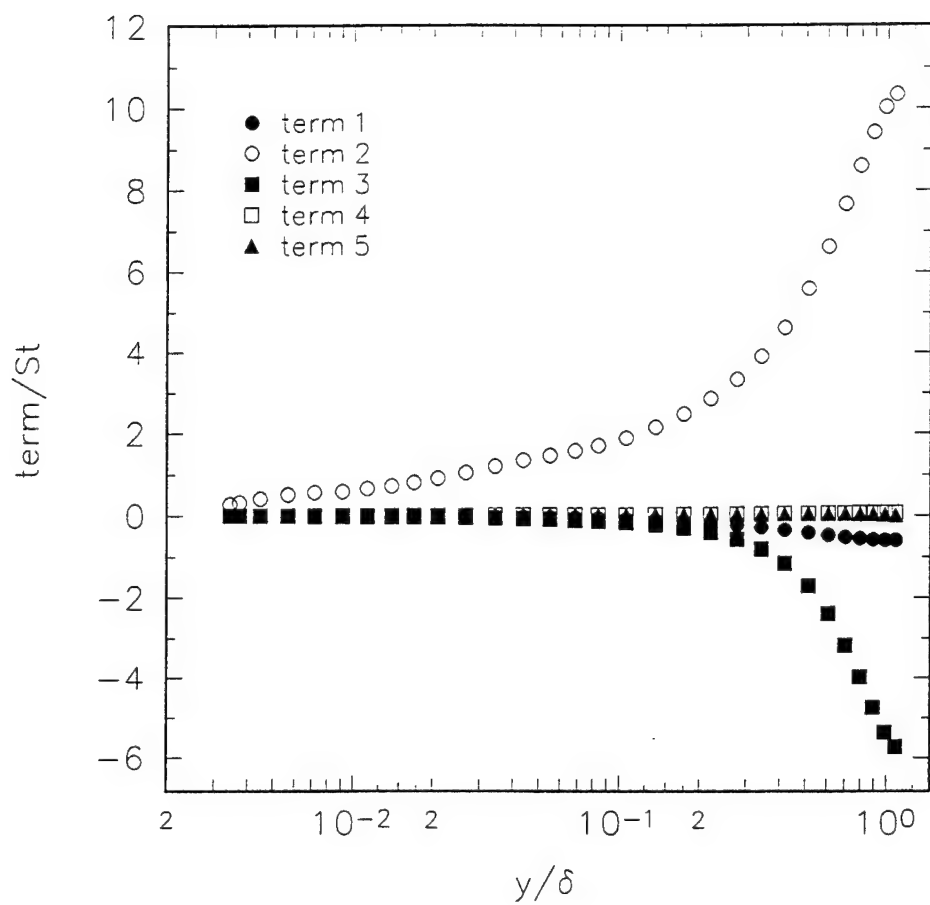


Fig. 7.44. Profiles of each term on the right-hand-side of Eq. (7.28) that contribute to $\overline{v\theta}/U_\infty$ at streamwise location $x = 301.0$ cm.

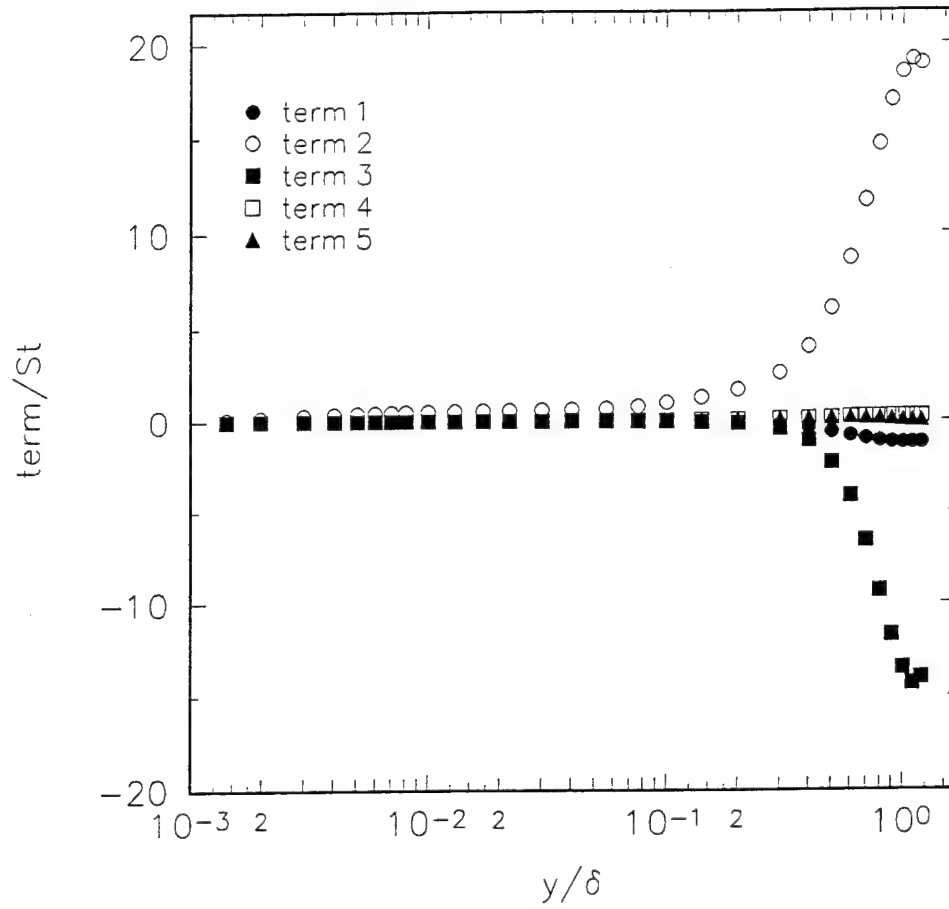


Fig. 7.45. Profiles of each term on the right-hand-side of Eq. (7.28) that contribute to $\bar{v}\theta/U_\infty$ at streamwise location $x = 341.63$ cm.

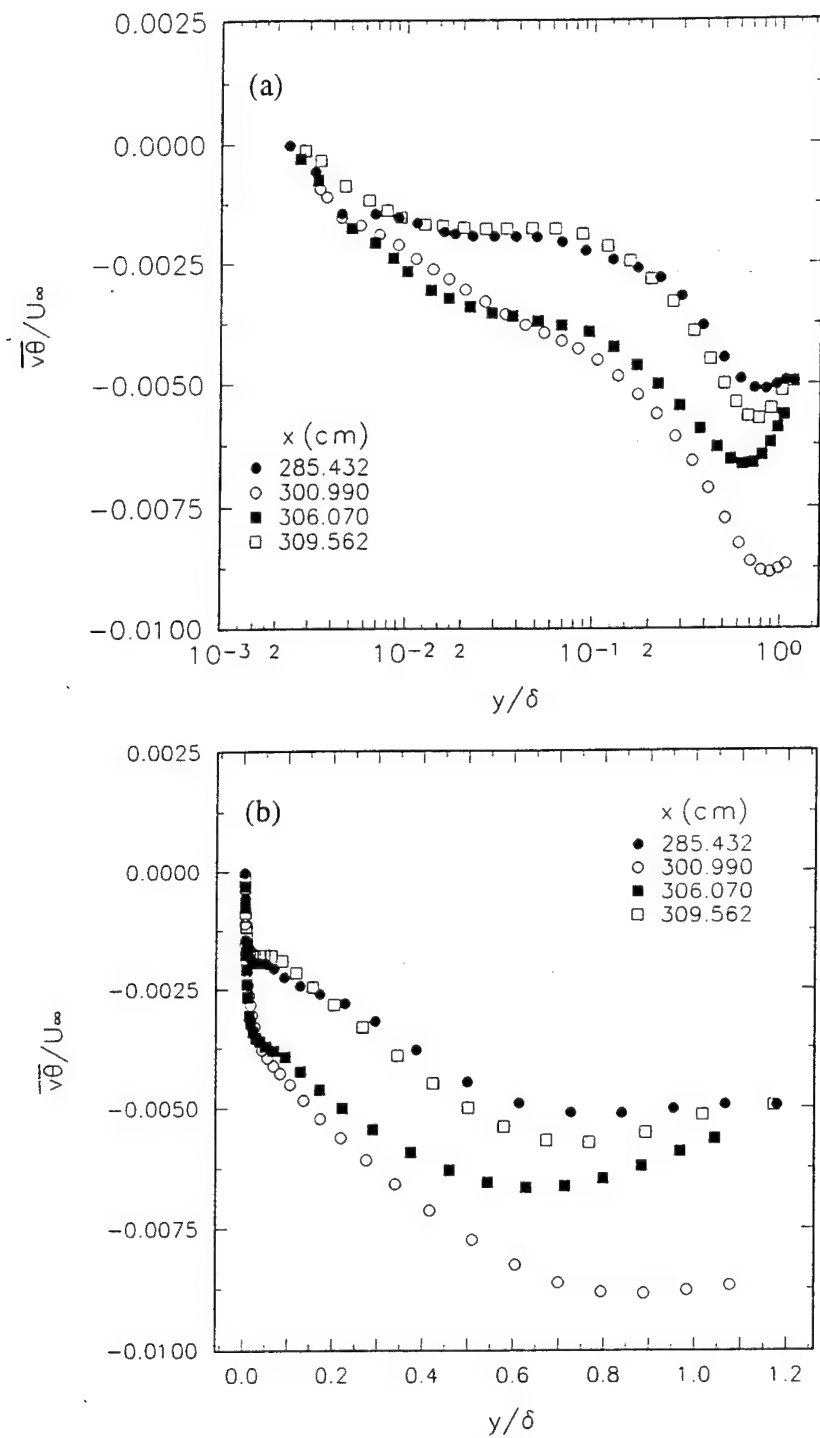


Fig. 7.46. Profiles of $\overline{v\theta}/U_\infty$ upstream of *incipient detachment* computed from integrating the energy equation. (a) inner region; (b) outer region.

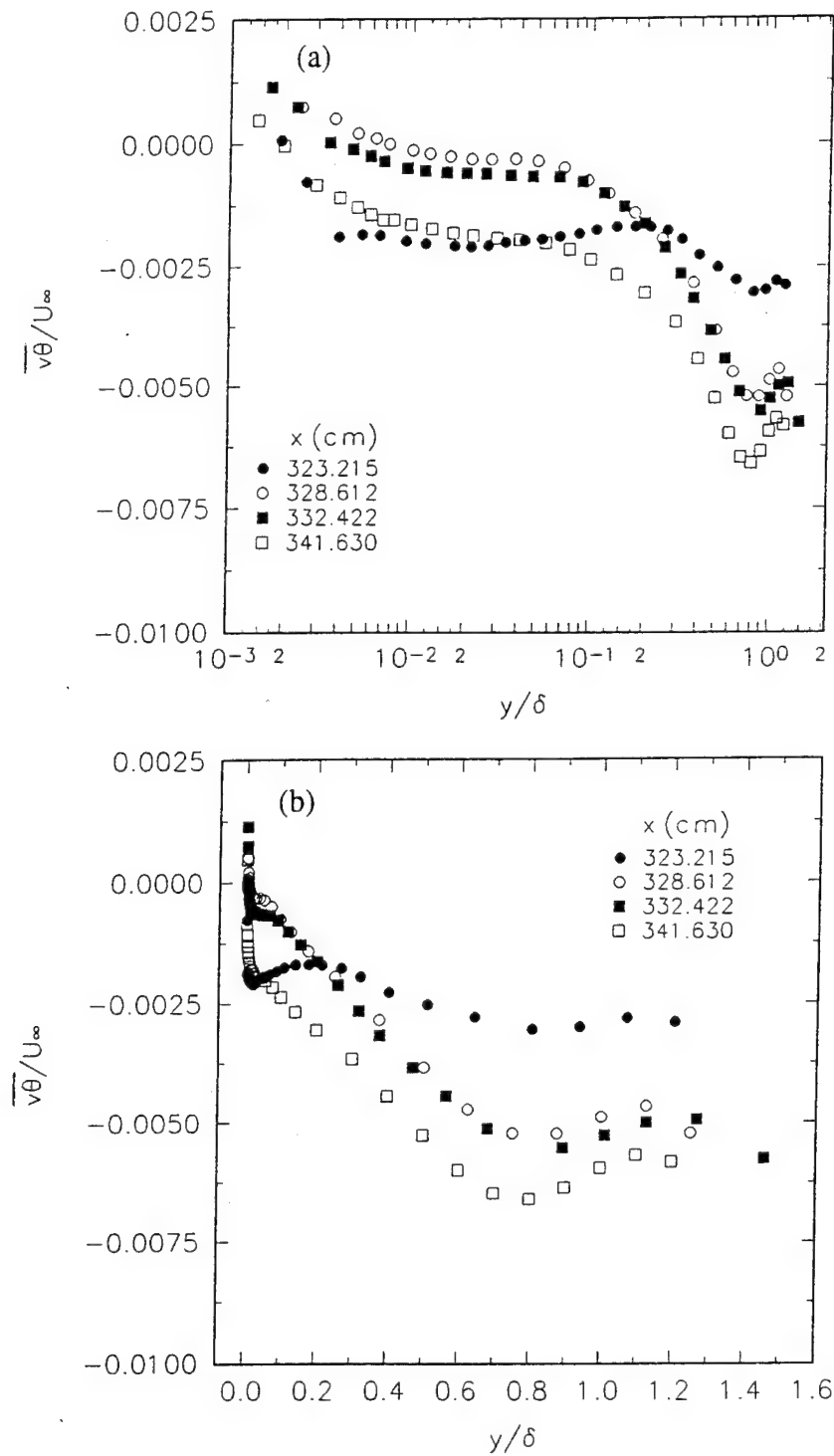


Fig. 7.47. Profiles of $\overline{v\theta}/U_\infty$ in the region between *incipient detachment* and detachment computed from integrating the energy equation. (a) inner region; (b) outer region.

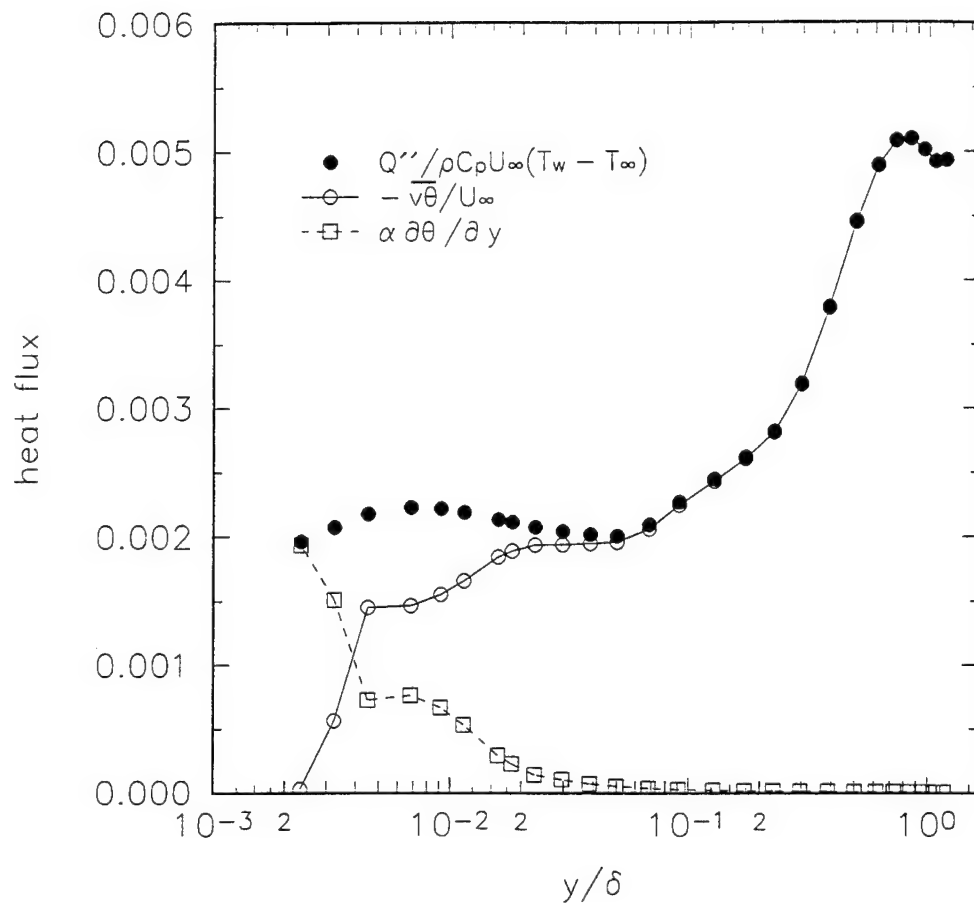


Fig. 7.48. Profiles of total, turbulent, and molecular heat transfer at streamwise location $x = 285.43$ cm.

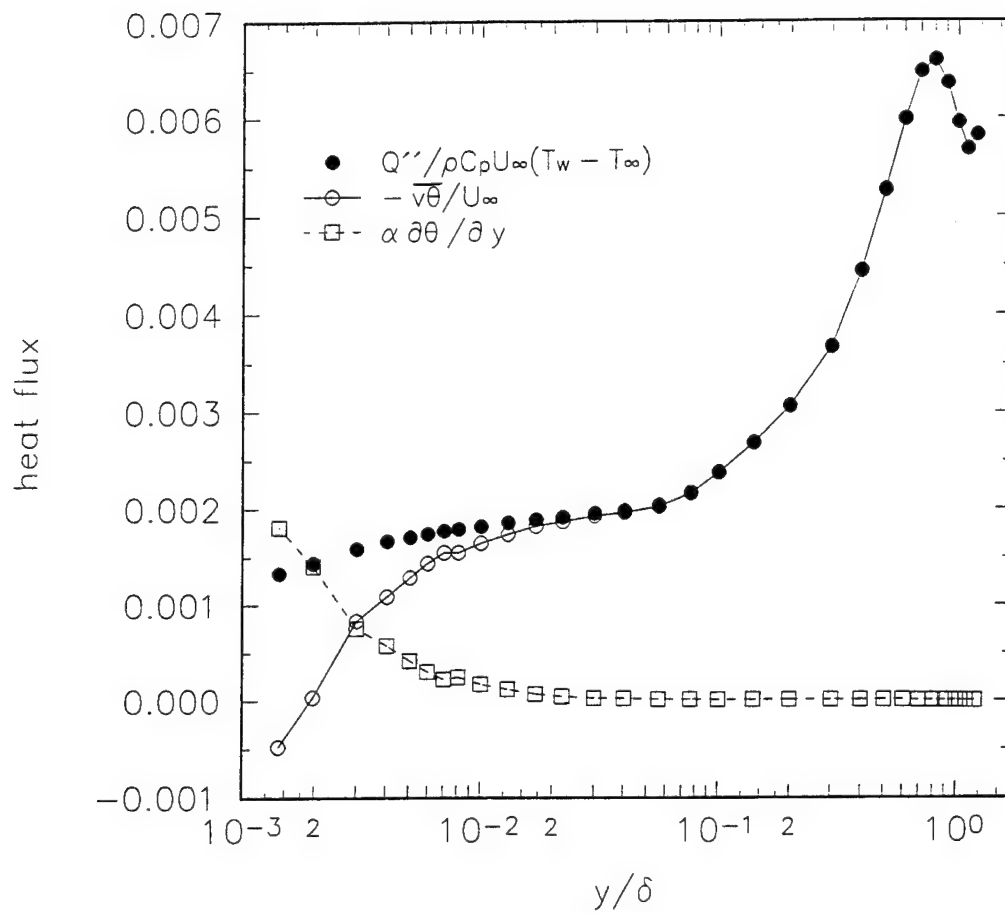


Fig. 7.49. Profiles of total, turbulent, and molecular heat transfer at streamwise location $x = 341.63$ cm.

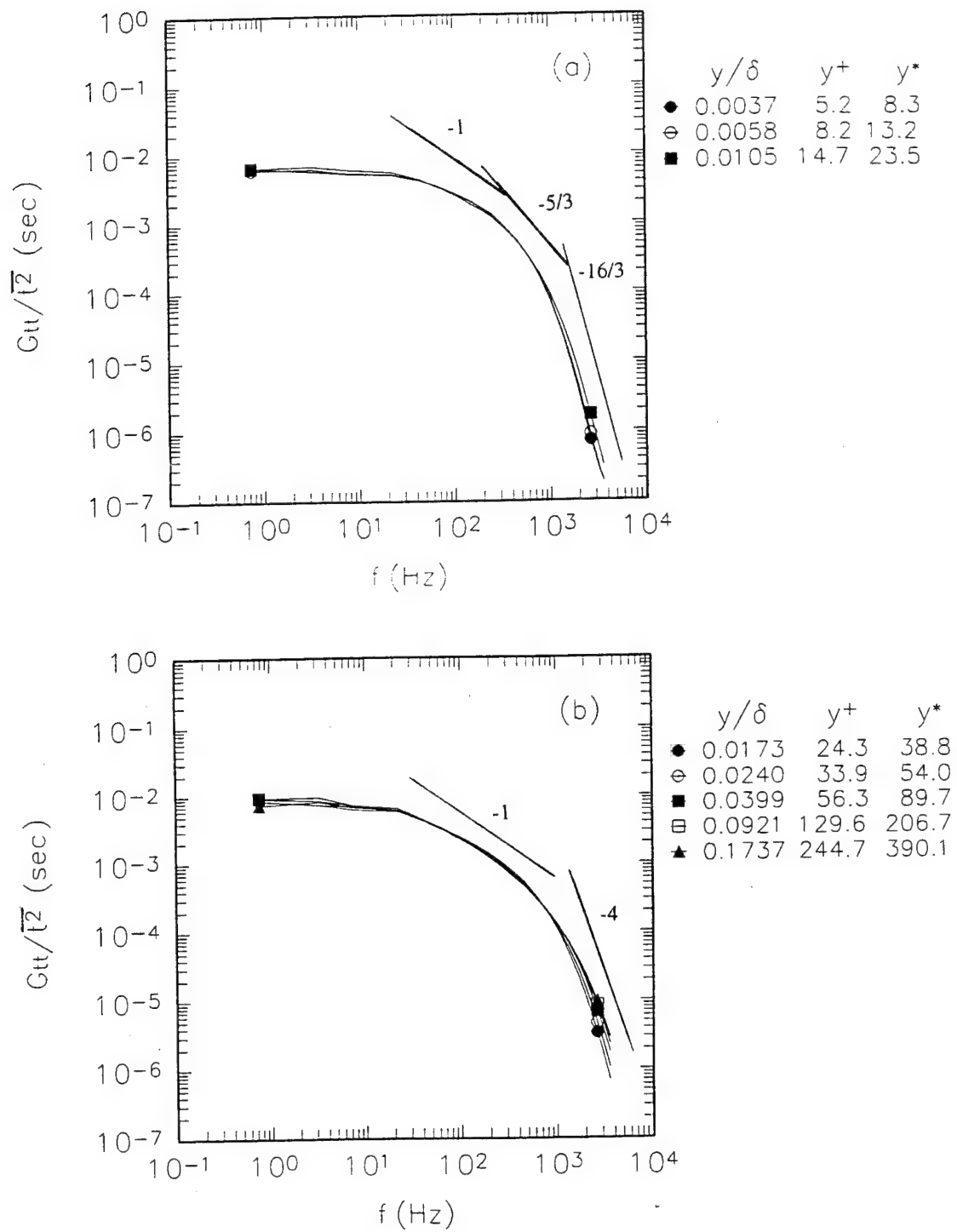


Fig. 7.50a,b. Normalized t power spectral distribution far upstream of detachment, at $x = 285.4$ cm. (a) in the buffer region; (b) in the fully turbulent region; (c) in the outer region.

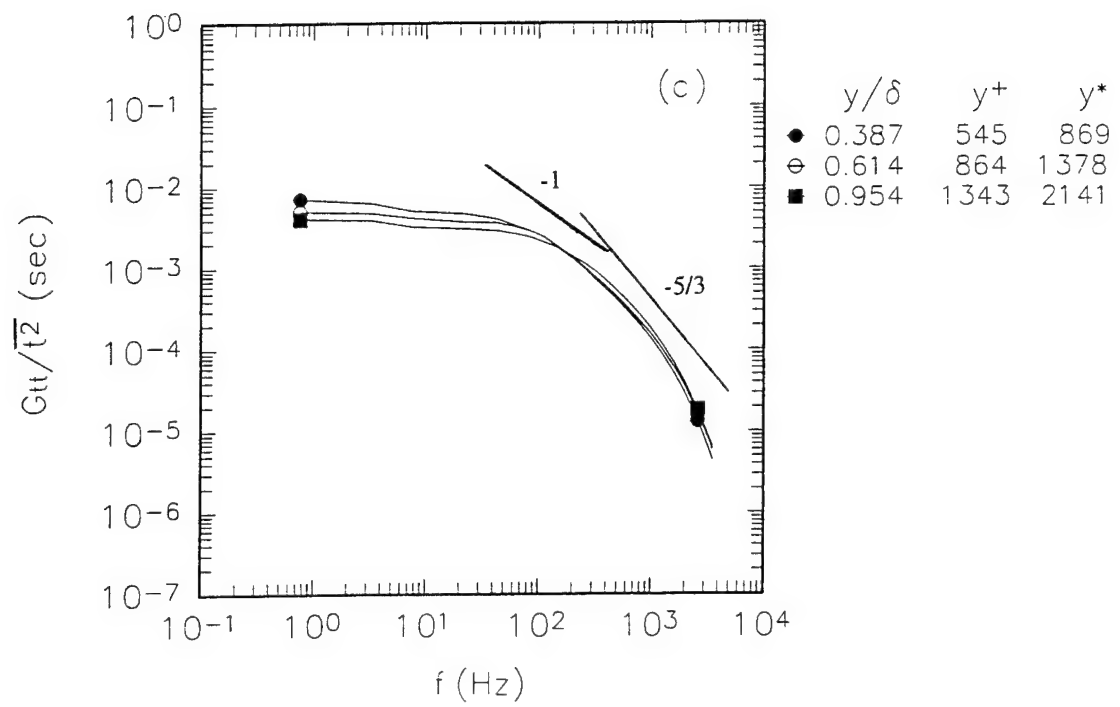


Fig. 7.50c. Normalized t power spectral distribution far upstream of detachment, at $x = 285.4$ cm. (a) in the buffer region; (b) in the fully turbulent region; (c) in the outer region.

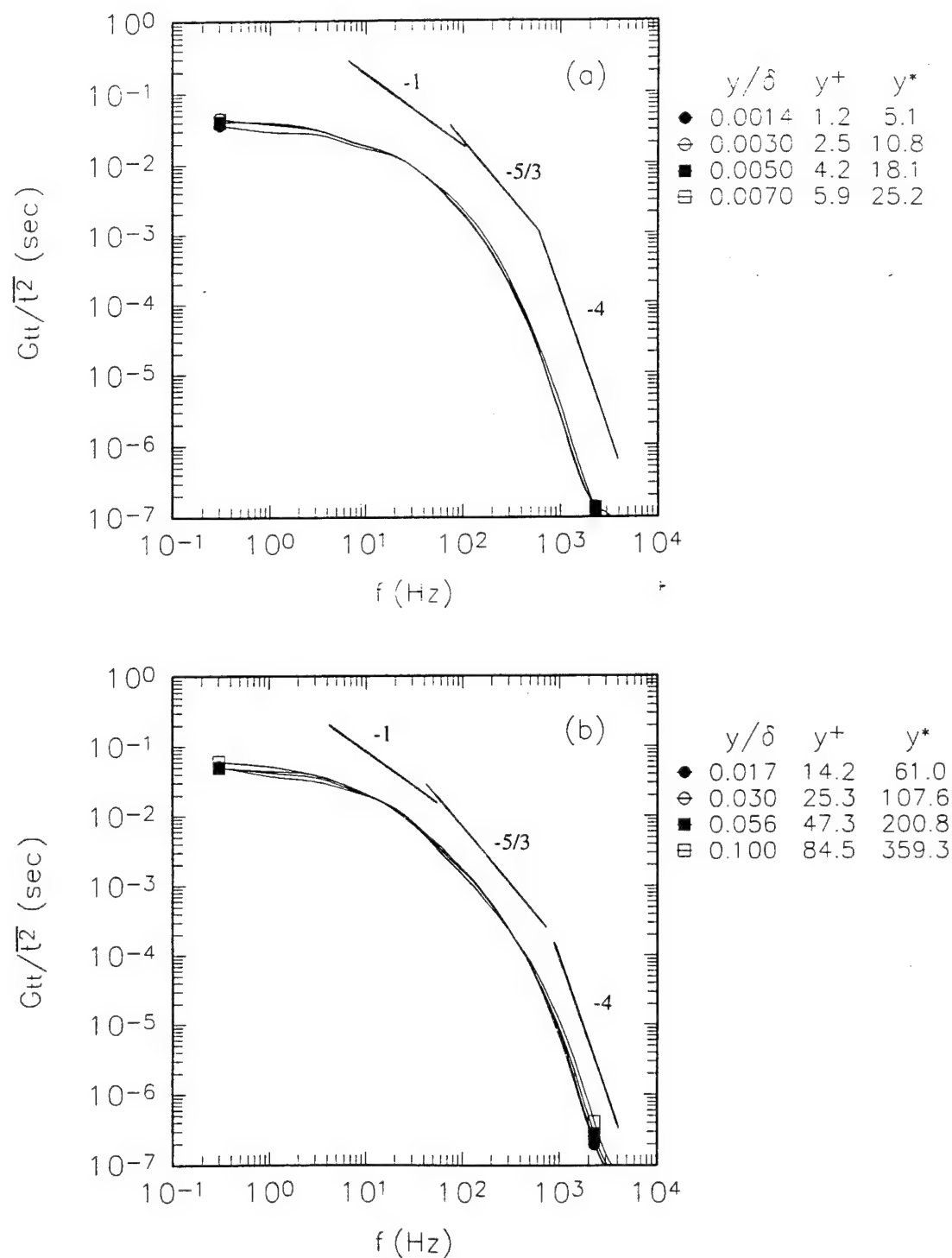


Fig. 7.51a,b. Normalized t power spectral distribution just upstream of detachment, at $x = 341.6$ cm. (a) in the buffer region; (b) in the fully turbulent region; (c) in the outer region.

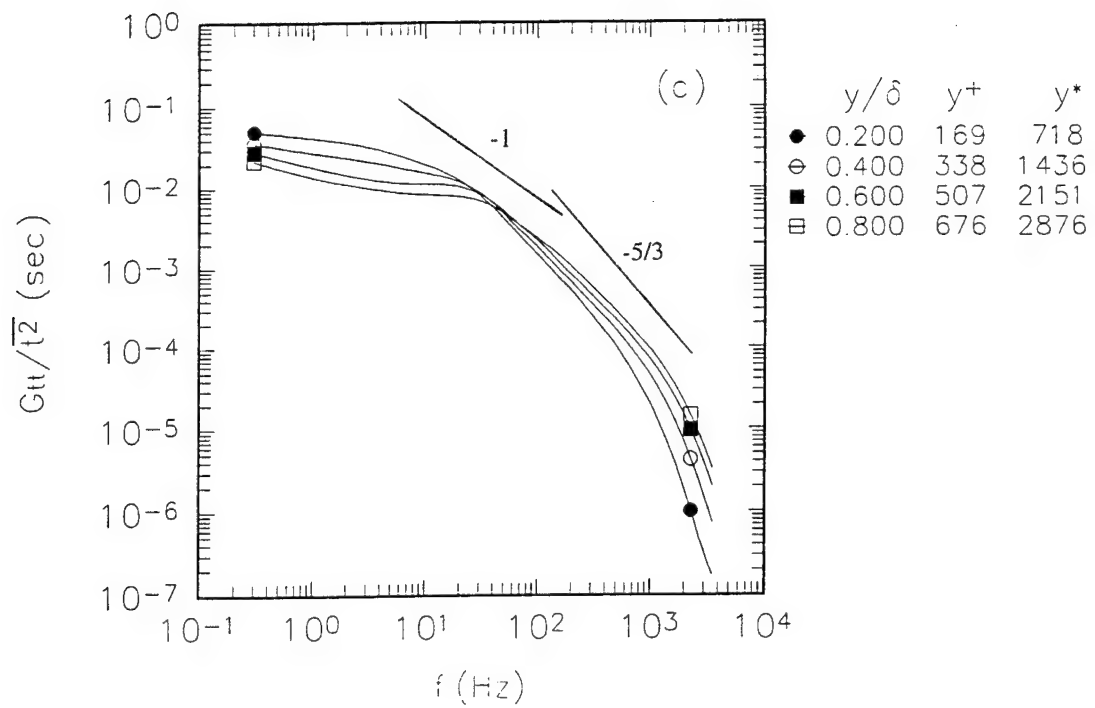


Fig. 7.51c. Normalized t power spectral distribution measured just upstream of detachment, at $x = 341.6$ cm. (a) in the buffer region; (b) in the fully turbulent region; (c) in the outer region.

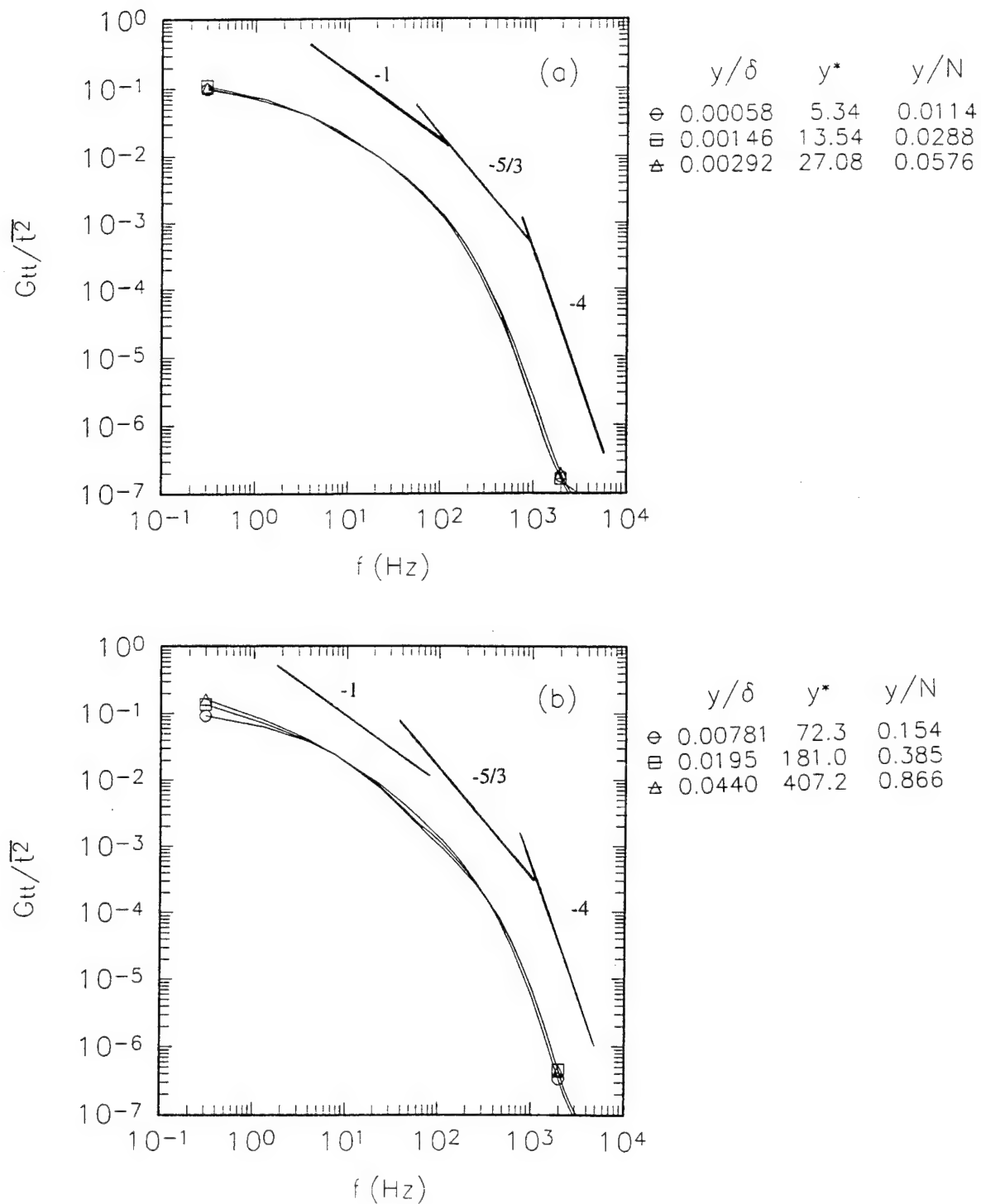


Fig. 7.52a,b. Normalized t power spectral distribution downstream of detachment, $x = 407.03$ cm. (a) in the near-wall region of the backflow; (b) in the outer backflow; (c) in transitional region; (d) in the outer region.

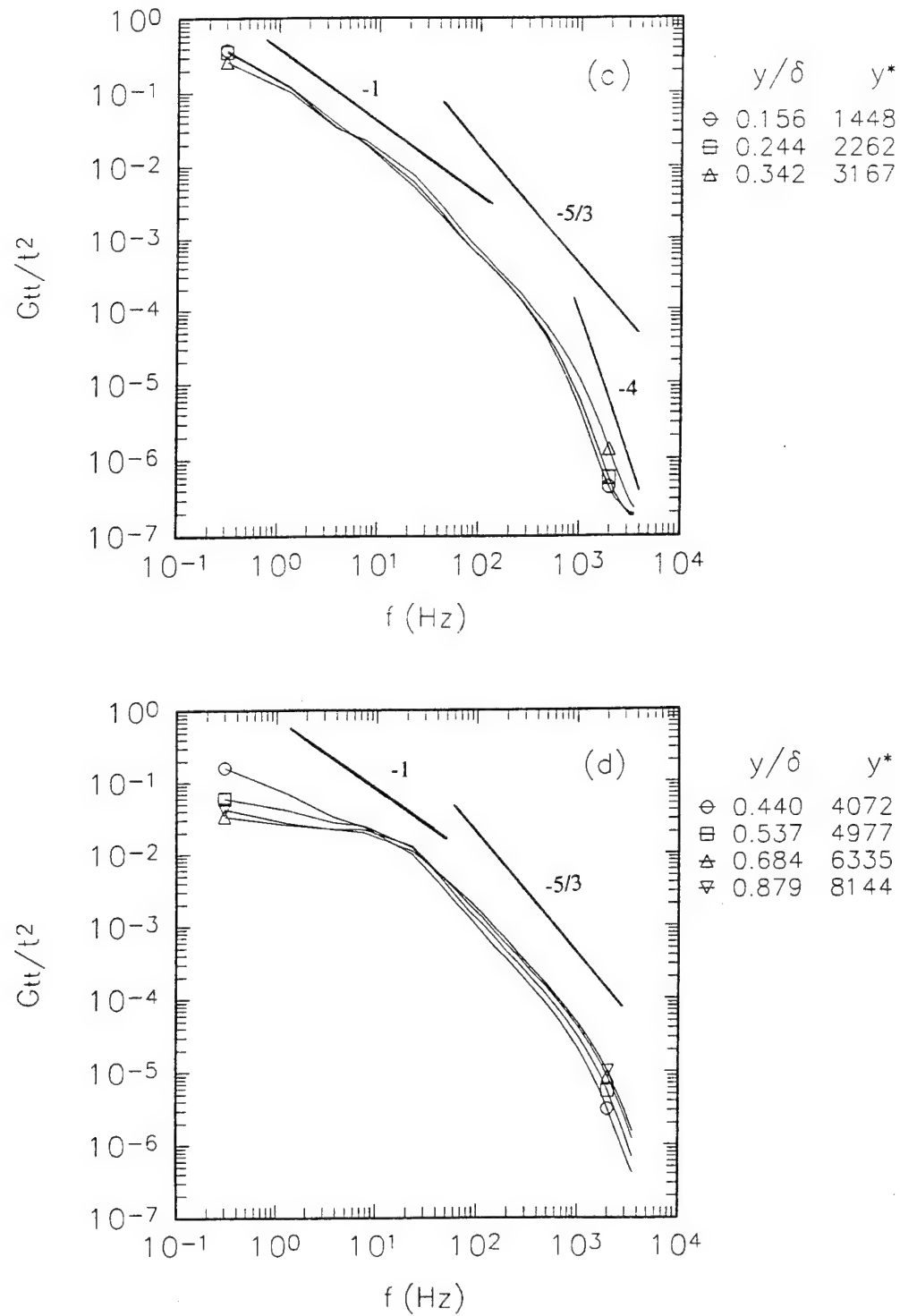


Fig. 7.52c,d. Normalized t power spectral distribution downstream of detachment, $x = 407.03$ cm. (a) in the near-wall region of the backflow; (b) in the outer backflow; (c) in transitional region; (d) in the outer region.

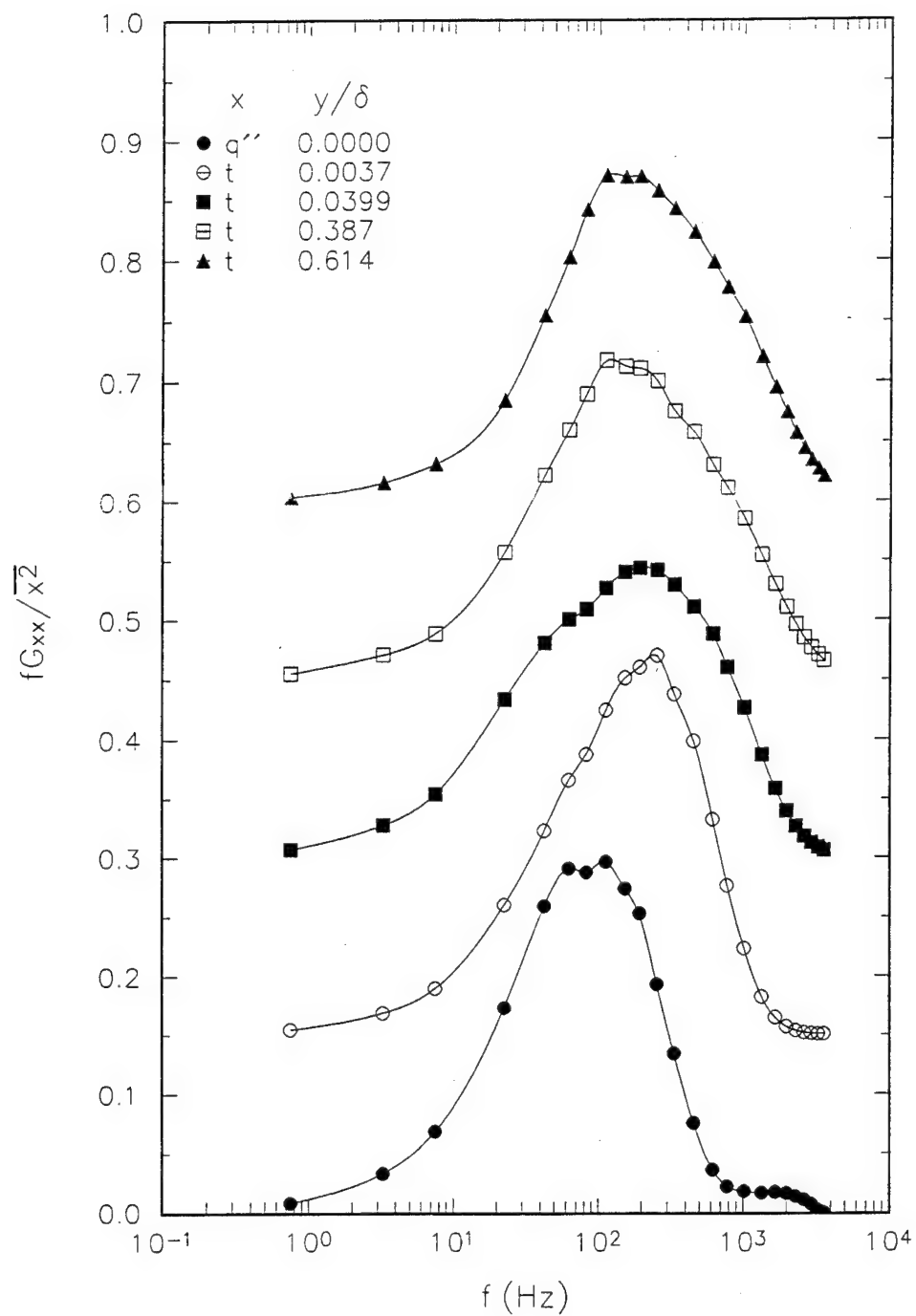


Fig. 7.53. Normalized first moment of q'' and t power spectral distribution far upstream of detachment, at $x = 285.4$ cm. Y-axis applies to surface heat flux spectra. Temperature spectra are offset successively by 0.15.

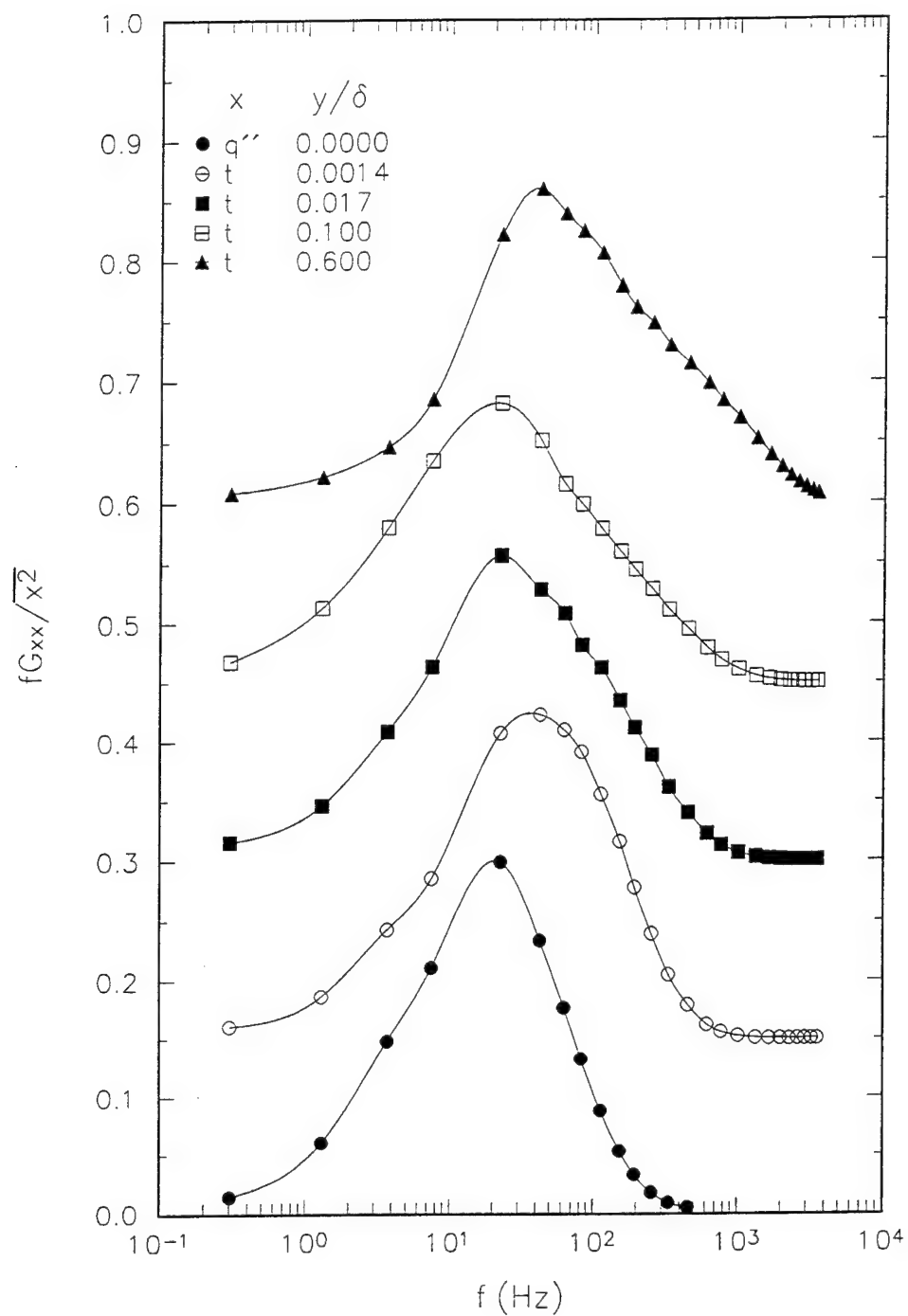


Fig. 7.54. Normalized first moment of q'' and t power spectral distribution just upstream of detachment, at $x = 341.6$ cm. Y-axis applies to surface heat flux spectra. Temperature spectra are offset successively by 0.15.

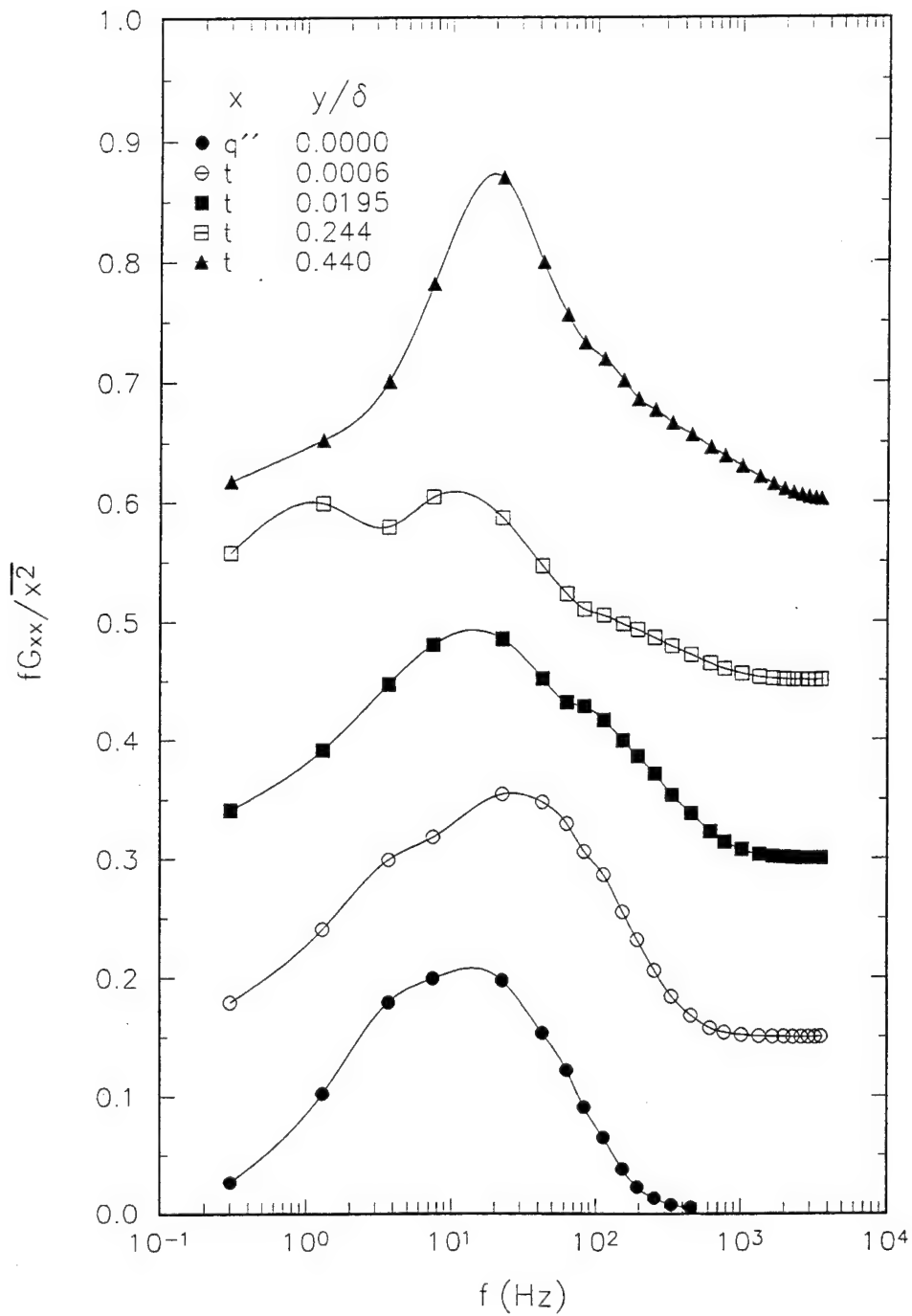


Fig. 7.55. Normalized first moment of q_0'' and t power spectral distribution downstream of detachment, at $x = 407.0$ cm. Y-axis applies to surface heat flux spectra. Temperature spectra are offset successively by 0.15.

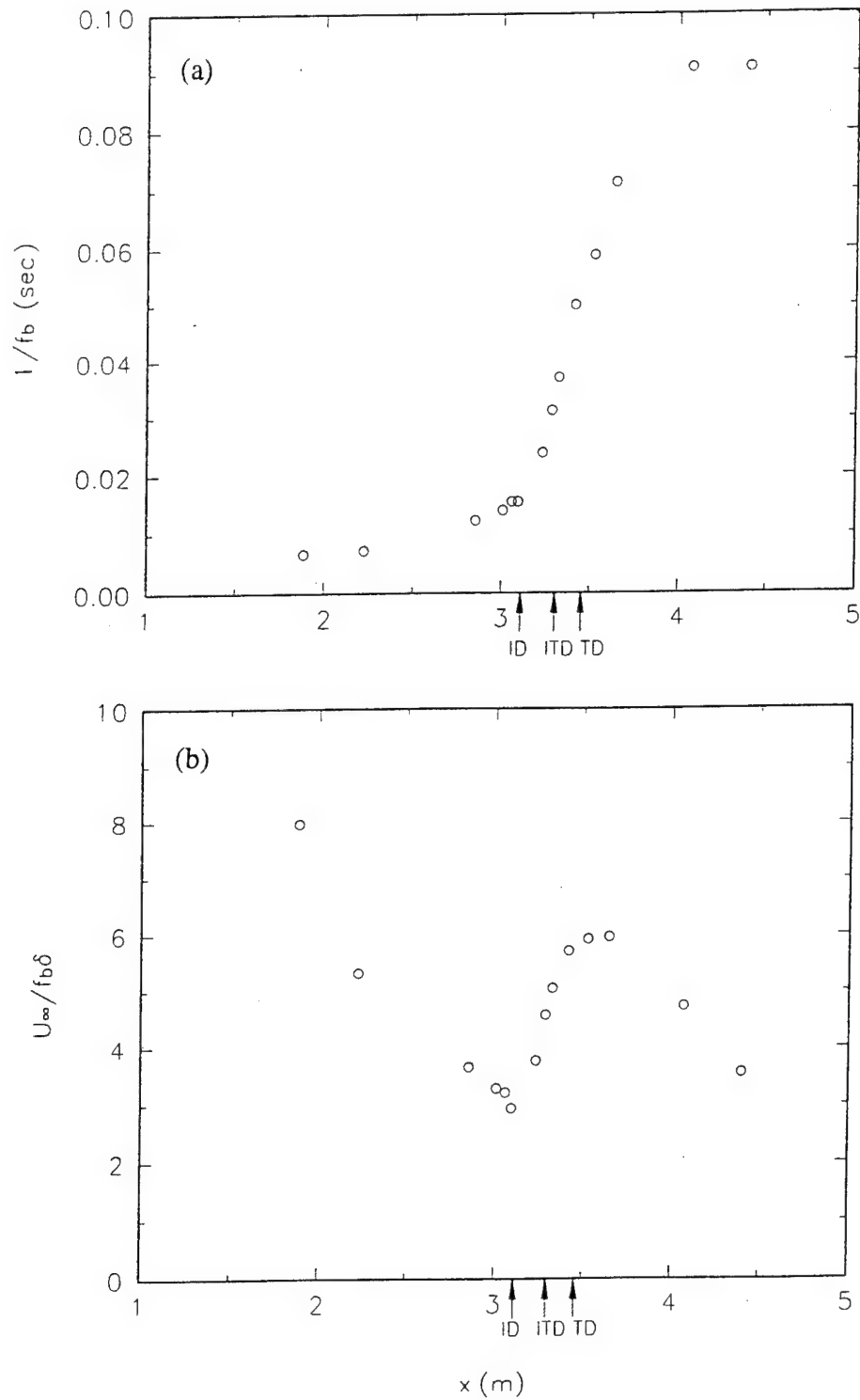


Fig. 7.56. Streamwise distribution of characteristic frequency from spectra of surface heat flux fluctuations. (a) dimensional period; (b) characteristic period normalized with outer flow velocity and length scale.

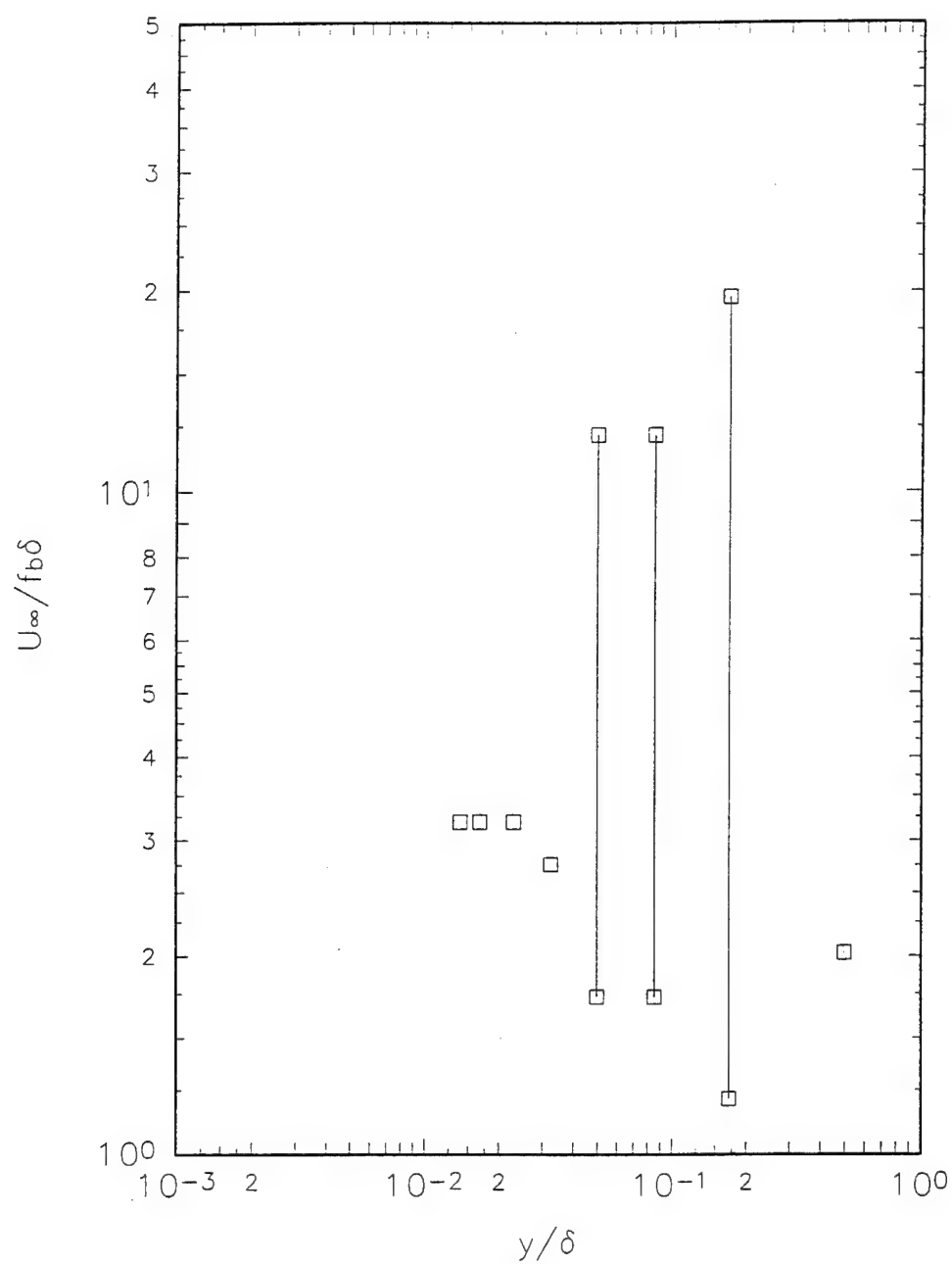


Fig. 7.57a. Profiles of characteristic frequency from spectra of temperature fluctuations at $x = 188.60$ cm.

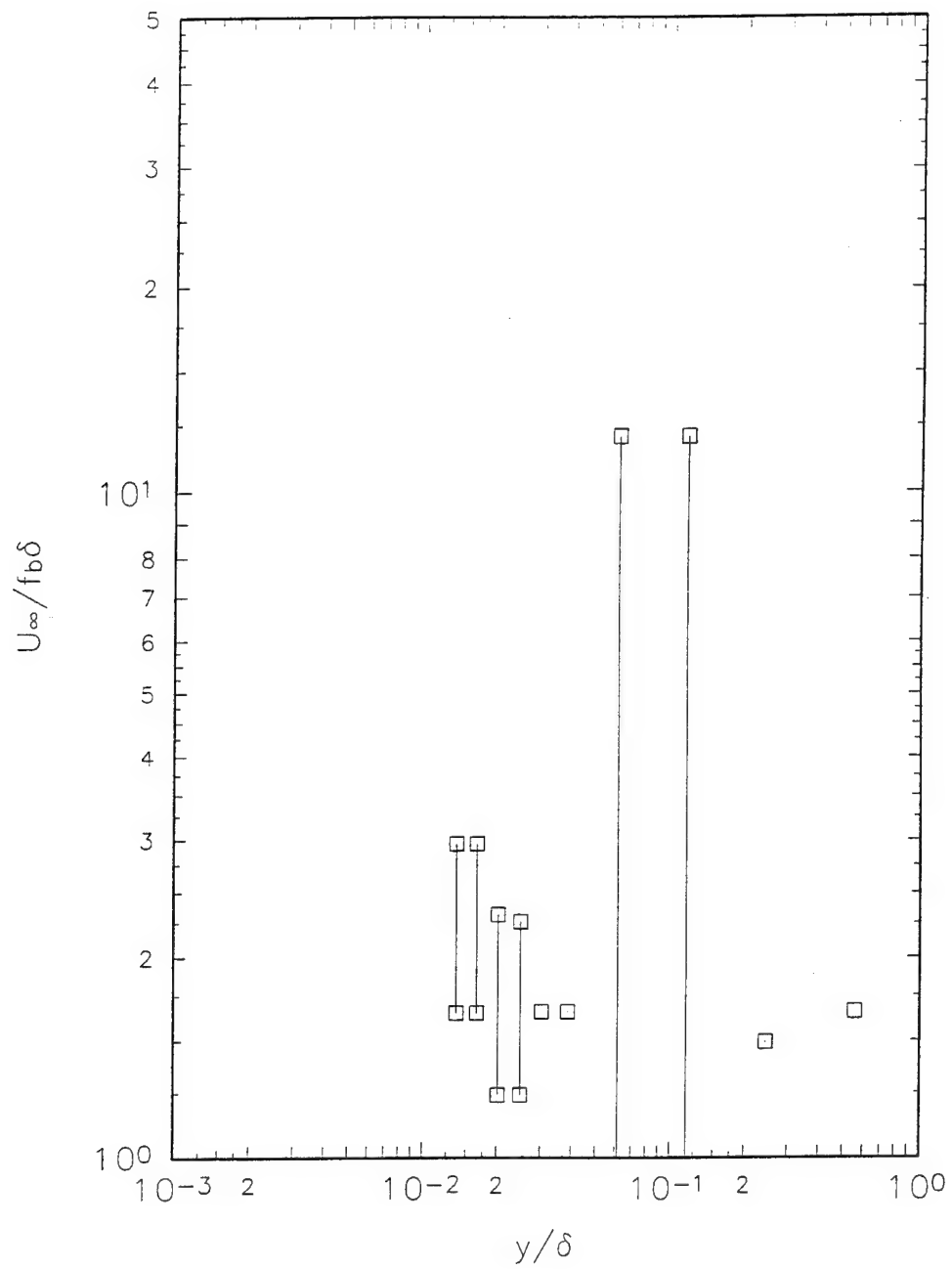


Fig. 7.57b. Profiles of characteristic frequency from spectra of temperature fluctuations at $x = 222.57$ cm.

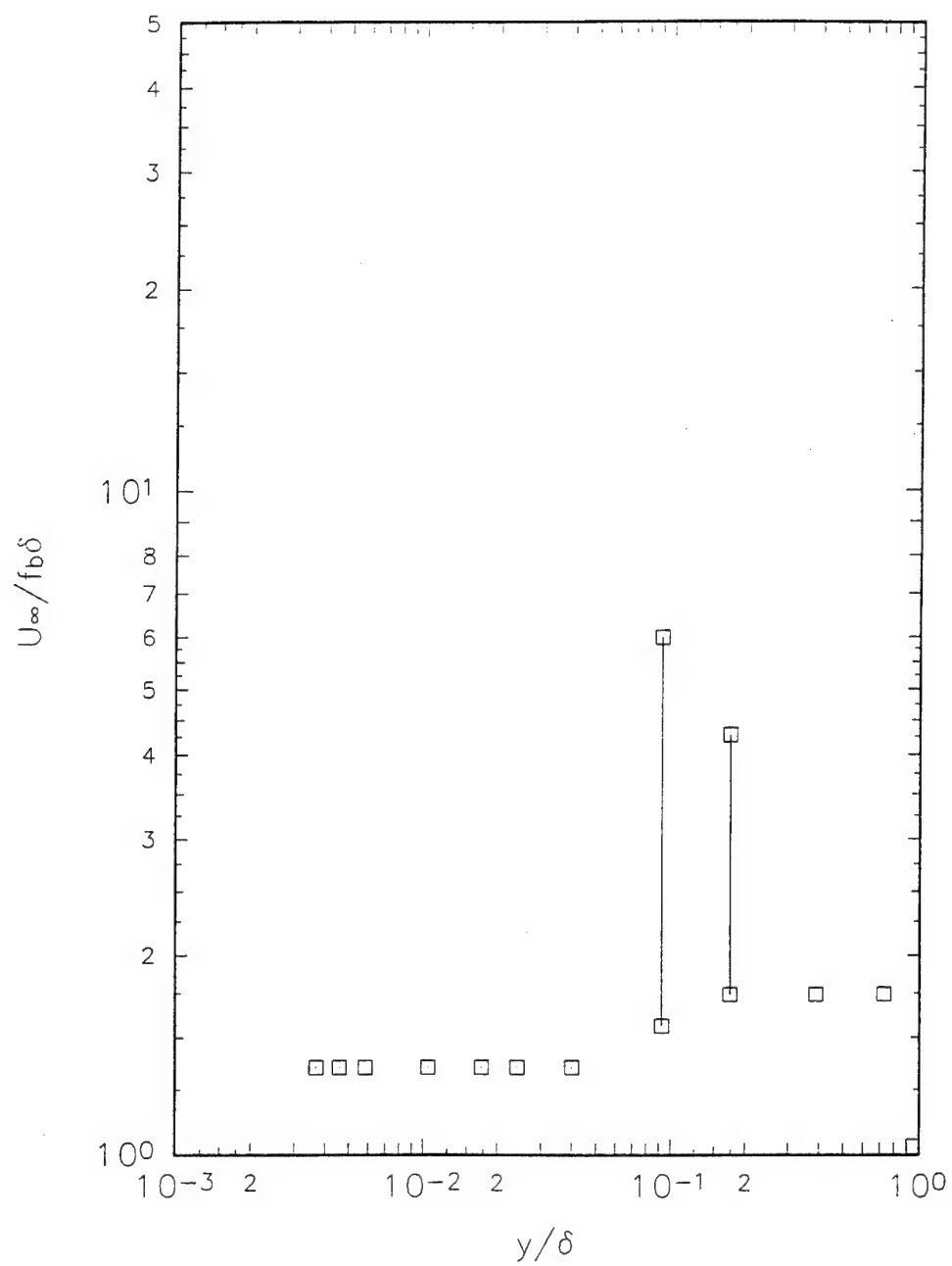


Fig. 7.57c. Profiles of characteristic frequency from spectra of temperature fluctuations at $x = 285.43$ cm.

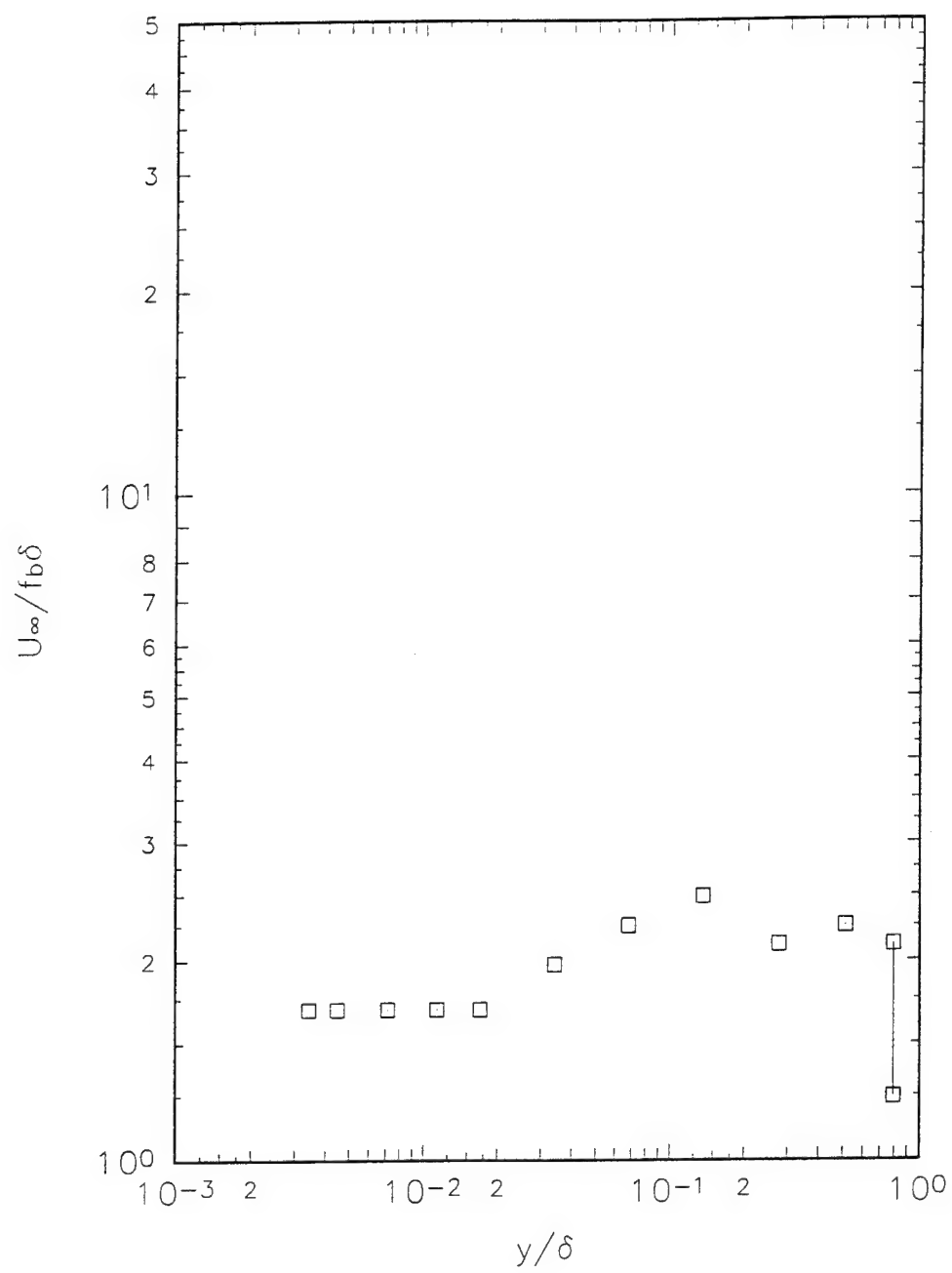


Fig. 7.57d. Profiles of characteristic frequency from spectra of temperature fluctuations at $x = 300.99$ cm.

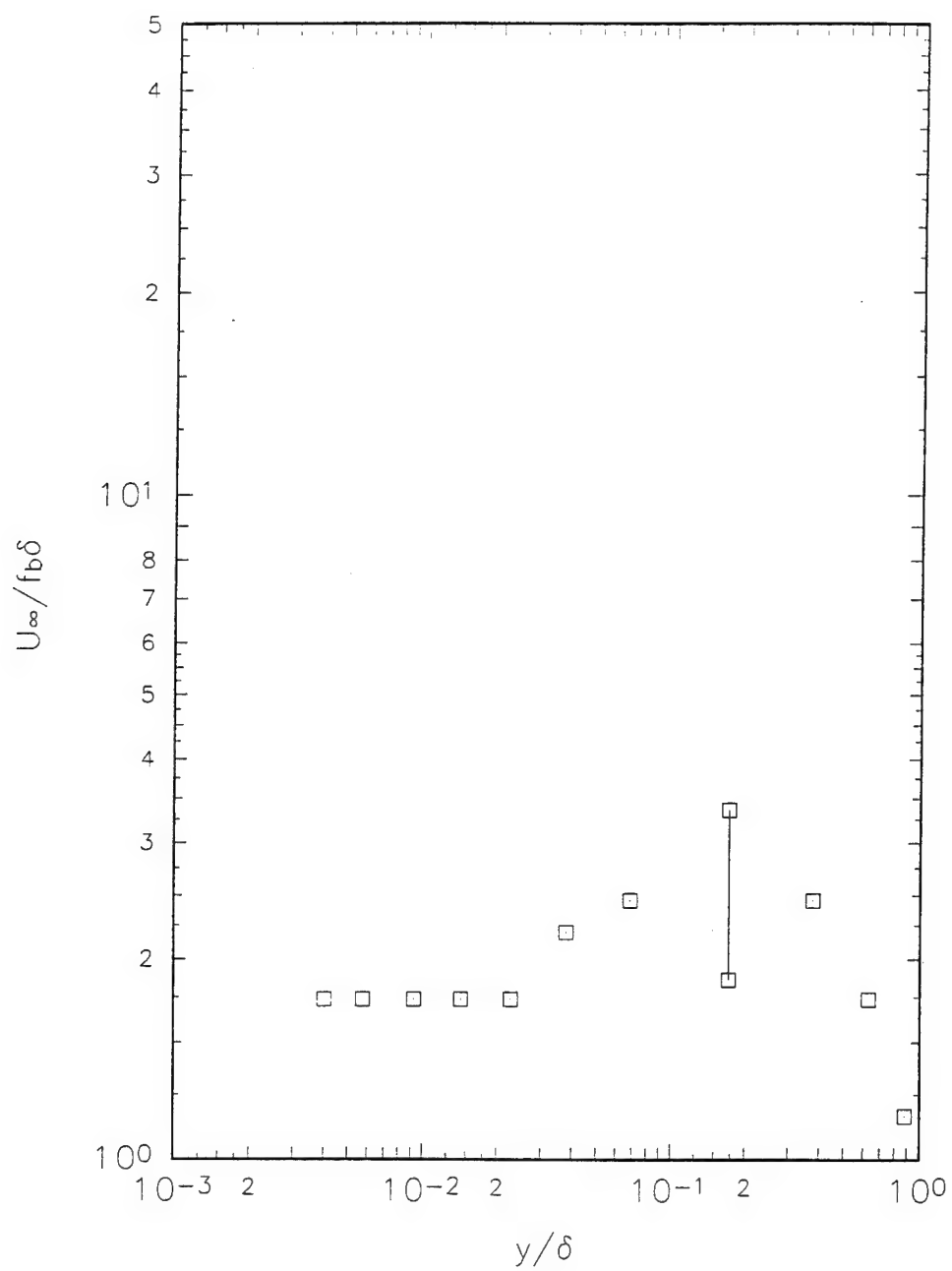


Fig. 7.57e. Profiles of characteristic frequency from spectra of temperature fluctuations at $x = 306.07$ cm.

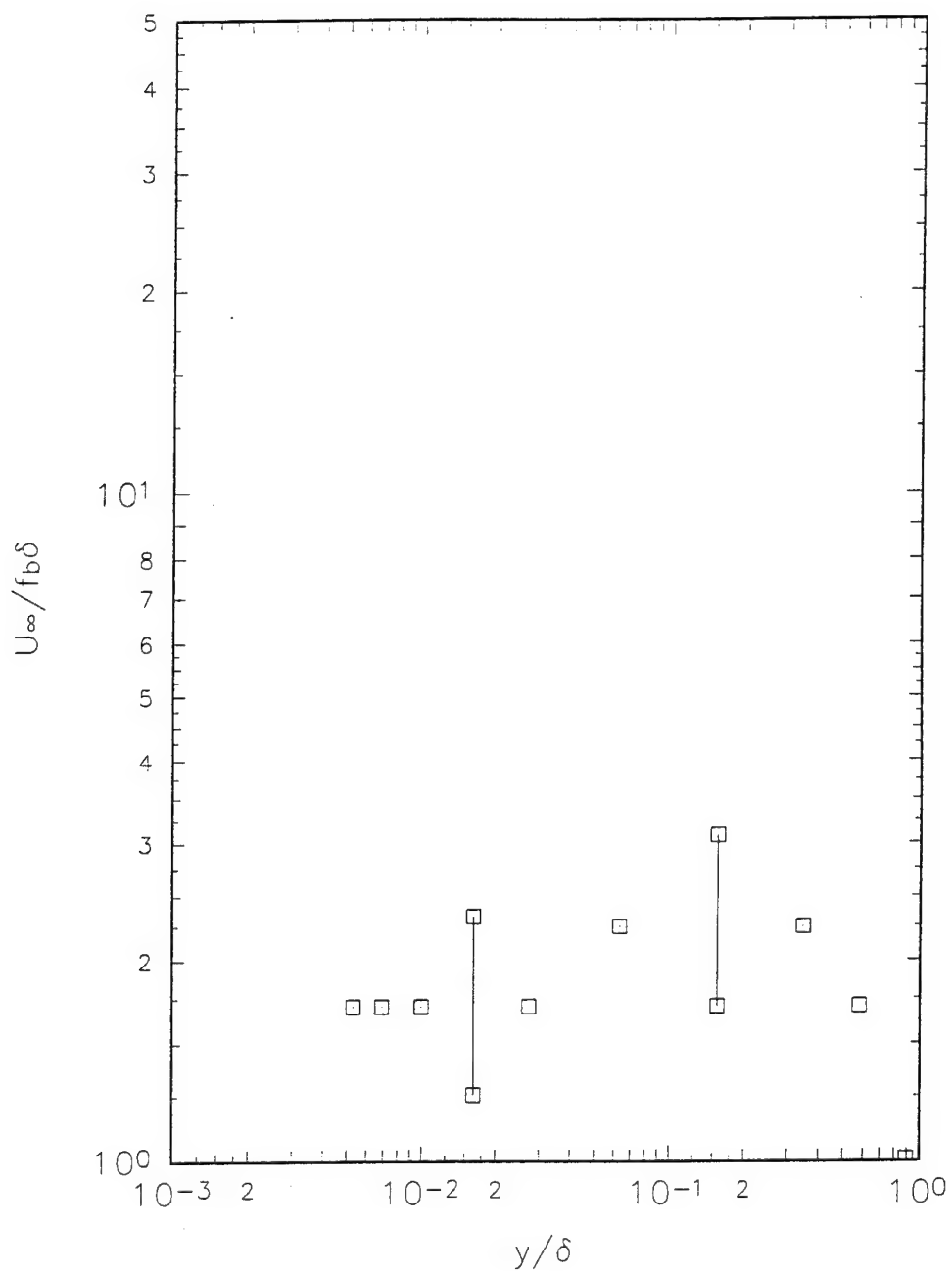


Fig. 7.57f. Profiles of characteristic frequency from spectra of temperature fluctuations at $x = 309.56$ cm.

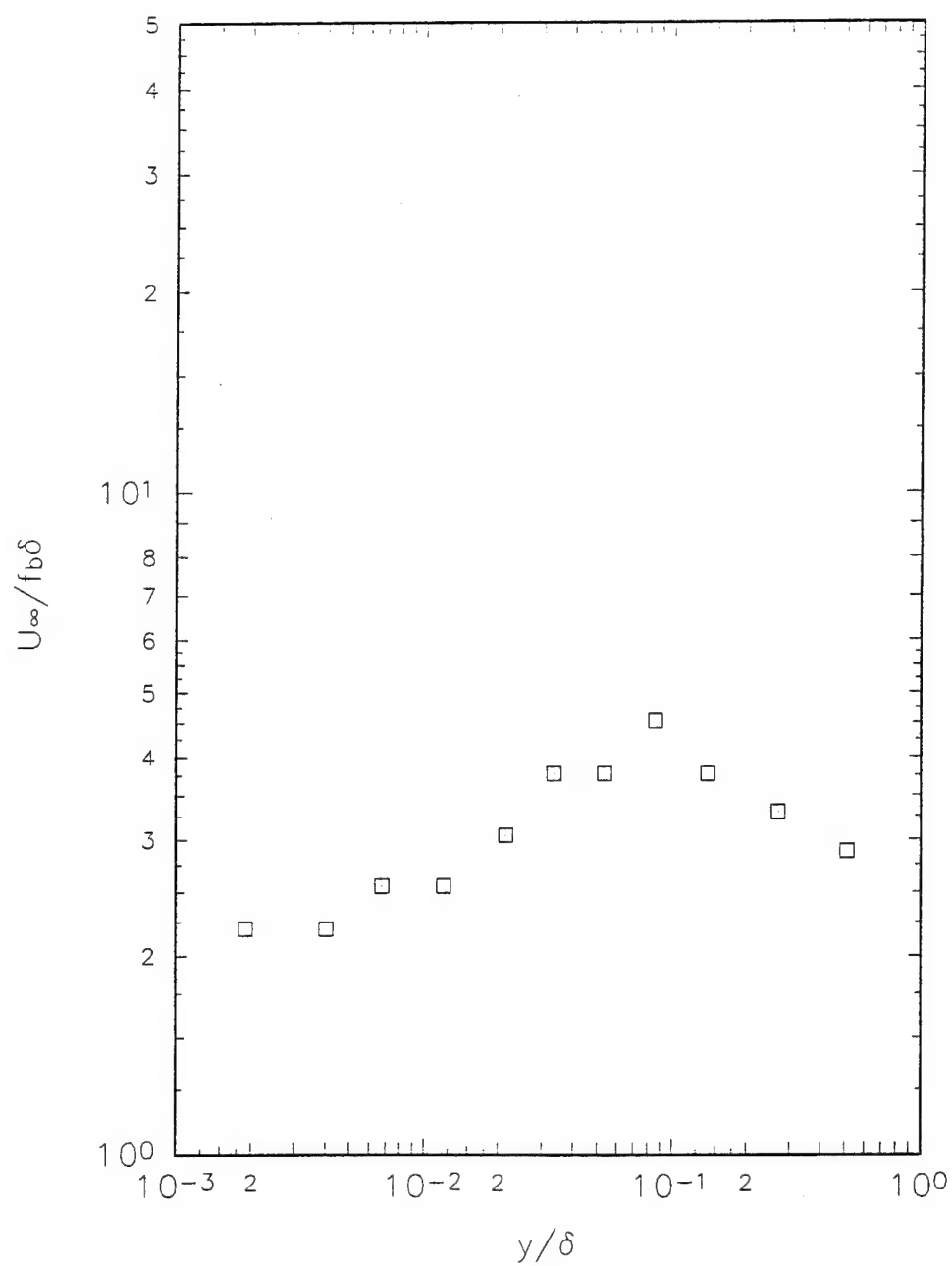


Fig. 7.57g. Profiles of characteristic frequency from spectra of temperature fluctuations at $x = 323.22$ cm.

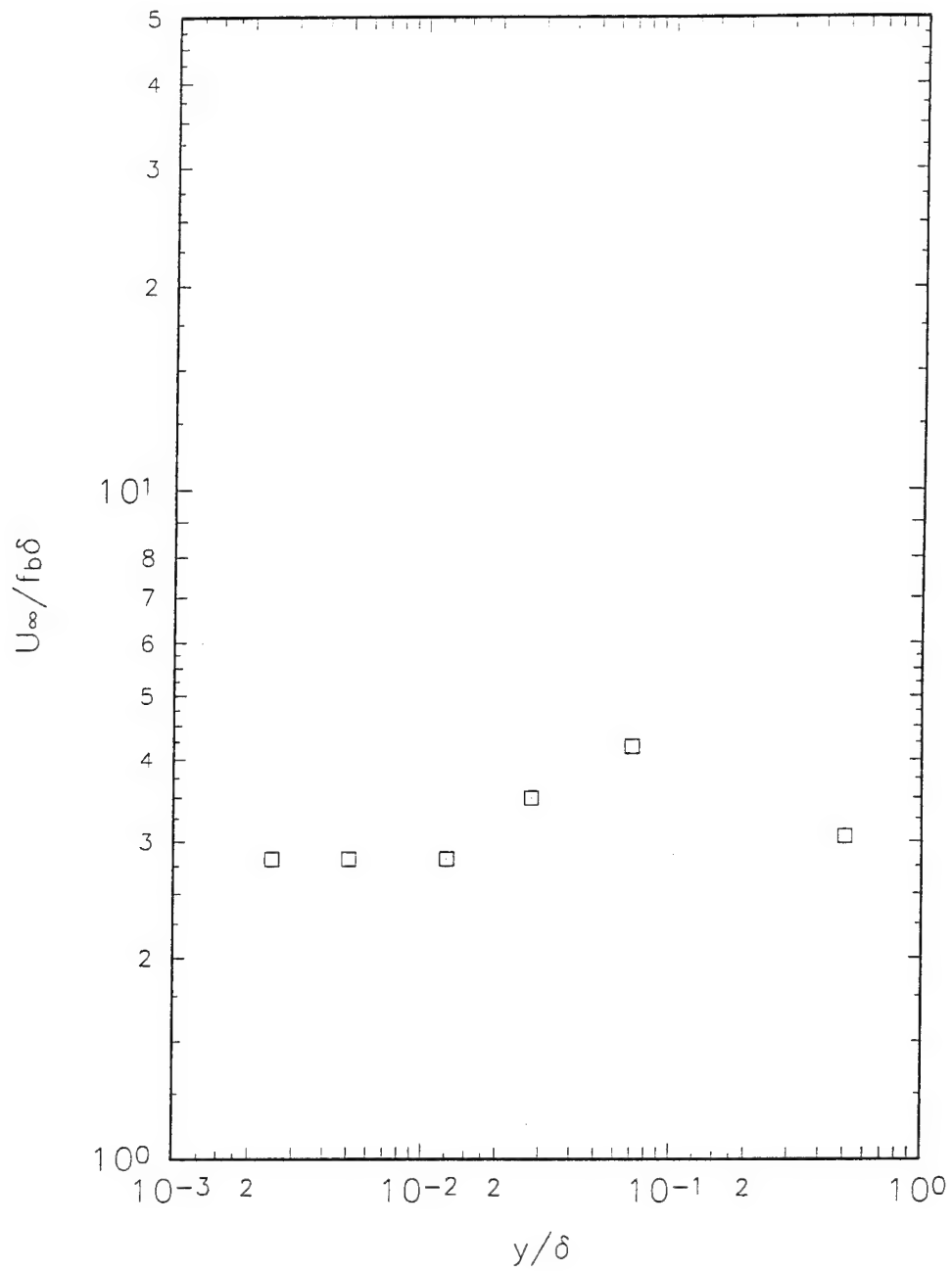


Fig. 7.57h. Profiles of characteristic frequency from spectra of temperature fluctuations at $x = 328.61$ cm.

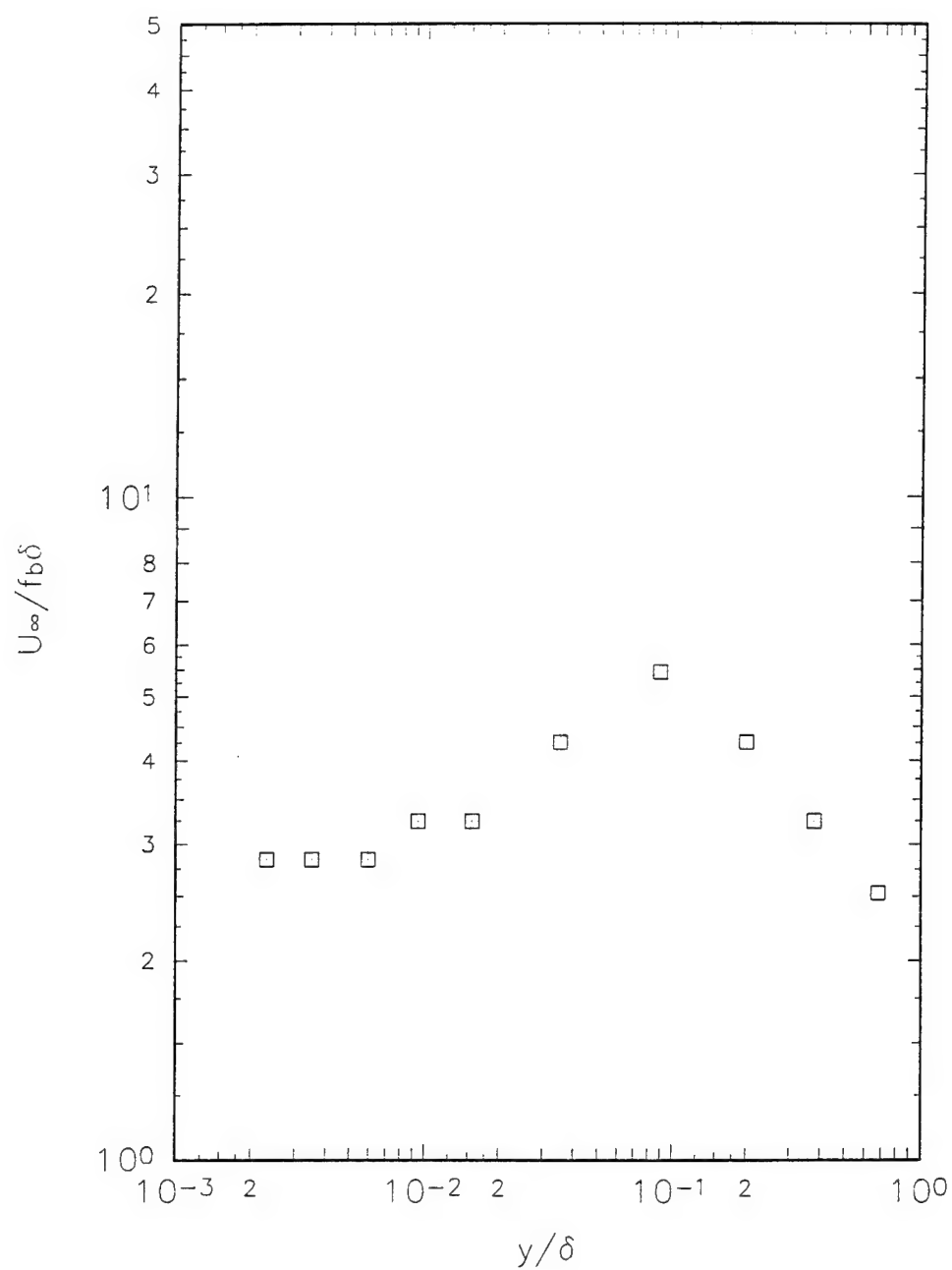


Fig. 7.57i. Profiles of characteristic frequency from spectra of temperature fluctuations at $x = 332.42$ cm.

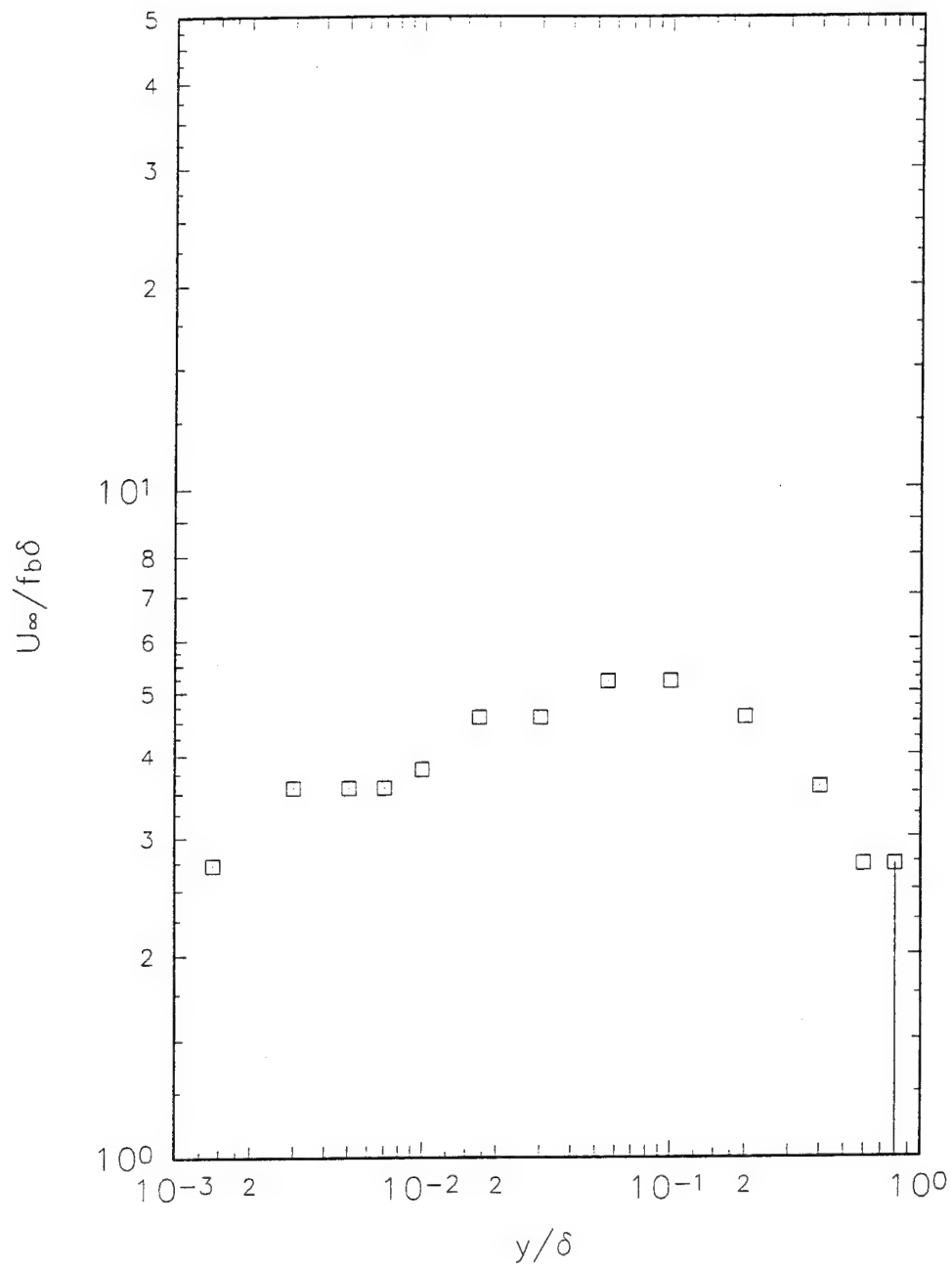


Fig. 7.57j. Profiles of characteristic frequency from spectra of temperature fluctuations at $x = 341.63$ cm.

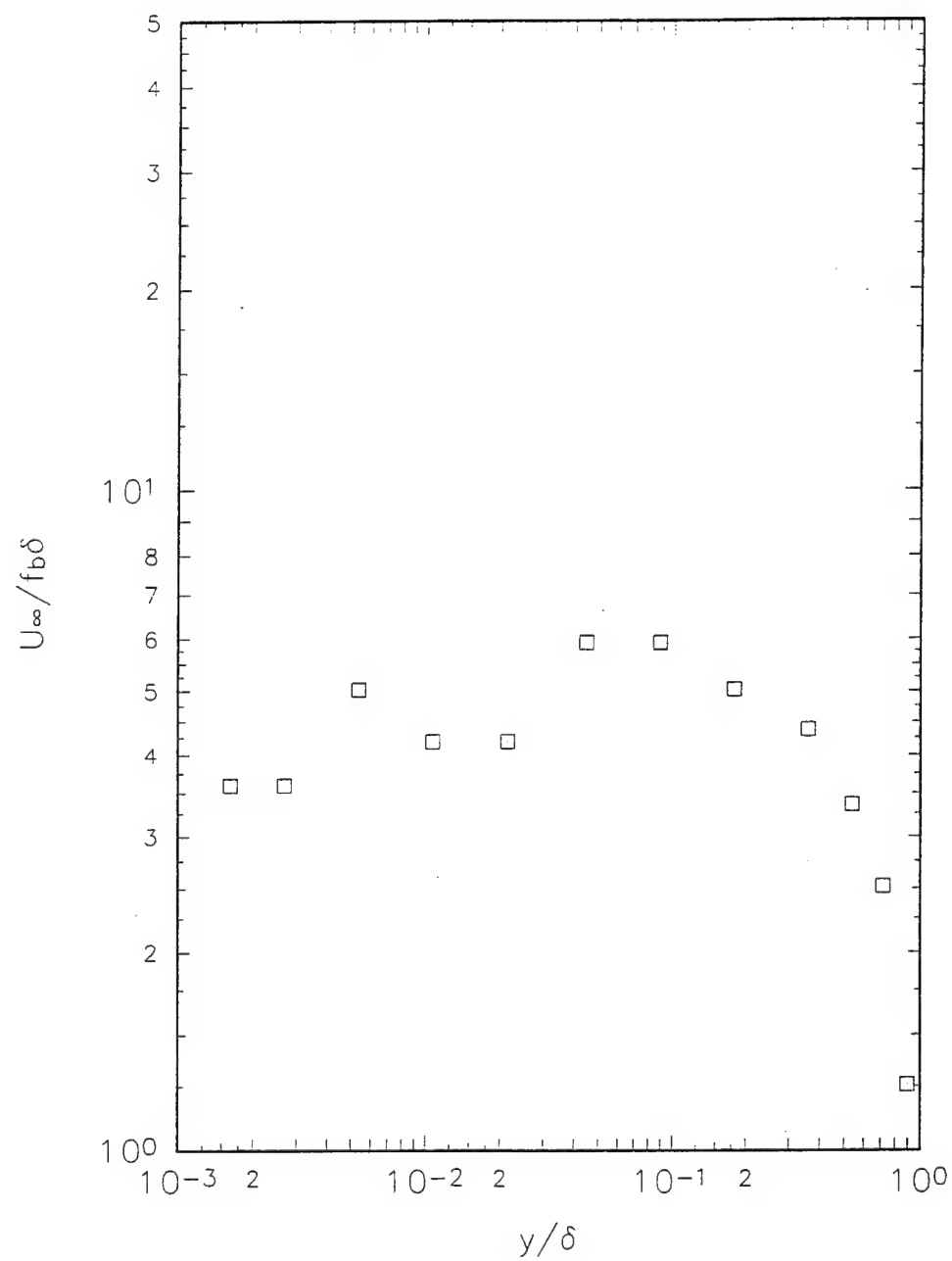


Fig. 7.57k. Profiles of characteristic frequency from spectra of temperature fluctuations at $x = 352.43$ cm.

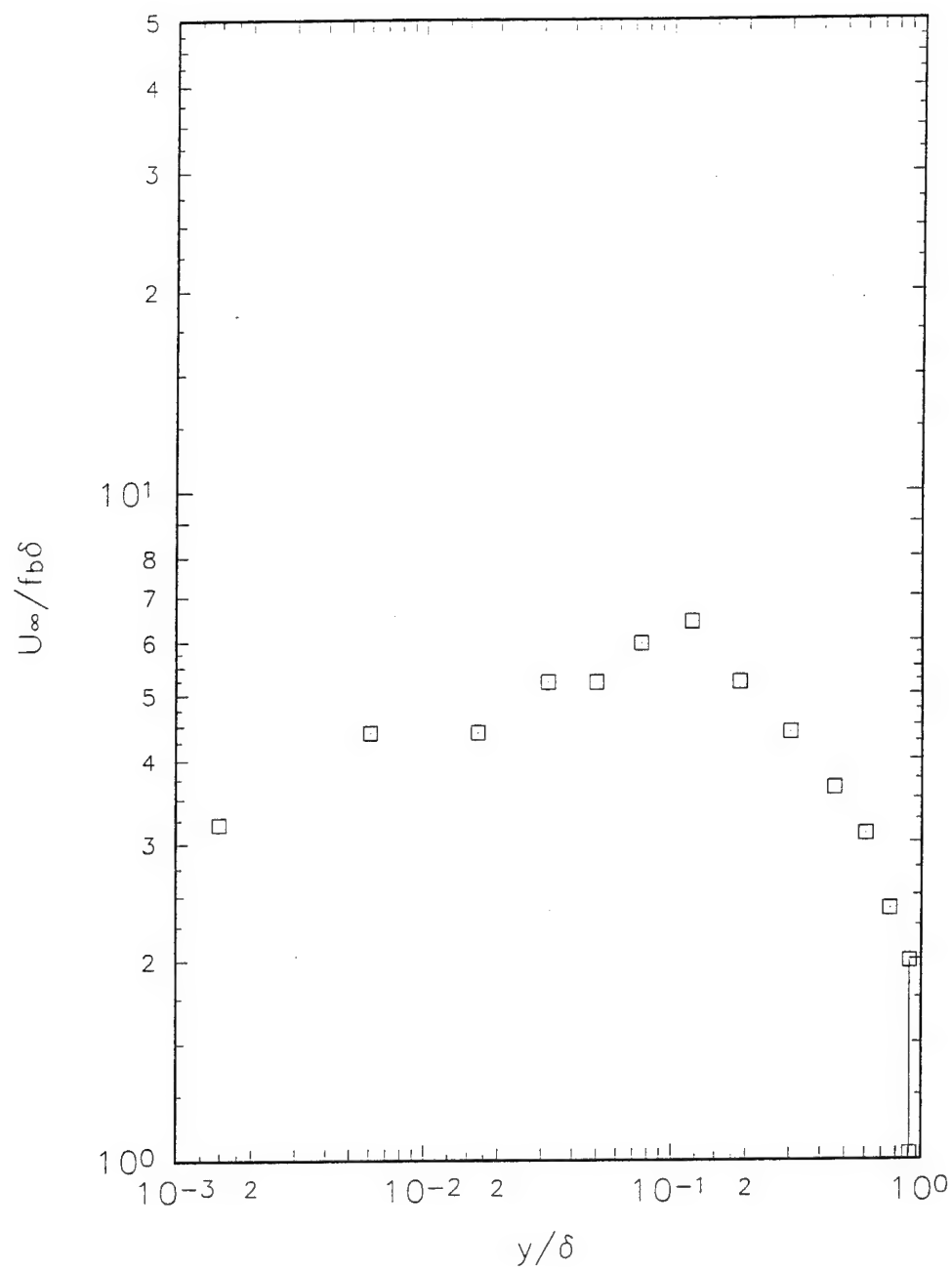


Fig. 7.571. Profiles of characteristic frequency from spectra of temperature fluctuations at $x = 364.49$ cm.

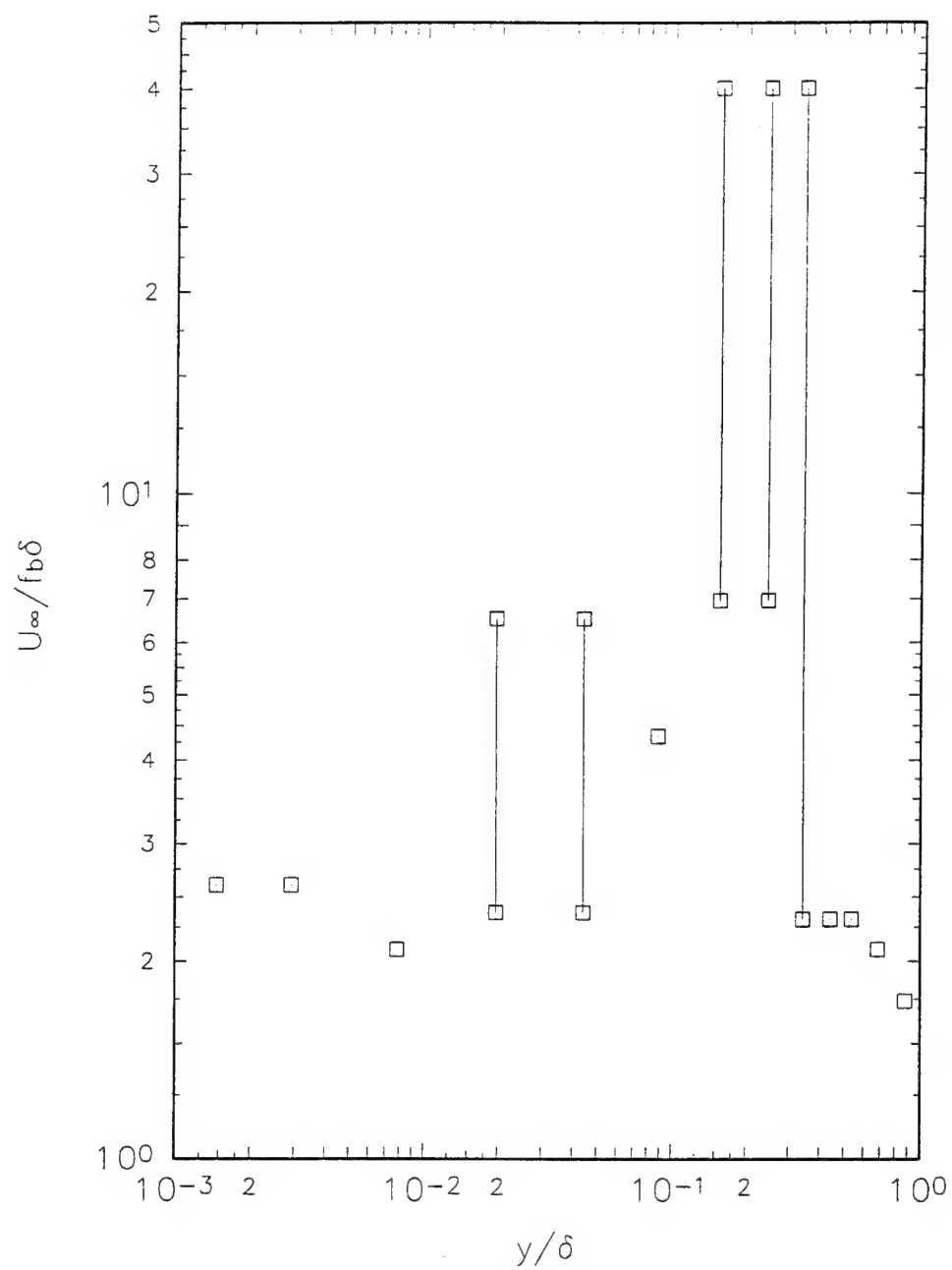


Fig. 7.57m. Profiles of characteristic frequency from spectra of temperature fluctuations at $x = 407.04$ cm.

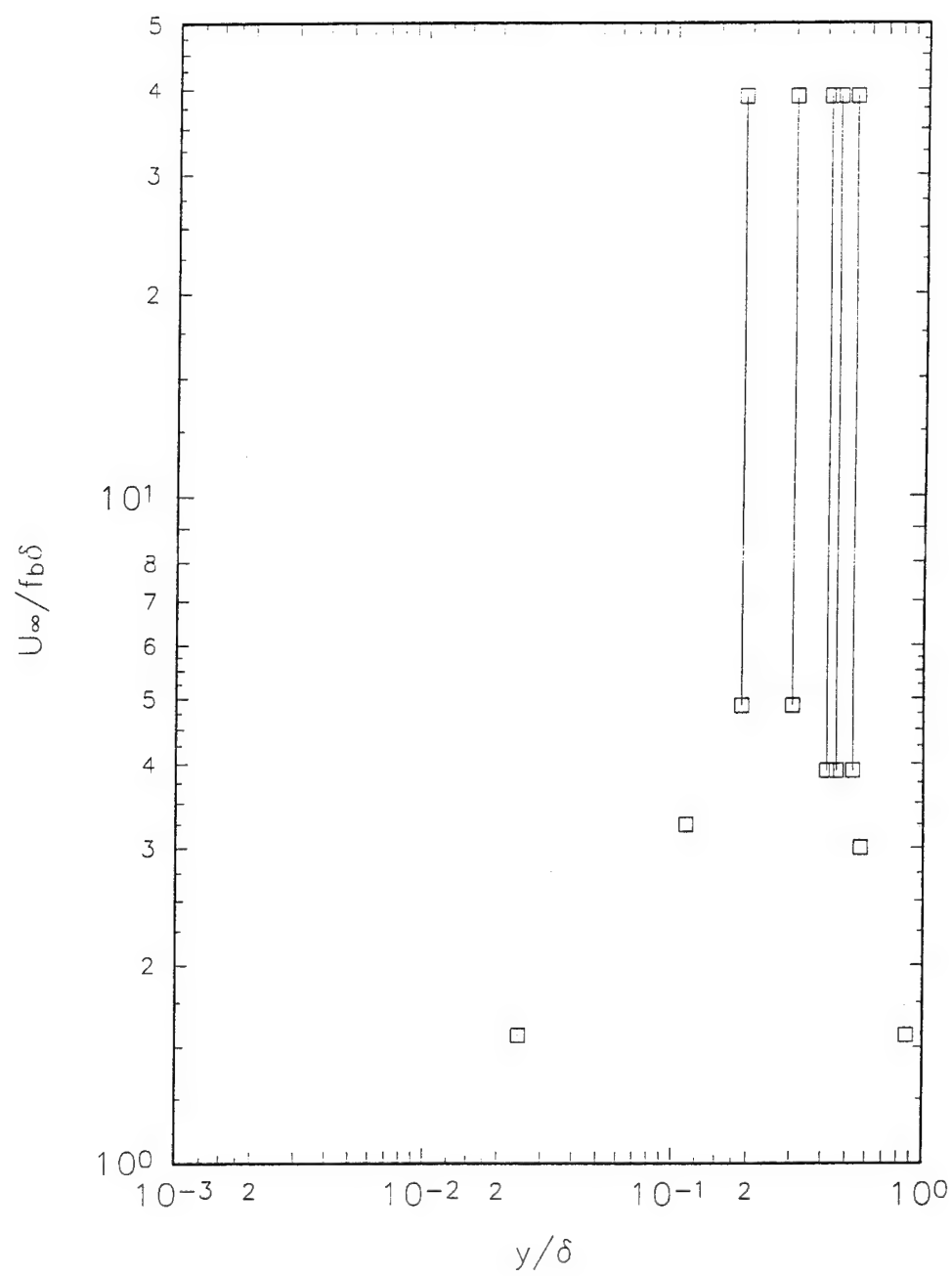


Fig. 7.57n. Profiles of characteristic frequency from spectra of temperature fluctuations at $x = 440.01$ cm.

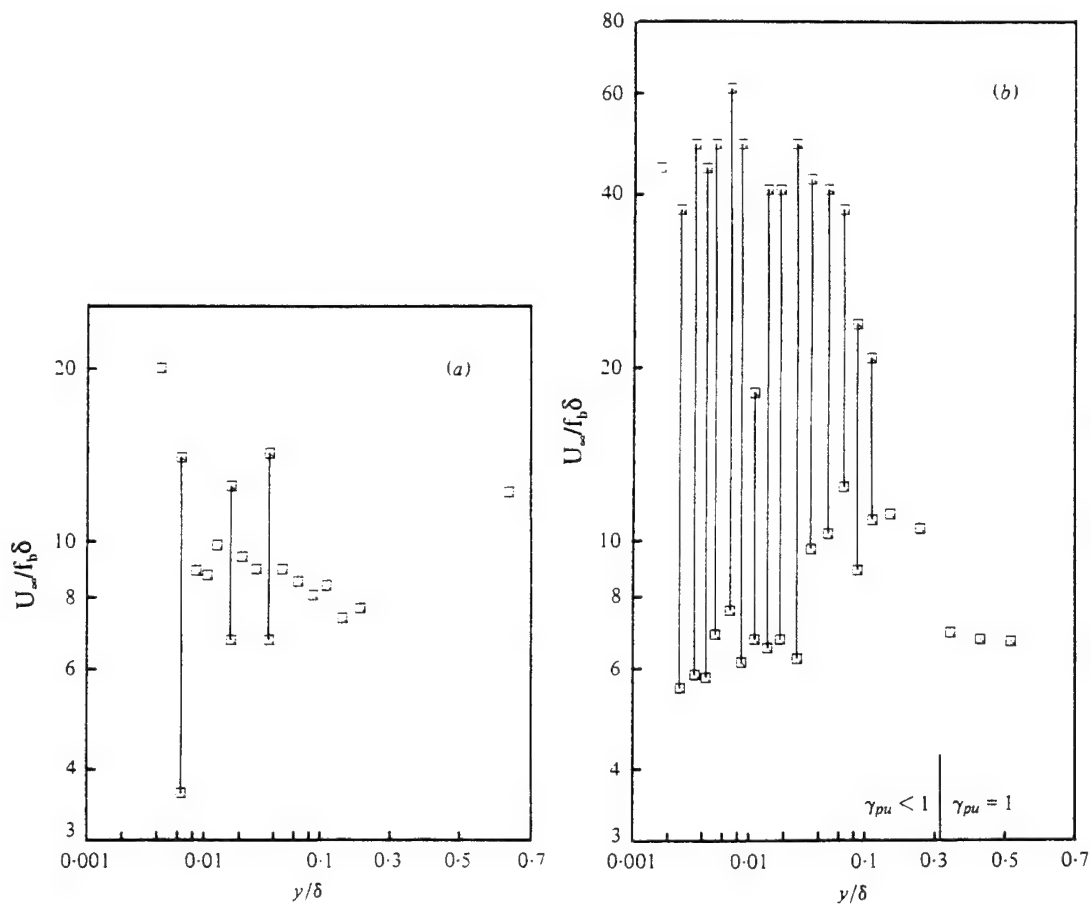


Figure 7.58. Characteristic frequency parameter $U_\infty/f_b\delta$ at (a) 285.50 cm., (b) 341.63 cm., and (c) 398.27 cm. Note the log-linear abscissa. (from Simpson et al., 1981 b)

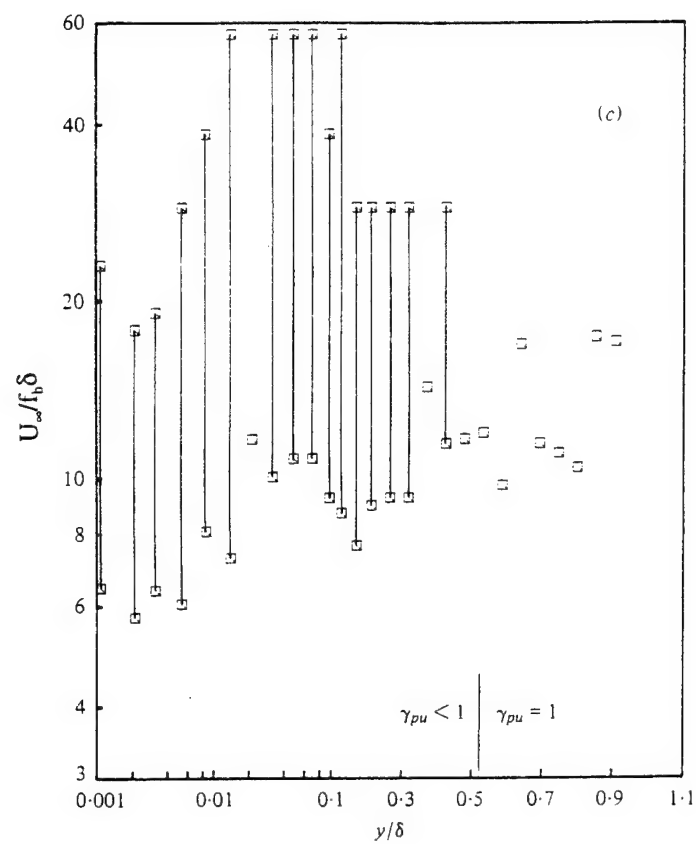


Figure 7.58c. Characteristic frequency parameter $U_\infty / f_b \delta$ at (a) 285.50 cm., (b) 341.63 cm., and (c) 398.27 cm. Note the log-linear abscissa. (from Simpson et al., 1981 b)

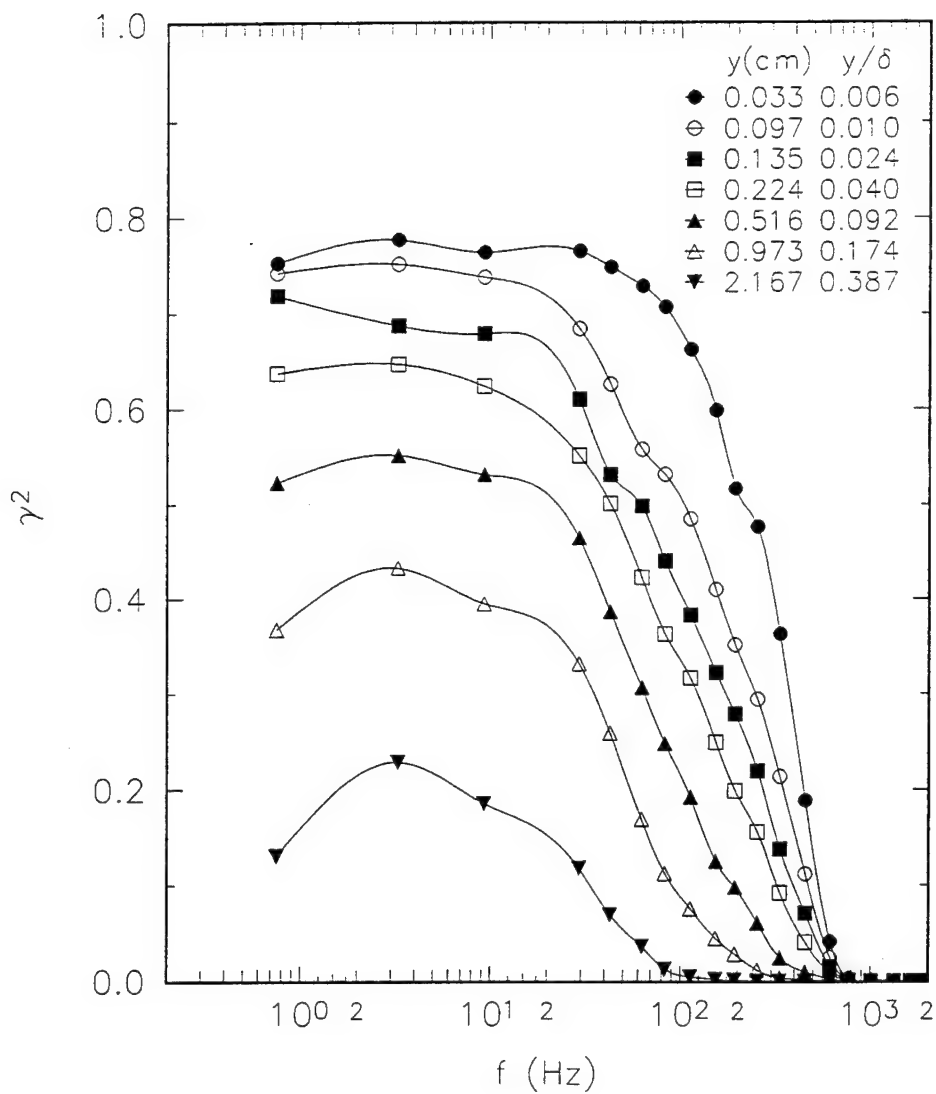


Fig. 7.59a. Spectral variation of coherency between surface heat flux and temperature at several distances from the wall far upstream of detachment, at $x = 285.4$ cm.

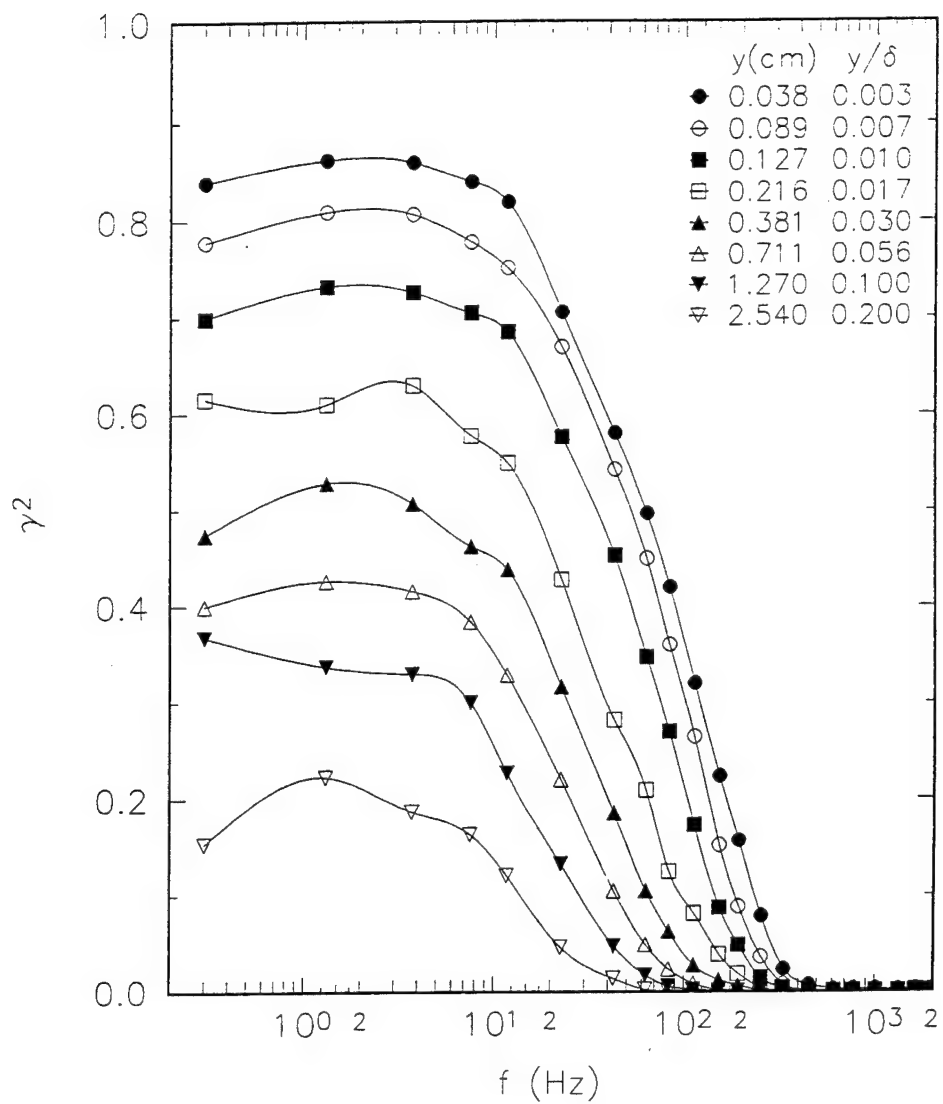


Fig. 7.59b. Spectral variation of coherency between surface heat flux and temperature at several distances from the wall just upstream of detachment, at $x = 341.6$ cm.

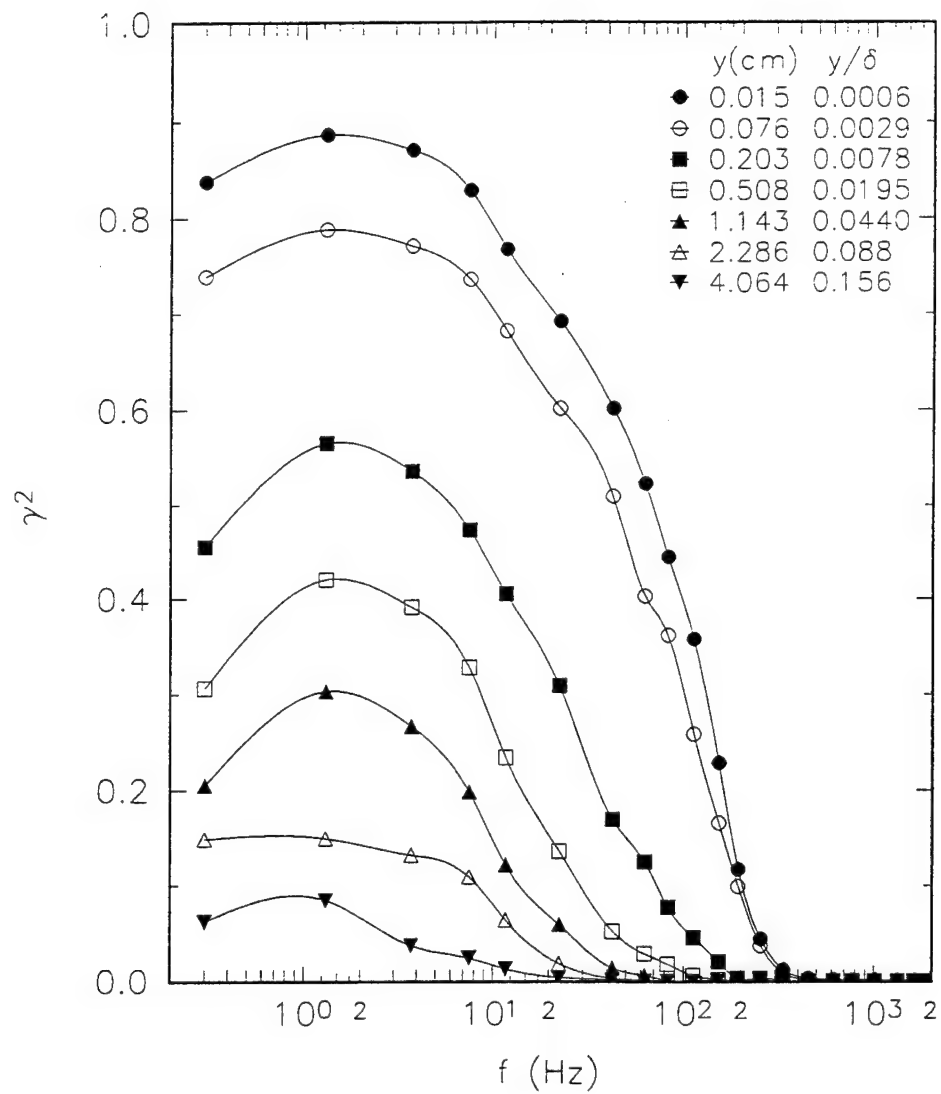


Fig. 7.59c. Spectral variation of coherency between surface heat flux and temperature at several distances from the wall downstream of detachment, at $x = 407.0$ cm.

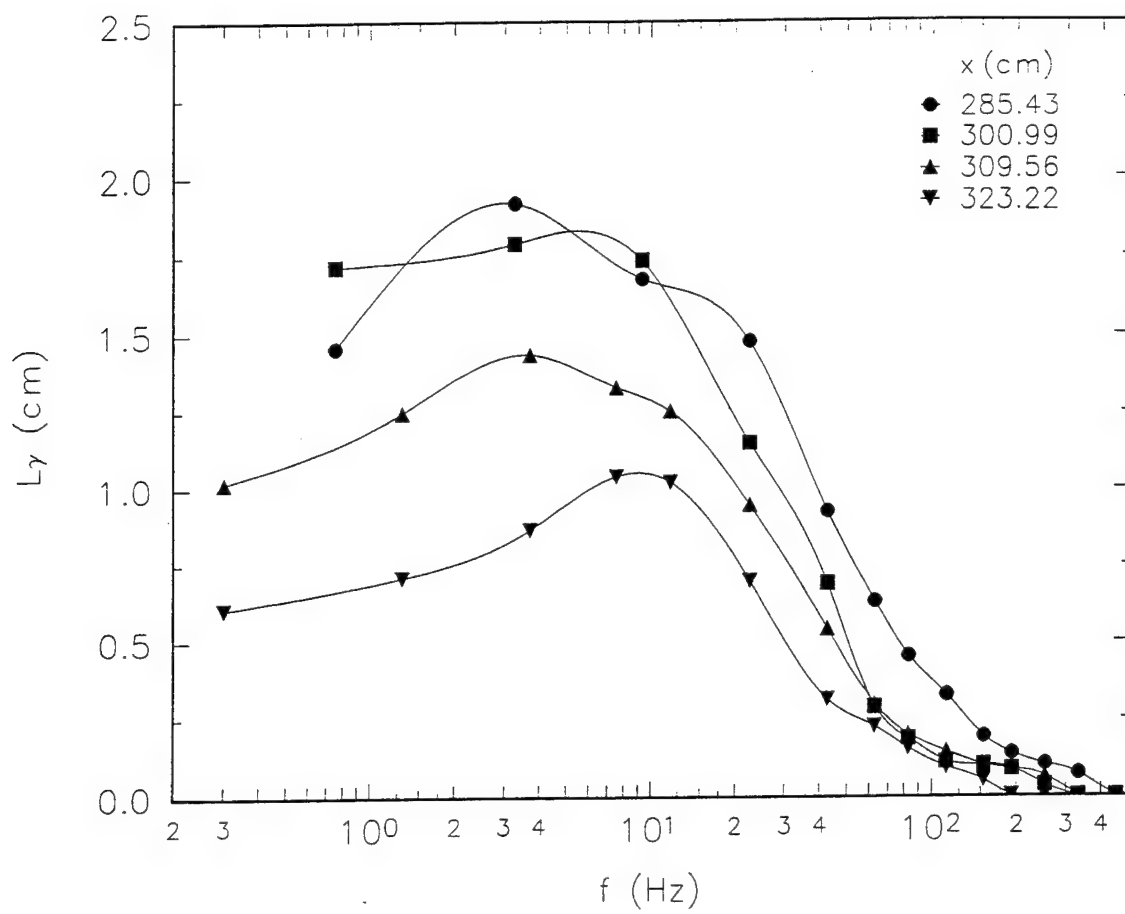


Fig. 7.60a. Spectral variation of coherence length scale far upstream of detachment.

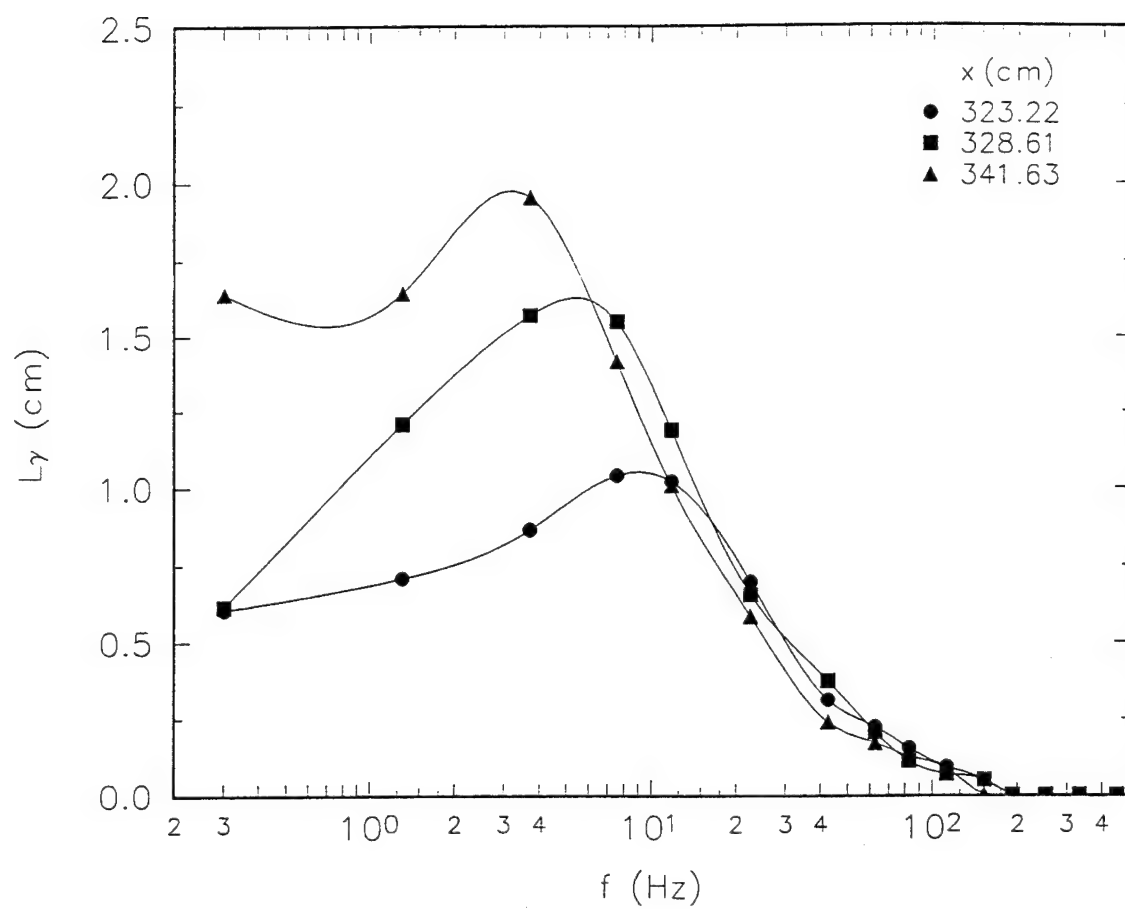


Fig. 7.60b. Spectral variation of coherence length scale in the region between *insipient detachment* and *detachment*.

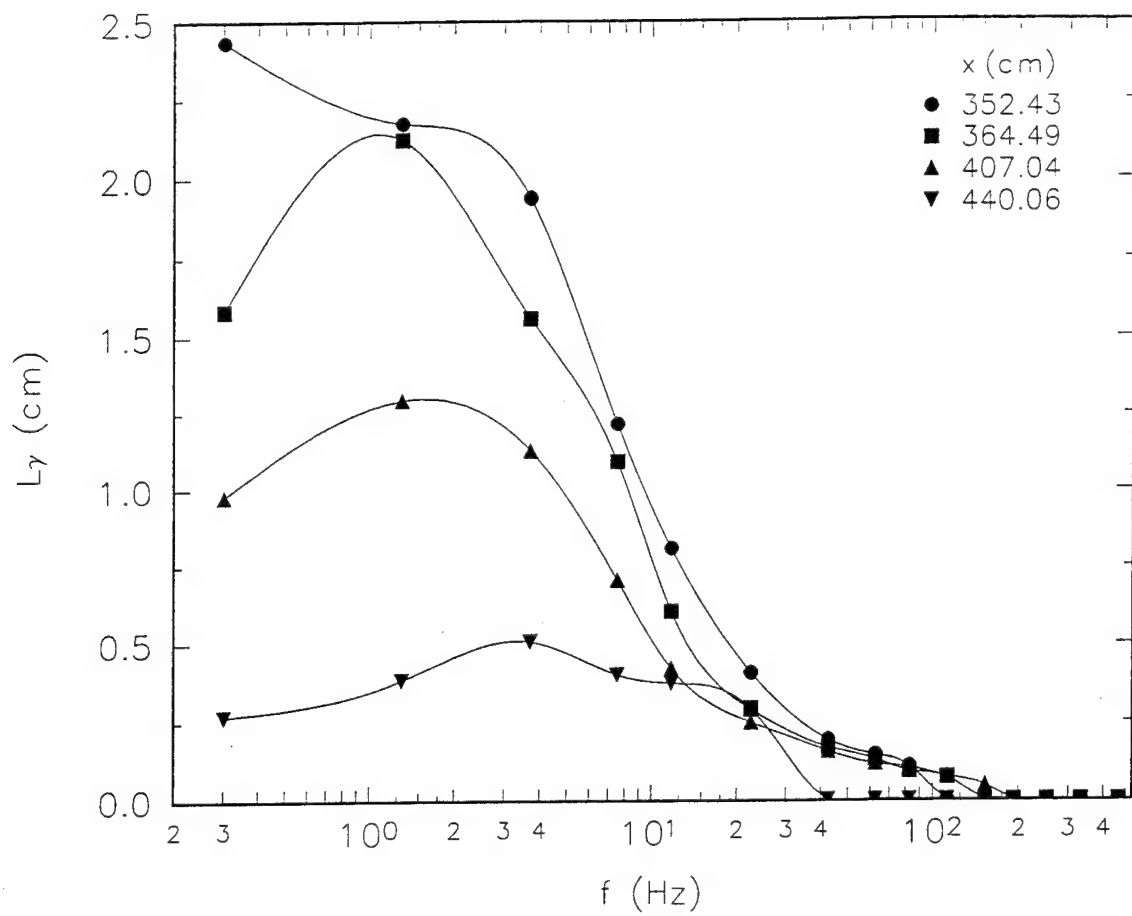


Fig. 7.60c. Spectral variation of coherence length scale downstream of detachment.

Appendix A. Calibrations

A.1 Convection Heat Flux Calibrations

A.1.1 Cylinder Stagnation Point Calibration

The Schmidt-Boelter gage was calibrated for convection heat transfer at the 2-D stagnation point of a cylinder in cross flow. The wind tunnel used was a blower type wind tunnel with a 6:1 contraction ratio. The potential core of the flow in the test section is uniform to within 2.1% with a turbulence intensity of 0.5% (Gundappa and Diller, 1985). The test section measures 124 cm in length and has a cross section of 74.1 cm by 52.9 cm. The walls of the test section are made of plexiglas and are machined to allow the cylinder to be placed in the flow. The test cylinder, shown in Fig. A.1, was constructed of 8.89 cm OD, 0.76 cm thick aluminum pipe, split lengthwise to facilitate assembly. Twenty-nine type-T thermocouples mounted in the cylinder walls were used to measure surface temperature. The Schmidt-Boelter gage was mounted in a 3.175 mm diameter threaded hole located near the axial center of the cylinder. The cylinder was heated by two independently controlled flexible silicone rubber electric resistance heaters held against the inside surface of the cylinder. Fiberglass insulation placed behind the

heaters held the heaters in place. The amount of power supplied to each heater was controlled by a Eurotherm 810 3-mode process controller and a Eurotherm 831 phase-angle-fired power supply. Tuning of the controllers allows the surface temperature of the cylinder to be held uniform and constant to within ± 0.5 °C over the entire center region.

After the cylinder was mounted inside the wind tunnel, the stagnation point of the cylinder was located by monitoring the heat flux output while rotating the cylinder. The stagnation point heat flux was varied by changing the tunnel free stream speed or by changing the temperature set point of the cylinder. Tunnel speed was adjusted by limiting the intake area of the blower. Runs were made at nominal tunnel speeds of 13.8, 20.5, and 27.2 m/s. For each tunnel speed, the temperature set point of the cylinder was set at 30, 35, 44, 55, 65, and 75 °C. At each set point, the heat flux signal, surface temperature, free-stream temperature, and tunnel speed were recorded. The cylinder was then heated to the next set point and the process was repeated. The output of the gage for each run was compared with the well documented Nusselt number prediction for the laminar stagnation point of a cylinder in cross flow (Kays and Crawford, 1980):

$$Nu_D = \frac{hD}{k} = 0.95Re_d^{1/2} \quad (A.1)$$

This relationship has been found to agree well with previous measurements made using this wind tunnel and cylinder (Simmons et al., 1990; Ancraka and Diller, 1985; Gundappa and Diller, 1985). The total heat flux was estimated from:

$$q = h(T_w - T) - \eta_g \sigma (T_w^4 - T^4) \quad (\text{A.2})$$

where the gage emissivity was 0.97. A sensitivity, $S = 4.0 \pm 0.2 \text{ mV}/(\text{W}/\text{cm}^2)$, was estimated from a linear regression between gage output voltage and total heat flux, shown in Fig. A.2.

The calibration curve obtained by the manufacturer was $S = 3.43 \text{ mV}/(\text{W}/\text{cm}^2)$. Due to the large difference between the manufacturers radiation calibration and the results of the convection calibration, a second method was used to predict the heat transfer at the cylinder stagnation point. The convection coefficient for the cylinder was measured using a previously calibrated Gardon gage in place of the Schmidt-Boelter gage. With the tunnel speed set at 27 m/s, measurements were made for temperature set points of 30, 35, 45, 55, and 65 °C. The output of the gardon gage was converted to a convection coefficient using the equations outlined by Borell and Diller (1987). The five measurements resulted in an average convection coefficient of $103.6 \pm 8.0 \text{ W}/\text{m}^2\text{°C}$ at 20:1 odds. The convection coefficient predicted using Eq. (A.1) was $h = 104 \text{ W}/\text{m}^2\text{°C}$ which is within the confidence interval for the Gardon gage results.

A.1.2 Jet Stagnation Point Calibration

The heat flux microsensor (HFM) was calibrated at the stagnation point of a perpendicular jet impinging on a flat plate using the apparatus shown in Fig. A.3. The jet was produced by a high pressure blower that pumps air into a plenum and through a 3.8

cm diameter orifice. The flat plate was a wooden cube encased by sheet metal. The HFM was mounted in a stainless steel tube which was wrapped with a resistance heater. The tube was mounted in a hole through the center of the wooden block so that the HFM surface was flush with the sheet metal surface. The block was placed with its front face perpendicular to the jet at a distance of three orifice diameters (11.43 cm). Power to the heater was controlled by a variac.

The convection heat transfer coefficient for this experimental system was measured using the Gardon gage described above. The Gardon gage was mounted in an aluminum plug in the stainless steel tube. The steady-state output was recorded for several temperature set points and the heat flux calculated according to the method of Borrell and Diller (1987). The resulting convection coefficient was $h = 205 \pm 2 \text{ W/m}^2\text{C}$ at 20:1 odds.

For calibration, the variac was turned on and the system was allowed to reach thermal equilibrium. The heat flux output, surface temperature, and plenum temperature were recorded and the heat flux was calculated according to Eq. (2.1). Different set-points were obtained by varying the power of the variac. Results of this calibration are shown in Fig. A.4. A linear least-squares regression resulted in a heat flux sensitivity of $66 \pm 10 \text{ mV/(W/cm}^2\text{)}$. Calibration of the Schmidt-Boelter gage in this apparatus resulted in a sensitivity of $3.9 \pm 0.2 \text{ Mv/(W/cm}^2\text{)}$.

A.2 Temperature Calibration

A.2.1. Static Cold-Wire Temperature Calibration

The cold-wire temperature probes and the resistance thermometer mounted on the surface of the heat flux microsensor were calibrated against the type-T thermocouple used to measure free-stream temperature. This ensured that the measured temperature difference between the wall, a point in the thermal boundary layer and the free stream would have minimum error. Calibration was performed in the uniform temperature oven which consisted of a cardboard box lined with wooden and styrofoam sheets. A resistance heater was placed on the bottom wall of the oven and covered with a 6.35 mm thick aluminum plate. Power to the heater was controlled by a variac.

When calibrating the cold wire, the cold wire and the thermocouple were inserted through a hole in the top of the oven. The distance between the wire and thermocouple was less than five mm. The output of the thermocouple was recorded by the TEGAM thermometer and the output of the HFM was recorded by a digital voltmeter. The heater was turned on and the oven was allowed to reach thermal equilibrium. A sample calibration run is shown in Fig. A.6.

When calibrating the RTS, a thermocouple was held against the top surface of the HFM substrate by an alligator clip. Zinc-Oxide ointment was used to ensure good thermal contact between the thermocouple and the HFM substrate. The HFM was then placed in the oven and enclosed with loose fiberglass insulation to ensure that the HFM and the

thermocouple would be at the same temperature. The procedure described above for the cold wire was repeated. The RTS calibration is shown in Fig. A.7. The uncertainty between measured temperature differences is approximately 0.17 °C. Uncertainty in absolute temperature is approximately 1 °C.

A.2.2. Dynamic Temperature Calibration

Neglecting radiation heat transfer and conduction heat transfer from the wire to the support needles, the frequency response of an uncompensated cold wire of length l , diameter d , and cross sectional area A , operating with a small constant current I , is that of a first order system (simple pole) with time constant (Lomas, 1990):

$$\tau_w = \frac{\rho c A l}{\pi d h l - I^2 \alpha R_0}. \quad (\text{A.3})$$

Here, h is the convection coefficient, ρ is the density of the sensor material, c is its specific heat, α is its temperature-resistance coefficient, and R_0 is the resistance at a reference temperature.

As noted by Bremhorst and Graham (1990) uncompensated cold wires do not have sufficient frequency response to permit the full temperature spectrum in typical laboratory flows to be measured without amplitude and phase distortion. The natural frequency response of a cold wire can be increased by the passive compensating network shown in Fig. A.8. The compensation network increases the cut-off frequency of the cold wire by

a factor:

$$K = \frac{\tau_{\text{new}}}{\tau_w} = \frac{R_1}{R_1 + R_2} \quad (\text{A.4})$$

The increase in frequency response is paid for by a loss of sensitivity in direct proportion. For correct compensation the compensator time constant must be matched to the wire time constant by adjusting either the resistor, R_1 or the capacitor C to match the time constant of the cold wire:

$$R_1 C = \tau_1 \quad (\text{A.5})$$

Standard practice has been to adjust R_1 . This causes a change in the DC gain and frequency response as shown in Eq. (A.4). A better method, suggested by Smits et al. (1978) is to use a variable capacitor.

Several methods have been used to determine the time constant of cold wires. The current perturbation method, first proposed by Kovasznay (1951) injects a square wave current to the constant cold-wire current. Bremhorst and Krebs (1976) have shown that significant error can occur with this method unless the bridge is balanced while the test signal is applied. This requires that the bridge be balanced at each measurement location which is not the case with a constant-current anemometer. Several external heating methods have been proposed. In these methods the anemometer bridge has no effect on the determination of the time constant. Fiedler (1978) used a pulsed laser to externally heat the cold wire. This method allows heating of both the wire and the support prongs. Fiedler (1978) also moved a cold wire between hot and cold air streams to create a step

change in temperature. This method was too slow to measure the wire time constant but is useful for measuring the time constant of the prong influence. Antonia et al. (1981) placed a cold wire downstream and normal to a hot-wire which was heated by a short-duration voltage pulse. The temperature spot was convected downstream and over the cold wire. Hojstrup et al. (1976) observed a cold wire's response to a external sinusoidal heating induced by a strong constant amplitude pressure field.

In a turbulent boundary layer, the convection coefficient, h , in Eq. (A.3) is a function of both the local flow velocity and turbulence intensity. Also, as discussed by Paranthoen et al. (1982), dust contamination causes the cold-wire time constant to increase over time. This means that the compensator must be adjusted *in-situ* at each measurement location in the boundary layer. Only the current perturbation method and the pulsed-laser method can be used for an *in-situ* measurement of the cold-wire time constant. For either technique, the cold wire is perturbed by a square wave (thermal or current injection) while exposed to the flow at the location to be studied. The compensator time constant (Eq. A.5) is adjusted until the output signal is optimized as shown in Fig. A.8. Since this optimization is performed while the wire is exposed to the turbulent flow, the output will contain the superposition of the wire's response to current and temperature fluctuations so the correct adjustment may not be as clear as Fig. A.8 suggests.

Of the two methods, the pulsed-laser method is preferred because of the error introduced by an unbalanced bridge and because the wire and the prongs are both heated by the radiation. The pulsed-laser method was implemented using the apparatus shown

in Fig. A.9. The wire was mounted in the AOE boundary layer tunnel. A beam from an INNOVA 90-6 argon-ion laser was split by a Bragg cell and one of the deflected beams was focused on the wire. The Bragg cell was adjusted so that the maximum energy was placed in the first of the deflected beams. An HP 3311A Function generator connected to the Bragg cell driver and was used to turn the bragg cell on and off, thus creating a thermal square wave. The output from this method is shown in Fig. A.10 for a 5- μm diameter tungsten wire placed in the freestream of a 32 m/s flow. Only the output during the cooling phase of the wire is valid. The time constant was 1 ms (cut-off frequency = 60 hz). The method described above was performed for several free-stream velocities to develop a relation between the wire time constant and free stream velocity. Unfortunately, the pulsed-laser method could not be used to set the compensation in the boundary layer tunnel. The long distance traveled by the laser beam and the shallow angle to the wall when the cold wire was placed in the near-wall region made it difficult to focus the beam on the wire.

Adjustment of the compensator using the current-injection method was attempted using the apparatus shown in Fig. A.11. The compensator gain was set to a value $K = 0.2$ ($\tau_w/\tau_{\text{new}}=5$). A square-wave current equal to a 1% step increase was added to the 0.2 mA anemometer current. A 1.25- μm dia. platinum wire was placed in a 27.5 m/s flow. Uncompensated wire response are compared with the compensated wire responses to injected square waves of 300 hz, 2000 hz, and 4000 hz in Figs. 4.12, 4.13. and 4.14 respectively. Unfortunately, this method did not work well in the near-wall region where compensation is required most due to the slower mean velocity. The wire's response due

to the large turbulent temperature fluctuations were an order of magnitude larger than the response to the injected current. This problem could not be overcome by injecting a larger current because the error in the measured frequency response is proportional to the square of the injected current (Bremhorst and Krebs, 1976). The dynamic compensation network was therefore not used. The spectral data are therefore only valid out to 2 kHz which is cut-off frequency for the 1.25- μm dia. wire at zero velocity. Future work should use a laser heating method with optics designed specifically for that purpose. Future temperature probes should be designed with the prongs further apart to reduce prong interference while keeping the sensing length of the wire less than 0.5 mm.

Table A.1. Sensitivities of heat flux gages.

Sensor Type	Calibration Type	Sensitivity $\mu\text{v}/(\text{W}/\text{cm}^2)$
Schmidt-Boelter	Cylinder stagnation point	4000 ± 200
Schmidt-Boelter	Jet stagnation point	3900 ± 200
Heat Flux Microsensor #1	Jet stagnation point	49 ± 10
Heat Flux Microsensor #2	Radiation	$66 \pm 5\%$
Heat Flux Microsensor #3	Radiation	$62 \pm 5\%$

Note: Radiation calibrations performed at Vatel Corp.
Uncertainties are 95% confidence intervals.

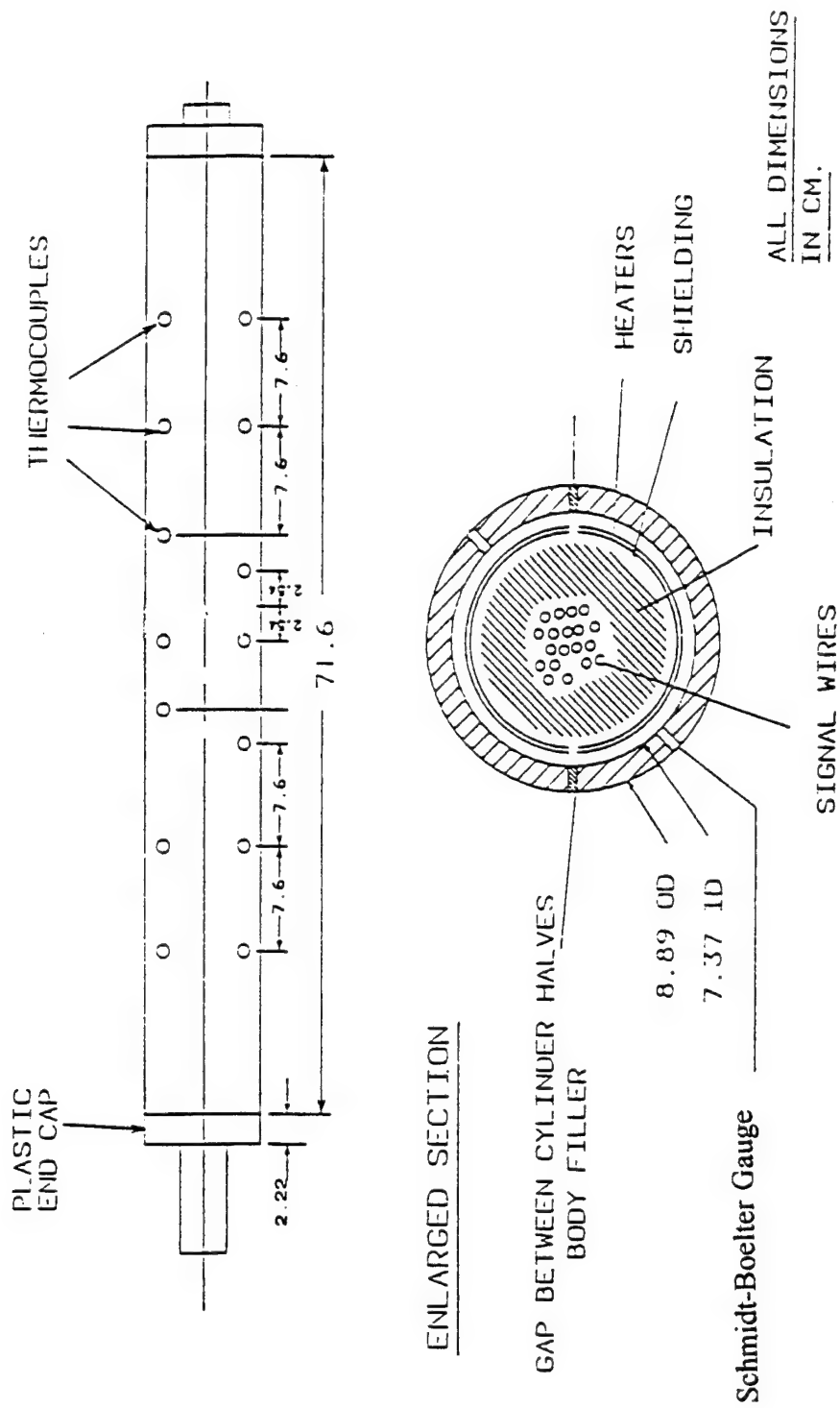


Fig. A.1. Sketch of test cylinder used for static convection calibration of Schmidt-Boelter gauge.
(from Gundappa and Diller, 1985).

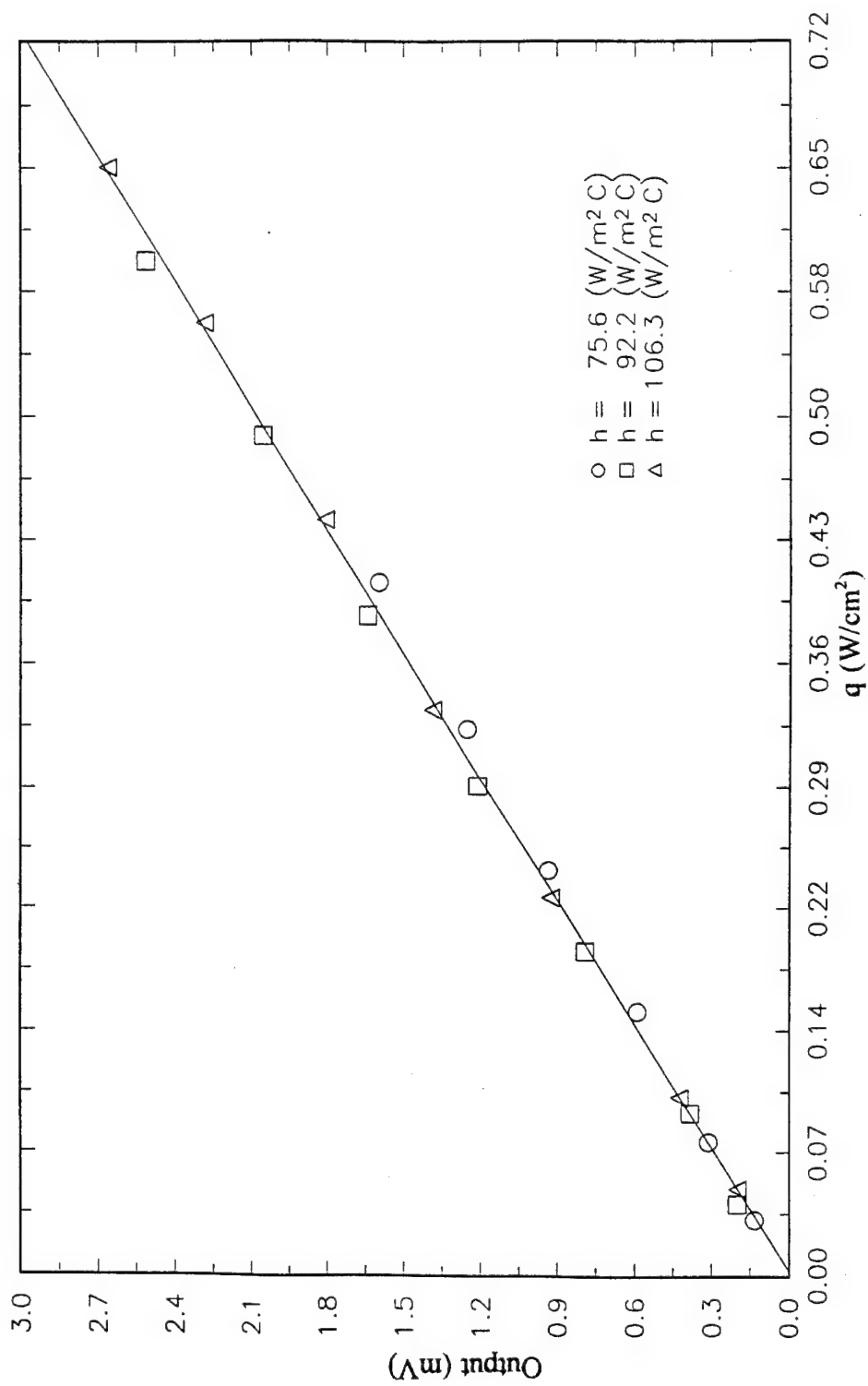


Fig. A.2. Static convection calibration of Schmidt-Boelter gauge using cylinder apparatus.

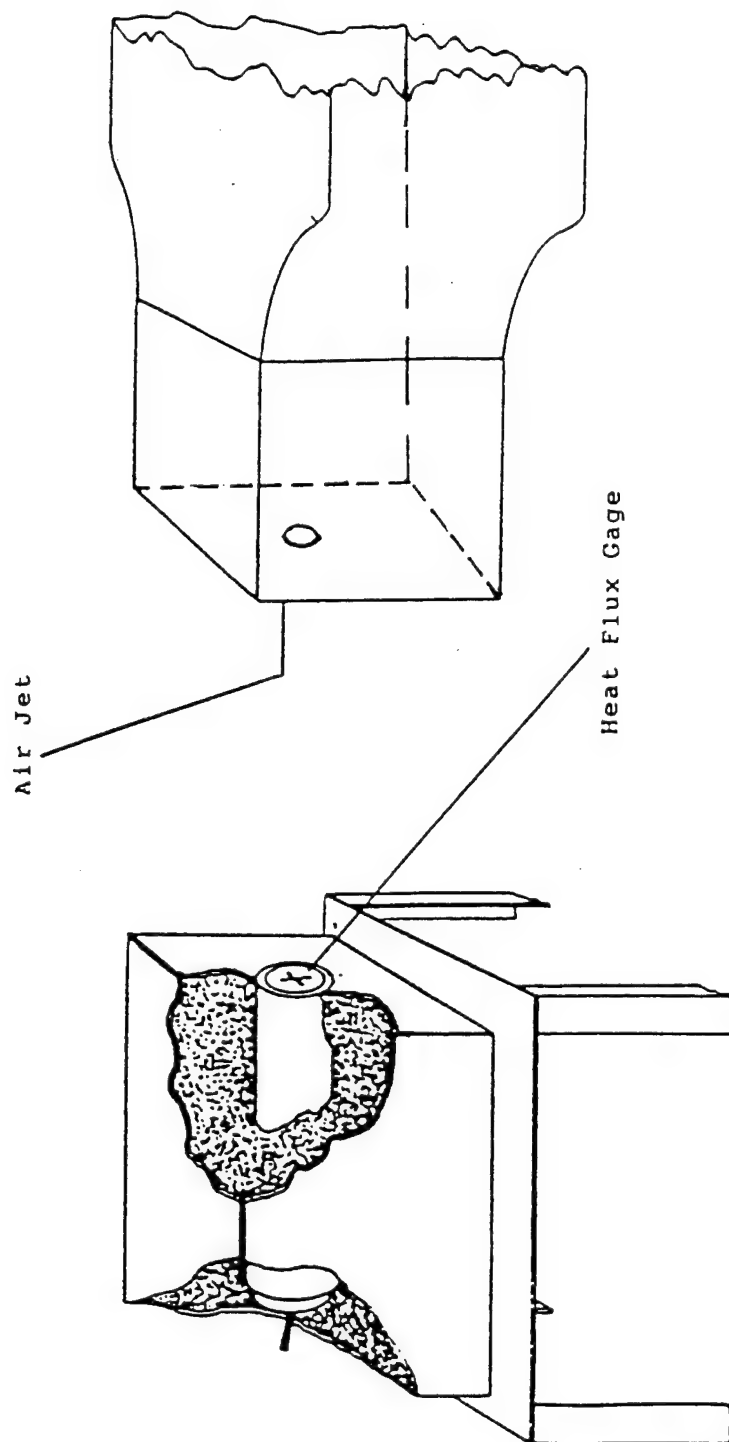


Fig. A.3. Sketch of the impinging-jet calibration apparatus. (from Hager et al., 1991c)

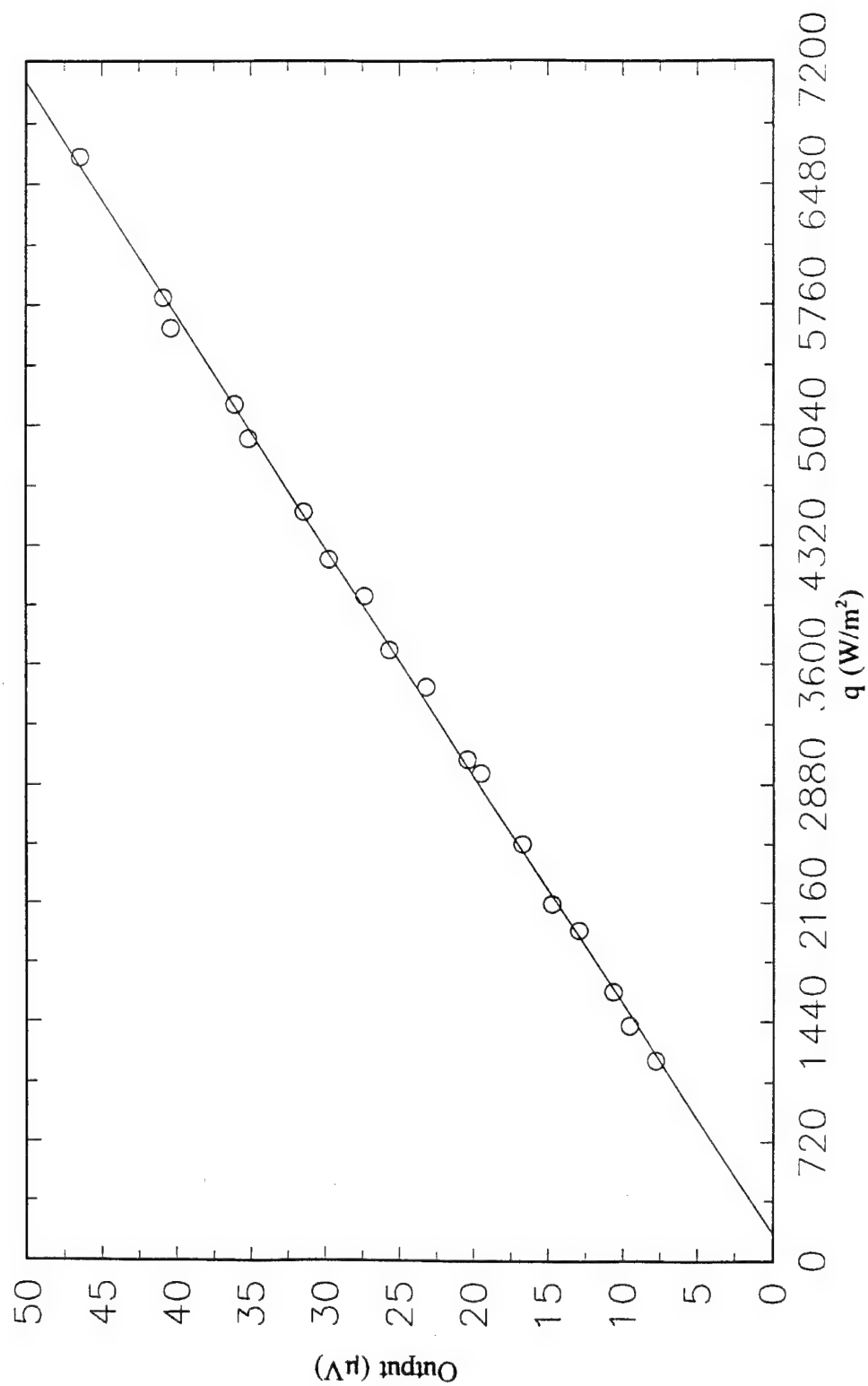


Fig. A.4. Static convection calibration of Heat Flux Microsensor in impinging-jet apparatus.

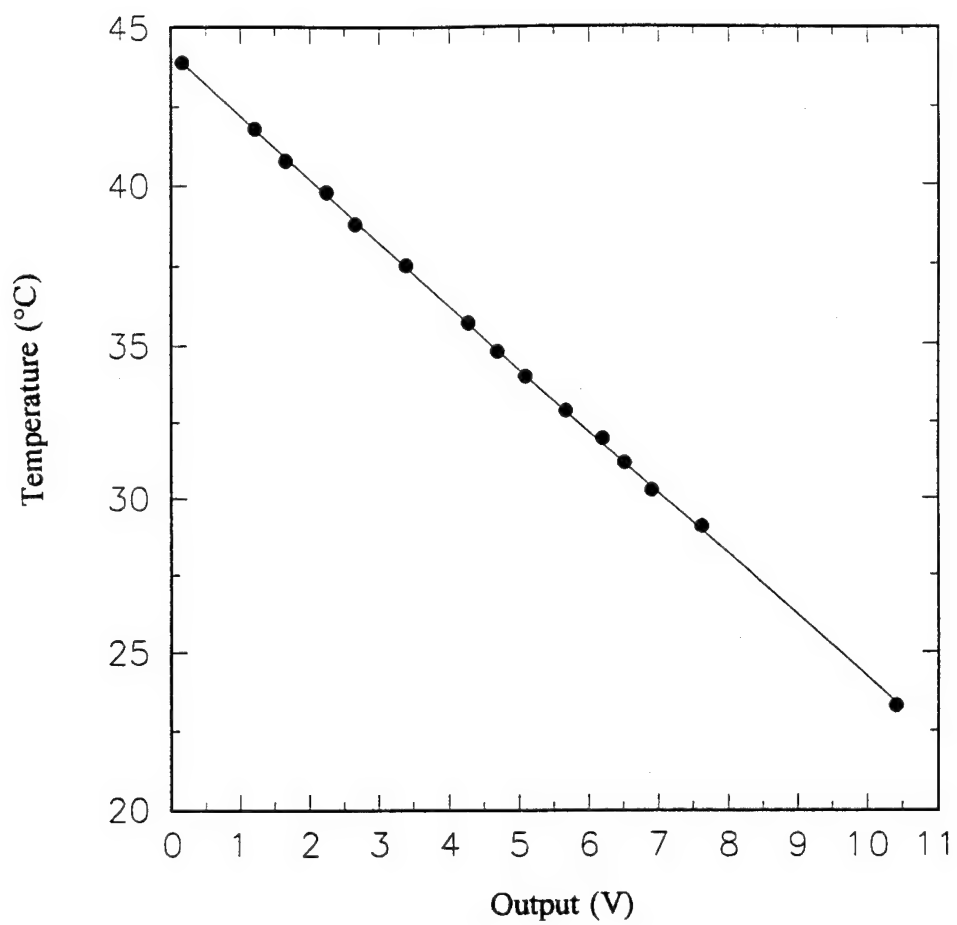


Fig. A.5. Static calibration of cold-wire temperature sensor.

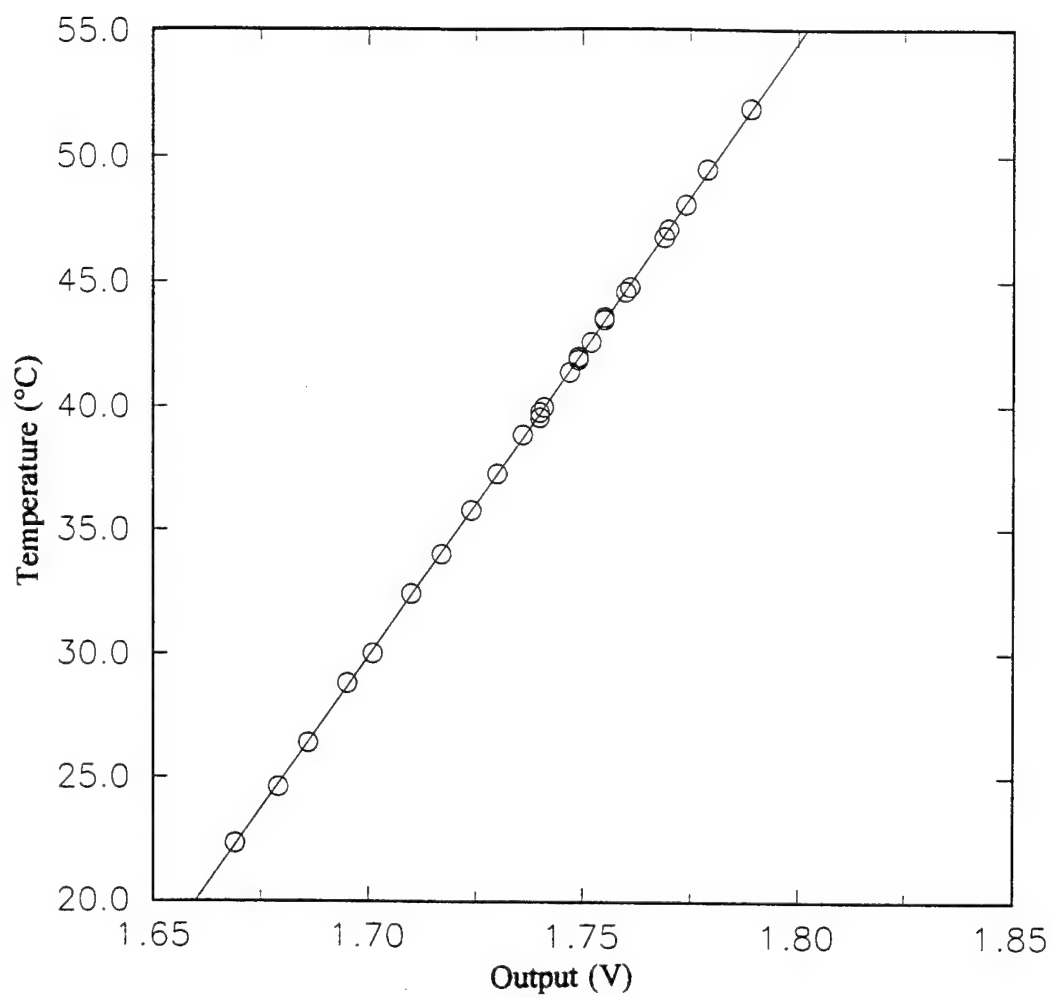
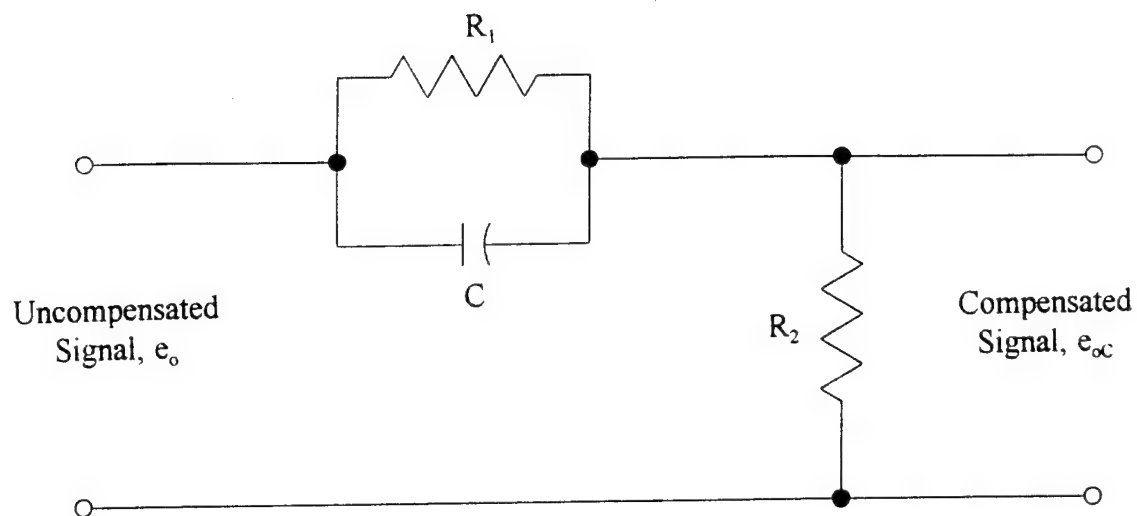


Fig. A.6. Static calibration of resistance temperature sensor on heat flux micorsensor.



$$\frac{e_{oc}}{e_o}(D) = \frac{\frac{R_2}{R_1 + R_2}(R_1 CD + 1)}{\left(\frac{R_2}{R_1 + R_2} R_1 CD + 1 \right)}$$

Fig. A.7. Sketch of passive dynamic compensation network.

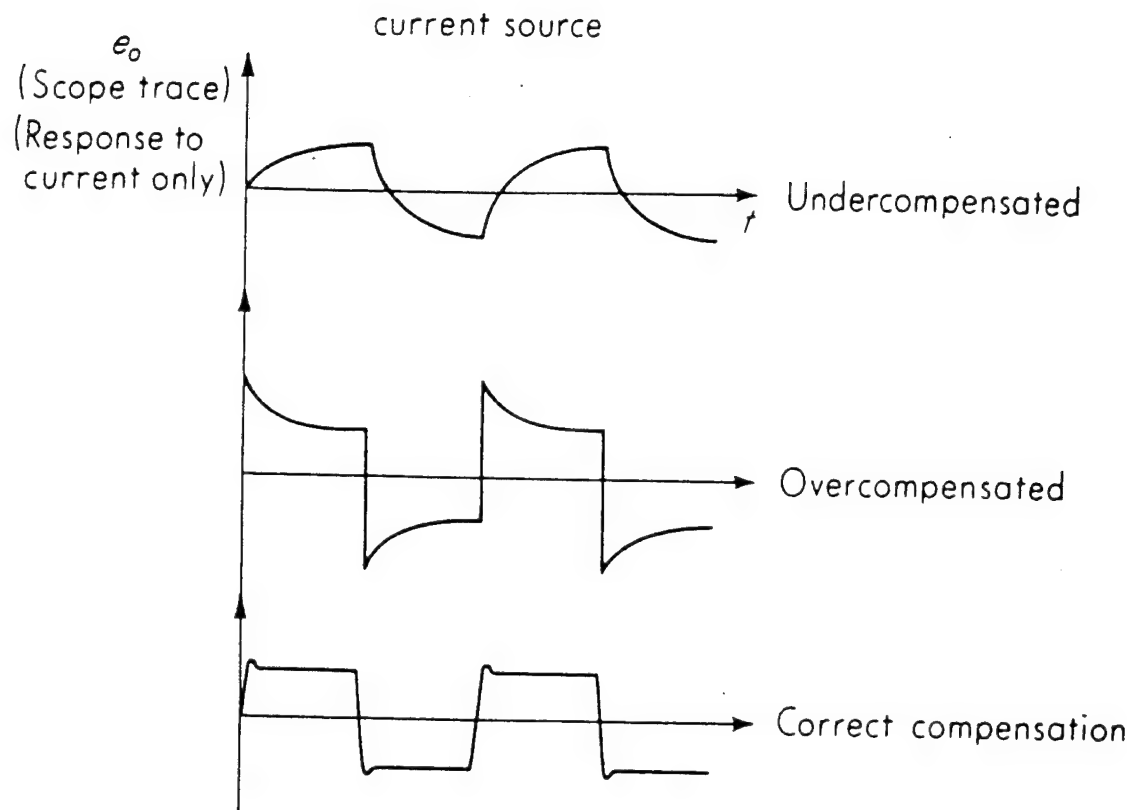


Fig. A.8. Compensation optimization scheme. (from Doebelin, 1990)

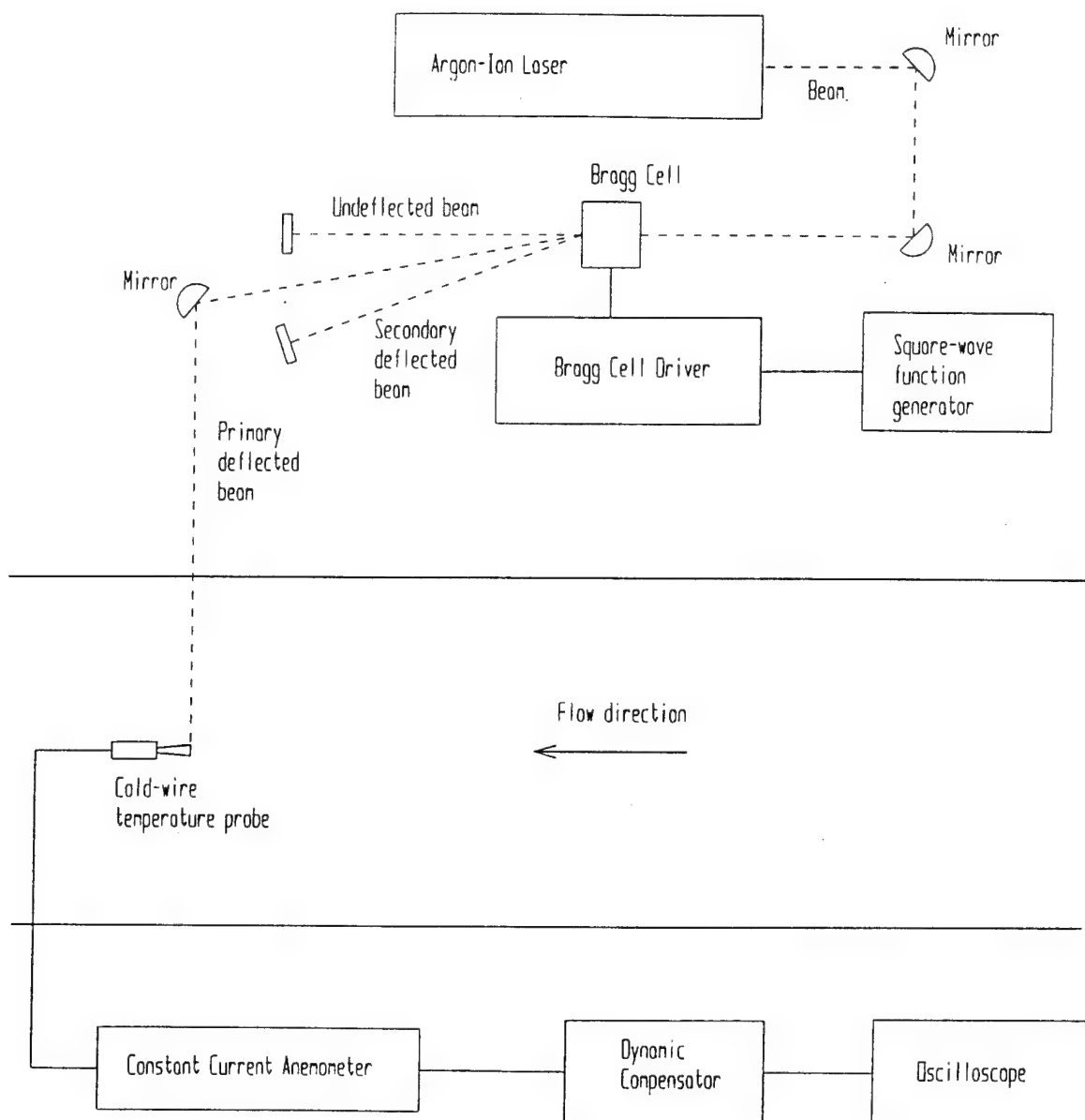


Fig. A.9. Apparatus used for pulsed-laser dynamic calibration of cold-wire sensor.

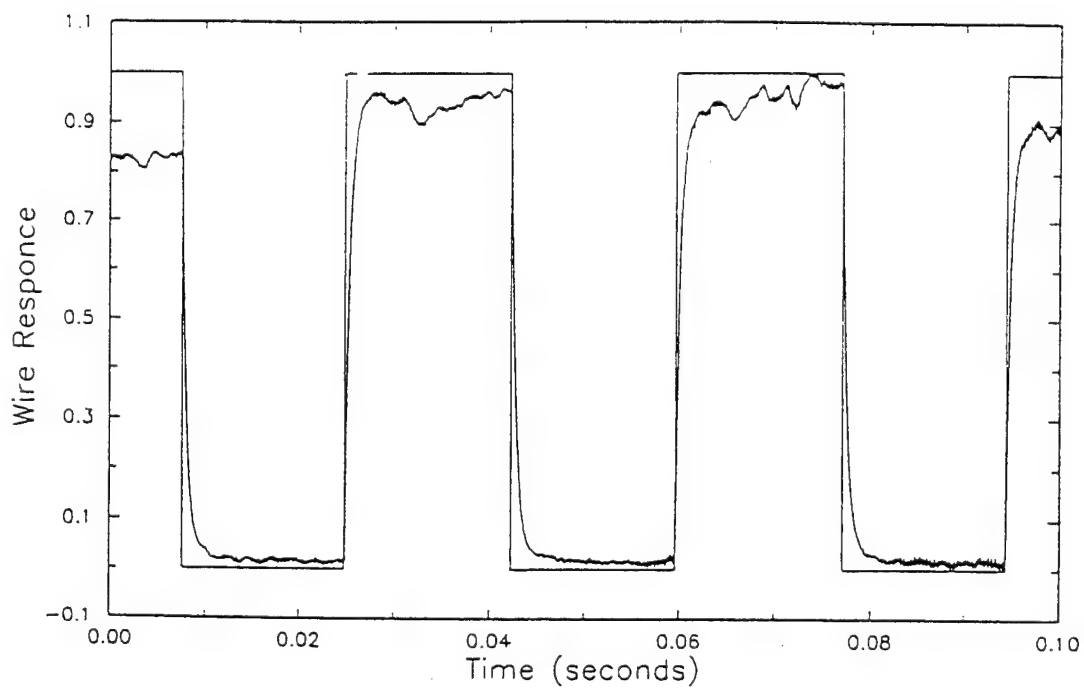


Fig. A.10. Dynamic calibration of 5- μ m dia. cold wire using pulsed-laser technique.

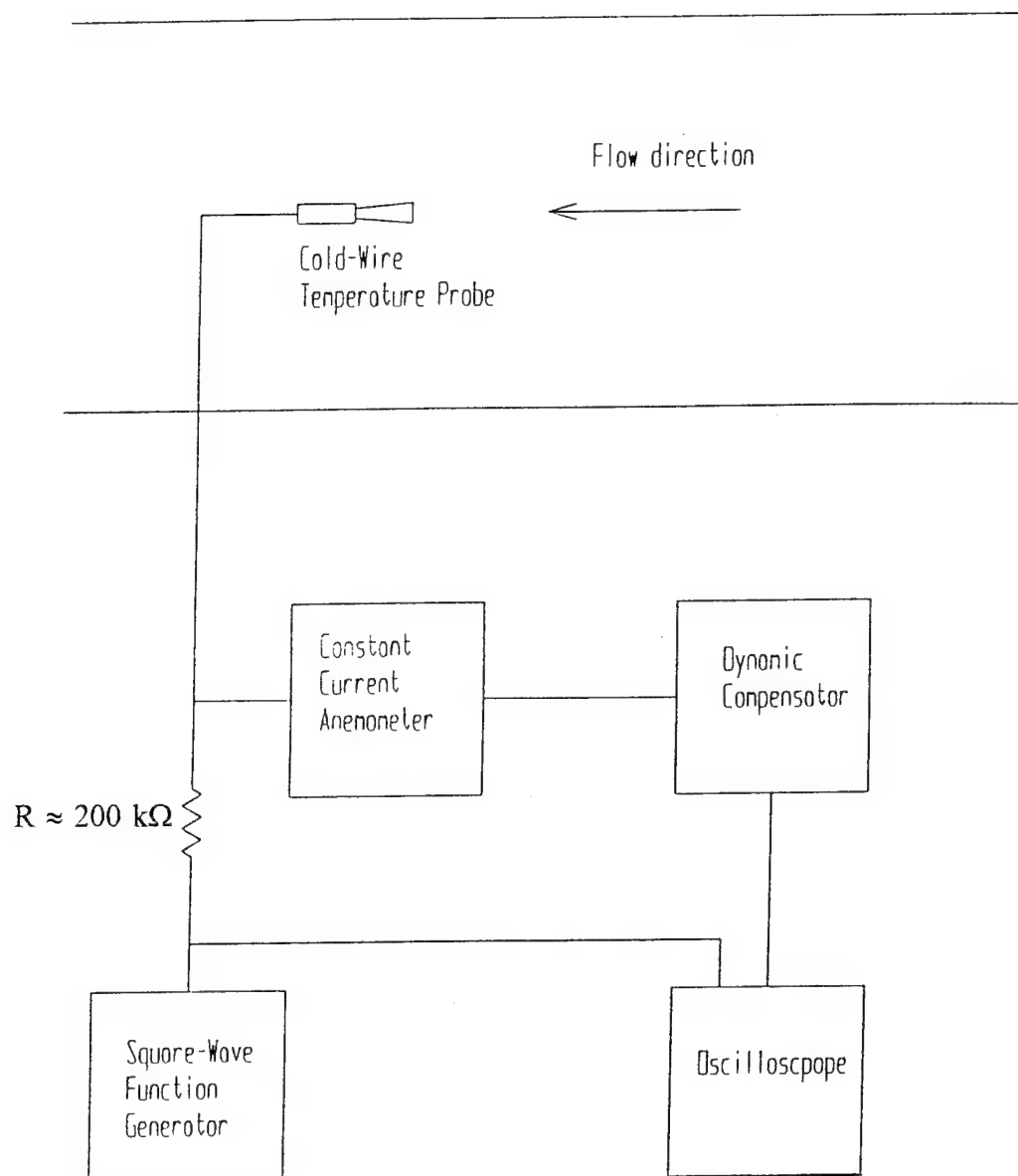


Fig. A.11. Apparatus used for current-injection technique for dynamic calibration of cold-wire temperature sensor.

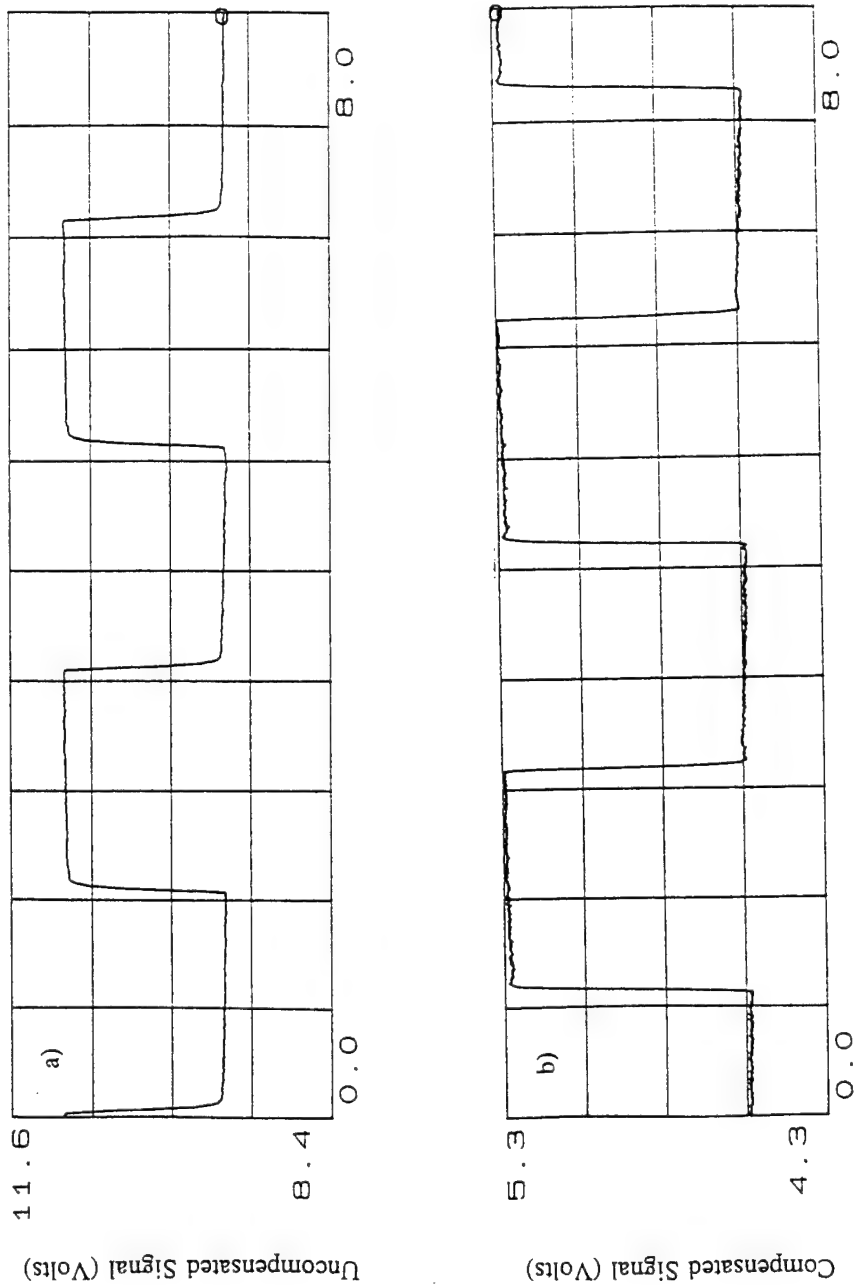


Fig. A.12. Response of cold-wire temperature probe to current injection of 300 Hz square wave. (a) uncompensated signal; (b) compensated signal.

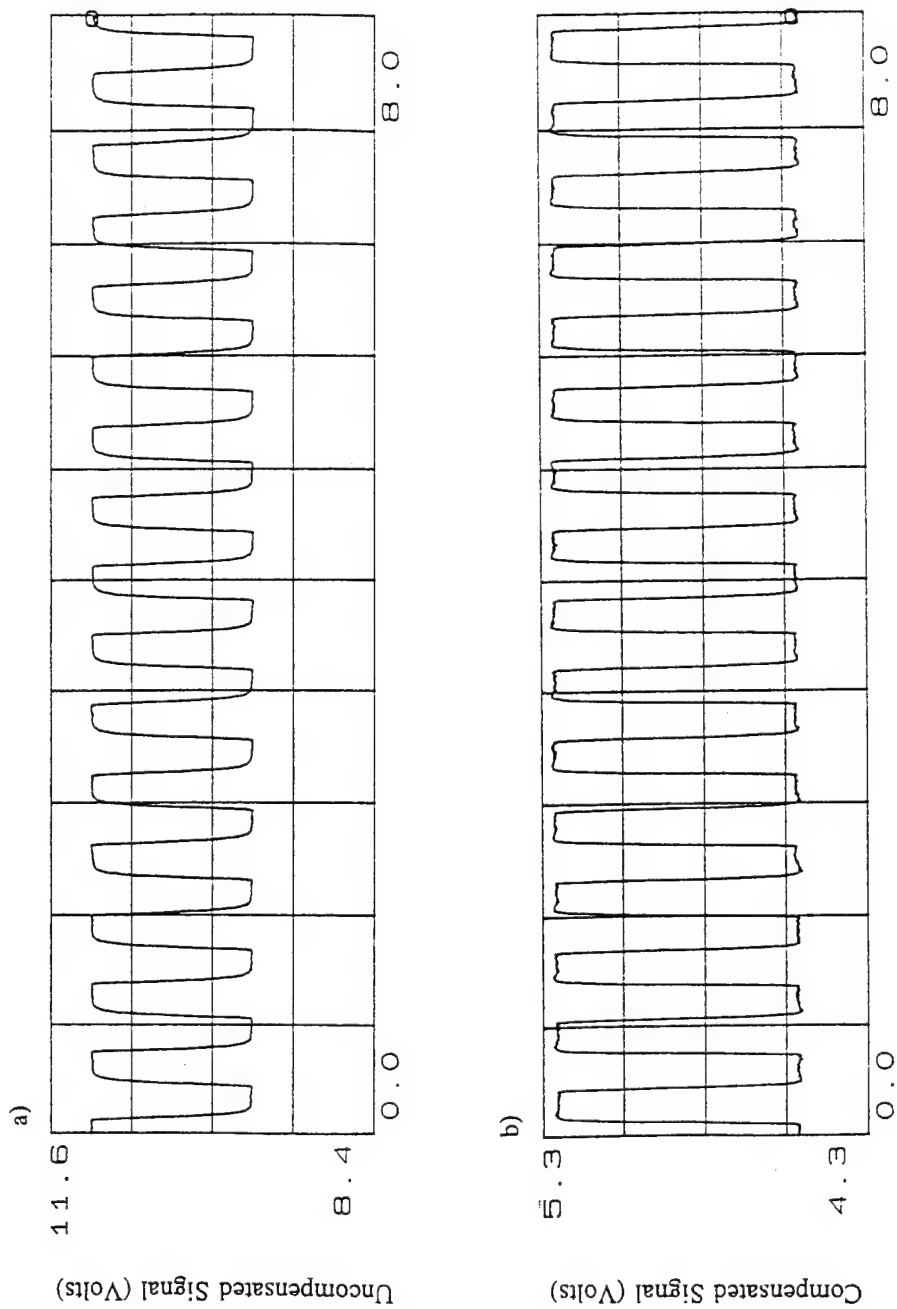


Fig. A.13. Response of cold-wire temperature probe to current injection of 2000 Hz square wave.
(a) uncompensated signal; (b) compensated signal.

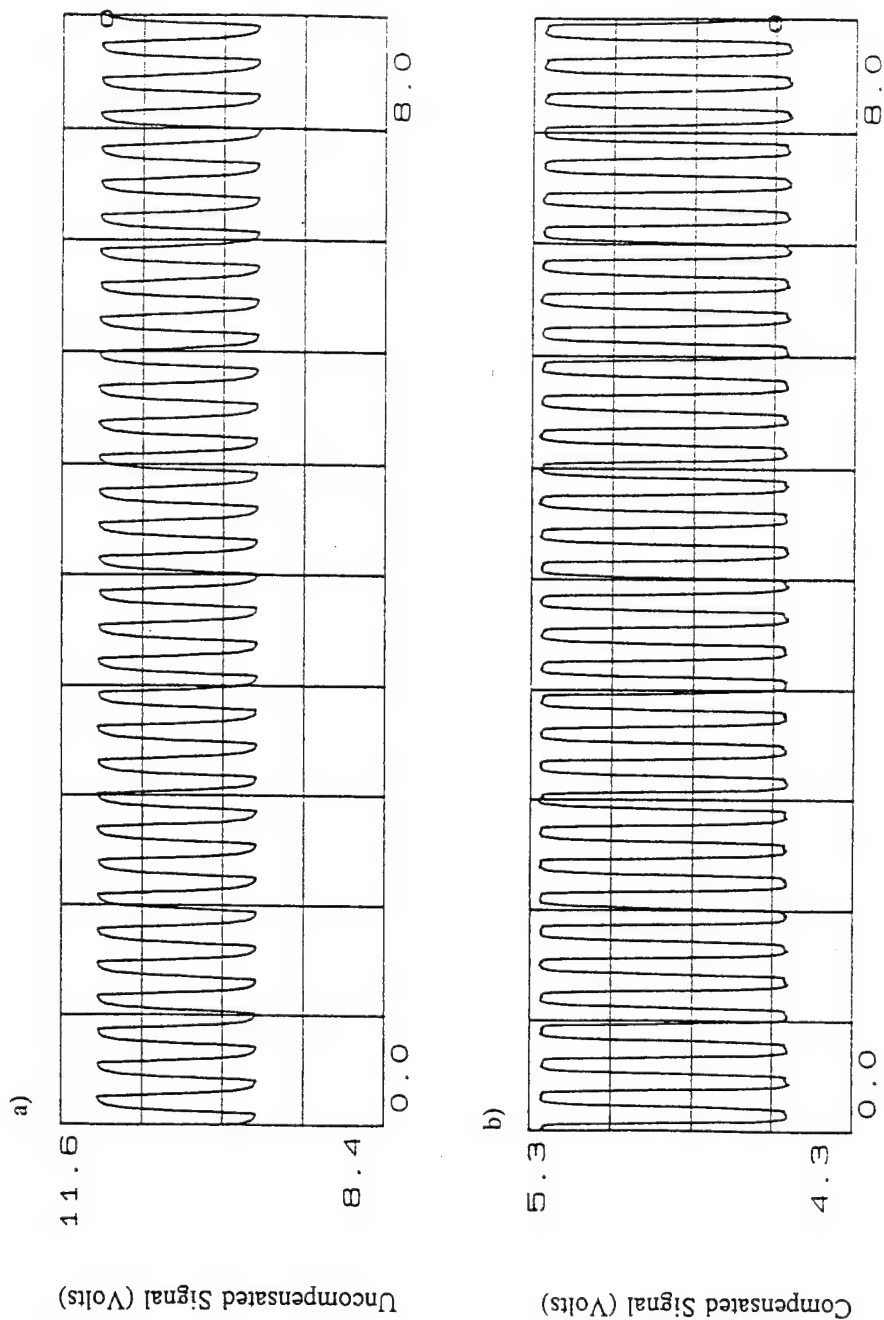


Fig. A.14. Response of cold-wire temperature probe to current injection of 4000 Hz square wave.
(a) uncompensated signal; (b) compensated signal.

Appendix B. Correction to Heat Flux Power Spectrum

Two sources of error in the surface heat flux spectra are considered. The first arises from the low signal to noise ratio of the heat flux microsensor. This signal to noise ratio decreases with increasing frequency. Corrections for this effect are discussed in Section B.1. The second source of error is due to the large surface area of the heat flux microsensor. Since the temporal scales of turbulence are created by the convection of eddies of a corresponding wavelength, temporal resolution in a turbulent flow is limited by spatial resolution. Corrections for spatial resolution are discussed in Section B.2.

B.1. Corrections due to background noise.

Measurements of the surface heat flux with the wind tunnel off revealed the noise floor of the background white noise. This noise appears in the heat flux spectra as a plateau at frequencies above 2000 hz (Fig. B.1). The noise floor decreases the measured roll-off rate of the spectra. To correct for this, the mean square white noise level was subtracted from the heat flux fluctuation energy spectra. Spectra at frequencies above 1000 hz (where the spectra are approximatedly 4 times the white noise level) were discarded as shown in Fig. B.1. The result is an increase in the roll-off rate at high

frequencies. Spectra in the energy-containing range are not affected. As shown in Fig. B.2, the location of the peak in the first moment of the heat flux fluctuations is not affected by this correction.

B.2 Corrections due to finite sensor size

The ability of a surface heat flux gage to resolve the temporal details of a turbulent flow is limited by the spatial resolution of the gage. Because the turbulence structure is convected at a speed comparable to the characteristic velocity of the flow, the gage spatially averages length scales less than the gage length. Consequently, a lack of resolution in space causes an apparent inability to resolve in time.

The attenuation of measured spectra of surface pressure fluctuations under a boundary layer due to finite transducer size has been investigated by Corcos (1963) and the results should apply to surface heat transfer as well. The attenuation of the power spectrum $\phi(\omega)$ is (Corcos, 1963):

$$\frac{\phi_m(\omega)}{\phi(\omega)} = \int_{-\infty}^{\infty} \int_{-\infty}^{\infty} \Theta\left(\frac{\epsilon_x}{L_x}, \frac{\epsilon_z}{L_z}, \frac{L_x}{L_z}\right) A\left(\frac{\omega L_x}{U_c} \frac{\epsilon_x}{L_x}\right) B\left(\frac{\omega L_z}{U_c} \frac{\epsilon_z}{L_z}\right) e^{\left(-i \frac{\omega L_x}{U_c} \frac{\epsilon_x}{L_x}\right)} d\left(\frac{\epsilon_x}{L_x}\right) d\left(\frac{\epsilon_z}{L_z}\right) \quad (\text{B.1})$$

where $\phi_m(\omega)$ is the measured power spectrum. For a rectangular face sensor with stream wise length L_x and spanwise length L_z , the function Θ in Eq. (B.1) is given by:

Equation (B.1) is a function only of the aspect ratio L_z/L_x and of the dimensionless

$$\Theta\left(\frac{\epsilon_x}{L_x}, \frac{\epsilon_z}{L_x}, \frac{L_z}{L_x}\right) = \frac{\left[1 - \left|\frac{\epsilon_x}{L_x}\right|\right] \left[\left|\left(\frac{L_z}{L_x}\right) - \left|\frac{\epsilon_z}{L_x}\right|\right]}{\left(\frac{L_z}{L_x}\right)^2}; \quad \left|\frac{\epsilon_x}{L_x}\right|, \left|\frac{\epsilon_z}{L_x}\right| \leq 1 \quad (\text{B.2})$$

$$= 0; \quad \text{otherwise}$$

frequency $\omega L_x/U_c$ where U_c is the convective speed of turbulent structures of frequency ω . For a round gage of radius $R = L_x$, the function Θ in Eq. (B.1) is given by:

$$\Theta\left(\frac{\epsilon_x}{L_x}, \frac{\epsilon_z}{L_x}\right) = \frac{2}{\pi^2 L_x^2} \left(\cos^{-1}\left(\frac{1}{2} \frac{\epsilon_r}{L_x}\right) - \left(\frac{1}{2} \frac{\epsilon_r}{L_x}\right) \left[1 - \left(\frac{1}{2} \frac{\epsilon_r}{L_x}\right)^2\right]^{1/2} \right); \quad \left|\frac{\epsilon_r}{L_x}\right| \leq 2 \quad (\text{B.3})$$

$$= 0; \quad \text{otherwise}$$

where $\epsilon_r^2 = \epsilon_x^2 + \epsilon_z^2$.

The parameters A and B in Eq. (B.1) relate the frequency-spectral density to the longitudinal and lateral cross-spectral densities respectively, through the relations

$$\Gamma(\omega, \xi, 0) = \Phi(\omega) A(\omega \xi/U_c) e^{-i\omega \xi/U_c} \quad (\text{B.4})$$

$$\Gamma(\omega, 0, \eta) = \Phi(\omega) B(\omega \eta/U_c) \quad (\text{B.5})$$

Since neither tabular data nor functional forms of $A(\omega \xi/U_c)$ and $B(\omega \eta/U_c)$ were given in Corcos (1963), values of A and B were taken from plots of $A(\omega \xi/U_c)$ and $B(\omega \eta/U_c)$ in Corcos (1963). These data are given in Tables B.1 and B.2. Approximations to the data were determined

$$A(\omega\xi/U_c) = e^{-0.115\omega\xi/U_c} \quad (\text{B.6})$$

$$B(\omega\eta/U_c) = 0.78898e^{-0.9\omega\eta/U_c} + 0.21102e^{-0.1451\omega\eta/U_c} \quad (\text{B.7})$$

The data $A(\omega\xi/U_c)$ and $B(\omega\eta/U_c)$ and the curvefits to Eq. (B.6) and Eq. (B.7) are shown in Figs. B.3 and B.4 respectively.

It was assumed that Eqns. (B.4) through (B.7) are also valid for surface heat transfer. Using Eqns. (B.6), (B.7), (B.2) and (B.3), Eq. (B.1) was numerically integrated for a round transducer and a square transducer ($L_z/L_x = 1$). The resulting attenuations are compared with the results from Corcos (1963) in Fig. B.5. The values of ϕ_m/ϕ obtained were slightly greater than those obtained by Corcos. This is most likely the result of the values of A and B used here being different than those used by Corcos. However, the values of A and B used here are within the experimental scatter in A and B published in a later report (Corcos, 1966) so no further adjustment of Eqs. (B.6) and (B.7) was attempted.

Equation (B.1) was numerically integrated for rectangular transducers with aspect ratios of $L_z/L_x = 1.625$ and $L_z/L_x = 0.6154$. The resulting attenuation is given in Table B.3 and shown in Fig. B.6. The results for $L_z/L_x = 1.625$ were used to correct the surface heat flux fluctuation power spectra for finite gage size. Results of the correction are shown in Fig. B.1. The correction decreases the roll-off rate at high frequencies and also increases the location of the peak in the first moment of the spectra.

Table B.1. Values of parameter "A" used in Eq. (B.4). Taken from Corcos (1963).

$\omega\xi/U_c$	A
0.0	1.0000
1.0	0.8749
2.0	0.7621
3.0	0.6847
4.0	0.6162
6.0	0.5153
8.0	0.4219
10.0	0.3415
12.0	0.2677
14.0	0.2096
16.0	0.1625
18.0	0.1338
20.0	0.1074
24.0	0.0717
28.0	0.0481
32.0	0.0368

Table B.2. Values of parameter "B" used in Eq. (B.5). Taken from Corcos (1963).

$\omega\eta/U_c$	B
0.0	1.0000
0.5	0.6728
1.0	0.4619
1.5	0.3429
2.0	0.2678
3.0	0.1882
4.0	0.1410
5.0	0.1108
6.0	0.0879
7.0	0.0781
8.0	0.0646
9.0	0.0573
10.0	0.0497

Table B.3. Attenuation of the frequency-spectral density by rectangular transducers of various aspect ratios.

$\omega L_x / U_c$	ϕ_m / ϕ		
	AR = 1.0	AR = 1.625	AR = 0.6154
0.000	1.0000	1.0000	1.0000
0.200	0.9423	0.9150	0.9598
0.400	0.8837	0.8356	0.9159
0.600	0.8249	0.7615	0.8689
0.800	0.7663	0.6924	0.8197
1.000	0.7085	0.6279	0.7688
1.200	0.6520	0.5677	0.7170
1.400	0.5970	0.5118	0.6649
1.600	0.5440	0.4599	0.6131
1.800	0.4933	0.4117	0.5621
2.000	0.4450	0.3672	0.5123
2.200	0.3994	0.3262	0.4643
2.400	0.3565	0.2885	0.4182
2.600	0.3166	0.2541	0.3746
2.800	0.2796	0.2227	0.3335
3.000	0.2457	0.1943	0.2952
3.200	0.2146	0.1687	0.2597
3.400	0.1865	0.1458	0.2272
3.600	0.1613	0.1254	0.1976
3.800	0.1387	0.1073	0.1710
4.000	0.1188	0.0915	0.1472
4.200	0.1014	0.0777	0.1262
4.400	0.0862	0.0659	0.1079
4.600	0.0732	0.0557	0.0920

4.800	0.0621	0.0471	0.0784
5.000	0.0529	0.0400	0.0670
5.200	0.0452	0.0341	0.0575
5.400	0.0389	0.0293	0.0497
5.600	0.0339	0.0254	0.0434
5.800	0.0299	0.0224	0.0385
6.000	0.0269	0.0200	0.0346
6.200	0.0246	0.0183	0.0318
6.400	0.0229	0.0170	0.0297
6.600	0.0217	0.0161	0.0282
6.800	0.0209	0.0155	0.0272
7.000	0.0204	0.0150	0.0266
7.200	0.0200	0.0148	0.0262
7.400	0.0198	0.0146	0.0260
7.600	0.0197	0.0144	0.0259
7.800	0.0195	0.0143	0.0257
8.000	0.0194	0.0141	0.0256
8.200	0.0191	0.0140	0.0253
8.400	0.0188	0.0137	0.0250
8.600	0.0185	0.0134	0.0245
8.800	0.0180	0.0131	0.0240
9.000	0.0175	0.0127	0.0233
9.200	0.0169	0.0122	0.0226
9.400	0.0162	0.0117	0.0217
9.600	0.0155	0.0112	0.0208
9.800	0.0148	0.0106	0.0198
10.000	0.0140	0.0101	0.0188

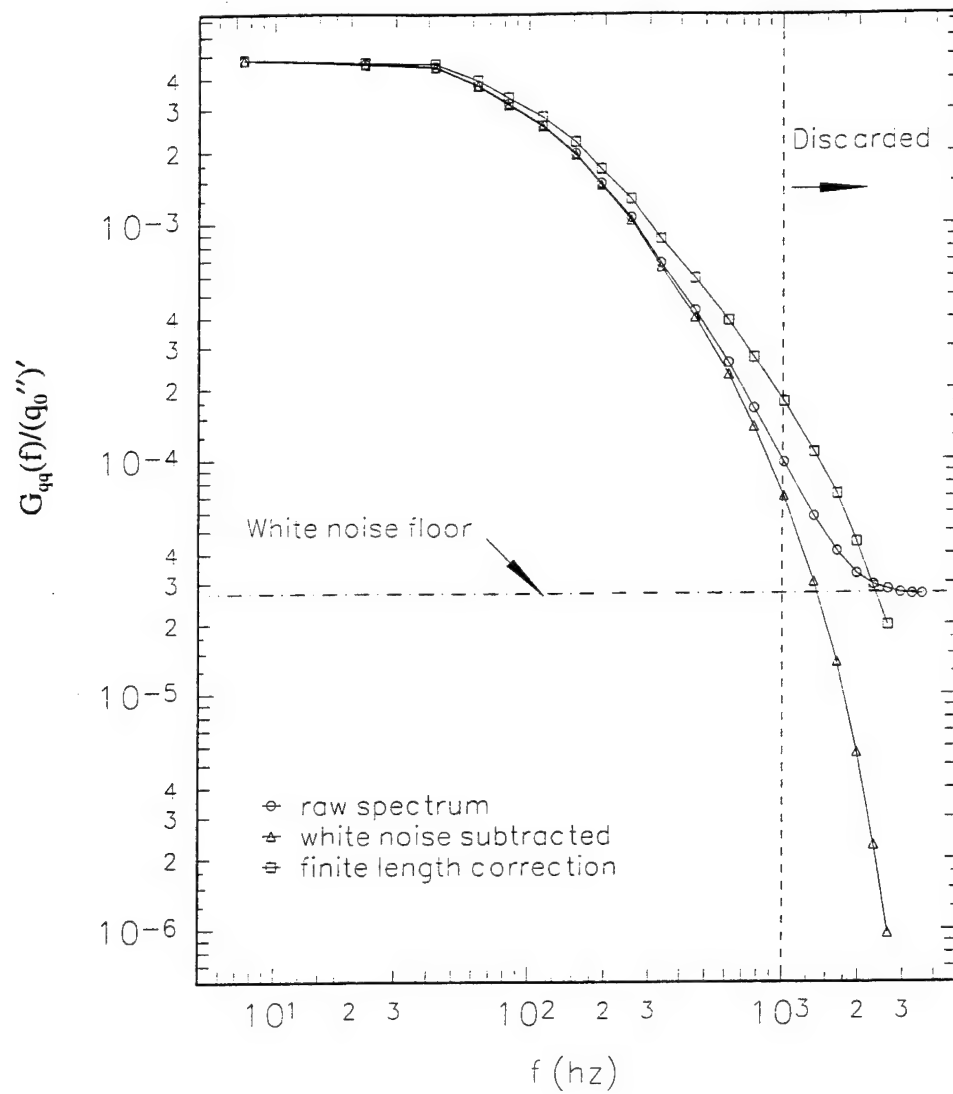


Fig. B.1. Corrections to surface heat flux fluctuation spectra at station #0 in 3-D TBL test case. \circ raw spectrum; Δ spectrum after white noise floor has been subtracted; \square spectrum after corrections for finite gage size.

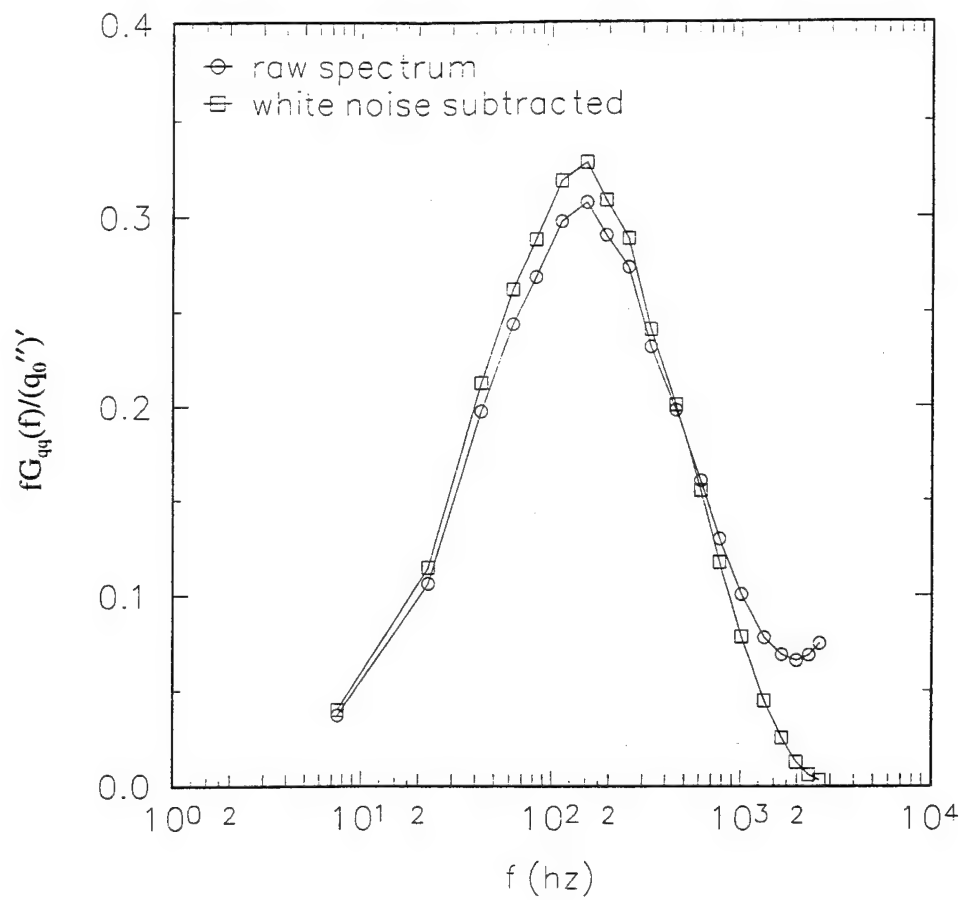


Fig. B.2. Corrections to first moment of surface heat flux fluctuation spectrum at station #0 in 3-D TBL test case..

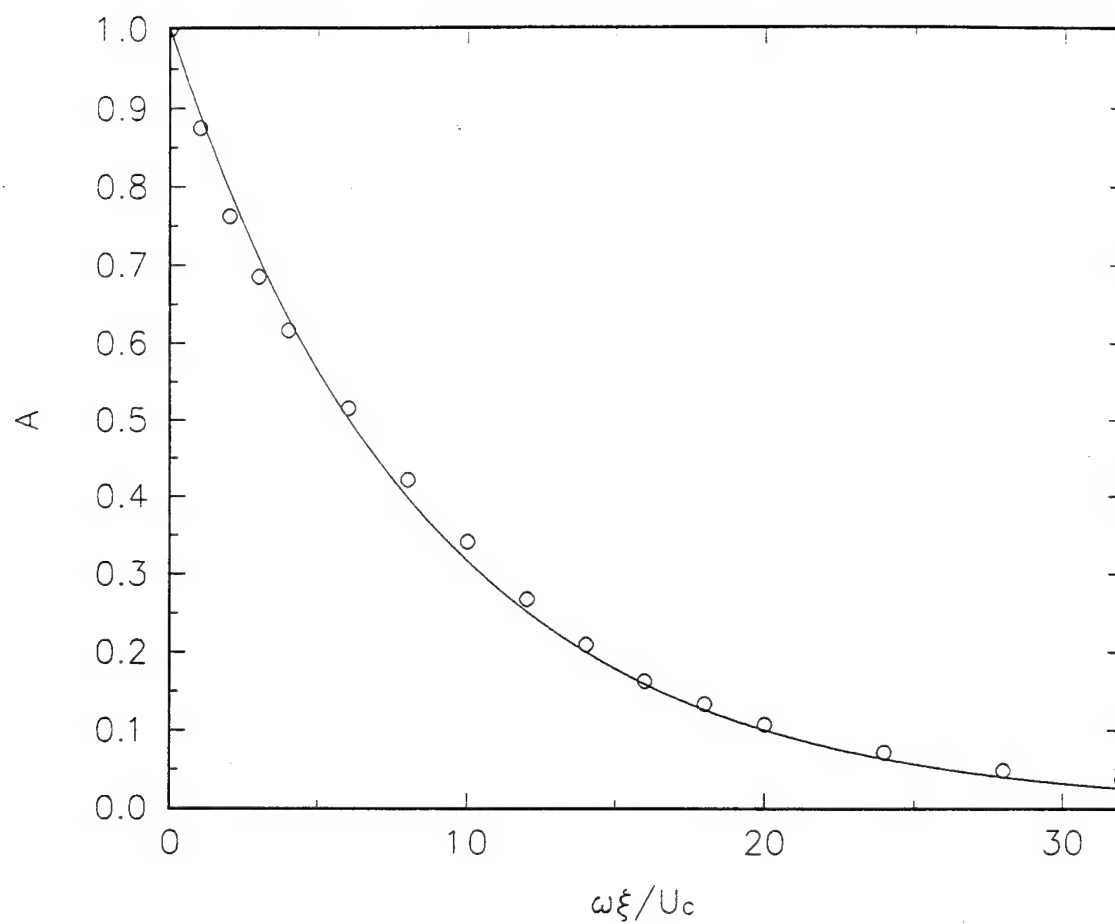


Fig. B.3. Values of parameter "A" which relates the frequency-spectral density to the longitudinal cross-spectral density through Eq. (B.4). O data from Corcos (1963); — curve fit to data, Eq. (A.6).

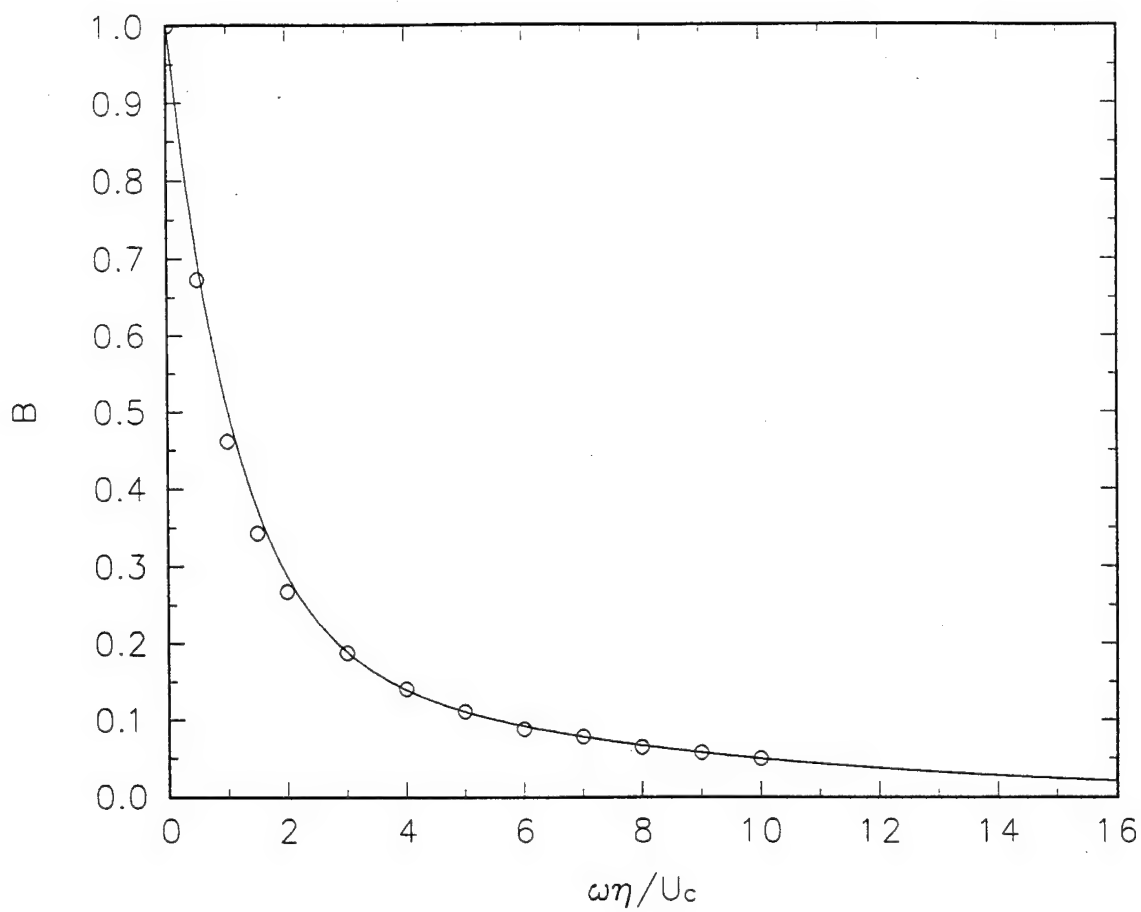


Fig. B.4. Values of parameter "B" which relates the frequency-spectral density to the lateral cross-spectral density through Eq. (B.5). O data from Corcos (1963); — curve fit to data, Eq. (A.7).

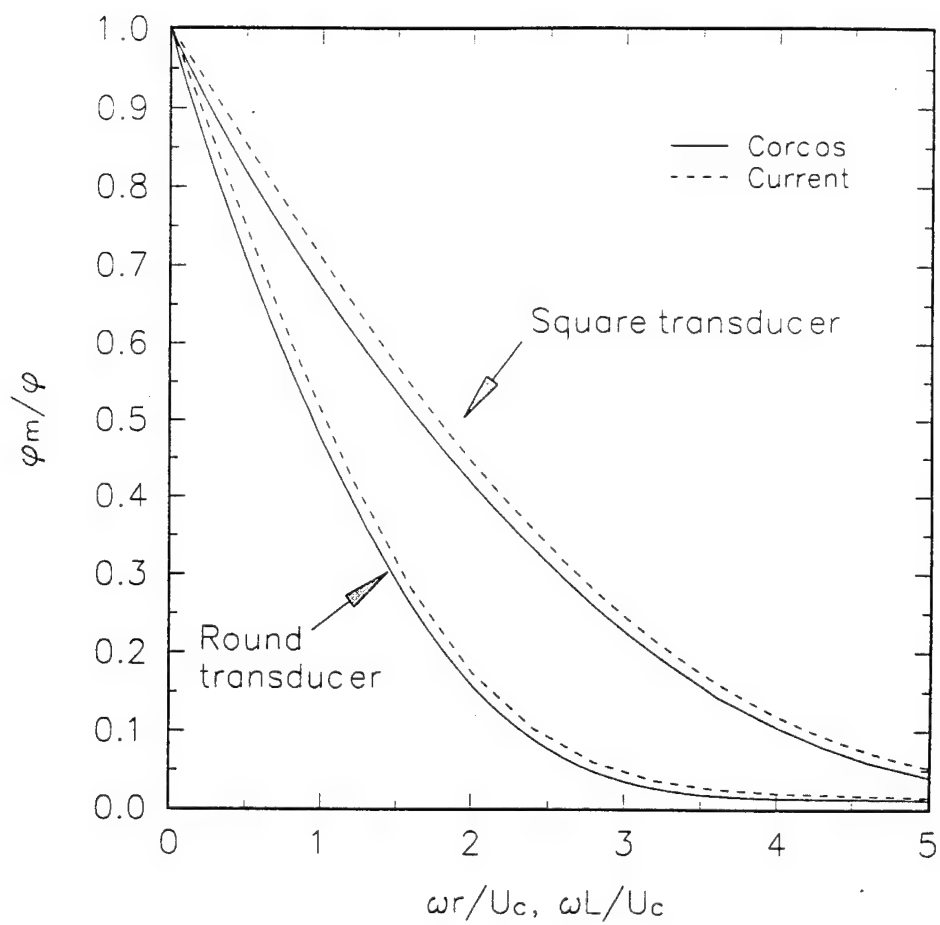


Fig. B.5. Attenuation of the frequency-spectral density due to finite surface area by a round and a square transducer. — Corcos (1963); ---- Integration of Eq. (A.1).

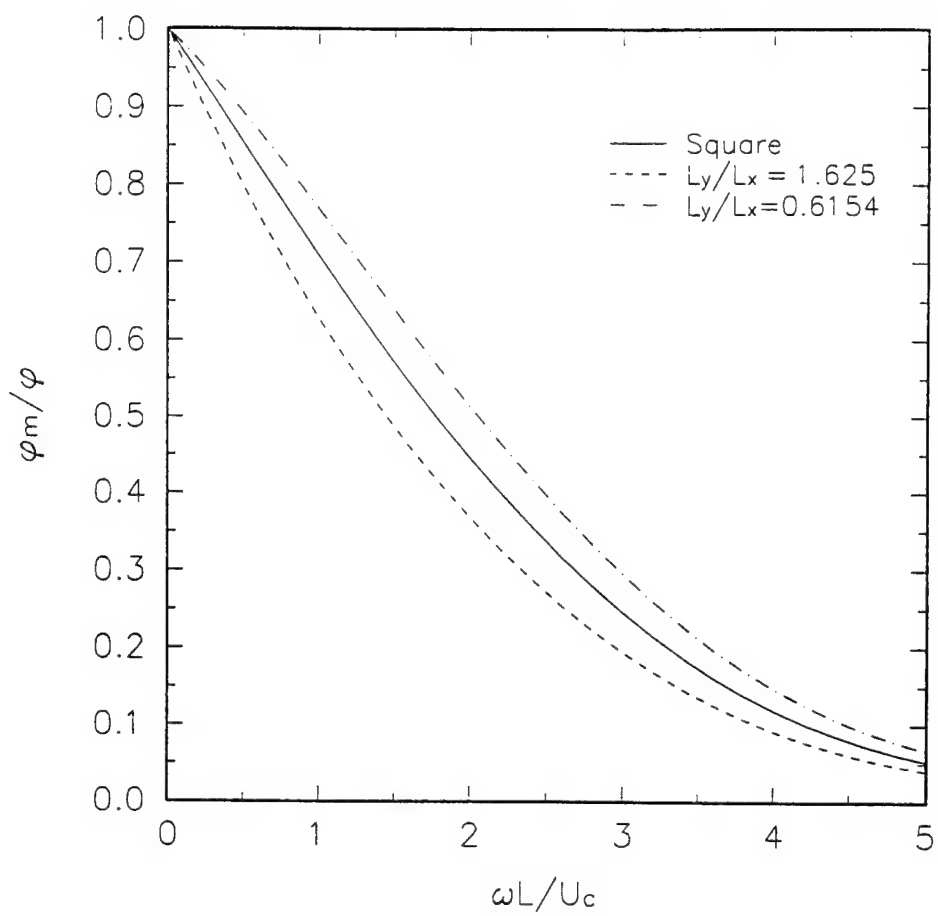


Fig. B.6. Attenuation of the frequency-spectral density due to finite surface area by a rectangular transducer of aspect ratio L_y/L_x .

Appendix C. Examination of Ha's (1993) Data:

C.1. Time-Averaged Turbulence-Structure Wavefronts

The mean inclination angle of the turbulent wavefront obtained by Ha (1993) was significantly different than the inclination angle obtained in the current study. Further, Ha's results differ from those of other researchers at station #0 which is nominally two-dimensional. Ha observed that the time-averaged wavefront at station #0 was linear and inclined at 49.3° to the wall. The inclination angle of the temperature structure obtained in the current investigation was 24.7° . The inclination angle of the turbulence in a two-dimensional flat plate boundary layer has been found to be 18° by Brown and Thomas (1977) and 20° by Head and Bandyopadhyay (1979).

Ha (1993) used a method similar to the one described in Chapter 6 except that he employed a rake of 13 hot wires with the wire nearest the wall at $y^+ = 40$. Ha computed the time-delayed correlation coefficient between adjacent wires and recorded the time delay at which the peak correlation coefficient occurred. Ha assumed that the convection velocity was a function of distance from the wall equal to the average of the local flow velocities at the two wire locations.

Several problems may exist in Ha's method. For the sampling frequency used (25 khz), the time delay where maximum correlation coefficient between two adjacent sensors

occurred was only 1 or 2 times steps. This results in an uncertainty of 50% - 100% in the time delay. Further, Ha's assumption that the convection velocity is equal to the local flow velocity may be incorrect. While small-scale structures may move at the local flow velocity, the large-scale structures which contribute most to the correlation coefficient should move at velocity proportional to the free-stream velocity.

Ha's data was reprocessed using a slightly different algorithm to compute the time-mean inclination angle of the turbulence structure. The uncertainty on the time-delay for maximum correlation was reduced by using the correlation coefficient between the wire nearest the wall and each of the wires above it rather than adjacent wires. The resulting correlation coefficients are shown for stations 0 - 6 in Fig. C.1a - C.1f respectively. These correlation coefficients are compared with correlation coefficients between surface heat flux and temperature shown in Fig. 6.2. For both the velocity and heat flux-temperature correlations, the peak correlation at station #0 is approximately 0.6. As distance from the wall increases, the peak in the correlation coefficient decreases and the time delay where the peak occurs increases. As distance from the wall is increased, the correlation coefficient between the near-wall and local velocity decreases faster than the correlation coefficient between surface heat flux and local temperature. The velocity correlation is significant ($\rho > 0.2$) out to $y/\delta = 0.3$ while the heat flux-temperature correlation is significant out to $y/\delta = 0.4$. Also as distance from the wall is increased the peak in the correlation coefficient becomes broader (due to increased length scale) so that for large time delays the correlation coefficient measured far from the wall is larger than the correlation coefficient near the wall.

At the downstream measurement stations, the correlation coefficient decreases

faster with distance from the wall. The shape of the correlation coefficient curve in the outer region becomes narrower indicating that the length scales become smaller. At station #5 and #6, the maximum velocity correlation coefficient occurs between sensors #1 and #3 rather than #1 and #2.

The convection velocity was assumed to be $0.7 U_{\infty}$ through the region of the boundary layer of interest ($0.05 < y/\delta < 0.6$). The location of the wave front relative to the sensor nearest the wall was calculated for each y location from $\Delta X = U_c \Delta T$. The resulting wave fronts are shown in Fig. C.2a - C.2g. In general the shapes are very similar to the temperature structures (Fig. 6.3) except that the temperature structures are inclined at a slightly greater angle. This agrees with the observations of Bagheri and White (1993). The mean inclination angles of the turbulent structure wavefronts and the temperature wave fronts are given in Table 6.1 along with the original inclination angles calculated by Ha (1993).

C.2. Convection Velocity

C.2.1. Spectral Variation of Convection Velocity

Ha (1993) used a parallel-sensor probe to measure the convection velocity across the boundary layer at each station in the 3-D TBL. The probe has two parallel 1.25-mm-length, 5- μ m-dia platinum-tungsten wires with a spacing of 4.81 mm between them. The probe was aligned with the wires parallel to the tunnel floor. Ha traversed the probe

across the boundary layer at stations 0 - 6. At each y location, the angular orientation of the probe was varied between $\beta_{FS} + 45^\circ$ to $\beta_{FS} - 10^\circ$ in steps of 5° and the coherency between the upstream and downstream sensors was measured. The convection velocity was determined from

$$U_c(f) = \frac{2\pi f \Delta s}{\Phi(f)} \quad (C.1)$$

where Φ is the phase difference between the upstream and downstream sensor and Δs is the separation distance between the sensors.

Ha's results show that the low-frequency contribution to the convection velocity in the near-wall region are in the range $20 < U_\infty/U_* < 25$. This result is unexplained and differs from observations made in 2D boundary layers (Ahn and Simpson, 1987). After examining Ha's data reduction codes, it was observed that Ha had computed the phase difference between unlinearized voltage signals. The convective wave speed was calculated for Ha's data with the probe aligned in the direction of maximum coherency between upstream and downstream sensors. His data reductions were repeated using the proper calibrations. Spectral variation of convective wave speed normalized on q is shown Figs. C.3a - C.3g for stations 0 - 6, respectively. Spectral variation of convective wave speed normalized on U_* is shown Figs. C.4a - C.4g for stations 0 - 6, respectively. Only wave speeds at frequencies below the frequency where $\gamma^2 < 0.27$ are shown. For these frequencies it was never necessary to add multiples of 2π to the values of Φ .

Only the results at station 4 are similar to those obtained in a two-dimensional boundary layer. At the other stations, the low-wave-number convection velocities at all

y locations are significantly larger than the local mean velocity.

C.2.2. Time-Averaged Convection Velocity

The mean frequency-averaged convection velocity was calculated as a function of distance from the wall for each measurement station from Ha's parallel sensor probe data. For each y-location the time-delayed correlation coefficient between the upstream and downstream wires was calculated using Eq. (2.6) and the time delay where the peak correlation coefficient occurred was noted. The convection velocity was calculated from $U_c = \Delta s / \Delta T$, where Δs ($= 4.81$ mm) is the spacing between the wires of the parallel sensor probe. Convection velocities were calculated for the parallel sensor probe aligned in the local free-stream direction at stations 0, 2, 4, and 6 and in the direction of maximum coherency for all stations. The direction of maximum coherency relative to the local free-stream direction is given for each measurement station in Table C.2. Figures C.5a and C.5b show profiles of the convection velocity normalized with U_∞ in the local free-stream and maximum-coherency directions respectively. Figures C.6a and C.6b show the same profiles normalized with U_∞ . The convection velocities collapse better in the maximum-coherency direction. In the near-wall region, the convection velocities range from $0.4 U_\infty$ to $0.6 U_\infty$ and increase slightly as the flow moves downstream. This may be due to misalignment of the constant maximum-coherency direction used here with the maximum-coherency direction in the near-wall region. Any misalignment would increase the measured convection velocity by decreasing the distance between the sensors. In region of the boundary layer used to compute the mean structure wavefront inclination angles

($0.05 < y/\delta < 0.5$) the convection velocity is between $0.55 U_\infty$ and $0.70 U_\infty$. When normalized on U_τ , the convection velocities in the near-wall region in the maximum-coherency direction are in the range $13 < U_\infty/U_\tau < 15$ which agrees with the results of Ahn and Simpson (1987).

One observation made concerning the convection velocities obtained here is that the uncertainty is rather large due to the sampling rate, $SF = 25$ khz. For most of the results in Figures 5 and 6, the peak correlation coefficient occurred for time delays in the range $6/SF < \Delta T < 8/SF$. The change in U_c resulting from a change in ΔT of one time step is approximately $3 U_\tau$. Since the uncertainty of the location of maximum correlation coefficient is at least ± 1 time step, the uncertainty in U_c is at least $\pm 3 U_\tau$. Thus a very high sampling rate is needed because of the small separation distance between the parallel sensor probes.

Table C.1. Angle of maximum coherency between upstream and downstream sensors of parallel sensor probe.

Station #	$\beta_m - \beta_{fs}$ (degrees)
0	5
1	5
2	5
3	10
4	10
5	10
6	10

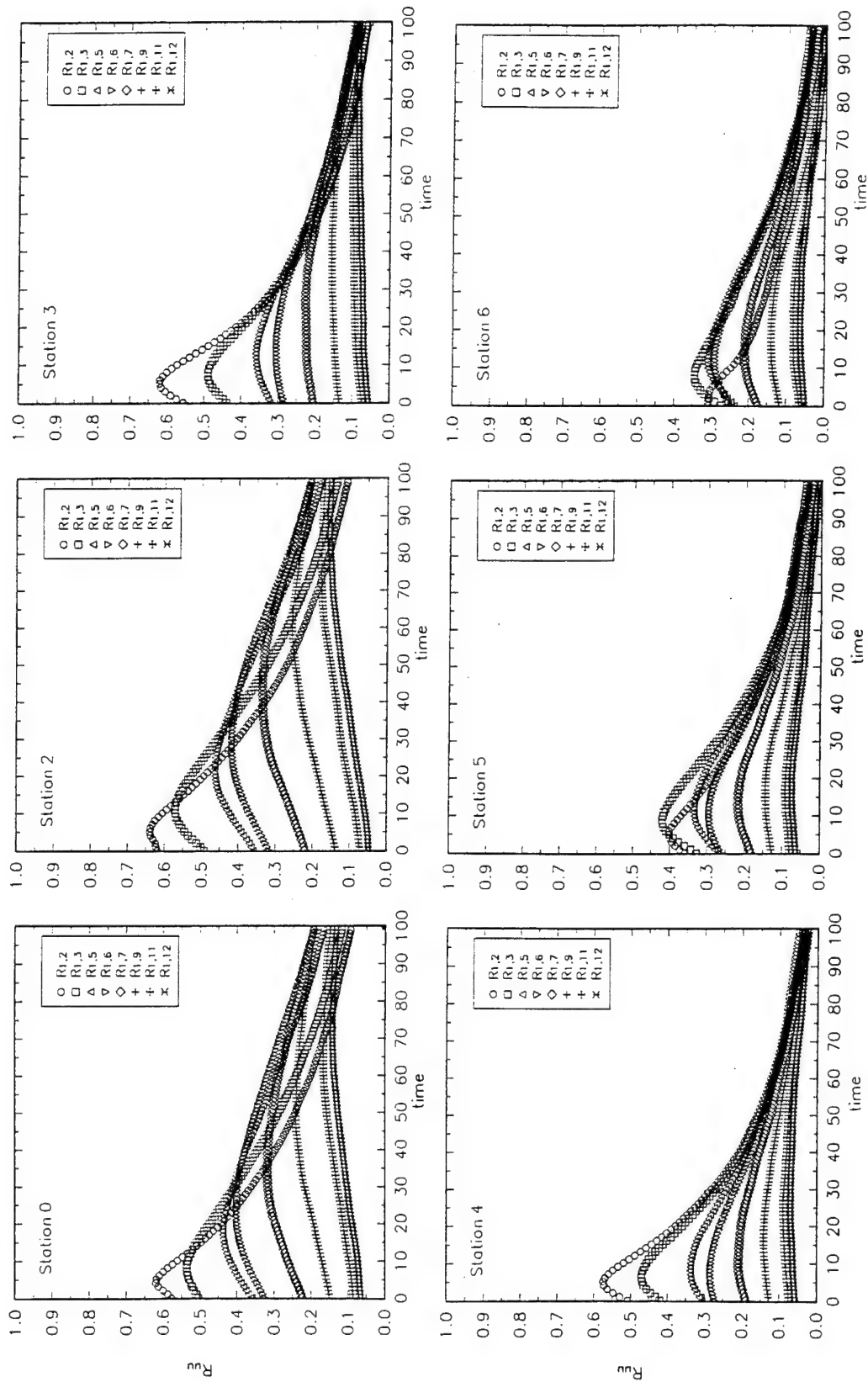


Fig. C.1. Time-delayed correlation coefficients between u fluctuations measured by the sensor closest to the wall and u fluctuations measured by each sensor of hot-wire rake.

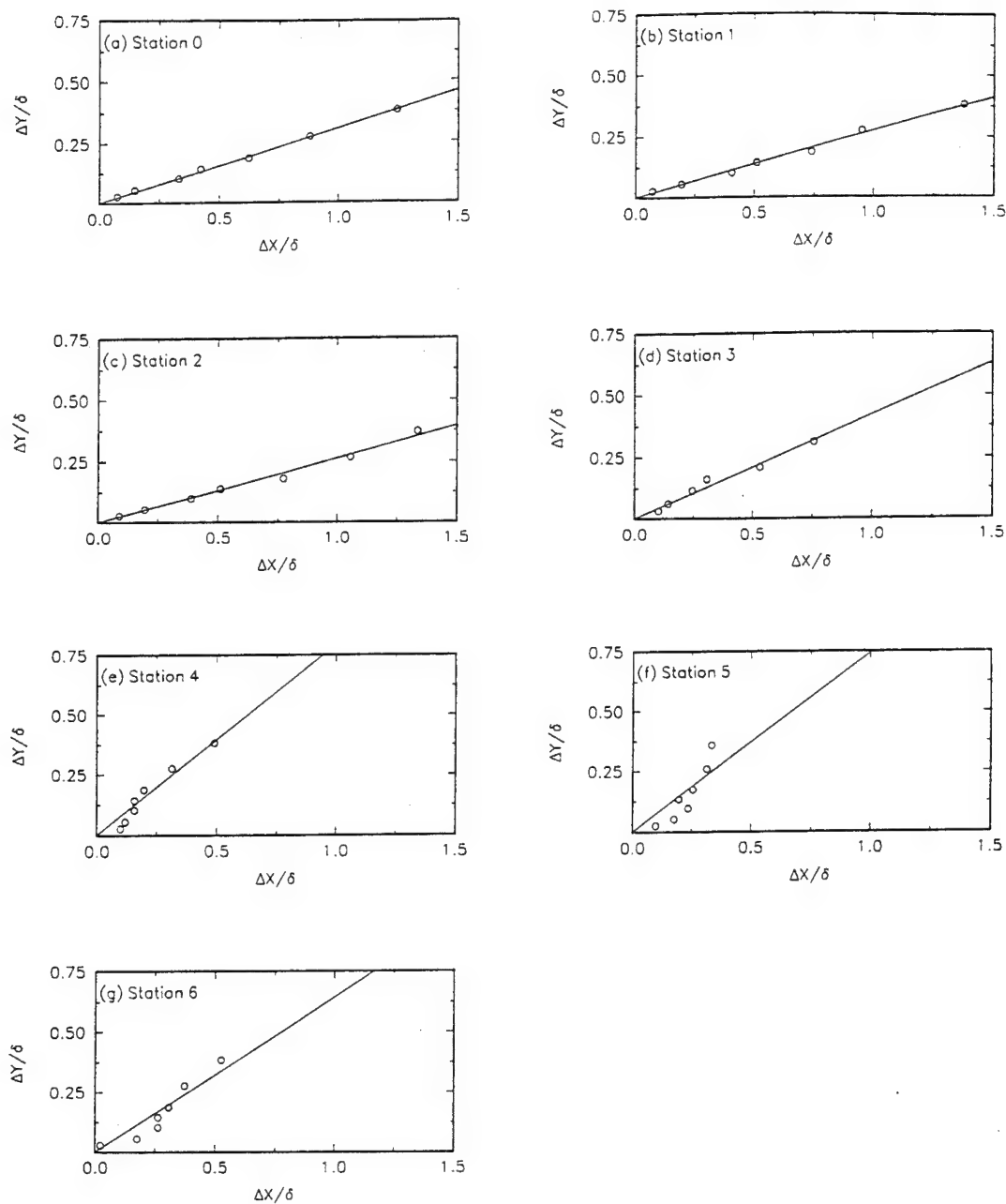


Fig. C.2. Time-averaged wavefronts in x_{FS} - y plane constructed from time-delayed correlations of u -fluctuations of hot-wire rake.

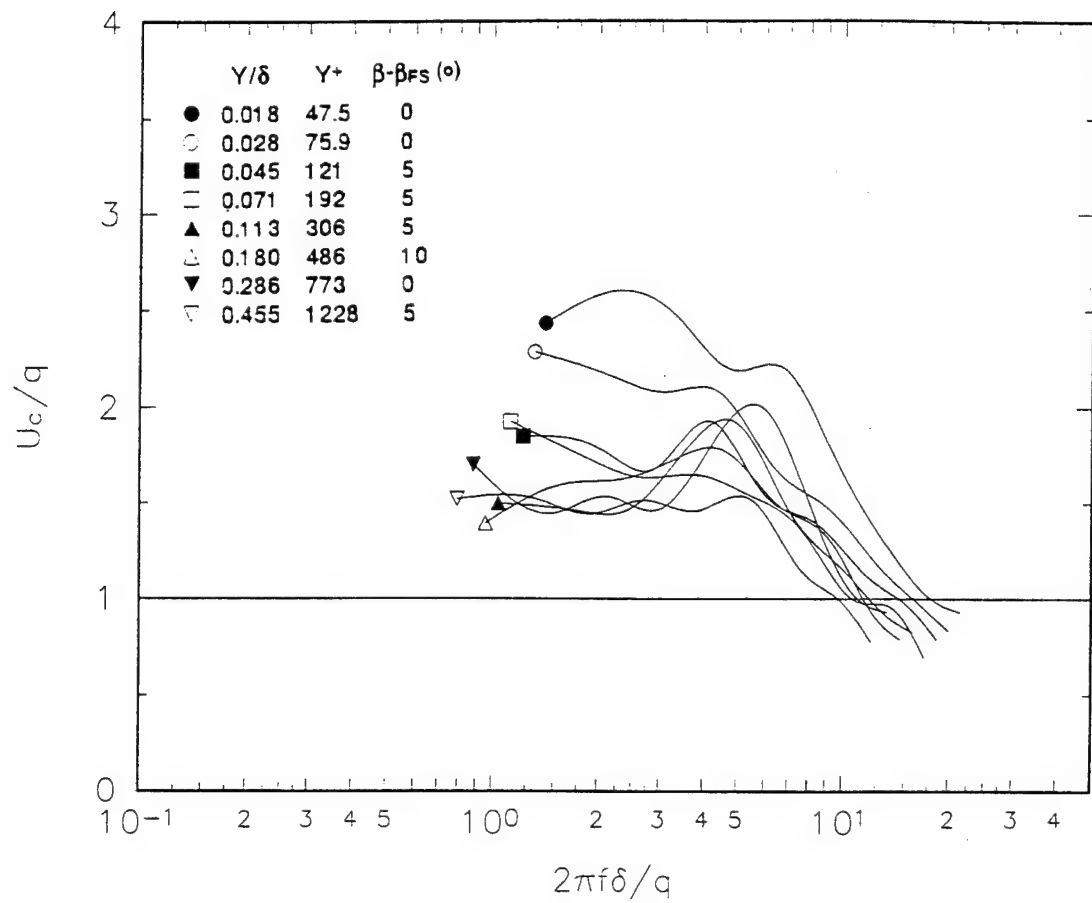


Fig. C.3a. Spectral variation of convective wave speed at station 0 normalized with outer scaling. $\beta = \beta_m$.

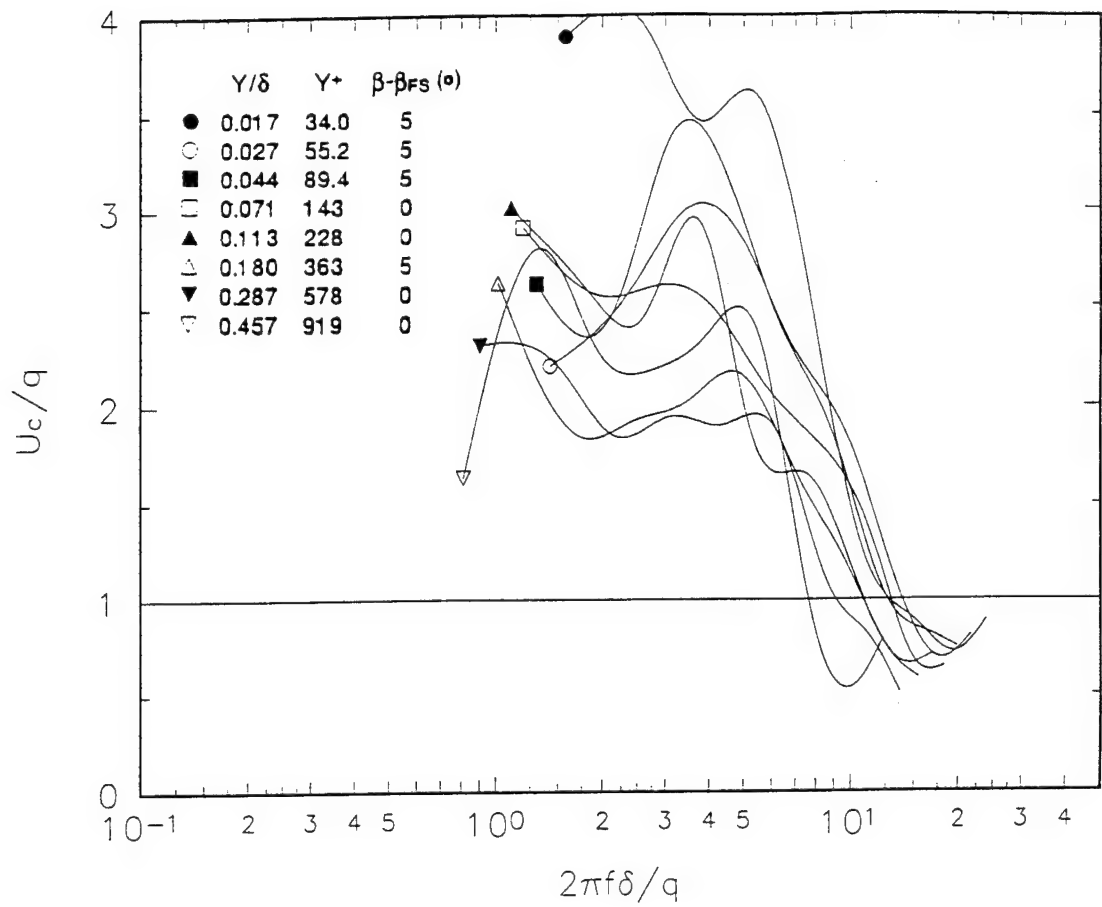


Fig. C.3b. Spectral variation of convective wave speed at station 1 normalized with outer scaling. $\beta = \beta_m$.

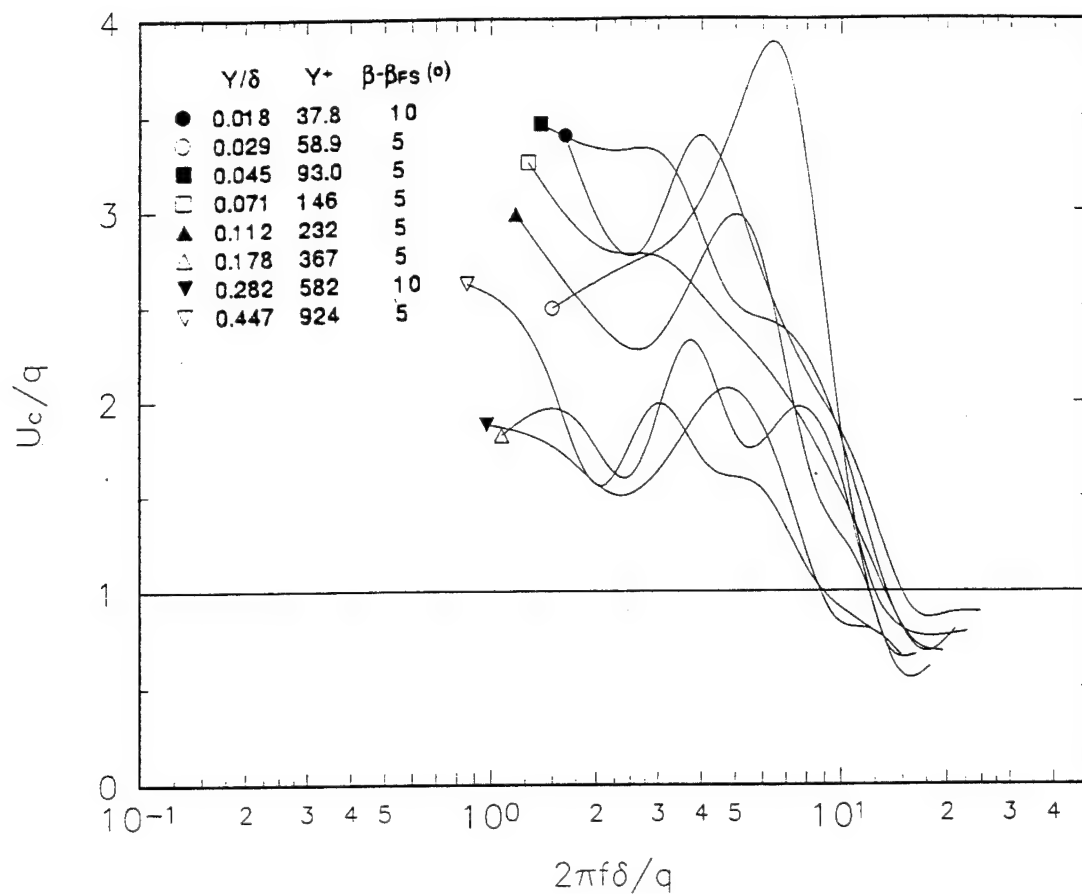


Fig. C.3c. Spectral variation of convective wave speed at station 2 normalized with outer scaling. $\beta = \beta_m$.

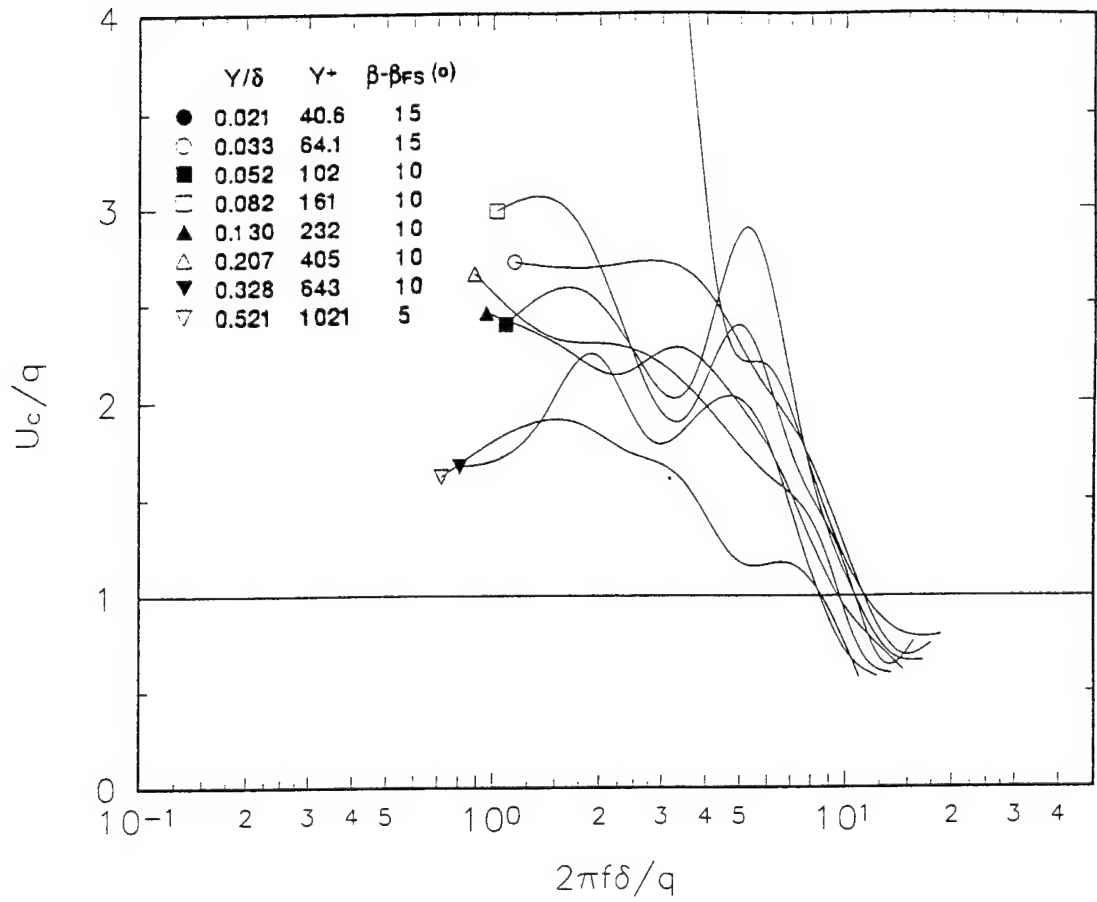


Fig. C.3d. Spectral variation of convective wave speed at station 3 normalized with outer scaling. $\beta = \beta_m$.

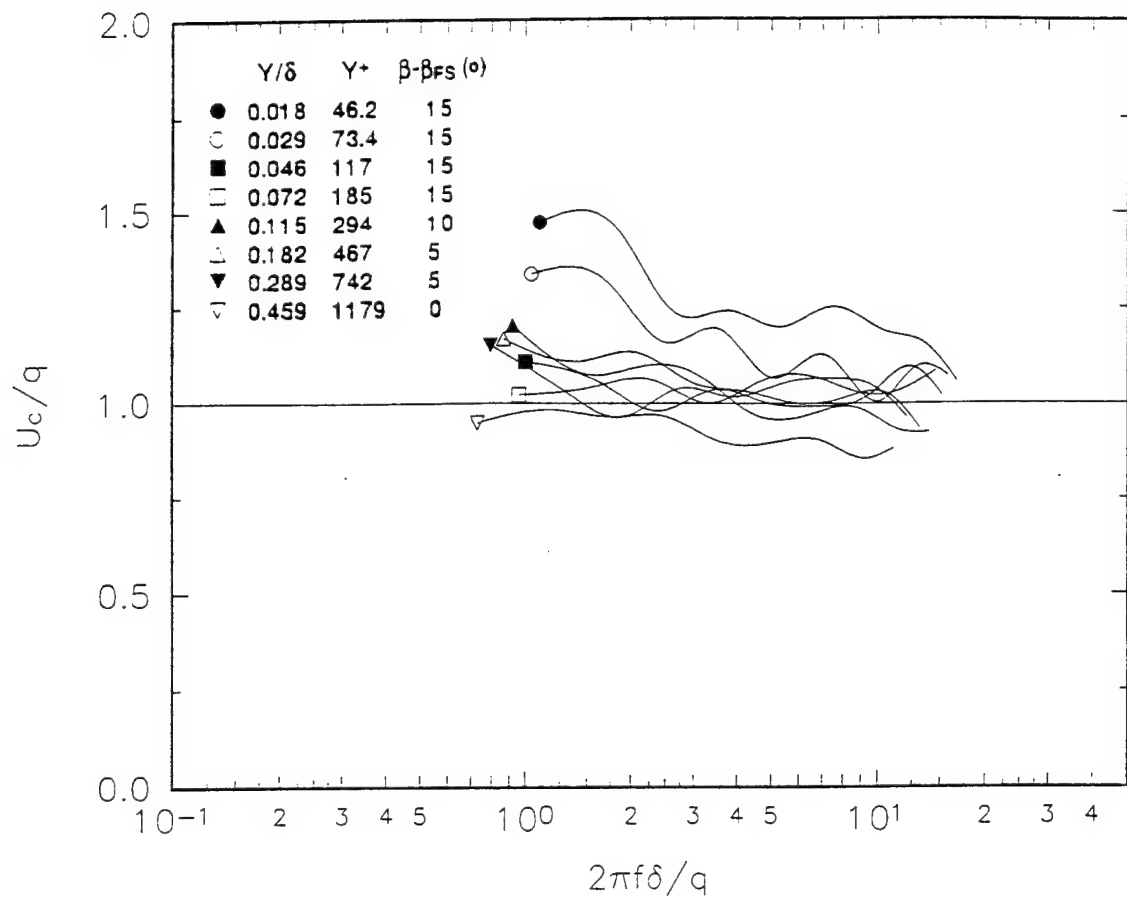


Fig. C.3e. Spectral variation of convective wave speed at station 4 normalized with outer scaling. $\beta = \beta_m$.

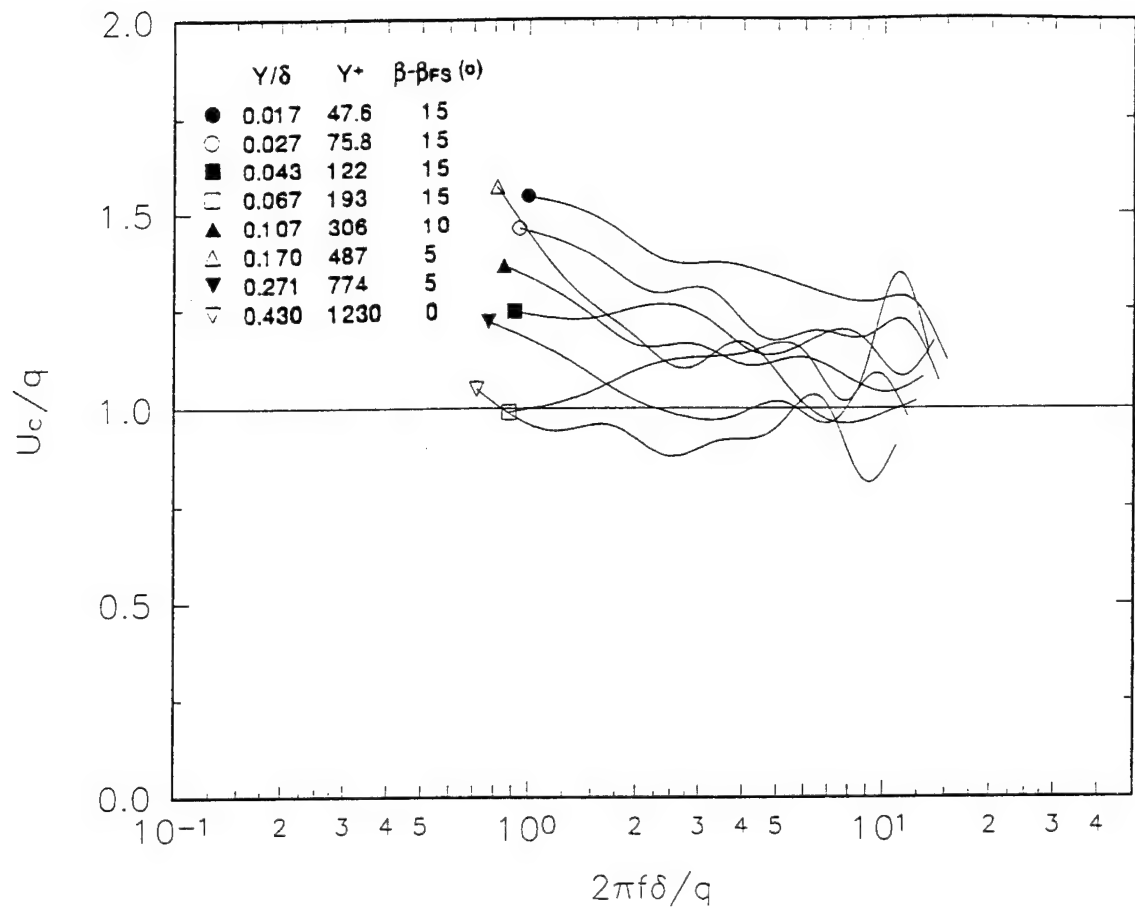


Fig. C.3f. Spectral variation of convective wave speed at station 5 normalized with outer scaling. $\beta = \beta_m$.

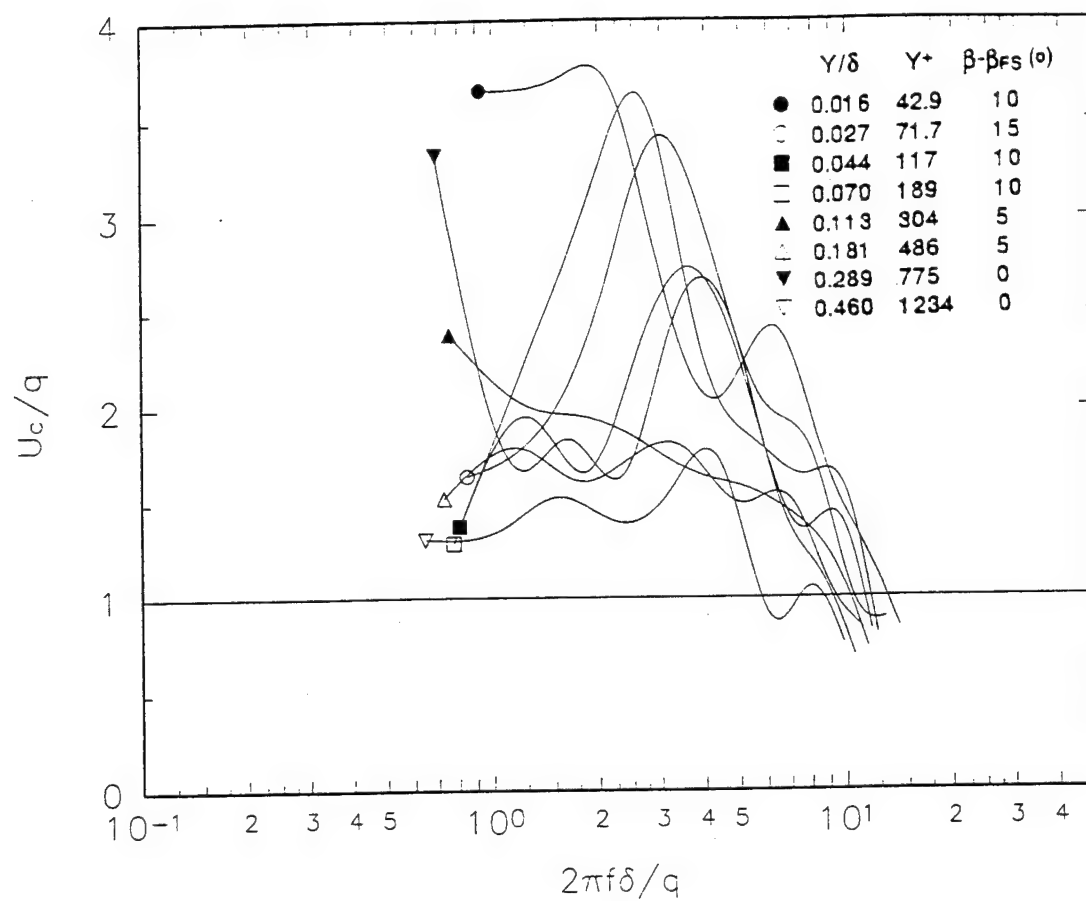


Fig. C.3g. Spectral variation of convective wave speed at station 6 normalized with outer scaling. $\beta = \beta_m$.

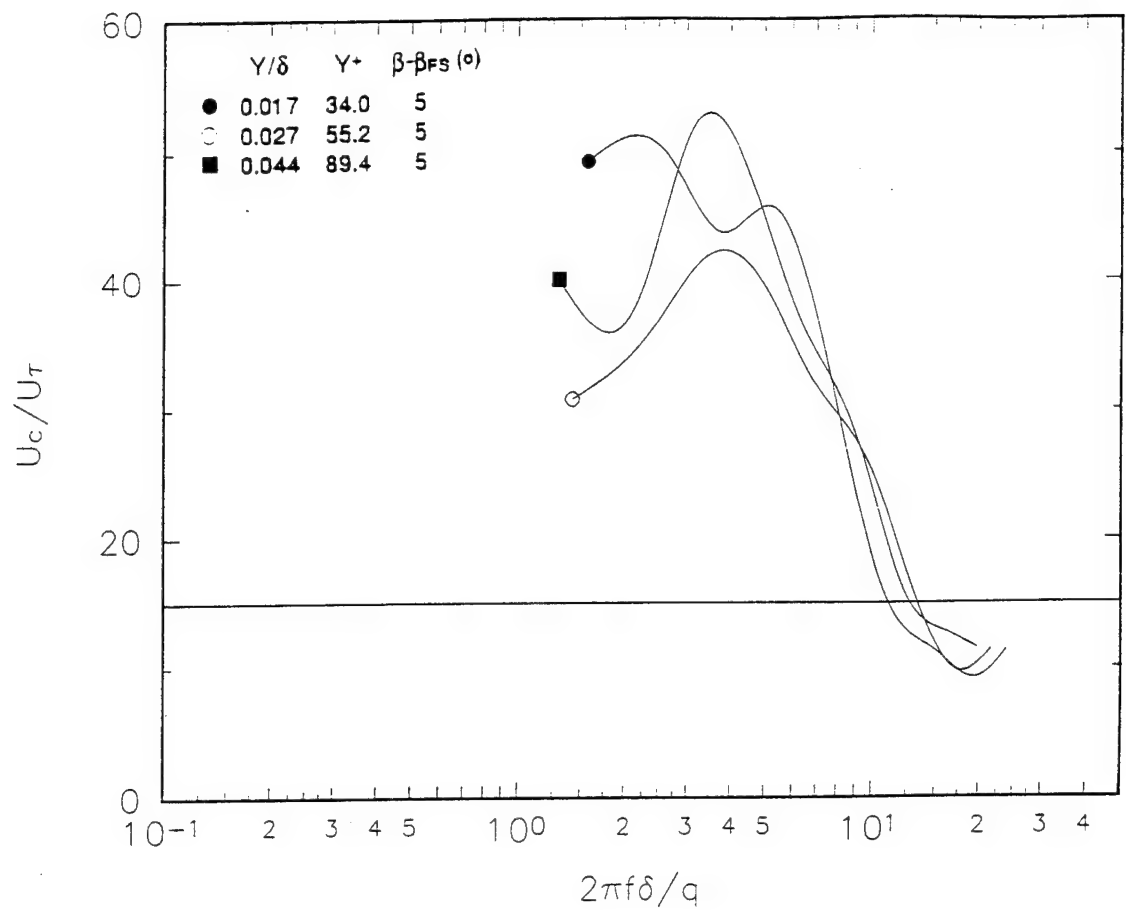


Fig. C.4b. Spectral variation of convective wave speed at station 1 normalized with inner scaling. $\beta = \beta_m$.

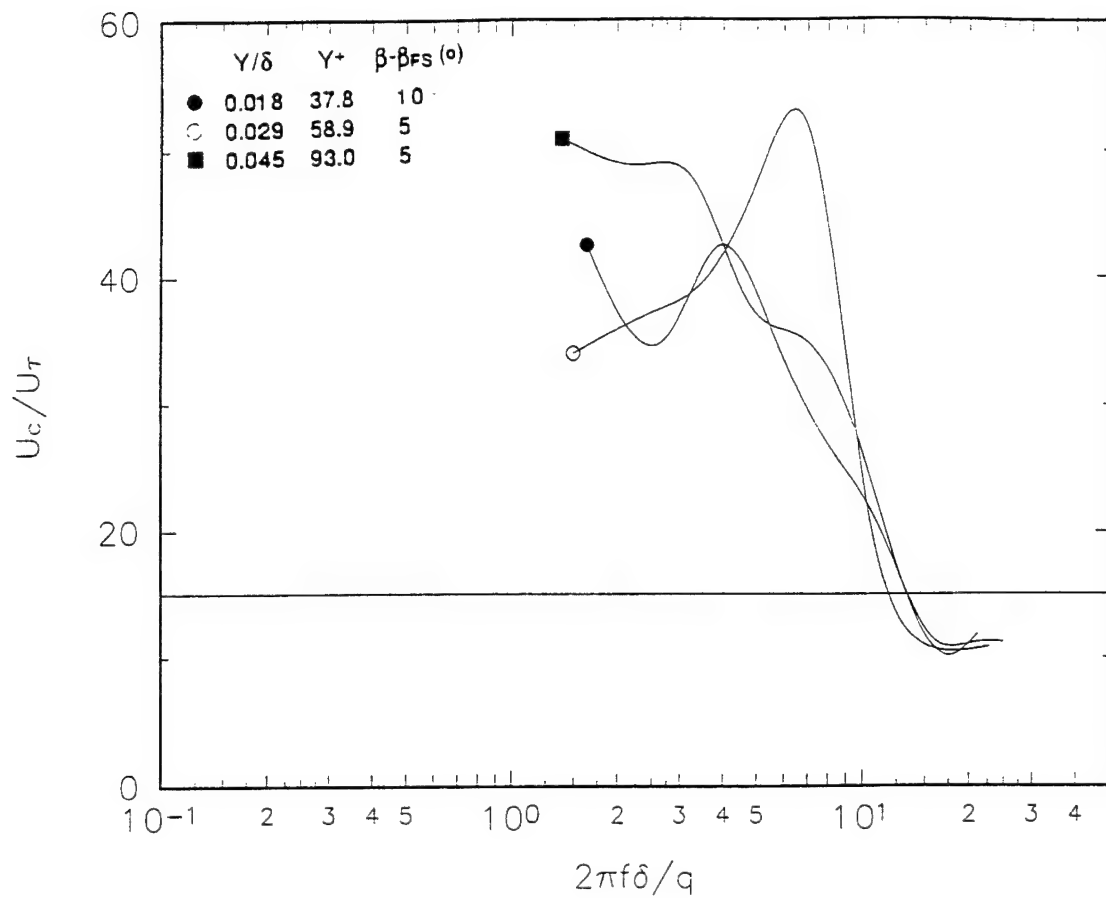


Fig. C.4c. Spectral variation of convective wave speed at station 2 normalized with inner scaling. $\beta = \beta_m$.

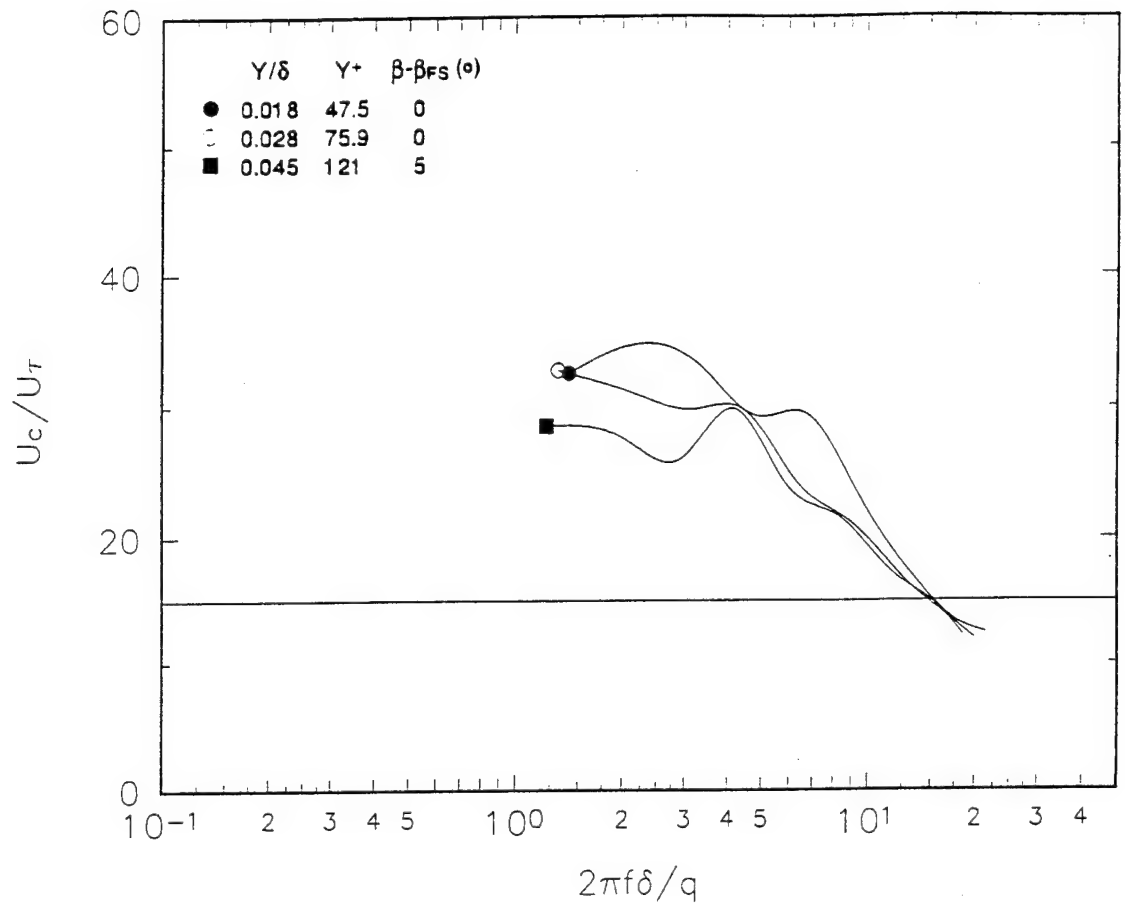


Fig. C.4a. Spectral variation of convective wave speed at station 0 normalized with inner scaling. $\beta = \beta_m$.

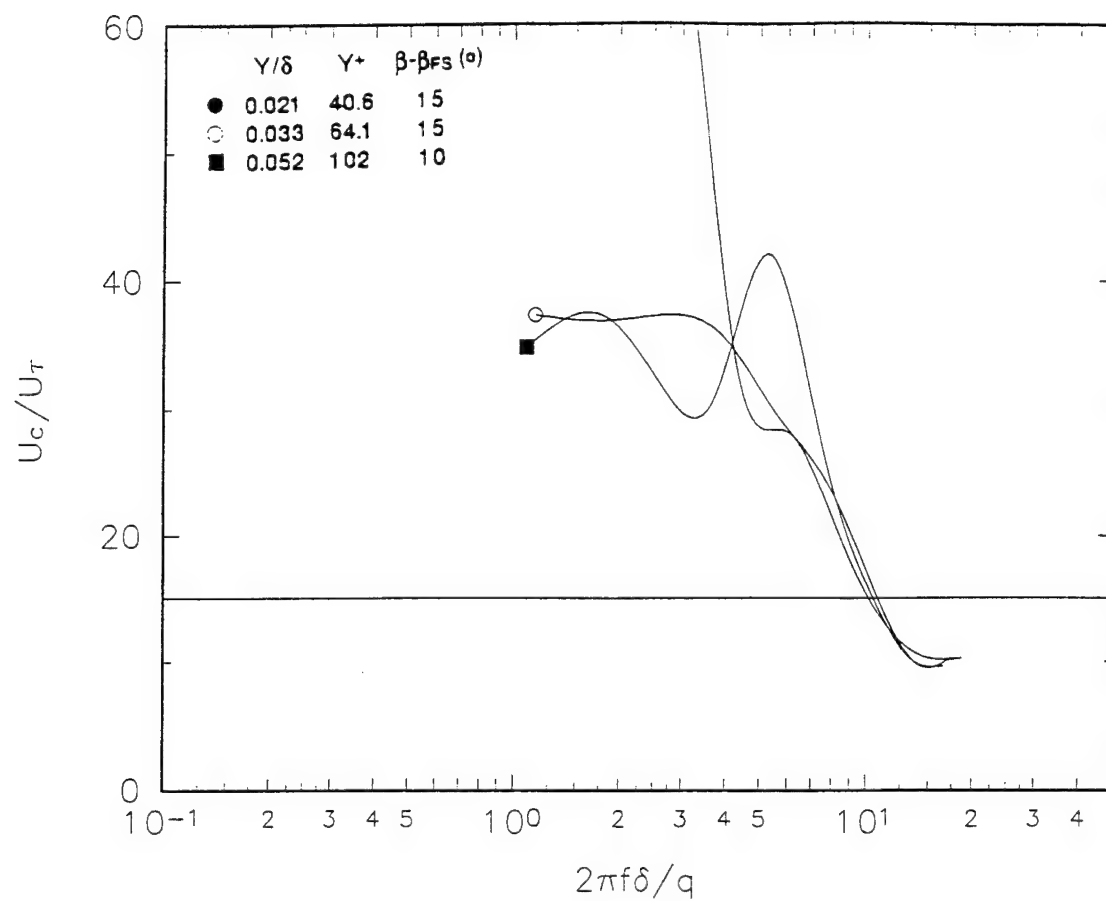


Fig. C.4d. Spectral variation of convective wave speed at station 3 normalized with inner scaling. $\beta = \beta_m$.

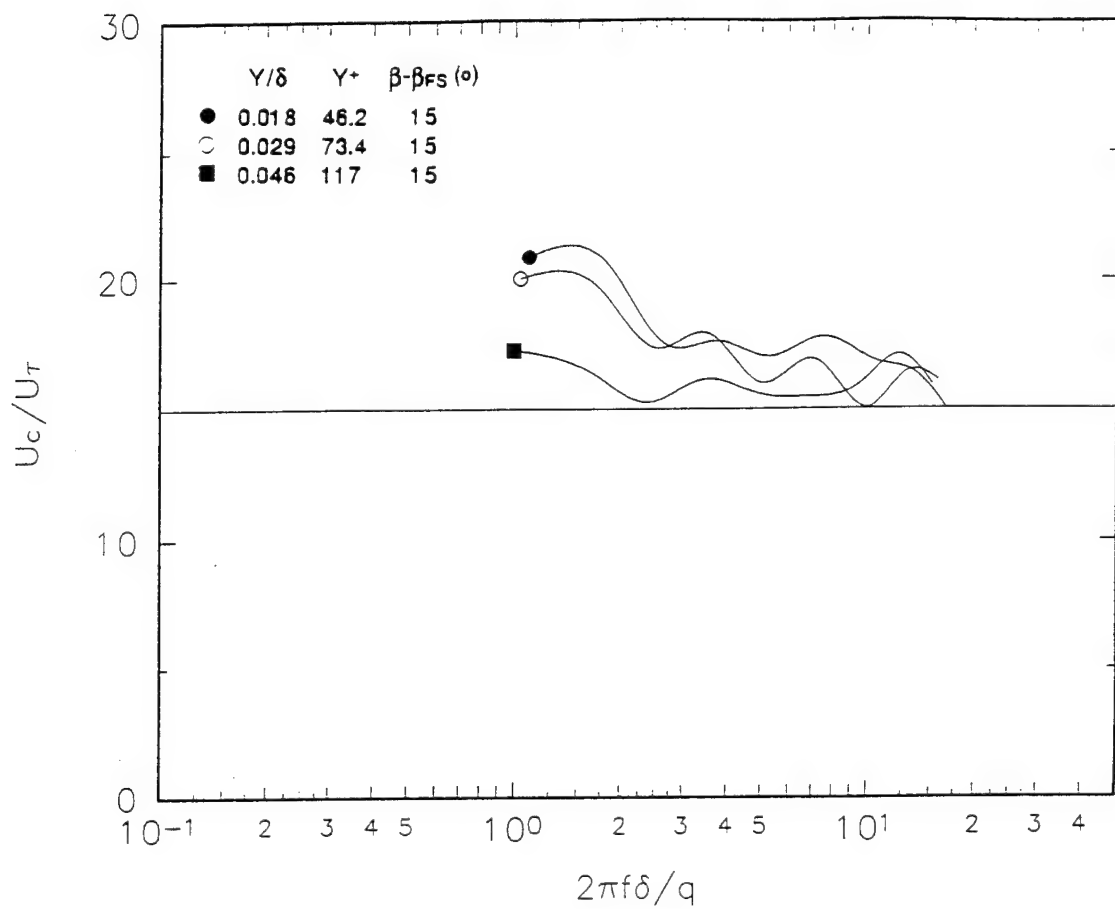


Fig. C.4e. Spectral variation of convective wave speed at station 4 normalized with inner scaling. $\beta = \beta_m$.

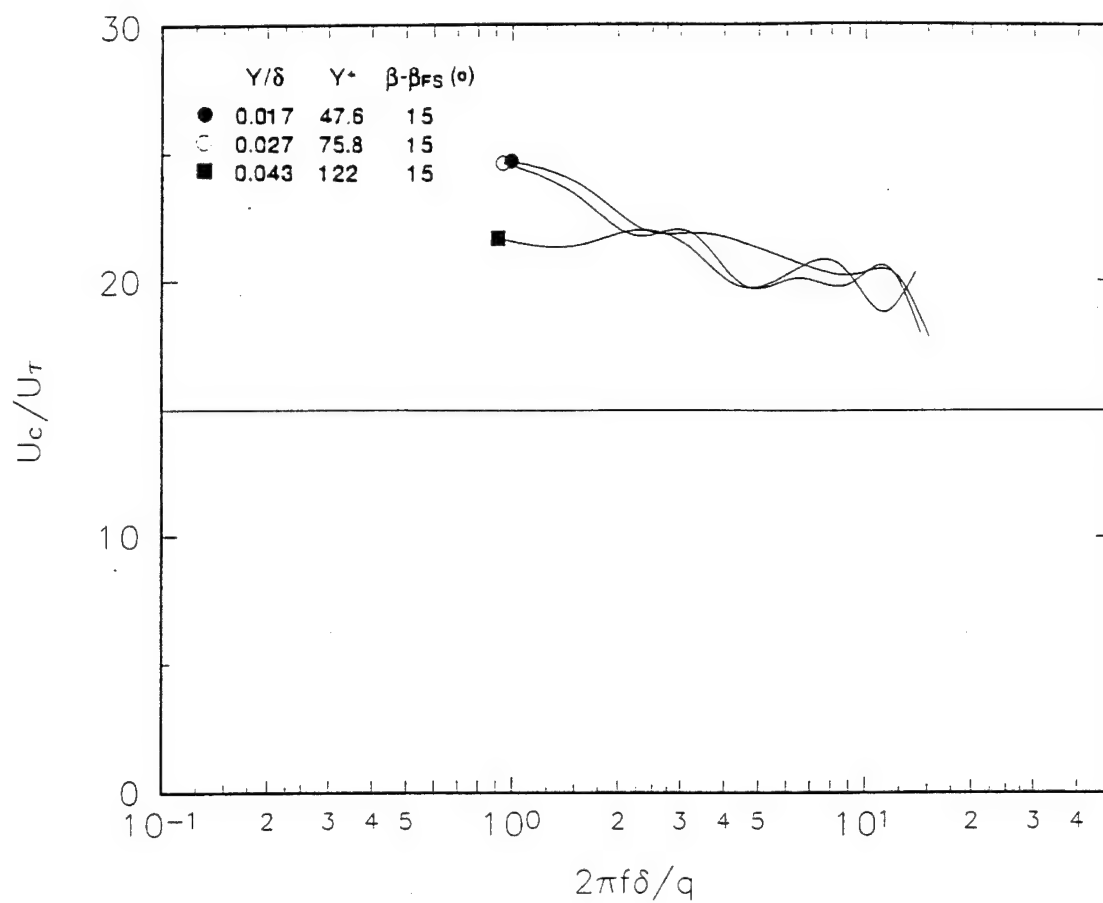


Fig. C.4f. Spectral variation of convective wave speed at station 5 normalized with inner scaling. $\beta = \beta_m$.

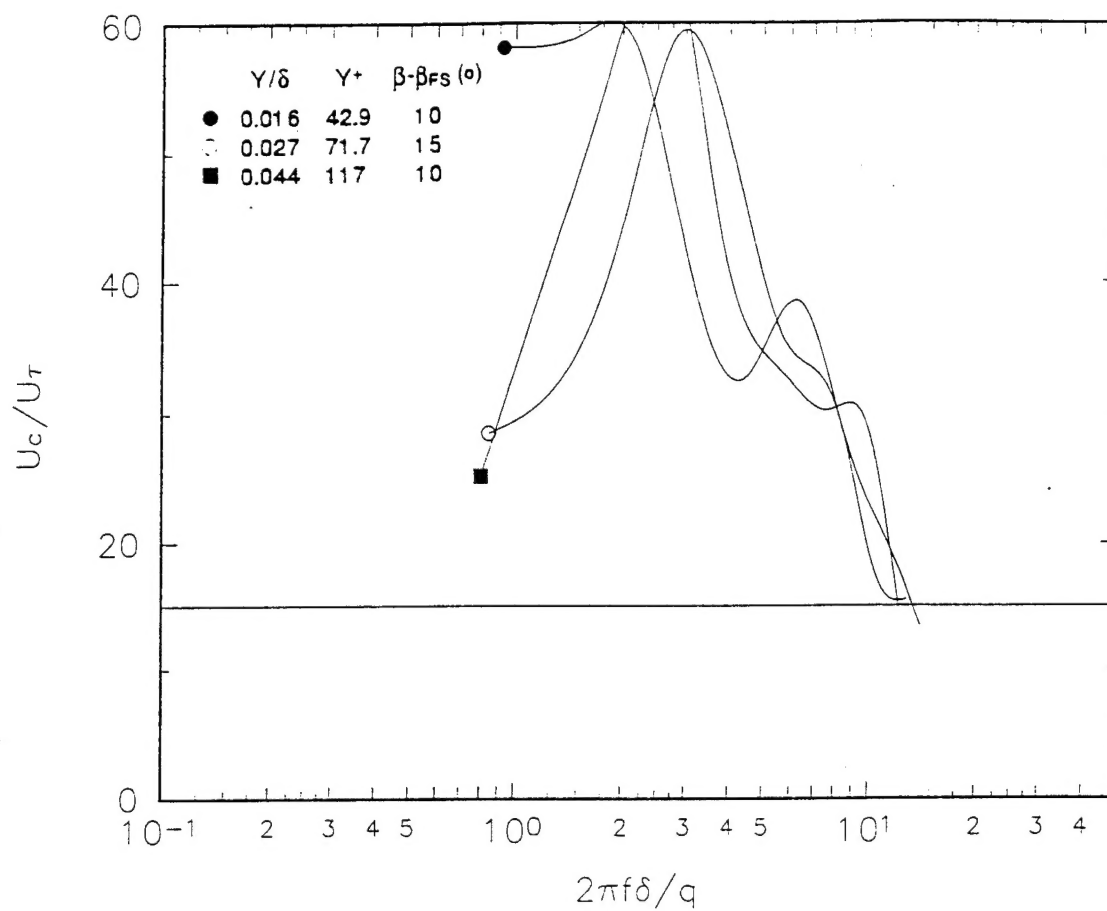


Fig. C.4g. Spectral variation of convective wave speed at station 6 normalized with inner scaling. $\beta = \beta_m$.

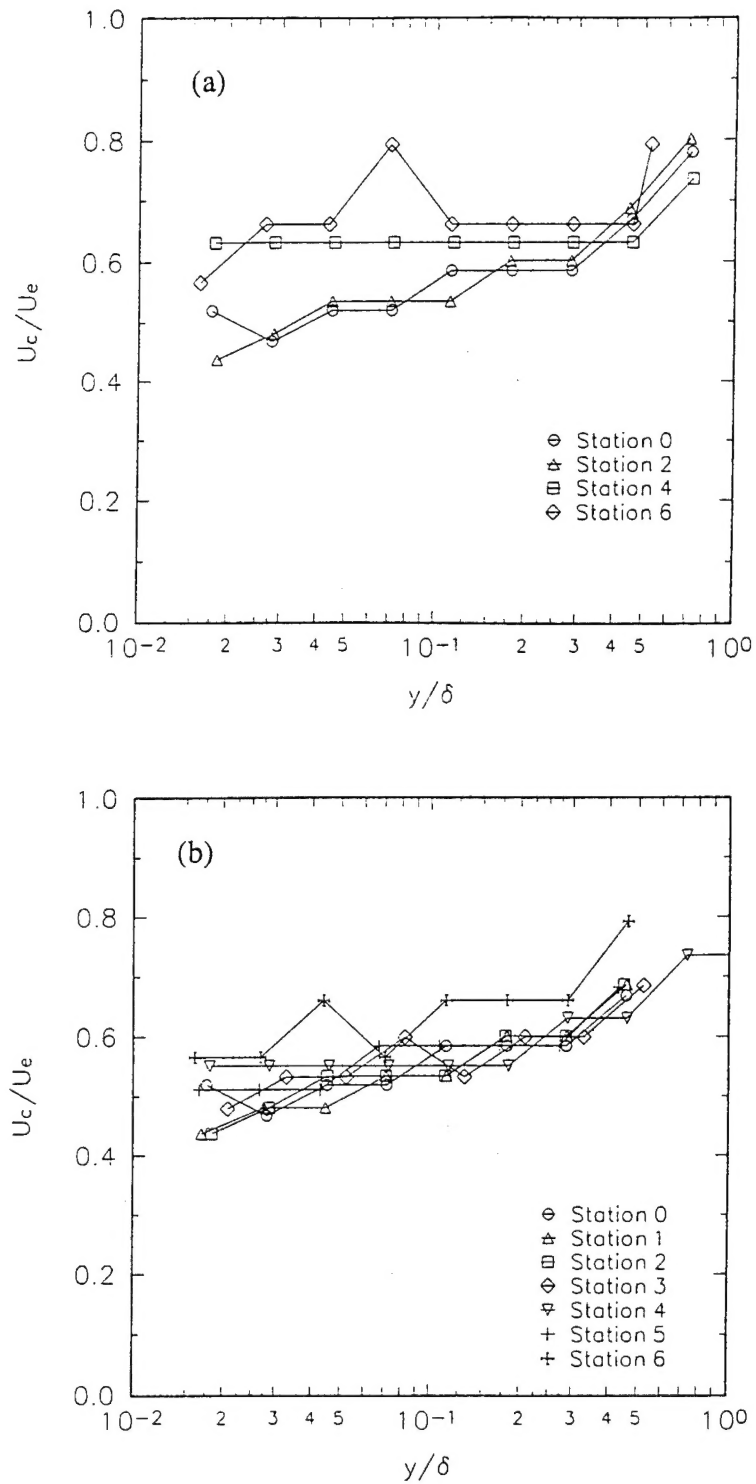


Fig. C.5. Profiles of convection velocity normalized with free-stream velocity measured by the parallel sensor probe aligned in (a) free-stream direction and (b) maximum-coherency direction.

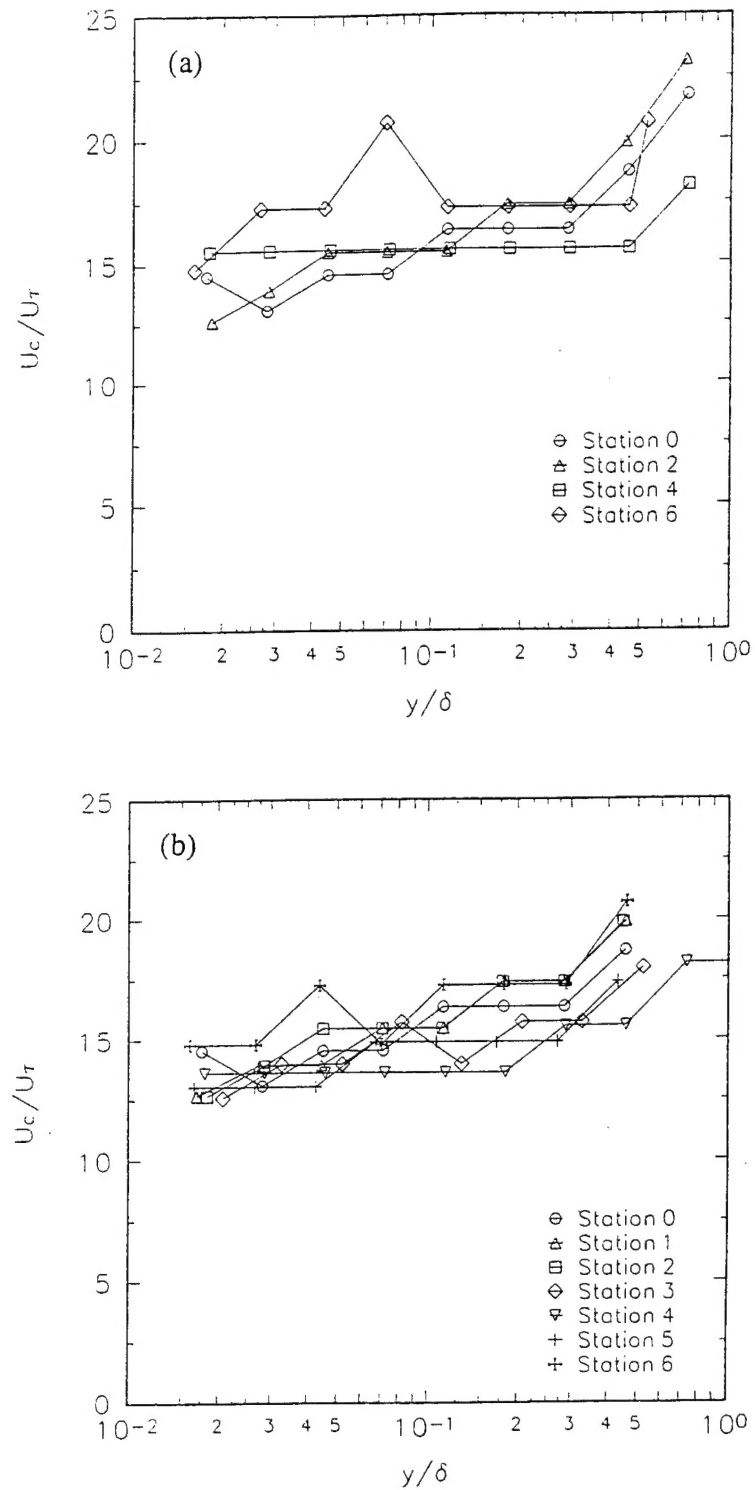


Fig. C.6 Profiles of convection velocity normalized with friction velocity measured by the parallel sensor probe aligned in (a) free-stream direction and (b) maximum-coherency direction.

Vita

The author was born June 4, 1966 in Cumberland, Maryland. After graduating from Bishop Walsh High School in 1984, he began his undergraduate studies at Virginia Tech. He received his Bachelor of Science degree in Aerospace and Ocean Engineering with honors in May 1988. Upon graduation, he immediately began studies toward his Master of Science in Aerospace Engineering from Virginia Tech which he completed in August 1990. After working as an engineer for Alleghany Ballistics Laboratory, he returned to Virginia Tech to pursue a Ph.D. in Aerospace Engineering in January 1991. Upon completion of this work, he will continue his career at the Naval Surface Warfare Center in Dahlgren, Virginia.

A handwritten signature in cursive script, reading "Joseph Lewis". The signature is written in dark ink and is positioned to the right of the main text block.